Energetic Radiation from Wakefield Acceleration and its Applications



Elias Gerstmayr

June 8, 2020

Submitted in partial fulfilment of the requirements for the degree of Doctor of Philosophy in Physics of Imperial College London and for the Diploma of Imperial College London.

Department of Physics
Imperial College London
Prince Consort Road
London SW7 2AZ

Abstract

The driving theme of this thesis is the experimental production and characterisation of high-energy gamma radiation using a laser wakefield accelerator (LWFA), and its application in the context of studies of fundamental QED phenomena.

An electron beam from shock injection of an energy up to 1.3 GeV was collided with a laser pulse at an intensity of $a_0 \sim 0.2-1$ producing 10's of MeV photons from linear inverse Compton scattering (ICS). The emitted radiation was used to diagnose the properties of the electron beam and of the laser pulse at the interaction. It was demonstrated that this can also be used to systematically facilitate the spatio-temporal overlap of the electron beam and the laser pulse in future radiation reaction studies.

A relativistic electron beam of energy $\epsilon > 500\,\mathrm{MeV}$ was collided with a tightly focused laser pulse with $a_0 \sim 10$. The interaction generated broadband synchrotron-like radiation from non-linear inverse Compton scattering (ICS) with critical energies $\epsilon_{crit} > 30\,\mathrm{MeV}$, which are the highest ICS photon energies reported from an all-optical setup at this time. The high photon energies in turn enabled a significant measurement of energy loss in the electron beam, rendering this the first published measurement of radiation reaction in an LWFA setup.

An electron beam from LWFA was used to commission a bremsstrahlung gamma-ray source reaching photon energies of several hundreds of MeV. Different materials and accelerator configurations were used to optimise the yield of photons and to mitigate the production of secondary particles. The energetic gamma rays were then collided with the X-ray field emitted by a hot plasma in order to attempt the production of electron-positron pairs from the Breit-Wheeler process.

Declaration of Originality

This thesis and the work presented in it are my original work. Material that was contributed by others or was taken from other sources is being referenced and acknowledged accordingly.

Elias Gerstmayr
June 8, 2020

Copyright Declaration

The copyright of this thesis rests with the author. Unless otherwise indicated, its contents are licensed under a Creative Commons Attribution-Non Commercial 4.0 International Licence (CC BY-NC).

Under this licence, you may copy and redistribute the material in any medium or format. You may also create and distribute modified versions of the work. This is on the condition that: you credit the author and do not use it, or any derivative works, for a commercial purpose.

When reusing or sharing this work, ensure you make the licence terms clear to others by naming the licence and linking to the licence text. Where a work has been adapted, you should indicate that the work has been changed and describe those changes.

Please seek permission from the copyright holder for uses of this work that are not included in this licence or permitted under UK Copyright Law.

Daß ich erkenne, was die Welt
Im Innersten zusammenhält.

So that I may perceive whatever holds
the world together in its inmost folds.

Johann Wolfgang von Goethe – Faust. Der Tragödie erster Teil.

Contents

Abstract **3**

Declaration of Originality **4**

Copyright Declaration **4**

Table of Contents **6**

List of Figures **11**

List of Tables **17**

Acknowledgements **18**

Role of the Author **19**

1 Introduction **20**
1.1 Particle accelerators 21
1.2 High-intensity lasers 23
1.3 Particle accelerators and high-intensity lasers 26
1.4 Thesis Outline 31

2 Single particle motions and radiation mechanisms **32**
2.1 Single particle motion in an electromagnetic field 33
2.1.1 Electron motion in a homogeneous electric field 33
2.1.2 Electron motion in a homogeneous magnetic field 34
2.1.3 Electron motion in a monochromatic plane EM wave 35
2.1.4 Ponderomotive Force 39
2.2 Radiation Production 40
2.2.1 Compton Scattering 41
2.2.2 Linear Inverse Compton Scattering 45
2.2.3 Nonlinear Inverse Compton Scattering 48
2.2.4 Bremsstrahlung 51

2.3 Radiation Reaction . . . 53
2.3.1 Regimes of Radiation Reaction . . . 53
2.3.2 Classical Radiation Reaction . . . 56
2.3.3 Quantum Radiation Reaction . . . 59
2.3.4 Signatures of radiation reaction in the electron spectrum . . . 60
2.4 Pair Production and Annihilation . . . 63
2.4.1 Dirac annihilation . . . 63
2.4.2 Breit-Wheeler pair production . . . 64
2.4.3 Bethe-Heitler pair production . . . 69
2.4.4 Schwinger pair production . . . 70

3 Laser Propagation and Wakefield Acceleration 72
3.1 Laser Propagation in an Underdense Medium . . . 72
3.1.1 Plasma Properties . . . 72
3.1.2 Plasma Formation . . . 73
3.1.3 Plasma Frequency . . . 74
3.1.4 Laser Propagation in Vacuum . . . 76
3.1.5 Laser Propagation in Plasma . . . 78
3.1.6 Nonlinear Refractive Index . . . 79
3.1.7 Relativistic Self-focusing and Self-guiding . . . 80
3.1.8 Pulse compression . . . 81
3.1.9 Photon acceleration . . . 82
3.2 Laser Wakefield Acceleration . . . 83
3.2.1 Wavebreaking . . . 83
3.2.2 Bubble regime . . . 84
3.2.3 Trapping and self-injection threshold . . . 84
3.2.4 Depletion . . . 85
3.2.5 Dephasing . . . 85
3.2.6 Maximum Energy Gain . . . 86
3.2.7 Injection Mechanisms and Accelerator Tailoring . . . 87

4 Experimental Methods 89
4.1 The Gemini laser system . . . 89
4.1.1 Laser properties . . . 89
4.1.2 Beam line geometries . . . 90
4.2 Laser Diagnostics . . . 91
4.2.1 Laser Energy . . . 91
4.2.2 Laser Pulse Duration . . . 91
4.2.3 Focal Spot Characterisation . . . 91

4.3 Dual-Beam Timing Diagnostics . . . 95
4.3.1 Photodiodes . . . 95
4.3.2 Interferometry . . . 97
4.3.3 Additional considerations for the synchronisation of beams . . . 100
4.4 Gas Targets . . . 105
4.4.1 Gas Jets . . . 107
4.4.2 Gas Cells . . . 108
4.4.3 Gas jets and cells in comparison . . . 109
4.4.4 Characterising Gas Targets . . . 109
4.5 Magnetic Energy Spectrometer . . . 114
4.6 Gamma-ray Diagnostics . . . 117
4.6.1 Profile Screen . . . 118
4.6.2 Spectrometer Array . . . 121

5 Linear ICS at Astra Gemini 137
5.1 Motivation . . . 137
5.2 Chapter Outline . . . 138
5.3 Experimental Setup . . . 139
5.4 Characterisation of Electron Spectra . . . 142
5.5 Laser raster scan . . . 145
5.6 Gamma spectra from inverse Compton scattering . . . 150
5.7 Number of scattered photons . . . 154
5.8 Energy-dependent detector response . . . 155
5.9 Estimate of laser beam size from photon yield . . . 160
5.10 Spectral Retrieval . . . 163
5.11 Compton scattering as electron beam diagnostic . . . 166
5.11.1 Resolving spatial features . . . 167
5.11.2 Beam Pointing . . . 172
5.11.3 Divergence and Ellipticity . . . 173
5.12 Conclusion . . . 176

6 Radiation Reaction at Astra Gemini 178
6.1 Experimental Motivation . . . 178
6.2 Chapter Outline . . . 184
6.3 Experimental Setup . . . 185
6.4 Identifying Successful Collisions . . . 187
6.5 Characterisation of the Electron Spectrum . . . 191
6.6 Estimating the laser intensity at the interaction . . . 198
6.7 Gamma spectra with and without interaction . . . 199

6.8 Agreement with models of radiation reaction . . . 201
6.9 Electron beam stability and model distinction . . . 203
6.10 Conclusion . . . 213

7 LWFA Bremsstrahlung Source for linear BW 215
7.1 Motivation and Introduction . . . 215
7.2 Chapter Outline . . . 219
7.3 Experimental Setup . . . 220
7.4 Characterisation of Electron Spectra . . . 225
7.5 Characterisation of Bremsstrahlung Targets . . . 228
7.6 Characterisation of Gamma Spectra . . . 238
7.7 Characterisation of X-ray spectra . . . 241
7.8 Spatio-temporal overlap of photon sources . . . 245
7.9 Variations in the number of produced pairs . . . 247
7.10 Status of the Breit-Wheeler Analysis . . . 252
7.11 Improvements for a future measurement . . . 254
7.11.1 Gamma-ray source . . . 254
7.11.2 X-ray source . . . 256
7.12 Conclusion . . . 257

8 Conclusion and Outlook 259
8.1 Summary of Results . . . 259
8.2 Discussion and Outlook . . . 260
8.2.1 Research Opportunities . . . 261
8.2.2 Experimental Considerations . . . 262
8.3 Concluding remarks . . . 274

A Symbols and constants 275
A.1 Symbols . . . 275
A.2 Abbreviations . . . 276
A.3 Notations . . . 277
A.4 Fundamental constants . . . 277

B Single particle motion 278
B.1 Electron in a cylindrically symmetric electric field . . . 278
B.2 Elec. in a cylindrically symmetric E field with axial field . . . 280

C Synchrotron radiation 282
C.1 Synchrotron Radiation . . . 282
C.2 Undulator and Wiggler Radiation . . . 283

C.3 Betatron Radiation 284

D Radiation Length **285**

E Bremsstrahlung **286**
E.1 Bremsstrahlung in the Born approximation 286
E.2 Bremsstrahlung including screening 287
E.3 Bremsstrahlung in terms of radiation length 287

F Nonlinear Compton Scattering **288**

G Quantum synchrotron function **289**

H Radiation Reaction **291**
H.1 Landau-Lifschitz Equation 291
H.2 Stochastic Operator 292

I Pair Production **293**
I.1 Nonlinear Breit-Wheeler cross section 293
I.2 Bethe-Heitler Pair Production 295

J Linear correlation coefficient **296**

Bibliography **297**

List of Figures

1.1 Aerial view of the LHC and Livingston Plot. 21
1.2 Evolution of focused laser intensities over time. 24
1.3 Aerial view of RAL and photo of the GEMINI laser area. 25
1.4 Overview of radiation reaction regimes and experiments as a function of η and a_0. 27
1.5 Visualisation of classical and quantum radiation reaction. 28
1.6 Visualisation of an electromagnetic particle shower. 29
1.7 Expansion of the polarisation and mass operator. 30

2.1 Electron motion in an infinite, linearly polarised, plane EM wave. 38
2.2 Feynman diagrams for Compton scattering for n incoming photons. 41
2.3 Feynman diagram for Compton scattering. 42
2.4 Kinematics diagram for Compton scattering. 42
2.5 Polar plot of photon energies and related differential cross section for Compton scattering. 44
2.6 Feynman diagram for nonlinear Compton scattering. 49
2.7 Angular energy distribution as a function of electron energy and redshifting of radiation as a function of a_0. 49
2.8 Differential emission rates for (nonlinear) Compton scattering at different intensities. 50
2.9 Feynman diagram for bremsstrahlung. 51
2.10 Differential cross section of bremsstrahlung for different electron energies. . 52
2.11 Overview of radiation reaction regimes and experiments. 55
2.12 Electron distribution before and after interaction with a laser pulse using different models of radiation reaction. 61
2.13 Feynman diagrams for pair annihilation and linear Breit-Wheeler pair production. 63
2.14 Total cross sections for Dirac annihilationand Breit-Wheeler pair production in the CM frame. 64

2.15 Polar plot of differential Breit-Wheeler cross sections in the centre-of-mass (CM) frame and polar plot of the particle energy distribution in the laboratory frame for different ratios of the incident photon energies. 65
2.16 Breit-Wheeler pair momentum vectors in the laboratory frame for a fixed centre-of-mass scattering angle and varying ratios of incident photon energies. 66
2.17 Feynman diagram for the nonlinear Breit-Wheeler process. 68
2.18 Feynman diagram for Bethe-Heitler process and bremsstrahlung as comparison. 69
2.19 Feynman diagram for the Schwinger process, and representation of nonlinear Breit-Wheeler and Schwinger process as ionisation processes. 70

3.1 Plasma frequency and wavelength as function of plasma density. 75
3.2 Group velocity at different densities and critical densities for different laser wavelengths. 79

4.1 Sketch of relevant focusing geometries used in experiments at GEMINI. . . 90
4.2 Spatial calibration target for a focal spot camera. 93
4.3 Examples of low-power focal spots from different focusing geometries, measured at GEMINI. 94
4.4 Photo of a photodiode used in experiment and timing scan using a delay stage and a photodiode. 96
4.5 Realising spatial interferometry as timing diagnostic in an experiment (sketch and example from an experiment). 99
4.6 Visibility of the interference pattern (fringes) as a function of the relative delay from a reference position. 100
4.7 Sketch of two counterpropagating laser pulses and how the interaction point shifts in different scenarios. 103
4.8 Temporal offset between the laser pulse (in vacuum) and the electron beam, $\Delta\tau$, as a function of the injection point relative to the start of the plasma. 104
4.9 Change in delay between the two GEMINI laser arms measured in the target area, using a spectral interferometry setup, and temperature fluctuations in the laser area as a function of time. 105
4.10 Images of a gas cell and a gas jet used in an experiment. 106
4.11 Gas jet and blade setup used at GEMINI. 107
4.13 Variable density and length gas cell used at GEMINI. 108
4.12 Sketch of nozzle design, distances in mm. 108
4.14 Shadowgraphy: Deflection of light rays in a cylindrically symmetric medium of varying density. 110
4.15 Comparison of two Mach-Zehnder interferometer geometries. 111

4.16 Example of a shadowgraphy and an interferometry image taken on an experiment at Gemini. 113
4.17 Visualisation of an electron deflected in a homogeneous magnetic field. . . 115
4.18 Visualisation of particle tracking in realistic fields. 116
4.19 Example images of an electron spectrometer screen. 117
4.20 Scintillator profile screen, photograph, GEANT4 representation and measured gamma signal. 119
4.21 Energy deposition in a gamma profile screen simulated in GEANT4. 120
4.22 Sketch of a gamma spectrometer setup in an experiment. 121
4.23 Photographs of scintillator arrays used in experiments. 122
4.24 Sketch of crystal orientations in the spectrometer arrays relative to the incident gamma rays. 123
4.25 Examples of raw response recorded on scintillator arrays. 124
4.26 GEANT4 representations of the two scintillator arrays used in the experiments 125
4.27 Images of the dual-axis spectrometer stack before and after background subtraction. 126
4.28 Response of a scintillator stack as measured by the detector and its pixelated response. 127
4.29 Example of simulated bremsstrahlung spectrum using electron spectra measured in experiment. 130
4.30 Determining a correction factor to match the in GEANT4 simulated and measured detector response. 131
4.31 Simulated detector response to mono-energetic photons and different detector setups. 132
4.32 Sketch of a combined setup of a gamma profile screen and a dual-axis spectrometer. 134
4.33 Dual-axis detector response to symmetric and asymmetric gamma sources. 135

5.1 Sketch of experimental setup to measure radiation from linear inverse Compton scattering. 140
5.2 Waterfall plot for electron spectra at fixed conditions. 143
5.3 Examples of 2D electron spectra measured in the experiment. 144
5.4 Histogram of fluctuations in the electron beam properties in this dataset. . 145
5.5 Shadowgram of the plasma channel with the focusing f/2 laser cone. 146
5.6 Montage of gamma profile measurements taken during an OAP raster scan. 147
5.7 Average integrated pixel counts and successful collisions at each OAP position of the laser raster scan. 148
5.8 Sketch of a (2D) laser raster scan. 149

5.9 Gamma energy produced in scattering a 1.55 eV photon with a relativistic electron beam in a head-on collision. 152
5.10 Example of two electron spectra with the corresponding ICS spectra. . . . 153
5.11 Average energy deposition in gamma profile detector simulated in GEANT4 as function of photon energy. 156
5.12 Energy-dependent contribution to yield on detector for a given electron spectrum. 157
5.13 Estimated number of scattered photons 159
5.14 Ratio of estimated number of scattered photons 160
5.15 Histograms of estimated beam radii of the laser pulse at the interaction. . . 161
5.16 Histograms of estimated intensities of the laser pulse at the interaction. . . 162
5.17 Gamma spectrometer responses with corresponding electron spectra and gamma profiles. 165
5.18 Montage of electron spectra and corresponding gamma profile measurements. 168
5.19 Example of a highly divergent electron beam and the corresponding ring-like gamma emission. 169
5.20 Electron spectrometer and gamma profile measurements of two electron beamlets. 170
5.21 Electron spectrometer and gamma profile measurements of an electron beam with narrow energy spread and small off-axis features. 170
5.22 Electron spectrometer and gamma profile measurements of a vertically tilted electron beam. 171
5.23 Electron spectrometer and gamma profile measurements of an electron beam with a low-charge off-axis wing. 171
5.24 Vertical beam pointing of the gamma beam and the electron beam. 172
5.25 FWHM divergences of the gamma profile and electron beam. 174
5.26 Ellipticity of the gamma profile and the electron beam as measured with the gamma profile screen. 175

6.1 Comparison of all-optical ICS experiments using LWFA. 183
6.2 Sketch of the experimental setup for the radiation reaction study. 185
6.3 Montage of gamma spectrometer and electron spectrometer images for collision and null shots. 187
6.4 Example of a measured gamma-detector signal. 188
6.5 Gamma-ray yield as a function of the electron beam energy squared for null and collision shots. 189
6.6 Gamma-ray signal above expected background signal. 190
6.7 Example of an electron spectrum measured on the radiation reaction campaign. 192

6.8 Photograph of the plasma channel and plasma self emission in a supersonic helium gas jet. . . . 193
6.9 Energy of the electron edge energy as a function of time. . . . 194
6.10 Laser energy as a function of time, and correlation of electron edge energy and laser energy. . . . 195
6.11 Distribution of electron edge energies and KDE. . . . 196
6.12 Gamma-ray signal as function of electron edge energy. . . . 197
6.13 Gamma-ray spectra for collision and non-collision shots. . . . 200
6.14 Critical energy of the gamma radiation as a function of the measured electron edge energy along with theory contours. . . . 202
6.15 Sketch of the experimental setup used on the Poder campaign. . . . 204
6.16 Example of a typical electron spectrum measured on the Poder radiation reaction campaign. . . . 205
6.17 Cutoff energy in the electron spectrum as function of the laser energy. . . . 206
6.18 Averaged electron spectra for Cole and Poder, along with their variance. . 207
6.19 Distribution of relative energy deviations from mean electron energy for Cole and Poder. . . . 208

7.1 Overview of fundamental QED processes shown in their Feynman representation along with the year the process was validated in experimentally. . . 216
7.2 Experimental setup for a photon-photon collider as proposed by Pike et al. in 2014 . . . 218
7.3 In pursuit of creating matter from light. Photograph of the magnetic chicane. 218
7.4 Sketch of the experimental setup for the Breit-Wheeler campaign. . . . 221
7.5 Example of electron spectra from high and low density accelerator setting. 226
7.6 Average electron spectra for the shot days. . . . 227
7.7 Average electron charge, energy, divergence and pointing measured on the relevant shot days. . . . 227
7.8 Montage of averaged gamma profile measurements for different materials and accelerator settings. . . . 229
7.9 Gamma-ray yield of the bremsstrahlung source for tungsten and bismuth at different accelerator settings. . . . 230
7.10 Divergence of the gamma-ray beam for tungsten, bismuth and different accelerator settings. . . . 231
7.11 Pointing of the gamma-ray beam for the different materials and accelerator settings. . . . 232
7.12 Gamma profile measurements with collimator in and out. . . . 233
7.13 Estimated through collimator transmitted gamma-ray yield for different materials and accelerator settings. . . . 234

7.14 On-shot TimePix3 data indicating identified candidate events and excluded events. . . . 235
7.15 Candidate events on the TimePix detectors as function of gamma-ray yield for tungsten (W), bismuth (Bi) and with the collimator in the beam path. 235
7.16 Total measured gamma yield at low density accelerator configuration for tungsten (W) and bismuth (Bi). . . . 236
7.17 Inverse of fitted gradient (yield over noise) from Figure 7.15 at low density accelerator configuration for tungsten (W) and bismuth (Bi). . . . 237
7.18 Example electron spectra and corresponding gamma spectra simulated in GEANT4 along with simulated and experimentally measured detector responses. . . . 239
7.19 Average gamma spectra for the relevant shot days based on simulations using electron spectra measured in the experiment. . . . 240
7.20 Variations of the gamma yield for the relevant shot days. . . . 240
7.21 X-ray spectra produced with the burn-through foil. Simulated and experimentally measured X-ray spectra. . . . 242
7.22 X-ray yield measured with the pinhole camera and the crystal spectrometer. 244
7.23 Average X-ray yield as measured by the crystal spectrometer on the different shot days. . . . 245
7.24 Alignment of the germanium (Ge) X-ray target relative to the wakefield beam axis. . . . 246
7.25 Sketch of the spatial overlap between the two high-energy photon sources. . 247
7.26 Breit-Wheeler cross section for a range of X-ray and gamma-ray energies. . 248
7.27 Estimated relative number of pairs produced for the three shot days assuming different angles and X-ray spectra. . . . 250

8.1 Sketch of a gas jet and diagnostics that characterise the plasma. . . . 263
8.2 Scattering geometries using either a head-on geometry or an off-axis parabola at an off-angle . . . 266
8.3 Scattering geometries for photon-photon colliders using an off-axis parabola at an oblique angle. . . . 267
8.4 Monitoring spatio-temporal overlap: crossed transverse probes and laser raster scan. . . . 269
8.5 Measuring high-energy radiation: combined gamma converter and scintillator array design, and crystal spectrometer. . . . 271
8.6 Sketch of an experimental setup to measure strong-field QED phenomena incorporating some of the ideas and concepts discussed in this work and this section. . . . 273

B.1 Particle trajectory of an electron in a cylindrically symmetric electric field with a constant axial accelerating field. 281

List of Tables

4.1 Gas targets and relevant injection mechanisms in this work. 106
4.2 Gas nozzle properties. 108
4.3 Scintillator arrays used as profile screens in experiments. 119
4.4 Scintillator arrays used as spectrometers in experiments. 125
4.5 Overview of bremsstrahlung converter targets used for the calibration. . . . 130

6.1 All-optical inverse Compton experiments using a plasma mirror. 180
6.2 All-optical inverse Compton experiments using two lasers. 181

7.1 Electron beam properties on relevant shot days. 228
7.2 Bremsstrahlung converter targets. 229

8.1 Comparison of scattering geometries under different aspects. 268

A.1 Overview of symbols. 275
A.2 List of abbreviations. 276
A.3 List of notations. 277
A.4 Summary of relevant fundamental constants. 277

Acknowledgements

Over the past couple of years, I had the immense privilege to work at world class research facilities alongside brilliant scientists, travel to international schools and conferences, and meet amazing people on the way. Frequent trips to RAL and long weeks spent at the shed that is Gemini have triggered a (sometimes painful) transformation from a practically inept phenomenologist to an experimental physicist. It has been a challenging journey, but I am grateful and have learned an awful lot.

I feel particularly lucky to have experienced the incomparable bond that is forged through coffee-fuelled late nights in climate-controlled labs. It is a fellowship united in a quest for 'that sweet data' but also in our suffering, to ultimately either share 'eternal glory' or see the sun rise without it on the final night of beam time. Experiments would not have been the same without on-point tunes, good craic and class people: amongst many others, Sav, Rob, Nic, Amina, Michael, and – the QED crew – Guillermo, Brendan, Dominik, Matt, Cary, Eva, the Chrises, Harsh, Christian, it was an honour and absolute pleasure to serve with you. A special shout out to Jason, Jon, Kris, Nelson and Christos for showing us the ropes and being absolute legends in their own way. Thanks also to the amazing staff at the CLF who work tirelessly to make our experiments a success.

A warm thank you, Stuart, for having been a great supervisor, a supportive guide and mentor on this journey, for always keeping your door open for stimulating discussions and reminding me of the big picture. I also want to thank you and Zulf for giving me the opportunity to work on so many fascinating (even if frustrating) experiments.

Thanks to Brendan, Sebastian, Steve and again Stuart for proofreading and offering words of encouragement, and to Tom for letting me use his beautiful figures.

A shout out to my cohort – Sav, Emma, Sam, Jon, Henry, Catalina, and in some way Meriame – and to everyone at Imperial who made this an unforgettable experience and kept me sane with tea breaks, crosswords, Christmas parties, orchestra rehearsals and pub visits. Thanks to Ollie and Rob for being there in the end and checking in on me.

Thanks to my friends outside the field, in particular Shayan, Patrick and Frederik, for having my back and for coping with sudden periods of radio silence.

To Judite, for experiencing the highs and lows together with me, for celebrating the successes and for supporting me on darker days, thank you for being there for me.

To my family, in particular my parents: thank you for always being there for me, for your unconditional love and unending support in every situation. This would not have been possible without your help.

Role of the Author

The results presented in this work were obtained on experimental campaigns at the Gemini laser of the Central Laser Facility (CLF), Rutherford Appleton Laboratory (RAL), UK. On all three experiments, the author was part of a sizeable experimental team supported by the capable local staff of engineers, laser and link scientists, that facilitated the success of these campaigns.

The analysis of the gathered data presented here was conducted by the author unless acknowledged or indicated otherwise. The specific role of the author and contributions of other researchers were as follows:

- **Chapter 5**: The author led the planning and coordination of the experimental campaign, during which he had the role of the Target Area Operator together with Matthew Streeter (IC) and Brendan Kettle (IC). Matthew Streeter characterised focal spots and FROG data. Cary Colgan (IC) analysed interferometry images and provided density profiles for the gas target.

- **Chapter 6**: During the experimental campaign, the author was mainly responsible for setting up the electron spectrometer. The author analysed the electron spectrometer data, surveyed data to find suitable datasets, and correlated the gamma spectrometer yield with the electron spectra to identify successful collisions. Tom Blackburn (Chalmers) provided simulations. Jason Cole (IC) and Keegan Behm (Michigan) analysed the gamma spectrometer data. Jason Cole correlated the experimental and the simulation results and wrote the paper.

- **Chapter 7**: The author was involved in planning and coordination of the campaign, and was Target Area Operator together with Brendan Kettle (IC) and Guillermo Marrero Samarin (QUB) during the experiment. The author analysed data from the electron and the gamma spectrometer. Brendan Kettle and Guillermo Marrero Samarin analysed the data from the gamma profile screen and the single-particle diagnostics. Cary Colgan (IC) and Brendan Kettle set up and analysed the X-ray diagnostics. Dominik Hollatz (Jena) set up and simulated the magnetic chicane.

Stuart Mangles (IC) was the principal investigator (PI) for all three experiments.

Chapter 1

Introduction

Developing a better understanding of the fundamental principles of nature lies at the very heart of science. Ultrarelativistic particle accelerators represent powerful 'microscopes', which provide invaluable insights into the fundamental building blocks of nature. The recent discovery of the Higgs boson [1–5] completes the *Standard Model* of particle physics [6], which classifies the zoo of known elementary particles and describes the interaction of the fundamental forces (except gravitation). Moreover, they have enabled many interdisciplinary applications, including ultra-bright FEL-based photon sources [7, 8].

Since the invention of the Nobel-prize awarded *chirped-pulse amplification* (CPA) technique [9], peak intensities of optical lasers have increased exponentially, while at the same time the number of high-intensity laser systems has surged [10]. This development has revolutionised our understanding of light-matter interactions and lead to disruptive transformations [11]. The advent of CPA created entire novel scientific fields, such as strong-field atom and molecular science [12–15], attosecond physics [16], relativistic and nonlinear optics [17], and laboratory astrophysics [18]. It also enabled the realisation of the plasma-based *laser wakefield acceleration* (LWFA) [19–21], where a laser pulse of relativistic intensities forms an accelerating cavity with high field gradients [22].

The marriage of both technologies – ultra-relativistic particle accelerators and ultra-intense lasers – is bound to boost our understanding of nature once again, by providing access to electromagnetic fields which reach and potentially exceed those encountered in extreme astrophysical environments, e.g., close to the surface of a neutron star [23, 24]. The fundamental scale, at which qualitatively new physics is expected, is the so-called *Schwinger field*, *Sauter field* or also *critical field of QED* [25–29]. This scale defines the *"strong-field frontier"*, which is complementary to the *"energy frontier"* [30], that is traditionally explored with accelerators. This regime bears ample research opportunities that will be explored at conventional accelerator facilities [31–34] and the next generation of multi-PW laser facilities [35–46] in laser-matter, light-light and even laser-vacuum interactions [47].

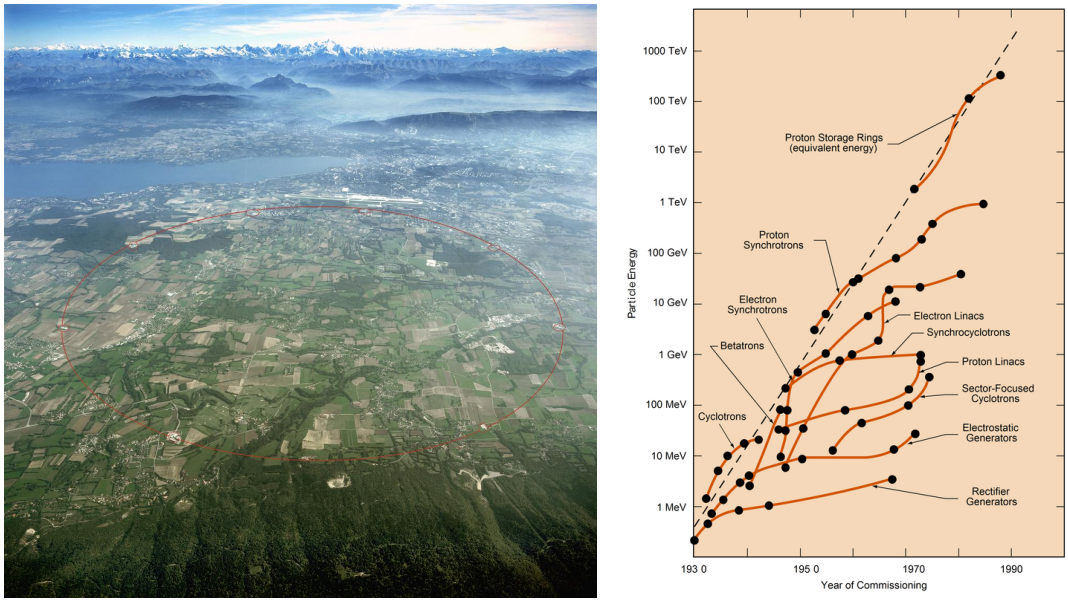


Figure 1.1: Left: Aerial view of the Large Hadron Collider (LHC) at CERN located near (Lake) Geneva [48]. Right: Livingston plot showing the particle energies achieved in particle accelerators as a function of their year of commissioning [49]. The dashed line indicates the increase of the maximum particle energy with time, increasing by a factor of 10 about every 6 years.

1.1 Particle accelerators

In an ordinary microscope, the smallest feature that can ultimately be resolved is determined by the wavelength of the optical light that is used to backlight the sample. More generally, we can postulate that the characteristic scale of the probe has to be smaller than the object it tries to resolve. The wavelength associated with a particle of momentum p is given by the *de Broglie wavelength* [50], $\lambda_{dB} = h/p$, where h is the Planck constant. As a consequence, this intuitively motivates that higher particle energies are required to resolve smaller scales. The equivalence of energy, ϵ, and mass, m, given by $\epsilon = mc^2$, on the other hand, indicates that higher energies enable the production of heavier particles in the interaction. The key quantity is the *centre-of-mass energy*, $\sqrt{s}$. For two ultrarelativistic, i.e. $\epsilon \gg mc^2$, particles of the same species that collide with each other at an angle θ, it is given by:

$$\boxed{s = \frac{(1 - \cos\theta)\epsilon_1\epsilon_2}{2m^2c^4}.} \tag{1.1.1}$$

Modern particle accelerators rely on radio-frequency (RF) cavities that support field strengths of up to $\sim 100\,\mathrm{MV/m}$, before reaching their breakdown limit [51].

One way to reduce the footprint of the accelerator is to force the particles onto a circular trajectory using sufficiently strong magnets and to re-use the same accelerator segments multiple times. The circular motion, however, requires that the particles are cosntantly accelerated and, as a consequence, they radiate. The associated emission power,

and the rate at which the particle loses energy, is the *Larmor emission power* [52]

$$\boxed{P_L = \frac{1}{6\pi\epsilon_0 c^5}\left(\frac{q}{m}\right)^4 \epsilon^2 B^2,} \tag{1.1.2}$$

where ϵ_0 is the dielectric constant, c the speed of light, q the charge of the particle, m its mass, ϵ its energy and B is the magnetic field. P_L increases quadratically with the energy of the particle, ϵ, and the strength of the applied magnetic field, B, which implies that higher energies require larger accelerators (stronger fields result in smaller bending radii). On the other hand, the emission power scales in particular with the charge to mass ratio by $(q/m)^4$, which indicates that this geometry is, for instance, more suited for protons than for electrons as $m_p/m_e \approx 1836$. Consequently, circular accelerators are typically only used to accelerate protons or heavy ions. Figure 1.1 (left) shows an aerial view of the Large Hadron Collider (LHC) at CERN with a circumference of 26.7 km at magnetic field strenght of $> 8\,\mathrm{T}$. The potential successor, the FCC(-hh) [53], is planned to reach 100 km in circumference requiring magnetic field strengths of $\sim 16\,\mathrm{T}$. Electron or other lepton accelerators are, on the other hand, typically linear accelerators. The Stanford Linear Accelerator (SLAC), for instance, reaches electron energies of $> 40\,\mathrm{GeV}$ over a distance of about 3 km. Future facilities like CLIC [54] or ILC [55] will exceed this scale to about $30 - 50\,\mathrm{km}$ total length.

The expanding size and infrastructure required to maintain these accelerators results in significant costs ranging in the billions of pounds. A complementary technology that could help reducing the size of accelerators, and consequently their cost, are plasma-based structures [56], which can in principle sustain orders of magnitude higher field gradients [57], e.g. $\sim 100\,\mathrm{GV/m}$ for a plasma of density $n_e = 10^{18}\,\mathrm{cm}^{-3}$, i.e. $E_p/E_{RF} \approx 10^3$.

An important distinction to note between hadron and lepton colliders is that hadron interactions are intrinsically much more complex due to the strong coupling constant in quantum chromodynamics (QCD), whereas lepton interactions are dominated by the 'simpler' quantum electrodynamics (QED) such that these interactions are much 'cleaner' and highly desirable. In hadron interactions, the energy is distributed amongst its constituents, the quarks and gluons, also referred to as partons, such that the effective collision energy per parton is reduced.

Despite the cost and the challenges associated with large particle accelerators, the centre-of-mass energy has continuously increased over the years, by a factor of 10 every ~ 6 years, which is visualised in a so-called *Livingston plot* [58] in Figure 1.1 (right) [49]. The increasing energies enabled the discovery of numerous new particles and a detailed study of their interplay, culminating in a rigourously confirmed Standard Model of particle physics that classifies the zoo of elementary particles and fundamental forces that they

are governed by. The discovery of the Higgs boson [1–5] provided the final experimental evidence to complete its current state. Other types of experiments and the next generation of facilities will be able to probe physics *beyond* the Standard Model.

The high-luminosity upgrade of the LHC (HL-LHC) [59], for instance, will increase the discovery reach of the LHC [60] and facilitates precision studies of rare processes [61] like (virtual) light-light interactions in ultra-peripheral scattering [62, 63] and the search for particle candidates outside of the Standard Model [64–66].

The radiation that accelerators can provide, on the other hand, has itself also proven to be a powerful tool to study, for instance, material properties, and the motion in atoms and molecules [67, 68].

1.2 High-intensity lasers

Whilst the centre-of-mass energy is the key driving factor for particle accelerators, for high-intensity lasers the *peak intensity* or *focused intensity* of the laser field determines the access to regimes of qualitatively different physics. The intensity is the energy delivered per unit area and time, commonly given in the units [W/cm^2]. The peak intensity, I_0, for a laser pulse which is Gaussian in time and space is given by [69]

$$\boxed{I_0 = 3.32 \times 10^{17}\,\mathrm{W/cm^2}\frac{\epsilon_J[J]}{(d[50\,\mu\mathrm{m}])^2\tau[50\,\mathrm{fs}]},} \tag{1.2.1}$$

where ϵ_J is the energy in the laser pulse, d its FWHM spatial size and τ its FWHM pulse duration. The evolution of the focused intensity over the past decades is shown in Figure 1.2 [11]: the invention of CPA resulted in an exponential increase of laser intensities from $< 10^{15}\,\mathrm{W/cm^2}$ to an excess of $10^{22}\,\mathrm{W/cm^2}$, passing through different regimes of interest. At the same time, the number of high-intensity lasers has increased rapidly as the range of their applications has expanded as well [10].

For instance, approaching the *atomic intensity* of $\sim 10^{16}\,\mathrm{W/cm^2}$ nonperturbative laser-atom interactions give rise to a wealth of strong-field phenomena, including tunnel ionisation and recollision-induced high-harmonic generation (HHG) [12–15].

Reaching intensities of $10^{18}\,\mathrm{W/cm^2}$, on the other hand, the electron motion in the electromagnetic field becomes relativistic, so that we call this the regime of *relativistic intensity*. These intensities are, for instance, achieved by the GEMINI laser of the Central Laser Facility shown in Figure 1.3. In this relativistic regime, the intensity, I, is commonly expressed in terms of the *normalised vector potential*, a_0 [70]:

$$\boxed{a_0 = \frac{eE_0}{m_e c\omega_L} = 0.856\sqrt{\frac{I\lambda^2}{10^{18}\,\mathrm{W/cm^2\mu m^2}},}} \tag{1.2.2}$$

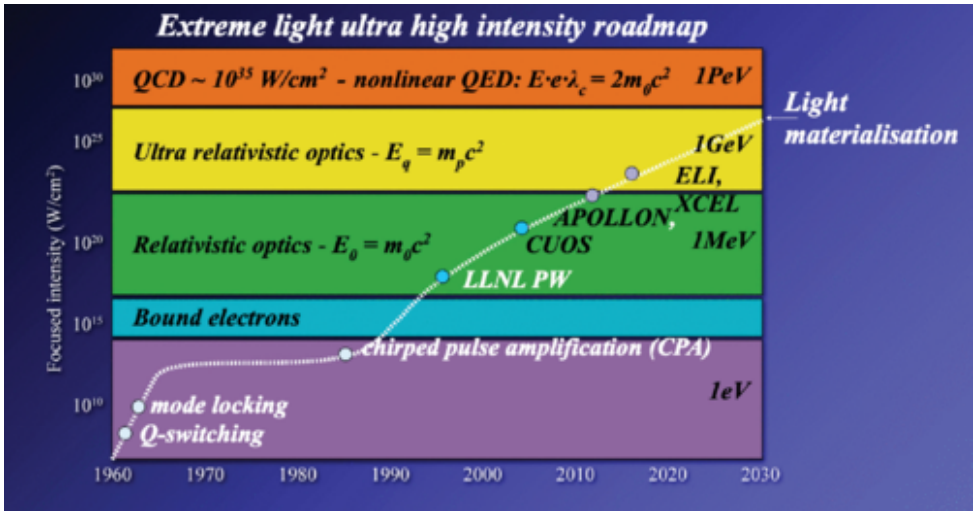


Figure 1.2: Evolution of focused laser intensity in W/cm^2 over the past decades along with relevant intensity regimes. Printed with permission, from [11].

where E_0 is the peak electric field, e the electron charge, m_e its mass, c the speed of light, ω_L the laser frequency, and λ its wavelength. An a_0 of unity indicates that the electric field is sufficiently strong to accelerate an electron within one laser oscillation by a momentum comparable to its rest mass. An electron in a laser field of relativistic intensity follows a 'figure-of-eight' trajectory, which results in the emission of higher harmonic radiation. Laser-matter interactions at relativistic intensities also give rise to phenomena in the realms of relativistic and nonlinear optics [17], e.g. relativistic focusing [71] and plasma mirrors [72].

One particularly relevant phenomenon in the context of this work is the *ponderomotive force* described by [70]

$$\boxed{F_p = -m_e c^2 \nabla \frac{\langle a^2 \rangle}{2},} \tag{1.2.3}$$

which pushes away electrons from regions of high-intensities, here expressed in terms of the vector potential, a. The ponderomotive force enabled the development of plasma-based accelerator techniques, in particular *laser wakefield acceleration* (LWFA), where an intense laser pulse travels through a plasma and expels electrons in its way [22]. The charge separation it forms in its wake, at high intensities called the 'bubble' [73], supports strong focusing and accelerating field gradients [74]. Electrons that are injected in the right phase of this cavity can be accelerated to relativistic energies in short distances. Following a breakthrough in 2004, yielding quasi-monoenergetic particle beams of hundred MeV [19–21], the quality of LWFA beams has continuously improved [75] and maximum electron energies have reached up to $\sim 8\,\mathrm{GeV}$ [76]. The structure of the bubble and the short laser pulses driving the accelerator also result in electron bunches that are intrinsically short in time [77] and typically of micrometre source size [78]. Whilst the overall quality

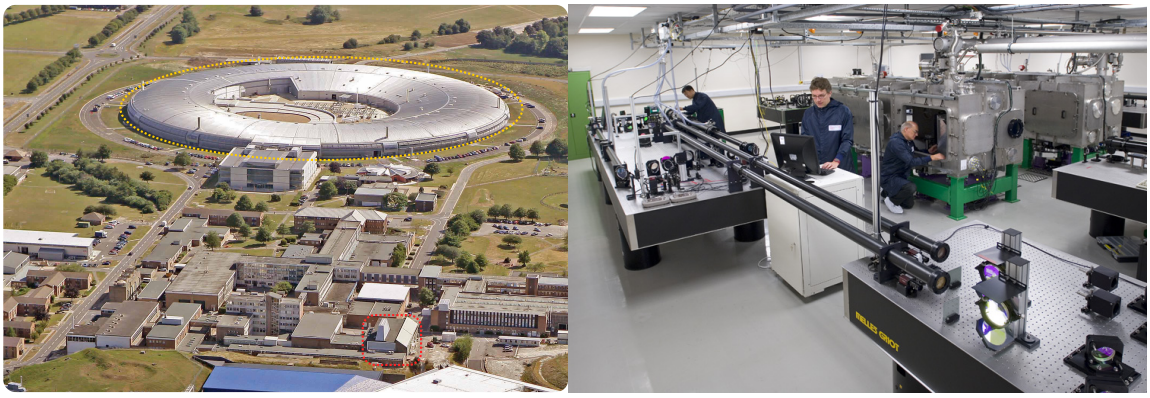


Figure 1.3: Left: Aerial view of the Rutherford Appleton Laboratory with the Diamond Light Source (yellow) and the Gemini *laser (red) of the Central Laser Facility. Right: View of the* Gemini *laser area, showing the two vacuum compressor chambers. The target area is located below this room. Figure courtesy of the CLF [84].*

of LWFA beams is to date still inferior to conventional accelerators, e.g. in terms of charge, emittance and reproducibility, it yields a large potential for more compact and cost-efficient generations of accelerators in the future. Currently, plasma-based accelerator technology is a subject of research at conventional and laser facilities alike.

Similarly as conventional particle accelerators, LWFA also acts as source of high-energy radiation. Electrons that are injected off-axis into the bubble start to oscillate due to the strong field gradients. These are called betatron oscillations, which result in the emission of betatron radiation in the X-ray regime [79]. Due to its broadband radiation, small source size and short pulse duration, betatron radiation is suitable for a range of applications [80, 81], e.g. phase-contrast imaging [82] and time-resolved measurements [83].

At even higher intensities of $\sim 10^{29}\,\mathrm{W/cm^2}$, far beyond the relativistic regime, the interaction with the vacuum itself becomes sizeable [25, 26], opening a qualitatively new regime of light-matter interactions [27–29, 47]. The associated electric field strength, referred to as the *Schwinger field*, *Sauter field* or *critical field of QED*, is given by

$$\boxed{E_S = \frac{m_e^2 c^3}{e\hbar} = 1.33 \times 10^{18}\,\mathrm{V/m},} \tag{1.2.4}$$

which is the electric field that performs work within a (reduced) Compton length equal to the rest mass of the electron. Whilst the next generation of multi-petawatt laser systems now commissioned across Europe [35, 36], Asia [38, 39] and the US [45] will reach unprecedented peak powers and peak intensities, these and any other laser system envisioned so far will not be able to reach this critical intensity with current amplification schemes [10]. One solution proposed to tackle this challenge is to combine multiple intense laser beams either coherently or incoherently [39]. Other challenges for future laser systems

include improving the efficiency and repetition rates to reach high average powers [10, 11], which is an analogous trend to the increase in luminosity at particle accelerators.

1.3 Particle accelerators and high-intensity lasers

High-intensity lasers and ultrarelativistic particle accelerators have separately revolutionised our understanding of nature. By combining both we are able to access a new regime of physics to explore qualitatively new physics [47].

Currently, they are already used in pump-probe experiments crucial for material, atom, molecular science and HEDP experiments, for instance, at XFELs [85, 86]. Intense lasers are also used to diagnose particle beams with a spatial correlation technique called 'laser wire' [87–95], which replaces traditional wire beam profile monitors [96]. Here a thin laser beam is scattered off the relativistic particle beam and experiences a relativistic Doppler shift. As a result, optical photons are backscattered at X-ray or gamma-ray energies, which can be used to diagnose the particle beam, and the generated radiation is also suited for nuclear studies [97]. This process is referred to as *Compton backscattering*, *inverse Compton scattering* (ICS) or, in its classical limit, *relativistic Thomson scattering* [98].

If we consider the interaction more carefully, we realise that the electric field in the rest frame of the relativistic electron is greatly enhanced. In other words, by colliding high-intensity lasers with ultra-relativistic electron beams, higher intensities become accessible in the electron rest frame than before due to the Lorentz boost, reaching up to $I' \sim 4\gamma^2 I$, where I is the intensity in the laboratory frame, I' is the intensity in the electron rest frame, and γ is the relativistic Lorentz factor. The most prominent example taking advantage of this geometry is the seminal E-144 experiment at SLAC, where a 46.6 GeV electron beam was collided with a laser of intensity $a_0 = 0.3$ producing highly energetic gamma radiation [99] and electron-positron pairs from the nonlinear Breit-Wheeler and the Trident process [100, 101]. The increase in laser intensities and accelerator technologies available now provides a motivation to revisit this geometry to probe phenomena in the vicinity of the critical field strength, governed by *strong field quantum electrodynamics* (SFQED).

In this context, we now consider the electric field the laser, E_L, in the rest frame of the electron, E_{RF}, which defines the *quantum nonlinearity parameter*, η. For a relativistic electron with energy, $\epsilon = \gamma m_e c^2$, colliding with a laser pulse with peak intensity, I_0, at an angle, θ, the parameter, η, is given by [102]

$$\begin{aligned} \eta &= \frac{E_{RF}}{E_S} = \frac{(1-\cos\theta)\gamma E_L}{E_S} \\ &\approx 0.1 \left(\frac{\epsilon}{500\,\mathrm{MeV}}\right)\left(\frac{I_0}{10^{21}\,\mathrm{W/cm^2}}\right)^{1/2}, \end{aligned} \tag{1.3.1a}$$

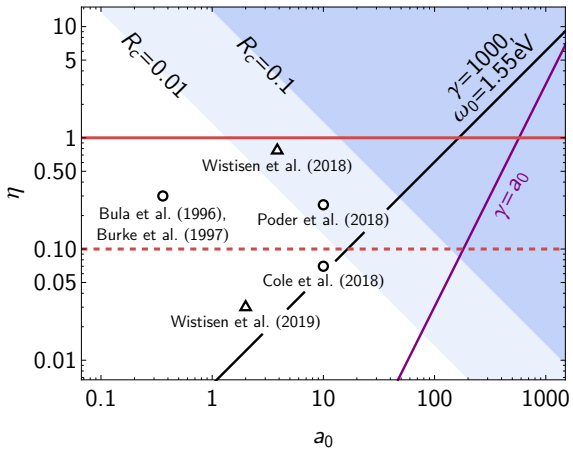


Figure 1.4: Overview of radiation reaction regimes and experiments as a function of the quantum nonlinearity parameter, η, and the normalised vector potential, a_0. The red lines indicate when quantum effects become significant (dashed) or dominate (solid). More details are provided in Section 2.3.1. Figure courtesy T. Blackburn, adapted from [102].

where $E_S = 1.33 \times 10^{18}\,\mathrm{V/m}$ is again the Schwinger field, corresponding to a laser intensity of $I_S \approx 10^{29}\,\mathrm{W/cm^2}$, and η is maximised in a head-on collision, i.e. if $\theta = 180°$. Higher values of η indicate stronger fields at the interaction and that quantum effects become more important. By combining high intensities and particle energies, we can then reach the critical field of QED already at existing or currently commissioned conventional accelerators and multi-petawatt laser facilities. In this so-called *nonperturbative strong-field regime of QED* ($I' \gtrsim I_S$ or $\eta \gtrsim 1$) [103–105], the recoil of emitted photons significantly perturbs electron/positron trajectories (strong-field radiation reaction) and prolific electron-positron pair production becomes substantial (vacuum breakdown). Figure 1.4 shows the parameters of SLAC E-144 and more recent strong-field experiments in terms of the peak normalised vector potential or intensity, a_0, and the quantum linearity parameter, η, incorporating the particle energy, γ, and the intensity. The red dashed line indicates $\eta = 0.1$ when quantum effects become significant. The solid red line, on the other hand, indicates when $\eta = 1$ above which interactions are dominated by SFQED.

Such extreme conditions can be encountered in violent astrophysical phenomena like gamma ray bursts [106] and supernova explosions [107], in the vicinity of pulsars and magnetars [23, 24], close to magnetized black holes [108], and in the early universe [109–112]. Due to stringent luminosity requirements, a future lepton collider (e.g., CLIC [54] or ILC [55]) will also reach the critical field strength at the interaction point [113, 114]. Moreover, it might be beneficial to exceed this scale by orders of magnitude [103], necessitating a better understanding of light and matter in extreme electromagnetic fields. At multi-petawatt laser facilities [35–46], laser-plasma interactions will probe an interplay

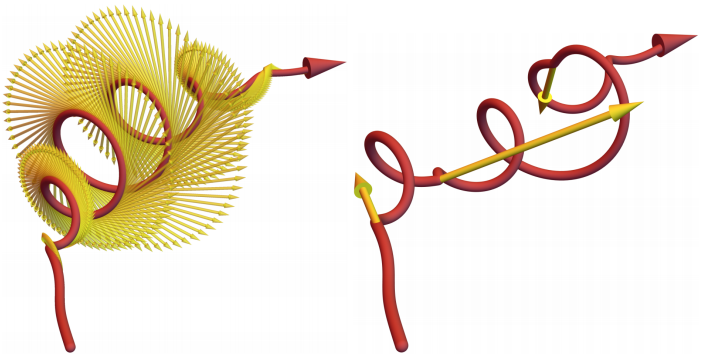


Figure 1.5: Trajectory (red) of an electron in a circularly polarised laser field. The radiation the particle emits is indicated by the yellow arrows. Left: The particle undergoes classical radiation reaction which acts as a slow continuous force. Right: The particle experiences quantum radiation reaction. The stochastic, incoherent emission of multiple high-energy photons leads to a significant alteration of the trajectory. Figure courtesy T. Blackburn, reprinted from [102].

between strong-field quantum and collective effects. These facilities will open an exciting new research field within high-energy-density physics (HEDP) [115–118].

The regime in the approach of $\eta \sim 1$ and beyond bears a wealth of interesting phenomena [47, 119]. For instance, it enables a detailed study of Compton scattering across a range of regimes from the classical limit [120], to the perturbative quantum description [99] and the non-perturbative strong-field regime [99, 121–126].

The high energies emitted in the process also give rise to significant *radiation reaction*, which is the knock-back force a particle experiences when it radiates. Radiation reaction is a very fundamental process but surprisingly there is no practicable description of radiation reaction that is valid across a wide parameter space [102]. Initial attempts to find a formulation that is self-consistent in classical electrodynamics resulted in non-physical runaway solutions with self-acceleration [127]. In the classical *Landau-Lifschitz (LL) radiation reaction force* [128], these unphysical solutions are removed, but it predicts energy losses beyond the initial energy of the electron in rapidly changing fields [129].

Approaching notable values of η, the classical descriptions lose validity and we have to consider *quantum radiation reaction* [130–135]. In the quantum regime, the description experiences mainly two corrections, one is the reduction in the emission power, the second is the stochasticity of the emission (opposite to the deterministic classical description), which gives rise to individual high energy emissions enabled through *energy straggling* [136] and also partially the suppression of emission events through *radiation quenching* [137], both of which are classically forbidden. Quantum radiation reaction is then the result of multiple incoherent and discrete emission events. The difference in the impact

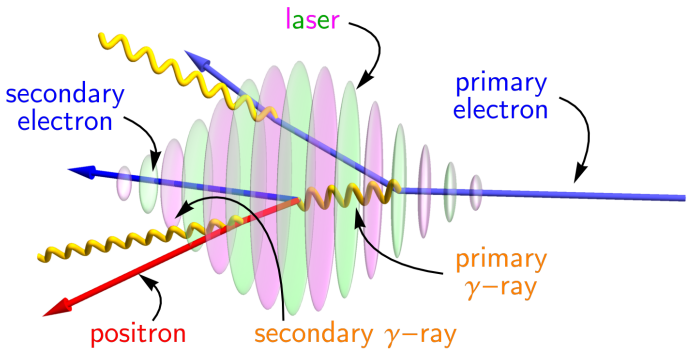


Figure 1.6: Ultrarelativistic electrons (blue) collide with an intense laser pulse (green, purple), and emit gamma-rays (yellow). Some of the gamma-rays interact with the laser field to produce an electron-positron pair (blue and red) via the nonlinear Breit-Wheeler process. The secondary particles can in turn interact with the laser field to emit more radiation. Figure courtesy T. Blackburn, adapted from [141].

of classical and quantum radiation reaction is visualised in Figure 1.5 [102]. In intense interactions it has also been predicted that beams can be spin-polarised through a fast analogue of the Sokolov-Ternov effect [138–140], which bears promising opportunities and applications in particle physics. At the same time, a detailed study of radiation reaction is also important to develop mitigation strategies for future accelerators.

At high-intensity laser facilities, particle accelerators and high-intensity laser pulses are conveniently co-located: laser wakefield accelerators (LWFA) driven by high-intensity lasers are well suited for these studies as the laser pulse and the electron beam are intrinsically synchronised to each other which facilitates the spatio-temporal overlap – one of the major challenges when dealing with femtosecond scale and micron sized objects. The small size of the electron beam also means that a tightly focused laser pulse can interact with a large fraction of the bunch at comparable intensities, such that the electron is a real probe of the laser pulse (probe has to be smaller than the 'object' it probes).

Conventional accelerators with access to high-intensity lasers will also be able to probe this regime and will benefit from their superior beam quality and stability, but will have to overcome challenges arising from synchronising the electron beam and the laser pulse. Moreover, spatial and temporal beam sizes are typically larger such that a large background of radiation from low-intensity interactions is expected.

Radiation reaction can also be probed in other geometries, for instance, in a standing wave formed by multiple intense laser pulses, in laser-solid interactions and in aligned crystals [142–146].

Strong-field interactions also enable studying a variety of *pair production processes*,

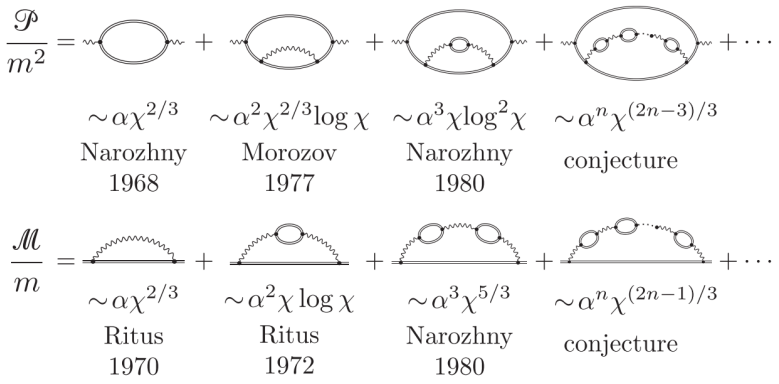


Figure 1.7: Dressed loop expansion of the polarisation (top) and mass operator (bottom). The double lines indicate dressed electron/positron states (here propagators), the wiggly lines indicate photons. The Ritus-Narozhny conjecture predicts that these diagrams are the dominant contribution at the n-th loop with an expansion parameter $\alpha\eta^{2/3}$ in the strong-coupling regime of QED at $\eta \gg 1$. Reprinted Figure 2 with permission from [103]. Copyright 2019 by the American Physical Society.

QED showers and cascades (see Figure 1.6 [141]), which are particularly relevant in the astrophysical context [115, 147, 148], or the production of *dense (QED) pair plasmas* which are of interest for high energy density physics [115–117].

By utilising the highly energetic radiation produced in interactions and combining it with a second light source, for instance another intense laser pulse, these geometries facilitate the study of light-light interactions and realisation of pure *photon-photon colliders*: Examples are the two (linear) [149, 150] and multi-photon (nonlinear) pair production [100, 151] via the Breit-Wheeler process. At $\eta \sim 1$ we gain access to pair production from the vacuum via *Schwinger pair production*, also referred to as *vacuum tunnel ionisation* or *vacuum breakdown* [27–29]. Note that light-light interactions are classically forbidden by the superposition principle. In this regime the vacuum itself acts as a nonlinear medium, with *vacuum birefringence* [152, 153] and *vacuum dichroism* [154] providing insights into the *quantum fluctuations* of the vacuum. Similarly, there are vacuum recollision processes [155, 156], which are reminiscent of atomic recollision physics.

Photon-photon colliders would also be powerful tools to probe physics beyond the Standard Model [64–66]. Note that here these interactions would occur between real photons and are hence qualitatively different to the virtual photon interactions measured in ultra-peripheral ion collisions, for instance at CERN.

Finally, deep in the supercritical regime when $\alpha\eta^{2/3} \sim 1$, i.e. $\eta \sim 1600$, radiative corrections become sizable, such that we access the conjectured *strong-coupling regime of QED* in these extreme fields [157–160], also referred to as *Ritus-Narozhny conjecture* (see Figure 1.7 [103]). At this frontier the current treatment of QED breaks down and bears resemblance to the strongly-coupled QCD.

1.4 Thesis Outline

This work focuses on the versatile capabilities of laser wakefield accelerators and high-intensity lasers to generate highly energetic radiation of varied spectral shape and across a wide energy range. It provides three experimental examples where laser wakefield accelerators were used to produce gamma radiation with photon energies from few to several hundreds of MeV, and highlights their application in studies of fundamental phenomena of quantum electrodynamics (QED).

The thesis starts by discussing single particle motions in electromagnetic fields, radiation mechanisms, radiation reaction and pair production in **Chapter 2**. **Chapter 3** introduces principles regarding the collective motion in plasmas and their interaction with an intense laser pulse, which are relevant for wakefield acceleration. This is followed by a discussion of experimental methods underpinning this work in **Chapter 4**. The experimental results that are at the core of this thesis are presented in **Chapters 5**, **6** and **7**:

5) **Linear Inverse Compton Scattering and Beam Profile Diagnostic:**
Relativistic electrons from a wakefield accelerator were collided with a defocused laser pulse at $a_0 \sim 0.2 - 1$ generating gamma radiation from linear inverse Compton Scattering in the 10's of MeV photon energy range. The radiation is used to diagnose the properties of the laser pulse at the interaction and its application as single-shot electron beam diagnostic is explored.

6) **Nonlinear Inverse Compton Scattering and Radiation Reaction:**
By scattering a tightly focused high-intensity laser pulse from a relativistic electron beam and generating gamma radiation from nonlinear inverse Compton Scattering, it was possible to measure radiation reaction in an experiment. The energy loss of the electron beam and the spectrum of the radiation were used to pinpoint the interaction conditions and their agreement with theoretical models was tested.

7) **Bremsstrahlung source and the Linear Breit-Wheeler Process:**
An electron beam from a wakefield accelerator was passed through a solid target to produce bremsstrahlung with photon energies of 100s of MeV. The source was optimised with regards to its yield of photons and energetic secondary particles. The high energy photons were then collided with a $\sim$ keV X-ray field generated by a second laser in an attempt to measure the elusive linear Breit-Wheeler process.

Finally, **Chapter 8** summarises the results and discusses future research opportunities. The findings and insights of the presented results are then used to discuss experimental considerations and make recommendations for future studies of strong-field phenomena like radiation reaction investigated in a colliding-pulse geometry.

Chapter 2

Single particle motions and radiation mechanisms

This Chapter lays the theoretical groundwork for the results presented later in this work, addressing the motion of single charged particles in electromagnetic fields, radiation mechanisms, and discussing the fundamental processes of radiation reaction and pair production.

First, equation of motions of charged single particles in electromagnetic fields are derived. This forms the basis for understanding the properties of electrons accelerated in wakefield accelerators, measuring their energy in magnetic spectrometers and calculating the radiation they emit in interaction with electromagnetic fields.

Subsequently, the production of radiation through two processes is discussed: (inverse) Compton scattering (ICS) in moderately (linear ICS) and highly intense laser fields (non-linear ICS), which is central to the work presented in Chapters 5 and 6, and the radiation process of bremsstrahlung which is in particular important for the experiment outlined in Chapter 7.

This leads over to the topic of radiation reaction, the knock-back force a charged particle experiences when emitting a photon. This can, for instance, be investigated in relativistic inverse Compton scattering. Whilst radiation reaction is a very fundamental phenomenon there is so far no universally accepted and practicable description for a wide parameter space. In this section, different proposed descriptions of radiation reaction are discussed, starting with the Lorentz-Abraham-Dirac equation, which is self-consistent in classical electrodynamics, followed by the classical Landau-Lifschitz equation and leading over to quantum corrections and their implications. Finally, the fundamental QED processes of pair annihilation and pair production through the Breit-Wheeler, Bethe-Heitler and Schwinger process are discussed.

2.1 Single particle motion in an electromagnetic field

The Lagrangian for a relativistic particle in an electromagnetic field with the potentials Φ and $\mathbf{A}$ is given by [52]

$$L(\mathbf{r}, \mathbf{v}, t) = -mc^2\gamma^{-1} + q\mathbf{v} \cdot \mathbf{A} - q\Phi, \tag{2.1.1}$$

where m is the mass of the particle, γ the relativistic Lorentz factor and q the charge. We use the Euler-Lagrange equation to obtain the equation of motion:

$$\frac{\mathrm{d}}{\mathrm{d}t}\frac{\partial L}{\partial \mathbf{v}} - \frac{\partial L}{\partial \mathbf{r}} = 0. \tag{2.1.2}$$

Using $\mathbf{A} = \mathbf{A}(\mathbf{r}, t)$, $\Phi = \Phi(\mathbf{r}, t)$, $\gamma^{-1} = \sqrt{1 - (v/c)^2}$ and this becomes

$$\frac{\mathrm{d}}{\mathrm{d}t}\left[\mathbf{p} + q\mathbf{A}\right] - \left[q\nabla\left(\mathbf{A} \cdot \mathbf{v}\right) - q\nabla\Phi\right] = 0, \tag{2.1.3}$$

where $\mathbf{p} = \gamma m\mathbf{v}$ is the relativistic momentum. Now using the convective derivative $\frac{\mathrm{d}}{\mathrm{d}t} = \frac{\partial}{\partial t} + \mathbf{v} \cdot \nabla$ and the vector identity $\nabla\left(\mathbf{v} \cdot \mathbf{A}\right) = (\mathbf{v} \cdot \nabla)\mathbf{A} + \mathbf{v} \times (\nabla \times \mathbf{A})$ this reads:

$$\frac{\mathrm{d}}{\mathrm{d}t}\mathbf{p} = q\left(\mathbf{v} \times \nabla \times \mathbf{A} - \frac{\partial \mathbf{A}}{\partial t} - \nabla\Phi\right). \tag{2.1.4}$$

With the definitions of the electric field $\mathbf{E}$ and the magnetic field $\mathbf{B}$ in terms of the potentials Φ and $\mathbf{A}$

$$\mathbf{E} = -\frac{\partial \mathbf{A}}{\partial t} - \nabla\Phi, \tag{2.1.5}$$

$$\mathbf{B} = \nabla \times \mathbf{A}, \tag{2.1.6}$$

the equation of motion takes the familiar shape of the Lorentz force:

$$\boxed{\frac{\mathrm{d}\mathbf{p}}{\mathrm{d}t} = q\left(\mathbf{E} + \mathbf{v} \times \mathbf{B}\right).} \tag{2.1.7}$$

2.1.1 Electron motion in a homogeneous electric field

Using the previously derived equation for the Lorentz force, we can now consider a first simple example. Consider the motion of a single electron in a homogeneous electric field without presence of a magnetic field, i.e. $\mathbf{B} = \mathbf{0}$. The Lorentz equation simplifies to:

$$\frac{\mathrm{d}\mathbf{p}}{\mathrm{d}t} = q\mathbf{E}. \tag{2.1.8}$$

If we choose the coordinate system such that $\mathbf{E} = (E, 0, 0)^t = E\mathbf{e}_x$, the electron feels a

constant force qE accelerating it in x at a linear energy gain. Its momentum, however, is unchanged in the other two directions, $\mathrm{d}p_x/\mathrm{d}t = \mathrm{d}p_y/\mathrm{d}t = 0$.

2.1.2 Electron motion in a homogeneous magnetic field

Consider the motion of a single electron in a homogeneous magnetic field extending over the entire region of interest. The equation for the Lorentz force simplifies with $\mathbf{E} = \mathbf{0}$ to:

$$\frac{\mathrm{d}\mathbf{p}}{\mathrm{d}t} = q\mathbf{v} \times \mathbf{B}, \tag{2.1.9a}$$

$$\frac{\mathrm{d}\mathbf{p}}{\mathrm{d}t} = \frac{q}{\gamma m}\mathbf{p} \times \mathbf{B}, \tag{2.1.9b}$$

in terms of the relativistic momentum $\mathbf{p} = \gamma m\mathbf{v}$. Note that in this case the purely magnetic Lorentz force does not do any work: the instantaneous rate of work (power) is $P = \mathbf{F} \cdot \mathbf{v}$, where the force $\mathbf{F}$ is by virtue of the cross product always orthogonal to $\mathbf{v}$ and the dot product vanishes. We choose the coordinate system such that $\mathbf{B} = (0, 0, B)^t = B\mathbf{e}_z$. The momentum vector is simply $\mathbf{p} = (p_x, p_y, p_z)^t$. The differential equations are then given by:

$$\dot{p_x} = \frac{qB}{\gamma m}p_y, \tag{2.1.10a}$$

$$\dot{p_y} = -\frac{qB}{\gamma m}p_x, \tag{2.1.10b}$$

$$\dot{p_z} = 0, \tag{2.1.10c}$$

which combines to

$$\ddot{p_x} = -\left(\frac{qB}{\gamma m}\right)^2 p_x, \tag{2.1.11a}$$

$$\ddot{p_y} = -\left(\frac{qB}{\gamma m}\right)^2 p_y. \tag{2.1.11b}$$

This second order, linear differential equation can be solved by a periodic motion of type $p_x(t) = C\sin(\omega t) + D\cos(\omega t)$ with $\omega = qB/\gamma m$. The dotted variables indicate the time derivatives with $\dot{p} = \mathrm{d}p/\mathrm{d}t$ and $\ddot{p} = \mathrm{d}^2p/\mathrm{d}^2t$.

$\mathbf{p}_\perp$ be the momentum vector of the particle perpendicular to the magnetic field lines and $\mathbf{p}_\parallel$ the component parallel to the magnetic field (z). For the initial conditions $p_x(t = 0) = |\mathbf{p}_\perp| = p_\perp$ and $p_y(t = 0) = 0$, we obtain for the momenta:

$$p_x(t) = p_\perp \cos(\omega t) \tag{2.1.12a}$$

$$p_y(t) = -p_\perp \sin(\omega t) \tag{2.1.12b}$$

The solution for the z-motion is trivial with $p_z = p_{z,0}$. Expressed in terms of the trajectories with initial conditions $x(0) = 0, z(0) = 0, y(0) = p_\perp/qB = r_L$, this reads

$$\boxed{\begin{aligned} x(t) &= r_L \sin(\omega t) \\ y(t) &= r_L \cos(\omega t) \\ z(t) &= \frac{p_{z,0}}{\gamma m} t \end{aligned}} \tag{2.1.13a}$$

$$y(t) = r_L \cos(\omega t) \tag{2.1.13b}$$

$$z(t) = \frac{p_{z,0}}{\gamma m} t \tag{2.1.13c}$$

The radius of the circular motion of the electron is called the Larmor radius, r_L. It depends on the total momentum in the x-y plane and the magnetic field strength, B:

$$\boxed{r_L = |\mathbf{p}_\perp|/eB,} \tag{2.1.14}$$

where e is the charge of the electron and $\mathbf{p}_\perp$ is the component of the momentum vector $\mathbf{p}$ that is perpendicular to the field component of the magnetic field.

The motion of the electron consists of two decoupled motions: one at the constant, initial velocity parallel to the magnetic field vector in z, the second motion is a circular motion in the x-y plane. This is called a cyclotron motion. For now we will ignore the dissipation of energy in form of radiation due to the acceleration of the electron and accept the result that the Lorentz force conserves the total momentum and energy of the particle in this case.

2.1.3 Electron motion in a monochromatic plane EM wave

We will now consider the case of an electron in a monochromatic plane wave. Writing the equation of motion in terms of the potentials $\mathbf{A}$ and Φ as in Equation (2.1.4) on page 33 gives [161]:

$$\frac{\mathrm{d}}{\mathrm{d}t}\mathbf{p} = q\left(\mathbf{v} \times \nabla \times \mathbf{A} - \frac{\partial \mathbf{A}}{\partial t} - \nabla\Phi\right). \tag{2.1.15}$$

Now using the convective derivative, $\mathrm{d}\mathbf{p}/\mathrm{d}t = \partial\mathbf{p}/\partial t + \mathbf{v}\cdot\nabla\mathbf{p}$ and the vector identity $\mathbf{v}\cdot\nabla\mathbf{p} = (\nabla\mathbf{p})\cdot\mathbf{v} - \mathbf{v}\times(\nabla\times\mathbf{p})$ again, the total time derivative of the momentum expands to

$$\frac{\mathrm{d}}{\mathrm{d}t}\mathbf{p} = \frac{\partial \mathbf{p}}{\partial t} + (\nabla\mathbf{p})\cdot\mathbf{v} - \mathbf{v}\times(\nabla\times\mathbf{p}). \tag{2.1.16}$$

With this result the equation of motion becomes

$$\frac{\partial \mathbf{p}}{\partial t} + (\nabla \mathbf{p}) \cdot \mathbf{v} - \mathbf{v} \times (\nabla \times \mathbf{p}) = q \left(\mathbf{v} \times \nabla \times \mathbf{A} - \frac{\partial \mathbf{A}}{\partial t} - \nabla \Phi \right),$$

$$\frac{\partial}{\partial t} (\mathbf{p} + q\mathbf{A}) + (\nabla \mathbf{p}) \cdot \mathbf{v} - \mathbf{v} \times (\nabla \times (\mathbf{p} + q\mathbf{A})) = -q \nabla \Phi,$$

$$\frac{\partial}{\partial t} \mathbf{u} + (\nabla \mathbf{p}) \cdot \mathbf{v} - \mathbf{v} \times (\nabla \times \mathbf{u}) = -q \nabla \Phi, \tag{2.1.17}$$

where we introduced in the last step the canonical momentum $\mathbf{u} = \mathbf{p} + q\mathbf{A}$. We can express $(\nabla \mathbf{p}) \cdot \mathbf{v}$ as follows

$$(\nabla \mathbf{p}) \cdot \mathbf{v} = \frac{1}{m\gamma} \nabla (p^2/2) = \frac{1}{m\gamma} \nabla (\gamma^2/2) = mc^2 \nabla \gamma. \tag{2.1.18}$$

Substituting $(\nabla \mathbf{p}) \cdot \mathbf{v}$ in Equation (2.1.17) by the expression in Equation (2.1.18):

$$\frac{\partial}{\partial t} \mathbf{u} = \mathbf{v} \times (\nabla \times \mathbf{u}) - \nabla \left(q\Phi + \gamma mc^2 \right). \tag{2.1.19}$$

Taking the curl of this equation results in:

$$\frac{\partial}{\partial t} \nabla \times \mathbf{u} = \nabla \times \left[\mathbf{v} \times (\nabla \times \mathbf{u}) \right], \tag{2.1.20}$$

where the second term disappeared as the curl of a gradient is always zero, so that if $\nabla \times \mathbf{u}$ is zero initially, it will remain so always. The condition is satisfied, for instance, for a plasma at rest before the laser pulse arrives. Assuming this condition, Equation (2.1.19) simplifies to

$$\frac{\partial}{\partial t} \mathbf{u} = -\nabla \left(q\Phi + \gamma mc^2 \right). \tag{2.1.21}$$

For a medium close to vacuum or an unperturbed plasma, one can assume $\Phi = 0$, resulting in:

$$\frac{\partial}{\partial t} \mathbf{u} = -\nabla \gamma mc^2. \tag{2.1.22}$$

In the case of an infinite plane wave, the transverse gradient $\nabla_\perp$ is zero. This means we obtain two separate components:

$$\frac{\partial}{\partial t} \mathbf{u}_\perp = 0, \tag{2.1.23a}$$

$$\frac{\partial}{\partial t} \mathbf{u}_\parallel = \nabla_\parallel \gamma mc^2. \tag{2.1.23b}$$

From the perpendicular component we see that the transverse canonical momentum is conserved: $\mathbf{p}_\perp + q\mathbf{A} = 0$. If $q = -e$ and $e\mathbf{A}_\perp = \mathbf{a}_\perp$, then $\mathbf{p}_\perp = \mathbf{a}_\perp$. In Cartesian coordinates, this means $p_x = a_x, p_y = a_y$.

For the parallel spatial component z, consider the substitution $z = ct$ for light. Thus, $\partial z = c\partial t$. The parallel-component of the vector potential $\mathbf{A}$ is zero, so $u_\parallel = p_\parallel = p_z$:

$$\frac{\partial}{\partial t}(cp_z - \gamma mc^2) = 0. \tag{2.1.24}$$

Assuming an unperturbed stationary plasma, the initial conditions are $\gamma(t = 0) = 1$ and $p_z(t = 0) = 0$. Integrating the previous equation gives:

$$cp_z + mc^2 = \gamma mc^2. \tag{2.1.25}$$

Using $E = \gamma mc^2 = \sqrt{mc^2 + (cp_\parallel)^2 + (cp_\perp)^2}$ and substituting, one obtains an expression for $p_\parallel = p_z$:

$$p_z = \frac{1}{2}mca^2, \tag{2.1.26}$$

where $a^2 = p_\perp^2$. We now have

$$p_x = mca_x, \tag{2.1.27a}$$
$$p_y = mca_y, \tag{2.1.27b}$$
$$p_z = \frac{1}{2}mca^2. \tag{2.1.27c}$$

Using $\mathbf{p} = \gamma m\mathbf{v}$ this can be written as:

$$\frac{\gamma}{c}\frac{\mathrm{d}x}{\mathrm{d}t} = a_x, \tag{2.1.28a}$$
$$\frac{\gamma}{c}\frac{\mathrm{d}y}{\mathrm{d}t} = a_y, \tag{2.1.28b}$$
$$\frac{\gamma}{c}\frac{\mathrm{d}z}{\mathrm{d}t} = \frac{a^2}{2}. \tag{2.1.28c}$$

Changing from t to proper time τ, we transform via $\mathrm{d}\tau = \gamma^{-1}\mathrm{d}t$, simply giving the equation of motions in term of τ:

$$\frac{1}{c}\frac{\mathrm{d}x}{\mathrm{d}\tau} = a_x, \tag{2.1.29a}$$
$$\frac{1}{c}\frac{\mathrm{d}y}{\mathrm{d}\tau} = a_y, \tag{2.1.29b}$$
$$\frac{1}{c}\frac{\mathrm{d}z}{\mathrm{d}\tau} = \frac{a^2}{2}. \tag{2.1.29c}$$

Let us assume a laser field with linear polarisation in x, described by the vector potential

$$\mathbf{a} = a_0\cos(kz - \omega t)\mathbf{e}_x = a_0\cos(\xi)\mathbf{e}_x, \tag{2.1.30}$$

where $\mathbf{e}_x$ is the unit vector in the x-coordinate, $\xi = kz - \omega t$ the waveframe coordinate and $k = \omega/c$ the wave number.

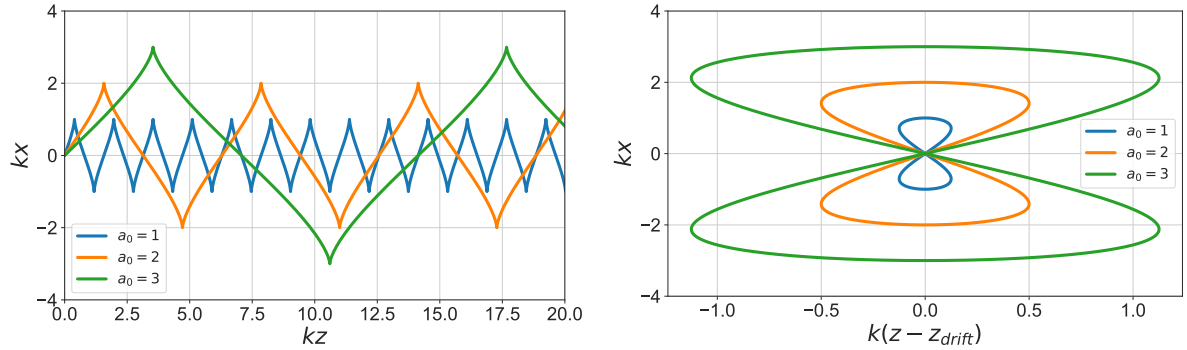


Figure 2.1: Electron motion in an infinite, linearly polarised, plane EM wave in the lab frame (left), with the wavenumber $k = \omega/c$. On the right the figure-of-eight motion in the drift frame.

Using this explicit vector potential:

$$\frac{\gamma}{c}\frac{\mathrm{d}x}{\mathrm{d}t} = a_0 \cos\xi, \tag{2.1.31a}$$

$$\frac{\gamma}{c}\frac{\mathrm{d}y}{\mathrm{d}t} = 0, \tag{2.1.31b}$$

$$\frac{\gamma}{c}\frac{\mathrm{d}z}{\mathrm{d}t} = \frac{1}{2}a_0^2 \cos^2\xi. \tag{2.1.31c}$$

and integrating the equation of motions, results in:

$$x(\xi) = \frac{a_0}{k}\sin(\xi), \tag{2.1.32a}$$

$$y(\xi) = 0, \tag{2.1.32b}$$

$$z(\xi) = \frac{a_0^2}{4k}\left(\xi + \frac{1}{2}\sin(2\xi)\right), \tag{2.1.32c}$$

where we chose the initial conditions $x(0) = y(0) = z(0) = 0$ and used $\mathrm{d}\xi/\mathrm{d}t = \omega/\gamma$. The electron performs a periodic oscillation in the x-axis, whilst the motion in the z-axis is composed of a constant drift and another oscillation [see Figure 2.1 (left)]. This is commonly referred to as the 'figure-of-eight' motion, which becomes more evident in the drift frame [see Figure 2.1 (right)]. For $a_0 \leq 1$ the motion in z is suppressed and the motion of the electron is dominated by the transverse oscillation. For $a_0 \gg 1$, the motion is predominantly longitudinal.

2.1.4 Ponderomotive Force

In laser wakefield acceleration (LWFA), a high intensity laser pulse propagates through an underdense plasma, expels electrons in its way and drives a wave. The driving force is the so-called ponderomotive force which is proportional to the gradient of the laser intensity.

The following relativistic derivation of the ponderomotive force is based on [161]. We start with the Euler-Lagrange equations after inserting the Lagrangian in terms of the potentials $\mathbf{A}$ and Φ as given as intermediate step in Equation (2.1.3) on page 33:

$$\frac{\mathrm{d}}{\mathrm{d}t}\left[\mathbf{p} + q\mathbf{A}\right] - \left[q\nabla\left(\mathbf{A}\cdot\mathbf{v}\right) - q\nabla\Phi\right] = 0. \tag{2.1.33}$$

This can be written in terms of the normalised quantities

$$\begin{aligned} \mathbf{a} &= -q\mathbf{A}/m_e c, & \phi &= -q\phi/mc^2, \\ \mathbf{v} \to \beta &= \mathbf{v}/c, & \mathbf{p} &\to \mathbf{p}/mc, \end{aligned} \tag{2.1.34}$$

resulting in

$$\frac{\mathrm{d}}{\mathrm{d}t}\left[\mathbf{p} - \mathbf{a}\right] - \left(c\nabla\mathbf{a}\right) - c\nabla\phi = 0. \tag{2.1.35}$$

Using the canonical momentum $\mathbf{u} = \mathbf{p} - \mathbf{a}$, the time derivative can now be re-written and we can also substitute $\mathbf{v} = \mathbf{p}/\gamma = (\mathbf{u} + \mathbf{a})/\gamma$:

$$\begin{aligned} \frac{\mathrm{d}}{\mathrm{d}t}\mathbf{u} &= c\nabla\phi - (c\nabla\mathbf{a})\cdot\frac{(\mathbf{u}+\mathbf{a})}{\gamma}, \\ \frac{\mathrm{d}}{\mathrm{d}t}\mathbf{u} &= c\nabla\phi - \frac{1}{\gamma}c\nabla\frac{\mathbf{a}^2}{2} - c\nabla\mathbf{a}\cdot\frac{\mathbf{u}}{\gamma}. \end{aligned} \tag{2.1.36}$$

In the scenario of an electromagnetic pulse at high frequency ω of long pulse duration $\tau \gg 1/\omega$ and sufficiently large spot size $w \gg 1/|k|$ in terms of the fast oscillations, fast and slow dynamics can be treated separately. When averaging over the time of a period $T = 2\pi/\omega$, the terms of linear order $\mathbf{a}$ and the potential ϕ amount to zero:

$$\boxed{\left\langle \frac{\mathrm{d}}{\mathrm{d}t}\mathbf{u} \right\rangle \sim -\left\langle \frac{1}{\gamma}c\nabla\frac{\mathbf{a}^2}{2} \right\rangle,} \tag{2.1.37}$$

which is the ponderomotive force $\mathbf{F}_p$ acting on a single electron. Since $\mathbf{F}_p \sim \nabla\langle\mathbf{a}^2\rangle$, this implies $\mathbf{F}_p \sim \nabla\langle I\rangle$, i.e. the ponderomotive force pushes electrons away from regions of high intensity and is hence a suitable force to drive LWFA.

On the other hand, the ponderomotive force is suppressed for ultrarelativistic particles as $1/\gamma \ll 1$ as considered in relativistic inverse Compton scattering geometries as used in studies of radiation reaction (see Chapters 5, 6 and [99, 100, 162, 163]).

2.2 Radiation Production

In the following, we will consider the production of radiation through processes that are relevant in the course of this work. First, we discuss *inverse Compton scattering* or, in its classical limit, *relativistic Thomson scattering*, where one (linear) or multiple photons (nonlinear) are scattered off a relativistic electron to produce highly energetic radiation. This is followed by a brief outline of the emission of bremsstrahlung by a relativistic electron in the nuclear Coulomb field.

There are two main routes to determine the spectrum of a specific radiative process: In a *classical* picture, we first have to derive the equation of motion of the charged particle and then analyse its trajectory in terms of relativistic Lienard-Wiechert potentials. Solving the corresponding radiation integrals through a Fourier analysis then provides the classical emission spectra [52]. Similar particle motions then provide similar radiation spectra which allows identifying similar behaviour in analogue scenarios. An example is the *figure-of-eight motion*, which can be found in the context of electrons in (alternating) magnetic fields, e.g. synchrotrons and insertion devices (see Appendix B and C), but similarly in an electron in a laser field (see Section 2.1.3). As a result, we identify a wiggler parameter, K, which in one case is related to the magnetic field strength [52] and in the other is the normalised vector potential, a_0 [98].

In a *quantum* picture, the cross sections and spectra are obtained by calculating the matrix element from the Feynman diagrams related to the process. The evaluation of a matrix element, even a simple fundamental tree-level diagram, is relatively tedious, but processes with a similar Feynman representation can be related to each other (crossing symmetry) [164] and the small coupling constant, $\alpha \approx 1/137$, allows a perturbative treatment such that more complicated processes contribute only little overall and can be neglected. However, at high field strengths the number of significantly contributing diagrams increases rapidly, e.g. at $\sim a_0^3$ for nonlinear Compton scattering [47], which makes the evaluation of standard Feynman diagrams not very feasible and computationally challenging. To restore a perturbative treatment *'dressed states'* are being introduced, which replaces, for instance, an electron interacting with many photons with one dressed electron, i.e. an electron in a background field. The dressed state uses the exact classical description of the background field, assuming that the quantum nature of the interaction does not originate in the field itself and that there is no backreaction of the particles to the field. This is referred to as the *Furry picture* [165]. In this picture one dressed or *Volkov state* [166] is equivalent to the infinite sum of standard Feynman diagrams [167].

A review of radiation mechanisms and sources in the context of wakefield accelerators can be found in [80] and [81]. A comprehensive review of high-field interactions is given in [47].

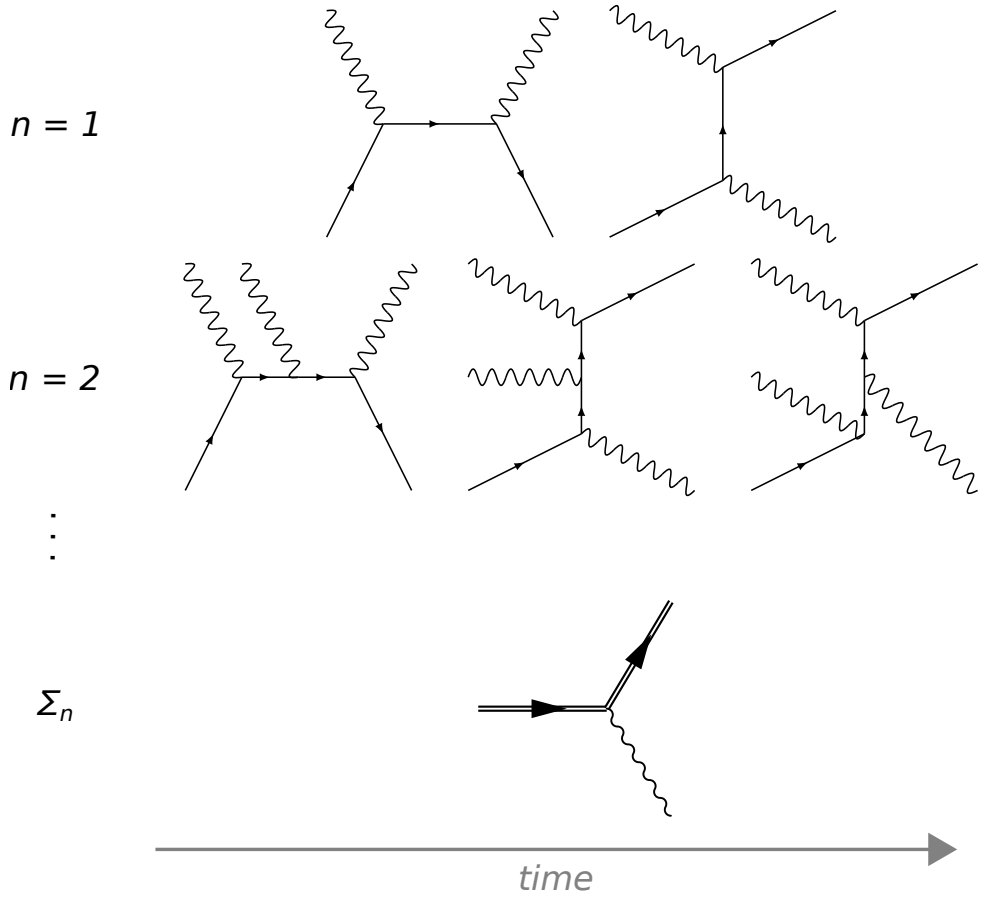


Figure 2.2: Feynman diagrams for Compton scattering for n incoming photons, showing the contributing diagrams for $n = 1$ (top row), $n = 2$ (second row). The bottom row shows the Feynman diagram for nonlinear Compton scattering using dressed electron states (Volkov states). This diagram is equivalent to the infinite sum of all n standard Feynman diagrams as it includes the exact treatment of the classical background field.

2.2.1 Compton Scattering

Compton scattering describes the inelastic scattering of a photon off a charged free or quasi-free particle, typically an electron [168, 169]. The photon transfers energy to the electron and as a result loses energy. In the low energy limit of the photon energy $\omega \to 0$, the interaction becomes fully elastic and is called *Thomson scattering* [170], i.e. Thomson scattering is the low-energy classical limit of Compton scattering. The interaction can be written as follows:

$$\gamma + e^- \longrightarrow \gamma + e^-, \tag{2.2.1}$$

with the corresponding Feynman diagram shown in Figure 2.3.

Kinematics

In the following, we will treat the electron and the incoming photon both as particles and calculate their final momenta relativistically based on energy and momentum conservation.

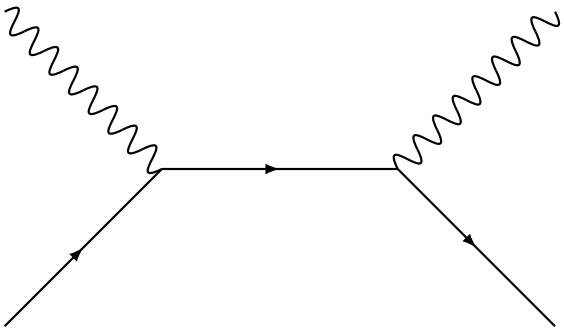


Figure 2.3: Feynman diagram for Compton scattering. The time axis is oriented from left to right. Wiggly lines indicate photons, the arrowed lines represent fermions (arrow towards positive time), here electrons.

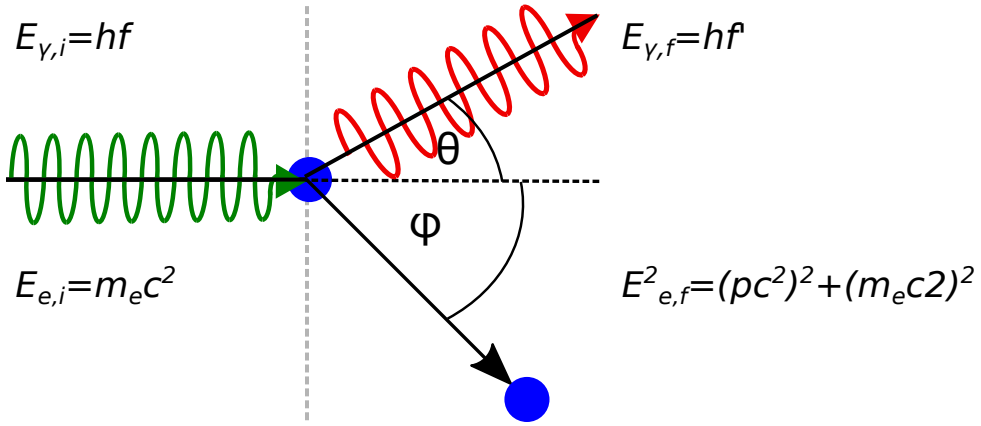


Figure 2.4: Sketch of the kinematics for Compton scattering. A photon of energy $E_{\gamma,i}$ (green) is incident onto an electron at rest (blue), i.e. $E_{e,i} = m_e c^2$, and scatters off it at an angle θ. The electron is scattered at an angle ϕ. The photon and the electron exchange momentum.

Assuming the electron has a negligible initial momentum $\mathbf{p}_{e,i} = \mathbf{0}$ as in Compton's original experiment [168], the total energy hence reduces to the rest energy of the electron $\epsilon_{e,i} = m_e c^2$. The subscript e stands for 'electron' and i for 'initial'. The photon on the other hand has an initial momentum $\mathbf{p}_{\gamma,i}$ and an energy $\epsilon_{\gamma,i} = p_{\gamma,i}c = hf$, where h is Planck's constant and f the frequency of the photon. The subscript γ represents the photon in this interaction. Relying on the conservation of energy, we can postulate that

the sum of energies before and after the interaction have to be equal:

$$\begin{aligned}
\epsilon_{e,i} + \epsilon_{\gamma,i} &= \epsilon_{e,f} + \epsilon_{\gamma,f}, \\
m_e c^2 + hf &= \sqrt{(p_{e,f}c)^2 + (m_e c^2)^2} + hf', \\
hf - hf' + m_e c^2 &= \sqrt{(p_{e,f}c)^2 + (m_e c^2)^2}, \\
\left(hf - hf' + m_e c^2\right)^2 - (m_e c^2)^2 &= (p_{e,f}c)^2, \\
(\epsilon_{\gamma,i} - \epsilon_{\gamma,f} + m_e c^2)^2 - (m_e c^2)^2 &= (p_{e,f}c)^2,
\end{aligned} \tag{2.2.2}$$

where f' is the frequency of the photon after the interaction. Similarly, we can use momentum conservation to find an expression for the momentum of the electron after the scattering:

$$\begin{aligned}
\mathbf{p}_{\gamma,i} &= \mathbf{p}_{e,f} + \mathbf{p}_{\gamma,f} \\
\mathbf{p}_{\gamma,i} - \mathbf{p}_{\gamma,f} &= \mathbf{p}_{e,f} \\
(\mathbf{p}_{\gamma,i} - \mathbf{p}_{\gamma,f})^2 &= (\mathbf{p}_{e,f})^2 \\
(p_{\gamma,i}c)^2 + (p_{\gamma,f}c)^2 - 2p_{\gamma,i}p_{\gamma,f}c^2\cos\theta &= (p_{e,f}c)^2, \\
\epsilon_{\gamma,i}^2 + \epsilon_{\gamma,f}^2 - 2\epsilon_{\gamma,i}\epsilon_{\gamma,f}\cos\theta &= (p_{e,f}c)^2,
\end{aligned} \tag{2.2.3}$$

where $\mathbf{p}$ is a momentum vector and $|\mathbf{p}| = p$ its corresponding length. θ is the angle between incoming and outgoing momentum vector of the photon (see Figure 2.4). Setting Equations (2.2.2) and (2.2.3) equal, we find the familiar equation for the angular dependent change in wavelength of a photon performing Compton scattering with an electron:

$$\lambda_{final} - \lambda_{initial} = \frac{h}{m_e c}\left(1 - \cos\theta\right) = \lambda_C\left(1 - \cos\theta\right), \tag{2.2.4}$$

where $\lambda_C = hm_e c$ is the Compton wavelength. Similarly, there is an equation for the emission angle of the electron:

$$\cot(\phi) = \left(1 + \frac{hf}{m_e c^2}\right)\tan(\theta/2). \tag{2.2.5}$$

In terms of photon energy we can write

$$\boxed{\epsilon_{\gamma,f} = \frac{\epsilon_{\gamma,i}}{1 + \frac{\epsilon_{\gamma,i}}{m_e c^2}(1 - \cos\theta)},} \tag{2.2.6}$$

where the final energy, $\epsilon_{\gamma,f}$, only depends on the energy of the incoming photon, $\epsilon_{\gamma,i}$, and the scattering angle, θ. Polar plots of the final photon energies for different initial photon energies are shown in Figure 2.5 (left). At low energies $\epsilon_{\gamma,i} \to 0$ and $\epsilon_{\gamma,f} \to E_{\gamma,i}$, and the

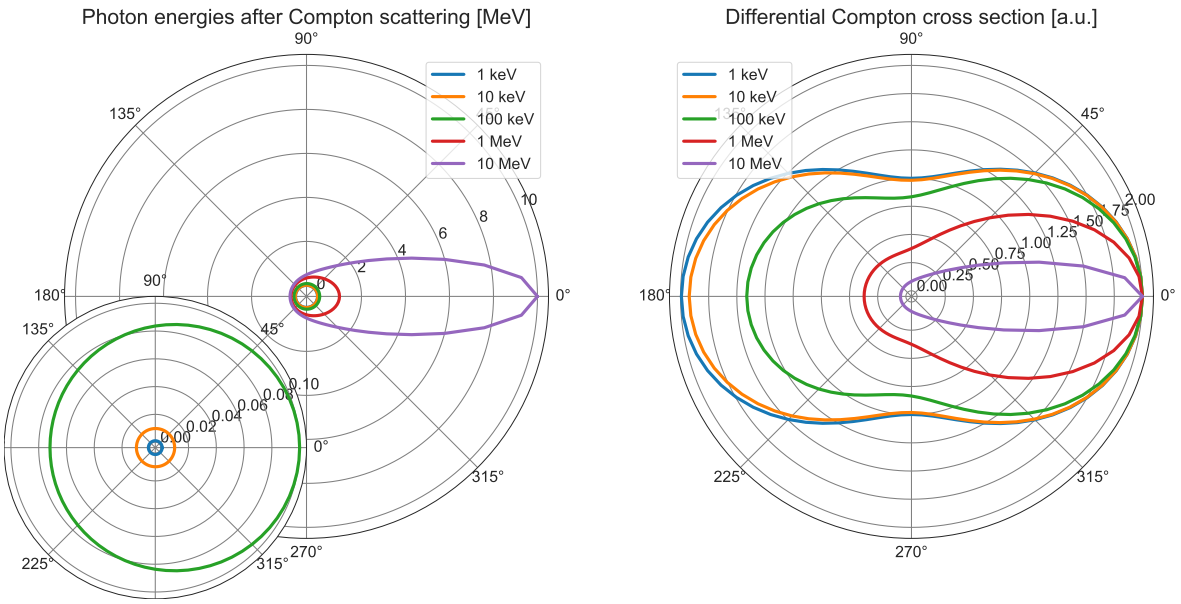


Figure 2.5: Left: Polar plot of photon energies after Compton scattering from an electron at rest for different incoming photon energies (legend) for up to 100 keV (left, inset) and up to 10 MeV (left). The incoming photon travels on the zero degree axis. The energy axis is linear and the numbers show the energy in MeV. Right: Polar plot of the differential cross section in arbitrary units for photon scattering angles calculated using Equation (2.2.7) *for different initial photon energies (legend).*

emitted energy becomes approximately independent of the scattering angle θ [see Figure 2.5 (left, inset)]. At higher energies $\epsilon_{\gamma,i} > m_e^2 c$, the energy distribution is being skewed towards the forward direction of the incoming photon and the energy of the photon after the interaction is maximised at zero degrees with $\epsilon_{\gamma,f} = \epsilon_{\gamma,i}$, i.e. no significant amount of energy is transferred to the electron [see Figure 2.5 (left)].

Cross-Section

The cross section for Compton scattering, again assuming the electron is initially at rest, is given by the spin-averaged *Klein-Nishina formula* [169]:

$$\boxed{\frac{\mathrm{d}\sigma_{\gamma e}}{\mathrm{d}\cos\theta} = \pi r_e^2 \left(\frac{\omega'}{\omega}\right)^2 \left(\frac{\omega'}{\omega} + \frac{\omega}{\omega'} - \sin^2\theta\right),} \tag{2.2.7a}$$

$$\boxed{\frac{\mathrm{d}\sigma_{\gamma e}}{\mathrm{d}\cos\theta} = \pi r_e^2 \left(\frac{\epsilon_f}{\epsilon_i}\right)^2 \left(\frac{\epsilon_f}{\epsilon_i} + \frac{\epsilon_i}{\epsilon_f} - \sin^2\theta\right),} \tag{2.2.7b}$$

in terms of the initial and final frequency and energy, respectively. For very low energetic photons in the limit $\omega \to 0$ and $\omega'/\omega \to 1$, the cross section simplifies to

$$\boxed{\frac{\mathrm{d}\sigma_{\gamma e}}{\mathrm{d}\cos\theta} = \pi r_e^2 (1 + \cos^2\theta),} \tag{2.2.8}$$

which is independent of photon energy and has a total cross section of $\sigma_{\gamma e} = \sigma_T = 8\pi r_e^2/3$, with $r_e = e^2/4\pi\epsilon_0 m_e c^2 = 6.65 \times 10^{-29}\,\mathrm{m}^2$ [52]. This is the classical Thomson scattering cross section, σ_T. The total cross section using the Klein-Nishina equation amounts to:

$$\boxed{\sigma_{\gamma e} = 2\pi r_e^2 \left[\frac{1+x}{x^3}\left(\frac{2x(1+x)}{1+2x} - \ln(1+2x)\right) + \frac{1}{2x}\ln(1+2x) - \frac{1+3x}{(1+2x)^2}\right],} \tag{2.2.9}$$

with $x = \epsilon_\gamma/m_e c^2$, so that in the two limits this becomes

$$\sigma_{\gamma e} = \sigma_T \times \begin{cases} (1 - 2x + \frac{26x^2}{5}) & \text{for } x \ll 1, \\ \frac{3}{8}\frac{1}{x}\left(\ln 2x + \frac{1}{2}\right) & \text{for } x \gg 1, \end{cases} \tag{2.2.10}$$

so that $\sigma_{\gamma e} \to \sigma_T$ for $x \to 0$, which is the limit of Thomson scattering, and $\sigma_{\gamma e} \to 0$ for $x \to \infty$, which indicates that ultra-relativistic photons are less likely to scatter.

The differential cross section is shown in a polar plot in Figure 2.5 (right) for different incoming photon energies. At low photon energies, the cross section and the photon spectrum are symmetric in forward and backward direction following Thomson scattering [see Equation (2.2.8)]. At increasing photon energies reaching the X-ray and gamma regime, the photon is preferentially scattered in the forward direction at lower momentum transfers and falling to 0 at $\theta = 0$.

2.2.2 Linear Inverse Compton Scattering

In the previous section, Compton scattering and its classical low-energy limit Thomson scattering were discussed for a single photon interacting with an electron that is initially at rest. Here, we will consider the special case of a relativistic electron of energy $\epsilon \gg m_e c^2$ interacting with a single photon. Whilst in 'standard' Compton scattering momentum is transferred from the photon to the electron, resulting in a longer wavelength of the scattered photon, we will see that in this scenario the photon gains considerable amount of energy from the electron. Due to this inversion of the energy balance relative to standard Compton scattering, this special case is referred to as *inverse* Compton scattering (ICS). In the limit discussed here, it is also referred to as relativistic Thomson scattering or Compton backscattering. In this section, we will neglect nonlinear effects such as the emission of higher harmonics or the relativistic mass gain of electrons in an intense laser field. These phenomena will be discussed in the following section related to nonlinear inverse Compton scattering.

Kinematics

To treat this scattering process similarly to the standard Compton scattering discussed in the previous section, we will shift to the rest frame of the electron, where the initial condition, that the electron is at rest, is again satisfied. In the following, quantities in the lab frame, S, will be denoted as before, for instance ϵ, θ. In the rest frame of the electron, S', quantities will be denoted as dashed quantities, i.e. ϵ', θ' and so on.

Assume a single relativistic electron with a relativistic Lorentz factor, γ, moving in x and a photon of energy ϵ_i with an incident angle θ_i relative to this axis. In the rest frame of the electron, the photon experiences a relativistic Doppler-shift so that its energy in this frame, ϵ_i', is

$$\epsilon_i' = \gamma\epsilon_i(1 - \beta \cdot \mathbf{e_k}) = \gamma\epsilon_i(1 - \beta\cos\theta) \approx \gamma\epsilon_i(1 - \cos\theta), \tag{2.2.11}$$

where we assumed that the electron is highly relativistic and $\beta \approx 1$. In a head-on collision ($\theta = \pi$), the photon energy in the electron rest frame is maximised by a factor of 2γ. The angles transform via

$$\sin\theta' = \frac{\sin\theta}{\gamma(1 + \beta\cos\theta)},\ \cos\theta' = \frac{\cos\theta + \beta}{1 + \beta\cos\theta}. \tag{2.2.12}$$

In this frame, the scattered photon energies follow the same relation as for standard Compton scattering [see Equation (2.2.6)], but in terms of dashed quantities:

$$\epsilon_f' = \frac{\epsilon_i'}{1 + \frac{\epsilon_i'}{m_e c^2}(1 - \cos\alpha')}, \tag{2.2.13}$$

where α' is the difference between the incident and outgoing angle and determined by

$$\cos\alpha' = \mathbf{n_f'} \cdot \mathbf{n_i'} = \cos\theta_i'\cos\theta_f' + \sin\theta_i'\sin\theta_f'\cos(\phi_i' - \phi_f'), \tag{2.2.14}$$

with the angles ϕ' denoting the azimuthal angles of the photon. In this frame, the photon is losing energy as it transfers momentum to the electron, as expected for Compton scattering. In a head-on collision in the lab frame for $\gamma \sim 1000$ and $E_i = 1\,\mathrm{eV}$, the energy in the electron rest frame becomes $\epsilon_i' = 2\,\mathrm{keV}$, with $\epsilon_i' \ll m_e c^2$ or in terms of lab-frame quantities $\epsilon_i \ll m_e c^2/\gamma$. This means that under these conditions this interaction corresponds to Thomson scattering.

In order to calculate the final photon energy in the laboratory frame, S, we have to boost back from the rest frame of the electron, S', which results in another amplifying factor of $\sim \gamma$:

$$\epsilon_f = \epsilon_f'\gamma(1 + \beta\cos\theta_f') \approx \epsilon_f'\gamma(1 + \cos\theta_f') \propto \gamma^2\epsilon_i, \tag{2.2.15}$$

where the angles have to be transformed back into the lab frame as well. We now see that in the lab frame $\epsilon_f > \epsilon_i$, so that the photon gains energy in the interaction and the name *inverse* Compton scattering is justified. The emitted energy is maximised in a head-on collision and when radiated in the propagation direction of the relativistic electron. The photon energy is then boosted by $(2\gamma)^2$ to $\epsilon_{f,max} = 2\gamma\epsilon'_f = 2\gamma\epsilon'_i = 4\gamma^2\epsilon_i$. In the rest frame of the electron, this corresponds to $\epsilon'_i = \epsilon'_f$, which again indicates Thomson scattering and motivates another common name for this process, *relativistic Thomson scattering*.

Cross-Section

$\epsilon_i = m_e c^2/\gamma$ would for $\epsilon_i = 1\,\mathrm{eV}$ require $\gamma \sim 5 \times 10^5$ or $\epsilon \sim 250\,\mathrm{GeV}$. As a result, $\epsilon_i \ll m_e c^2/\gamma$ holds for all relevant scenarios and the interaction is in the rest frame accurately described by the Thomson cross section as given in Equation (2.2.8), but in quantities of the rest frame S':

$$\frac{\mathrm{d}\sigma'}{\mathrm{d}\cos\theta'} = \pi r_e^2 \left(1 + \cos^2\theta'\right). \tag{2.2.16}$$

For $\gamma \gg 1$ the transformation of the angles results in the so-called 'headlight' or 'searchlight effect' since $\cos\theta \to 1$ [see Equation (2.2.12)], so that the photons are preferentially emitted in the direction of the electron momentum vector. If we consider a cross section normal to the direction of the boost $\sigma' \to \sigma$ and $\sigma = \sigma_T$, the Thomson cross section, so that the cross section is again independent of energy as long as $\epsilon_i \ll m_e c^2/\gamma$.

Total emitted energy

In the Thomson limit, the cross section of the interaction is independent of the photon and electron energy. The total number of scattered photons, N_X, is then given by the Thomson cross section multiplied by the number of electrons, N_e, and photons, N_L, in an area πw_0^2 [81]:

$$\boxed{N_X = \frac{\sigma_T}{\pi w_0^2} N_L N_e.} \tag{2.2.17}$$

The total energy emitted in this interaction is simply the sum of the individual photon energies. The total energy emitted by an electron bunch of distribution $\mathrm{d}N_e/\mathrm{d}\gamma$ is

$$\boxed{\mathcal{E}_{total} = \int \epsilon_f(\gamma) \frac{\sigma_T}{\pi\omega_0^2} N_L \frac{\mathrm{d}N_e}{\mathrm{d}\gamma} \mathrm{d}\gamma \approx \langle\epsilon_f\rangle N_X \propto \langle\gamma^2\rangle N_X,} \tag{2.2.18}$$

where we would generally have to integrate over all incoming and outgoing angles and photon energies to obtain the emitted energy. Since the number of photons, N_L, is proportional to the intensity and N_e to the charge Q, we also find $\mathcal{E}_{total} \propto a_0^2 \langle\gamma^2\rangle Q$.

Experimental modifications of the spectrum

In a real setting, the ICS spectrum is modified by experimental parameters that result in an energy spread of the emitted radiation, $\Delta\epsilon_f$. These are, for instance, the energy spread of the electron beam, the bandwidth of a realistic laser pulse, and a range of angles between the electrons and photons introduced by the divergence of the electron bunch and the focusing of the laser pulse. The effective spectrum has, for instance, been investigated experimentally in a laser wakefield setup in [171]. In addition, when the normalised vector potential approaches unity, nonlinear effects start to modify the spectrum. This is discussed in the following section.

2.2.3 Nonlinear Inverse Compton Scattering

At higher intensities, i.e. $a_0 \to 1$ and $a_0 > 1$, the character of Compton scattering changes as nonlinear effects gain significance and the electrons experience a relativistic mass increase while performing a figure-of-eight motion (see Section 2.1.3). In a classical picture, a Fourier analysis of the particle trajectories shows that this gives rise to higher harmonic radiation [98]. In a quantum picture, the contributions of multi-photon interactions described by higher-order Feynman diagram become increasingly significant (see Figure 2.2). The relativistic mass increase results in red-shifting of the emitted radiation [98]. This behaviour draws parallels in the description of electrons in insertion devices that is also described by the figure-of-eight motion (see Section 2.1.3 and C.2). There, the wiggler parameter, K, indicates whether distinct harmonics ($K \ll 1$) or broadband radiation is emitted ($K \gg 1$). In the case of (inverse) Compton scattering, a *laser wiggler*, the parameter a_0 replaces K, so that linear ICS corresponds to the undulator regime ($a_0 \ll 1$) and nonlinear ICS to the wiggler regime ($a_0 \gg 1$). The emission angle (divergence) is then similarly $\sim a_0/\gamma$ in the polarisation axis for $a_0 \gg 1$ [172].

The process of n photons scattering from a single electron resulting in the emission of one more energetic photon is described by

$$n\gamma_L + e^- \longrightarrow \gamma + e^-, \tag{2.2.19}$$

which is represented by the Feynman diagram shown in Figure 2.6.

Kinematics

Assuming all n photons have the same energy ϵ_i and are parallel to each other, the relativistic kinematics for the multi-photon process are identical to the single-photon process discussed in the previous section by simply substituting $\epsilon_i \to n\epsilon_i$. As a result, the

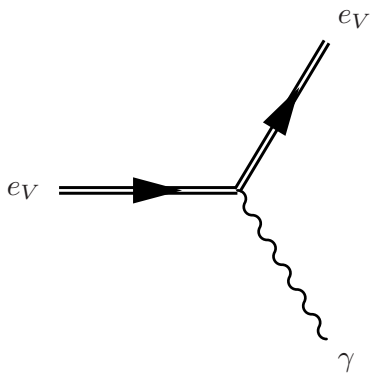


Figure 2.6: Feynman diagram for nonlinear Compton scattering. The double lines with arrows indicate dressed electron states. The time axis is oriented from left to right.

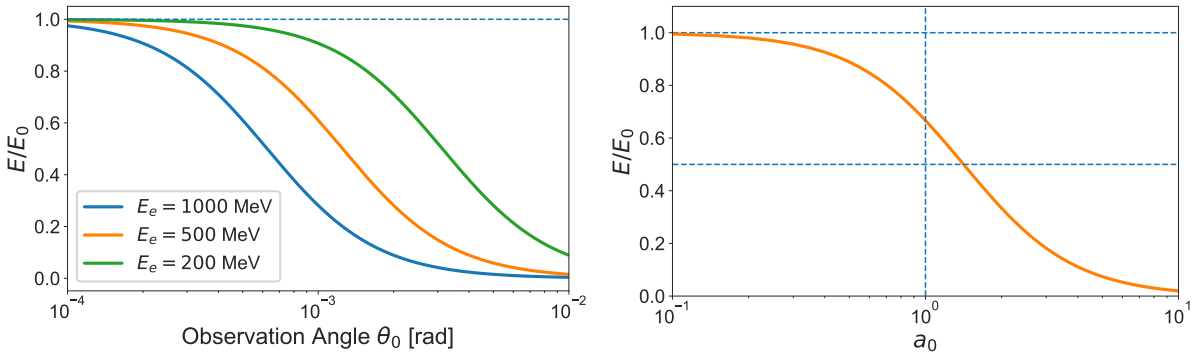


Figure 2.7: Left: Energy of the emitted radiation relative to the peak energy, E_0, as a function of the observation angle θ_0 for different electron energies (legend). Right: Decrease in the peak photon energy (redshifting) relative to the peak photon energy in the limit $a_0 \to 0$ as a function of a_0 (right).

energy of the scattered photon in the rest frame, E'_f, is then

$$\epsilon'_f = \frac{n\epsilon'_i}{1 + \frac{n\epsilon'_i}{m_e c^2}(1 - \cos\alpha')}, \tag{2.2.20}$$

including the effect of the mass increase $\left(m_e \to m_e^* = m_e\sqrt{1+a_0^2}\right)$, the energy of the radiation in the laboratory frame is then given by [98]

$$\boxed{\epsilon_f \approx \frac{2\gamma^2(1-\cos\theta)n\epsilon_i}{1 + a_0^2/2 + (\gamma\theta_0)^2},} \tag{2.2.21}$$

where the contribution $(\gamma\theta_0)^2$ leads to a fall-off of the photon energy off-axis, so that it reaches $\epsilon_f/2$ at about $\theta_0 \sim 1/\gamma$ and the emitted radiation is confined to a cone of that opening angle [see Figure 2.7 (left)].

The equation also shows that higher a_0 leads for a fixed harmonic n to a redshifting of the radiation, $\epsilon_f \propto 1/a_0^2$ for $a_0 \gg 1$. This decrease in energy from the case of $a_0 \to 0$

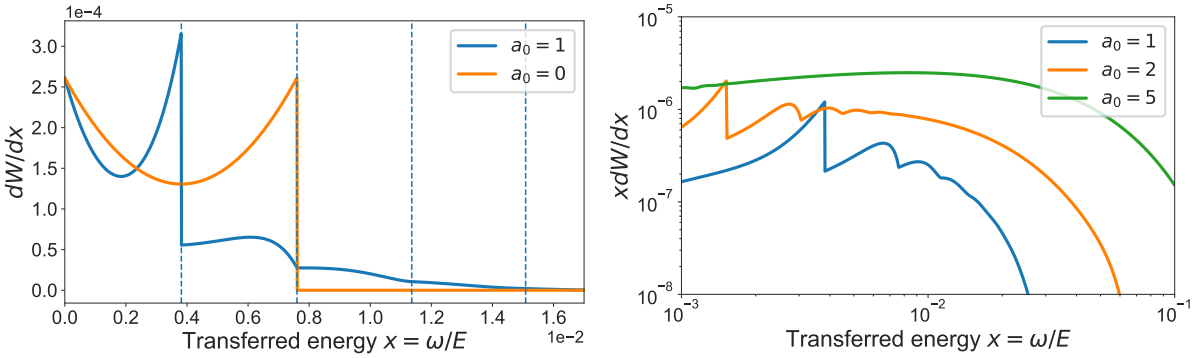


Figure 2.8: Left: Differential emission rates for Compton scattering (circular polarisation) at an intensity of $a_0 = 1$ (blue) and in the linear limit of $a_0 \to 0$ (orange) as a function of the energy transferred from the electron to the emitted photon. Right: Energy times differential emission rates for Compton scattering (circular polarisation) at increasing intensities from $a_0 = 1$ (blue), 2 (orange) to 5 (green) as a function of the energy transferred from the electron to the emitted photon. The spectral shape smooths out with increasing a_0 and resembles a synchrotron spectrum. Both axes are logarithmic. The plots are adapted from [173].

is shown for a fixed harmonic in Figure 2.7 (right) as a function of a_0. At $a_0 = 10$, for instance, the photon energy has reached a value less than 10% of its original value. Whilst a fixed harmonic loses energy with increasing a_0, high a_0's give rise to a larger number of higher harmonics, such that the emitted energy in an interaction increases overall. This behaviour will be discussed in more detail in the following.

Cross-Section

Since the equation of motion takes the form of a figure-of-eight motion, it is not surprising that the related emission rate consists of a series of Bessel functions, similarly as an undulator or wiggler. For instance, the scattering rate (spin-averaged and unpolarised states in/out) for n scattered photons of frequency ω for circular polarisation is in natural units given by [131, 173]

$$\frac{\mathrm{d}W_n}{\mathrm{d}x} = \frac{\alpha m^2}{4\epsilon}\left[-4J_n^2 + a_0^2\left(1 - x + \frac{1}{1-x}\right)\left(J_{n-1}^2 + J_{n+1}^2 - 2J_n^2\right)\right], \tag{2.2.22}$$

where we have to evaluate the sum of n differential cross sections to reproduce the complete spectrum, and x is the fraction of the energy that is transferred from the electron into radiation. α is the fine-structure constant, ϵ the energy of the electron and m its mass. J_n denotes a Bessel function of first kind of order n with the argument z:

$$z = \frac{2a_0}{\sqrt{1+a_0^2}}\frac{\sqrt{x[nu-(1+nu)x]}}{u(1-x)}, \qquad u = \frac{4\epsilon\omega}{m^2(1+a_0^2)}. \tag{2.2.23}$$

Also note that the emission rates for the n-th harmonic depend on the laser polarisation. The rates for linear polarisation are given in Appendix F.

Figure 2.8 shows the emission rate, $\mathrm{d}W/\mathrm{d}x$, as a function of the transferred energy for values of a_0. First, for the limit of $a_0 \to 0$ (orange), which corresponds to linear Compton scattering, i.e. $n = 1$, and the result from the Klein-Nishina equation. The spectrum rises up to the Compton edge (dashed line) where it sharply falls off. The blue line shows the emission rates evaluated for $a_0 = 1$: the distinct Compton edge is down-shifted to about half of its original energy. On the other hand, higher harmonics, up to $n = 4$, are emerging and are also down-shifted, with a maximum energy of about twice the Compton edge for $a_0 \to 0$.

The most significant contribution is still the red-shifted fundamental order, but even for a moderate intensity of $a_0 = 1$ we already had to evaluate the emission rates of $n = 4$ harmonics to reproduce the high-energy tail of the spectrum accurately. The highest significant order scales as $\sim a_0^3$ [47], such that the number of additional harmonics and related emission rates that have to be evaluated increases rapidly, e.g. $n = 1000$ for $a_0 = 10$. As a result, this approach becomes infeasible relatively quickly. As an alternative, we can for $a_0 \gg 1$ approximate the emission spectrum by the *quantum synchrotron function* [162, 173] (see Appendix G). Figure 2.8 (right) shows the emission rate (times energy) for increasing values of a_0. Even for these moderate intensities, the high-energy component and relatively quickly also lower energy band structures disappear, and give rise to a smooth synchrotron-like emission spectrum, which indicates that this approach is valid (see for instance [173] for a more rigorous comparison). Whilst the highest significant order increases at a_0^3, the energy of the emitted radiation is red-shifted at $\epsilon_f \propto 1/a_0^2$ for $a_0 \gg 1$, such that the net energy gain is linear in a_0.

2.2.4 Bremsstrahlung

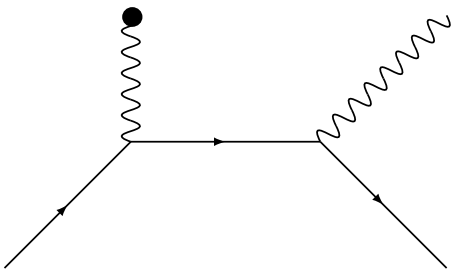


Figure 2.9: Feynman diagram for bremsstrahlung. The time axis is oriented from left to right. Wiggly lines indicate photons, the dark circle shows the nuclear field. The arrowed lines represent fermions, here electrons.

A charged particle can interact with the nuclear Coulomb field to produce bremsstrahlung,

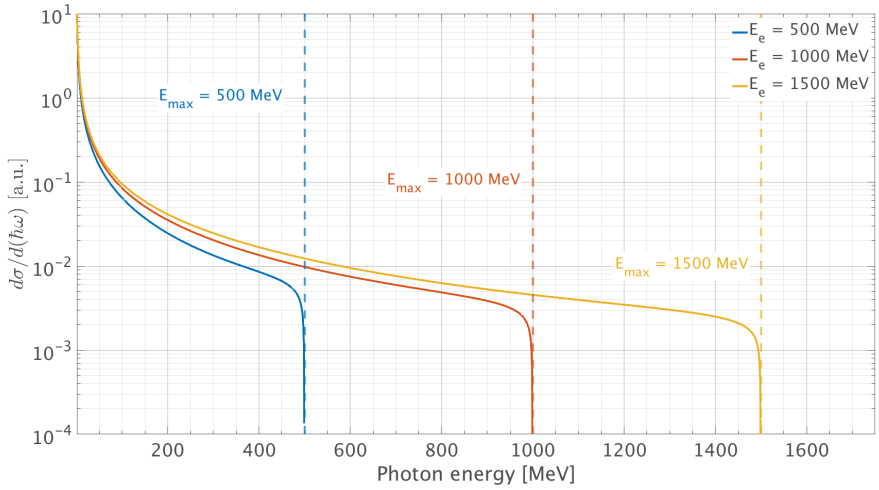


Figure 2.10: Differential cross section of bremsstrahlung for different electron energies as a function of the emitted photon energy calculated using Equation (2.2.25)*. The dashed lines indicate the high-energy cut-off or maximum energy, E_{max}, that is equal to the electron energy.*

which roughly translates from German into 'braking radiation'. For an electron, this process is described by

$$Z + e^- \longrightarrow Z + e^- + \gamma \tag{2.2.24}$$

or in terms of the Feyman diagram shown in Figure 2.9. In the quantum picture, the electron exchanges momentum with a virtual photon from the Coulomb field before radiating a photon. From the classical view, the charged particle is decelerated ('braked') in the Coulomb field which results in the production of radiation.

In the limit of small photon energies relative to the initial electron energy, $\hbar\omega \ll \epsilon$, and relativistic initial and final electron energies, $\epsilon, \epsilon' \gg mc^2$ the differential cross section can be written as [52]:

$$\frac{d\sigma}{d(\hbar\omega)} \approx \frac{16}{3}\frac{Z^2e^2}{c}\left(\frac{z^2e^2}{mc^2}\right)^2\left(1 - \frac{\hbar\omega}{\epsilon} + \frac{3}{4}\frac{(\hbar\omega)^2}{\epsilon^2}\right) \times \left[\ln\left(\frac{2\epsilon(\epsilon - \hbar\omega)}{mc^2\hbar\omega}\right) - \frac{1}{2}\right], \tag{2.2.25}$$

where Z is the charge number of the nucleus and z the number of electrons in the atomic orbit. For $\hbar\omega \ll \epsilon$ the doubly differential cross is then

$$\frac{d^2\sigma}{d\omega d\Omega_\gamma} = \left[\frac{3}{2\pi}\gamma^2\frac{(1 + \gamma^4\theta^4)}{(1 + \gamma^2\theta^2)^4}\right] \cdot \frac{d\sigma}{d\omega}, \tag{2.2.26}$$

which indicates that for highly relativistic electron the emitted radiation is confined to a narrow forwards-pointing cone of angle $\ln\gamma/\gamma$ for $\gamma \gg 1$. The emission of photons at energies $\hbar\omega \ll E$ is strongly favoured, whereas the cross section falls off towards the maximum emitted energy which is the initial energy of the electron (see Figure 2.10). The

complete cross section for bremsstrahlung in the Born approximation can be found in the Appendix E.1, along with a description including screening in Appendix E.2.

2.3 Radiation Reaction

In the previous sections, we discussed the emission of radiation from charged particles, in particular through inverse Compton scattering. Based on conservation rules, the particles lose energy in the process and also have to experience a knock-back force whenever they radiate. Such a knock-back, commonly referred to as *radiation reaction (force)* or *radiation friction (force)*, can significantly alter the particle dynamics in strong electromagnetic fields. Whilst the instantaneous force felt by the emitting particles is small in most settings, it is particularly important in the astrophysical context [109, 136] and will be the subject of research at high-intensity laser facilities [35–39]. Here, a single particle can emit multiple energetic photons in a short span of time and the radiation reaction force becomes comparable to the Lorentz force. In extreme cases, the energy emitted by the particle approaches its initial energy, which then occurs in a regime where the process has to be modelled in a quantum picture, i.e. we then have to consider *quantum radiation reaction* [130–132, 174].

Radiation reaction can be investigated in different experimental geometries using intense laser pulses. Suitable geometries are, for instance, the collision of a relativistic electron beam with an intense laser pulse [130, 162, 163], laser-solid interactions [116] and an electron in the standing wave of multiple intense laser pulses [175]. Another approach is the use of aligned crystals [142, 145], where an electron or positron is undulated by the varying atomic potential of the crystal lattice. In this work, we will focus on the measurement of radiation reaction in the collision of a relativistic electron beam with an intense laser pulse.

Radiation reaction is a fundamental phenomenon of electrodynamics, but surprisingly there is no universally accepted and practicable description across a variety of regimes. In the following, different descriptions will be introduced, starting with classical descriptions of radiation reaction highlighting their motivation and limitations, followed by the quantum corrections and modifications to these, indicating how they differ qualitatively, for instance, with respect to their experimental signatures in the post-interaction electron spectrum. This section uses in large parts [102] and [132] as guidance. A more detailed overview of this topic can be found in parts of [47] and in [102].

2.3.1 Regimes of Radiation Reaction

There are different parameters that indicate the significance of radiation reaction effects and signal the appropriate description that describes the dynamics most accurately in a

particular regime.

The *classical radiation reaction parameter*, R_c, for instance, indicates how much energy is radiated in a single cycle relative to the electron energy in the average rest frame, $f = \epsilon_{rad}/(\gamma' m) = 4\pi R_c/3$. R_c is in natural units and in terms of experimental variables given by [102, 174]:

$$\boxed{\begin{aligned} R_c &= \frac{\alpha a_0^2 \gamma_0 (1+\beta_0)\omega_0}{m} \\ &\approx 0.13 \left(\frac{\epsilon_0}{500\,\mathrm{MeV}}\right)\left(\frac{I_0}{10^{22}\,\mathrm{W/cm^2}}\right)\left(\frac{\lambda}{\mu\mathrm{m}}\right), \end{aligned}} \tag{2.3.1a}$$

where α denotes the fine-structure constant, a_0 the normalised vector potential, ω_0 is the laser frequency and m is the electron mass, λ is the laser wavelength, I_0 the peak intensity and ϵ_0 the initial energy of the electron. $\gamma' = (1+a_0^2)^{1/2}$ and $\beta' = a_0(1+a_0^2)^{-1/2}$. Significant radiation damping occurs for $R_c \geq 0.24$ [133], when the energy loss per period approaches 10% of the electron energy. For $R_c \geq 1$ [174], we reach the *radiation-dominated regime*.

We can also, on the other hand, estimate the magnitude of a specific radiation reaction force relative to the Lorentz force. In the context of the collision of a relativistic electron beam of energy γ with a laser pulse of intensity a_0, the relative magnitude of the Landau-Lifschitz radiation reaction force (see Section 2.3.2), for instance, is given by [133]

$$\boxed{\psi = \gamma^2 a_0 \frac{2 r_e \omega}{3c},} \tag{2.3.2}$$

where $\psi \ll 1$ indicates that radiation reaction effects are negligible and $\psi \to 1$ that the radiation reaction force becomes comparable to the Lorentz force.

Beyond these classical descriptions, we can also find a parameter that indicates how 'quantum' an interaction will be. The *quantum nonlinearity parameter*, for instance, indicates the strength of the electric field (in the rest frame) relative to the critical field of QED:

$$\eta = E_{RF}/E_{crit}, \tag{2.3.3}$$

with the critical field for quantum electrodynamics $E_{crit} \approx 1.33 \times 10^{18}\,\mathrm{Vm^{-1}}$ [25, 26]. In the collision of an electron and a laser pulse at an angle θ this becomes

$$\boxed{\eta = \frac{(1-\cos\theta)\hbar\omega_0 \gamma a_0}{m_e c^2},} \tag{2.3.4}$$

where ω_0 is the laser frequency, m_e the electron mass, c the speed of light, γ the Lorentz

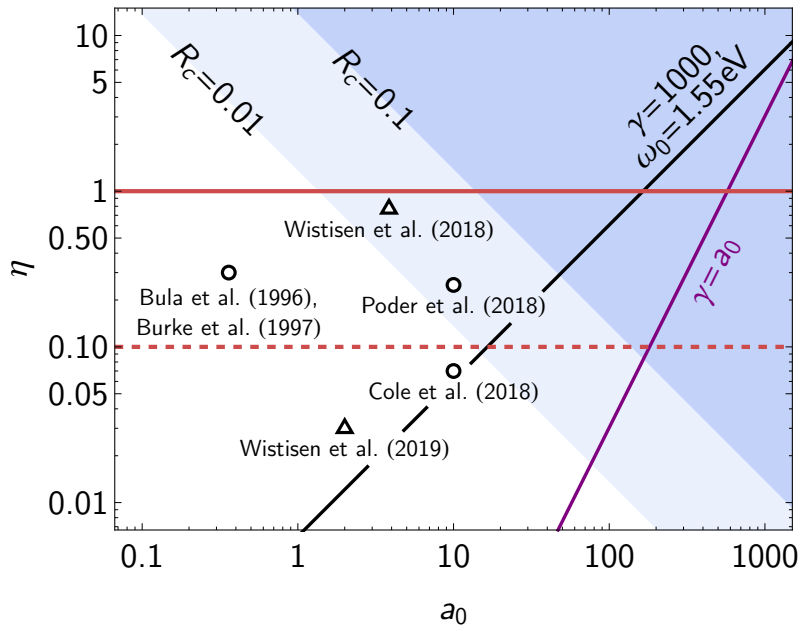


Figure 2.11: Overview of radiation reaction regimes and experiments as a function of quantum nonlinearity parameter, η, and the normalised vector potential, a_0. Note that both axes are logarithmic. Moving upwards on the y-axis increases the quantum character of an interaction, whereas moving sideways increases the nonlinearity. The diagonal black line indicates how we move at a fixed electron energy when increasing a_0. The red lines indicate when quantum effects become significant (dashed) and dominate (solid), whereas the blue shaded region show when we enter the classical radiative dominated regime based on R_c. Circles indicate experiments colliding an electron beam and a laser pulse. The triangle denotes an experiment based on planar channeling. Reprinted from [102].

factor of the electron and a_0 is the normalised vector potential. Quantum effects dominate when $\eta \to 1$, which can be achieved by high intensities and electron energies. This also coincides with the onset of vacuum pair production, where the electric fields become so strong that virtual pairs can be extracted directly from of the vacuum (see Section 2.4.4). We can similarly give a relation in terms of a_0 and γ_0 to show a threshold when quantum effects dominate

$$a_0\gamma_0 > \frac{m_e c^2}{2\hbar\omega_0}, \tag{2.3.5}$$

where we assumed $\theta = 180°$.

Figure 2.11 is a map of η and a_0, that shows significant regimes for the parameters η and R_c, as well as previous experimental measurements of radiation reaction. Circles indicate colliding-pulse experiments, whereas the triangle shows the parameter of an experiment using aligned crystals. The shaded regions indicate (on a logarithmic scale) the corresponding values of R_c, which increase diagonally across the image. The black line indicates the position on the plane when increasing the intensity of the laser a_0 in an interaction with an electron beam of fixed energy $\gamma = 1000$, which corresponds to moving

diagonally on the plane. The red lines indicate different values of η. At $\eta = 0.1$ (dashed) quantum effects become significant, whereas the solid red line indicates the threshold to the quantum dominated regime. Moving upwards on this graph (increasing η) translates into more 'quantum', whereas moving in x (a_0) results in a higher degree of nonlinearity in the interaction.

Locally constant field approximation

An important assumption that is commonly used in radiation reaction models is that the electric field remains constant over the *formation length* of the photon, l_f. The formation length can be estimated geometrically by comparing its overlap with its emission cone [102]

$$\frac{l_f}{C} \approx \frac{1}{2\pi a_0}, \tag{2.3.6}$$

where $C = 2\pi r'$ and

$$r' = \frac{a_0}{\gamma_0(1+\beta_0)\omega_0}, \tag{2.3.7}$$

where $l_f/C \ll 1$ is satisfied for large a_0. If we also include the requirement that $a_0^3 \gg \eta$, this approximation is then called the *locally constant field approximation* (LCFA). Requiring $a_0 \gg 1$ and $a_0^3 \gg \eta$ means that the particle has to be ultrarelativistic and the background field is weak compared to critical field of QED. Within the LCFA the background field can be treated classically and it can be assumed that, whilst emission events are governed by (strong-field) QED, the particle trajectories between emission events can be determined classically. As a result, this enables a semi-classical treatment of high-field (radiation reaction) processes, for instance, in numerical implementations.

2.3.2 Classical Radiation Reaction

There is a variety of classical descriptions of radiation reaction rooted in classical electrodynamics [176]. We will focus on the two most commonly applied models and their implications: the Lorentz-Abraham-Dirac (LAD) equation [127] and the Landau-Lifschitz (LL) description [128].

Lorentz-Abraham-Dirac Equation (LAD)

An intuitive way to derive an expression for a radiation reaction force is considering the conservation of energy [52]. The synchrotron emission power, P, of an electron with charge e is given by the Larmor power formula:

$$P = \frac{e^2}{6\pi\epsilon_0 c^3}\dot{\mathbf{v}}^2, \tag{2.3.8}$$

where $\mathbf{v}$ is the velocity vector of the particle and $\dot{\mathbf{v}}$ its acceleration, c the speed of light and ϵ_0 the dielectric constant. By requiring that the emitted radiation power corresponds to the work done on the radiating particle by the radiation reaction force, we can write

$$\int_{t_1}^{t_2} \mathbf{F}_{rad} \cdot \mathbf{v} \mathrm{d}t = -\int_{t_1}^{t_2} P \mathrm{d}t, \tag{2.3.9}$$

$$= \frac{e^2}{6\pi\epsilon_0 c^3} \int_{t_1}^{t_2} \ddot{\mathbf{v}} \cdot \mathbf{v} \mathrm{d}t - \frac{e^2}{6\pi\epsilon_0 c^3} (\dot{\mathbf{v}} \cdot \mathbf{v}) \Big|_{t_1}^{t_2}, \tag{2.3.10}$$

where we used integration by parts. For a periodic motion or $\dot{\mathbf{v}} \cdot \mathbf{v} = 0$ at $t = t_1$ and $t = t_2$, we can write:

$$\int_{t_1}^{t_2} \left(\mathbf{F}_{rad} - \frac{e^2}{6\pi\epsilon_0 c^3} \ddot{\mathbf{v}} \right) \cdot \mathbf{v} \mathrm{d}t = 0, \tag{2.3.11}$$

so that we can identify the radiation reaction force, $\mathbf{F}_{rad}$, as

$$\mathbf{F}_{rad} = \frac{e^2}{6\pi\epsilon_0 c^3} \ddot{\mathbf{v}} = m\tau\ddot{\mathbf{v}}, \tag{2.3.12}$$

with the *characteristic time*, τ:

$$\tau = \frac{e^2}{6\pi\epsilon_0 m c^3}, \tag{2.3.13}$$

which for electrons amounts to $\tau = 6 \times 10^{-24}\,\mathrm{s}$. A sudden force acting on a similar time scale as τ will result in a significant modification of the motion through radiative effects. The equation of motion then reads

$$m(\dot{\mathbf{v}} - \tau\ddot{\mathbf{v}}) = \mathbf{F}_{ext}. \tag{2.3.14}$$

This equation of motion, sometimes referred to as *Abraham-Lorentz equation*, depends on the second derivative of the velocity in time, which requires a knowledge of the acceleration as initial condition and also results in runaway solutions. For a vanishing external force, we obtain two solutions for $\dot{\mathbf{v}}$:

$$\dot{\mathbf{v}}(t) = \begin{cases} \mathbf{0}, \\ \mathbf{a}e^{t/\tau}, \end{cases} \tag{2.3.15}$$

where $\mathbf{a}$ is the acceleration at $t = 0$. If $\mathbf{a} \neq 0$ leads to a self-acceleration of the particle in absence of an external force, which is clearly unphysical and also results in $(\dot{\mathbf{v}} \cdot \mathbf{v}) \neq 0$ at t_1 and t_2, which we used to derive this expression. The relativistic generalisation of this equation is referred to as *Lorentz-Abraham-Dirac equation (LAD)* and is for an electron of charge $-e$ and mass m_e given in terms of the four-velocity u [47, 127]:

$$\boxed{\frac{\mathrm{d}u^\mu}{\mathrm{d}\tau} = -\frac{e}{m_e} F^{\mu\nu} u_\nu + \frac{e^2}{6\pi m_e} \left(\frac{\mathrm{d}^2 u^\mu}{\mathrm{d}\tau^2} + u^\mu \frac{\mathrm{d}u^\nu}{\mathrm{d}\tau} \frac{du_\nu}{\mathrm{d}\tau} \right),} \tag{2.3.16}$$

with the radiation reaction force

$$g^\mu = \frac{e^2}{6\pi m_e}\left[\frac{\mathrm{d}^2 u^\mu}{\mathrm{d}\tau^2} - u^\mu\left(\frac{\mathrm{d}u^\nu}{\mathrm{d}\tau}\right)\left(\frac{\mathrm{d}u_\nu}{\mathrm{d}\tau}\right)\right], \tag{2.3.17}$$

where τ is the proper time and $F_{\mu\nu}$ is the field tensor for an applied electromagnetic field. The second derivative of the momentum, $\mathrm{d}^2u/\mathrm{d}\tau^2$, leads again to pathological runaway solutions as described for the Abraham-Lorentz equation.

Landau-Lifschitz (LL) Equation

The first self-consistent solution to including radiation reaction into a classical model was achieved by the *Landau-Lifschitz (LL) equation* [128]. Here it is assumed that the radiation reaction force is small compared to the Lorentz force in a suitable frame of reference. The expression $\mathrm{d}u/\mathrm{d}\tau$ is substituted by $e/mF^{\mu\nu}u_\nu$, which reduces the order of the differential equation and removes the runaway solutions [102]:

$$\boxed{\frac{\mathrm{d}u^\mu}{\mathrm{d}\tau} = -\frac{e}{m}F^{\mu\nu}u_\nu + \frac{e^4}{6\pi m_e}\left[-\frac{m_e}{e}(\partial_\alpha F^{\mu\nu})u_\nu u^\alpha + F^{\mu\nu}F_{\nu\alpha}u^\alpha + (F^{\nu\alpha}u_\alpha)^2 u^\mu\right],} \tag{2.3.18}$$

with the radiation reaction force

$$g^\mu = \frac{e^4}{6\pi m_e}\left[-\frac{m_e}{e}(\partial_\alpha F^{\mu\nu})u_\nu u^\alpha + F^{\mu\nu}F_{\nu\alpha}u^\alpha + (F^{\nu\alpha}u_\alpha)^2 u^\mu\right]. \tag{2.3.19}$$

This description only holds for length scales larger than the Compton wavelength, $L \gg \lambda_C \approx 2.43 \times 10^{-12}\,\mathrm{m}$, and electric field strengths much smaller than the critical field strength, $E \ll E_{cr}/\alpha \approx 1.89 \times 10^{20}\,\mathrm{V/m}$, in the instantaneous rest frame of the electron.

In the Landau-Lifschitz model, we can also find an analytic expression of the energy loss, $\Delta\gamma$, an electron experiences. For an electron of initial energy γ_0 interacting with a plane wave with a Gaussian temporal envelope, this is given by [133, 177]

$$\frac{\Delta\gamma}{\gamma_0} = \frac{\sqrt{\pi/2}\tau_0 t_L \omega_0^2 \gamma_0 a_0^2}{1 + \sqrt{\pi/2}\tau_0 t_L \omega_0^2 \gamma_0 a_0^2}, \tag{2.3.20}$$

where $\tau_0 = e^2/6\pi\epsilon_0 m_e c^3 = 6 \times 10^{-24}\,\mathrm{s}$ is again the 'characteristic time' for an electron, t_L is the FWHM laser pulse duration, λ the wavelength of the laser pulse, and a_0 is its normalised vector potential. This is valid if quantum effects are negligible, $\gamma_0 a_0 \ll m_e c^2/2\hbar\omega_0$ (Section 2.3.1). Strong radiation reaction effects are expected for $\gamma a_0^2 > (10\sqrt{2\pi^3}\omega_0\tau_0\gamma_0)^{-1/2}$.

Whilst this description is free from runaway solutions unlike the LAD equation, it violates in some cases energy conservation when considering abruptly changing fields,

causing the energy loss to exceed the initial energy of the particle [129]. Note also that all physical solutions of the LAD equation are also solutions of the LL description [178].

2.3.3 Quantum Radiation Reaction

At high electron energies and electric field strengths, when the quantum nonlinearity parameter, η, approaches unity, i.e. the electric field in rest frame approaches the critical field of QED, the assumptions under which the classical treatments were derived are not valid any more and we expect quantum effects to dominate the particle dynamics. The deviations or quantum corrections to the classical description are fundamentally two-fold:

First, the emission spectrum of the classical model overestimates the emission power and in extreme cases allows more emission than the original particle energy. This is fixed by replacing the classical synchrotron function by the *quantum synchrotron function*. As a result, the classical radiation reaction force is modified by the Gaunt factor, which is defined as the ratio of the quantum and classical synchrotron emission power, $g(\eta) = P_q/P_{cl}$, where $0 \leq g \leq 1$ (see Appendix G):

$$\mathbf{F}_{mod,cl} = g\mathbf{F}_{cl}. \tag{2.3.21}$$

Second, the emission is not continuous and deterministic but stochastic in nature so that we have to consider discrete emission events and related emission probabilities, rather than deterministic one-to-one relations. Quantum radiation reaction is then the overall recoil experienced by an electron undergoing multiple simultaneous incoherent photon emission events. In the collision of an electron and a laser pulse, the finite radiation lifetime allows the electrons to enter field regions that are classically forbidden, which can result in more energetic photon emissions. This is referred to as *(energy) straggling* [136]. Similarly, an electron might also pass through the entire laser pulse without emitting a single photon, which is then called *quantum quenching of radiation losses* [137].

We can estimate the importance of stochastic effects by comparing the typical timescale between emission events, Δt, with the time scale of the laser pulse, ω_0, [102]:

$$\omega_0 \Delta t = \begin{cases} 44 a_0^{-1} & \eta \ll 1, \\ 58[\gamma\omega_0/(a_0 m_e)]^{1/3} & \eta \gg 1. \end{cases} \tag{2.3.22}$$

Δt is given by $\Delta t = \langle\omega\rangle/P$, where P is the emission power $P_q = 2\alpha m^2 \eta^2 g(\eta)/3$ and $\langle\omega\rangle$ is the average photon energy. Stochastic effects are most significant for $\omega_0\Delta t \geq 1$, when the total number of emissions is small but η is large.

Finally, when η approaches unity, we also have to consider prolific pair production and

subsequent QED cascades that might deplete the laser pulse and energy of the electron beam.

2.3.4 Signatures of radiation reaction in the electron spectrum

Here, we will now consider the signatures or observables of radiation reaction in the post-interaction spectrum of relativistic electrons in the interaction with an intense laser pulse, following [132]. The two key signatures are the change in the momentum, predominantly observed through energy loss, the second is the variance or energy spread of the electron spectrum. The evolution of these two properties is characteristic for different models of radiation reaction, such that these are suitable experimental indicators for radiation reaction and facilitate discrimination between the models. The optimum conditions to distinguish different models is investigated in more detail, for instance, in [179, 180] using the same formalism as [132].

Evolution of momentum or energy loss

The evolution of the average electron momentum interacting with a laser pulse, $\langle \mathbf{p} \rangle$, is determined by the synchrotron power, P [132]:

$$\boxed{\left(\frac{\mathrm{d}\langle \mathbf{p} \rangle}{\mathrm{d}t}\right) = -\frac{\langle P\hat{\mathbf{p}} \rangle}{c},} \tag{2.3.23}$$

where $\hat{\mathbf{p}}$ is the unit momentum vector and c is the speed of light. The minus sign indicates that the average momentum decreases over time, i.e. the electrons lose energy equal to the radiated energy.

In a classical model, the emission power is the Larmor power, P_{cl}, whereas the average emission power is reduced in the quantum description (see quantum synchrotron in Appendix G) by the *Gaunt factor*, g, i.e. $P_q = gP_{cl}$. The Gaunt factor is analytically approximated by [181]

$$g(\eta) = [1 + 4.8(1+\eta)\ln(1+1.7\eta) + 2.44\eta^2]^{-2/3}, \tag{2.3.24}$$

where η is the quantum nonlinearity parameter, and $0 \leq g \leq 1$ such that the emission power is reduced relative to the classical value. More information on the Gaunt factor and the quantum synchrotron function is provided in Appendix G.

The equation describing the evolution of the average electron momentum including the quantum correction is obtained by modifying Equation (2.3.23) by g:

$$\boxed{\left(\frac{\mathrm{d}\langle \mathbf{p} \rangle}{\mathrm{d}t}\right)_{mod,cl} = -\frac{\langle gP_{cl}\hat{\mathbf{p}} \rangle}{c}.} \tag{2.3.25}$$

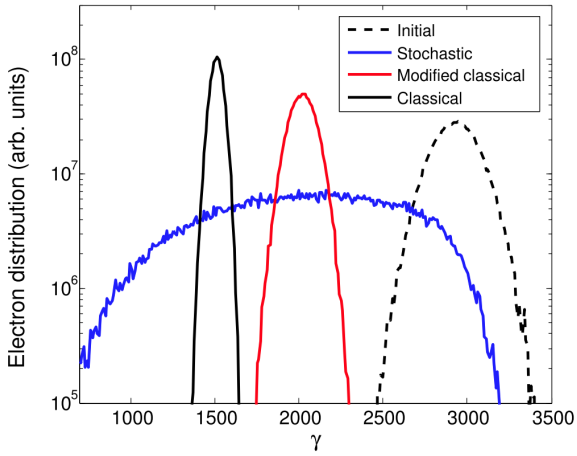


Figure 2.12: Electron distribution as a function of energy before (dashed) and 10.5 fs *after interaction (full) with a laser pulse using different models of radiation reaction. The initial electron beam is a Gaussian with mean* $\gamma_0 = 3000$*, the laser pulse has a peak intensity of* $10^{21}\,\mathrm{W/cm^2}$ *and is a half-Gaussian with* 1 fs *rise time. Reprinted from [132].*

Figure 2.12 [132] shows the simulated spectrum of an electron beam before (dashed line) and after (solid lines) the interaction with an intense laser pulse, where different colours indicate the different radiation reaction models that were used to obtain the post-interaction spectrum. For now we only consider the mean energy of the spectrum: The classical description (solid black) results in the strongest shift in energy to about half of its initial energy, whereas the other two models labelled 'stochastic' (blue) and 'modified classical' (red) predict a lower energy loss, consistent with the reduced emission power used in Equation (2.3.25). As a result, the amount of energy the electron beam loses on average in an interaction is a good observable in an experiment to signal when quantum corrections become significant, and the classical and quantum descriptions depart from each other. See, for instance, [179] for a discussion on the overlap of these models for a range of experimental parameters.

Evolution of the variance or energy spread

The second observable we consider is the evolution of the variance or the energy spread of the electron spectrum. Classical models are deterministic and as such yield one-to-one predictions of the final energy of an electron undergoing an interaction with an intense laser pulse. Since higher electron energies are linked to higher energy losses, the energy spread of an electron beam experiencing a classical radiation reaction force always decreases in an interaction. The evolution of the variance in the Lorentz factor of the electron, $\sigma^2 = \langle\gamma^2\rangle - \langle\gamma\rangle^2$, is then described by [132]

$$\boxed{\left(\frac{\mathrm{d}\sigma^2}{\mathrm{d}t}\right)_{cl} = -2\frac{\langle\Delta\gamma P_{cl}\rangle}{m_e c^2},} \tag{2.3.26}$$

where P_{cl} is again the classical emission power, c the speed of light, m_e is the electron mass, and $\Delta\gamma = \gamma - \langle\gamma\rangle$. The minus sign indicates that the variance always decreases. Considering the emission power reduced by g resulting from quantum corrections, the corresponding predicted decrease in variance is reduced by the same factor

$$\boxed{\left(\frac{\mathrm{d}\sigma^2}{\mathrm{d}t}\right)_{mod,cl} = -2\frac{\langle\Delta\gamma g P_{cl}\rangle}{m_e c^2}.} \tag{2.3.27}$$

If we apply not only the reduced emission power but also consider the stochasticity of the quantum nature, we obtain an equation complemented by a term $\sim S$:

$$\boxed{\left(\frac{\mathrm{d}\sigma^2}{\mathrm{d}t}\right)_{st} = -2\frac{\langle\Delta\gamma g P_{cl}\rangle}{m_e c^2} + \frac{\langle S\rangle}{m_e^2 c^4},} \tag{2.3.28}$$

where S is a measure of stochasticity and is given in Appendix H.2. Whereas the deterministic models predict a decrease in variance under all circumstances, we see that this equation consists of two terms with opposite signs such that the variance can increase or at least decrease at a slower rate if the stochasticity is significant. For a Gaussian electron beam spectrum with mean $\langle\epsilon_i\rangle$ and width σ_{ϵ_i} the crossover point below which stochastic broadening dominates is for $\sigma_{\epsilon_i} \ll \langle\epsilon_i\rangle$ given by [179]

$$\frac{\sigma_{\epsilon_i}}{\langle\epsilon_i\rangle} \approx 0.7\sqrt{\langle\eta\rangle}. \tag{2.3.29}$$

Note that the effective η in an interaction is not constant, such that the interaction might be dominated by stochastic broadening for parts of the interaction, followed by a strong cooling resulting from lower electron energies due to energy loss.

Returning to Figure 2.12 [132] again, we can now also consider the shape of the electron distributions. We see that the width of the distribution has narrowed for both the classical (black solid) and the modified classical (red) models as they are deterministic models, where the classical model has narrowed the distribution more. This is again consistent as the emission power in the modified classical model is reduced by the Gaunt factor and $g \leq 1$. The model including stochasticity (blue) has, on the other hand, widened significantly whilst losing on average the same amount of energy as the electron beam experiencing the modified classical radiation reaction force. This indicates that whilst the average energy loss is a good indicator to discriminate purely classical models and those that include quantum corrections, the variance of the spectrum can serve as powerful observable to distinguish deterministic and probabilistic models, such that by measuring both quantities they can serve as complementary measurements. An analysis of the impact of stochasticity on different beam shapes has been discussed in [182].

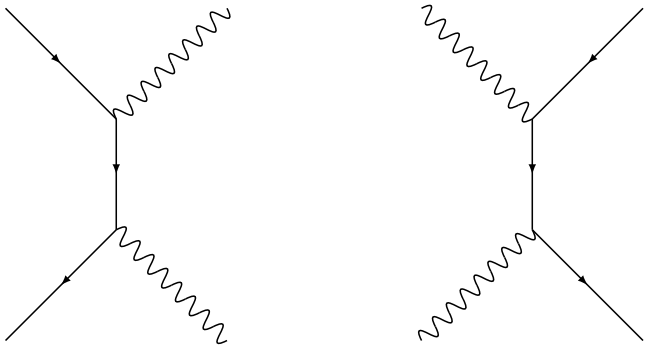


Figure 2.13: Feynman diagrams for pair annihilation (left) and linear Breit-Wheeler pair production (right). The time axis is oriented from left to right. Wiggly lines indicate photons, whereas lines with arrows represent fermions (arrow towards positive time), here electrons, and anti-fermions (arrow in negative time direction), here positrons.

2.4 Pair Production and Annihilation

One of the most intriguing predictions of quantum electrodynamics (QED) is the transformation of light into matter and vice versa matter into light. In this context, the two most fundamental processes are the annihilation of an electron with its antiparticle, the positron, into two photons (Dirac annihilation) [183], and the inverse process where two photons create an electron-positron pair (Breit-Wheeler pair production) [184]. If multiple photons annihilate into an electron-positron pair, this is referred to as the nonlinear Breit-Wheeler process [99, 100].

Another means of producing electron-positron pairs is, for instance, the interaction of photons with the Coulomb field of the nucleus and atom (Bethe-Heitler process) [185], which is closely related to the radiative process of bremsstrahlung. A third example of pair production is the so-called Schwinger pair production [27], where an extremely high electric field 'pulls' virtual electron-positron pairs directly out of the vacuum. These field strengths can, for instance, be achieved in the rest frame of a relativistic electron colliding with an intense laser pulse [130, 162, 163] or in the standing wave of two (or more) such laser pulses [175]. The following section briefly discusses the cross sections and scaling laws associated with these mechanisms, where the focus lies on the (linear) Breit-Wheeler process that is central to the results presented in Chapter 7.

2.4.1 Dirac annihilation

An electron and a positron can annihilate into two photons, i.e. transform their matter into light. This process is referred to as *pair annihilation*, two-photon annihilation or *Dirac annihilation* named after Paul Dirac, who postulated the existence of the positron and also its annihilation with an electron [183, 186]. Both were confirmed experimentally

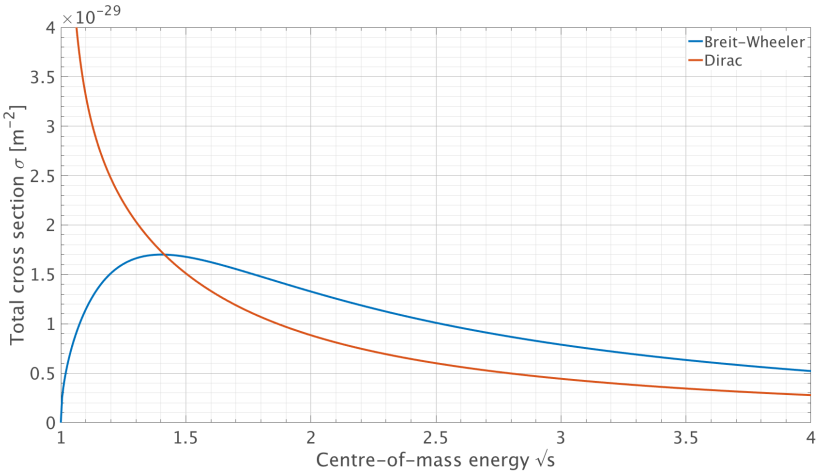


Figure 2.14: Total cross sections for Dirac annihilation (see Equation (2.4.2)) and Breit-Wheeler pair production (see Equation (2.4.4)) in the CM frame in units of m^{-2} as a function of centre-of-mass energy, $\sqrt{s}$.

briefly afterwards [187–189]. It can be described by the following equation

$$e^+ + e^- \longrightarrow \gamma + \gamma, \tag{2.4.1}$$

or in terms of the Feynman diagram in Figure 2.13 (left). The annihilation of electron-positron pairs is commonly found in radioactive decays. There relatively 'slow' pairs collide and the emitted gamma rays are emitted (in the centre-of-mass frame) at 180 degrees with $E_{ph} = m_e c^2$ each. This is, for instance, used in coincidence measurements in radio-isotope therapy to localise tumours [190].

The total cross section, $\sigma_{e^+e^-}$, is given by [109]:

$$\boxed{\sigma_{e^+e^-} = \pi r_e^2 \frac{(1-\beta^2)}{4\beta^2}\left[(3-\beta^4)\ln\left(\frac{1+\beta}{1-\beta}\right) - 2\beta(2-\beta^2)\right],} \tag{2.4.2}$$

where $r_e = e^2/4\pi\epsilon_0 m_e c^2$ is the classical electron radius, $\beta = \sqrt{1-1/s}$ is the centre-of-mass velocity and $s = (\epsilon_{CM}/m_e c^2)^2$ the square of the centre-of-mass (CM) energy. In the limit of ultrarelativistic energies, i.e. $s \to \infty$, $\beta \to 1$ and as a result $\sigma_{e^+e^-} \to 0$. At low energies, $s \to 1$ reducing the energy to the rest mass, $\beta \to 0$ and the total cross section diverges, $\sigma_{e^+e^-} \to \infty$, due to the logarithm $\ln[(1+\beta)/(1-\beta)]$. The total cross section is shown as a function of the centre-of-mass energy, $\sqrt{s}$, in Figure 2.14.

2.4.2 Breit-Wheeler pair production

The inverse mechanism of Dirac annihilation is the two-photon (linear) *Breit-Wheeler process* [184]. Here two photons combine to produce an electron-positron pair, i.e. matter

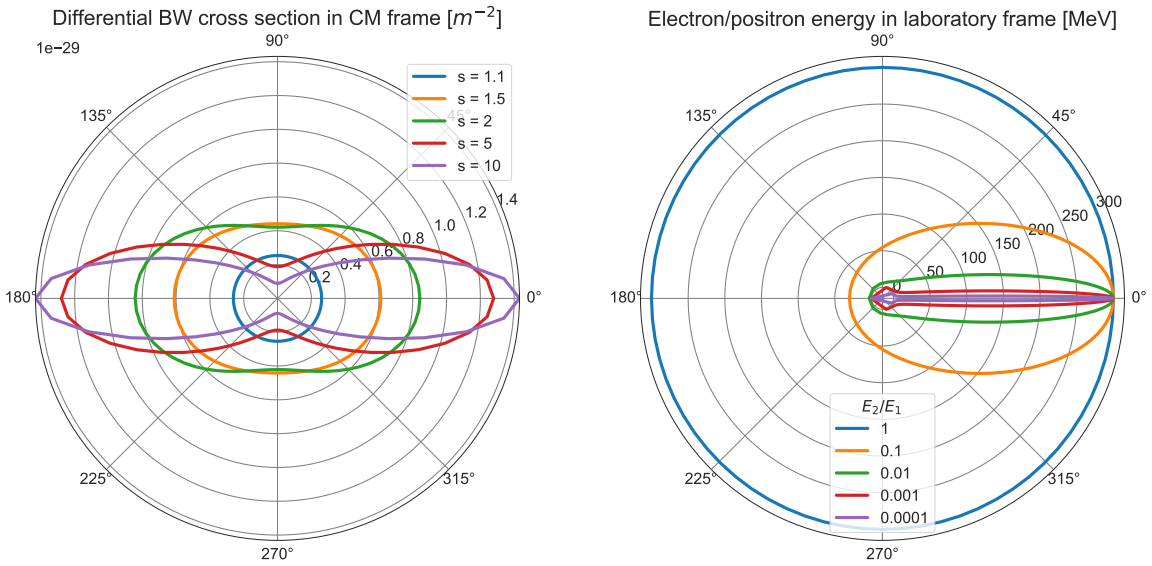


Figure 2.15: Left: Polar plot of differential Breit-Wheeler cross sections in the centre-of-mass (CM) frame calculated using Equation (2.4.5) *for different centre-of-mass energies, s. Right: Polar plot of the particle energy distribution in the laboratory frame for different ratios of the incident photon energies, with photon 1 propagating at zero degrees and $E_1 = 300\,\mathrm{MeV}$ and photon 2 at* 180°.

is created from light. The process is described by the equation

$$\gamma + \gamma \longrightarrow e^+ + e^-, \tag{2.4.3}$$

or in terms of the corresponding Feynman diagram shown in Figure 2.13 (right).

Cross section

In the CM frame, the total cross section for the process is given by [109, 191] (see Figure 2.14):

$$\boxed{\sigma_{\gamma,\gamma} = \frac{\pi r_e^2}{2}(1-\beta^2)\left[(3-\beta^4)\ln\left(\frac{1+\beta}{1-\beta}\right) - 2\beta(2-\beta^2)\right] = 2\beta^2\sigma_{e^+e^-},} \tag{2.4.4}$$

where again $s = (\epsilon_{CM}/m_e c^2)^2 = \epsilon_{\gamma 1}\epsilon_{\gamma 2}(1-\cos\phi)/2m_e^2c^4$, and $\beta = \sqrt{1-1/s}$, so that it is again required that $s \geq 1$. We see that for a head-on collision ($\theta = \pi$) $s = \epsilon_1\epsilon_2/m_e^2c^4$ and for a right-angle scattering ($\theta = \pi/2$) only half of this, $s = \epsilon_1\epsilon_2/2m_e^2c^4$.

The total cross section of the pair annihilation and the pair production process are related by the factor $2\beta^2$ [109], which immediately implies that $\sigma_{\gamma,\gamma} \to 0$ for $s \to 1$, opposite to the behaviour of the annihilation cross section. Equally, it then indicates that also $\sigma_{\gamma,\gamma} \to 0$ for $s \to \infty$. Both cross sections are balanced for $\beta = 1/\sqrt{2}$ or $s = 2$, which

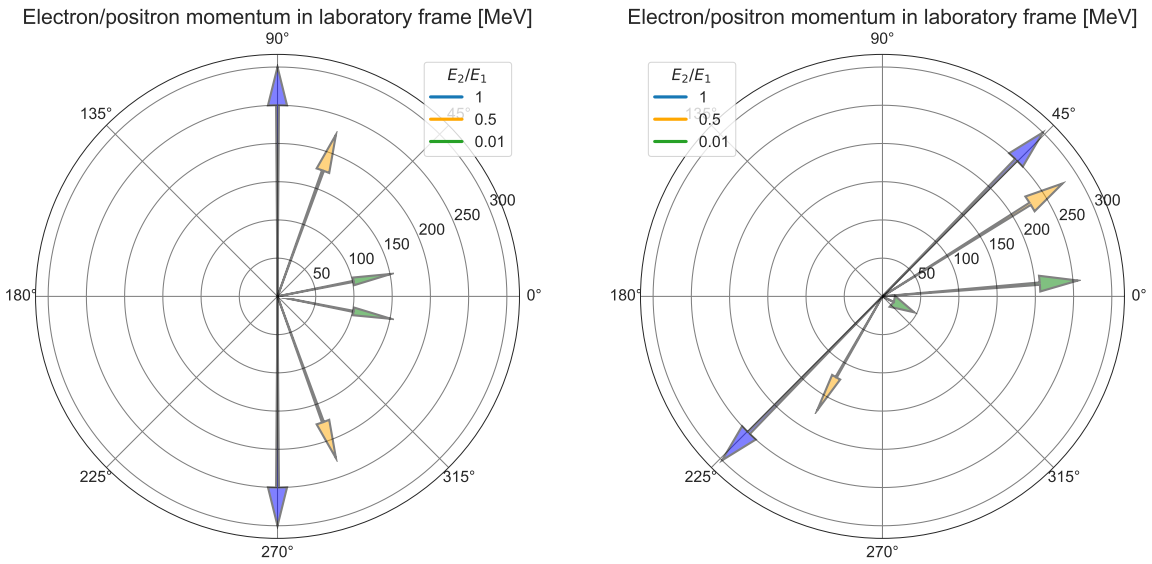


Figure 2.16: Momentum vectors of an emitted electron-positron pair in the laboratory frame for a fixed scattering angle in the centre-of-mass frame, θ_{CM}, and varying ratios of E_2/E_1 (vector colours), left at $\theta_{CM} = 90° \pm 180°$ and on the right at $\theta_{CM} = 45° \pm 180°$. The distribution is symmetric for electrons and positrons.

is also approximately the maximum of $\sigma_{\gamma,\gamma}$. The differential cross section in the CM frame is given by [110, 150]

$$\boxed{\frac{\mathrm{d}\sigma_{\gamma,\gamma}}{\mathrm{d}\Omega} = r_e^2 \beta(1-\beta^2)\left[\frac{1+2\beta^2\sin^2\theta_{CM} - \beta^4 - \beta^4\sin^4\theta_{CM}}{(1-\beta^2\cos^2\theta_{CM})^2}\right].} \tag{2.4.5}$$

The differential cross section is shown for different values of s in a polar plot in Figure 2.15 (left). At $s \sim 1$ the distribution is isotropic, but with increasing s forward and backward emissions ($\theta = 0, \pi$) become preferential. The differential cross section is symmetric under the transformation $\theta \to \theta + \pi$ as we are in the centre-of-mass frame.

Kinematics

After having calculated the differential cross section in the CM frame, we now want to know what the energy and momentum distribution of the particles is in the laboratory frame. For this we have to relativistically transform the quantities from the CM to the laboratory frame. We are in particular interested in how the distribution changes with increasing energy asymmetry between the two colliding photons. Finally, we will consider how the energy is distributed between the electron and positron when being emitted in the process.

The particle energy and momenta in the laboratory system are calculated using [192]

$$\epsilon_{3,4} = \gamma_{CM}\left(\epsilon_{3,4}^{CM} + \boldsymbol{\beta}_{CM}\cdot\mathbf{p}_{3,4}^{CM}\right), \tag{2.4.6}$$

$$\mathbf{p}_{3,4} = \mathbf{p}_{3,4}^{CM} + \frac{\gamma_{CM}-1}{\beta_{CM}^2}\left(\boldsymbol{\beta}_{CM}\cdot\mathbf{p}_{3,4}^{CM}\right)\boldsymbol{\beta}_{CM} + \gamma_{CM}\epsilon_{3,4}^{CM}\boldsymbol{\beta}_{CM}, \tag{2.4.7}$$

with $\gamma_{CM} = (\epsilon_1+\epsilon_2)/\sqrt{s}$ and $\boldsymbol{\beta}_{CM} = (\mathbf{p}_1+\mathbf{p}_2)/(\epsilon_1+\epsilon_2)$. Figure 2.15 (right) shows the angular energy distribution in the laboratory frame for different ratios of the two photon energies ϵ_1/ϵ_2, with $\epsilon_1 = 300\,\mathrm{MeV}$. For $\epsilon_1 = \epsilon_2$ the laboratory frame and the CM frame are identical (blue). Here the emitted energies are isotropic, but for $s > 1$ preferentially emitted at $\theta = 0, \pi$. At a fixed value of ϵ_1 and $\epsilon_1 > \epsilon_2$, a decreasing energy of the second photon, ϵ_2, i.e. $\epsilon_2/\epsilon_1 < 1$, higher energies are emitted in forward direction as momentum has to be conserved. Combined with the differential cross section, we are expecting that particles of energy $\sim \epsilon_1$ are emitted predominantly in forward direction. Note that the energy distribution and the differential cross section are identical for electrons and positrons.

We will now discuss how this asymmetry affects how energy and momentum is shared between the two emitted particles. For this purpose we will consider two specific examples of scattering angles in the centre-of-mass frame to symptomatically indicate their behaviour. Figure 2.16 shows the energy distribution between the two particles in the laboratory frame at a fixed scattering angle in the CM frame of $\theta_{CM} = 90° \pm 180°$ (left) and $45° \pm 180°$ (right) for three ratios of ϵ_1/ϵ_2. For $\epsilon_1 = \epsilon_2$ the particles are emitted back-to-back as the CM and the laboratory frame are equivalent. With increasing asymmetry as $\epsilon_2/\epsilon_1 < 1$, the centre-of-mass velocity β_{CM} increases in forward direction and results in a head-light effect that rotates the momentum vectors towards $\theta = 0$. As a result, for a large centre-of-mass velocity all particles are emitted in forward direction, a phenomenon sometimes referred to as pair-beaming [193]. In the case of $\theta_{CM} = 90°$, the transformation back into the laboratory frame conserves the symmetry of the emission angle relative to the zero-degree axis such that both particles carry the same energy, $(\epsilon_1+\epsilon_2)/2$. For a non-perpendicular scattering angle, here at the example of $\theta_{CM} = 45°$, the relativistic boost results in an increasingly unequal distribution of the energies amongst the two particles, strongly favouring the forward scattered particle whereas the backward scattered particle only carries a small fraction of the total energy. This example describes the typical emitted momentum distribution for the setup presented in Chapter 7 most accurately, whilst an equal momentum distribution is only produced in the special case of scattering perpendicular to the beam axis ($\theta_{CM} = 90° \pm 180°$), which is further suppressed as the centre-of-mass energy, s, increases.

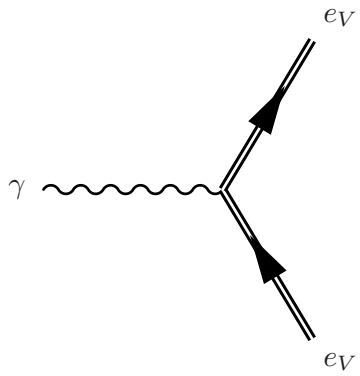


Figure 2.17: Feynman diagram for the nonlinear Breit-Wheeler process. The double lines with arrows indicate dressed electron states. The time axis is oriented from left to right.

Nonlinear Breit-Wheeler process

At high photon densities multiple photons ($n > 1$), γ_n, can interact with one high energy photon, γ, to produce a single electron-positron pair. The equation for this *nonlinear Breit-Wheeler process* then becomes:

$$\gamma + n\gamma_n \longrightarrow e^+ + e^-. \tag{2.4.8}$$

Similarly as for nonlinear Compton scattering (Section 2.2.3), the multiphoton process requires the evaluation of higher order Feynman diagrams or, in the Furry picture, the use of Volkov states to sum over all possible states (see Section 2.2). The corresponding Feynman diagram is shown in Figure 2.17.

Considering the special case of one high-energy photon colliding with n identical low-energy photons [99, 100], for instance optical photons from a laser, the corresponding centre-of-mass energy can simply be written as $s = (\epsilon_{CM}/m_e c^2)^2 = \epsilon_\gamma n \epsilon_{\gamma_n}(1-\cos\phi)/2m_e^2c^4$. The total rate for the Breit-Wheeler pair production is (in natural units) given by [173]

$$\boxed{W_\pm = \frac{\alpha}{\tau_C}\frac{mc^2}{\hbar\omega}\chi T(\chi),} \tag{2.4.9}$$

where $\tau_C = \hbar/mc^2 = 1.288 \times 10^{-6}$ fs is the Compton time, and $T(\chi)$ can be parametrised by [194]

$$T(\chi) \approx \frac{0.16}{\chi} K_{1/3}^2\left(\frac{2}{3\chi}\right), \tag{2.4.10}$$

where $K_{1/3}$ is a Bessel function of the second kind. $T(\chi)$ can also be approximated in two limits of χ [194]

$$T(\chi) = \begin{cases} \frac{3\sqrt{3}}{8\sqrt{2}}\exp\left(-\frac{4}{3\chi}\right) & \chi \ll 1, \\ 0.6\chi^{-1/3} & \chi \gg 1. \end{cases} \tag{2.4.11}$$

$\chi = \hbar\omega E_L/2m_e c^2 E_S$ is a quantum parameter, with the electric field of the laser, E_L, and the Schwinger field, $E_S = 1.33 \times 10^{18}\,\mathrm{Vm}^{-1}$. The total production rate is exponentially suppressed for low χ and increases at $\chi^{2/3}$ for large values of χ. The differential cross section for the process is given in Appendix I.1.

2.4.3 Bethe-Heitler pair production

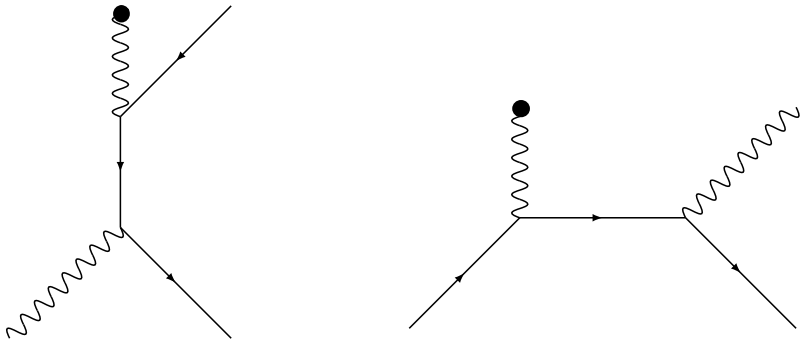


Figure 2.18: Feynman diagram for Bethe-Heitler process (left) and bremsstrahlung (right) as comparison. The time axis is oriented from left to right. Wiggly lines indicate photons, the dark circle shows the nuclear field. The arrowed lines represent fermions (arrow towards positive time), here electrons, and anti-fermions (arrow in negative time direction), here positrons.

A photon of energy $> 2m_e c^2$ can produce an electron-positron pair in the nuclear Coulomb field. This is called the *Bethe-Heitler process* [185], described by the equation

$$\gamma + Z \longrightarrow Z + e^+ + e^-, \tag{2.4.12}$$

with the corresponding Feynman diagram shown in Figure 2.18 (left) along with the diagram for bremsstrahlung (right). The differential cross section for the process is related to the bremsstrahlung cross section via crossing symmetry as follows

$$\frac{d\sigma_{\gamma Z}}{dE_+}(\omega, x) = -\frac{1}{\hbar x^2}\frac{d\sigma_{eZ}}{d\omega}(-\omega, x), \tag{2.4.13}$$

where $x = \hbar\omega/\epsilon_+$, the ratio of the initial photon to the final positron energy. The full cross section is given in Appendix I.2. In the ultrarelativistic case, the total cross section for a photon of energy ω to produce a pair is [109, 195, 196]

$$\sigma_{\gamma Z} = \frac{28}{9} Z^2 \alpha r_e^2 \left(\ln\frac{2\omega}{m_e} - \frac{109}{42} - f(Z\alpha) \right), \tag{2.4.14}$$

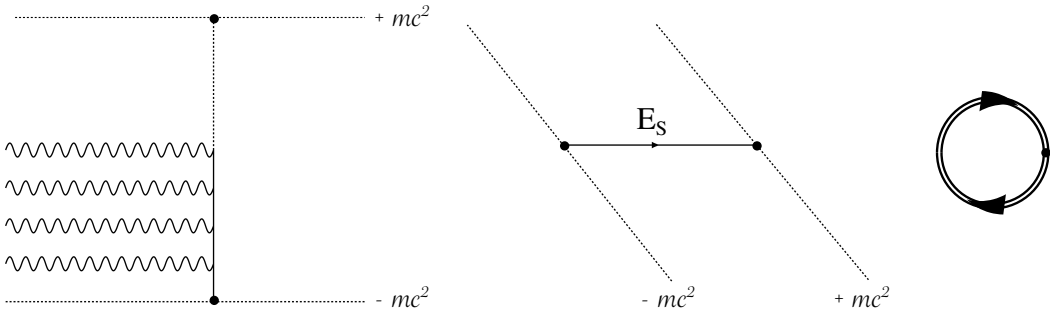


Figure 2.19: Representation of the nonlinear Breit-Wheeler as multiphoton ionisation equivalent (left) and Schwinger pair production as tunneling ionisation (centre) with the potential $\sim mc^2$. Feynman diagram for the Schwinger process (right).

with

$$f(Z\alpha) = (Z\alpha)^2 \sum_{n=1}^{\infty} \frac{1}{n[n^2 + (Z\alpha)^2]}, \tag{2.4.15}$$

with $f(Z\alpha) \to 0$ for $Z\alpha \ll 1$ [185].

2.4.4 Schwinger pair production

At extreme field strengths electron-positron pairs can be created directly from the (quantum) vacuum, where virtual electron-positron pairs are constantly created and anihilated in quantum fluctuations. This process is called *Schwinger pair production* [27], with the associated *Schwinger field* or *critical field of QED* [25, 26]:

$$\boxed{E_S = \frac{m_e^2 c^3}{e\hbar} \approx 1.33 \times 10^{18}\,\mathrm{Vm}^{-1},} \tag{2.4.16}$$

where we see by rearranging that

$$eE_S \bar{\lambda}_C = m_e c^2, \tag{2.4.17}$$

which provides an intuitive explanation of significance of this field strength: E_S is then the static electric field required to accelerate an electron to an energy of $m_e c^2$, equivalent to its rest mass, within a (reduced) Compton wavelength, $\bar{\lambda}_C$. Figure 2.19 (right) shows the associated Feynman diagram.

Another interpretation of the Schwinger process is to understand it as an analogue process to tunnel ionisation in a Coulomb potential. For a static field, $l_f \ll \lambda$, we can then find an analogue of the Keldysh parameter, $\gamma_K = \omega\sqrt{2mI_p}/eE$, where we then identify the electron rest mass as 'ionisation potential' $I_p \sim mc^2$, such that $\gamma_K \sim 1/a_0$. In other words, by applying an electric field of strength $\sim E_S$, the virtual particles can tunnel out of the Dirac sea through the rest mass potential into real space. If we can understand the Schwinger process as tunnel ionisation, the nonlinear Breit-Wheeler process then becomes

in this picture the analogue to multi-photon ionisation [see Figure 2.19 (left and centre)].

The pair production rate, $R_{e^+e^-}$, scales as [47]

$$R_{e^+e^-}(\eta) \propto \begin{cases} \eta^2 \exp\left(-\frac{\pi}{\eta}\right) & \eta \ll 1, \\ \eta^2 & \eta \gg 1, \end{cases} \tag{2.4.18}$$

where η is again the quantum nonlinearity parameter indicating the magnitude of the electric field relative to the Schwinger field. The scalings of the production rate coincide for static [27] and oscillating fields [28, 29], and resemble ionisation rates.

The field strength of E_S is, however, incredibly high: it corresponds to a laser intensity of $\sim 10^{29}\,\mathrm{W/cm^2}$, which is well beyond current capabilities and what will be achievable in the foreseeable future [10]. In the laboratory these field strengths are, for now, only accessible in the rest frame of a relativistic electron beam, where the electric field of the laser pulse is boosted. However, even in the rest frame of an electron it is challenging to really reach these high values as the energy loss from radiation reaction and the production of pairs from the nonlinear Breit-Wheeler process increases strongly when $\eta \to 1$, which can initiate QED showers and cascades depleting the laser pulse [148]. As a result, the effective η might drop significantly without reaching an η of unity. Proposed solutions to this dilemma include, for instance, the tailoring of the laser wave front and colliding the laser pulse and the electron beam at an oblique angle [104].

Chapter 3

Laser Propagation and Wakefield Acceleration

This Chapter addresses the propagation of a laser pulse in an underdense plasma and its evolution at high-intensities, which give rise to interesting phenomena such as self-focusing and self-guiding, pulse compression and photon acceleration. In contrast to the previous Chapter that was concerned with the motion of individual charged particles and consequences thereof, e.g. radiation production and radiation reaction, here the interaction of an intense laser pulse with a plasma, a medium exhibiting collective behaviour, is discussed. This leads over to the topic of laser wakefield acceleration (LWFA): here an intense laser pulse drives a plasma wave through the ponderomotive force and the resulting charge separation in its wake generates strong electric fields that are suitable to capture and accelerate electrons to relativistic energies. In the context of this discussion, key quantities like the maximum energy gain and its fundamental limiting factors, dephasing and depletion, are introduced, along with a brief note on different injection mechanisms relevant to this work.

3.1 Laser Propagation in an Underdense Medium

3.1.1 Plasma Properties

A plasma is an on average charge-neutral medium that consists of charged particles, in the context of wakefield acceleration ions and free electrons. This property is called *quasi-neutrality* and can mathematically be expressed as [197]

$$-en_e + Zen_i \approx 0, \tag{3.1.1}$$

where e is the fundamental charge, n_e the electron number density, n_i the ion number density and Z the charge number of the ions. Whilst this balance might locally not be

true at every moment in time, the mobility of the charges enable their redistribution and lead to shielding at length scales larger than the Debye length, λ_D [198]:

$$\lambda_D = \left(\frac{\epsilon_0 k_B T_e}{n_e e^2} \right)^{1/2}, \tag{3.1.2}$$

where ϵ_0 is the dielectric constant, k_B the Boltzmann constant and T_e the electron temperature. This phenomenon, referred to as *Debye shielding*, is an example of a collective response of the plasma to a small perturbation. In a plasma, particles can act together on macroscopic scales through long range electromagnetic forces to form instabilities and waves. Even small imbalances can stimulate a significant response of the medium. This means that even though plasmas can be modelled as fluids and simulated using hydrodynamic codes, introducing electromagnetic forces will give rise to more complex and exotic phenomena than in fluids dominated by gravitational forces [197].

3.1.2 Plasma Formation

In the context of this work, the process of forming a plasma is achieved by ionising a neutral gas in the electric field of an intense laser pulse. The resulting collection of unbound electrons and ions is a plasma. After a certain time, the electrons will return to the ionic cores of the atoms and back again to a bound energy state emitting any excess energy in form of radiation in the process. This process is called *recombination* and the emitted radiation *recombination light*.

There are different mechanisms through which an oscillating laser field ionises a gas. In single and multi-photon ionisation [199], one electron is excited by absorbing one or multiple photons, respectively, before decaying to its original ground state. Another mechanism relies on the collision of electrons and atoms [200]. The electric field of the laser can also distort the Coulomb potential of the atom, resulting in a finite probability for electrons to tunnel into the continuum [201].

The dominant ionisation mechanism is indicated by the Keldysh parameter, γ_K, considering the strength of the electric field E relative to the binding potential V and the frequency of the oscillating field ω:

$$\gamma_K = \omega \frac{\sqrt{2 m_e V}}{eE}. \tag{3.1.3}$$

At $\gamma_K \gg 1$ *multiphoton ionisation* dominates, whereas for small $\gamma_K < 0.5$ *tunnel ionisation* is expected to be important. If the electric field is larger than the binding Coulomb potential, the atom is immediately ionised: this is called *barrier-suppression ionisation* [202]. In the simple example of a hydrogen-like atom in an external electric field E, the

potential V at a distance r from the core is given by

$$V(r) = -\frac{Ze^2}{4\pi\epsilon_0 r} - eEr, \tag{3.1.4}$$

where the position of the maximum potential is given by $r_{max} = (Ze/4\pi\epsilon E)^{1/2}$. Hence, the electric field required for complete barrier suppression of an ionisation potential V_e amounts to

$$E = \frac{\pi\epsilon_0 V_e^2}{Ze^3} \approx 173.6 \times \left(\frac{V_e}{eV}\right)^2 \frac{1}{Z}\,\mathrm{MV/m}, \tag{3.1.5}$$

or in terms of intensity using $I = \frac{c\epsilon_0}{2}|E|^2$ in (near) vacuum:

$$I = \frac{c\epsilon_0^3\pi^2 V_e^4}{2e^6 Z^2} \approx 4 \times 10^9 \left(\frac{V_e}{eV}\right)^4 \frac{1}{Z^2}\,\mathrm{W/cm^2}. \tag{3.1.6}$$

For hydrogen with $V_e = 13.6\,\mathrm{eV}$, the lower bound intensity required for barrier-suppression ionisation amounts to $1.37 \times 10^{14}\,\mathrm{W/cm^2}$, for helium with $Z = 2$ and $V_e = 54.4\,\mathrm{eV}$ the equation gives $I = 8.76 \times 10^{15}\,\mathrm{W/cm^2}$. The laser intensities in LWFA experiments routinely reach peak intensities above $10^{18}\,\mathrm{W/cm^2}$. Hence, one can safely assume that ionisation effects are negligible for low-Z gases. Higher-Z gases like nitrogen are not as easily fully ionised: in hydrogen-like nitrogen the last electron is bound by a potential of $V_e = 667\,\mathrm{eV}$ at $Z = 7$, which translates in intensities required in excess of $10^{19}\,\mathrm{W/cm^2}$. Even very intense laser pulses might struggle to fully ionise a nitrogen gas at all and one can not assume any longer that a fully ionised plasma is in place when the main part of the laser pulse arrives. The gas might then reach higher degrees of ionisation only at peak fields of the laser either through full barrier suppression or by triggering an increased tunnelling rate: this is taken advantage of in an injection scheme for laser wakefield acceleration called 'ionisation injection' [203, 204].

3.1.3 Plasma Frequency

The plasma frequency, ω_p, is the natural frequency at which electrons will oscillate in a plasma when being displaced [197]. It constitutes the typical time scale and the corresponding plasma wavelength, λ_p, the typical length scale of a plasma response.

Assume a uniform and neutral plasma, i.e. $n_e = Zn_i = n_{e0}$, where n_e is the electron number density, Z the charge number of the ions, n_i the ion number density, and the initial electric field be $\mathbf{E} = \mathbf{0}$. Now consider displacing a slab of charge by X in an arbitrary axis x. Starting with Gauss' Law we obtain:

$$\nabla \cdot \mathbf{E} = \frac{\rho}{\epsilon_0} = \frac{\partial E_x}{\partial x}, \tag{3.1.7}$$

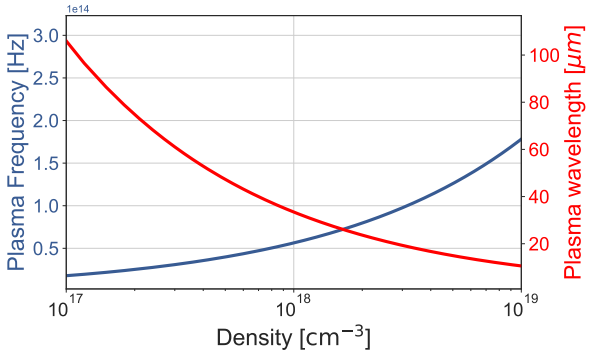


Figure 3.1: Plasma frequency (blue) in Hz and wavelength (red) in micrometres as function of plasma density assuming $v_{ph} = c$.

where we used that the displacement is only along x, simplifying the Nabla operator to a spatial derivative in x. We assume a uniform plasma so that the charge density is a constant $\rho = en_{e0}$. Integrating the previous equation then gives a constant factor times the displacement X:

$$E_x = \frac{1}{\epsilon_0}\int_0^x \rho(x')dx' + E_x(0) = \frac{en_{e0}}{\epsilon_0}X,$$
$$E = \frac{en_{e0}}{\epsilon_0}X. \tag{3.1.8}$$

If we now consider a force based on this field, we immediately see that this is equivalent to the equation of motion of a harmonic oscillator:

$$m_e\frac{\mathrm{d}^2X}{\mathrm{d}t^2} = -\frac{e^2n_{e0}}{\epsilon_0}X = -m_e\omega_p^2X, \tag{3.1.9}$$

with the (plasma) frequency, ω_p:

$$\boxed{\omega_p = \sqrt{\frac{n_{e0}e^2}{\epsilon_0 m_e}},} \tag{3.1.10}$$

and the corresponding wavelength $\lambda_p = 2\pi v_{ph}/\omega_p$, where v_{ph} is the phase velocity of the wave. A typical wakefield accelerator in the context of this work operates at an electron density of around $10^{18} - 10^{19}\,\mathrm{cm}^{-3}$. This corresponds to a plasma frequency of $(5.6 - 17.7) \times 10^{13}\,\mathrm{Hz}$ or a plasma wavelength of $\lambda_p \approx 33 - 10\,\mu\mathrm{m}$ for $v_{ph} = c$ (see Figure 3.1).

3.1.4 Laser Propagation in Vacuum

An electromagnetic wave of arbitrary shape u has to satisfy Maxwell's equations and hence also the wave equation [52]

$$\left(\nabla^2 - \frac{1}{v^2}\frac{\partial^2}{\partial t^2}\right) u = 0, \tag{3.1.11}$$

where $v = c/\sqrt{\mu\epsilon}$ and in vacuum $v = c$. In the case of waves with an electric field $\mathbf{E} = \mathbf{E}(\mathbf{r}, t) = \mathbf{u}(\mathbf{r})v(t)$, where the spatial and temporal dependencies can be separated, the components solve two separate differential equations

$$\left(\nabla^2 + k^2\right) \mathbf{u} = 0, \tag{3.1.12}$$

$$\left(\frac{\partial^2}{\partial t^2} + k^2\right) v = 0, \tag{3.1.13}$$

where $k = \sqrt{\mu\epsilon}\omega/c$. The spatial component is called the Helmholtz equation. For an an electric field $\mathbf{E} = \mathbf{E_0}(r, z)e^{i(kz-\omega t)}$ with cylindrical symmetry in the paraxial approximation $|k\mathbf{E}_0| \gg |\partial_z \mathbf{E}_0|$, the Helmholtz equation takes the form

$$\left(\frac{\partial^2}{\partial r^2} + \frac{1}{r}\frac{\partial}{\partial r} - 2ik\frac{\partial}{\partial z}\right) \mathbf{E}_0 = 0. \tag{3.1.14}$$

For an in x-direction linearly-polarised electric field moving in z, the solution is

$$\mathbf{E}(r, z, t) = E_0 \frac{w_0}{w(z)} \exp\left(-\frac{r^2}{w(z)^2}\right) \exp\left[-i(kz - \omega t) - ik\frac{r^2}{2R(z)} + i\zeta(z)\right] \hat{\mathbf{x}}. \tag{3.1.15}$$

This family of solutions is referred to as Gaussian modes and the physical properties of the beam are captured in the different parameters of the wave function. The function $\mathbf{E}$ describes a beam converging from $z < 0$ at a size $w(z)$ onto a minimum at $z = 0$ achieving the highest field strengths, before diverging again for $z > 0$.

$w(z)$ is the *waist size* of the Gaussian beam at position z and indicates the transverse size of the beam when the intensity drops to $1/e^2$ of its maximum:

$$\boxed{w(z) = w_0\sqrt{1 + \left(\frac{z}{z_R}\right)^2},} \tag{3.1.16}$$

where w_0 is the waist size at focus, $z = 0$, and z_R is the *Rayleigh length* defined as

$$\boxed{z_R = \frac{\pi w_0^2}{\lambda}.} \tag{3.1.17}$$

z_R is the distance over which a Gaussian beam expands from w_0 to $\sqrt{2}w_0$ and is hence

an indicator for how quickly a beam diverges or in other words over which distance it maintains an intensity close to its maximum. Assuming the beam is a Gaussian in both time and space, the intensity at the focal plane $z = 0$ is given by

$$I(r,t) = I_0 \exp\left(-\frac{2r^2}{w_0^2}\right) \exp\left(-\frac{2t^2}{\tau^2}\right). \tag{3.1.18}$$

The intensity is commonly expressed in terms of the normalised vector potential a_0

$$\boxed{a_0 = \frac{eE_0}{m_e c\omega},} \tag{3.1.19}$$

where e is the electron charge, m_e the electron mass, c the speed of light, ω the frequency of the laser and E_0 the amplitude of the electric field. The intensity of the wave is given by $I = \epsilon_0 c E_0^2/2$, so that we can express a_0 in useful units for this work:

$$\boxed{a_0 = 0.856 \times \sqrt{I[10^{18}\mathrm{W/cm}^2]}\lambda[\mu\mathrm{m}].} \tag{3.1.20}$$

$R(z)$ is the radius of curvature of the wavefront

$$R(z) = z\left[1 + \left(\frac{z_R}{z}\right)^2\right]. \tag{3.1.21}$$

The wavefront is strongly curved around the focus $z < z_R$ and flattens out for $z \gg z_R$ and at $z = 0$. The difference in radii of curvature for beams with different Rayleigh length can be used in spatial interferometry applied in the context of synchronising two laser pulses in time. ζ, the final term in Equation (3.1.15), is called the Guoy phase and is an additional phase term that changes signs once the Gaussian mode passes through its focus.

When focusing a beam with an optic, for instance an off-axis parabola or spherical mirror, the ratio of the focal length, f, and the beam diameter, d, is a useful quantity that indicates how tightly a beam is focussed. It is called the f-number, $f_\# = f/d$, and is in shorthand typically written as $f/2$ for $f_\# = 2$, $f/40$ for $f_\# = 40$ and so on. Expressing some of the previous quantities in terms of the f-number gives

$$w_0 = \frac{2\sqrt{2}}{\pi}\lambda f_\# \approx 0.9\lambda f_\#, \tag{3.1.22}$$

and the distance over which a laser pulse remains intense

$$z_R = \frac{\pi w_0^2}{\lambda} \approx 2.5\lambda f_\#^2. \tag{3.1.23}$$

However, real laser beams in experiments are typically not Gaussian but mostly flat-top

beams. In addition, changes in the wave front, curvature profile, spatio-temporal couplings and so on consist further deviations from an ideal beam. These are commonly expressed in terms of the parameter M^2, with the minimum spot size being the ideal diffraction-limited spot size times M^2 and $M^2 > 1$ [69].

3.1.5 Laser Propagation in Plasma

Consider a quasi-neutral plasma (charge density $\rho \approx 0$) with a current density $\mathbf{j} = -en_e\mathbf{v}$, depending on the velocity $\mathbf{v}$ of the electrons in the plasma and the electron density n_e. The wave equation for the electric field $\mathbf{E}$ becomes

$$\nabla^2\mathbf{E} = -\mu e n_e \frac{\partial \mathbf{v}}{\partial t} + \frac{1}{c^2}\frac{\partial^2 \mathbf{E}}{\partial t^2}. \tag{3.1.24}$$

The acceleration of the electrons is due to the electric field of the wave, i.e. $\partial\mathbf{v}/\partial t = -e\mathbf{E}/m_e$. Now using the solution for a plane wave with $\mathbf{E} = \mathbf{E_0}\exp\left[i(\mathbf{k}\cdot\mathbf{r} - \omega t)\right]$, the dispersion relation is given by $\omega = ck\left[1 - \left(\frac{\omega_p}{\omega}\right)^2\right]^{-1/2}$, and hence the group velocity v_g and the phase velocity v_p are given by:

$$v_p = \frac{\omega}{k} = \frac{c}{\sqrt{1 - \left(\frac{\omega_p}{\omega}\right)^2}}, \tag{3.1.25}$$

$$v_g = \frac{\partial\omega}{\partial k} = c\sqrt{1 - \left(\frac{\omega_p}{\omega}\right)^2}, \tag{3.1.26}$$

where ω is the frequency of the electromagnetic wave. At $\omega \ll \omega_p$ this the expression can be approximated by a Taylor series:

$$v_p = \frac{\omega}{k} \approx c\left(1 + \frac{1}{2}\frac{\omega_p^2}{\omega^2}\right), \tag{3.1.27}$$

$$v_g = \frac{\partial\omega}{\partial k} \approx c\left(1 - \frac{1}{2}\frac{\omega_p^2}{\omega^2}\right). \tag{3.1.28}$$

The group velocity reaches zero for $\omega_p = \omega$, where ω_p is the plasma frequency, derived in the previous section and given by $\omega_p = (n_e e^2/\epsilon_0 m_e)^{1/2}$. Solving this for the density, we obtain a relation for the *critical density*, n_c (see also Figure 3.2):

$$\boxed{n_c = \frac{m_e\epsilon_0\omega^2}{e^2},} \tag{3.1.29}$$

which only depends on the frequency of the incident electromagnetic wave, and so we can write the refractive index $\eta = c/v_p$ in terms of the electron density n_e and the critical density n_c:

$$\eta = \sqrt{1 - \left(\frac{\omega_p}{\omega}\right)^2} = \sqrt{1 - \frac{n_e}{n_c}}. \tag{3.1.30}$$

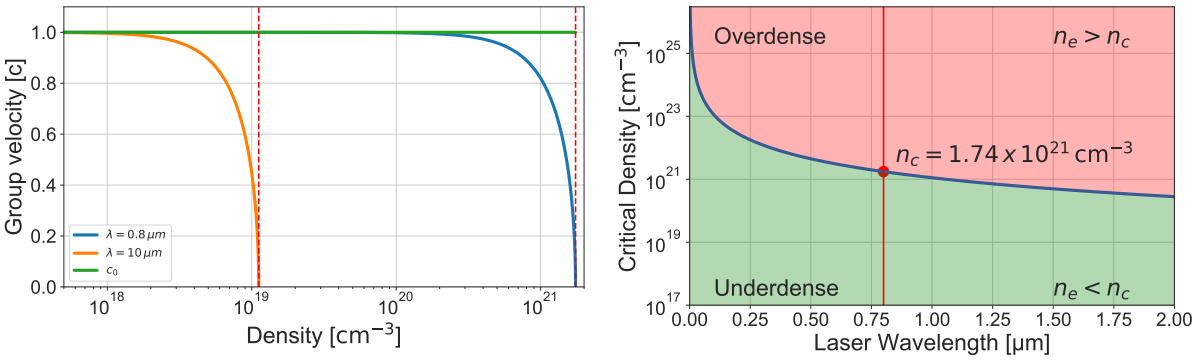


Figure 3.2: Left: Group velocity at different densities for photons of wavelength $\lambda = 0.8\ \mu m$ (blue) and 10 μm (orange) in units of the vacuum speed of light (indicated in green). The red dotted line shows the density at which the group velocity reaches zero, called the critical density. Right: Critical density for wavelengths up to 2 μm (blue). The critical density corresponding to a central wavelength of 0.8 μm, as for the commonly used titanium-doped sapphire (Ti:Sa) lasers, is marked in red on the graph. The region above the critical density (blue line) is called overdense, below underdense.

For $n_e > n_c$, an 'overdense plasma', the refractive index is imaginary and the wave becomes evanescent in the medium. This means a wave can only enter the material up to a skin depth before being reflected again. A plasma with a density $n_e < n_c$ is transparent and 'underdense'. LWFA requires the laser pulse to propagate through the plasma to drive the wave and hence targets used are typically operating at densities of only a fraction of n_c, whilst many ion acceleration mechanisms are based on overdense media.

3.1.6 Nonlinear Refractive Index

As seen previously, electrons interacting with a highly intense laser perform a relativistic motion (see Section 2.1.3). This results into a relativistic mass increase and in turn to a modification of the plasma frequency and the refractive index [17]:

$$\eta = \frac{c}{v_p} = \left(1 - \frac{\omega_p^2}{\gamma_\perp \omega^2}\right), \tag{3.1.31}$$

where $\gamma_\perp = 1 + \frac{1}{2}a_0^2$. Taking into consideration local modifications of the plasma density, laser frequency and laser intensity

$$n = n_0 + \frac{\delta n}{n_0} n_0, \tag{3.1.32}$$

$$\omega_L = \omega_0 + \frac{\delta \omega_L}{\omega_0} \omega_0, \tag{3.1.33}$$

$$\langle \gamma \rangle = 1 + \frac{a_0^2}{4}, \tag{3.1.34}$$

the nonlinear refractive index then becomes

$$\boxed{\eta = 1 - \frac{1}{2}\frac{\omega_p^2}{\omega_0^2}\left(1 + \frac{\delta n}{n_0} - \frac{2\delta\omega_L}{\omega_0} - \frac{a_0^2}{4}\right),} \tag{3.1.35}$$

assuming that the perturbations are small and higher order terms vanish.

3.1.7 Relativistic Self-focusing and Self-guiding

The diffraction of a Gaussian mode near focus ($z < z_R$) can be calculated by differentiating the waist size, w [205]:

$$\frac{\partial w}{\partial \tau} = \frac{\partial z}{\partial \tau}\frac{\partial w}{\partial z}, \tag{3.1.36}$$

$$\frac{\partial^2 w}{\partial \tau^2} = \frac{4c^4}{\omega_0^2 w_0^3}, \tag{3.1.37}$$

which takes a positive value resulting in an increase of the waist size. On the other hand, using the expression of the nonlinear refractive index and focusing on the term involving the vector potential of the laser we find

$$\frac{\partial^2 w}{\partial \tau^2} = \frac{c^2}{\eta}\frac{\partial \eta}{\partial r} = -\frac{c^2}{8}\frac{\omega_p^2}{\omega_0^2}\frac{\partial}{\partial r}a^2(r,z) \approx -\frac{1}{8}\frac{\omega_p^2}{\omega_0^2}\frac{a_0^2}{w_0}c^2, \tag{3.1.38}$$

which has a negative sign indicating focusing and counteracts the diffraction term in Equation (3.1.37). To find the conditions when diffraction and focusing balance each other, we set both terms equal

$$\begin{aligned} w_0^2 a_0^2 &= 32\frac{c^2}{\omega_p^2}, \\ w_0 &= \frac{\sqrt{32}}{a_0}\frac{c}{\omega_p}, \end{aligned} \tag{3.1.39}$$

and expressed in terms of laser power [71]:

$$\boxed{P_c = \frac{8\pi\epsilon_0 m_e^2 c^5}{e^2}\frac{\omega^2}{\omega_p^2} \approx 17\frac{\omega_0^2}{\omega_p^2}\,\mathrm{GW} = 17\frac{n_c}{n_e}\,\mathrm{GW},} \tag{3.1.40}$$

where P_c is the *critical power* or minimum power required to outweigh diffraction by relativistic self-focusing. This is referred to as *self-guiding* as it enables guiding without external guiding structures [206, 207]. When balancing both terms, the laser pulse remains focused over several Rayleigh lengths while oscillating in size [208]. The waist evolution is

described by

$$\frac{\mathrm{d}^2 w}{\mathrm{d}z^2} = \frac{w_0^2}{z_R^2 w^3}\left(1 - \frac{P}{P_c}\right). \tag{3.1.41}$$

In the 'bubble' regime [73], a highly intense laser pulse completely clears the laser axis from electrons forming a cavity of radius $r_b = 2\sqrt{a_0}\frac{c}{\omega_p}$, the bubble radius. This cavity is void of electrons $n_e = 0$ and no focusing occurs within it. The guided spot size is matched to r_b as smaller spots diffract and larger spots are focused again.

3.1.8 Pulse compression

In a wakefield accelerator, an intense laser pulse propagates through a plasma and expels the electrons in its way. As a result, the front and the back of the laser pulse witness different electron densities. This in turn corresponds to a variation in group velocities [see Equation (3.1.28)] leading to a change in the length of the laser pulse over time [17, 205].

Consider two points in the laser pulse at z_1 and z_2, separated by a distance $L = z_2 - z_1$, and travelling at a group velocity of v_{g1} and v_{g2}, respectively. If the laser pulse propagates for a time interval, Δt, the difference in the group velocities, Δv_g, will translate into a change in the separation of the two points by ΔL

$$\Delta L = (v_{g2} - v_{g1})\Delta t = \Delta v_g \Delta t. \tag{3.1.42}$$

If we write the difference in group velocities as rate of change in the group velocity over the pulse length, L,

$$\Delta v_g \approx \frac{\partial v_g}{\partial z} L, \tag{3.1.43}$$

such that

$$\Delta L \approx L \frac{\partial v_g}{\partial z} \Delta t. \tag{3.1.44}$$

If we only consider the variation of the refractive index, η, due to a change in the electron density, n_e, we obtain

$$\frac{\partial v_g}{\partial z} = \frac{\partial}{\partial z}(c\eta) \approx \frac{\partial}{\partial z} c\left(1 - \frac{n_e}{2n_c}\right) = -\frac{c}{2n_c}\frac{\partial n_e}{\partial z}, \tag{3.1.45}$$

where n_c is the critical density. In the bubble regime, the leading edge of the laser pulse sees a density $n_e = n_0$, whereas the remaining pulse propagates approximately in vacuum with $n_e \approx 0$. If we assume that the density transition occurs linearly over a distance l, i.e. $\partial_z n_e = n_0/l$, then

$$\frac{\partial L}{\partial t} \approx L\frac{\partial v_g}{\partial z} \approx -L\frac{c}{2n_c}\frac{\partial n_e}{\partial z} = -L\frac{n_0 c}{2n_c l}, \tag{3.1.46}$$

which can be solved by the exponential function

$$L(t) = L_0 e^{-cn_0 t/(2n_c l)}, \tag{3.1.47}$$

where L_0 is the initial separation. This indicates that sharper density transitions (small l) lead to faster pulse compression.

3.1.9 Photon acceleration

In the previous section, we motivated that a laser pulse travelling through a density gradient can experience pulse compression. In the context of LWFA, the density gradient is produced by the intense laser pulse itself. A compression of the pulse duration as described has to be accompanied by an increase of the bandwidth of the laser pulse.

Similarly as before, consider two points in the laser pulse at z_1 and z_2 with phase velocities v_{p1} and v_{p2}, respectively. If we impose that the wavefronts at these points are separated by a phase of 2π, then the spatial separation corresponds to the wavelength $\lambda_0 = z_2 - z_1$. After a time interval Δt, the spatial separation of the wavefronts is now modified by $\Delta\lambda$

$$\lambda_0 + \Delta\lambda = \lambda_0 + (v_{p2} - v_{p1})\Delta t. \tag{3.1.48}$$

Substituting similarly as in the previous section

$$(v_{p2} - v_{p1}) \approx \frac{\partial v_p}{\partial z}\lambda_0, \tag{3.1.49}$$

so that

$$\frac{\partial \lambda}{\partial t} \approx \lambda_0 \frac{\partial v_p}{\partial z}, \tag{3.1.50}$$

or in terms of the wave frame variables ξ and τ, and the refractive index η:

$$\frac{\partial \lambda}{\partial \tau} = -\lambda_0 \frac{c}{\eta^2}\frac{\partial \eta}{\partial \xi}, \tag{3.1.51}$$

$$\frac{1}{\omega_L}\frac{\partial \omega}{\partial \tau} = \frac{c}{\eta^2}\frac{\partial \eta}{\partial \xi}. \tag{3.1.52}$$

This equation now describes how the wavelength or frequency shifts as a function of the density gradient. A positive density gradient results in an increase of the frequency, ω, i.e. blue-shifting or 'photon acceleration'. A negative gradient, on the other hand, would lead to a decrease in the frequency, i.e. red-shifting or 'photon deceleration'. In the previous section, we considered pulse compression as a result of a positive density gradient. Now we see that pulse compression is accompanied by photon acceleration. This phenomenon has been more rigourously investigated theoretically in [209, 210] and has been confirmed in experiment [211].

3.2 Laser Wakefield Acceleration

In laser wakefield acceleration (LWFA), a short (10's fs), intense and focused laser pulse ($a_0 \geq 1$) travels through an underdense plasma, driving a plasma wave by pushing the electrons out of its way by means of the ponderomotive force (see Section 2.1.4). In beam-driven plasma wakefield acceleration (PWFA), the ponderomotive force is replaced by the Coulomb force. On the time scale of the laser pulse, the ions remain static and the Coulomb force pulls the electrons back onto the laser axis, setting up a density wave. A highly intense pulse ($a_0 \geq 2$) almost completely evacuates the region in its wake, producing a cavity with strong longitudinal and transverse electromagnetic fields, which are suited to focus and accelerate electrons to relativistic energies. This is commonly referred to as the non-linear or 'bubble' regime, which enables the production of quasi-monoenergetic electron beams, first reported in 2004 [19–21]. By now maximum electron energies of beams produced in LWFA have reached the multi-GeV level in one [69, 76, 212, 213] or two coupled acceleration stages [214, 215].

A comprehensive overview on this topic explaining the fundamental physics is given in [22]. A more recent overview on the progress and status of experiments in the laser wakefield community can be found in [216].

3.2.1 Wavebreaking

At large electric fields, neighbouring electron sheets in the plasma start to cross and the plasma wave loses coherence. This is referred to as *wavebreaking* and marks the breakdown of the fluid approximation of the plasma. The maximum electric field that can be sustained by a plasma wave is

$$E_0 = \frac{m_e c \omega_p}{e}, \tag{3.2.1}$$

which is also called the *cold non-relativistic wavebreaking limit* [22, 57]. In useful units we can write:

$$E_0[\mathrm{GV/m}] \approx 96\sqrt{n_0[10^{18}\mathrm{cm}^{-3}]}, \tag{3.2.2}$$

which indicates that the maximum field sustained by a wave in a plasma of density $10^{18}\mathrm{cm}^{-3}$ is roughly 100 GV/m. Nonlinear plasma waves can exceed this value and the wavebreaking limit for a 1D relativistic, non-linear periodic plasma wave is, for instance, given by [217]

$$E_{WB} = \sqrt{2(\gamma_p - 1)}E_0, \tag{3.2.3}$$

where in the 1D low-intensity limit $\gamma_p \approx \omega/\omega_p$, and E_0 is again the cold non-relativistic wave breaking limit given above.

3.2.2 Bubble regime

A short and relativistic laser pulse can fully expel the electrons in its way. The pure ion cavity left behind is an approximately spherical 'bubble' of radius r_b [73]:

$$\boxed{r_b = 2\sqrt{a_0}\frac{c}{\omega_p},} \tag{3.2.4}$$

which can be derived by balancing the ponderomotive force with the Lorentz force acting on the electrons (see e.g. [218]). This is a highly non-linear regime leading to wavebreaking such that wakefields are only sustained for few periods. The electromagnetic fields associated to the cavity are given by [74, 205]

$$E_z = \frac{n_0 e}{\epsilon_0}\frac{\xi}{4}, \tag{3.2.5}$$

$$E_r = \frac{n_0 e}{\epsilon_0}\frac{r}{4}, \tag{3.2.6}$$

$$B_\theta = n_0 e \mu_0 \frac{r}{4}, \tag{3.2.7}$$

where n_0 is the background ion density in the bubble and $\xi = z - v_{ph}t$ is the waveframe coordinate. Here the region in which electrons are accelerated and focused is half of the cavity $r_b \approx \lambda_p/2$. The effective focusing field on an relativistic electron beam is given in useful units by [22]

$$E_r[\mathrm{GV/m}] = 9.06 \times n_e[10^{18}\,\mathrm{cm}^{-3}]\sigma_r[\mu\mathrm{m}], \tag{3.2.8}$$

where σ_r is the size of the electron beam. This focusing field forces off-axis electrons onto the axis, as a result of which the electron beam performs betatron oscillations.

3.2.3 Trapping and self-injection threshold

In order to trap electrons from the ambient plasma in the wakefield cavity, the following condition has to be satisfied [219]:

$$\boxed{r_b \geq \frac{2c\sqrt{\ln(2\gamma_{ph}^2 - 1)}}{\omega_p},} \tag{3.2.9}$$

where $\gamma_{ph} = \omega/\omega_p \approx \sqrt{n_c/(3n_e)}$ and r_b is the radius of the plasma bubble. This process is referred to as *self-trapping* and triggering the injection of electrons into the cavity solely through the evolution of the laser pulse is called *self-injection*.

Based on the trapping condition above, the minimum power required to reach self-injection, the self-injection threshold, is for the depletion-limited case estimated by [220]

$$\boxed{\frac{\alpha P}{P_c} > \frac{1}{16}\left[\ln\left(\frac{2n_c}{3n_e}\right) - 1\right]^3,} \tag{3.2.10}$$

with α the fraction of energy contained in the FWHM of the laser focal spot, and P, the laser power. P_c is the laser power at which relativistic self-focusing and diffraction are balanced, with $P_c \approx 17 n_c/n_e$ GW (see Section 3.1.7).

3.2.4 Depletion

As the laser pulse propagates through the plasma, it slowly loses energy through diffraction and driving the wake. The energy loss is concentrated at the front of the laser pulse that is interacting with the medium and thus slowly etches away at a velocity v_{etch} [221]

$$v_{etch} = \frac{\omega_p^2}{\omega_0^2} c. \tag{3.2.11}$$

The wakefield phase velocity or front velocity, v_f, is then given by the group velocity reduced by the etch velocity, v_{etch},

$$\boxed{v_f = v_g - v_{etch} \approx c\left(1 - \frac{3}{2}\frac{\omega_p^2}{\omega^2}\right).} \tag{3.2.12}$$

After a certain distance, the pump-depletion length L_{pd}, the pulse is not intense enough any more to drive a stable wave with sufficient field gradients - the cavity collapses. The depletion length in the 3D bubble regime is given by [222]

$$\boxed{L_{pd} = \frac{\omega^2}{\omega_p^2}\frac{\omega_p}{k_p}\tau \propto \frac{1}{n_e}.} \tag{3.2.13}$$

Higher plasma densities lead to faster etching of the pulse and shortens the depletion length, whilst reducing the density allows sustaining the accelerating structure over longer distances.

3.2.5 Dephasing

In the high field gradients of the wake, electrons are relatively quickly accelerated to relativistic energies, reaching velocities close to the speed of light. The driving laser pulse, on the other hand, propagates through the plasma at a group velocity smaller than c. As a result, the electrons slowly catch up with the driver and leave the accelerating phase of the cavity, hence called *dephasing*. The relativistic electrons are moving close to the speed

of light ($\beta_e \to 1$), whilst the plasma wave moves at a velocity β_p (in the 1D linear case):

$$\beta_p = \frac{v_g}{c} = \left(1 - \frac{n_e}{n_c}\right)^{\frac{1}{2}}, \tag{3.2.14}$$

where n_e is the electron and n_c the critical density. Using this one can estimate the time it takes the electrons to move out of the acceleration phase of the wave sizing half the length of the plasma wave:

$$t_d = \frac{\lambda_p}{2c\,(\beta_e - \beta_p)} \approx \frac{\lambda_p}{c}\frac{n_c}{n_e}. \tag{3.2.15}$$

The distance over which electrons leave the acceleration phase, the dephasing length L_{dp}, is then for the 1D linear regime

$$L_{dp} = \lambda_p \frac{n_c}{n_e} \propto n_e^{-\frac{3}{2}}. \tag{3.2.16}$$

The dephasing length for the 3D bubble regime is given by [222]

$$\boxed{L_{dp} = \frac{2}{3}\frac{\omega^2}{\omega_p^2} r_b = \frac{4}{3}\frac{\omega^2}{\omega_p^2}\frac{\sqrt{a_0}}{k_p} \propto \sqrt{a_0} n_e^{-\frac{3}{2}},} \tag{3.2.17}$$

which is similar to the 1D linear case but using the bubble radius and considering the front velocity, v_f, which is reduced due to the etching [see Equation (3.2.12)]. A higher plasma density reduces the front velocity of the laser pulse and the dephasing length.

3.2.6 Maximum Energy Gain

Wakefield cavities support several orders of magnitude higher electric fields than conventional radio-frequency cavities. For a 3D non-linear wake, the maximum electric field that can be supported by the plasma wave is given by [222]

$$\boxed{E_{max} = \sqrt{a_0} m_e c \omega_p / e \propto \sqrt{a_0 n_e}.} \tag{3.2.18}$$

A higher plasma density results in a larger amount of separated charge and hence a stronger electric field which is desirable for our accelerator.

On the other hand, both limiting factors introduced in the previous sections, depletion and dephasing, are inversely proportional to the plasma density. Whilst the depletion length can be extended by using a more intense laser pulse, the dephasing length at a constant plasma density remains a fixed limitation. Solutions to overcome this limit include, for instance, increasing the density either gradually or abruptly to rephase the electrons [223] and/or employ multiple lasers [224] and acceleration stages injecting the electron bunch into the accelerating phase of the new wakefield [214].

The maximum energy gain is the optimised product of the electric field and the acceleration distance. By assuming that ultimately the dephasing length is the limiting factor, the maximum energy gain W_{max} for a 3D non-linear wake at matched conditions is given by [222, 225]

$$\boxed{W_{max} = \frac{2}{3} a_0 \left(\frac{\omega_L}{\omega_p}\right)^2 m_e c^2 \propto \frac{a_0}{n_e}.} \tag{3.2.19}$$

This gives the counter-intuitive result that one has to choose low plasma densities (corresponding to lower field gradients) to accelerate particles to higher energies. A variety of injection mechanisms have been proposed to optimise the properties of the electron beam (internal [204, 226–228] and external [214, 229]).

3.2.7 Injection Mechanisms and Accelerator Tailoring

In Section 3.2.3, we introduced the self-trapping condition and the threshold for self-injection. In 1D this threshold is equivalent to the wavebreaking limit, whereas in 3D the crossing of electron sheets that trigger the injection can also occur without catastrophic wavebreaking. Other injection mechanisms have been developed to produce electron beams with specific properties, for instance high charge or low energy spread. Out of the plethora of different techniques, we will only introduce the mechanisms used in the context of this thesis, which are, besides self-injection, ionisation and shock injection.

Ionisation Injection

Electrons can be released directly into the bubble cavity through delayed ionisation of the atoms or molecules close to the peak intensity of the laser pulse. Higher-Z gases bind electrons strongly and require higher field strengths to release them. When the intense laser pulse passes through the plasma, it triggers an increased rate of tunnel ionisation near the centre of the pulse (see Section 3.1.2 on plasma formation). The released electrons can then be trapped and subsequently accelerated. This is called *ionisation injection*.

Typically, a gas with low ionisation threshold like helium or hydrogen is used as base, which is then doped with a few percent of high-Z gas, for instance nitrogen, to provide the injection events. The interplay of the laser, its evolution and intensity, and the properties of the dopant determine the amount of charge released into the cavity and the duration of the injection event. The duration of the injection translates into energy spread (Liouville's theorem, see e.g. [205]) and hence provides a way to tune the properties of the accelerated electron beam.

Shock Injection

The accelerating structure in a wakefield depends on the complex interplay of the driving laser pulse and its evolution in interaction with the surrounding medium. An evident handle onto the shape and behaviour of the cavity is the plasma density as $r_b \sim 1/\sqrt{n_e}$ and the changes in the group velocity $\Delta v_g \sim -\Delta n_e$.

An abrupt fall-off in plasma density leads to a temporary elongation of the bubble in the longitudinal direction as the effective velocity of the back of the bubble is reduced for a short time. Electrons can now be trapped inside the cavity as part of a very localised injection event. Since such a sharp density transition can in experiments be achieved by inducing a shock into the gas, this injection mechanism is called *shock injection*. Shock injection has been demonstrated as powerful tool to produce high-quality electron beams of high charge, stability and tunable energy [228, 230]. Similarly, but less localised, an extended density gradient can also trigger the injection of electrons by gradually extending the bubble size, then called *downramp injection* [231]. In contrast, a positive density gradient will lead to a decrease in the size of the bubble. A decrease in bubble size is not suitable to capture electrons but it moves the centre of the cavity closer to the laser pulse shifting the accelerating phase. This can be used to keep electrons for a longer distance in an accelerating phase to delay dephasing, and is hence referred to as *rephasing* [223].

Chapter 4

Experimental Methods

The following Chapter introduces a selection of experimental methods and techniques relevant in the context of the experimental results presented in this thesis and other laser wakefield acceleration (LWFA) experiments. The three main ingredients of an LWFA experiment are covered: a high-intensity laser, gas targetry and diagnostics for particles and secondary radiation. The measurement of high-energy gamma radiation will be discussed more extensively as it is central to this work.

The Chapter starts by introducing the Gemini laser system, the dual-beam high-intensity laser used to conduct the experiments in this work, along with diagnostics and methods to characterise high-intensity laser pulses. It then continues with a section on gas targets and techniques to diagnose the plasma, followed by particle diagnostics. Finally, the chapter focuses on diagnostics for high-energy radiation in the gamma regime, in particular a scintillator array used to infer gamma spectra. A comprehensive review of diagnostics used in LWFA experiments is, for instance, provided in [232].

4.1 The Gemini laser system

All experimental results presented here were acquired at Target Area 3 using the Gemini laser [233, 234] of the Central Laser Facility, Rutherford-Appleton Laboratory, UK.

4.1.1 Laser properties

The titanium-sapphire Gemini laser system provides two beams every 20 seconds at a compressed pulse duration of down to 30 fs and up to 15 J energy on each arm at a central wavelength of 800 nm [84]. The collimated beams that enter the target chamber have a diameter of just under $\sim$ 150 mm, a flat-top intensity profile and are focused with a spherical mirror or off-axis parabolas (OAPs). Adaptive optics (AOs) are deployed on both laser arms in conjunction with wavefront sensors to remove aberrations and flatten

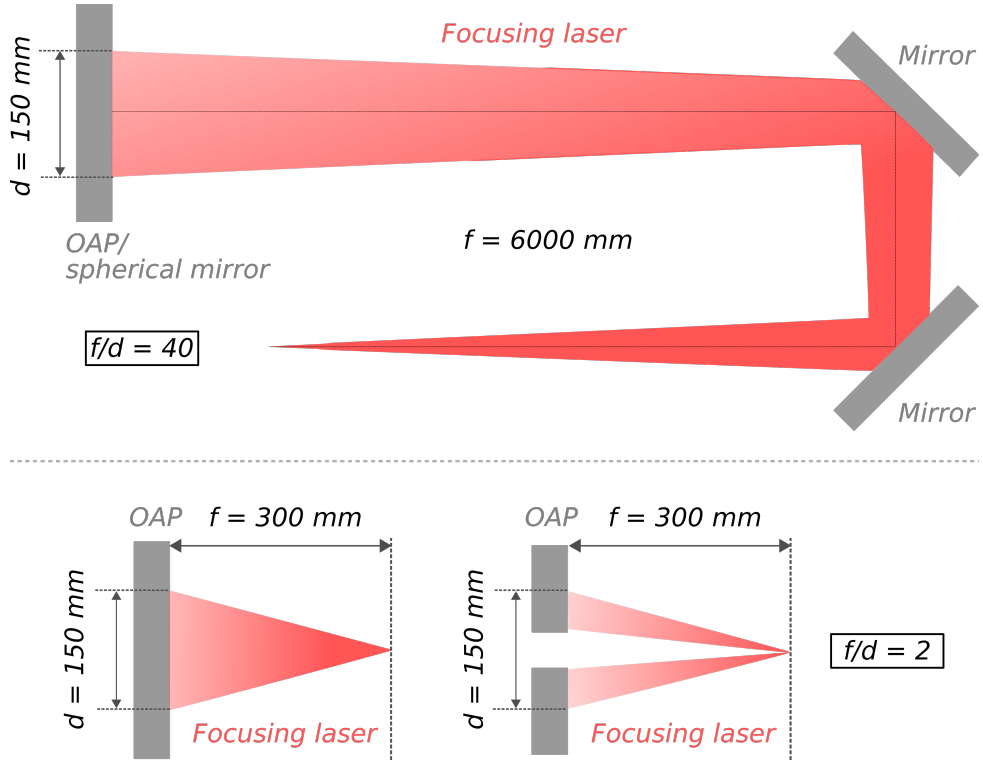


Figure 4.1: Sketch of focusing geometries used in experiments at Gemini *discussed in this work. Top: A long-focal-length geometry using an $f/40$ spherical mirror or off-axis parabola (OAP) used to drive a wakefield accelerator. Bottom: A short-focal-length $f/2$ geometry for a scatterer or heater beam using a full off-axis parabola (left) or an optic with a central hole (right).*

the wavefront. In addition to its full-power capabilities, a diode continuous-wave mode for alignment and a low power pulsed mode at 10 Hz repetition rate are available.

4.1.2 Beam line geometries

In the context of the LWFA experiments discussed later, typically two types of beam line geometries are of relevance at Gemini (see Figure 4.1): First, a long-focal-length geometry using either an $f/40$ spherical mirror or an off-axis parabola with focal length $f = 6\,\mathrm{m}$ to provide an intense laser pulse with normalised vector potential $a_0 > 1$ and a long Rayleigh length, z_R, to drive LWFA efficiently over long distances. This geometry is used for the wakefield driver beam in all experiments discussed in this work. Due to the long focal length and the limited size of the target area and the vacuum chamber, the beam has to be reflected or 'folded' at least once during the focusing process, in recent setups about halfway between optic and focal plane (see Figure 4.1, top). As a result, the maximum energy usable in this laser arm is limited by the damage threshold of these 'folding' mirrors or, in other words, by the fluence (optical energy delivered per unit area) the mirrors can sustain. The threshold at which damage occurs depends on several factors, including

the beam quality and beam size, the quality of the mirror coating and cleanliness of the chamber. In this work, it was found to be $\sim 0.175 \pm 0.035\,\mathrm{J/cm^2}$.

The second focusing geometry is the short-focal-length scatterer (see Figure 4.1, bottom) which is typically an $f/2$ off-axis parabola with focal length $f = 300\,\mathrm{mm}$. In the experiments discussed in Chapters 5 and 6, an off-axis parabola with a central fitted hole was used to enable a head-on counter-propagating geometry in conjunction with the long-focal-length beam line.

4.2 Laser Diagnostics

4.2.1 Laser Energy

At GEMINI, the laser energy is measured on every shot by collecting the laser light that is transmitted through the back of a highly-reflective dielectric mirror in the laser area and by imaging it onto a CCD camera chip. The integrated number of counts on the CCD is calibrated using a laser energy meter (Gentec QE8SP-B-BL-D0) and the filtering is adjusted for different power modes. A laser energy meter is also used to measure the reflectivity of the compressor gratings, at GEMINI typically between 60 and 70 percent, and the energy reaching the interaction point (energy on-target).

4.2.2 Laser Pulse Duration

At GEMINI, frequency-resolved optical gating (FROG) [235] is used to measure the pulse duration of the laser and characterise its temporal intensity profile. A FROG trace is taken on every shot by collecting laser light that is transmitted through highly-reflective dielectric mirrors, similarly as for the on-shot energy measurement.

The FROG is a diagnostic to measure the intensity and spectral phase of ultrashort laser pulses as present at GEMINI ($\sim 40\,\mathrm{fs}$). The setup is similar to an autocorrelator and is optically gated by combining two beams in a non-linear medium, typically a second-harmonic-generation crystal. The radiation is then spectrally resolved (hence frequency-resolved/*FR*OG) and provides information about the spectral phase. See, for instance, [235] and [236] for more details.

4.2.3 Focal Spot Characterisation

The ability to characterise the properties of a focused laser pulse, in particular its size and peak intensity, is crucial for high-intensity laser experiments as it enables the optimisation of the focal spot shape for the respective application in an active feedback loop [237], and also enables diagnosing the physical phenomena the laser is employed to probe or induce.

In LWFA a short-pulse laser is focused down to reach high intensities to drive a wake, but has to guide itself over a long range at the same time. Only energy contained in the beam centroid is efficiently guided, whilst energy in the 'wings' of the beam is lost and reduces the peak intensity of the laser pulse [220]. For Compton-backscatter experiments, on the other hand, a high intensity increases the yield of X-rays and is prerequisite to access nonlinear phenomena [80]. Since the energy in the laser pulses is limited and the temporal compression is also bounded (and not always desirable), the spatial shaping of the focal spot is a critical tool to reach high intensities efficiently.

A *direct* measurement and characterisation of a high-intensity laser focus, also referred to as *focal spot*, or even just its peak intensity is, however, very challenging. For this reason, an attenuated low-power laser pulse is characterised at GEMINI instead. In the low-power mode, the laser pulses are amplified in all but the final amplification stage (see, for instance, [69] for more details on the laser beam line), propagate on the same beam path and through the same materials, and are manipulated by the same optics. As a result, the focal spot in the low-power and high-power mode are expected to be very similar, with exception of certain thermal effects.

At GEMINI the low-power focal spot is imaged through a special long-working-distance microscope objective (Mitutoyo near-infrared infinity-corrected apochromatic) onto the CCD chip of an AVT Manta G-033B. To characterise the focal spot of the $f/40$ beam line (applicable to all experimental results) and the $f/2$ focal spot with phase plate (Chapter 7), a microscope objective with magnification $\times 10$ was used. A $\times 20$ objective was used to image the focal spot from the $f/2$ beam line in the colliding-pulse experiments (Chapters 5 and 6). A thin metal wire $\sim 100\,\mu\text{m}$ was used to localise a well-defined spatial plane for the position of the focus, relative to which other components in the setup were then positioned.

In order to produce an intensity profile of the laser pulse, we require a measurement of the energy in the laser pulse, its temporal structure and spatial properties. The diagnostics for on-shot laser energy and pulse duration measurements were already presented in the previous section. The measurement of the spatial properties of the focal spot and how to relate the focal spot image to an intensity distribution are presented in the following.

Spatial calibration

The imaging system for the focal spot characterisation was spatially calibrated by imaging well defined line pairs on a transmissive resolution target, specifically a 1951 US Air Force Target (R1DS1P, Thorlabs). Figure 4.2 (left) shows an image of the central part of the USAF target, containing the smallest line pairs, with a sketch of the full USAF target pattern (negative) presented on its right side. A simple diode laser was used as backlighter. Each line pair is identified by its element and group number, and the related spatial

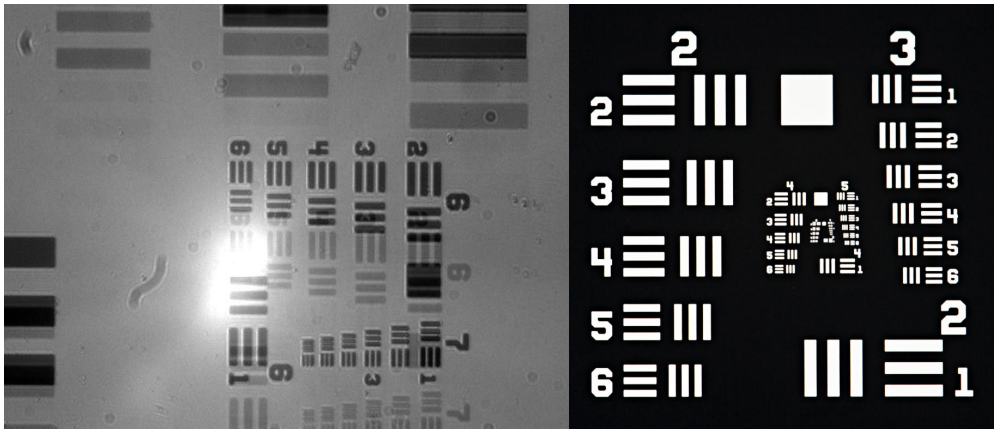


Figure 4.2: USAF targets to spatially calibrate the imaging system of the focal spot camera. Left: Central part of a transmissive USAF target backlit by a diode laser. Right: Full (negative) USAF pattern from the Thorlabs website. The groups in the centre (numbers not legible) correspond to the groups shown on the left.

dimension is given on the website of the manufacturer in units of line pairs per millimetre, lp/mm. By multiplying the size of a line pair on the image (pixels per line pair) with the dimensions given on the data sheet (line pairs per mm), we obtain the number of pixels corresponding to one millimetre or in inverse the size of one pixel, i.e. the spatial calibration of the image. The magnification of the imaging system, M, on the other hand, is then simply the physical size of one camera pixel, which can be found on the datasheet of the camera in use, divided by the determined spatial scale that corresponds to one pixel on the image:

$$M = \frac{image\,pixel\,size\,[\mu m/pxl]}{camera\,pixel\,size\,[\mu m/pxll]} = \frac{pixels\,per\,line\,pair/line\,pairs\,per\,mm}{camera\,pixel\,size\,[\mu m]}. \qquad (4.2.1)$$

Using the image shown in Figure 4.2 as an explicit example: One line pair of the second element of the 6th group measures 15 pixels. According to the data sheet this element has a scale of 71.8 lp/mm, such that we obtain for the image 1077 pixels/mm or 0.93 µm/pixel. The camera was of type AVT Manta G-033B with 9.9 µm physical pixel size, which then gives a magnification of 10.65.

Intensity Distribution and Peak Intensity

The image of the low-power focal spot on the CCD is a temporally integrated measurement of the profile of the laser pulse. Given an appropriate background subtraction, no saturation on the image and given that the entire focal spot is captured on the image, the total pixel count corresponds to the total energy in the laser pulse and the distribution of the counts in turn corresponds to the spatial energy distribution. This also applies to the high-power focal spot as we assume that the low-power laser pulse is representative of the high-power pulse.

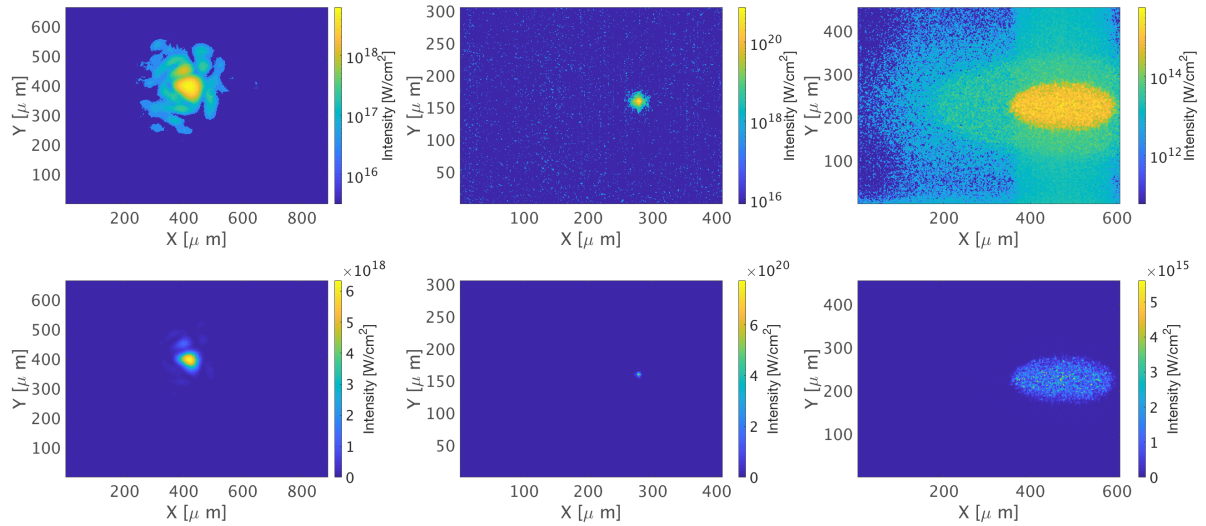


Figure 4.3: Examples of low-power focal spots from different focusing geometries, measured at Gemini *in 2019 (left, centre) and 2018 (right). The x- and y-axes show the horizontal and vertical spatial scale in micrometres, the colour scale shows the peak intensity in units of W/cm^2 on a linear scale (bottom row) and a logarithmic scale (top row). The focusing optics were an $f/40$ off-axis parabola (left column) and an $f/2$ off-axis parabola (central and right column). A phase plate was inserted into the collimated beam path of the laser pulse shown in the right column. The halo around this spot causes scattering in the imaging system which leads to the apparent rectangular region of intensity visible on the logarithmic scale (top) but is not a physical representation of the spot itself.*

By relating the on-shot energy measurement (see Section 4.2.1) to the total pixel count on the image, we obtain an energy calibration in units of $J/pixel\,counts$. Since the image is spatially calibrated, we can assign each pixel in turn a fluence, $pixel\,counts/area \rightarrow J/area$. If we now fold in the time over which this fluence is delivered, we obtain the intensity, energy per unit time and area, here given in the units W/cm^2. By considering the entire pulse duration (see Section 4.2.2), this corresponds to the average intensity. If we extract the peak power from the pulse envelope (FROG trace), we can determine the peak intensity, which is the driving quantity in most LWFA and colliding-pulse experiments. Finally, as a result, we obtain the spatial distribution of the peak intensity of the focal spot.

Figure 4.3 shows the intensity distributions of three example focal spots from different focusing geometries (note different spatial scales). The colour scale indicates the intensity in W/cm^2 on a logarithmic scale (top) and a linear scale (bottom), respectively. The laser pulses were focused by an $f/40$ off-axis parabola (left column) and an $f/2$ off-axis parabola (centre and right). A phase plate [238] was inserted into the collimated beam to obtain the wide, speckled focal spot on the right, which was used as X-ray heater beam in the experiment described in Chapter 7. The other two focal spots were measured on a Gemini campaign in 2019 (Chapter 5).

4.3 Dual-Beam Timing Diagnostics

All experiments discussed in this thesis use both laser arms of GEMINI, so that their laser pulses have to be overlapped in space and synchronised in time, or in other words they have to be 'timed' to each other. This section discusses the two diagnostics, photodiodes and (spatial) interference, that were used to measure the temporal separation of the two laser pulses. Photodiodes measured relatively 'large' separations on the nanosecond to few picosecond level, which was by itself sufficient for the experimental setup described in Chapter 7. The colliding-pulse experiments described in Chapters 5 and 6, on the other hand, required a femtosecond level synchronisation of the laser pulses, for which interference was used in addition. Two plane waves crossing at an angle produce an interference pattern of parallel straight lines, whereas a plane wave interfering with a spherical wave front results in a circular pattern. Two laser pulses that expand at different f-numbers, here $f/2$ and $f/40$, behave similarly as the latter case as the radii of curvature of their wave fronts differ strongly. The presence of a circular interference pattern then signals temporal overlap within their coherence length at an accuracy of tens of femtoseconds. At its end, this section considers the implications for electron-laser timing from a perspective of laser-laser timing, and effects from other experimental procedures specific to GEMINI, such as the pump-down of the vacuum chamber or the attenuation of the laser pulses.

At GEMINI both laser arms are 'intrinsically' synchronised as they originate from the same source (oscillator), but might arrive at the interaction point at different times as they travel on different beam paths. By measuring the difference in the time of arrival of both laser pulses, $\Delta\tau$, the length of the beam paths can be adjusted accordingly, such that $\Delta\tau \to 0$, i.e. the laser pulses are 'timed'. Temporal separations on the nanosecond level are typically corrected by extending the beam path of the 'early' laser pulse by several optics. Smaller adjustments corresponding to temporal shifts of tens of picoseconds or less are performed using a motorised linear stage (Newport M-ILS250) on the 'split-and-delay' (SAD) table in the laser area. The SAD delay stage adds or removes beam path in double-pass at micrometre or correspondingly few femtosecond precision.

4.3.1 Photodiodes

In the experiments described in this thesis, two attenuated (low power) laser pulses were spatially overlapped at the interaction point. The pulses are then either directed onto the active chip of a photodiode or are scattered from an object placed at the interaction point, for instance a piece of lens tissue, which the photodiode then faces. Each laser pulse triggers a response in the photodiode that can be measured with an oscilloscope. Since each pulse is only $\sim 40\,\mathrm{fs}$ long, almost instantaneous for the diode, the response for each pulse is a symmetric peak with the rise/fall time as width. The relative time of arrival can

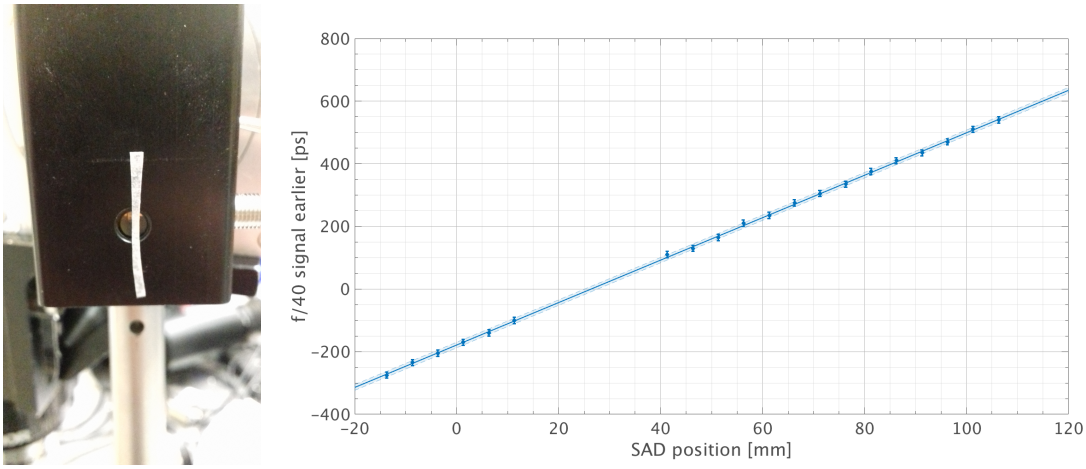


Figure 4.4: Left: Photodiode (black) used in the experiments in this work (EOT-4000 GaAs). The active area is inside the round 'window'. The white strip is used to scatter the laser and increase the signal yield. Right: Temporal separation between two laser pulses ($f/40$ and $f/2$) measured with a fast diode and oscilloscope. The plot shows how much earlier the $f/40$ laser pulse arrives as a function of the position of the delay stage (SAD position). In the region between 15 and 40 picoseconds, the peaks start to merge and measurement of the separation becomes unreliable. The linear fit can be used to identify the delay required to match the time of arrival of both laser pulses. The shaded region indicates the 95 percent confidence interval for the fit.

then be determined by measuring the separation of the two peaks. At GEMINI the fast EOT-4000 GaAs photodetector (see Figure 4.4) with a rise/fall time of < 30 ps was used in conjunction with a Lecroy WaveMaster 813Zi-B oscilloscope (> 13 GHz). The detectors were only used in air and were not tested for vacuum use.

Photodiodes and oscilloscopes are relatively straightforward to set up and use, but due to their typical rise/fall time of several tens of picoseconds, the accuracy of an individual measurement using an appropriate oscilloscope is ~ 10 ps. The accuracy of the synchronisation can be improved by conducting multiple measurements across a range of relative temporal delays and then interpolating between the data points to obtain the zero-delay point. At GEMINI the delay stage on the SAD table can be moved to adjust the relative delay of both laser arms. Since the stage moves at micrometre precision, the main experimental error for each measurement is the reading error on the oscilloscope.

The result of such a scan in relative delay is shown in Figure 4.4 (right) for data taken on the experimental campaign presented in Chapter 5: the relative delay of the two laser pulses (here in terms of how much earlier the $f/40$ laser pulse arrives) as measured with the photodiode and the oscilloscope is shown as a function of the SAD position. When both pulses arrive within each other's rise or fall time, the diode responses merge and the peaks can not be properly distinguished, which is why there are no data points around the zero-delay point. The linear fit to the data points is parametrised by $y_{fit} = 6.78\,[\text{ps/mm}] \times x_{SAD}[\text{mm}] - 178.72\,[\text{ps}]$ which indicates that the zero point is

at $x_0 = (26.36 \pm 0.68)\,\mathrm{mm}$. The error on the SAD position (equivalent to $\sim 2\,\mathrm{ps}$) was estimated using the 95% confidence interval of the linear fit (shaded area in Figure 4.4).

4.3.2 Interferometry

Diode timing as described in the previous section can measure up to nanosecond temporal separations but is limited to an accuracy of a few picoseconds. It is a suitable technique to synchronise the two laser pulses 'roughly'. Interference of the two laser pulses can be used to synchronise the two laser pulses to the femtosecond level.

Considering the electric fields of two plane waves with the identical frequency ω and polarisation but different wave vectors $\mathbf{k_1}$, $\mathbf{k_2}$, time of arrival t_1, t_2 and initial phase ϕ_1, ϕ_2 can be written as:

$$\mathbf{E_1}(\mathbf{r}, t_1) = E_1 e^{i(\omega t_1 - \mathbf{k_1}\cdot\mathbf{r} + \phi_1)}\mathbf{e_x},\ \mathbf{E_2}(\mathbf{r}, t_2) = E_2 e^{i(\omega t_2 - \mathbf{k_2}\cdot\mathbf{r} + \phi_2)}\mathbf{e_x}, \tag{4.3.1}$$

where $\mathbf{e_x}$ is a unit vector indicating the polarisation, $\mathbf{r}$ is the position vector and E_1, E_2 are the amplitudes of the electric fields. The combined intensity of both plane waves, for instance at the plane of the detector, is

$$I = \frac{1}{4}\epsilon_0 \mathbf{E}\cdot\mathbf{E}^*, \tag{4.3.2}$$

where $\mathbf{E}^*$ is the complex conjugate of $\mathbf{E}$, and $\mathbf{E} = \mathbf{E_1} + \mathbf{E_2}$, or more specifically

$$I = \frac{\epsilon_0}{4}\left|E_1^2 + E_2^2 + E_1 E_2 \cos(2ky\sin\theta - \omega\Delta\tau + \Delta\phi)\right|, \tag{4.3.3}$$

where θ is the angle between the two plane waves, $\Delta\tau$ the difference in their time of arrival and $\Delta\phi$ the difference in the initial constant phase. The relation shows that the crossing plane waves produce a straight interference pattern due to the angle, θ, between them which vanishes when both wave vectors are parallel, i.e. $\theta = 0$. The contrast, the difference between the maxima and minima $(I_{max} - I_{min})/(I_{max} + I_{min})$, is optimised for equal field amplitudes, $E_1 = E_2$. If we consider a plane wave and a spherical wave instead, the resulting interference pattern will produce concentric rings due to the radius of curvature:

$$I \sim 1 + \cos\left(\frac{\pi r^2}{\lambda R}\right), \tag{4.3.4}$$

where we simplified the relation by assuming that the wave vectors are parallel and $\Delta\tau = 0$, $\Delta\phi = 0$, i.e. in contrast to the previous case the interference pattern does not vanish for parallel waves. In the limit of $R \to \infty$, this approaches the case of two plane waves.

A focusing and defocusing Gaussian laser pulse changes its radius of curvature, R,

where the wave front is strongly curved near the focus (within few Rayleigh lengths, z_R), especially for tightly focused beams, and asymptotically flat at a distance $|z| \gg z_R$ away from the focus or weakly focused beams (see Section 3.1.4). As a consequence, one can produce straight or circular fringes by interacting two Gaussian laser pulses either close or far away from their foci, or by focusing one with a low f-number and the other one with a high f-number optic.

Ultrashort laser pulses require large bandwidths, Δf, such that the coherence length, l_{coh}, is very short ($l_{coh} \propto 1/\Delta f$), here shorter than the pulse duration. As a result, the variation in the interference pattern due to a change in the term $\omega\Delta\tau$ can be neglected when varying the relative delay between two pulses. The interference pattern only appears when both pulses arrive at the detector plane within their coherence time. Since the coherence time is here shorter than the pulse duration, the effective time window over which interference is observed is approximately the combined duration of both laser pulses. For two laser pulses of comparable pulse duration, the contrast of the pattern is optimised when the beams are centred on each other in space and time as then the entirety of the pulses interfere. This method is here referred to as *spatial interferometry*. Since the 'active' time window in which the pattern appears is very small an initial 'rough' timing using the photodiodes described in the previous section is of advantage.

On the other hand, it is possible to increase the coherence length by dispersing both laser pulses with a grating such that the individual frequency components interact separately, assuming both pulses are identically chirped. This method is referred to as *spectral interferometry*. See for instance [239] for a detailed description. Depending on the dispersion, this enables an active window of hundreds of picoseconds and in turn allows using the variation of $\omega\Delta\tau$ to quantitatively determine the temporal separation of the laser pulses as it is now encoded in the wavelength of the interference pattern.

Experimental Implementation

In the experiments discussed in Chapters 5 and 6, spatial interferometry was used to synchronise two counterpropagating laser pulses of pulse duration $\sim 45\,\mathrm{fs}$, one focused by an $f/2$ off-axis parabola (OAP), the other by an $f/40$ OAP or spherical mirror. The laser pulses are cross-polarised and the timing measurements were performed in an attenuated low-power mode. A 90-degree reflective knife-edge prism (Thorlabs, protected aluminium/dielectric) was placed at the interaction point to combine and reflect the counterpropagating beams collinearly onto the CCD chip of a camera (see Figure 4.5, left). By gradually translating the prism away from the CCD, the two laser beams move closer to the knife edge of the prism and in the process closer together until only one half of each beam is reflected (see dotted prism outline in Figure 4.5, left). By now moving the CCD

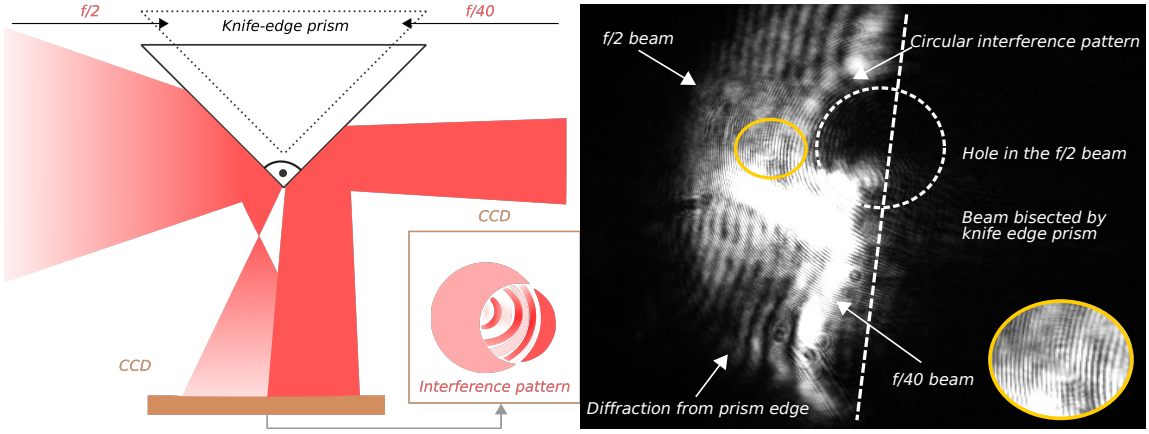


Figure 4.5: Realising spatial interferometry as timing diagnostic in an experiment. Left: Sketch of a spatial interferometry setup used in the experiments described in this work. Two counterpropagating laser beams are reflected collinearly from a 90-degree knife-edge prism and onto a CCD (brown). One laser pulse is highly divergent ($f/2$, left), the other one has a comparatively long Rayleigh length ($f/40$, right). The different radii of curvature result in a circular interference pattern when both laser pulses are overlapped in space and time. The prism can be translated to only reflect half of each beam (dotted prism). Right: Example of spatial interferometry (circular interference pattern) measured in an experiment using a setup as sketched out on the left with an attenuated (low-power) pulsed $f/2$ (OAP with hole) and an $f/40$ beam. Both beams aligned such they are effectively bisected by the knife-edge prism (spatial overlap, see dotted prism in the sketch on the left). As a result, the $f/2$ beam shows straight diffraction patterns in its near field. The hole in the $f/2$ beam is also clearly visible and the circular interference pattern is centred on it which indicates that both beams are close to parallel and the interference pattern mainly originates from the different radii of curvature.

in the opposite direction, the beams diverge and overlap with each other: we achieved spatial overlap. When both pulses are also synchronised in time, a circular interference pattern will appear which allows a synchronisation of both beams to about $\sim 30\,\mathrm{fs}$. An example of this final configuration from the experiment described in Chapter 5 is shown in Figure 4.5 (right), where the large half circle with the central hole is the divergent $f/2$ laser pulse and the bright spot is the $f/40$ beam that expands only slowly. The straight, vertical interference pattern is due to diffraction from the knife edge, whereas the circular, more closely spaced circular pattern results from the interference between both two pulses.

The camera was equipped with a long-working-distance microscope objective ($\times 10$ Mitutoyo Plan Apochromat Near-Infrared) and a linear polariser. The polariser is prerequisite for interference but was also be used to adjust the relative brightness of both beams to increase the contrast of the interference pattern. The contrast was also adjusted by taking advantage of the different divergences of the beam and moving the imaging plane closer or further away from the focus. Once the contrast was maximised, the visibility of the pattern was optimised to determine the temporal overlap more accurately. The accuracy of the synchronisation can be improved through statistical measurements, similarly as described

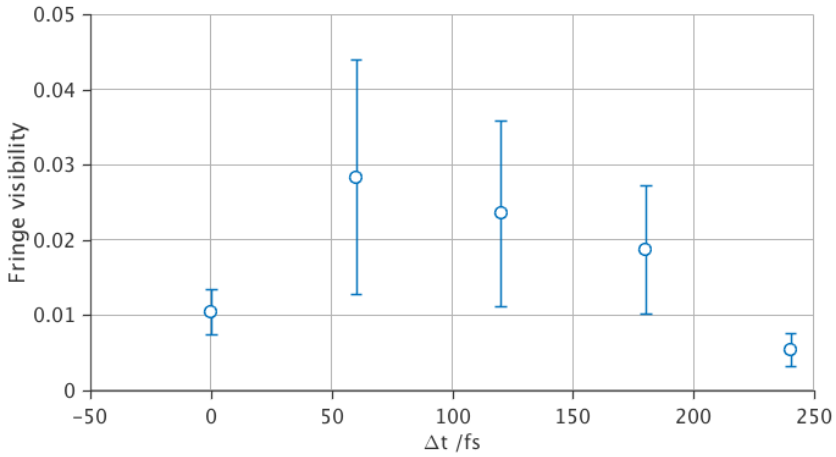


Figure 4.6: Visibility of the interference pattern (fringes) as a function of the relative delay from a reference position for data taken on an experimental campaign at Gemini *in 2015. Figure courtesy of J. Cole (Imperial College).*

for the diode timing. Figure 4.6 shows the 'fringe' (interference pattern) visibility as a function of the SAD position, using data analysed for [162] by J. Cole (Imperial College). The position for the optimum overlap was determined through a fitting routine. The uncertainty of this technique was estimated to be $\sim 17\,\text{fs}$.

4.3.3 Additional considerations for the synchronisation of beams

The synchronisation of two laser pulses to each other or of a laser pulse with an electron beam to the femtosecond level is very challenging (even if we neglect the spatial overlap to the micrometre level). This section will discuss certain factors that affected the timing procedure in the context of the experiments at Gemini discussed later in this thesis.

One key fact to remember is that light moves slower through media than through vacuum. The group velocity, v_g, is reduced by the refractive index, η, to $v_g = c/\eta$ or more specifically in a plasma to $v_g \approx c(1 - 1/2(\omega_p/\omega)^2)$ (see Section 3.1.5), where ω is the frequency of the laser and ω_p is the plasma frequency (see Section 3.1.3). Introducing or removing media asymmetrically from beam paths changes the relative time of arrival of the laser pulses. Typical examples at Gemini for this are moving from air to vacuum (pumping down the vacuum chamber), opening or closing the transparent gate valves, or attenuating beams using glass slides when switching between different power modes.

Shifting beam paths from air to vacuum

The refractive index of vacuum is $\eta_0 = 1$, whereas the refractive index of air, for instance, at 20° Celsius, 45% relative humidity and atmospheric pressure is $\eta_{air} = 1.00027$ for light of wavelength $\lambda = 800\,\text{nm}$ [240]. The difference in time, Δt, it takes a laser pulse to travel

a distance d in vacuum or air is then proportional to the difference in the refractive indices:

$$\Delta t = \frac{d}{c}\left(\eta_{air} - \eta_0\right), \\ \Delta t \approx 0.9\,\mathrm{ps} \times \frac{d}{1\,\mathrm{m}}, \tag{4.3.5}$$

which means that it takes the laser pulse 0.9 ps longer to travel one metre in air than in vacuum. If the beam paths of two laser pulses are of different length, the difference in their beam path will result in a shift in the relative time of arrival at the interaction point when transitioning from air to vacuum.

At Gemini the laser arm used as wakefield driver typically covers a beam path of over 10 m distance due to the long-focal-length geometry with $f = 6\,\mathrm{m}$, whilst the scatterer beam only covers about half of the distance. If both beams arrive at the same time at the interaction point when the chamber is at air, then a difference in 5 m, for instance, would mean that in vacuum the laser pulse following the long-focal-length beam line arrives at the interaction point 4.5 ps after the scatterer.

As a result of the pump-down process, the components in the vacuum chamber and the vacuum chamber itself experience changes in pressure and temperature which in turn result in stress on the materials. This can lead to a steering of the laser beams which affects the alignment in general but also modifies the beam path.

Opening and closing gate valves

Another step in the pump-down process at Gemini is opening the transparent gate valves that separate the target chamber, which is often at air or lower quality vacuum, from the relatively permanent and high quality vacuum of the two laser compressors. Once the pressure in the target chamber reaches a sufficiently low value and the turbo pumps are engaged, the gate valves can be opened. Both gate valves at Gemini are made of sapphire glass, but measurements found a slight difference in thickness of around $\Delta x = 60 \pm 3\,\mu\mathrm{m}$ [241] corresponding to $\Delta t = 350 \pm 17\,\mathrm{fs}$ at a wavelength of $\lambda = 800\,\mathrm{nm}$. The gate valve of the laser arm that is predominantly used as wakefield driver was found to be thicker.

Attenuation of beams

The previous two examples can be cross-checked by repeating some of the timing procedures after the pump-down, for instance using again spatial interferometry, whereas the following example can not. At Gemini glass slides are used as beam attenuators in the low-power modes and can be used in conjunction with polarisers and waveplates to improve the contrast of the interference pattern in spatial interferometry (see Section 4.3.2). In some

cases, this will require inserting material asymmetrically in both laser arms in order to optimise the visibility of the pattern.

The attenuators are 2 mm thick fused silica glass slides with refractive index $\eta = 1.4533$ [242]. The slides are inserted at 45 degrees angle relative to the laser beam axis which delays the laser pulse by 4.24 ps for each glass slide. The attenuators were found to be identical to each other to within $\Delta x < 10\,\mu\text{m}$, such that an equal number of attenuators in each beam path does not introduce a measurable relative delay. An unequal number of attenuators in each beam, on the other hand, requires an adjustment of the beam paths relative to the configuration at which the interference pattern is observed.

Synchronisation of an LWFA electron beam with a laser pulse

Using spatial interferometry, the two laser pulses can be synchronised in vacuum to an estimated accuracy of 30 fs. This timing is only valid if both laser pulses travel through vacuum. In a shooting scenario, however, the driving laser pulse propagates through plasma to accelerate electrons via LWFA. The propagation in a medium reduces the group velocity of the laser pulse and delays its arrival relative to the vacuum timing. In the colliding-pulse experiments discussed in Chapters 5 and 6, we are in addition trying to overlap the scattering beam with the electrons accelerated by the driver pulse rather than the driver itself. The LWFA electron bunch trails behind the driving laser pulse and arrives later at the interaction point. Since the scattering beam arrives before both at its focal plane and the designated interaction point, the real collision will occur beyond this point. The sketch in Figure 4.7 illustrates this for the relevant scenario of a vacuum interaction point right at the end of a wakefield accelerator (plasma).

The following analysis considers the scenario illustrated in Figure 4.7 and explicitly derives Equation 2 in [162]. It is based on work by Jason Cole (Imperial College). We assume that the laser pulse travels through a plasma of electron density n_e at the standard non-linear group velocity reduced by the etching velocity, $v_f/c \approx 1 - \frac{3}{2}\frac{n_e}{n_c}$ (called front velocity in [221]), where n_c is the critical density. Given a plasma of thickness d the laser pulse of the scattering beam travels in the same time a distance $d' = dc/v_f > d$. Both laser pulses now meet at a distance δz_1 past the focal plane of the scattering beam (see Figure 4.7, central row):

$$\delta z_1 = \frac{1}{2}\left[d\frac{c}{v_f} - d\right] = \frac{d}{2}\left[\left(1 - \frac{3}{2}\frac{n_e}{n_c}\right)^{-1} - 1\right] \approx \frac{d}{2}\left(1 + \frac{3}{2}\frac{n_e}{n_c} - 1\right) = \frac{3d}{4}\frac{n_e}{n_c}. \tag{4.3.6}$$

The electrons in turn trail around N plasma wavelengths, λ_p, behind the driving laser pulse and meet the scattering pulse midway (see Figure 4.7, bottom row), neglecting the

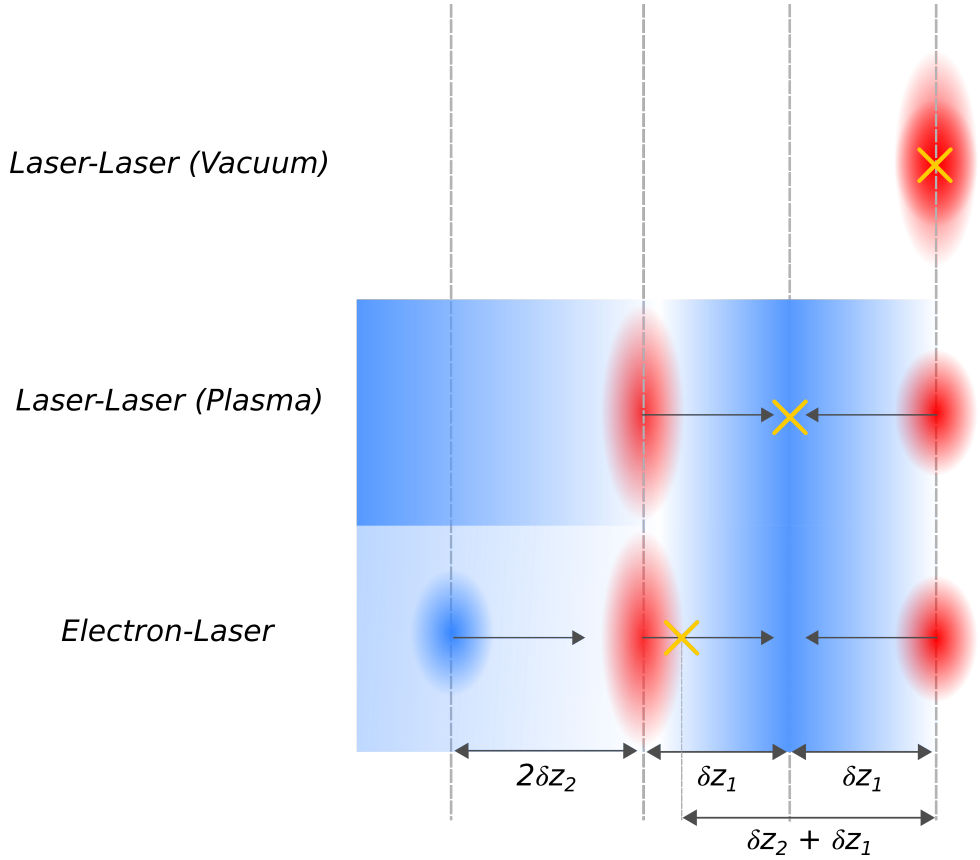


Figure 4.7: Top row: Two counterpropagating laser pulses (red) are synchronised to each other in vacuum so that they meet at a designated interaction point (yellow cross) $z = 0$ at $t = 0$. Central row: The laser pulse entering the sketch from the left now propagates through plasma and is slowed down such that at $t = 0$ it is a distance $2\delta z_1$ separated from the designated interaction point (see Eqn. (4.3.6)). The laser pulses then meet halfway at $z = \delta z_1$ (yellow cross). Bottom row: An LWFA electron bunch is trailing behind the laser pulse at $2\delta z_2$ distance (see Eqn. (4.3.7)). The effective interaction point is now at $\delta z = \delta z_1 + \delta z_2$ (see Eqn. (4.3.8)).

reduced group velocity over this short distance:

$$\delta z_2 = \frac{1}{2} N \lambda_p = \frac{1}{2} N \frac{2\pi c}{\omega_p} = \frac{1}{2} N \frac{2\pi c}{\omega} \frac{\omega}{\omega_p} = N \frac{\lambda_0}{2} \sqrt{\frac{n_c}{n_e}}. \tag{4.3.7}$$

The smallest possible value of N, assuming a homogeneous plasma, is $N = 1/2$ which is when the acceleration is close to its dephasing limit. Under these assumptions the electron bunch and the scattering beam meet at δz distance from the intended collision point:

$$\boxed{\delta z = \frac{3d}{4} \frac{n_e}{n_c} + N \frac{\lambda_0}{2} \sqrt{\frac{n_c}{n_e}},} \tag{4.3.8}$$

where in this context d is the distance of the injection point from the front of the plasma. We can instead also determine, similar as before, the temporal offset, $\Delta\tau$, relative to the

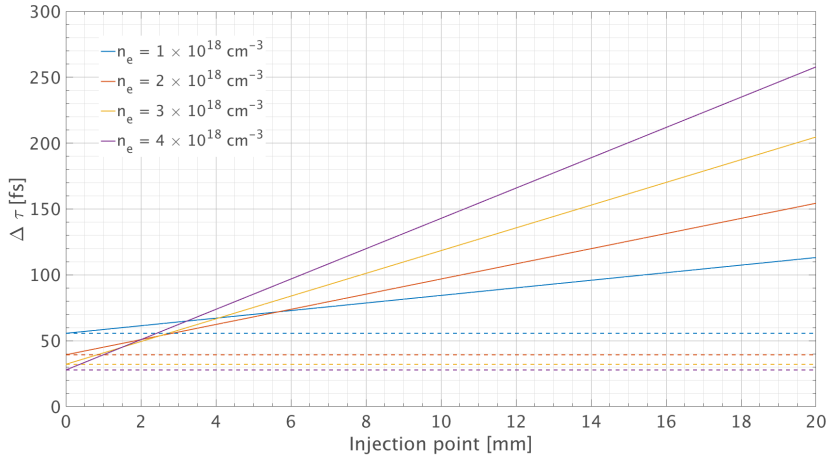


Figure 4.8: Temporal offset between the laser pulse (in vacuum) and the electron beam, $\Delta\tau$, as a function of the injection point relative to the start of the plasma, d, for the dephasing limited case, $N = 1/2$, for different electron densities, n_e. The dashed lines indicate the delay $\Delta\tau$ for $d = 0$ (immediate injection) for the respective electron density in the same colour.

vacuum laser-laser timing:

$$\boxed{\Delta\tau = \frac{2\delta z}{c} = \frac{3d}{2c}\frac{n_e}{n_c} + N\frac{\lambda_0}{c}\sqrt{\frac{n_c}{n_e}},} \tag{4.3.9}$$

or in terms of practical units:

$$\Delta\tau[\text{fs}] \approx 5 \times 10^3 \times d[\text{mm}]\,\frac{n_e}{n_c} + 3.34 \times \lambda_0[\mu\text{m}]\,N\sqrt{\frac{n_c}{n_e}}, \tag{4.3.10}$$

and specifically for $\lambda_0 = 0.8\,\mu\text{m}$

$$\Delta\tau[\text{fs}] \approx 2.88 \times d[\text{mm}]\,n_e[10^{18}\text{cm}^{-3}] + 1.11 \times 10^2 \times N\left(n_e[10^{18}\text{cm}^{-3}]\right)^{-\frac{1}{2}}, \tag{4.3.11}$$

where the second term dominates if the injection point is within the first few millimetres. Figure 4.8 shows $\Delta\tau$ as a function of d for a range of electron densities, n_e, assuming $N = 1/2$.

Stability of synchronisation over extended periods of time

After having discussed some of the considerations related to *achieving* a temporal synchronisation of two laser pulses, or a laser pulse and an electron beam, we will now consider the challenges associated to *maintaining* this synchronisation over an extended period of time. At GEMINI, the laser pulses propagate typically several 10's of metres distance across mutiple laser areas before being directed into the target area. Minor changes in

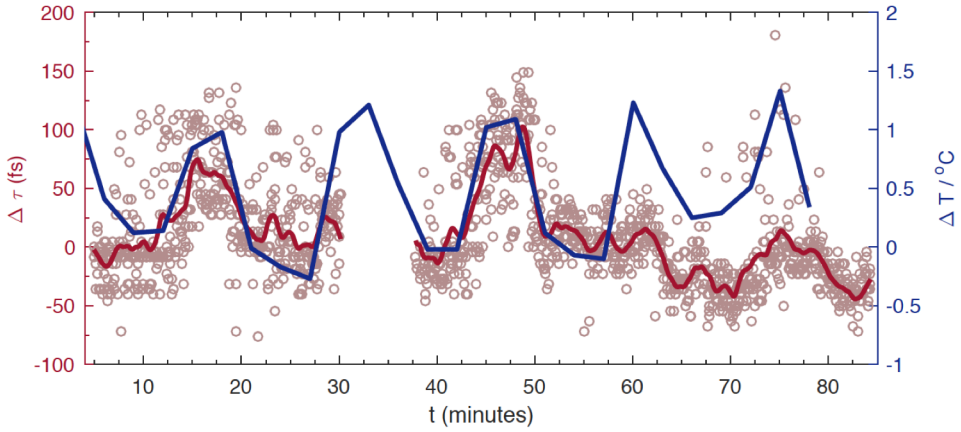


Figure 4.9: Change in delay between the two Gemini *laser arms measured in the target area using a spectral interferometry setup as a function of time (moving average in red line). The relative changes in temperature as measured in the laser area are shown in blue, and are caused by the faulty synchronisation of different climate control units. Reprinted from [243] with permission of the author, R. Shalloo (Oxford University).*

the environment, e.g. humidity or temperature, can lead to an expansion or contraction, for instance, of optical tables and optics mounts leading to a drift of the alignment and the relative timing over a period of time. In Figure 4.9, the relative delay between the two Gemini laser beams measured in the target area is shown as a function of time (red) along with variations in the temperature in the laser area (blue) [243]. The measurements indicate fluctuations in the relative delay of $> 100\,\text{fs}$ over the course of ~ 20 minutes associated with temperature changes of $\sim 1°$ Celsius. This highlights the importance of a stable environment in the laser and target area to ensure that the sensitive alignment and synchronisation can be maintained for longer periods of time, but also indicates that it is crucial to monitor and identify drifts as seen in Figure 4.9.

4.4 Gas Targets

In laser-wakefield acceleration (LWFA), the laser pulse propagates through a plasma and sets up a density modulation. This requires a plasma with a density below the critical density, $n_c = m_e\epsilon_0\omega^2/e^2$. A medium with electron density $n_e < n_c$ is referred to as 'underdense'. For a laser of wavelength $\lambda = 800\,\text{nm}$, these are typically gaseous targets. 'Overdense' targets with a density higher $n_e \geq n_c$ are for titanium-sapphire lasers mostly solid or liquid targets that are used for ion acceleration schemes, e.g. (Target Normal) Sheath Acceleration [244, 245], or to generate X-rays [246].

Gas and liquid targets can be destroyed and replenished in a short amount of time without significant re-alignment and debris production, and are suitable for high-repetition



Figure 4.10: Gas targets under fire. Left: Variable length and density gas cell target by N. Lopes (Imperial College/IST) used at Gemini *in 2018. The laser propagates from left to right. The straight bright line is the plasma channel inside the cell, whereas the blue plume is gas that left the cell and was subsequently ionised by back-reflected laser light. Right: Picture of a diverging supersonic gas jet with* 15 mm *diameter. The emerging helium gas is ionised by the laser and lights up. Picture taken at* Gemini *in December 2015.*

Gas Targets in this work				
Chapter	**Target Type**	**Length**	**Gas**	**Injection Mechanism**
5	Jet + Blade	15 mm	Helium	Shock Injection
6	Jet	15 mm	Helium	Self + Shock Injection
7	Cell	20 mm	Helium + N_2	Self + Ionisation Injection

Table 4.1: Overview of gas targets in this work and relevant injection mechanisms.

experiments. The factors limiting the repetition rate are then the performance of the vacuum system, the time it takes the gas flow or liquid to reach equilibrium, the durability of nozzles and other components, and the repetition rate of the laser system itself.

Examples of gas targets that are routinely used for wakefield experiments are gas jets [247], gas cells [75] and capillaries [212, 248]. In some cases, several targets of the same or different type or combined and staged together to achieve more favourable results [214, 215]. The target size, i.e. the distance the laser pulse propagates through the medium, has to be matched with the laser in use, considering depletion and dephasing lengths (see Section 3.2) to optimise the particle and radiation output, and to use the energy of the laser pulse efficiently. As a result, there is a large variety of different targets, each tailored to a different application. Here, we will focus on examples of gas jets and cells relevant to the work presented in thesis. Table 4.1 provides an overview of these targets.

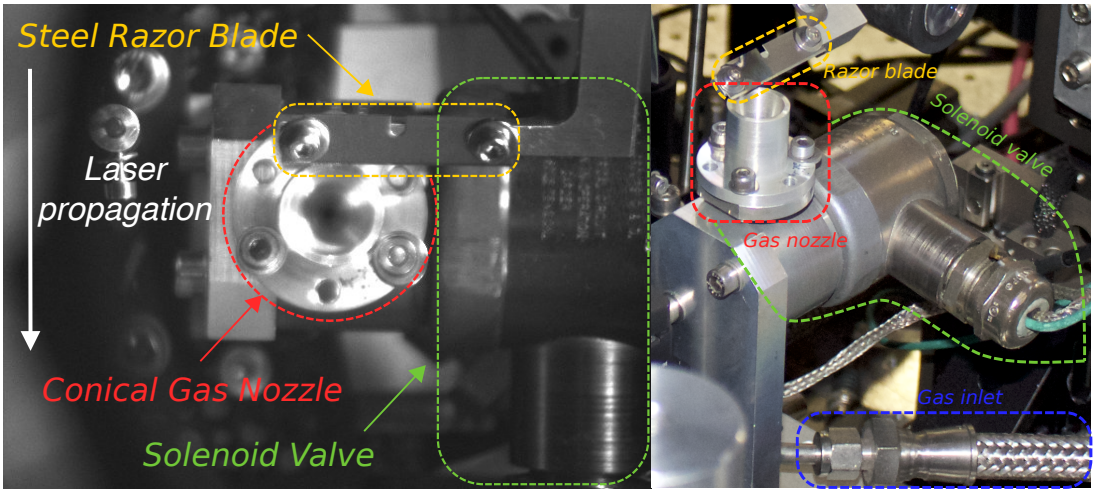


Figure 4.11: Gas jet and blade setup used at GEMINI *in 2019 (see Chapter 5), shown from a top-down view (left) and from the side (right). A 15 mm diameter conical aluminium gas nozzle (red) is mounted on a Peter-Paul solenoid valve (green). A razor blade (yellow) is introduced to induce a shock front on-shot (not shown).*

4.4.1 Gas Jets

In the experiments discussed in Chapters 5 and 6, conical aluminium gas nozzles were used to produce a supersonic gas flow [247]. The gas was stored in a reservoir at backing pressures between 70 and 100 bar, and was released through a Peter-Paul solenoid valve (EH22). The resulting density profile was typically a flat-top with short density ramps on either side, providing electron densities of few $10^{18}\,\mathrm{cm}^{-3}$. The characteristic parameters of the conical nozzle (see Figure 4.12) are its orifice size, D_{crit}, its maximum inner diameter, D_{exit}, and the opening angle, θ, and are listed for both nozzles that were used in Table 4.2. Both nozzle types have the same orifice size, $D_{crit} = 1\,\mathrm{mm}$, and exit diameter, D_{exit}, so that they only differ in their opening angles of $\theta = 19.56°$ (designed by Stuart Mangles, Imperial College) and $\theta = 16.72°$ (designed by Stefan Kneip, Imperial College), respectively.

In the experiment described in Chapter 5, a steel blade was inserted 1.2 mm into the gas flow at 4 mm height above the nozzle at $-32.4 \pm 0.3°$ vertical tilt from the laser axis. The blade was mounted on a rotation and translation stage that allowed changing the height and angle of the blade and its position in the jet. Figure 4.11 shows photos of this setup.

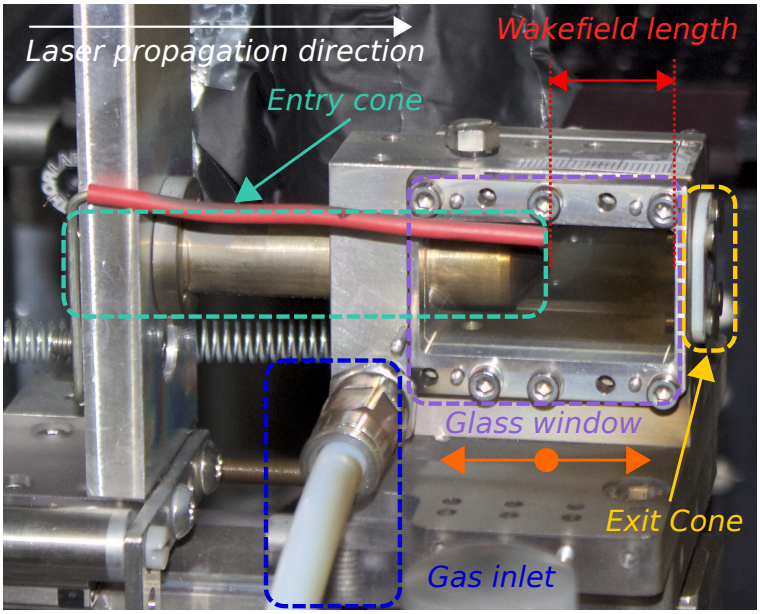


Figure 4.13: Variable density and length gas cell used at GEMINI *in 2018 (see Chapter 7). The length of the accelerator (red) is varied by translating the cell (orange arrow) and keeping the position of the entry cone (turquoise) fixed. The plastic exit cones are regularly replaced to maintain the cell performance. Glass windows (purple) enable diagnostic access to the plasma.*

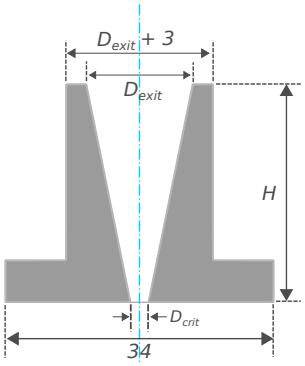


Figure 4.12: Sketch of nozzle design, distances in mm.

Gas Nozzles				
Chap.	D_{crit}	D_{exit}	H	θ
5	1 mm	15 mm	19.7 mm	19.56°
6	1 mm	15 mm	23.3 mm	16.72°

Table 4.2: Overview of gas nozzle properties.

4.4.2 Gas Cells

The experiment discussed in Chapter 7 employs a variable density and length aluminium gas cell with a maximum length of 20 mm [82]. The gas cell was designed, built and maintained by Nelson Lopes (Imperial College/IST). Figure 4.13 shows a photo of the gas cell and its components. The gas cell is equipped with replaceable glass windows (purple) for optical probing and plastic exit cones (yellow) to counteract the constant deterioration of the cell performance. The exit cone was typically replaced once or twice per shot day, whereas the durable entry brass cone remained in place throughout the campaign. The length of the accelerator (red) was varied by shifting the position of the entry cone tip

inside the cell. In order to preserve the relative position of the focal plane of the laser and the start of the accelerator, the entry cone is fixed in space whilst the rest of the cell is being translated (orange arrows). The electron density was varied by adjusting the backing pressure of the gas reservoirs connected to the cell (blue). Typical backing pressures were around $100's$ mbar to reach an electron density of few $10^{18}\,\mathrm{cm}^{-3}$.

4.4.3 Gas jets and cells in comparison

Gas jets and cells are both frequently used in experiments and 3D printing techniques allow for fast prototyping [249, 250]. Gas cell targets have sometimes produced superior results from gas jets using the same laser system, e.g. compare [251] and [69], in terms of charge, shot-to-shot stability [75, 252] and maximum energy gain [76]. However, some of the most stable LWFA sources have been achieved using gas jet targets [226] and the open geometry of gas jets allows for diagnostic access and colliding pulse experiments as well as a route to high repetition rate operation. In addition, gas jets are relatively easy to align and sharp density transitions can be introduced by obstructing the gas flow [228, 230]. The alignment of gas cells, on the other hand, requires more precision as otherwise parts might be damaged and in turn deteriorate the performance. Moreover, large pointing fluctuations of the laser can cause damage, in particular at the entry and exit of the cell where plasma might defocus the laser pulse. The diagnostic access is typically enabled by glass windows, but the casing of the cell leads to a reduction of the field of view and debris can render the windows over hundreds of shots opaque. The variety of gas targets, their performance and the performance of the specific laser system make it difficult to compare gas cells and jets in general with each other. Comparisons can in most cases only be done between individual specimens and conclusions drawn from such a comparison might only be valid in this limited context.

4.4.4 Characterising Gas Targets

In wakefield experiments, a variety of diagnostics can be used to gain an insight into the behaviour of the laser pulse in the plasma, the wake itself or the injection mechanisms. A commonly used tool is an optical probe that is passed through the plasma transverse to the main beam, where density perturbations induced by the main beam modulate the phase of the probe beam. In this work, a shadowgraphy and interferometry setup translate these phase shifts back into a measurement of the plasma density and strong density gradients or features. The two methods and their experimental implementation at Gemini are introduced in the following.

Shadowgraphy

In shadowgraphy a light source, here a laser, is used to backlight a transparent medium and the transmitted light is imaged onto a detector [198]. The medium is in this case an underdense plasma (see Section 3.1.5), where gradients in density translate into gradients in the refractive index. These gradients cause light to refract and to accumulate at the boundaries of these regions (see Figure 4.14). Because of this behaviour shadow images or *shadowgrams* are a useful tool to see features in a plasma, such as the edges of a plasma channel or a shock front. Whilst features become very apparent, the absolute density itself can not be derived from a single projection without further reference.

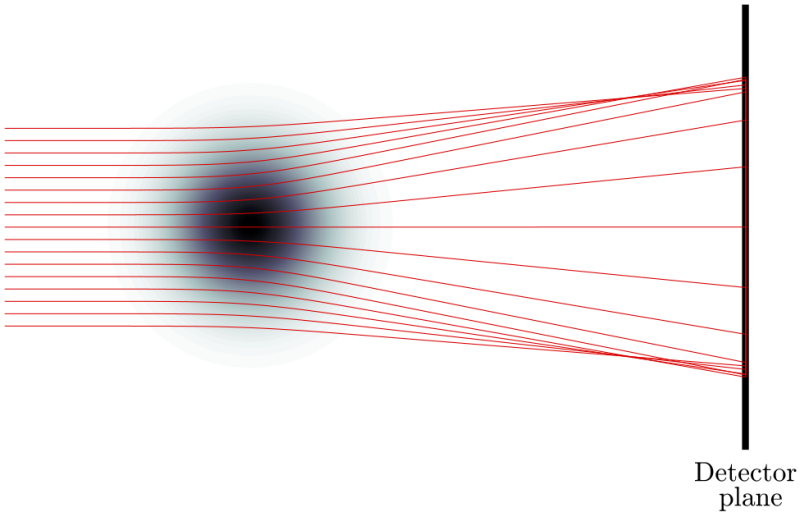


Figure 4.14: Rays of light (red), entering the sketch from the left, propagate through a cylindrically symmetric density profile and are then incident onto a detector plane. The density is encoded in the colour scale, where darker regions are denser than light regions. The rays are deflected away from large density gradients, resulting at the detector plane in an accumulation of rays at the edges of the dense region and fewer rays inside of it. Figure courtesy O. Ettlinger and G. Hicks (Imperial College).

The relative change in local intensity a beam experiences when travelling in z through a medium of refractive index η is for small deflections given by [205]:

$$\frac{I(x,y,L) - I_0}{I_0} = -L\nabla^2 \int \log \eta(x,y,z) \mathrm{d}z, \tag{4.4.1}$$

where I_0 is the initial intensity distribution and $I(x,y,L)$ the final distribution measured at a detector at distance L. In an experimental setup, however, an imaging system consisting of one or multiple lenses is typically used, such that L then corresponds to the size of the density perturbation, e.g. the diameter of a plasma channel. The Laplacian, ∇^2, indicates

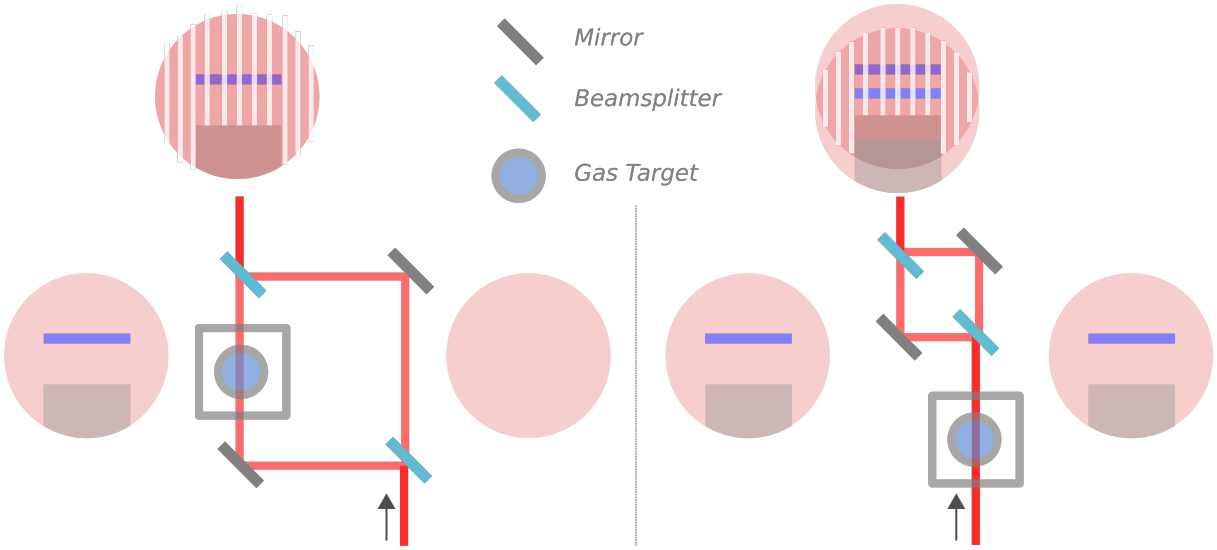


Figure 4.15: Comparison of two Mach-Zehnder (MZ) interferometer geometries. The laser beam (red) enters the sketch from the bottom and reaches the detector at the top. On its path it passes through a gas target (grey ring filled blue) in a vacuum chamber (grey box), where it images a plasma channel (blue-purple line). The pink circles indicate the respective beam properties on each arm. Left: Standard MZ setup. One propagates through the plasma, whereas the other beam bypasses it to act as reference. Both are fully overlapped to effect interference. Right: MZ setup used in the experiments at GEMINI. *A single beam passes through the plasma. The beam is then split up into two identical copies which are recombined with a spatial offset. Different regions of the beam act as reference and others as signal regions. Adapted from [205].*

that the intensity is strongly modulated by steep gradients in the refractive index, η, corresponding to abrupt changes in density. Figure 4.16 (bottom) shows a shadowgram measured during an experimental campaign at GEMINI in 2019 (see Chapter 5).

Interferometry

In interferometry two beams are overlapped with a phase difference resulting in an interference pattern. One beam acts as the unperturbed reference, the second beam probes the perturbation of interest at the interaction point. Starting from the original interference pattern, the 'fringes' will shift as the second beam collects phase shifts when propagating through the interaction region. In this context, the phase shift, $\Delta\phi$, occurs due to density modulations in the plasma which are reflected in changes to the refractive index, η [198, 253]:

$$\Delta\phi(y,z) = \frac{2\pi}{\lambda}\int_{-\infty}^{\infty}(\eta(r,z)-1)\mathrm{d}x, \tag{4.4.2}$$

where the refractive index, η, is for underdense plasmas, $n_e \ll n_c$, approximated by $\eta \approx 1 - n_e/(2n_c)$.

$$\Delta\phi(y_0) = \frac{\pi}{n_c\lambda}\int_{-\infty}^{\infty} n_e(x, y_0)\mathrm{d}x = \frac{2\pi}{n_c\lambda}\int_{y_0}^{R}\frac{n_e(r)r}{\sqrt{r^2 - y_0^2}}\mathrm{d}r, \tag{4.4.3}$$

substituting $x = \sqrt{r^2 - y_0^2}$ and $\mathrm{d}r = r\mathrm{d}r/\sqrt{r^2 - y_0^2}$. Assuming radial symmetry, the plasma density $n_e(r)$ is then inferred using an Abel inversion [254]:

$$n_e(r) = -\frac{n_c\lambda}{\pi^2}\int_{r}^{R}\frac{\mathrm{d}}{\mathrm{d}r}\Delta\phi(y)\frac{\mathrm{d}y}{\sqrt{y^2 - r^2}} \tag{4.4.4}$$

More instructive details on this method can be found in [205].

In the experiments at GEMINI described in this work, a Mach-Zehnder interferometer was used. However, instead of splitting the beam before the interaction, the beam is only entering the Mach-Zehnder setup after the interaction, such that both copies are identical (see Figure 4.15). Since the plasma channel that is diagnosed only takes up a small fraction of the image, the remaining area of neutral gas can be used as reference. Similarly as in a Wollaston interferometer, the two beams are offset relative to each other to overlap 'active' with 'passive' regions. As a result, two copies of the plasma channel with inverted phase shifts can be seen. An example of an interferometry measurement from an experiment performed at GEMINI is shown in Figure 4.16 (top).

Experimental Implementation

In the LWFA experiments in this work, the optical probe is split off the main wakefield driver beam by collecting the fraction of light that is transmitted through a highly reflective dielectric mirror. The transmitted light is telescoped down from $\sim 150\,\mathrm{mm}$, the beam diameter of the collimated main laser pulse, to about one inch using an $f/7$ off-axis parabola and a suitable lens. The final diameter is chosen based on the field of view required for the respective application.

The collimated probe beam is then following a beam path of the same length as the main beam to ensure that both arrive at the interaction point simultaneously. The probe is sent through the gas target at the interaction point and collects phase shifts encoding the density and its variation in the plasma. If the probe arrives before the main driver at the gas target, no plasma has been formed yet. If the probe arrives much later than the main beam, the plasma channel it formed has expanded. As a result, the density measured is not representative of the conditions the driver beam experienced and in turn does not describe the wakefield dynamics correctly either. A motorised linear stage can be used to

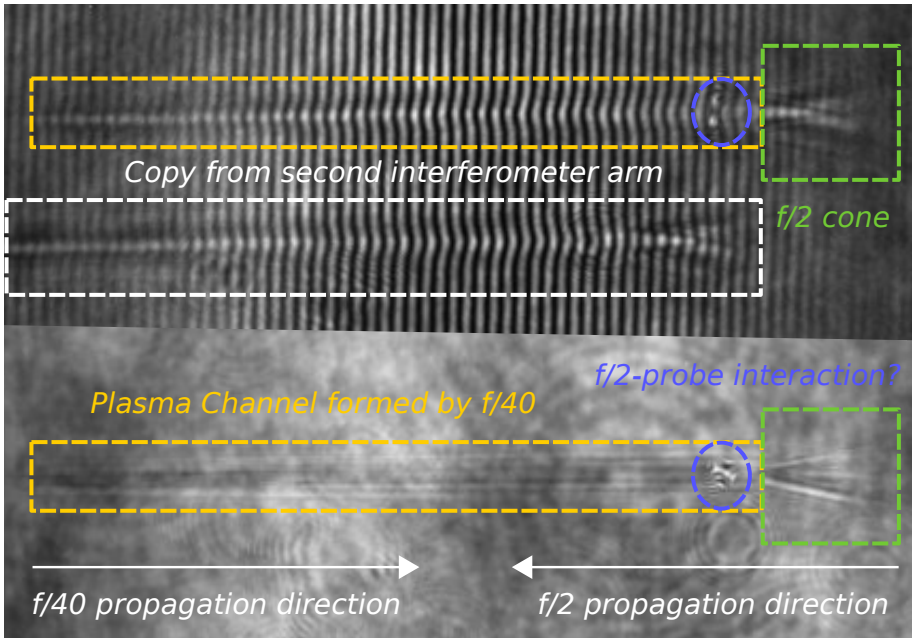


Figure 4.16: Example of an interferometry image (top) and a shadowgram (bottom) taken on an experiment at Gemini *(see Chapter 5) on the same shot. Two laser pulses counterpropagate through a gas jet and form a plasma. One laser pulse is focused in an $f/40$ geometry (left to right), the other tightly by an $f/2$ off-axis parabola. The common features on both diagnostics are indicated in the same colour on both images.*

add or remove beam path dynamically (delay stage) to adjust the relative arrival time of the probe and the main beam.

After the plasma the probe beam is attenuated by reflecting off glass wedges to prevent nonlinear effects when the laser pulse leaves the vacuum chamber through a glass window (B-integral). A set of lenses is used to image the plane of the gas target onto the prospective detector plane. On the way to the detector plane, the probe pulse is split up by a beam splitter into two parts: one is directly incident on a CCD chip to act as shadowgraphy, the other pulse travels through a symmetric, compact Mach-Zehnder setup before also arriving at a CCD camera chip forming an interferometry diagnostic as outlined in the previous section.

Figure 4.16 shows an example interferometry (top) and shadowgraphy (bottom) image, taken with an optical probe on the same shot. The data was taken on an experimental campaign at Gemini in 2019 (see Chapter 5). On the images an $f/40$ laser pulse is travelling through a helium gas jet and forms a plasma channel (gold). The centre of the channel is slightly darker and the edges form a bright line as discussed in the previous section. In the interferometry image, on the other hand, a shift of the interference pattern indicates the formation of a plasma channel. Due to the special setup of the Mach-Zehnder interferometer, two copies of the same channel can be seen (white), where the only difference between the two is the inverted phase shift. On the right side, the cone

of a counterpropagating, tightly focused $f/2$ beam is visible (green). The particularly bright outline of the cone seen in the shadowgraphy indicates a large gradient in density. The distinct feature at the crossing of both pulses is potentially caused by an interaction between the optical probe pulse and the $f/2$ beam.

4.5 Magnetic Energy Spectrometer

The energy of electrons in wakefield experiments can be determined with a magnetic spectrometer, where electrons are dispersed in a magnetic field and then detected on a scintillating Lanex screen. To determine the deflection angle, θ, in such a magnetic field analytically, we will consider an external magnetic field restricted to a circle of radius r_b embedded in an otherwise completely field-free region [255]:

$$\begin{aligned} \mathbf{B} &= B\mathbf{e_z} && r \leq r_b, \\ &= \mathbf{0} && r > r_b \end{aligned} \tag{4.5.1}$$

The angular deflection of a particle in this case can be solved analytically using the Larmor radius and simple geometry. This is visualised in Figure 4.17 (left). Since the sum of all angles in a triangle is π:

$$2\alpha + \theta = \pi, \tag{4.5.2}$$

where θ is the deflection angle and α the angle indicated in the sketch in Figure 4.17 (left). The angle α is geometrically related to the two radii:

$$\tan\alpha = \frac{r_L}{r_b}. \tag{4.5.3}$$

By combining these results and expressing this in quantities relevant in an experiment, we obtain

$$\begin{aligned} \tan\frac{\theta}{2} &= \frac{r_b}{r_L}, \\ &= \frac{eBr_b}{p_\perp}, \end{aligned} \tag{4.5.4}$$

which indicates that at a fixed magnetic field strength, B, and field region, r_b, the deflection angle, θ, is larger for a lower particle momentum, $p_\perp$, the momentum component perpendicular to the magnetic field lines. In a typical LWFA experiment, $p_\perp$ will be dominated by the component in the laser propagation axis, i.e. if the propagation axis were z, $|\mathbf{p}_\perp| \approx p_z$.

In a realistic scenario, the field regions are not perfectly homogeneous and field gradients

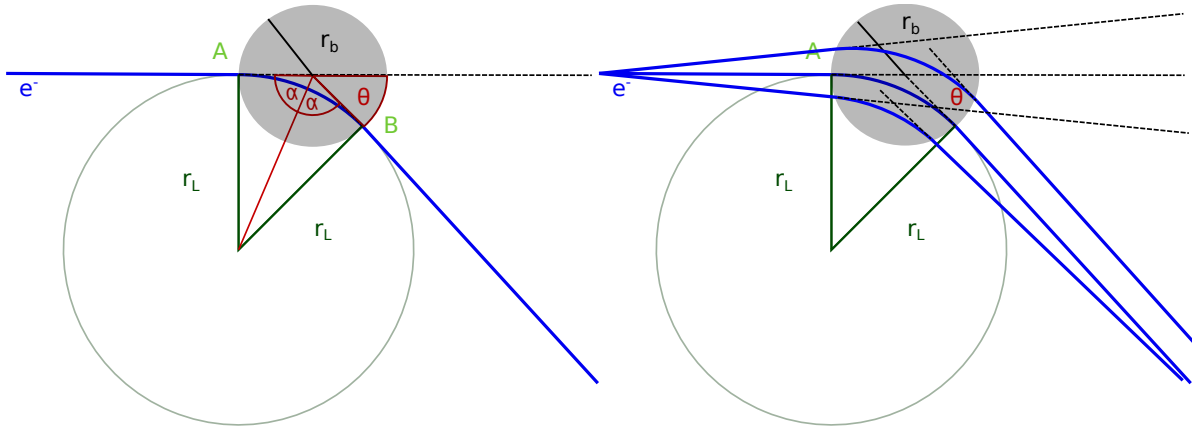


Figure 4.17: Left: Visualisation of an electron deflected in a homogeneous circular magnetic field (grey) with radius r_b. The larger (empty) circle indicates the Larmor radius, determining the electron trajectory (blue) from the point of entry into the field (A) to its exit point (B) resulting in a total deflection θ. Right: Similar visualisation as on the left but considering three electrons entering the same field at different angles and positions.

have to be considered. The magnetic fields can be measured, for instance, using a Hall probe and the particle trajectories are determined with numerical methods. To measure the magnetic dispersion as diagnostic, a scintillating Lanex screen is positioned behind the magnet. By measuring the magnetic field strength of the magnet and the distances between the components, and by calculating the trajectories for a range of energies, each position on the screen can be linked to a specific electron energy. In this work, a Matlab-based particle tracking code by Jonathan Wood (Imperial College) and another code by Matthew Streeter (Imperial College) were used (see Figure 4.18 for a visualisation from M. Streeter's code simulating the particle trajectories for the magnet configuration used in the photon-photon collider experiment outlined in Chapter 7).

If all electrons enter the magnet at one defined position and angle, each position on the detector screen is uniquely related to one electron energy. For a distribution of angles and positions, each position on the screen can correspond to multiple energies (see Figure 4.17, right). In LWFA experiments, variations in angle and position typically originate from two sources: first, the entire beam might be ejected from the accelerator at an angle relative to a reference axis that varies from shot-to-shot. This is referred to as *beam pointing* and shifts the entire dispersed beam on the detection plane relative to the reference axis, i.e. leads to a systematic shift in the inferred energy if not considered. Multiple detector screens or spatial references can be used to identify and correct for beam pointing [69, 256, 257].

Second, the beam has a finite divergence such that electrons entering the magnetic field have a distribution of angles, even at a fixed energy. As a result, one energy is not mapped onto a single point but a spot of finite size, i.e. the dispersion or energy axis and spatial components of the beam are mixed (instrument function).

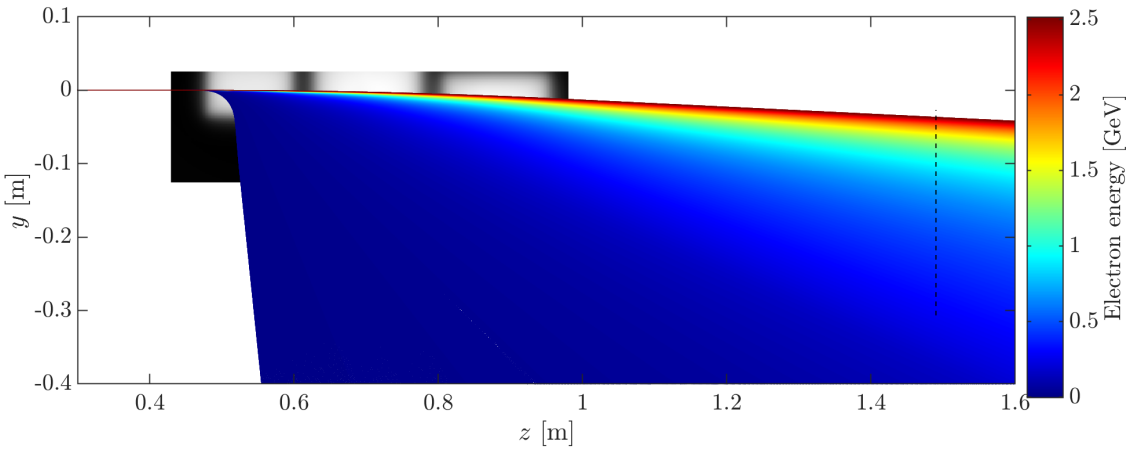


Figure 4.18: Example of particle tracking simulation using a code by M. Streeter (Imperial College). Electrons enter a three-piece magnet from the left side and are dispersed according to their energy (colour bar in electron energy). The perpendicular field magnet field component, $B_\perp$, is colour-coded, with black indicating zero and white $B_\perp = 1\,T$. The magnetic fields outside the black rectangle vanish but are also shown in white. The vertical dashed line indicates the position of a measurement screen.

The momentum component of the electron beam that is parallel to the magnetic field lines is unperturbed by the magnetic field as the magnetic Lorentz force vanishes for parallel vectors. If the size of the electron beam is very small at the end of the accelerator, measuring its width in the non-dispersed direction at the detector plane and the distance from the detector to the accelerator can be used to infer the magnitude of $p_\parallel$ relative to $p_\perp$, $p_\parallel/p_\perp$. This ratio is in the small-angle approximation equivalent to the angle to a reference axis z, with $z \parallel \mathbf{p}_\perp$, or applied to an entire beam the *divergence*, θ.

In the experiments discussed in this thesis, the detectors are scintillating Lanex screens (Kodak Standard or Biomax) imaged by cooled 16-bit CCD Andor Neo cameras. Since the imaging of the screens was non-normal but at an oblique angle to avoid placing the cameras into the path of the electrons, the spatial scale is not constant across the image. Spatial references on the image, here rulers attached to the frame holding the Lanex screen, can then be used to apply a projective transform that morphs the image onto a linear spatial scale [69, 205]. The linear spatial scale can then be translated into an energy axis in the dispersion direction, by applying the results from the particle tracking code described above, and into beam divergence in the non-dispersion direction (see Figure 4.19, right). This is shown in Figure 4.19 at an example image (from a Gemini campaign in 2015, experiment is described in more detail in Chapter 6). The panel on the left shows the raw reference image, with the rulers clearly visible on both sides and higher energies (less dispersion) at the top of the image. A projective transform has been applied to generate the image in the centre. Both sides are now straight and the spatial scale

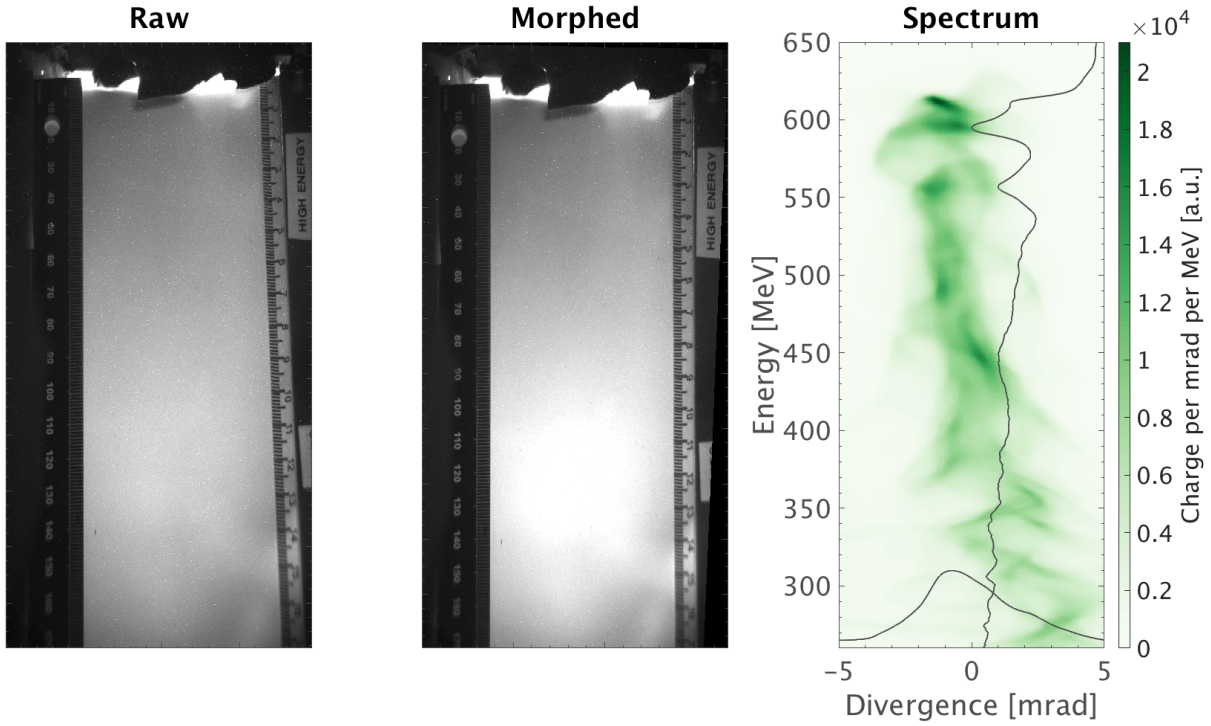


Figure 4.19: Example images of an electron spectrometer screen. Left: Raw reference image of a Lanex spectrometer screen. The vertical axis is the dispersion axis, with the top part corresponding to less dispersion (higher energy), and the horizontal axis corresponds to divergence. Centre: Image on the left after applying a projective transform. Right: Example electron spectrum obtained using this setup and using particle tracking results to translate the spatial scale into an energy scale. This image was also background subtracted and cropped. The colour scale indicates charge per divergence and energy in arbitrary units (darker regions indicate more charge).

is slightly stretched in the upper part. The panel on the right shows an example 2D electron spectrum, obtained by replacing the spatial scale with an energy (vertical) and a divergence axis (horizontal) using the results from the tracking code, as well as subtracting background and cropping the image. The colour scale indicates charge per divergence and energy in arbitrary units. The signal recorded from the Lanex screen can be related to the absolute number of electrons by cross calibrating with an imaging plate [218].

4.6 Gamma-ray Diagnostics

In the following, diagnostics measuring the profile and spectrum of energetic radiation are introduced. Both detectors consist of a pixelated scintillator array imaged by a CCD camera. In one case, the transverse profile of the radiation is measured, in the other case the gradual decay throughout several scintillating layers is used to infer the spectrum of the incident radiation.

At photon energies $> 10-30\,\mathrm{keV}$, the quantum efficiency of CCD chips decreases

significantly such that a direct measurement of the radiation using these becomes infeasible. Moreover, at photon energies $> 1\,\mathrm{MeV}$, particle showers are produced that can damage electronics in the radiation path. As a consequence, commercially available indirect detection X-ray cameras, e.g. Andor iKon, that directly couple a scintillating layer to a silicon-based readout chip are also not recommended for use in these energy ranges. By separating the two components spatially, i.e. placing the scintillator in the radiation path and the CCD sufficiently far away, this problem can be circumvented.

A scintillator placed into the path of the energetic radiation emits scintillation light when energy is deposited in the scintillator. A suitable imaging system collects the light and directs it onto the CCD detector. Commonly used scintillators emit light in a spectral bandwidth matched to the quantum efficiency of silicon-based detectors with a material-dependent characteristic emission spectrum. For photon energies relevant in this context, the light yield of the scintillator is proportional to the energy deposited in it [258], with a material-dependent conversion efficiency from deposited energy to number of emitted photons. The light emission is isotropic in a 4π solid angle [259], which can lead to a spreading of the signal comparable to the thickness of the scintillator. This spreading can be reduced by either using a thin scintillator or by dividing the detection area into smaller scintillators such that light from one crystal can not enter another and vice versa. The result in the latter case is then a pixelated detector, where the spatial resolution is determined by the transverse width of the crystals such that deep (longitudinal) crystals can be used to increase the light yield without loss of spatial resolution. To increase the fraction of collected light, the crystal faces are often polished and some sides are coated or covered with a reflective surface, so-called reflectors, such that the emitted scintillation light can be directed.

4.6.1 Profile Screen

The radiation profile is a useful measure of, for instance, the pointing of the radiation cone and its divergence, or an indicator of the total radiation yield. In the context of inverse Compton scattering or nonlinear relativistic Thomson scattering, where a relativistic electron beam collides with an intense laser pulse, the elongation of the radiation profile in the laser polarisation direction has also been proposed as measurement of the laser intensity at the interaction [120, 172, 260].

In the experiments described in this work, a pixelated scintillating screen is placed into the path of the radiation, normal to the beam axis, and is then imaged by a sensitive EMCCD camera (Andor iXon) with a bandpass filter. An overview of the different arrays used in the experiments is given in Table 4.3. The imaging was in all cases done close to normal to the scintillator surface, either directly or by placing a mirror into the radiation path, to maximise the collection efficiency of the scintillation light which is directed due

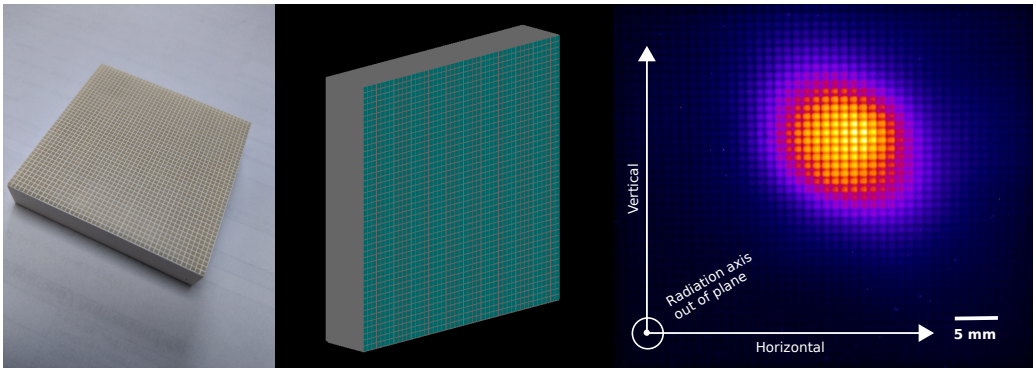


Figure 4.20: Example of a scintillator stack ('Jena') used as profile screen in experiment. Photograph of the scintillator screen (left) along its GEANT4 representation (middle) and a false colour image of a gamma signal from linear inverse Compton scattering (right) measured with the stack in an experiment at GEMINI *in 2019 (Chapter 5).*

to the reflectors. This also reduces the required post-processing of the images to small rotations and background subtractions. In this setup, the required spatial resolution of the imaging system is low as the intrinsic spatial resolution of the detector is given by the width of the scintillator voxels which are $\sim 1\,\text{mm}$ or more. The scintillating material that was used is caesium-iodide doped with thallium which has one of the highest light conversion efficiencies of available crystals releasing $\approx 5.4 \times 10^4$ optical photons at a central wavelength of 550 nm for each MeV energy deposited in the crystal [261].

Overview of Scintillating Profile Screens

Name	Chapter	Crystals	Crystal Dim.	Front Plate	Divider
QUB	7, BW	20×20	$2 \times 2 \times 20$ mm	Al 10 mm	Al 0.02 mm
Jena	5, linICS	45×45	$1 \times 1 \times 10$ mm	TiO2 0.5 mm	TiO2 0.2 mm
DESY	5, linICS	30×30	$1.5 \times 1.5 \times 10$ mm	TiO2 0.5 mm	TiO2 0.2 mm
RAL	6, RR	47×33	$5 \times 5 \times 50$ mm	None	Al 1 mm

Table 4.3: Overview of caesium-iodide arrays used as radiation profile screens in the context of this thesis. Columns from left to right: Name or 'affiliation' of the screen, chapter related to an experiment using this particular profile screen, size of the array in number of crystal columns and rows, spatial dimensions of an individual crystal in the array, material and thickness of the front plate or coating on the front side facing the beam, divider material and thickness between crystals.

Figure 4.20 shows a photograph of one of the scintillating arrays used in this work (left, labelled 'Jena' in Table 4.3) along with a GEANT4 representation (centre) and a false-colour image of a detector response produced by a gamma-ray beam from inverse Compton scattering measured in the experiment at GEMINI discussed in Chapter 5. Each

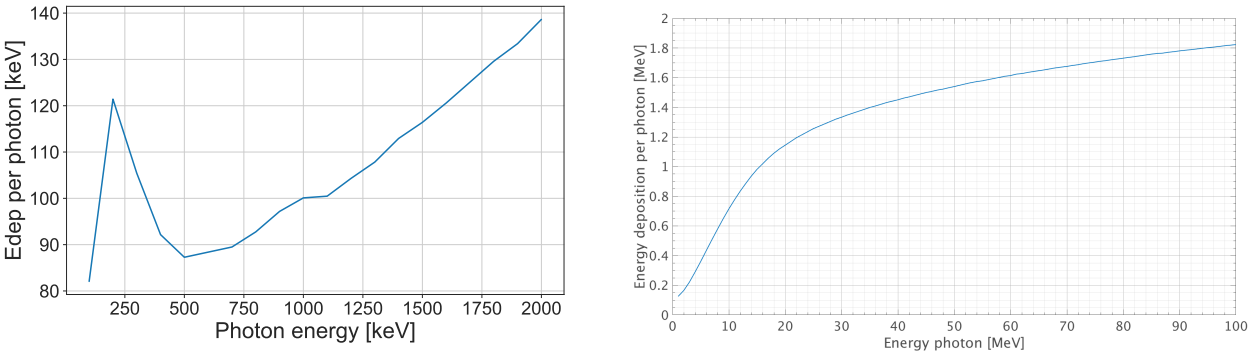


Figure 4.21: Energy deposition per photon in the 'Jena' profile screen simulated in GEANT4 as a function of photon energy for 100 to 2000 keV (left) and 1 to 100 MeV photon energies (right).

square corresponds to one crystal or voxel in the array.

Energy dependent detector response

To determine the energy deposited in the scintillating crystals, one has to consider the scattering of the radiation, secondary particles and their energy deposition through various mechanisms. This complex interplay of different mechanisms is most conveniently modelled in a Monte-Carlo code such as GEANT4 since collective effects are not significant. Here, a GEANT4 code based on work by J. Cole and K. Poder (Imperial College) was used. The simulation geometry includes the composition of the detector and the relevant materials in the beam path of the radiation as measured on the respective experiment. Individual photons within a range of energies are then launched towards the detector and the energy deposition is recorded as a function of the incident photon energies. For each photon energy, 10^6 photons are simulated to account for statistical fluctuations. Figure 4.21 shows the energy deposited on average per incident photon in the 'Jena' profile screen as a function of the incident photon energy for an energy range of 100 to 2000 keV (left) and for 1 to 100 MeV. It is assumed that the light yield of the scintillator and the energy deposition are linearly related [258] and that there are no saturation effects to be considered in this scenario. With exception of a peak in energy deposition at just under 200 keV photon energy, the energy deposited in the screen increases monotonically with photon energy. The distribution can in most parts approximated by two linear functions, one with a steep gradient up to a photon energy of 15 MeV and a second function with a lower gradient after this value.

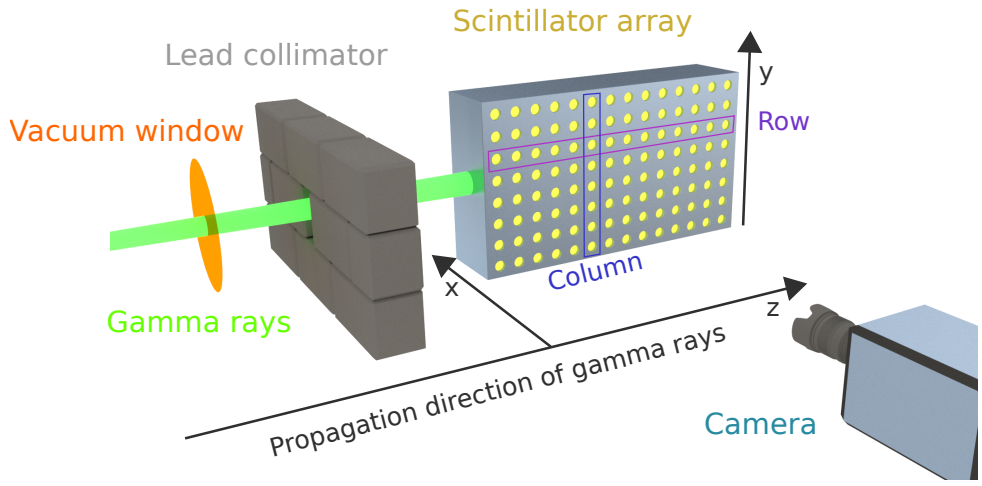


Figure 4.22: Sketch of a gamma spectrometer setup in an experiment. The gamma rays (green) traverse from the left a vacuum window (orange) and then in air through a lead collimator onto an array of scintillators (yellow) housed in a casing. The stack is predominantly extended in the longitudinal direction (z) but can also resolve one transverse dimension (here y). A camera directly images the open side of the scintillator array.

4.6.2 Spectrometer Array

Experimental Setup

A long array of scintillating crystals is placed in the beam path and its scintillation light is measured with a CCD. The spectrum of gamma radiation passing through the crystals is inferred by simulating the response of the array in GEANT4 [262] and comparing it to the response measured in the experiment [263]. Figure 4.22 shows a conceptual sketch of the experimental setup: a beam of gamma rays (green) enters from the left side of the sketch, passes through a vacuum window (orange) into air, then traverses a lead collimator and enters the scintillator array. The crystals are indicated in yellow. The response of the detector is imaged by a camera (bottom right corner).

The individual scintillators are caesium-iodide crystals doped with thallium, with the spatial dimensions $5 \times 5 \times 50\,\text{mm}$. The long side of the crystals is oriented transversely to the propagation direction of the gamma rays (z), in the sketch shown in Figure 4.22 this is the horizontal axis x (see also Figure 4.24). This maximises the light yield as the response of the detector is integrated along this axis (x) but at cost of spatial resolution. The crystals are arranged in a two-dimensional grid of columns (z) and rows (y). Crystals along the longitudinal axis z measure the decay of the radiation and can be used to infer the spectrum. The response in the y-axis encodes the vertical divergence of the radiation.

The crystals are separated from each other by light-tight spacers such that each crystal is enclosed from all but one side, from which the scintillation light leaves the crystal. This crystal side faces in x direction and the scintillation light is measured on a CCD. In all the experiments discussed in this thesis, cooled 14-bit EMCCD cameras of type Andor

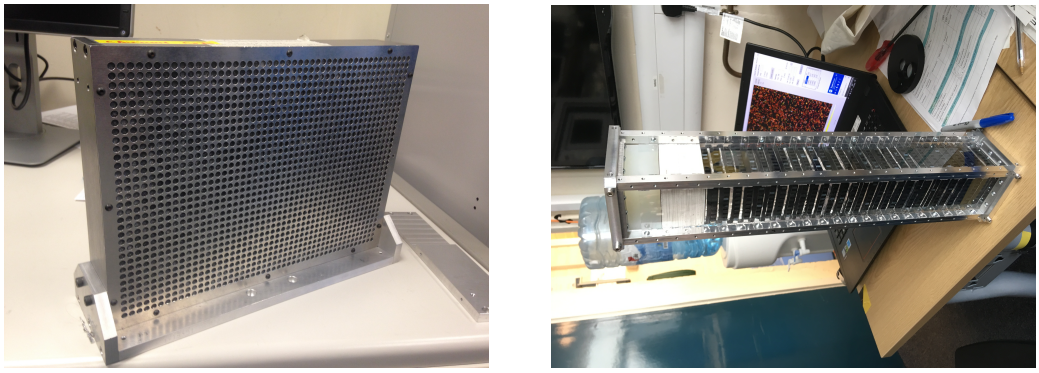


Figure 4.23: Photographs of scintillator arrays used in experiments. Left: 'RAL' stack of 47×33 *crystals. Right: Long dual-axis stack consisting of* 10×70 *crystals. More details can be found in Table 4.4*

iXon were used, which are very sensitive and allow for high gain but in turn also require efficient light shielding. The cameras were equipped with suitable objectives and bandpass filters that only transmit light in the bandwidth of the scintillation light at a wavelength of 546 ± 10 nm. A reflective casing for the crystals along with polishing and reflective coating of the crystals can increase the light output.

The material and thickness of the dividers between the crystal columns determine how fast the incoming radiation decays which can be used to 'tune' the response of the detector to the right spectral range. The separation and thickness of the crystals in the y-axis, on the other hand, determines the vertical spatial or, with respect to the radiation source, the angular resolution.

Two different scintillator stack designs were used as gamma spectrometers in the experiments described in this thesis. An overview of the dimensions and the materials used in the arrays is provided in Table 4.4 and photos of the stacks are shown in Figure 4.23. Examples of raw images from both detectors are shown in Figure 4.25.

The experiment outlined in Chapter 6 employed a 47×33 [longitudinal (z) $\times$ vertical (y)] array of crystals, housed in an aluminium casing[1] (see Figure 4.23, left). The long side of the crystals was oriented along the horizontal direction (x) to maximise the light yield. The crystals were separated in z and y by 1-mm-thick light-tight aluminium spacers. On the sides (x) the array is held together by 1-mm-thick aluminium plates. One plate is solid, on the other side 4 mm diameter holes over the crystal faces allow the scintillation light to escape. The aluminium spacers and the solid plate reflect the light and direct the photons towards the only open side. The front and back side of the stack (z) are fortified with 9 mm thick steel plates.

The experiment described in Chapter 7 used the same scintillator array as above for

[1]Designed and built by Rob Clarke (CLF).

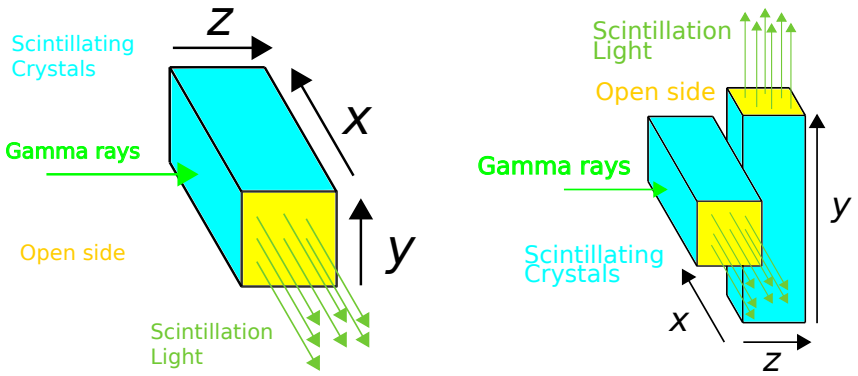


Figure 4.24: Sketch of crystal orientations (cyan) in the spectrometer arrays relative to the incident gamma rays (green) for the RAL stack (left) and the alternating layers in the long dual-axis stack (right). The yellow faces indicate the open sides out of which the scintillation light (green) leaves the crystal.

the setup described in Chapter 6, but the thick steel front plate is replaced by a 1-mm sheet of plastic (PTFE) to reduce the attenuation of the incident radiation. In this setup, a scintillating profile screen is placed in front of the spectrometer array (see previous section). The additional material of the profile screen roughly compensates the effect of the thinner front plate and matches the response of the detector to its previous configuration.

The campaign described in Chapter 5 fielded a longer array of 10×70 [transverse (x, y) $\times$ longitudinal (z)] crystals[2] (see Figure 4.23, right). Since the gamma beam produced in these experiments is highly-directional, the signal measured in previous experiments on the array described above was concentrated on a few central rows with a large number of crystals being left unused. In this design, the transverse dimension is reduced in favour of an extension in the z axis that is spectrally relevant. In addition, lighter spacing materials are used to slow down the decay and stretch out the signal over more crystal columns (z).

The crystals rows (x, y) are spaced by black polyethylene dividers and the columns by 0.5 mm sheets of black nylon. The small faces of the crystals that are not imaged are covered with reflective aluminium foil. The front plate of the stack is a 2 mm thick aluminium plate. The entire stack is held together by an aluminium skeleton, with the 4 long sides being covered by transparent PTFE plastic sheets. The positioning and visibility of the crystals is less regular than in the other stack since this array was assembled from hundreds of individual components which were partly not matching the requested dimensions, requiring manual (and hence not completely repeatable) corrections. In addition, the light shielding of the extremal rows [see Figure 4.25 (top)] appears to require improvement as well.

Another new feature of this array is the alternating orientation of the crystals (see Figure 4.24, right): the long side of the crystals is now in every other column rotated from

[2]Proposed by Stuart Mangles (IC), designed and built by D. Treverrow (CLF) and C. Baird (CLF).

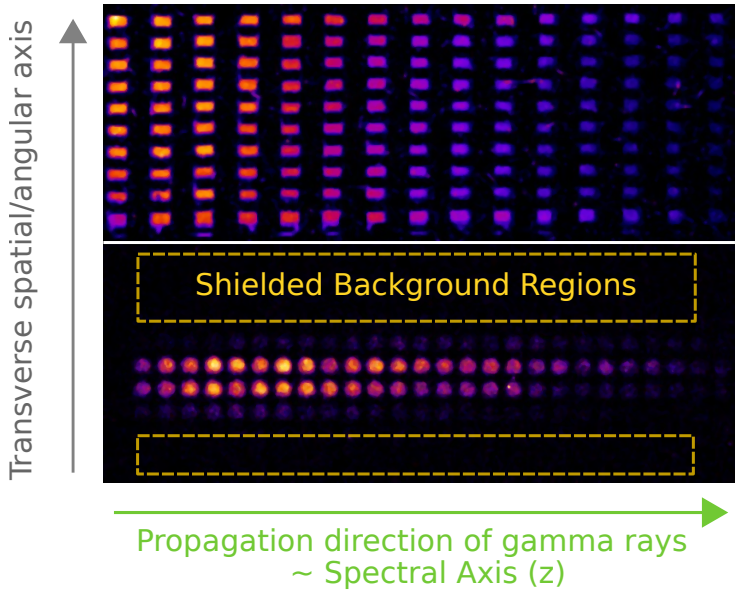


Figure 4.25: Examples of raw response recorded on scintillator arrays in false colour, where black indicates low and orange a high signal. The radiation propagates into the stack from left to right, such that radiation of higher energy penetrate deeper into the stack. The vertical axis encodes spatial/angular information. Top: Top view of the first 15 crystal columns of the dual-axis stack. The response was measured at Gemini *in 2019. Each square is an individual crystal, where the different dimensions are due to a large variation in the size of the transverse spacers that were used in the assembly. Top: Response of the 'RAL' spectrometer stack to gamma radiation from inverse Compton scattering measured at* Gemini *in late 2015 (see Chapter 6). The stack was housed in a lead enclosure with a circular aperture (lead collimator) such that the signal area is restricted to the centre. The shielded regions can be used as background measurement. The crystals in this array have also rectangular faces but the casing holding the crystals in place has round apertures.*

the x-axis (horizontal) by 90 degrees to align with the y-axis (vertical). Each odd and even layer now integrates the response of the detector in a different transverse dimension. The preserved non-integrated spatial component then also alternates with each subsequent column. This is discussed in more detail at the end of this section.

In the setup outlined in Chapter 5, the top of the detector (y) was imaged directly and a long rectangular mirror was placed at 45 degrees next to the other side, reflecting the scintillating light from even and odd layers onto the same CCD chip to use the area of the rectangular CCD chip most efficiently. Due to the length of the stack (z), two cameras were used, one for the front section and one for the back.

GEANT Simulation Setup

The attenuation and energy deposition of the radiation is simulated using the Monte Carlo code GEANT4 [262], as the impact of secondary radiation and particles as well as 3D effects such as side-scattering become important. The specific GEANT4 code used in this

Overview of Spectrometer Arrays				
Name	**Chapter**	**Crystals**	**Front Plate**	**Divider**
RAL	6, RR	47×33	Steel 9 mm	Al 1 mm
RAL	7, BW	47×33	PTFE 1 mm	Al 1 mm
Dual	5, linICS	10×70	Al 2 mm	Nylon 0.5 mm

Table 4.4: Overview of scintillator arrays used in the experiments discussed in this thesis and their properties, namely the array size, divider and front plate material. The material of all crystals that were used is caesium-iodide doped with thallium and have the spatial dimensions $5 \times 5 \times 50$ *mm.*

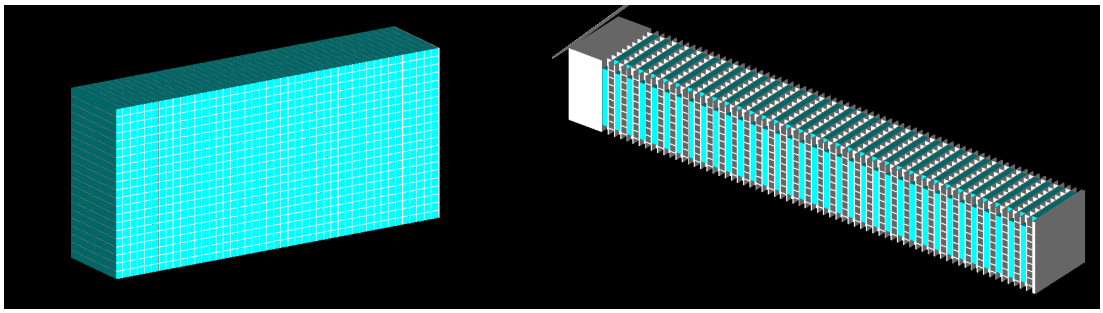


Figure 4.26: GEANT4 representations of the two scintillator arrays used in the experiments without their outer casing. The cyan blocks indicate the caesium-idodide crystals and the energy deposited in those volumes is recorded as detector response. Divider materials, front- and end plates are indicated in white. Photos of the stacks are shown in Figure 4.23.

work builds on previous work by K. Poder and J. Cole (Imperial College).

Typically 10^6 individual photons or 10^5 electrons are simulated, assuming collective or multi-photon/-particle processes are negligible, such that individual photon responses can be combined cumulatively. The specific experiment geometries are reconstructed in GEANT4 including the detector geometry and materials in the pathway as well as distances measured in the experiment. The GEANT4 representations of the two spectrometer designs are shown in Figure 4.26. The electrons and gamma rays are emitted from a point source and low divergence, close to an idealised pencil beam. The code measures the energy deposition in the scintillator material, but does not model the physics of the scintillation process itself or the light transport. It is assumed that the energy deposited within the scintillator crystals is linearly related to the light yield of the scintillator, i.e. the number of fluorescence photons emitted, independent of the process of energy deposition [258].

Image processing and background subtraction

The response of the scintillator array is recorded as an image on a CCD and the images require processing before analysing them. The specific steps vary from setup to setup

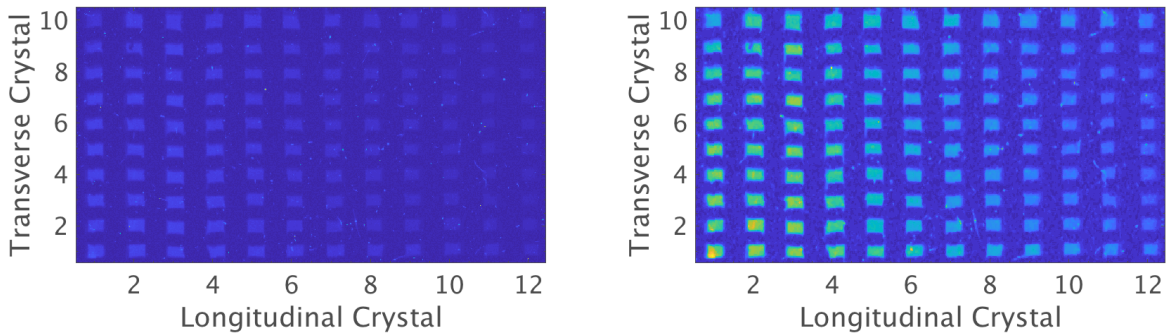


Figure 4.27: Images of the dual-axis spectrometer stack before (left) and after background subtraction (right), excluding treatment of bremsstrahlung. The colour scale is matched to the lowest and highest pixel value on the respective image.

depending on the imaging system. The open side of the crystals (see Figure 4.24) were imaged close-to-normal to collect a large fraction of the scintillation light, which also removed the necessity of morphing the image as required for the magnetic spectrometer screen (see Section 4.5).

The images contain background noise from different sources that has to be removed. The background can roughly be divided into continuous off-shot background and on-shot noise. The off-shot noise includes the intrinsic 'dark noise' on the camera chip and counts related to ambient light. This background can be characterised by taking a series of images at dark conditions which are then subtracted from on-shot data.

In high-intensity laser-plasma interactions, energetic radiation and particles are produced, which can directly hit CCD chips resulting in 'hard hits' or 'hot pixels'. In addition, scattered laser light and bremsstrahlung might produce a signal on the detectors. Scattered laser light can be mitigated by light shielding and by adding bandpass filters to the imaging system with a transmission matched to the bandwidth of the scintillation light. Hard hits, single pixels with high or saturation value, can be removed by applying a median filter which results in some blurring of the image. The treatment of the bremsstrahlung background is more complicated and will be discussed later.

In the experiment outlined in Chapter 6, the radiation signal is constrained to a narrow, central part of the image due to the lead collimator and the remaining image can be used as on-shot reference to account for off-shot noise and on-shot noise from stray light (see Figure 4.25). In Chapters 5 and 7, the signal occupies large parts of the image and the regions in between the crystals are used instead to estimate the background. An explicit example of a background subtraction is shown in Figure 4.27. On the left an image of the raw detector response to hard betatron radiation is shown. The colour scale indicates the number of pixel counts and is scaled to the minimum and maximum values on the image. Due to efficient shielding the camera is not affected much by 'hard hits', but some of the crystals (squares) are barely visible. On the right the image after the

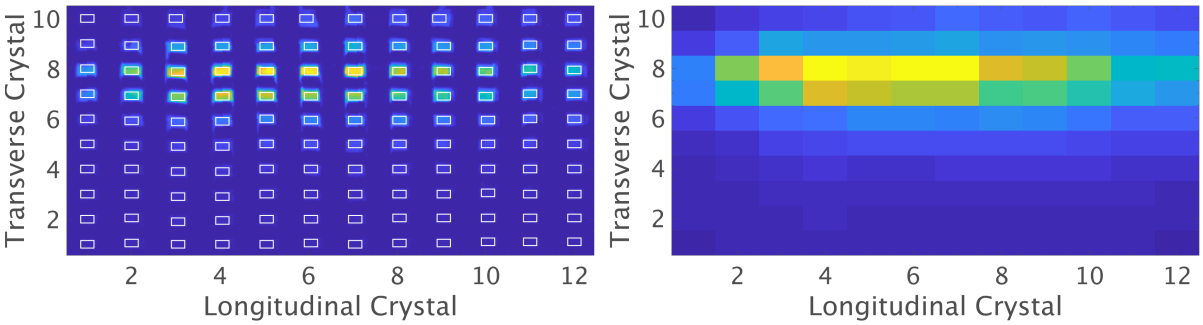


Figure 4.28: Response produced by an LWFA bremsstrahlung source measured using the dual-axis spectrometer stack. The radiation enters the stack from the left side and propagates to the right. Left: Image of the scintillator stack after background subtraction. The white rectangles indicate the regions of interest where the crystals are located. The dark regions in between the crystals are occupied by spacers. Right: Corresponding pixelated response retrieved from the image on the left by integrating over the regions indicated by the rectangles.

background subtraction is shown, where the colour scale is again matched to its minimum and maximum values. The contrast has improved significantly, such that each crystal is clearly visible.

Even with efficient filling of the field of view, the crystals emitting the scintillation light only occupy a fraction of the total image. To further reduce the impact of noise and to focus on the signal-relevant parts of the image, we select the regions of the individual crystals (see Figure 4.28) and extract the content of the crystals. The result is a pixelated response of the detector, only using its active parts. The shape of the decay in the longitudinal direction is characteristic of the spectral content, whereas the transverse dimension indicates the angular divergence. The transverse width of the crystal and spacers determine the transverse spatial resolution.

On-shot bremsstrahlung background and shielding

In the experiment setups described in this thesis, electrons are accelerated and dispersed in a magnetic spectrometer. While traversing the chamber and also when leaving it, the electrons interact with a range of solid materials, resulting in scattering, generation of secondary particles and showers of bremsstrahlung being produced. This is another source of on-shot noise. Since the radiation from this process is highly energetic, a lot of energy is potentially deposited in the scintillator crystals dominating the detector response.

Consequently, it is important to reduce the amount of noise reaching the detector by identifying the main source and shielding the direct line of sight to the detector efficiently. In the setup described in Chapter 5, the electrons were dispersed sideways and the detector

was shielded with lead on both of its sides. In the campaign reported of in Chapter 6, the electrons were dispersed upwards. The main source of noise is the roof of the vacuum chamber and the ceiling of the target area. After measuring the shower of radiation from above on the detectors, the top of the detector was shielded with lead which reduced the noise level. A lead collimator was also used to limit the acceptance angle for radiation coming from upstream (see Figures 4.22 and 4.25). For the measurements in Chapter 7, the electrons were primarily dispersed downwards into the thick breadboard of the vacuum chamber, the chamber itself and the floor of the target area. Two lead walls with narrow apertures and a large aperture 60-cm-long magnet were blocking the direct line of sight downstream to the detector (see Figure 7.4). The primary magnet was in some instances removed from the setup and the second magnet was used to characterise the electron beam by dispersing it horizontally. To account for this scenario, the sides of the detector were shielded with lead as well.

Since the primary noise source is off-axis, efficient shielding of the direct line of sight reduces the measured signal significantly. Most of the remaining radiation is then entering the detector on the same path as any radiation signal we would want to characterise. As a result, it is impossible to shield this component without infringing on the signal itself, but the response of the detector can be used to characterise the background. On shots with the background and the signal present, on the other hand, the detector response is then the combined response to both, and depending on their relative yields the spectral retrieval of the signal might be affected.

In the results presented in this thesis, gamma rays produced by three methods are characterised. Each generation method requires a slightly different approach to deal with the bremsstrahlung background which are briefly discussed here.

1. Linear inverse Compton scattering (Chapter 5): The background was characterised by a series of null shots, i.e no scattering laser, but the full electron beam. The spectral shape of the background was found to be stable and its total yield proportional to the total squared energy in the electron beam, $Q\langle\gamma^2\rangle$, where Q is the total beam charge and γ is the electron Lorentz factor. As linear inverse Compton scattering does not affect the energy of the electron beam this allows the measured electron spectrum on full shots to be used to estimate the bremsstrahlung background on each shot.

2. Non-linear inverse Compton scattering (Chapter 6): The background was characterised on a series of null shots and was also found to be proportional to $Q\langle\gamma^2\rangle$. Although the energy spectrum is affected by collision with the laser on full shots, the bremsstrahlung sources are likely to be from interaction of electrons with material

downstream from the collision point. This means it is reasonable to assume that the background on full shots is determined by the post-collision $Q\langle\gamma^2\rangle$.

3. Bremsstrahlung (Chapter 7): The background, characterised on shots without the converter in place, was much lower than the signal measured on shots with the converter. The background therefore has a negligible affect on the measured spectrum when the converter was used.

Detector Calibration using Bremsstrahlung

The conversion efficiency of the scintillator varies from crystal to crystal. This might be due to differences in quality of the crystal, radiation damage or age. The light emitted from the stack might also vary due to small changes in the dividers, polishing, or positioning of the crystal. Finally, the relative measured signal is also affected by a varying viewing angle and collection efficiency across the image.

To be able to compare the simulated response and the experimentally measured response, we have to match both through a suitable calibration. In order to correct all the different factors using one calibration, we have to use a well understood comparable test signal in the right energy range that we can simulate and measure in an experiment. By comparing the simulated and measured response, we then obtain a correction factor for each crystal.

A well understood mechanism with a spectrum covering a wide range is bremsstrahlung from relativistic electrons interacting with solid foils. The overall spectral shape is also only weakly dependent on the spectral shape of the used electron spectrum. Using a relativistic electron beam, we can produce a directed bremsstrahlung source.

In the experiments described in this thesis, electrons are accelerated via LWFA and characterised using a magnetic spectrometer. A foil of known material and thickness is then inserted into the path of the undispersed electrons to produce a directed beam of bremsstrahlung generating a detector response. If we know the properties of the electron beam and the converter material (material, thickness), we can simulate the expected bremsstrahlung spectrum and the corresponding detector response in GEANT4 to compare with the experimentally measured response. Throughout this work various background methods were used, which are summarised in Table 4.5.

In Figure 4.30, an example of an experimentally measured and a simulation result for one detector row is presented. The simulated response is very smooth in comparison to the measured response, where the peaks in the experimental data are results of the varying light efficiency of the crystals (intrinsic to the crystals and the setup). By dividing the simulated response by the experimentally measured response, we obtain one correction

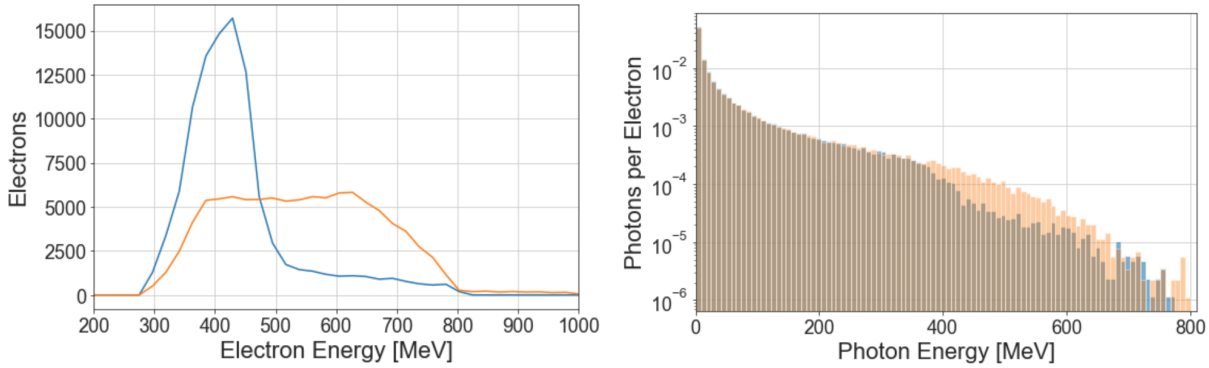


Figure 4.29: Left: Two examples of electron spectra measured in an experiment that are used as input for GEANT4 bremsstrahlung simulation. Right: Corresponding simulated bremsstrahlung spectrum produced using 1 mm of bismuth as converter material. The spectrum is normalised by the number of electrons in the simulation.

Calibration Targets and Methods			
Chapter	**Converter**	**On-/Off-Shot**	**Collimation**
5	1.6 mm PTFE	on-shot	Narrow
6	9 mm Pb	off-shot, statistical	Wide
7	4 mm W	off-shot, statistical	Wide

Table 4.5: Overview of bremsstrahlung converter targets used for the calibration. The PTFE converter enables measuring the electron beam on-shot, whereas the other targets lead to strong scattering and the electron beam is characterised statistically.

factor, $c_{corr}(i,j)$, for each crystal in an array of $(i \times j)$ crystals:

$$c_{corr}(i,j) = \frac{R_{sim}(i,j)}{R_{exp}(i,j)}, \qquad c_{corr} = R_{sim} \oslash R_{exp}. \tag{4.6.1}$$

This correction factor now accounts for deviations in the efficiency independently of its origin (e.g. imaging setup, intrinsic crystal efficiency). To reduce the experimental error, this can also be averaged over several shots, but experimental data has shown that bremsstrahlung is a very reliable and reproducible source [263]. However, if the detector is moved or the imaging is being changed, the procedure has to be repeated. The 'corrected' response, R_{corr}, is then being obtained by multiplying the experimental response of crystal (i,j) in the array, $R_{exp}(i,j)$, by the corresponding correction factor $c_{corr}(i,j)$:

$$R_{corr}(i,j) = R_{exp}(i,j) \cdot c_{corr}(i,j), \qquad R_{corr} = R_{exp} \circ c_{corr}. \tag{4.6.2}$$

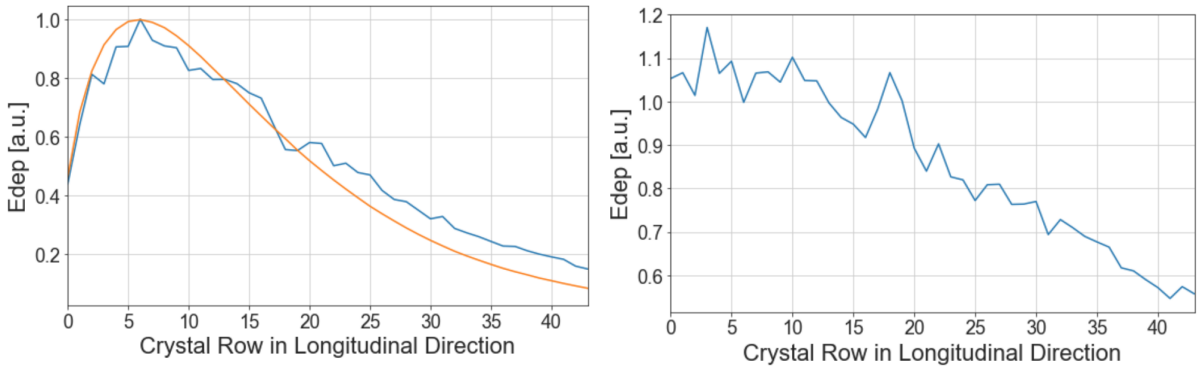


Figure 4.30: Left: Measured experimental response of the detector for bremsstrahlung (blue) and the corresponding in GEANT4 simulated response curve (orange). Both curves are normalised to their maximum value. Right: Correction factor for the crystal rows obtained by dividing the simulated by the experimentally measured detector response (Eqn. (4.6.2)*).*

Detector response for gamma-ray spectra

Since we obtained the background-subtracted detector response and corrected the response for experimental deviations from an idealised detector, we can proceed to characterise the energy-dependent response and infer a gamma spectrum from experimental data. As we will use the same setup and detector to characterise different types of radiation with different spectral shapes, we will use a generalised technique that will flexibly work in different scenarios.

First, we run GEANT simulations similarly as before for the bremsstrahlung calibration, but now for mono-energetic gamma rays covering the energy range of interest. The characteristic shape of the energy deposition in the longitudinal crystal rows and its variation with photon energy can be seen in Figure 4.31 (left) for up to 500 MeV gamma rays. The simulated energy deposition ramps up to a peak before decaying, with the peak moving further into the stack with increasing photon energies. This is a result of the showers of secondary radiation and particles the energetic photons produce when interacting with the material of the stack. The position of this peak is hence an indicator of the length of this cascade and the energy of the radiation that is incident on the stack.

Figure 4.31 (right) shows the crystal which records the highest energy deposition as a function of photon energy. The different curves show how this changes in different detector geometries. By adding more material before the stack or using dense high-Z materials, the highest energy deposition occurs earlier and, inversely, using plastic instead of metal can be used to move the peak further into the stack. This means that the choice of materials can be used to compress or stretch parts of the signal over more or fewer crystals.

We now simulated the energy deposition for a range of incoming photon energies in terms of energy deposition for crystals in longitudinal direction for a given photon energy.

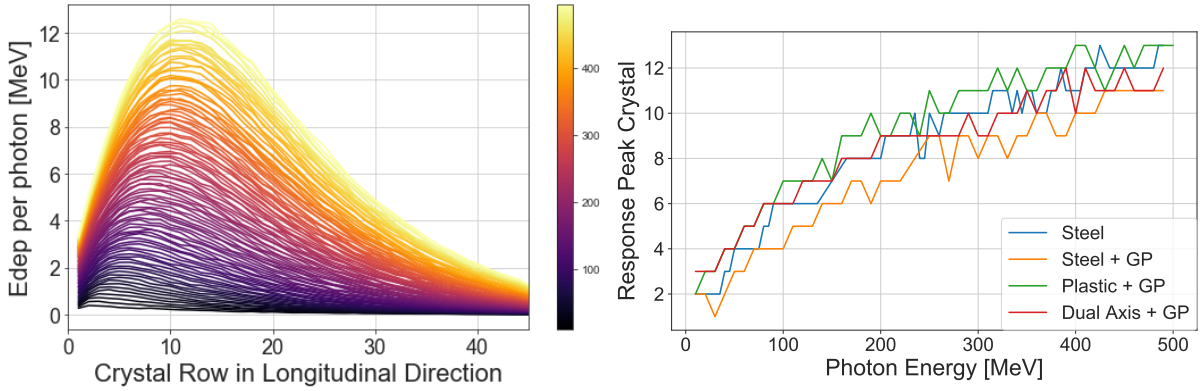


Figure 4.31: Left: Detector response to mono-energetic gamma-rays simulated in GEANT4, using a setup as in Chapter 7. The energy deposited per photon from energies 10 to 500 MeV is shown as function of the longitudinal crystal row. The photon energy is encoded in the colour axis from low (black) to high (white). The energy deposition per crystal rises to a maximum and then decays further into the stack. Right: Crystal recording the highest energy deposition as a function of photon energy for different detector geometries: 'RAL' stack with steel front plate (blue), additionally a gamma profile screen ('QUB'), 'RAL' stack with front plate replaced by PTFE and profile screen, dual-axis detector with profile screen (see also Tables 4.3 and 4.4). In general, the peak of the response increases with increasing photon energies, where fluctuations are probably caused by statistical fluctuations in the simulated data and would vanish for larger simulation sets.

We assume this is linearly converted into light output [258] and that the experimental measurement has been corrected as described previously. For each photon energy E_i, we obtain an array of deposited energies $\mathbf{R_i}$ in the longitudinal crystal columns C_1 to C_n

$$\mathbf{R_i} = \begin{array}{c} \\ E_i \end{array} \begin{array}{c} \begin{array}{cccc} C_1 & C_2 & \dots & C_n \end{array} \\ \begin{pmatrix} R_{i1} & R_{i2} & \dots & R_{in} \end{pmatrix} \end{array} \tag{4.6.3}$$

where R_{ij} is the energy deposited in crystal j by a photon of energy E_i. We can expand this to a matrix of energies in one direction and energy deposition in a particular longitudinal row. To reduce the number of simulations we require, we can interpolate the detector response on a finer grid of photon energies, filling in energies between the simulated photon energies. The energy deposition is normalised such that it represents the energy deposited by one single photon of the respective energy. If we do this for m different photon energies for a longitudinal array of n crystals, we obtain an $m \times n$-sized matrix $\mathbf{R}$:

$$\mathbf{R} = \begin{array}{c} \\ E_1 \\ E_2 \\ \vdots \\ E_m \end{array} \begin{array}{c} \begin{array}{cccc} C_1 & C_2 & \dots & C_n \end{array} \\ \begin{pmatrix} R_{11} & R_{12} & \dots & R_{1n} \\ R_{21} & R_{22} & \dots & R_{2n} \\ \vdots & \vdots & \ddots & \vdots \\ R_{m1} & R_{m2} & \dots & R_{mn} \end{pmatrix} \end{array} \tag{4.6.4}$$

An entry R_{ij} is then the energy a photon of energy E_i deposits in the longitudinal crystal row j. Each row is the individual contribution of one photon at a defined energy and by summing several rows and weighting them according to a spectrum, we determine the combined response of the detector. This can also be expressed more generally in terms of a matrix multiplication. Define a vector $\mathbf{N}$ of length m. Each entry is the number of photons or relative weight N_i of energy E_i in an arbitrary gamma spectrum.

$$\mathbf{N} = \begin{matrix} E_1 & E_2 & \dots & E_m \end{matrix} \\ \begin{pmatrix} N_1 & N_2 & \dots & N_m \end{pmatrix} \tag{4.6.5}$$

Multiplying the vector $\mathbf{N}$ containing the spectral information of the gamma spectrum with the response matrix $\mathbf{R}$ is equivalent to calculating the combined response or signal $\mathbf{S}$ of all photons in the spectrum defined by $\mathbf{N}$. $\mathbf{S}$ is then a vector of length n, the number of longitudinal crystals.

$$\mathbf{S} = \mathbf{NR} = \begin{matrix} E_1 & \dots & E_m \end{matrix} \\ \begin{pmatrix} N_1 & \dots & N_m \end{pmatrix} \quad \begin{matrix} C_1 & \dots & C_n \end{matrix} \\ \begin{pmatrix} R_{11} & \dots & R_{1n} \\ R_{21} & \dots & R_{2n} \\ \vdots & \ddots & \vdots \\ R_{m1} & \dots & R_{mn} \end{pmatrix} = \begin{matrix} C_1 & \dots & C_n \end{matrix} \\ \begin{pmatrix} S_1 & \dots & S_n \end{pmatrix} \tag{4.6.6}$$

Each entry of $\mathbf{S}$ is then

$$S_i = \sum_{j=1}^{m} R_{ij} N_j, \tag{4.6.7}$$

i.e. the sum of responses for the longitudinal crystal row i for all photon energies weighted by the spectrum $\mathbf{N}$. Provided we have access to a sufficiently populated matrix that spans a wide energy range, we can calculate the response of the detector associated to any arbitrary spectral shape.

Since this is a matrix operation, the experimental response of the detector can in theory be inverted to obtain the input spectrum. Unfortunately, noise and the low sensitivity of the detector response to smaller changes in the spectral shape make an inversion an unsuitable technique. Instead, we assume a parametrised spectral shape, calculate the response for a range of parameters and find the best fit to the experimentally measured response, for instance using a least-square fit. Other work has shown that the gamma spectrum can be retrieved without assumption of the spectral shape if a second independent measurement is performed, for instance using a Compton or pair spectrometer [264].

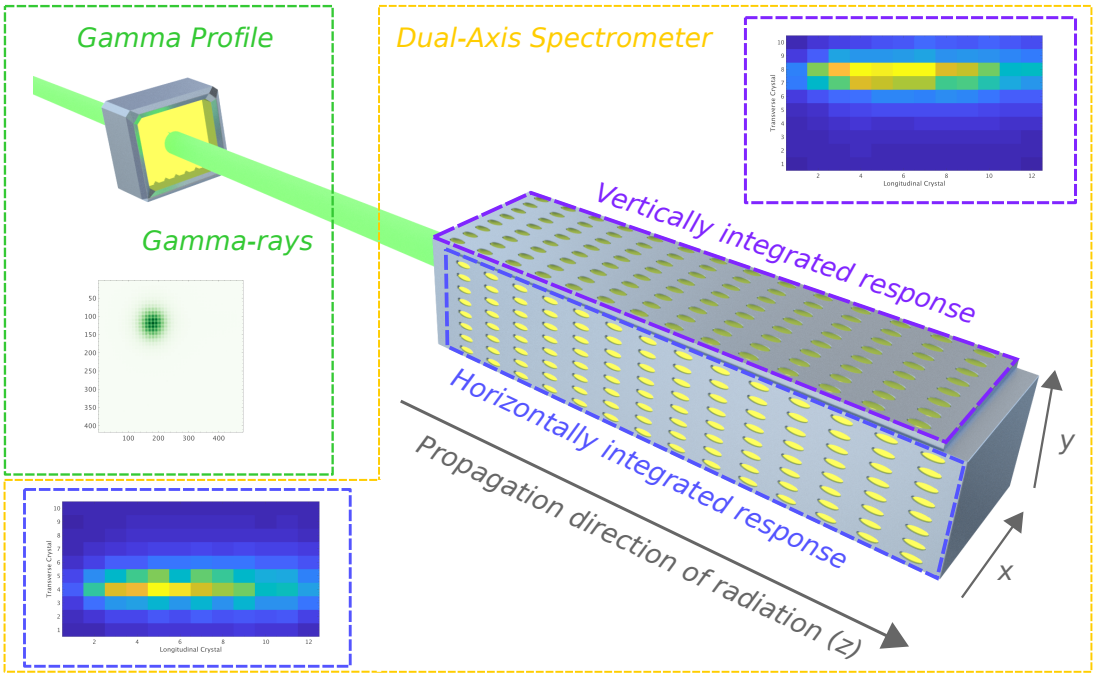


Figure 4.32: Sketch of a combined setup of a gamma profile screen (green) and a dual-axis spectrometer (gold) along with example data from a bremsstrahlung source at GEMINI. *For the dual-axis spectrometer the two views enabled by the alternating crystal layers are indicated in purple (vertically integrated) and blue (horizontally integrated), with the associated experimental data marked in the same colours.*

Resolving spatial features

Due to the comparatively large crystals used in the spectrometer arrays, the spatial resolution of both detectors is poor compared to the profile screens introduced in the previous section. In addition, the long crystals that are used to increase the light yield also destroy one of two transverse spatial components of the radiation. In the dual-axis stack, however, the orientation of the crystals is alternated and, as a result, the spatial dimension that is resolved (or destroyed) alternates as well (see Figure 4.24).

Figure 4.32 shows a sketch of a combined setup using a profile screen (green) and the dual-axis spectrometer (gold) along with example on-shot data for the diagnostics from bremsstrahlung that was taken on an experiment at GEMINI (see Chapter 5). The experimental data is shown in a larger format in Figure 4.33 (top). The gamma beam from bremsstrahlung is narrow and symmetric such that it produces a small circle on the gamma profile screen (left) and is concentrated only on one or two crystal rows in the vertically integrated (centre) and horizontally integrated response (right). Assuming that the gamma beam is confined to an expanding cone centred around an axis parallel or at a small angle to the nominal laser axis, the centroid and the bright rows visible on the two projections can be used to confirm the relative position of the two detectors within their spatial/angular resolution. At the specific example of the data provided in Figure 4.33

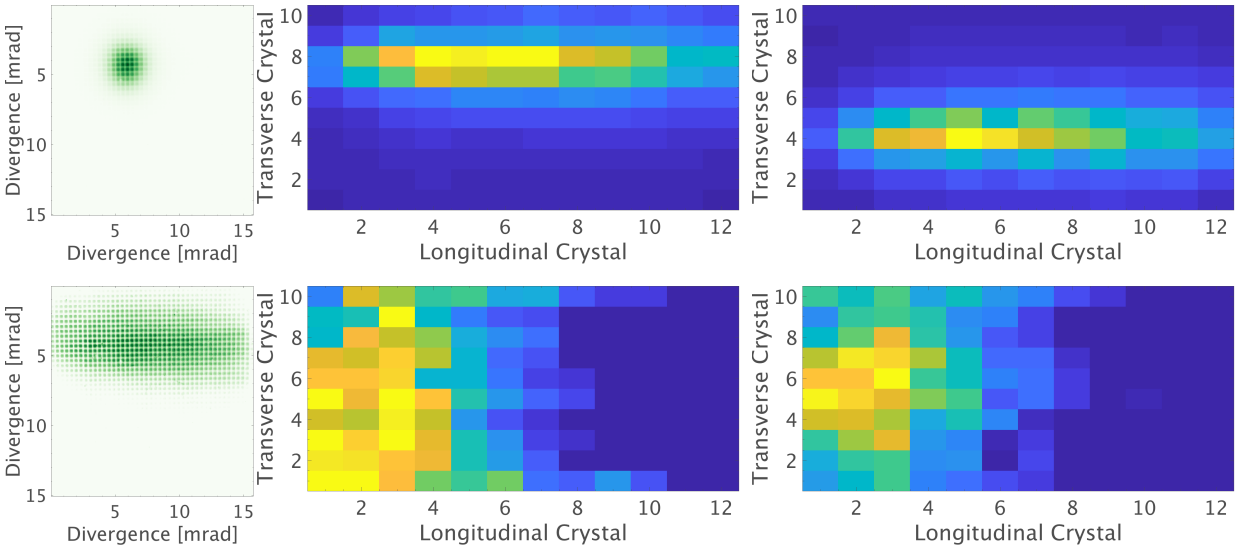


Figure 4.33: Gamma signal measured in experiment with a gamma profile screen (left) and the corresponding pixelated detector response of the dual-axis scintillator stack. Two views of the array, integrated vertically (middle) and horizontally (right), are shown for a symmetric bremsstrahlung source (top) and elongated betatron radiation (bottom). The transverse crystal (y-axis) indicates pointing and the spatial extent of the source. The symmetric source produces a comparable response in both views. The betatron source produces a narrow response in the horizontally integrated axis as most energy is deposited in a single crystal, whereas its response is spread widely in the other axis.

(top): the positions of crystal row 8 on the vertically integrated view and row 4 on the horizontally integrated response correspond to the area around pixel $(x, y) \sim (180, 120)$ on the gamma profile screen. This can be confirmed further by observing how the signal shifts on all three views relative to each other as a result of beam pointing.

The spatial resolution is determined by the size of the crystals and their spacing, which is $5 + 1$ mm for the RAL stack and $5 + 0.5$ mm for the dual-axis stack (see Table 4.4). The RAL stack is very wide and covers a height of 198 mm, whereas the dual-axis stack covers 55 mm. At 3 m distance from the source this then corresponds to an angular resolution of 2 mrad and 1.83 mrad at a field of view of 66 mrad and 18.33 mrad, respectively.

In Figure 4.33 (bottom), on the other hand, the response of an asymmetric gamma beam from hard betatron radiation is shown. On the profile screen (left), we see that the gamma beam is much wider in the horizontal plane than high. This is reflected in the two projections of the dual-axis spectrometer: on the vertically integrated view most of the first crystal columns are lit up brightly (yellow), whereas on the horizontal projection the bright signal is mainly concentrated on ~ 3 rows. The response is mainly confined to the first columns as the betatron radiation is much less energetic than the gamma rays from bremsstrahlung. The lower energy of the radiation also results in less energy being deposited in the detector which in turn translates into worse contrast.

Measuring the spatial profile of radiation is interesting for different applications. In

the context of inverse Compton scattering, it can be used as beam diagnostics in the linear case [171] and to infer the intensity at the interaction from the ellipticity in the non-linear case [120, 172, 260]. For betatron radiation produced from wakefield accelerators, for instance, the ellipticity is an indicator for the wiggler parameter. However, a plain spatial analysis of the profile is easier done using a scintillator with better resolution (Fig. 4.33).

On the other hand, if not only the spatial component is of relevance but the spectral distribution across the profile, then a profile screen alone is not sufficient and this capability could become useful. The different rows allow in principle a separate spectral retrieval if simulated appropriately. The ellipticity of a source and its decay could be tracked throughout this stack as another way to characterise radiation through a double-differential or to infer a full 3D spectrum (two spatial and one energy dimension: x, y, E). This is not further investigated in this context, but represents a proof-of-principle that this detector is able to resolve the different dimensions and that the spectral retrieval can be done independently.

Chapter 5

Linear Inverse Compton Scattering at Astra Gemini

5.1 Motivation

Photons scattering off a relativistic electron are Doppler-upshifted due to the relativistic Lorentz boost, converting, for instance, optical photons from a laser into energetic X-rays and gamma radiation. This process is called *inverse Compton scattering* (ICS), *relativistic Thomson scattering* or *Compton backscattering*. *Linear* inverse Compton scattering, the low-intensity limit of this process, is widely used in conventional accelerators as high-energy radiation source to study nuclear processes [97], and as versatile beam diagnostic to measure, for instance, the beam energy [95, 265], position [92], emittance [91] and polarisation [87, 93, 266].

More recently, it has also found increasing application in laser wakefield accelerators (LWFA) [80, 81, 232], for instance, as X-ray source for imaging applications, including high-Z materials [267]. Since the radiation inherits the ultrafast nature of the LWFA electron beam [77], it also has potential as X-ray probe for fast processes like laser-driven shocks in materials [268] or structural transitions such as non-thermal melting [81]. In the context of LWFA, linear ICS has also been considered as diagnostic to measure properties of the accelerated electron beam [171, 269, 270].

At conventional accelerators and in LWFA experiments, the beam is typically diagnosed by scanning or rastering the laser over multiple shots through the electron beam (see 'laser wire' [88–94]). In all-optical setups, the laser is focused tightly in order to produce a significant number of X-rays or gamma-rays [171]. In conventional accelerators, the typical beam charges are much higher such that Fabry-Perot cavities excited by a continuous-wave laser can be used [94]. A statistical characterisation of the electron beam is only meaningful if the beam source is either reproducible, as in conventional setups, or a particle beam transport is used to focus the electron bunch onto a fixed point in space. The

performance of LWFA sources has improved greatly in the recent years [216], also in terms of reproducibility and repetition rates, which are key development areas to be competitive with other light sources and accelerator concepts [81].

A sufficiently intense laser pulse, on the other hand, can produce a significant yield of scattered photons at a beam diameter comparable to the size of the electron beam or exceeding it. In such a setup, the Compton source could act as single-shot diagnostic similar to a beam profile monitor, measuring electron beam pointing, divergence and ellipticity, and their statistical fluctuations. The same setup could then be used at high intensities in *nonlinear* inverse Compton scattering where the ellipticity of the emission profile has been proposed as on-shot intensity measurement of the interaction [120, 172, 260]. A statistical characterisation of the electron beam would be a useful tool to discriminate experimental uncertainties, e.g. caused by the intrinsic fluctuations of the wakefield accelerator, and model uncertainties related to radiation reaction.

5.2 Chapter Outline

This Chapter presents results from an experimental campaign undertaken at the GEMINI laser system in early 2019, aimed at conducting precision measurements of radiation reaction by colliding highly relativistic electron beams from a laser wakefield accelerator with an intense laser pulse. Unfortunately, we were not able to perform interactions at high-intensities as we lost access to the scattering laser beam towards the end of the campaign. However, we succeeded in colliding a relativistic electron beam with a defocused laser pulse at $a_0 \sim 0.2 - 1.0$ over the course of hundreds of shots, and measured the emitted high-energy radiation produced from linear inverse Compton scattering in the process. In this Chapter, we demonstrate how to use the properties of the emitted radiation to diagnose both, the scattering laser pulse and the electron beam.

After outlining the experimental layout of the campaign, we proceed with a characterisation of the electron spectra taken at fixed experimental conditions (Section 5.4). These electron beams interacted with the laser pulse and acted as Compton source.

Then, results from a laser raster scan are presented (Section 5.5): the scattering beam is shifted relative to the electron bunch and the presence or absence of a bright gamma signal is measured on the gamma profile detector to establish the size of the laser beam at the interaction plane. Here, the electron beam is small and approximately fixed in space so that it acts as a probe rastering the laser beam profile. This technique can be used to corroborate the spatio-temporal electron-laser alignment, and to estimate the change in their relative arrival time required to achieve high-intensity interactions.

Based on the estimated laser beam parameters at the interaction and the characterised electron beams, the spectral shape of the generated radiation is discussed (Section 5.6).

This is followed by an estimate of the total number of high-energy photons produced in the interaction (Section 5.7), and how different spectral components of the electron beam contribute to the total yield measured on the gamma-ray detectors (Section 5.8). The photon yield is then used to infer the beam size and intensity at the interaction (Section 5.9), and could be used to diagnose the temporal fluctuations in the synchronisation of the laser pulse and the electron beam. Subsequently, the radiation spectrum is inferred for specific example shots (Section 5.10).

Finally, we discuss the feasibility of this light source as single-shot non-invasive electron beam diagnostic, in particular its ability to measure the beam divergence, pointing and to resolve spatial features of the electron beam (Section 5.11).

5.3 Experimental Setup

This experiment was performed at the GEMINI facility in 2019 using both laser arms of the dual beam facility. Figure 5.1 shows a sketch of the relevant components of the setup.

Laser wakefield accelerator

The driver beam for the wakefield accelerator was focused by an $f/40$ off-axis parabola (OAP) onto the leading edge of a 15 mm conical supersonic helium gas jet. The pulse duration was measured to be 61 ± 5 fs FWHM with an average energy on-target of 12.5 ± 0.2 J, reaching a peak power of 195 ± 3 TW. The size of the focal spot measured $(48.6 \pm 3.2) \times (39.2 \pm 1.6)$ µm FWHM, amounting to a peak normalised vector potential of $a_0 = 1.88 \pm 0.04$ in vacuum[1]. The laser pulse was polarised in the horizontal plane.

The exit of the gas nozzle was positioned 14 ± 0.1 mm below the laser beam axis to avoid damage from the second, more divergent laser beam. A steel razor blade was introduced 4 ± 0.1 mm above the nozzle edge at $-32.4° \pm 0.3°$ angle in vertical direction relative to the laser axis to produce a shock front. The tip of the blade was inserted 1.2 ± 0.1 mm into the gas flow from the same side that the driver beam entered from. The gas target was characterised on-shot by a transverse optical probe synchronised with the driver beam ending in a shadowgraphy and a Mach-Zehnder interferometry setup. The electron density determined interferometrically[2] without inserting the blade was $(1.4 \pm 0.2) \times 10^{18}\,\mathrm{cm}^{-3}$. When inserting the blade, the density profile exhibited a sharp peak in density, a shock, reaching about $(2.4 \pm 1.4) \times 10^{18}\,\mathrm{cm}^{-3}$, which is up to twice the ambient density. The errors indicate the statistical variation in density rather than the resolution of the retrieval. Especially around the shock front, the retrieval might suffer from systematic errors, that

[1]The focal spot data and FROG trace were analysed by Matthew Streeter (Imperial College)
[2]The interferometry data was evaluated by Cary Colgan (Imperial College)

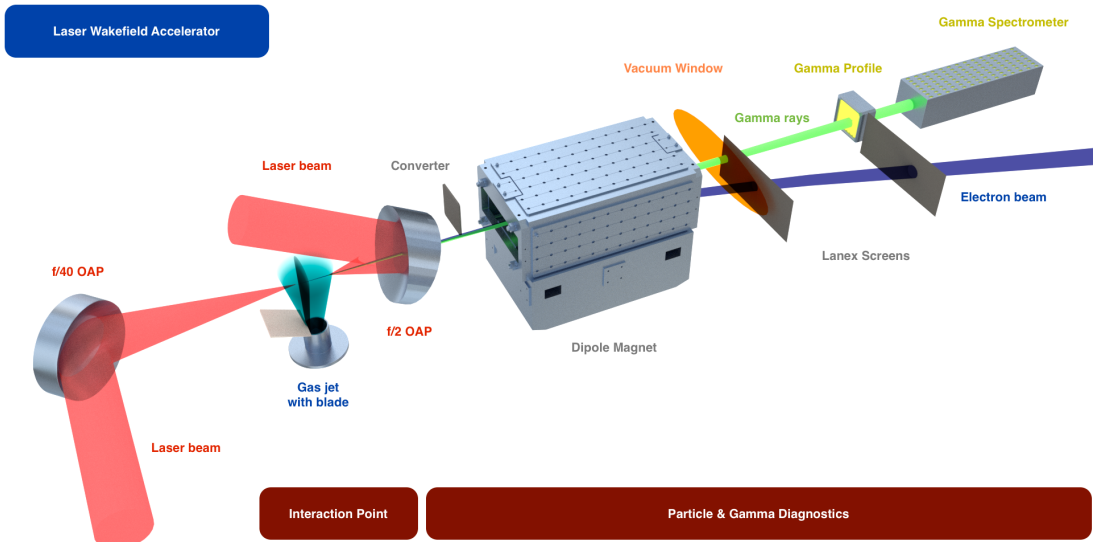


Figure 5.1: Sketch of the experimental setup to measure radiation from linear inverse Compton scattering. The first laser pulse (red, left) is focused down by an $f/40$ OAP into a gas jet and accelerates electrons (blue) from LWFA, where the density perturbation induced by the blade affects the injection mechanism. A second laser is focused down by an $f/2$ OAP and counter-propagates with the electron beam. Gamma radiation produced from linear inverse Compton scattering (green) is emitted in the propagation direction of the electron beam and is measured downstream by a scintillating profile screen and a stack of scintillating crystals used as spectrometer (right). A solid target behind the $f/2$ OAP can be used to convert the electron beam into an energetic source of bremsstrahlung to calibrate the gamma diagnostics. The electrons are dispersed horizontally by a permanent dipole magnet onto a set of Lanex screens. The accelerator, the interaction point and the magnet are in vacuum, whereas the measurement screens and gamma diagnostics are located at air separated by a thin vacuum window (orange).

are subject of ongoing analysis: e.g. an angled shock breaking the symmetry of the Abel inversion, intensity modulations from shadowgraphy convolved with shifts in the interference pattern, or if the shock front is spatially not sufficiently resolved. In addition to the optical probe, the gas target and the recombination light emitted by the plasma channel were imaged by a Canon DSLR camera from the side and a CCD camera from the roof of the chamber.

Scattering beam

A second laser pulse was focused by an $f/2$ off-axis parabola (OAP) at the opposite edge of the gas jet in a head-on geometry. The $f/2$ OAP had a 21-mm-diameter hole in the centre that allowed the electrons, laser light and radiation on-axis to propagate through. A plastic ring of outer radius 28 mm and inner radius 11 mm was fitted around the hole to protect the optic and the laser chain upstream from laser light that was potentially scattered or strongly defocused in the plasma. This reduced the energy on-target by 16 percent assuming a perfect top-hat laser profile and that the collimated beam incident on

the OAP had a diameter of 150 mm. To protect the optic from potential debris, a thin plastic layer with anti-reflective coating ('pellicle') and a suitable hole was attached to the mount of the OAP. The on-shot energy of the laser after the compressor was 9.73 ± 0.15 J and 8.17 ± 0.13 J on-target due to the hole in the OAP. In the dataset presented, the beam diameter at the interaction was estimated through a raster scan to be 400 ± 100 µm (see Section 5.5). This translates into a normalised vector potential of $a_0 \sim 0.28 \pm 0.04$ at a pulse duration of 45 fs. The laser pulse was linearly polarised in the vertical plane, cross-polarised to the wakefield driver beam.

Two-beam timing

Both laser beams were synchronised to each other in vacuum to an accuracy of ±30 fs using spatial interferometry [162]. A 90-degree dielectric knife-edge prism (Thorlabs MRAK25-E03) was inserted at the interaction point, deflecting both beams collinearly onto the CCD chip of a camera (AVT Manta G-033B) equipped with a ×10 long-working-distance infinity-corrected microscope objective (Mitutoyo NIR). The different radii of curvature of both beams, especially near the focus of the $f/2$ beam, produced a circular interference pattern when the beams were overlapped in space and time (see Section 4.3).

Particle and Radiation diagnostics

The radiation, the remaining driver laser and the electrons propagated through the hole in the $f/2$ OAP into a large aperture [10 cm × 30 cm (vertical × horizontal)] permanent dipole magnet[3] of integrated magnetic field strength $\int B(x)\mathrm{d}x = 0.35$ Tm. The electrons were dispersed in the horizontal plane. Electrons of an energy below 220 MeV collided with the yoke of the magnet, resulting in an effective low-energy cut-off. The dispersed beam left the vacuum chamber through a two-layer wide-aperture vacuum window[4] of dimensions 580 mm × 70 mm (horizontal × vertical). The layer facing the vacuum consisted of 25 µm of Kapton, the outside layer is 375 µm of Kevlar (chemical equation $C_{14}H_{14}N_2O_4$, density $\rho = 1.44\,\mathrm{g/cm^3}$ [271]) providing additional mechanical stability and fibre support that acted as mechanical fail-safe. A scintillating sensitive Lanex screen (Kodak Biomax) was placed just after the window, at 1.61 m distance downstream of the interaction point, to measure the spectrum of the dispersed electron beam. The screen also extended beyond the laser and radiation axis. The light and thin material of the window and the short distance to the Lanex screen minimised the impact of multiple small-angle scattering on the measurement [272, 273]. A second Lanex screen (Kodak Standard) measured the spectrum 700 ± 1 mm further downstream (2.31 m from the interaction point) and can in conjunction with the first screen be used to account for the pointing of the beam [256, 257].

[3] designed, and assembly and positioning supervised by Dominik Hollatz (Jena)
[4] designed and tested by the Mechanical Engineering Division at the CLF, in particular Daniel Treverrow.

The screens were each imaged by a cooled 16-bit CCD camera (Andor Neo) equipped with a suitable objective and a bandpass filter transmitting light of wavelength $546 \pm 10\,\mathrm{nm}$.

High-Z metal converter targets (bismuth, tungsten, iron) were fixed to a 1.6 mm plastic (PTFE) base and mounted on a motorised linear stage between the mount of the $f/2$ OAP and the dipole magnet. The targets were driven into the beam path to intercept the electron beam and to produce gamma radiation from bremsstrahlung [274] to calibrate the gamma-ray diagnostics [263]. The high-Z targets enabled efficient conversion of the electron beam energy into radiation, but did not allow measuring the electron spectrum at the same time. The PTFE base itself was also used as converter that was less efficient in terms of radiation yield but allowed a synchronous measurement of the electron and gamma-ray beam.

Radiation traversed the magnet on the laser axis, then passed through a 120 µm aluminium laser beam block that terminates the wakefield driver beam, and through the Kevlar-Kapton window mentioned before. Bright radiation in the right bandwidth was also captured by the Lanex screen as it extended beyond the laser and radiation axis. An array of 45×45 scintillating caesium-iodide crystals doped with thallium (CsI:Tl) of dimensions $1\,\mathrm{mm} \times 1\,\mathrm{mm} \times 10\,\mathrm{mm}$ measured the profile of the radiation $700 \pm 1\,\mathrm{mm}$ downstream from the plane of the first Lanex screen. The crystals were each separated transversely by a 0.2 mm thick TiO_2 coating and were held together by a TiO_2 front plate of thickness 0.5 mm. The stack covered a field of view corresponding to a cone of half opening angle 11.7 mrad. The spatial resolution including the coating separating the individual crystals was then $1.2\,\mathrm{mm}/2.31\,\mathrm{m} = 0.52\,\mathrm{mrad}$. $704 \pm 1\,\mathrm{mm}$ further downstream from the profile screen another elongated array of caesium-iodide crystals was positioned to measure the spectrum of the gamma radiation. Both scintillator arrays, the profile screen and the spectrometer, were imaged using cooled 14-bit EMCCD cameras (Andor iXons). The diagnostics are described in more detail in Section 4.6.

5.4 Characterisation of Electron Spectra

In this experiment, the electrons were injected through density perturbations in the supersonic gas flow, which were introduced by a steel blade [230] and subsequently accelerated to relativistic energies via laser wakefield acceleration (LWFA). The electron spectrum was measured by scintillating Lanex screens as part of a magnetic spectrometer setup (see [69, 205] and Section 4.5). Here, we will only consider the measurements from the first Lanex screen and ignore potential errors in the inferred electron energy that result from pointing fluctuations [256, 257].

We consider a dataset that consists of a series of shots taken at nominally fixed

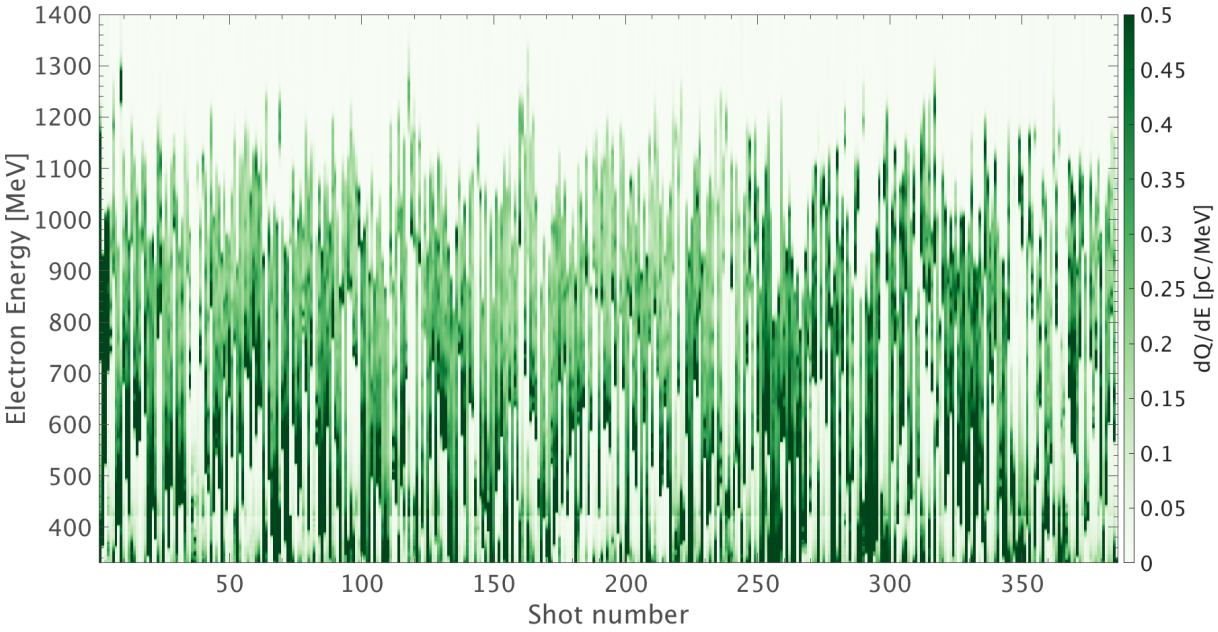


Figure 5.2: Waterfall plot of electron spectra measured at fixed experimental conditions. The y-axis indicates the electron energy in MeV, the x-axis shows the order the shots were taken in. The electron spectra measured on the Lanex screens were integrated in the non-dispersion axis and each occupy one column in this waterfall plot. The colour scale indicates the charge per MeV in the beam.

experimental conditions to investigate fluctuations in the accelerator performance. The electron beams measured on these shots were collided with a second laser pulse to produce radiation from inverse Compton scattering, which will be analysed in more detail in the following sections. The dataset consists of 386 shots, taken at constant backing pressure of the gas jet and fixed blade position (1.2 ± 0.1 mm into the gas flow from the entry point of the driver beam). Figure 5.2 shows a waterfall plot of the 1D electron spectra integrated in non-dispersion direction. Despite nominally constant conditions, the properties of the electron beams vary strongly from shot-to-shot and take on a wide range of shapes, maximum energies and energy spreads. Figure 5.3 provides a few examples of the 2D electron spectra from this dataset. The spectral bandwidth of the beams varies strongly with some exhibiting an almost flat spectrum spanning hundreds of MeV (see 4 left panels in Figure 5.3). These spectrally very wide electron beams show signatures of strong transverse oscillations, which indicate their potential to act as a bright betatron source [80]. In other instances, electron beams with narrow energy spread around 1 GeV are measured (right panels in Figure 5.3).

The striking variability of the electrons produced at seemingly fixed experiment conditions is not consistent with experimental results reported from other LWFA experiments at other laser systems using shock injection [230]. These setups typically provide reproducible electron beams with narrow energy spread [228, 230, 275, 276].

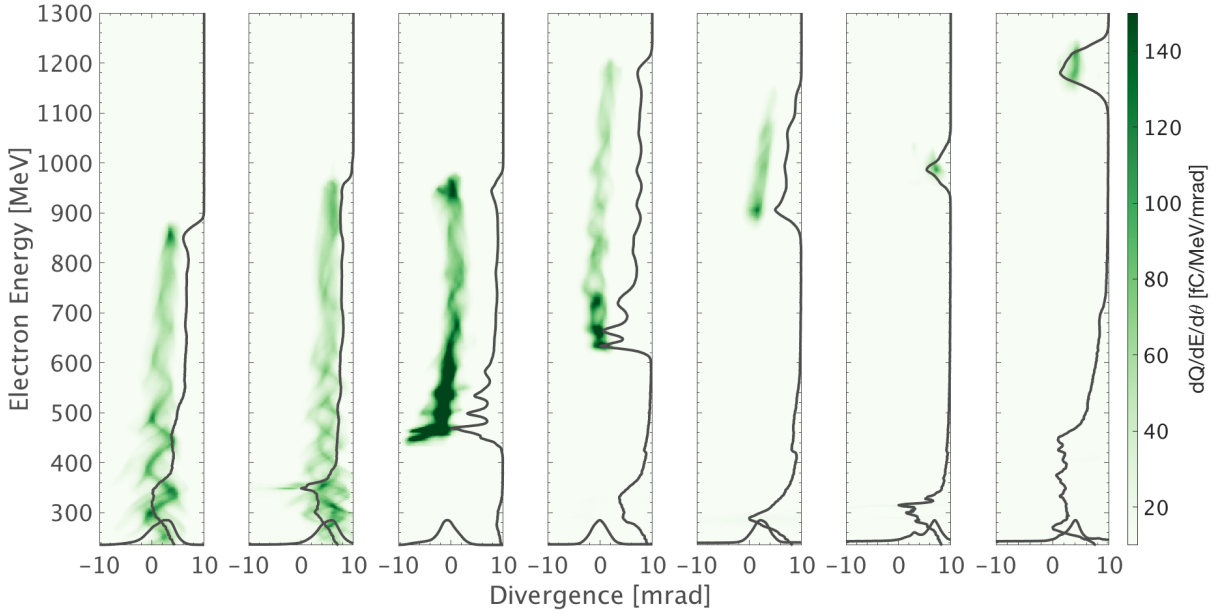


Figure 5.3: Examples of 2D electron spectra measured in the experiment. The y-axis is the dispersion axis and shows the electron energy in MeV on a linear scale, the x-axis indicates the divergence in mrad. The colour scale indicates the amount of charge per MeV per mrad in the beams and is fixed for all plots. Projections of the 2D spectra are shown on the respective axes (grey). The amplitude of the projections is set to the maximum within the respective panel and is not indicative of the relative charge between the panels.

Figure 5.4 summarises the key properties of the electron beams in form of histograms showing charge, maximum electron energy, vertical (non-dispersion axis) divergence, beam pointing and on-shot laser energy of the wakefield driver beam. The maximum energy of the electron beam, here defined as the energy when the spectral intensity reaches 10 percent of its peak value, measured on average $944 \pm 139\,\mathrm{MeV}$ (error indicates standard deviation based on normal distribution), with some shots reaching up to 1.3 GeV. The charge of the beam varied in particular due to the varying spectral range of the bunch with a median of $225(+67/-56)\,\mathrm{pC}$, where the error interval indicates the quarter and three quarter quantile, respectively, as the distribution is not normal. The divergence of the beams was measured to be $2.1(+0.6/-0.5)\,\mathrm{mrad}$, using the same convention as for the charge, and the vertical position of the beam centroid was fluctuating by 2.2 mrad, assuming a normal distribution. The on-shot laser energy was on average $12.3 \pm 0.5\,\mathrm{J}$, assuming a normal distribution. The linear correlation coefficient for the laser energy and the maximum electron energy is 0.03 which indicates that the quantities are not correlated. This is consistent with shock injection, where the position of the density perturbation, the injection point, determines the maximum energy, and also indicates that the injection point varies from shot to shot, potentially due to a variation in the shock position and angle. The charge in the beam is only moderately correlated with the laser energy at a

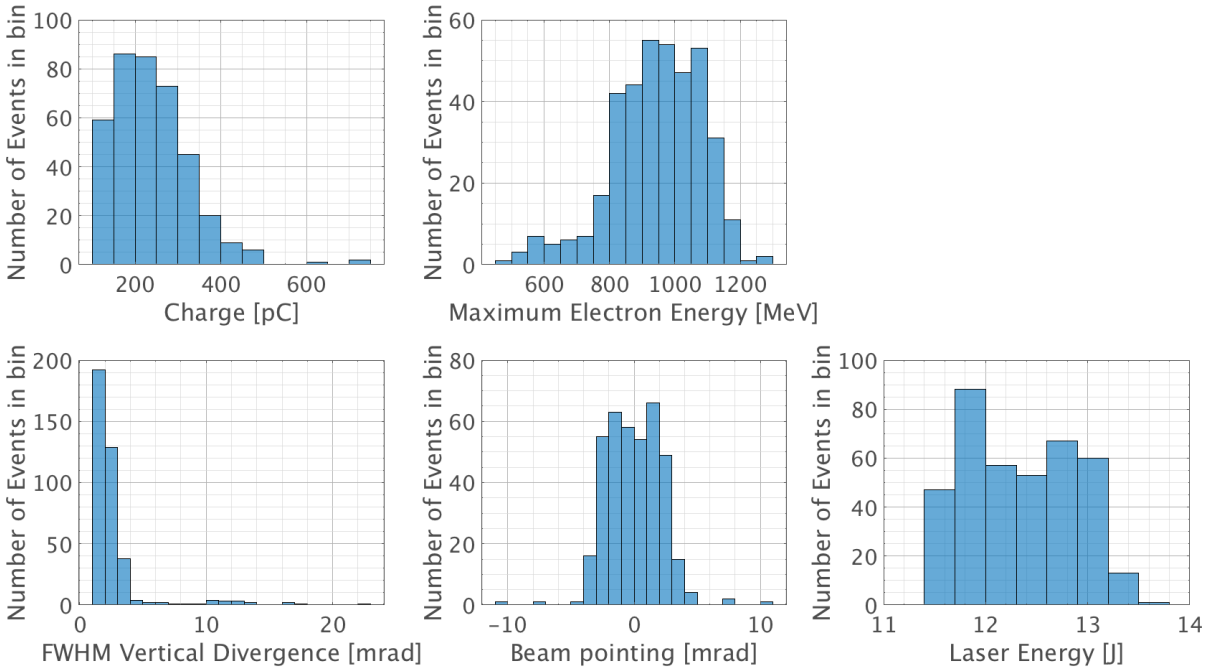


Figure 5.4: Histograms showing the fluctuations of electron properties in this dataset (386 shots). Top left: Total charge of the electron beams measured from 220 MeV upwards. Top right: Maximum electron energy, defined as energy at which the spectral intensity falls to 10 percent of its peak value. Bottom left: vertical divergence (non-dispersion axis, FWHM*) in mrad. Bottom centre: Beam pointing fluctuation in mrad from the mean position. Bottom right: On-shot laser energy of the wakefield driver beam in Joules.*

coefficient of 0.29.

The wide range of electron beams produced in this setup is interesting in the context of radiation production from linear inverse Compton scattering (ICS). Since the properties of the beams this accelerator generates vary strongly, the radiation these electron beams are capable to produce in a well-defined linear ICS interaction will also vary significantly. This means that this accelerator is in principle also able to produce a wide range of radiation spectra from broadband to strongly peaked radiation. However, an increased control over the accelerator would be required to shape the spectral emission and develop a tunable radiation source that can be optimised for a specific application. An improved stability of the shock position could facilitate this control.

5.5 Laser raster scan

The laser pulses from the two laser arms were overlapped in space and time using a photodiode and spatial interferometry in vacuum (see Section 4.3). The focal plane of the scattering $f/2$ beam was positioned in the gas jet for alignment purposes. On full-power

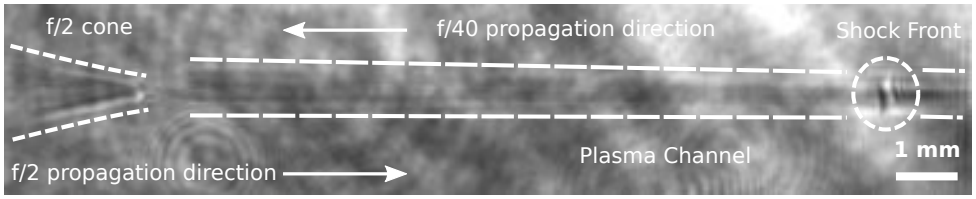


Figure 5.5: Cut-out of a shadowgram of the gas jet taken with the transverse optical probe (horizontal plane). The wakefield driver beam enters the gas jet from the right side and generates a plasma channel. The dark line on the right side results from a shock front. The second scattering beam is focused tightly into the plasma from the left side, where a converging cone becomes visible. The spatial scale is indicated in the bottom right corner.

shots, the cone of the $f/2$ laser pulse focusing into the plasma is visible on the transverse (horizontal plane) shadowgraphy diagnostic (see Figure 5.5, left side) along with the plasma channel from the wakefield driver beam and the shock leading to the injection of electrons into the wakefield accelerator (dark line in the plasma channel on the right side).

On full-power shots with both laser beams and an electron beam produced by the wakefield accelerator, we consistently measured a bright circular or oval signal on the gamma profile screen indicating an interaction of the laser pulse and the electron beam (inverse Compton scattering). The consistency of the collisions implies that the laser beam is much larger than the electron beam, and the combined fluctuations in the relative position of the scattering beam and the electron beam. This in turn indicates a systematic offset of the interaction point from the focal plane of the $f/2$ laser pulse as the laser pulse and the electron bunch would there be of comparable size and are expected to miss each other frequently [162].

To establish the transverse size of the scattering laser pulse at the interaction point, the scattering laser beam was shifted horizontally by translating the position of the $f/2$ off-axis parabola (OAP) in 50 µm steps, assuming that the laser beam translates by the same amount for small motions. The remaining experimental parameters and the alignment of the wakefield driver beam were kept constant during this procedure. At least 5 full-power dual-beam shots were taken at each OAP position. In some cases, more shots were required to accumulate 5 suitable data points, when at least one of the lasers was not firing or no electron beam was measured on-shot. The response of the gamma profile screen was recorded and the number of visibly bright signals was noted down. Subsequently, the OAP was then translated again by 50 µm and the procedure was repeated. Figure 5.6 shows a montage of the gamma profile screens at each position of a horizontal scan in the OAP position, where the relative position from the established beam centre is indicated on the x-axis. Figure 5.7, on the other hand, shows the corresponding average integrated gamma yields on the profile screen and the fraction of successful collisions at each position. The absence of bright signals at two consecutive OAP positions was deemed to be a suitable

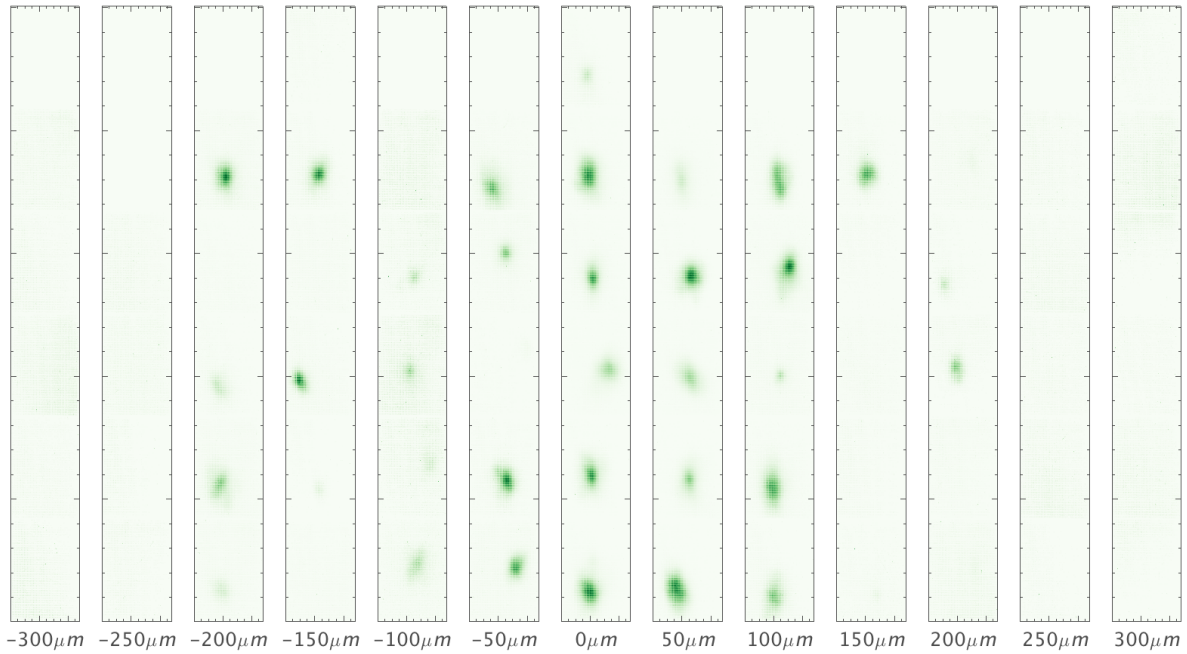


Figure 5.6: Montage of gamma profile measurements at different transverse OAP positions. Each panel shows the measured gamma profile images for a series of shots taken at a fixed OAP position. The panels are labelled with the relative transverse offset of the OAP for that particular dataset. The colour scale indicates the yield of scintillation light which is proportional to the energy deposited in the profile stack. The scale varies across the panels.

indication of lacking overlap of the laser beam and the electron bunch. The distance mapped by this method includes the diameter of the laser beam at the plane of the interaction, the size of the electron beam, and the relative pointing fluctuations between them. Since the finite step size in the OAP translation (50 μm) is much larger than the expected electron beam size $\sim$ μm and the relative pointing fluctuations ($\sim$ mrad $\times$ mm), the dominant measurement error on the transverse size of the laser beam is the step size.

In the raster scan presented in Figure 5.6 and Figure 5.7, the interaction region and hence, following our argument, the combined size of the laser beam and the electron beam along with variations in the relative beam pointing was 400 ± 100 μm. The integrated gamma yield in Figure 5.7 also shows signs of a drop in intensity throughout the scan, potentially when crossing the hole in the beam. At an energy on-target of 9.73 ± 0.15 J, this amounts to a normalised vector potential of $a_0 \approx 0.28 \pm 0.04$, where we assumed a perfect flat-top beam profile and hence ignored the reduction of the energy in the beam due to the hole in the $f/2$ OAP, as this does not affect the local photon density in the near-field. For an $f/2$ geometry, this also indicates that the interaction plane is at $\sim 1.1 \pm 0.1$ mm distance from the focal plane. Based on the alignment procedure in the experiment, we suspect that the interaction occurs prior to the focus of the scattering beam (left hand side in Figure 5.5). The interaction still takes place in the plasma, so that pointing fluctuations are reduced and the electron beam is only $\sim$ μm in size [78]. Similarly, off-axis distributions

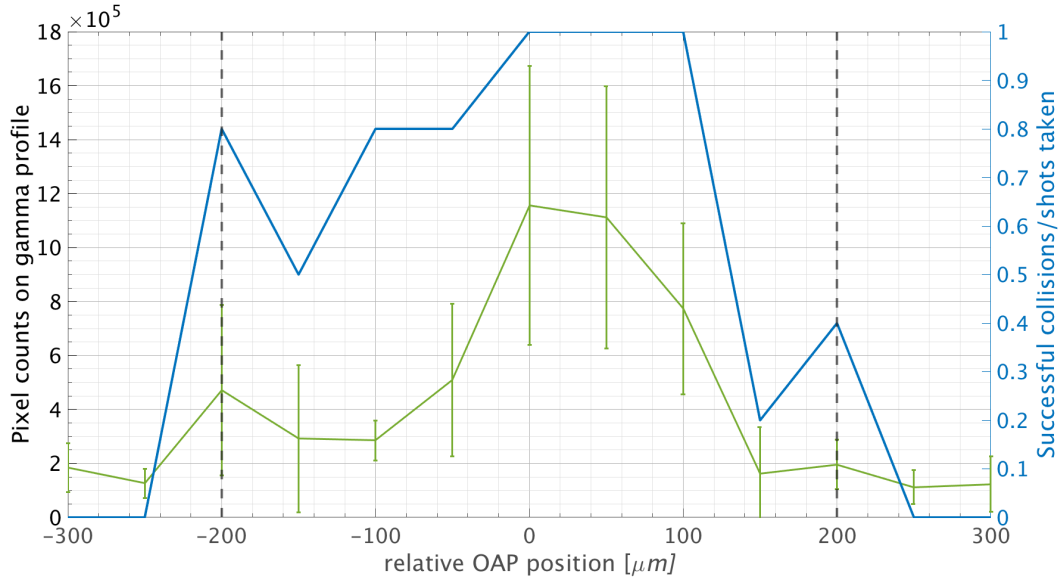


Figure 5.7: Green: Average integrated pixel counts on the gamma profile screen as a function of the relative OAP position. The error bars indicate one standard deviation from the mean based on a normal distribution. Blue: Fraction of successful collisions at each OAP position. The grey dashed lines indicate the determined beam size.

resulting from betatron oscillations are small with amplitudes $r_\beta \sim$ µm [80]. Since the beam pointing of the $f/2$ beam is demagnified due to the short focal distance, the raster scan mainly reflects the dimensions of the scattering beam and this is hence a suitable method to determine the size of the laser beam.

If we assume that this method successfully determines the size of the laser pulse at the interaction plane, we can also pinpoint its centre by shifting the OAP to the central position between the outermost OAP positions on which a significant gamma signal was measured. By repeating this procedure in the vertical axis, we can then centre the scattering laser pulse on the electron beam accurately in both transverse dimensions, provided that the relative pointing fluctuations and the electron beam size are negligible as assumed. The accuracy of this procedure can be improved by repeating the steps in the first transverse dimension in a third pass and by reducing the step size of the OAP translation. The principle of this 'raster scan' resembles the 'laser wire' or spatial cross-correlation technique where a scattering laser beam is focused tightly onto an electron beam to produce energetic from linear inverse Compton scattering and to diagnose the electron beam [88–96, 122, 171, 269, 270]. The laser focus is typically smaller than the electron beam and the transverse size of the electron beam can be determined by translating the laser focus over multiple shots. The emission spectrum and angular distribution of the backscattered radiation can also be used as diagnostic for other beam properties. The name 'laser wire' is derived from the physical wire scanners that were used as beam diagnostics in conventional accelerator facilities [96]. In the case presented here, the electron beam, however, is much smaller

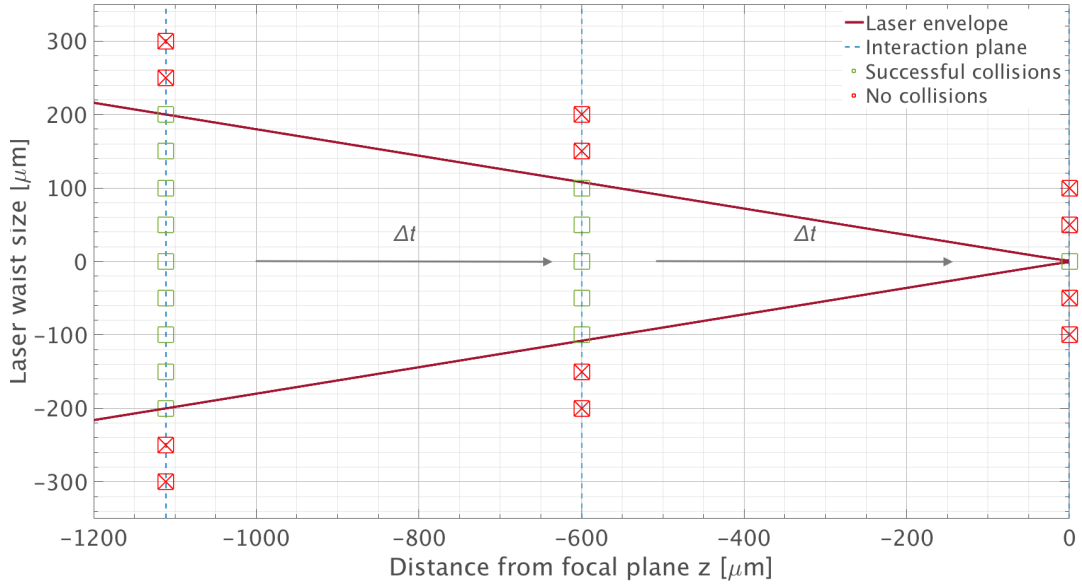


Figure 5.8: Sketch of a (2D) laser raster scan. The laser waist size (red) is shown as a function of the distance from the focal plane, $z = 0$. The laser is translated in space such that electron beam interacts with a different part of the laser pulse (boxes). If the electron beam intersects the laser pulse, energetic radiation from inverse Compton scattering is emitted (green boxes). If the laser pulse and the electron miss each other, no radiation is produced (red boxes with crosses). By adjusting the relative time of arrival between the driving laser pulse and the scattering beam, the plane of the interaction is shifted (dashed blue lines) and the procedure can be repeated.

than the laser beam. Even though the laser pulse is translated and the electron remains approximately fixed, here the electron beam effectively acts as the probe and diagnoses the laser beam at the interaction plane, inversely to the laser wire.

Laser raster scan as tool to achieving high-intensity interactions

This spatial correlation technique determines the size of the laser beam at the interaction, its centre and, knowing the focusing geometry, the plane of the interaction. As a result, we can not only characterise the properties of the beam at the interaction, but we can use this information to change the relative arrival time of both laser pulses to shift the interaction towards a more intense region of the focusing beam. The procedure can then be repeated at the new interaction plane to confirm that the laser pulse is indeed smaller and more intense (see Figure 5.8). When the beam size of the scattering laser pulse and the electron bunch become comparable, we also expect a particularly high gamma-ray yield due to the high laser intensity but also more frequently 'missed' shots, when the laser pulse and the electron beam pass by each other as the pointing fluctuations are comparable with their sizes.

If we perform this raster scan at a high resolution (small step size) in both transverse

dimensions, at various focal planes (multi-dimensional raster scan) and with multiple shots at each position, we immediately see that this requires a large number of shots in total. A route to reducing the number of required shots to identify the ideal high-intensity conditions is using a Bayesian inference model and to automate this process. Bayesian inference models can reduce the number of data points required for optimisation in a multi-dimension scan [277, 278]. For any interaction far away from the focus, i.e. $z \gg z_R$, the key optimisation quantity would be the gamma ray yield measured with the profile screen, potentially also correlated with the electron beam charge and energy if these quantities fluctuate strongly (see Chapter 6). Closer to the focus, we would have to consider the number of successful collisions as well as part of the algorithm. Machine learning has been used, for instance, in different forms for optimisation and alignment procedures in conventional [279] and plasma-based accelerators [280], whereas automated control of laser pulses is widely used in laser laboratories for alignment and optimisation purposes. The advantage of this method for future measurements would be that it would facilitate taking large amounts of data (precision measurement), which is required to generate a large confidence and to outweigh statistical fluctuations of the beam. The algorithm ideally also corrects drifts in alignment and timing automatically.

Unfortunately, the final step of shifting the interaction plane to the high-intensity focus of the scattering laser pulse was not possible in the experiment. A lens in the beam expander telescope of the scattering beam broke during this dataset and we were not able to continue the campaign with dual-beam shots and potential high-intensity collisions. Nonetheless, we were able to show consistent overlap in space and time and a good control over the spatio-temporal alignment. The laser raster scan promises to become a useful technique to estimate the laser intensity at the interaction plane and to achieve high-intensity collisions in a future measurement of radiation reaction systematically.

5.6 Gamma spectra from inverse Compton scattering

A photon of energy ϵ_{ph} that is scattered off a relativistic electron is Doppler up-shifted due to the relativistic Lorentz boost. The energy of the scattered photon, ϵ_X, is given by [98]:

$$\epsilon_X \approx \epsilon_{ph} \times \frac{2(1-\cos\theta)\gamma^2}{1 + a_0^2/2 + \gamma^2\theta_0^2}, \tag{5.6.1}$$

where θ is the angle between the electron and the incoming photon, a_0 is the normalised vector potential and θ_0 is the observer angle relative to the propagation direction of the electron.

The electron beams shown in Section 5.4 were collided with a laser pulse at an intensity of $a_0 \sim 0.28$, as estimated in the previous section (Section 5.5). As $a_0 < 1$, we can ignore at

first order the contribution of higher harmonic radiation and only consider the fundamental harmonic from linear inverse Compton scattering [98]. Since $a_0^2 \ll 1$, we can also ignore the term $a_0^2/2$ in the denominator, which accounts for red-shifting of the radiation when the longitudinal component of the electron motion becomes significant (see Section 2.1.3 for 'figure-of-eight motion').

GEMINI has a wavelength of $(800 \pm 15)\,\mathrm{nm}$ [281], with a corresponding photon energy, $\epsilon_{ph} = (1.55 \pm 0.03)\,\mathrm{eV}$. The bandwidth of the laser introduces a spread in the photon energy of $\Delta\epsilon_{ph} \sim 0.06\,\mathrm{eV}$ or $\Delta\epsilon_{ph}/\epsilon_{ph} < 4\%$, which we will ignore in the following.

For a beam focused by an $f/2$ optic, the angle between the outer rays and the central axis, $\Delta\theta$, is up to 14.48 degrees which corresponds to < 2 percent spread in energy. Since the electron beam ($w_0 \sim$ µm) only interacts with a small fraction of the full beam with radius r, i.e. $\pi w_0^2/\pi r^2 \ll 1$, the rays in the interaction region are approximately collinear and this contribution can be ignored as well. A systematic shift of the radiation by 3 percent due to the relative pointing of the electron beam and the laser pulse within this solid angle is also negligible for our considerations ($\Delta\epsilon_X < 1\,\mathrm{MeV}$ at $30\,\mathrm{MeV}$).

In linear ICS, scattered photons will be emitted in a narrow cone of divergence $\sim 1/\gamma \ll 1$ [80]. The observation angle, on the other hand, introduces a strong position-dependent modulation of the emitted energy within the emission cone as it is paired with the Lorentz factor, γ, in $(\gamma\theta_0)^2$.

Here, the electron beams are in most cases confined to a divergence cone of few milliradians. For a beam of divergence 4 mrad, the difference introduced by the electron angles in the $\cos\theta$ term, assuming a collimated light source, is less than 0.001%, which means that we can ignore a broadening of the spectrum from electron angles as well. The divergence is typically larger than the emission cone $1/\gamma$, such that the total emission loses its strong correlation of position and energy, but the modulation of all emission cones overlap and merge. As a result, we assume that the emission spectrum is on average homogeneously distributed over the profile, maybe with exception of the borders.

Lastly, for $\gamma \sim 2500$ ($\epsilon \sim 1.3\,\mathrm{GeV}$) and $a_0 = 0.3$

$$\psi = \gamma^2 a_0 \frac{2 r_e \omega}{3c} \ll 1, \tag{5.6.2}$$

which indicates that radiation reaction effects are negligible and the interaction with the laser pulse does not perturb the electron beam significantly as a whole [81, 133]. Combining these assumptions and considering a head-on collision ($\theta = 180°$), Equation (5.6.1) above simplifies to

$$\boxed{\epsilon_X \approx \frac{4\gamma^2 \epsilon_{ph}}{1 + (\gamma\theta_0)^2},} \tag{5.6.3}$$

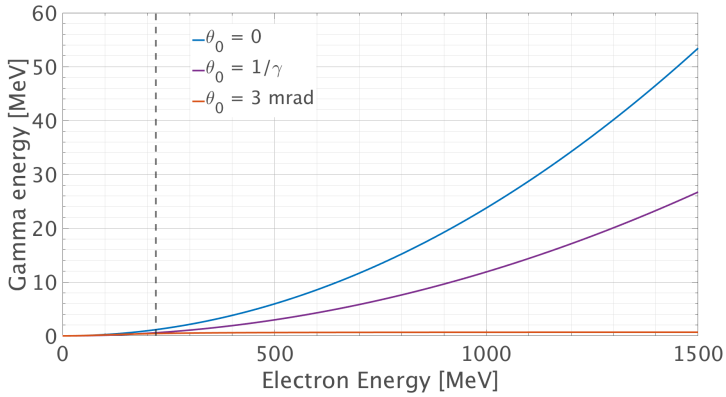


Figure 5.9: Gamma energy in MeV produced by scattering a 1.55 eV photon with a relativistic electron beam in a head-on collision ($\theta = \pi$) as a function of electron energy in MeV for $\theta_0 = 0$ (blue), $1/\gamma$ (purple) and 3 mrad (orange). The lines are calculated using Equation (5.6.3), which ignores energy broadening or reductions due to redshifting, the laser bandwidth, and relative angles between the electron beam and laser pulse. The dashed line indicates the low-energy cut-off in the electron spectrometer at 220 MeV.

with a maximum energy of

$$\boxed{\epsilon_{X,max} \approx 4\gamma^2 \epsilon_{ph}.} \tag{5.6.4}$$

Based on the simplified Equation (5.6.4) above, we then obtain a quadratic one-to-one mapping of the electron energy to a corresponding maximum gamma-ray energy (see Figure 5.9 (blue)). Overall, we will integrate Equation (5.6.3) over the observation angle, θ_0, to obtain the full emission spectrum.

Since the properties of the electron beam vary strongly in this experiment, we also expect the spectrum of the radiation produced from linear ICS to reflect this behaviour. Here the cross section is independent of the electron energy [81], such that the spectral shape of the electron beam is to some extent preserved in the gamma spectrum. Figure 5.10 shows two examples of electron spectra (top) and the corresponding gamma-ray spectra calculated with Equation 5.6.3 (bottom). The first electron beam is spectrally very broad (red) with significant spectral intensity spread from below the measurement threshold of 220 MeV up to 1200 MeV, resulting in a gamma-ray spectrum spanning few to 35 MeV with a peak around 8 MeV. The other beam (blue) is strongly peaked at just under 1.2 GeV with narrow energy spread of $< 10\%$, which has the potential to be converted into a gamma-ray spectrum peaked at 31 MeV. The dashed and dottes lines in Figure 5.10 (bottom) indicate that the accuracy of the calculated gamma spectra would be improved by including additional broadening effects. However, the differences are small and the leading order effect remains the $(\gamma_0\theta)^2$ term in Equation (5.6.3). We expect significant deviations due to redshifting and higher harmonic radiation once $a_0 \to 1$.

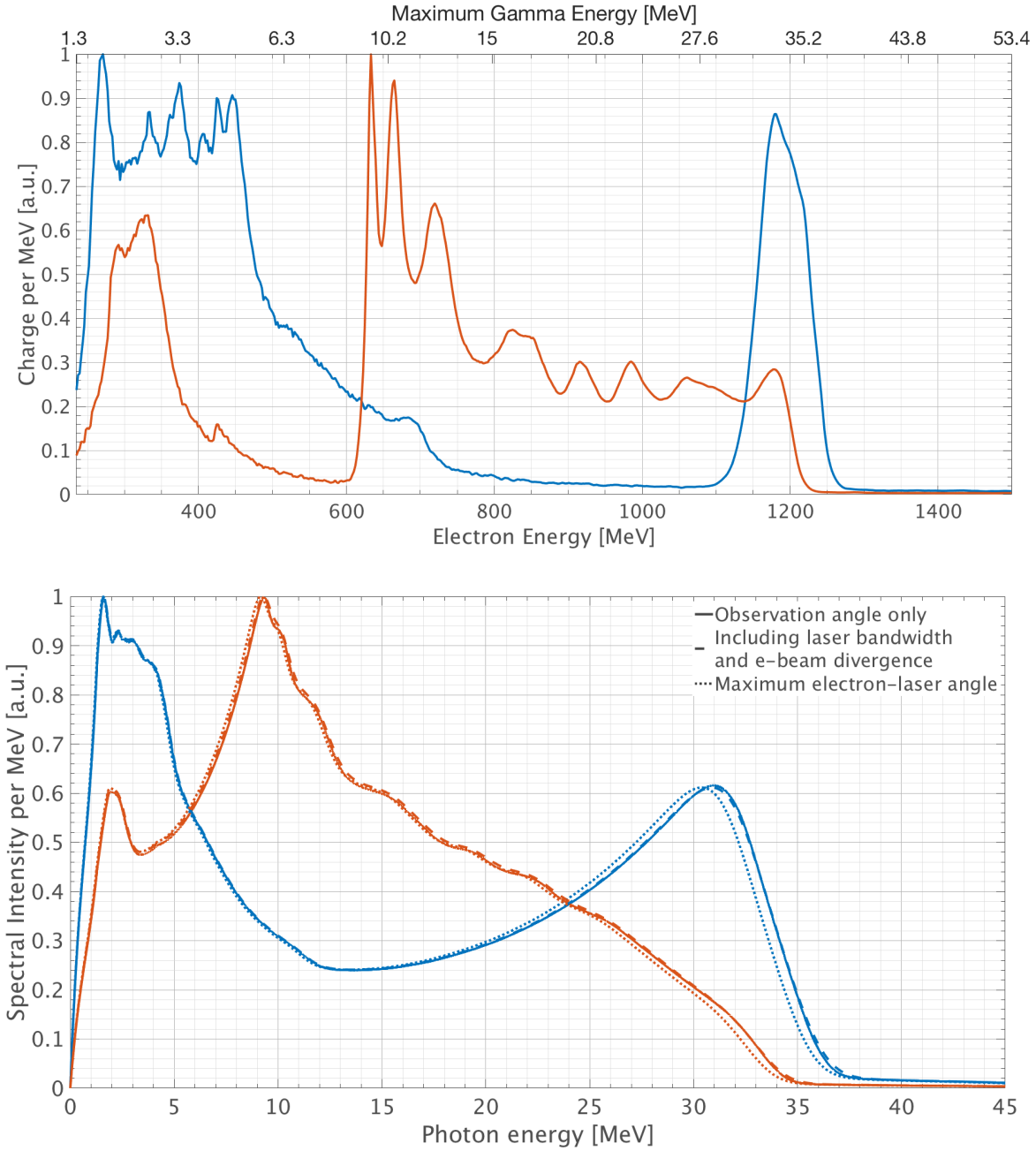


Figure 5.10: Top: Example of two electron spectra integrated in the non-dispersion axis. The y-axis indicates the charge per MeV and the x-axis the electron energy in MeV. The spectra are normalised to their maximum y-value. The maximum gamma-ray energies corresponding to the electron energies, calculated using Equation (5.6.4)*, are indicated in a second non-linear x-axis on the top. Bottom: Spectral intensity of ICS spectra per MeV as a function of the photon energy corresponding to electron spectra shown above (same line colours). The gamma spectra take into account the broadening due to the* $(\gamma_0\theta)^2$ *term in Equation* (5.6.3) *(solid), and the finite laser bandwidth and the divergence of the electron beam (dashed). The dotted lines show the gamma spectra for an interaction at the maximum angle between the laser rays and the electron beam,* $\theta = 180° \pm 14.48°$*, and include all previous broadening terms. We assumed* $a_0 \ll 1$ *for all spectra.*

5.7 Number of scattered photons

Based on the conditions in the experiment and the inferred intensity at the interaction (see Section 5.5), the interaction is accurately described by linear ICS in its classical Thomson limit (see Section 2.2.2). The total number of scattered photons or the number of gamma-rays, N_X, produced in the interaction of the laser pulse with an electron beam of size w_0 is then given by [81]

$$\boxed{N_X = \frac{\sigma_T}{\pi w_0^2} N_{ph} N_e,} \tag{5.7.1}$$

where $\sigma_T = 6.65 \times 10^{-29}\,\mathrm{m}^2$ is the Thomson scattering cross-section, N_e the number of electrons, and N_{ph} is the number of photons in the same area. In this limit, the cross-section and the total number of produced photons are independent of the electron and photon energy.

Since the laser beam is much larger than the electron bunch, we assume that the entire electron bunch passes through the laser pulse and that all electrons encounter the same photon density, hence also contribute equally to the total emitted radiation as the cross-section is constant across the energies. As a result, the number of electrons, N_e, is obtained by dividing the beam charge measured on-shot, Q, by the electron charge, i.e. $N_e = Q/e$.

In order to determine the number of photons, N_{ph}, sharing the interaction volume, we will make the following assumptions. The Rayleigh length, z_R, of an $f/2$ beam is approximately $2.5\lambda f_{\#}^2 \approx 8\,\mu\mathrm{m}$. At a diameter of $400 \pm 100\,\mu\mathrm{m}$, the beam is at $\sim 1100 \pm 275\mu\mathrm{m}$ distance from the focal plane, which corresponds to $> 100 z_R$, so that the laser beam is in its near field at this plane. As discussed before, we ignore relative angles between the laser and the electron beam. As the duration of the laser pulse and the electron bunch [77] are short, the duration over which the interaction occurs is also brief. As a result, we can ignore focusing effects and the electrons encounter a static photon field. The number of photons overlapping with an electron beam of transverse area πw_0^2, N_{ph}, is given by the laser energy in this area divided by the energy of a single photon, ϵ_{ph}. Assuming a homogeneous flat-top laser profile, with exception of the hole in the OAP, the energy in this area is simply given by the fraction this area holds relative to the total beam area multiplied by the total energy in the laser pulse, ϵ_J:

$$N_{ph} = \left[\frac{\epsilon_J}{\epsilon_{ph}} \frac{\pi w_0^2}{\pi r^2} \right], \tag{5.7.2}$$

where r is the full radius of the laser beam at the plane of the interaction. Note that ϵ_J is the total energy in the laser pulse measured on-shot. This neglects the reduction due to

the hole in the OAP, since this does not affect the local photon density of the laser pulse far away from the focal plane and sufficiently far away from the hole in the beam. We then obtain for the number of scattered photons, N_X:

$$N_X = \frac{\sigma_T}{\pi w_0^2}\left[\frac{\epsilon_J}{\epsilon_{ph}}\frac{\pi w_0^2}{\pi r^2}\right]\left[\frac{Q}{e}\right], \tag{5.7.3}$$
$$= \frac{\sigma_T}{\pi r^2}\left[\frac{\epsilon_J}{\epsilon_{ph}}\right]\left[\frac{Q}{e}\right].$$

The region of the interaction defined by the electron beam size, w_0, cancels out as the photon density is in this approximation constant across any region and only depends on the size of the full laser beam, r, and its total energy content, ϵ_J. We can then write in useful units:

$$\boxed{N_X = 5.32 \times 10^{10} \times \epsilon_J[J] \times Q[100pC] \times r[\mu m]^{-2}.} \tag{5.7.4}$$

For the conditions measured or inferred in this experiment ($\epsilon_J = 9.73 \pm 0.15$, $Q = 239 \pm 92\,\mathrm{pC}$ and $r = 200\,\mu\mathrm{m}$), this equation estimates that on average $(3.1 \pm 1.2) \times 10^7$ photons are scattered in total, $(75 \pm 8)\%$ of which at an energy $\epsilon_X > 1\,\mathrm{MeV}$. This is of comparable order of magnitude as reported for similar Compton experiments and bright betatron sources [282, 283], where we can assume that the radiation has a pulse duration and source size comparable to the electron beam.

However, considering the experimental parameters, it becomes clear that a linear Compton source could be achieved in a much more economical way by scaling down the energy and the beam size at the interaction, whilst still preserving a permanent overlap within the shot-to-shot fluctuations of the laser and the accelerator. Assuming a fixed charge in the electron beam, the number of scattered photons then only depends on the ratio of the laser energy and the beam size $\propto \epsilon_J/r^2$. By reducing the beam radius from 200 µm to 25 µm, a factor of 8, the corresponding energy in the scattering beam can be reduced by a factor of 64, to about 150 mJ, to produce the same number of photons as before. Using an $f/2$ OAP as in this case, the plane of the interaction would be more than 10 Rayleigh lengths, z_R, away from the focal plane and which is still in the near-field of the laser, where the profile is flat and smooth, such that any changes in response would predominantly reflect the properties of the electron beam.

5.8 Energy-dependent detector response

In the previous sections, we calculated how an electron spectrum translates via linear inverse Compton scattering (or relativistic Thomson scattering) into a gamma spectrum, and estimated the number of high-energy photons produced in such an interaction, finding

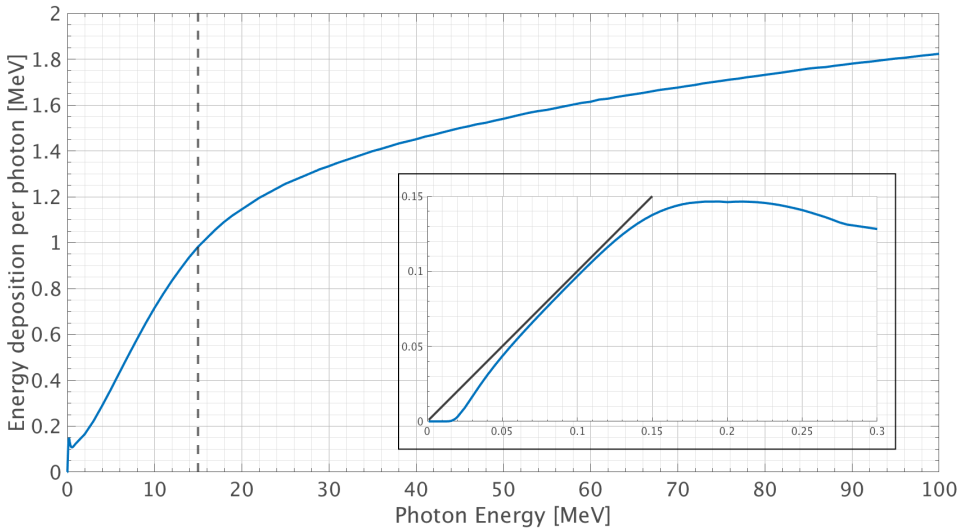


Figure 5.11: Average energy deposition per photon in the gamma profile stack simulated in GEANT4 as a function of the incident photon energy in MeV. The grey dashed line at 15 MeV indicates roughly the separation between two regimes, in the first of which the energy deposition increases more per increase in incoming photon energy than in the second. The inset enlarges low photon energies up to 300 keV. The energy of the incoming photons is almost completely absorbed, i.e. $\epsilon_{dep} = \epsilon_X$ (black line), for 50 to 150 keV.

that the cross-section in this regime is independent of the electron or gamma-ray energy, respectively.

However, whilst the cross-section for an interaction is independent of energy and, as a result, also the number of emitted photons per electron and energy band, the contribution to the yield measured on the gamma profile detector will not necessarily be constant across different energies. The gamma profile detector used in this experiment is not a calorimeter and only absorbs a fraction of the total radiation passing through it. Since there is a range of mechanisms coming into play at the tens of MeV photon energy range, the energy deposition in the profile screen was simulated using GEANT4 [262].

Figure 5.11 shows the simulated average energy deposited by one individual photon incident on the profile stack as a function of the photon energy, ϵ_γ. The energy deposition increases steadily between $\epsilon_\gamma = 1$ and 15 MeV, before slowing down (grey dashed line) and increasing at a slower rate over the remaining simulated energy range. This behaviour is important as the corresponding electron energies coincide with this energy band. It has to be considered particularly when attempting to measure absolute quantities such as the total number of photons. The energy-dependency shown in Figure 5.11 contrasts the almost flat energy deposition of relativistic electron beams in Lanex [284].

Figure 5.12 shows an example electron spectrum and how different parts of the spectrum contribute in relative terms to the total energy deposition. The response of the detector is here dominated by the high energy peak, whilst the radiation from lower energy electrons

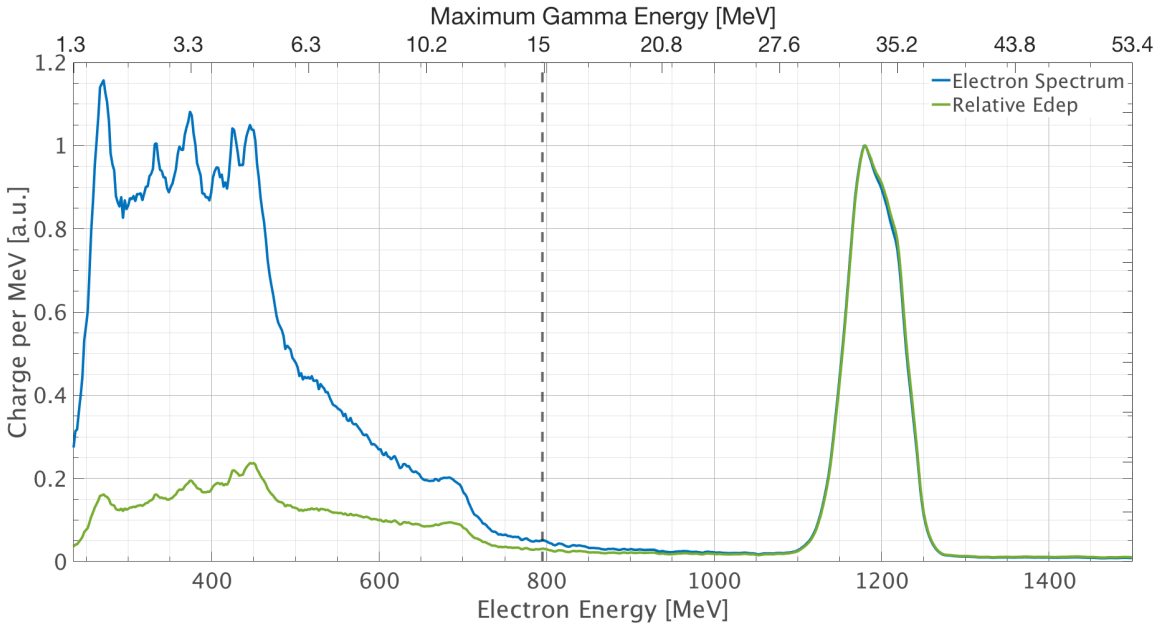


Figure 5.12: Example electron spectrum and weighted contribution to the total yield on the gamma profile screen. The y-axis shows the charge per MeV as function of the electron energy (x-axis). The x-axis on the top indicates the corresponding maximum gamma-ray energy from linear ICS. The blue curve shows the spectrum as before. In the green curve, the y-value is weighted by the energy deposited per photon. Both curves have been normalised such that the peak value at 1200 MeV takes the value 1. The grey dashed line indicates the point at which the energy deposition per photon energy slows down (see Figure 5.11).

is suppressed in relative terms. In this experiment, the response of a profile screen then mainly reflects the properties of the high-energy tail of the beam, in contrast to an electron beam profile diagnostic using a Lanex screen. In radiation reaction studies, the highest energies are of particular interest as they are expected to experience the strongest interaction and largest energy loss, such that this property might be of advantage in this scenario.

Using the simulated result as a lookup-table for the energy deposition, $\epsilon_{dep}(\gamma)$, and relating the photon energy to the electron energy, the total energy deposition, $\mathcal{E}_{dep}$, can be calculated for a given electron spectrum, $\mathrm{d}N_e/\mathrm{d}\gamma$, as follows:

$$\boxed{\mathcal{E}_{dep} = \int \epsilon_{dep}(\gamma) \frac{\sigma_T}{\pi w_0^2} N_{ph} \frac{\mathrm{d}N_e}{\mathrm{d}\gamma} \mathrm{d}\gamma \approx \langle \epsilon_{dep}(\gamma) \rangle N_X .} \tag{5.8.1}$$

The energy-dependent response of the detector becomes in particular important when the electron and gamma spectrum cover a wide energy range, as is the case here. More energetic radiation contributes in relative terms more to the response of the profile.

The simulated response of the detector can also be used to calibrate the gamma profile screen with a radioactive source. Here, we used caesium-137 which emits gamma-rays

predominantly at 661.7 keV photon energy [285], for which the GEANT4 simulation estimates an energy deposition of ~ 90 keV per photon. The response measured on the profile screen during the exposure with the radioactive source then gives a conversion factor from the total pixel counts on the CCD camera, S_γ, to energy deposition in MeV, $\mathcal{E}_{dep,\gamma}$, i.e. an absolute energy calibration:

$$\mathcal{E}_{dep,\gamma} = S_\gamma \times c_{S\to\mathcal{E}}, \tag{5.8.2}$$

where $c_{S\to\mathcal{E}}$ is in units of [MeV/pixel counts] and incorporates the conversion efficiency of energy to light and the collection efficiency of the detector setup.

In turn, using Equation (5.8.1) in conjunction with this calibration, we can then determine the number of photons emitted on-shot, $N_{X,\gamma}$, by measuring the energy deposited in the gamma profile screen, $\mathcal{E}_{dep,\gamma}$, and the on-shot electron spectrum, $\mathrm{d}N_e/\mathrm{d}\gamma$. Since the energy deposition is proportional to the number of photons, we can compare the initial guess, $N_{X,0}$ (see Equation (5.7.4)), with the experimentally measured quantity, $N_{X,\gamma}$:

$$\boxed{N_{X,\gamma} \approx N_{X,0}\frac{\mathcal{E}_{dep,\gamma}}{\mathcal{E}_{dep,0}},} \tag{5.8.3}$$

where $\mathcal{E}_{dep,0}$ is the energy deposited by $N_{X,0}$ photons. $\mathcal{E}_{dep,0}$ and $\mathcal{E}_{dep,\gamma}$ rely on the same on-shot electron spectrum, beam charge, and its relation to the gamma spectrum and energy deposition. Within these assumptions, any difference in the estimated photon numbers is then related to errors in the absolute calibration, $c_{S\to\mathcal{E}}$, or the photon density N_{ph}. The first forms to some extent a systematic pre-factor that is constant on all shots, whilst the photon density is expected to fluctuate from shot to shot.

We will now compare these quantities in the dataset discussed previously. The analysed dataset consists of two parts, here simply referred to as A and B: B includes the laser raster scan presented in Section 5.5 with an estimated average intensity of $a_0 \sim 0.28$ at a laser beam radius of $r = 200 \pm 50\,\mu$m. In dataset A, the beam size was not determined through the raster scan technique and the exact beam diameter is for now unknown, but based on the consistency of laser-electron interactions, we infer that the laser beam is again much larger than the electron bunch, i.e. $r \gg w_0$.

Figure 5.13 shows the number of photons estimated from the gamma profile measurement, $N_{X,\gamma}$, as a function of $N_{X,0}$ for A (blue) and B (purple), using the on-shot measurement of the laser energy and the on-shot spectrum of the electron beam. The solid lines show the linear fits to the data of the respective dataset, the green line indicates where $N_{X,\gamma} = N_{X,0}$. The linear fit for B (purple) matches the green line closely, whereas $N_{X,\gamma}$ in A (blue) is systematically higher than $N_{X,0}$. In addition, the values in A are more

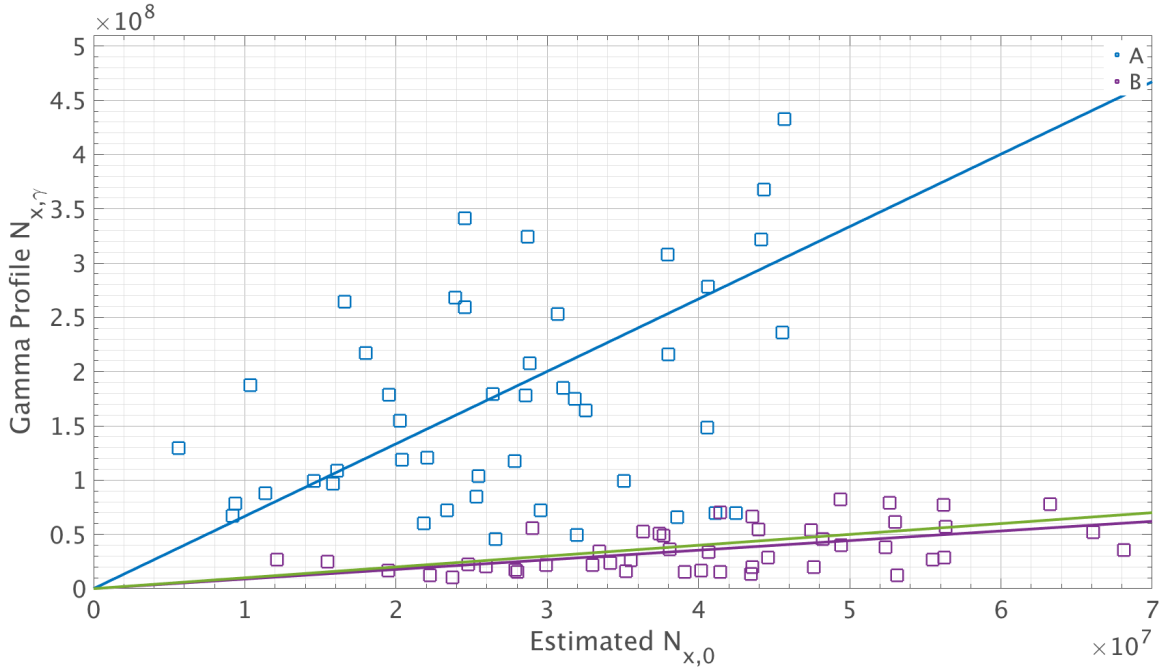


Figure 5.13: Estimated number of scattered photons based on the gamma profile measurement (see Equation (5.8.3)*),* $N_{X,\gamma}$ *as a function of the yield estimated by Equation* (5.7.4)*,* $N_{X,0}$*, for* $r = 200 \pm 50\,\mu\text{m}$*. Both equations rely on the electron spectrum measured on-shot. Dataset* B *refers to the laser raster scan data, whereas* A *has been taken without definitive beam size measurement. The green line shows* $N_{X,\gamma} = N_{X,0}$*.*

scattered than in B, i.e. the shot-to-shot variations are stronger. This is also reflected in their linear correlation coefficients of 0.3 and 0.5, respectively. The systematic difference between A and B indicates different experimental conditions.

The histogram in Figure 5.14 shows the ratio of $N_{X,\gamma}$ to the predicted value (green line), $N_{X,0}$, i.e. $N_{X,\gamma}/N_{X,0}$, following the same colour scheme as before. The average ratio is 0.92 ± 0.47 for the data from the laser raster scan (B), where the error is the statistical error and not the measurement error of the technique. The mean value of $N_{X,\gamma}$ is within $< 10\%$ in good agreement with $N_{X,0}$. The estimated number of photons for this part of the dataset was $(4.08 \pm 1.03) \times 10^7$ photons, with $(3.65 \pm 2.1) \times 10^7$ photons measured on the gamma profile screen. The ratio for A is higher at an average of 7.74 ± 5.59 with a large statistical variance, and single events even above a ratio of 10. The estimated number of photons, $N_{X,0}$, was $2.75 \pm 1.06 \times 10^7$ photons compared to $1.93 \pm 1.49 \times 10^8$ photons measured on the gamma profile screen. The physical implications of this discrepancy are investigated in the following section.

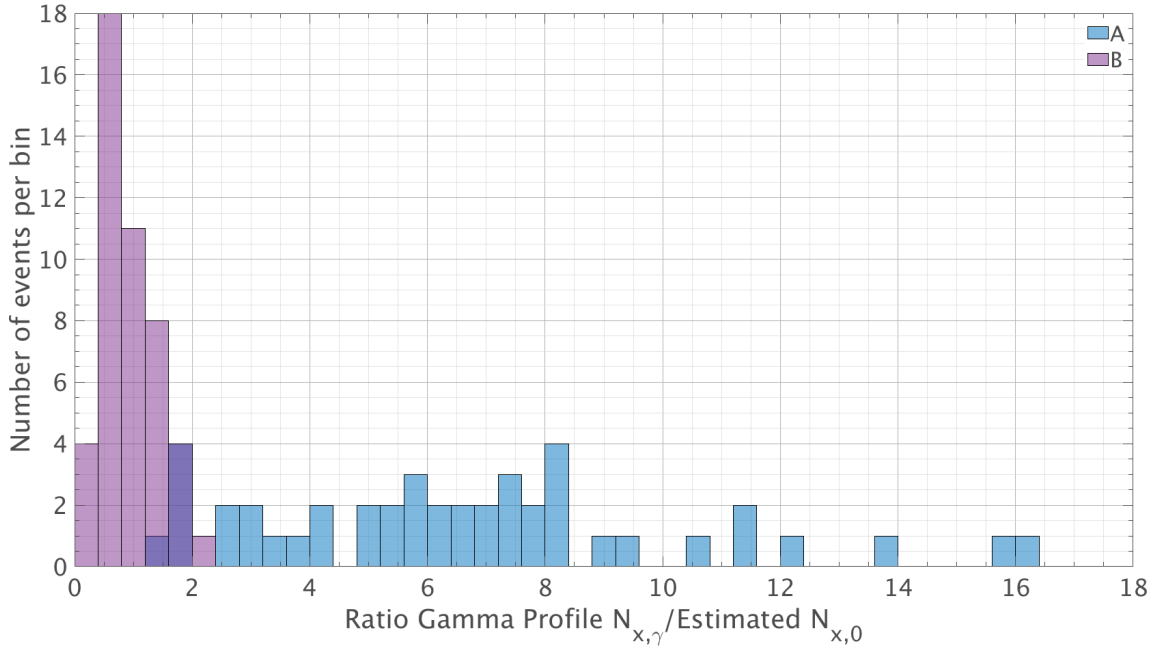


Figure 5.14: Histogram of the ratios $N_{X,\gamma}/N_{X,0}$ for the datasets A *(blue) and* B *(purple).* B *includes the laser raster scan that was discussed in Section 5.5.*

5.9 Estimate of laser beam size from photon yield

If we now consider the ratio of the energy depositions, $\mathcal{E}_{dep,\gamma}/\mathcal{E}_{dep,0}$, again and substitute for N_{ph} from Equation (5.7.2), we realise that the ratio is directly related to the beam radius of the laser pulse at the interaction plane:

$$\frac{\mathcal{E}_{dep,\gamma}}{\mathcal{E}_{dep,0}} = \frac{\int \epsilon_{dep}(\gamma)\frac{\sigma_T}{\pi w_{0,\gamma}^2}N_{ph,\gamma}\frac{\mathrm{d}N_e}{\mathrm{d}\gamma}\mathrm{d}\gamma}{\int \epsilon_{dep}(\gamma)\frac{\sigma_T}{\pi w_{0,0}^2}N_{ph,0}\frac{\mathrm{d}N_e}{\mathrm{d}\gamma}\mathrm{d}\gamma} = \frac{N_{ph,\gamma}/w_{0,\gamma}^2}{N_{ph,0}/w_{0,0}^2} = \frac{\epsilon_J/\left(\epsilon_{ph}r_\gamma^2\right)}{\epsilon_J/\left(\epsilon_{ph}r_0^2\right)} = \frac{r_0^2}{r_\gamma^2}, \tag{5.9.1}$$

where the subscripts 0 and γ for N_{ph}, w_0, r and $\mathcal{E}_{dep}$ indicate again the quantities using either the initial estimate from the raster scan (0) or the yield on the gamma (γ) profile screen. Most terms simply cancel out as we used the same on-shot electron spectrum, $\mathrm{d}N_e/\mathrm{d}\gamma$, and on-shot measurement of the laser energy, ϵ_J, for both values of $\mathcal{E}_{dep}$.

Since the results in the previous section indicated that the absolute calibration of the gamma profile screen is accurate, we can use the ratio of the estimated scattered photons introduced in the previous section to infer the size of the scattering laser pulse at the interaction plane:

$$\boxed{r_\gamma = \sqrt{\frac{\mathcal{E}_{dep,0}}{\mathcal{E}_{dep,\gamma}}}r_0 = \sqrt{\frac{N_{X,0}}{N_{X,\gamma}}}r_0,} \tag{5.9.2}$$

where $N_{X,0}$ is the number of scattered photons at radius r_0 estimated initially, and $N_{X,\gamma}$ is the number of photons inferred from the gamma profile measurement. The corresponding

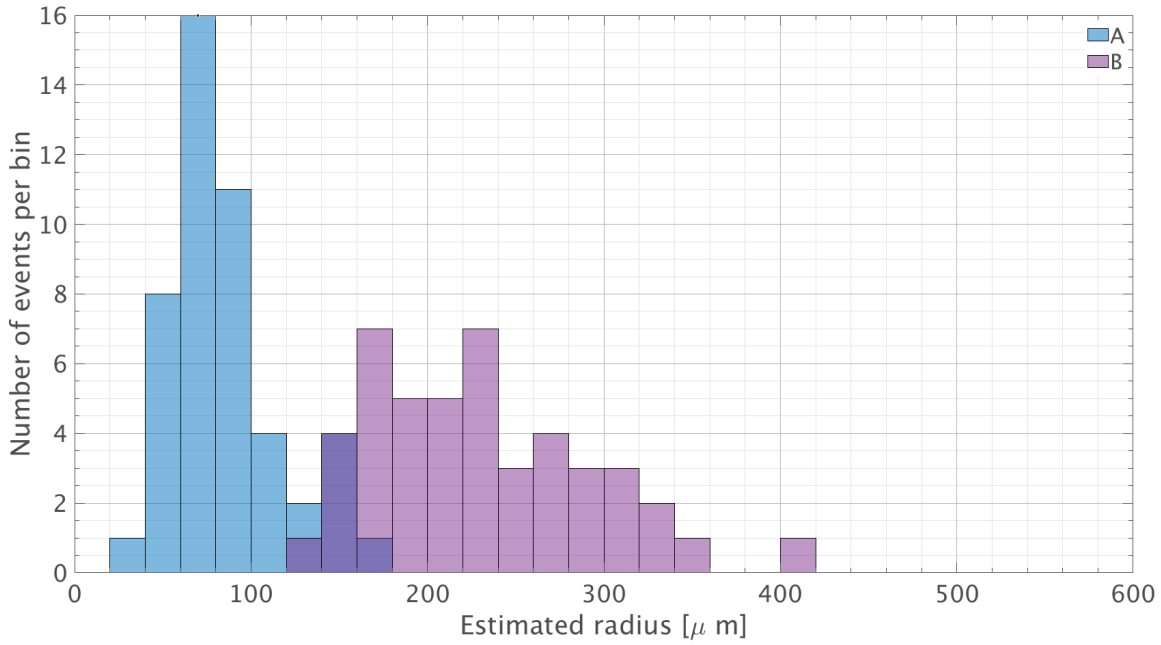


Figure 5.15: Histograms of estimated beam radii of the laser pulse at the interaction based on the gamma profile measurement using Equation (5.9.2) *for both parts of the dataset. Dataset* B *refers to the laser raster scan that was discussed in Section 5.5.*

laser intensity in turn is then approximately

$$a_0 \approx 0.85\lambda[\mu m]\sqrt{I[10^{18}W/cm^2]} \approx 0.286 \times \sqrt{\epsilon[10J]}(r[200\mu m])^{-1}, \tag{5.9.3}$$

where we assumed a pulse duration $\tau = 45\,\text{fs}$. This then reads in terms of the ratio of the estimated number of scattered photons

$$\boxed{a_0 \approx 0.286 \times \sqrt{\epsilon_J[10J]\frac{N_{X,\gamma}}{N_{X,0}}\frac{1}{r_0[200\mu m]}}.} \tag{5.9.4}$$

The histograms in Figures 5.15 and 5.16 show the inferred beam radius and laser intensity at the interaction for the raster scan in dataset B (purple) and dataset A (blue) using the ratios from Figure 5.14.

In the previous section, we found good agreement between $N_{X,0}$ and $N_{X,\gamma}$ for dataset B (see Figure 5.14). Similarly, the corresponding estimates for the beam radius and intensity agree well within errors at $r = 230 \pm 63\,\mu\text{m}$ and $a_0 = 0.28 \pm 0.07$ with $r = 200 \pm 50\,\mu\text{m}$ and $a_0 = 0.28 \pm 0.04$ estimated by the raster scan.

We can now estimate the relative beam diameter in the dataset A that was not evaluated with the raster scan. The inferred number of photons in dataset A is systematically higher than in B, which indicates that the beam size is here consistently smaller by a factor $\sim \sqrt{7.74} \approx 2.78$. Equation (5.9.2) suggests a radius of $r \approx 75 \pm 32\,\mu\text{m}$ which corresponds

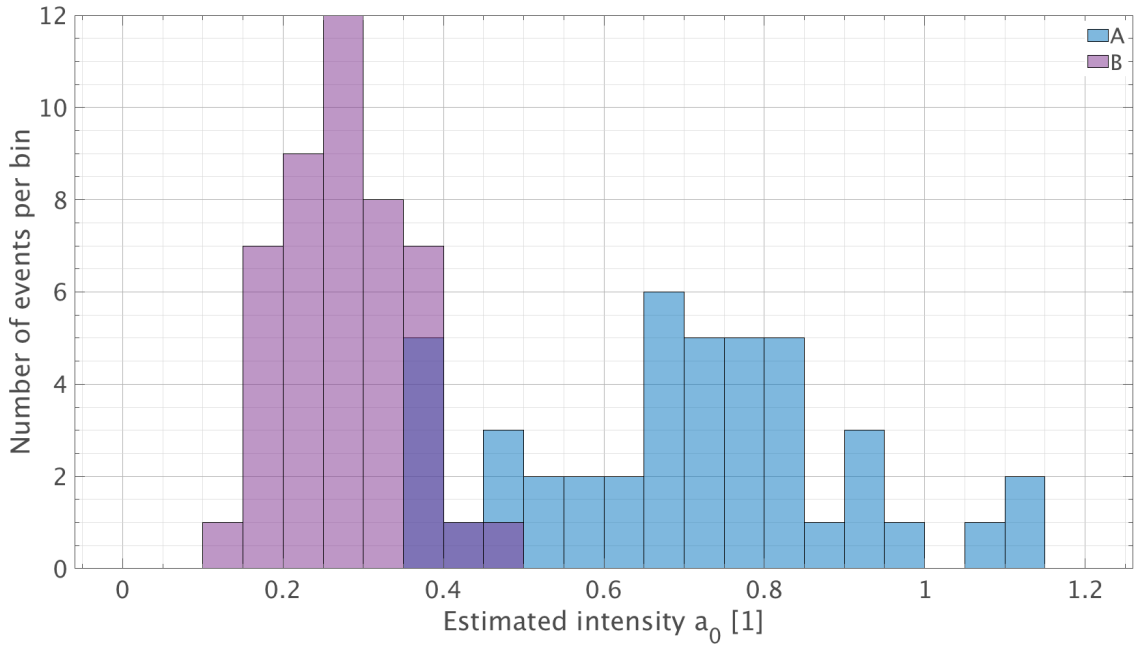


Figure 5.16: Histograms of estimated intensities of the laser pulse at the interaction based on the gamma profile measurement using Equation (5.9.4) *for both parts of the dataset. Dataset* B *refers to the laser raster scan.*

to an average intensity of $a_0 \approx 0.74 \pm 0.26$ (see Figure 5.16), where the error bars are the statistical error assuming a normal distribution. The values at the higher end reach or surpass $a_0 \sim 1$, where nonlinear affects like higher harmonics and redshifting become significant (see Section 2.2.3 and [98]). In this weakly nonlinear regime, our assumptions regarding the spectral shape of the gamma emission break down and the estimate of the beam size based on the deposited energy becomes less reliable, although it can be used to identify the onset of more intense interactions. Other work demonstrated that the production of higher harmonic radiation and their relative contribution to the spectrum can be used to estimate the intensity in the weakly nonlinear regime [171], but a highly resolved spectral measurement is more challenging in the MeV photon energy range.

This technique seems to be a promising single-shot diagnostic to estimate the laser intensity and beam diameter at the interaction point at lower intensities $a_0 < 1$, and will become particularly useful in combination with the laser raster scan presented in Section 5.5 applied to radiation reaction studies. Here in both datasets either the beam position (raster scan) or the relative delay was varied, with the second dataset being close to the onset of weakly nonlinear effects where some of the assumptions break down. In a future measurement at fixed conditions and strictly low intensities $a_0 < 1$, the varying deviation from a reference photon number, $N_{X,0}$ could be used to diagnose the fluctuations in the relative arrival time of the electron beam and the laser pulse. Combined with an on-shot

measurement of the relative fluctuations in the delay of both laser pulses, for instance using spectral interferometry [239], this could distinguish variations in the arrival time of the electron beam due to fluctuations in the relative delay of the laser pulses or due to changes in the injection point. Moreover, this technique could be refined by corroborating the absolute calibration of the gamma profile screen with a second radioactive source or different calibration method.

5.10 Spectral Retrieval

In the previous sections, we established the experimental conditions at the interaction, and identified how the electron spectra and the emitted radiation are related to each other (Section 5.6). In this section, we will confirm whether this relation holds in the experiment by retrieving the gamma spectrum for specific examples. Due to time constraints, we will not make use of the full capabilities of the detector and neglect alternating crystal rows (see Section 4.6.2). We will use the electron beam measured on-shot to estimate the gamma spectrum and fit the simulated response for this spectrum to the experimentally measured detector response [263]. Since the detector response will be dominated by the part of the electron spectrum containing the most charge, we will also fit the simulated response to the average electron energy.

Figure 5.17 shows three examples of electron spectra (centre) along with the gamma profile (left) and the gamma spectrometer response (right) measured on the same shot. The top two rows were taken from dataset B, the laser raster scan, and the example on the bottom is part of dataset A, which was estimated to include interactions at systematically higher intensities. The experimentally measured response of the gamma spectrometer, treated for bremsstrahlung background and varying crystal efficiencies etc. (see Section 4.6.2), is shown in blue as a function of the longitudinal crystal row (higher numbers are deeper in the stack). The yellow curve shows the simulated response to a monoenergetic spectrum fitting best to the experimental data, determined by a least square regression where the photon energy and amplitude were varied. The red curve shows the simulated response to the ICS gamma spectrum calculated from the electron beam measured on-shot.

The experimental and both simulated responses agree very well with each other in all three cases. Smaller deviations are within errors, e.g. increased yield in the experimental response for the second example (centre), and we need to analyse more gamma spectra to identify systematic differences. The inferred gamma energies are consistent with linear inverse Compton scattering and the assumptions we made about the conditions at the interaction. However, the fact that the simulated response to monoenergetic gamma rays and the ICS spectra are so similar indicates that this detector is not able to resolve the

shape of the spectrum but predominantly reflects its average energy. That makes sense as the response of the detector to the photons is in most parts not spectrally separated, e.g. as in an electron spectrometer. As a consequence, we can not *infer* the spectral shape from the response itself, but have to *assume* a spectral shape based on the experimental conditions and can only use this detector to determine its characteristic energy, e.g. a critical energy in a synchrotron spectrum or here the mean energy. The photon energies of the best fitting responses were (from top to bottom) 15.5 MeV, 11.4 MeV and 12.5 MeV, with average gamma energies calculated from the electron spectra of 15.9 MeV, 11 MeV and 12.1 MeV, respectively, which shows a good agreement between the results.

Future measurements of gamma radiation would greatly benefit from an increased sensitivity of the spectral retrieval, in particular to be able to infer the spectrum without imposing an assumed spectral shape. One proposed diagnostic that could achieve this in the future combines a scintillator stack as used here with a Compton or pair spectrometer [32, 264, 286] (see also Section 8.2.2). This would be, for instance, interesting for a detailed study of inverse Compton scattering at comparable intensities as the data presented here. The spectral shape is particularly sensitive to nonlinear effects in this intermediate regime between a purely linear and nonlinear treatment. As a consequence, this would be a useful tool to infer the intensity at the interaction to a high accuracy [287]. At very high intensities, on the other hand, it would allow to distinguish a classical synchrotron spectrum from the quantum synchrotron function (see Appendix G) and identify potential signs of stochastic quantum effects like energy straggling [136], which is of interest for radiation reaction studies [102] (see Section 2.3.3).

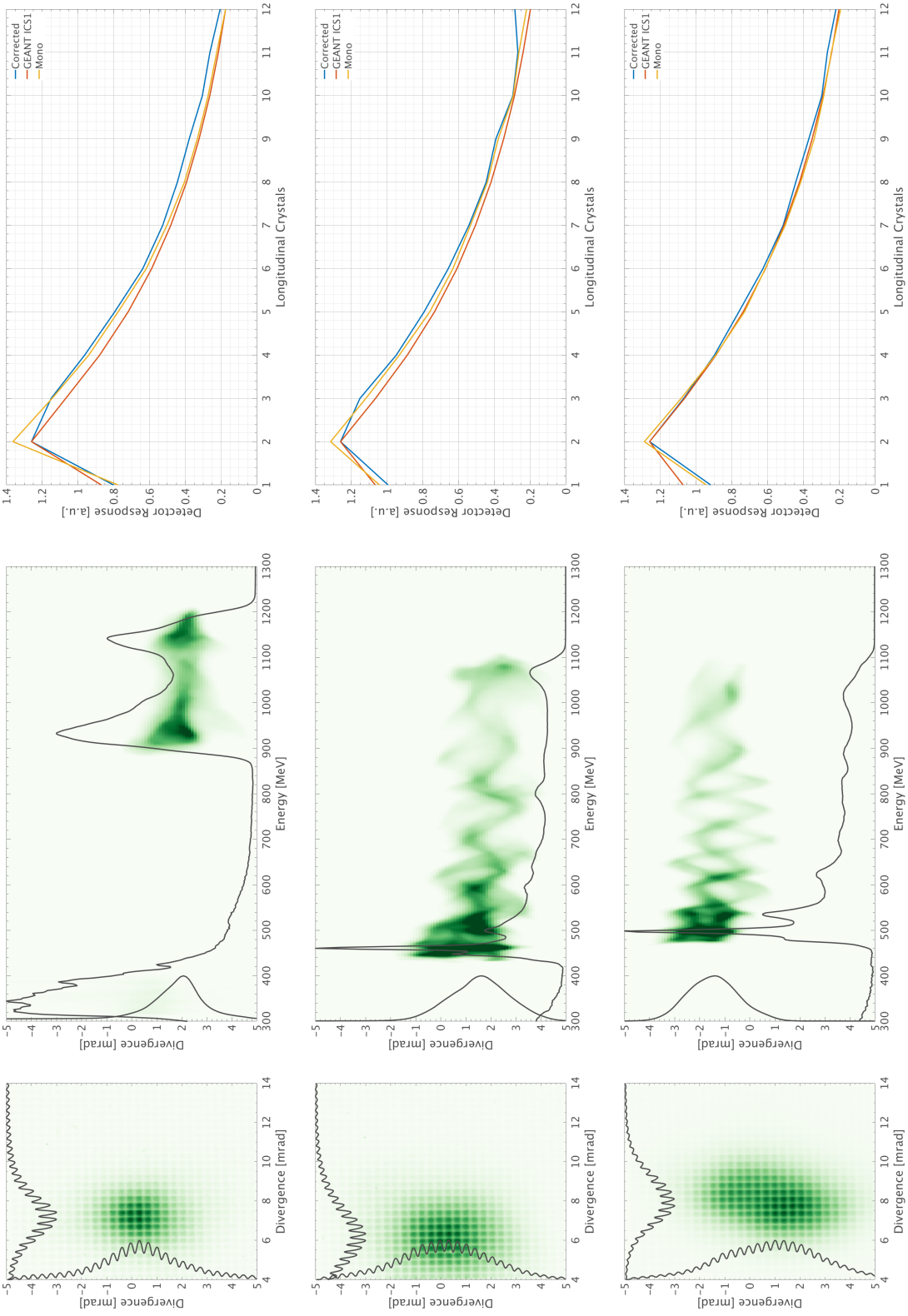


Figure 5.17: Gamma spectrometer responses (right) with corresponding electron spectra (centre) and gamma profiles (left). The experimentally measured detector response is shown in blue. Two simulated responses are fitted to the experimental data, one using a monoenergetic gamma spectrum (yellow), the other one relying on the electron spectrum (see centre) to calculate a spectrum from linear inverse Compton scattering (red). The top two examples are from dataset B*, the bottom one was taken from* A*.*

5.11 Compton scattering as electron beam diagnostic

Linear Compton scattering of an electron beam and a laser pulse is at these low intensities non-invasive and well understood, which signals its potential as diagnostic. Moreover, we have shown that the electron bunch and the laser beam can be overlapped over extended periods of time due to the large size of the laser beam. In the previous sections, we have already demonstrated that linear ICS can be used to diagnose the size of the laser pulse and its intensity at the interaction. We will now discuss its potential to diagnose the electron beam instead.

Linear ICS has already been used as beam diagnostics [171] to determine the energy [95], beam size [90], emittance [270], transverse and longitudinal charge distribution [89] or polarisation [87, 93, 266] of electron beams at conventional and plasma-based accelerators. However, it is typically used as a *multi-shot* diagnostics that involves scans in order to determine the properties of the electron beam, similar to the laser raster scan we presented earlier in Section 5.5. In these setups, the laser has to be focused tightly to produce a measurable yield of gamma-rays such that the focus is typically smaller than the transverse size of the electron bunch at that plane. Here, we propose to use the emission from linear ICS in conjunction with the gamma profile screen as *single-shot* beam profile measurement. Similarly to a physical beam profile monitor, as used frequently on laser wakefield experiments, this would be used to measure the beam pointing and the divergence of the electron beam (see for instance [232]).

A physical beam profile screen is in the context of radiation reaction studies not ideal as it would produce bremsstrahlung on-axis, which would make the spectral retrieval of the ICS spectrum more challenging (see Section 4.6.2). Such a profile screen, e.g. Lanex, would also require a static laser beam dump to terminate the wakefield driver beam or a plasma mirror as protection, both of which would result in the emission of bremsstrahlung and increasing complexity of the setup. A laser beam dump and the beam profile monitor would also lead to small-angle scattering of the electron beam, affecting the spectral measurement further downstream. In LWFA setups, the electron beam is typically spectrally dispersed close to the accelerator to reduce uncertainties in the inferred energy measurement resulting from beam pointing and divergence. As a consequence, any beam profile measurement of the non-dispersed beam has to be conducted close to the accelerator (or the magnet has to be retractable/tunable). The short distance limits the spatial resolution. In addition, any scattering of the beam will propagate long distances, reducing the beam quality and a subsequent measurement of the beam energy. An early non-invasive measurement would benefit from a potentially improved spatial resolution as it can in principle be propagated indefinitely to increase the spatial resolution via geometric magnification. Moreover, wakefield accelerators often produce a large number of electrons at few MeV energy that are typically not resolved by magnetic spectrometers

but will dominate the response of the beam profile screen [284].

The magnetic electron spectrometer in this experiment measures the beam pointing and divergence in the non-dispersion direction. In general, we expect that the electron beam and its divergence show some extent of cylindrical symmetry as the accelerating cavity (the 'bubble') will. Asymmetric injection and beam oscillations can, however produce elliptical beams. Any beam pointing in the dispersion axis affects the accuracy of the energy inferred from the spectrometer setup. Two-screen setups have been used previously in LWFA experiments to infer the beam pointing [256, 257] and were also used in this experiment. However, two-screen setups require a finite drift space between the screens to reach a sufficient resolution and contrast (if spatial references are used), whilst scattering induced from vacuum windows and Lanex screens will counteract the beneficial effect of the drift, limiting the resolution of the measurable beam pointing intrinsically.

Linear ICS promises to measure the beam pointing and divergence without impacting any further measurement of the beam properties and its transport. It seems in particular of interest as tool to characterise the fluctuations of the electron beam en route to high-intensity interactions for radiation reaction studies. In the highly non-linear regime, the interaction becomes invasive due to energy loss in the electron beam [133], but here the deformation of the emitted radiation cone in turn gives additional information about the intensity at the interaction point [120, 172, 260], simply using the same setup. We will in the following explore the feasibility of this diagnostic.

5.11.1 Resolving spatial features

This section investigates the relation of the measured gamma profile and the spatial structure of the electron beams. For this purpose, we will compare the measurements of the electron spectrometer with the corresponding gamma profile screen measurements at the example of particularly structured electron bunches.

Figure 5.18 shows a montage of electron beams measured in the dataset along with the corresponding gamma beam profile measured on the profile screen (on the left of the respective electron spectrometer image). Similarly as the electron beam varies strongly from shot to shot the gamma profile also changes shape, reflecting distinct features in the electron beam. The example on the top left of the Figure, for instance, shows an electron beam with distinct oscillations in the vertical axis. This is accompanied by an elongated gamma profile measurement, which indicates that the oscillations are predominantly in the vertical direction and that the elongation of the beam is less pronounced in the dispersion direction. The example on the top right shows an electron beam that is tilted in the vertical direction. The gamma beam also indicates a vertical offset, but also shows that the tilt is not only in the vertical but also in the horizontal axis.

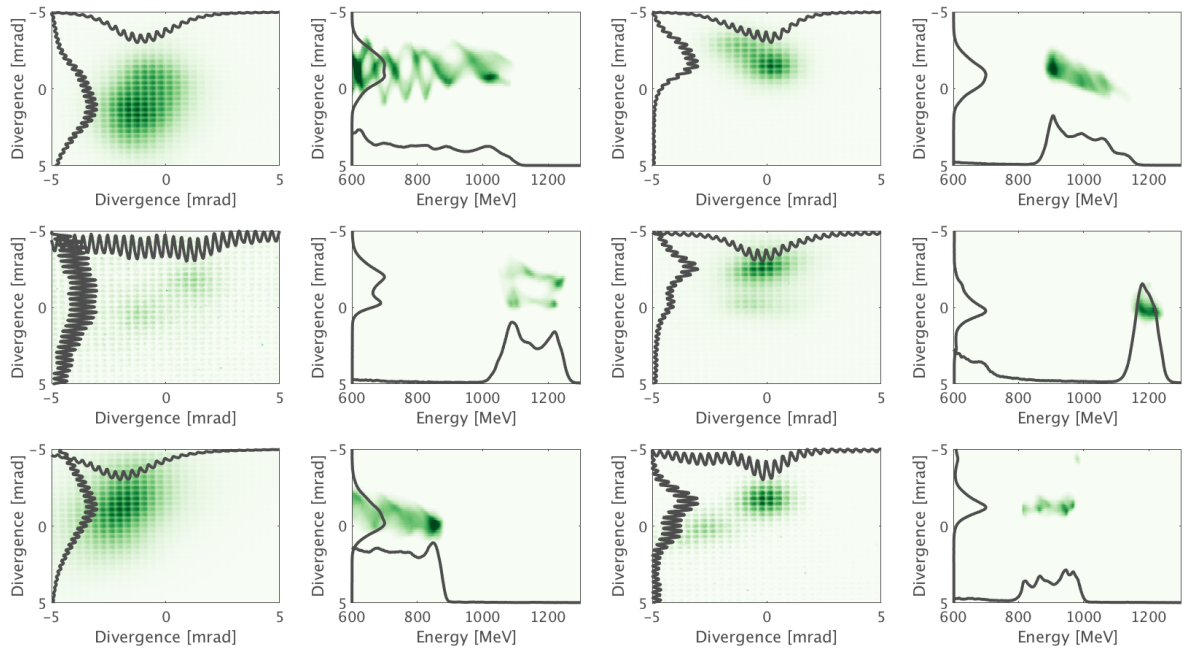


Figure 5.18: Montage of electron spectra and corresponding gamma profile measurements (on their right side) for a selection of shots. The axes for the gamma profile screens show the horizontal (x-axis) and vertical (y-axis) divergence. The axes for the electron spectrometer images are the vertical divergence (y-axis) and the electron energy (x-axis). The colour scale is proportional to the energy deposited in the gamma profile screen per $mrad^2$, and to the charge of the electron beam per $mrad \times MeV$. The lineouts on the x- and y-axes are the 2D images projected onto that respective axis. The maximum height of the lineouts changes for each image. Note that electron and gamma pointing deviate from each other in some instances (see Section 5.11.2).

Figure 5.19 shows a highly divergent electron beam around 450 MeV energy. On the electron spectrometer image, the electrons are mainly seen concentrated in one point with a straight line in the vertical direction. The gamma profile screen, on the other hand, reveals a highly divergent ring-like radiation pattern with a beamlet in the centre, which is not evident from the spectrometer screen.

Figure 5.20 shows two beamlets at similar energies separated in the vertical direction. The corresponding gamma-ray beam measured with the profile (left) shows that the beams are not only separated vertically but also in the horizontal axis. More examples are shown in Figures 5.21, 5.22 and 5.23.

These examples show that the measured radiation profiles are capable of reproducing spatial features visible in the electron spectra and but are also able to provide an additional insight into the composition of the electron beam that is hidden in the dispersion direction of the electron beam.

In addition to this qualitative insight, we want to investigate how well the radiation profile measured on the gamma profile screen reflects the spatial features of the electron

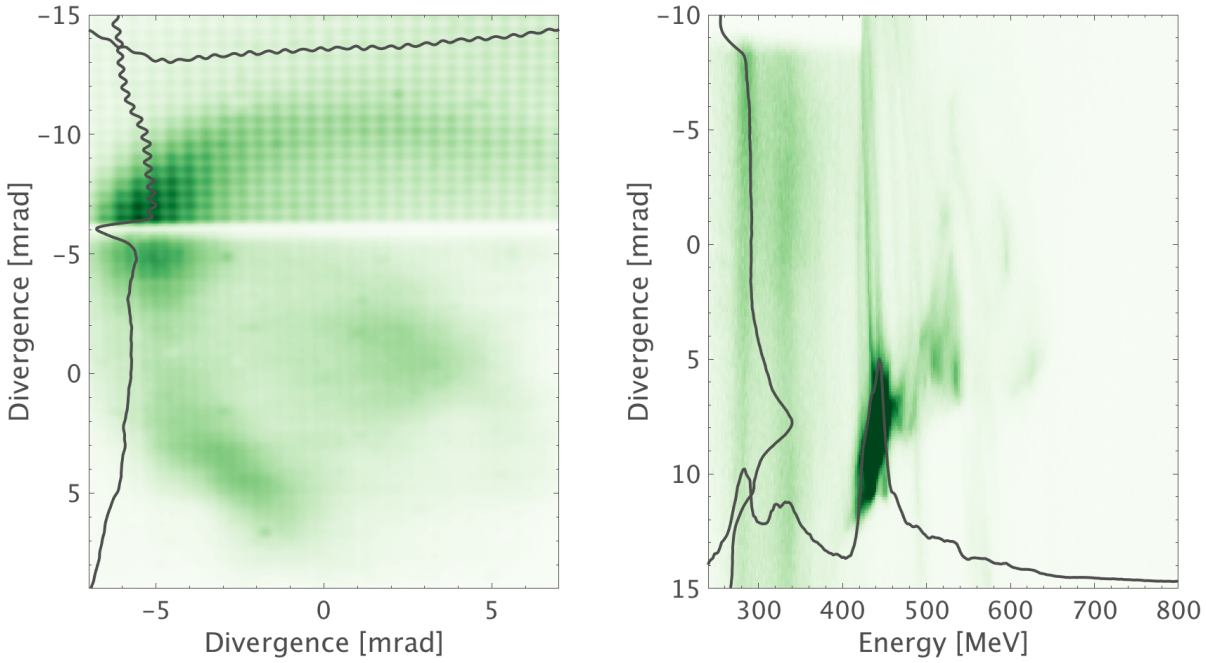


Figure 5.19: Example of a highly divergent electron beam at $\epsilon < 500$ MeV (right) and the corresponding gamma-ray emission measured on the profile screen (left). Due to the high-divergence the gamma radiation extends beyond the profile screen onto a second scintillator stack placed on top.

spectra in terms of their spatial scale and relative signal strength. Figures 5.20, 5.21, 5.22 and 5.23 show four examples, where this time the gamma profile measurement and the electron spectrum are complemented by a third panel that compares the projections onto the y-axis of both the gamma profile and electron spectra. The first observation is that the gamma-ray measurements consistently show broader profiles as the electron measurements (see for instance Fig. 5.20). This is expected as the emitted radiation has a larger divergence than the electron beam.

Figure 5.20 shows two vertically separated beamlets of similar charge. The spatial separation agrees well on both integrated signals (bottom), on the electron spectrometer screen (blue) and the gamma profile (yellow). The relative height of both peaks is also well reproduced by the gamma measurement (yellow). Since the energy deposited by photons produced at electron energies between $1 - 1.2\,\mathrm{GeV}$ does not change much, the related radiation profile is also not expected to be altered significantly (red curve).

Figure 5.21 shows a narrow-energy spread beam of $\sim 1.2\,\mathrm{GeV}$ central electron energy. The main beam is accompanied by two lower charge beamlets on either vertical side at ~ -1.2 and $\sim 2.5\,\mathrm{mrad}$ on the vertical axis of the spectrometer screen. The integrated gamma profile signal (yellow) shows a secondary peak at a comparable distance to the main peak as the spectrometer lineout (blue). The radiation related to the second beamlet is not measured and might be outside of the field of view of the detector. The amplitude of the

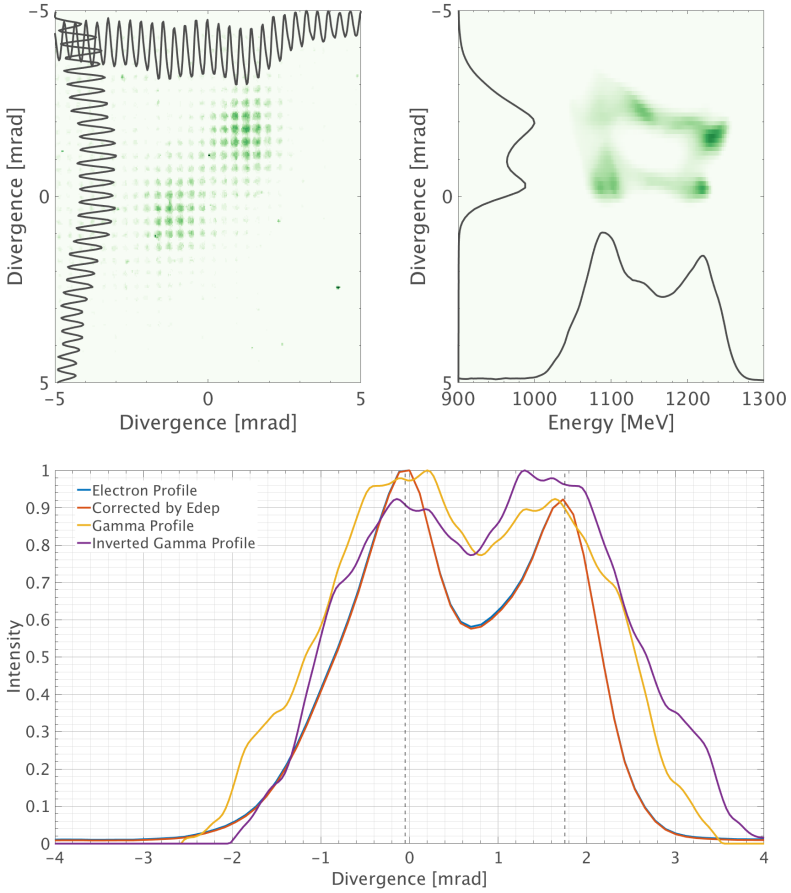


Figure 5.20: Two vertically separated electron beamlets measured on the electron spectrometer (top right) and their corresponding gamma-ray signal on the beam profile (top left). Bottom: Projected y-lineouts of the electron spectrometer (blue), corrected for the relative energy deposited by radiation related to that electron energy (red), the gamma profile signal (yellow) and its spatial inversion (purple).

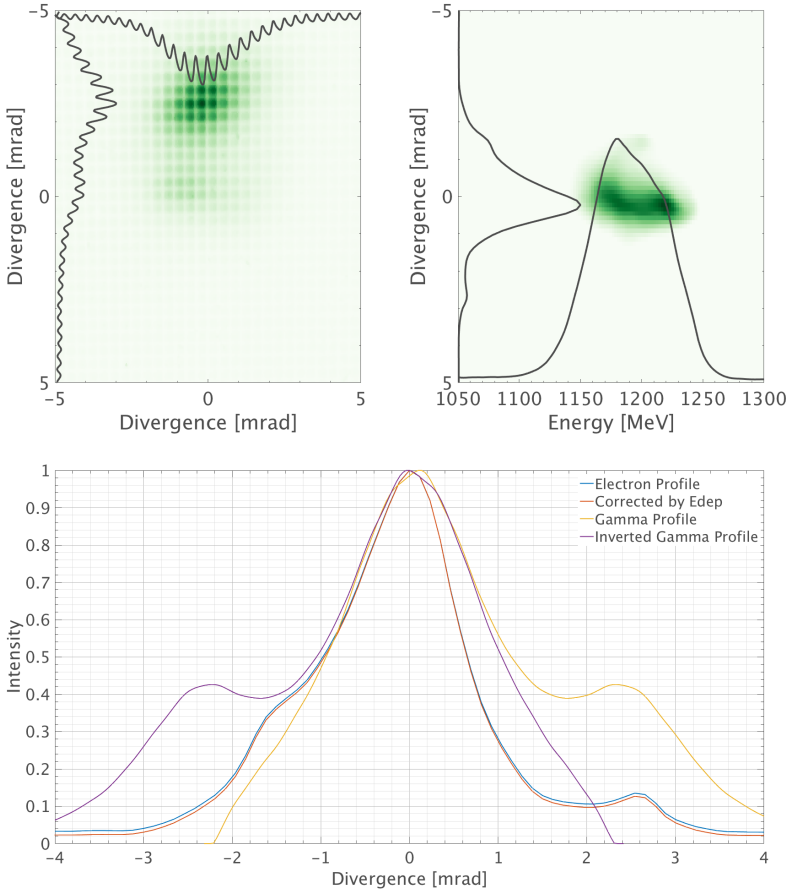


Figure 5.21: Electron spectrometer (top right) and gamma profile measurements (top left) of an electron beam with narrow energy spread and small off-axis features. Bottom: Projected y-lineouts of the electron spectrometer (blue), corrected for the relative energy deposited by radiation related to that electron energy (red), the gamma profile signal (yellow) and its spatial inversion (purple).

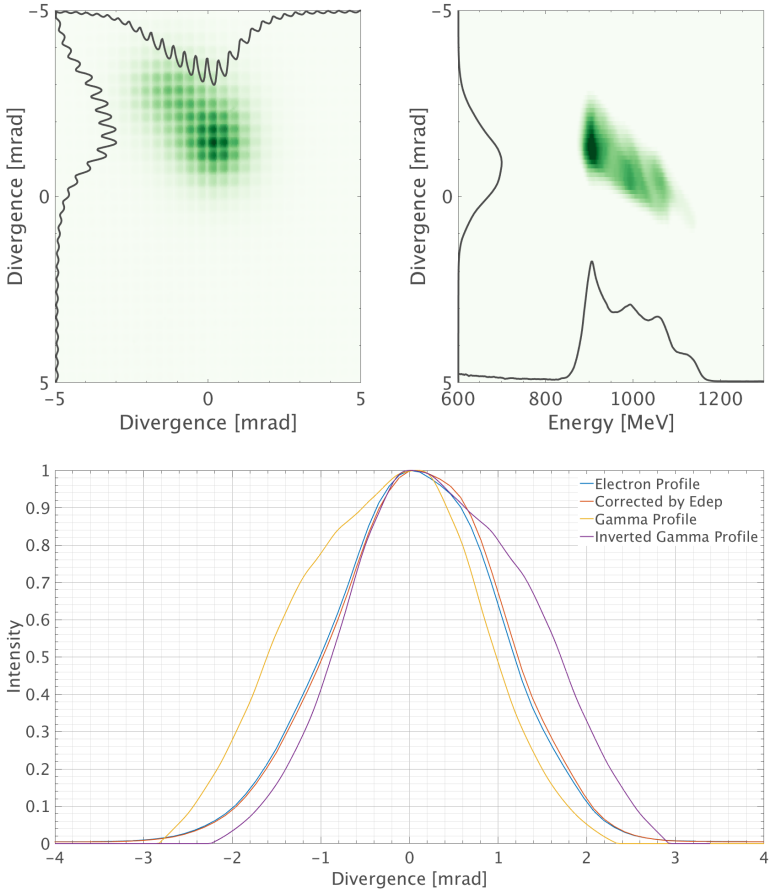


Figure 5.22: Electron spectrometer (top right) and gamma profile measurements (top left) of a vertically tilted electron beam. Bottom: Projected y-lineouts of the electron spectrometer (blue), corrected for the relative energy deposited by radiation related to that electron energy (red), the gamma profile signal (yellow) and its spatial inversion (purple).

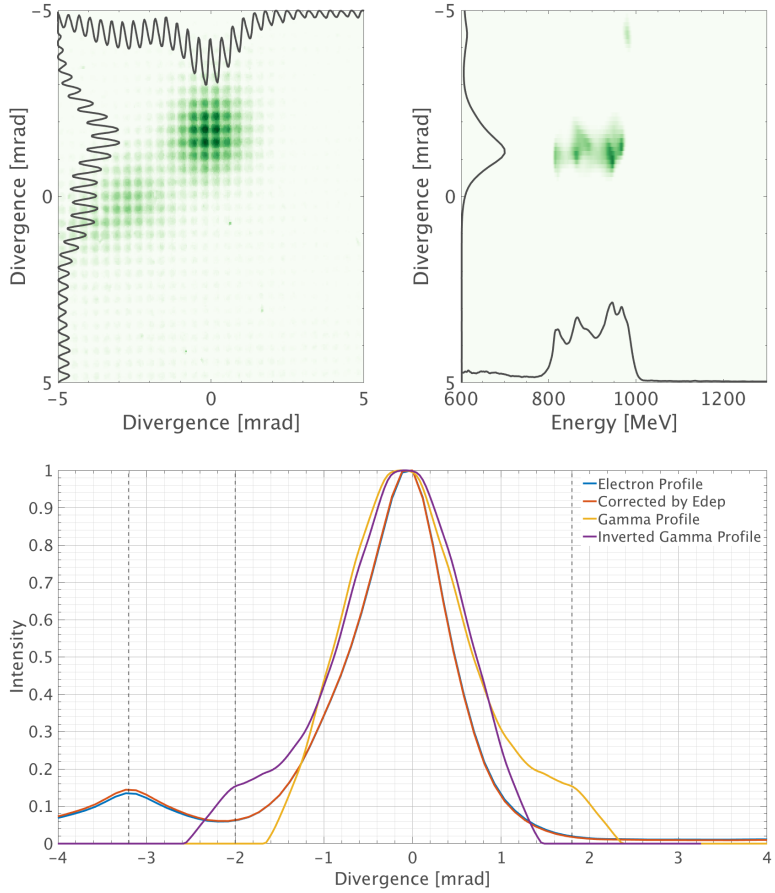


Figure 5.23: Electron spectrometer (top right) and gamma profile measurements (top left) of an electron beam with a low-charge off-axis wing. Bottom: Projected y-lineouts of the electron spectrometer (blue), corrected for the relative energy deposited by radiation related to that electron energy (red), the gamma profile signal (yellow) and its spatial inversion (purple).

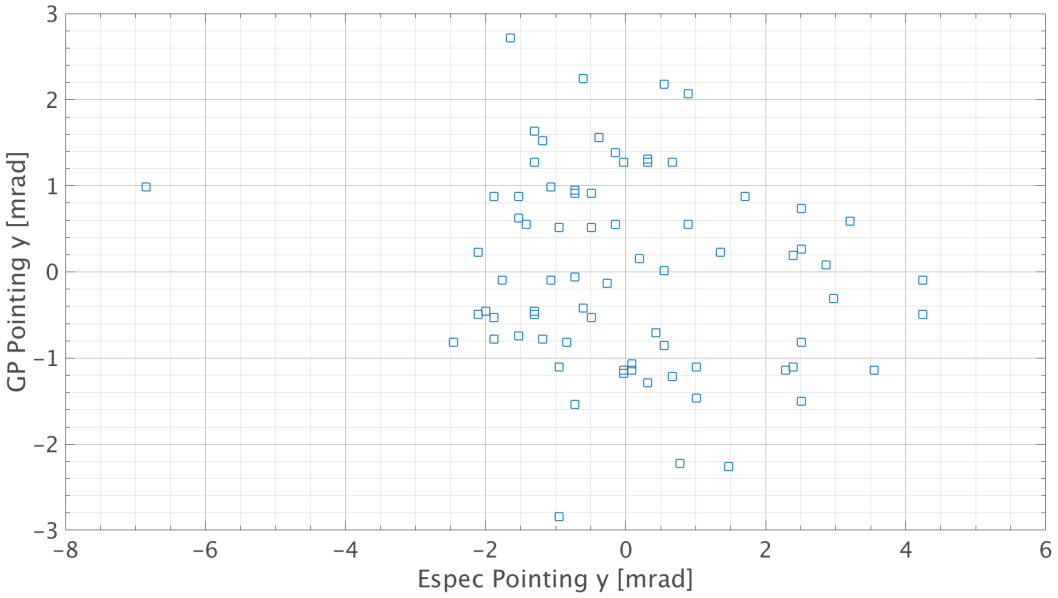


Figure 5.24: Vertical beam pointing (position of the beam centroid) in mrad measured on the gamma profile screen as function of the relative beam pointing of the electron beam. The observables do not show any significant correlation at a correlation coefficient of -0.15.

gamma signal for the beamlet is much larger than the relative charge on the spectrometer screen. Its amplitude, however, matches the other 'missing' beamlet.

Considering Figure 5.23, we see now more clearly that the vertical profile on the electron spectrometer screen (blue) and the gamma profile (yellow) are seemingly inverted relative to each other (purple). The electron beam has a secondary beamlet offset by about $\sim -3.2\,\mathrm{mrad}$ from the main beam (dashed line), whereas the gamma profile shows a secondary peak on the other side at $\sim +1.8\,\mathrm{mrad}$.

The interaction of the laser pulse and the electron beam occurred in the plasma which could be related to the discrepancy of the gamma profile and the electron beam. This could be related to betatron oscillations or the evolution of the accelerating cavity ('bubble') through changes in the plasma density. The data is, however, too ambiguous and sparse to provide conclusive evidence. Despite some discrepancy on some of these examples, this section showed that the gamma profile reproduces features in the electron beam, including their relative signal strength and spatial separation. We have also seen that the profile measurement can give further insight into the spatial arrangement of the electron beam that are not visible on the spectrometer screen.

5.11.2 Beam Pointing

In ICS, the photons are backscattered in the propagation direction of the electron beam, due to the Lorentz boost of the electron beam. As a result, the photon distribution is a

reflection of the momentum vector of the electrons. Figure 5.24 shows the vertical pointing of the gamma ray beam, in terms of the relative deviation from a reference point on a screen, as a function of the vertical pointing of the electron bunch measured with the electron spectrometer. Surprisingly, both quantities do not seem to be correlated significantly at a linear correlation coefficient of -0.15. Since the interaction with the laser pulse occurs in the plasma, it could be suspected that the electron beam pointing is still changing throughout its remaining propagation in the plasma, such that the pointing variations of the gamma radiation do not correlate well with the final beam properties. This aligns with the discrepancies in the signals discussed previously. Consequently, the interaction should take place outside of the plasma, i.e. in vacuum, where the momentum distribution of the electron bunch is fixed to render this a useful on-shot pointing diagnostic.

5.11.3 Divergence and Ellipticity

The profile screen measures the size of the radiation cone at the plane of the detector, σ_D. Using the small-angle approximation, it is given by:

$$\sigma_D \approx \theta_f d + \sigma_S \approx \theta_f d, \tag{5.11.1}$$

where d is the distance from the source to the detector plane, σ_S is the source size and θ_f is the divergence of the emission cone. The contribution of the source size, σ_S, is negligible, i.e. $\theta_f d \gg \sigma_S$, since $d \sim$ m and $\theta \sim$ mrad but $\sigma_S \sim$ µm. As a consequence, the profile screen measures effectively the divergence of the radiation cone, θ_f.

The divergence of the full gamma ray beam, θ_f, incorporates the divergence of the electron bunch, θ_e, and the gamma emission cones around each individual electron, θ_γ:

$$\theta_f = \sqrt{\theta_e^2 + \theta_\gamma^2}, \tag{5.11.2}$$

$$\Rightarrow \theta_\gamma = \sqrt{\theta_f^2 - \theta_e^2}, \tag{5.11.3}$$

where the $\theta_\gamma \sim 1/\gamma$, i.e. radiation from linear ICS is emitted in a narrow cone of divergence $\sim 1/\gamma$. γ is the relativistic Lorentz factor of the electrons. Within an electron beam, the divergence, θ_e, and charge distribution might vary with electron energy, which we will ignore for now and instead consider the profile of the full electron beam integrated over all energies. We also assume that the laser pulse interacts with the entire electron bunch. If $\theta_\gamma \ll \theta_e$, then the divergence of the total emitted radiation cone, θ_f, is simply the sum of both, i.e. $\theta_f \approx \theta_e + \theta_\gamma$.

In the experiment, the electron beam is dispersed in the horizontal axis, here x, to measure its energy, which destroys its spatial component in x. The vertical axis on the electron spectrometer, y, is preserved and can be used to measure the divergence of the

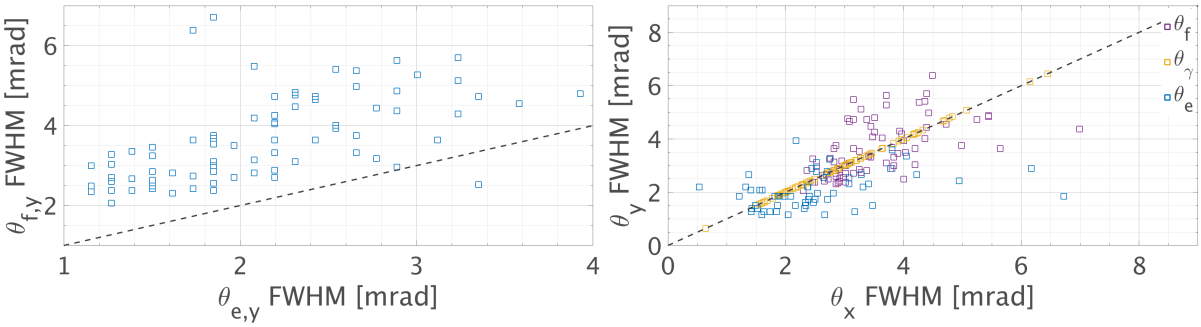


Figure 5.25: FWHM *divergences of the gamma profile and electron beam. Left: Vertical divergence of the gamma profile, $\theta_{f,y}$, as a function of the vertical divergence measured on the electron spectrometer screen, $\theta_{e,y}$. The dashed line indicates $\theta_{f,y} = \theta_{e,y}$. Right: Vertical divergence, θ_y, as a function of horizontal divergence, θ_x, for the full gamma profile, θ_f (purple), the contribution of the gamma emission cone, θ_γ (yellow, using Equation (5.11.3)), and the electron divergence, θ_e (blue). The dashed line indicates $\theta_y = \theta_x$.*

beam, $\theta_{e,y}$. If we assume cylindrical symmetry for the electron beam, the divergence in the horizontal axis is simply identical, i.e. $\theta_{e,x} = \theta_{e,y} = \theta_e$. On the other hand, we can instead assume that the contribution of θ_γ is constant in both axes, i.e. $\theta_\gamma = \theta_{\gamma,x} = \theta_{\gamma,y}$, which holds for $a_0 \ll 1$. We can then use the divergences measured on the profile screen, $\theta_{f,x}$ and $\theta_{f,y}$, and the divergence of the electron beam measured on the electron spectrometer, $\theta_{e,y}$, to infer the divergence of the electron beam in the horizontal axis, $\theta_{e,x}$:

$$\begin{aligned} \theta_{e,x} &= \sqrt{\theta_{f,x}^2 - \theta_\gamma^2} \\ &= \sqrt{\theta_{f,x}^2 - [\theta_{f,y}^2 - \theta_{e,y}^2]}, \end{aligned} \tag{5.11.4}$$

where we only obtain a real value for $\theta_{f,x} \geq \theta_\gamma$ and similarly $\theta_{f,y} \geq \theta_{e,y}$ for θ_γ. Figure 5.25 (left) shows that the condition $\theta_{f,y} \geq \theta_{e,y}$ holds for most of the dataset, except for one outlier. The condition $\theta_{f,x} \geq \theta_\gamma$, however, does not hold for a significant number in the dataset for which we can not calculate $\theta_{e,x}$. This means that the relation between the measured quantities is not suitable in these or maybe all instances. This could either be due to integrating over the entire spectrum, missing a large amount of electrons below the low-energy cut-off of the electron spectrometer, or a change in the electron beam properties after the interaction as indicated in the previous sections.

Figure 5.25 (right) shows the measured and calculated divergences in the $x - y$ plane, where only divergences with real values are shown. The values for the full divergence, θ_f (purple), are mostly larger than the electron divergences, θ_e (blue), as expected by this selection. The scatter around the dotted axis indicates non-symmetric beams, i.e. for which $\theta_x \neq \theta_y$. The average electron divergences are $\langle\theta_{e,y}\rangle = 2.14 \pm 0.65\,\text{mrad}$ (measured) and $\langle\theta_{e,x}\rangle = 2.52 \pm 1.13\,\text{mrad}$ (inferred). The values for θ_γ (yellow), calculated using Equation (5.11.3), lie on the dashed line where $\theta_x = \theta_y$ as we assumed symmetry. θ_γ varies

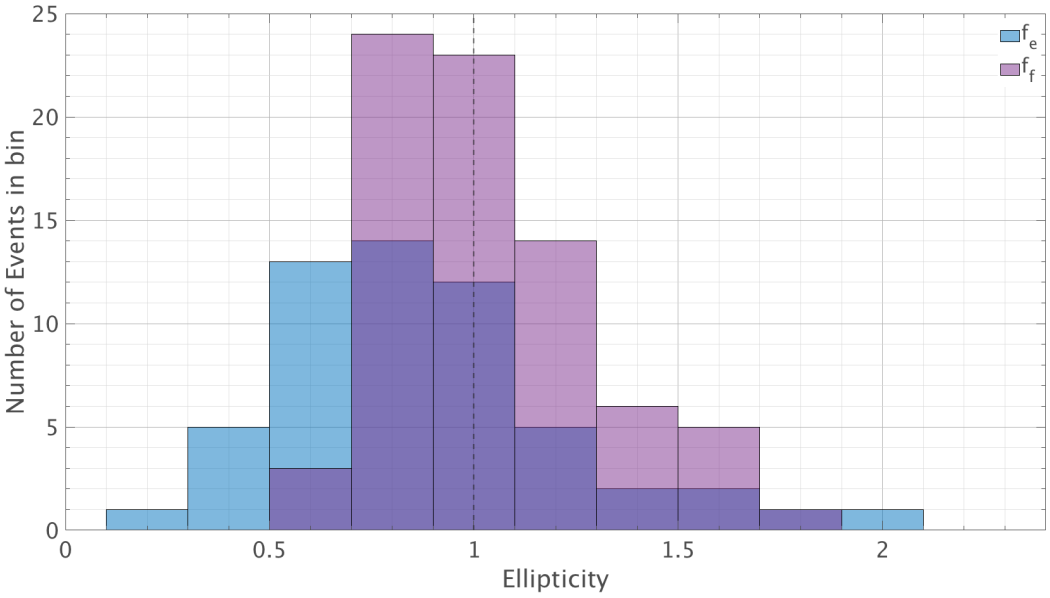


Figure 5.26: Histogram of the ellipticity of the gamma beam as measured on the gamma profile screen (purple) and the ellipticity of the electron beam inferred from it (blue) using Equation (5.11.5)*. The dashed grey line indicates $f = 1$, i.e. a symmetric beam.*

strongly from shot to shot from $\theta_\gamma < 1\,\text{mrad}$ to $> 6\,\text{mrad}$, which is either related to the strong fluctuations in the electron spectrum or it simply absorbs the potential change in the electron divergence after the interaction, i.e. does not represent the actual value of θ_γ. The discrepancies in some parts of this dataset should be investigated in a future measurement.

Nonetheless, using the part of the dataset where we were able to calculate all divergences, we can now determine the ellipticity for both, the electron beam and the gamma beam. The ratio of these divergences is called the ellipticity:

$$f_\gamma = \frac{\theta_{f,\parallel}}{\theta_{f,\perp}} = \sqrt{\frac{\theta_{e,\parallel}^2 + \theta_\gamma^2}{\theta_{e,\perp}^2 + \theta_\gamma^2}}, \tag{5.11.5a}$$

$$f_e = \frac{\theta_{e,\parallel}}{\theta_{e,\perp}} = \frac{\theta_{e,\parallel}}{\sqrt{\theta_{e,\parallel}^2 + \theta_{f,\perp}^2 - \theta_{f,\parallel}^2}}, \tag{5.11.5b}$$

where f_γ is the ellipticity of the total radiation cone that can be measured directly and f_e is the ellipticity of the electron beam that is inferred. A value of unity indicates that the beam is symmetric. If $\theta_\gamma \ll \theta_e$, then $f_\gamma \approx f_e$, and we can obtain the ellipticity of the electron beam directly from the gamma profile measurement. The results shown in Figure 5.25 suggest that this might not always be the case, but this has to be investigated in more detail. Figure 5.26 shows the ellipticities of the full gamma-ray beam (using only measured quantities), f_f (purple), and the inferred values for the electron beam, f_e

(blue). The median value for the gamma-ray beam is $0.97(+0.22/-0.11)$ which indicates on average symmetry. The deviations reach up to 0.5 and 2, which correspond to an elliptical beam where the long axis is twice the size of the short axis. The electron beam, on the other hand, has a median value of $0.81(+0.2/-0.12)$ which indicates a slight asymmetry of the beam on average. However, considering the inconsistencies in some parts of the dataset, the values might not be reliable for all shots. It would be desirable to repeat these measurements in vacuum instead of plasma to confirm that this removes these inconsistencies and improves other correlations, e.g. for beam pointing.

The profile of the emitted radiation is of great interest for radiation reaction studies as it indicates the intensity of the laser pulse at the interaction [120, 260]. The ellipticity, in particular, permits a model-independent inference of the intensity [172]. There $a_0 \gg 1$, such that we are in the nonlinear regime of Thomson or Compton scattering and the symmetry of the emission cone is broken, i.e. $\theta_{\gamma,\parallel} \neq \theta_{\gamma,\perp}$. The fluctuating ellipticity of the e-beam motivates similar statistical measurements as part of radiation reaction studies that use this inference method and to estimate the error associated with these fluctuations. For this purpose, it is paramount to refine the methods outlined here and investigate discrepancies systematically. An independent measurement of the electron beam ellipticity, on the other hand, would remove this error on a shot-to-shot basis and allow to use the absolute divergence of the radiation profile to probe different models of radiation reaction.

5.12 Conclusion

In this Chapter, we presented experimental results from an all-optical colliding pulse setup. We successfully collided relativistic electron beams from a laser wakefield accelerator of up to 1.3 GeV energy, injected by a density modulation, with a second laser pulse of intensities between $a_0 \sim 0.2 - 1.0$. The laser-electron interaction consistently produced collimated gamma-ray beams from linear inverse Compton scattering. Due to the variability of the electron beams produced in this setup, the spectral shape of the gamma radiation varied similarly ranging from narrow-band to broadband radiation of a few MeV to photon energies in excess of 30 MeV. The radiation was used to diagnose the properties of the laser pulse and the electron beam.

In Section 5.5, it was demonstrated that by translating the laser beam relative to the fixed electron beam axis (raster scan or spatial correlation technique), we can infer the diameter of the laser pulse and, as a result, determine the plane of the interaction relative to the focus and the intensity of the laser pulse at the interaction.

In Section 5.9, on the other hand, the radiation yield measured on the gamma profile

diagnostic was used to infer the diameter and intensity of the laser pulse at the interaction in a single shot. Future measurements would be improved by performing interactions in vacuum instead of plasma and by including additional broadening effects in the modelling of the gamma spectra, in particular redshifting and higher harmonics when $a_0 \to 1$.

Both techniques promise to become useful diagnostics in radiation reaction studies that facilitate high-intensity interactions systematically by measuring the spatio-temporal synchronisation of the electron beam and the laser pulse, rather than fluctuations between two laser pulses that are characterised, for instance, using spectral interferometry.

In Section 5.11, we then discussed the application of linear inverse Compton scattering as single-shot non-invasive electron beam diagnostic. The radiation profile measured on the gamma profile screen resolved spatial features in the electron beam, for instance smaller off-axis beamlets, and was used to retrieve information on the spatial distribution of the beam in both transverse dimensions, including the dispersion axis that is spatially not resolved in the magnetic spectrometer. The divergences measured with the gamma profiler and the electron spectrometer were then used to infer the ellipticity of both, the gamma beam and the electron bunch. This ability will be in particular useful in the context of intensity measurements in highly non-linear Compton scattering [120, 172, 260].

However, several discrepancies, e.g. a lack of correlation in the pointing of the electron bunch and the gamma beam, indicated that the electron beam was evolving between the interaction with the laser pulse and the end of the accelerator. This suggests that future measurements should interact the electron bunch and the laser pulse outside of the plasma, i.e. in vacuum, to make sure that the radiation properties reflect the properties of the final electron beam.

In summary, we demonstrated that linear inverse Compton scattering can act as a useful *non-invasive diagnostic of both laser and electron beam properties* in *multi* and *single-shot* techniques, and will be particularly crucial to facilitate and diagnose high-intensity electron-laser collisions and their statistical variations in future radiation reaction studies.

Chapter 6

First Measurements of Radiation Reaction at Astra Gemini

6.1 Experimental Motivation

Inverse Compton Scattering

In relativistic *inverse Compton scattering* (ICS), sometimes also referred to as Compton Backscattering (CBS) or, in the classical limit, relativistic Thomson scattering, one (linear) or multiple (non-linear) photons scatter from a relativistic electron of energy ϵ, with $\epsilon/m_e c^2 = \gamma \gg 1$. The scattered photons experience a relativistic Doppler-shift and are re-emitted in a narrow cone of divergence $\sim 1/\gamma$ in the direction of the electron propagation, carrying a higher energy based on the electron energy and the intensity of the laser field. The emitted photon energy, ϵ'_{ph}, is maximised in a head-on collision: $\epsilon'_{ph} = 2\gamma^2(1-\cos\theta)\epsilon_{ph}$ (see e.g. [98, 288] or Section 2.2.2), where ϵ_{ph} is the photon energy before the interaction and θ is the angle between the photon and the electron. Higher electron energies result in a stronger shift of the radiation towards higher energies, also called 'hardening of the spectrum', and an increase of the corresponding energy loss the electrons experience. A more intense laser field ($a_0 > 1$), on the other hand, enables non-linear interactions and increases the number of photons interacting with an electron, resulting in the generation of $\sim a_0^3$ higher harmonics [47] but also redshifting and broadening of the spectrum due to the relativistic mass increase [98, 288–290]. As a result, the rapidly rising number of higher harmonics blend together to form a broadband synchrotron-like spectrum and the characteristic energy of the spectrum, $\epsilon_{ICS} = 3\gamma^2 a_0 \hbar\omega_0$, increases linearly with a_0.

ICS provides a promising route to generate bright beams of high energy radiation reaching 100's of keV or even MeV photon energy, suitable for medical [291, 292] and imaging applications (also of high-Z objects) [274, 293] and to stimulate nuclear resonances [97, 294], even at small-scale facilities [81]. It also provides a useful tool to measure

beam properties [171, 295], including polarisation [87, 93]. In addition, the high photon energies offer the opportunity to directly measure the effect of *radiation reaction* on the beam dynamics itself and to observe energy loss, if the emitted photon carries an energy comparable to the energy of the electron $\gamma^2 a_0 \frac{2r_e\omega}{3c} \sim 1$ [81], where r_e is the classical electron radius. The attempt to solve radiation reaction self-consistently within classical electrodynamics exhibits unphysical predictions like self-acceleration, resulting in runaway solutions, or an unbounded emission spectrum, i.e. energy loss higher than the initial energy of the electron is allowed [102]. A universally accepted practicable description of radiation reaction has not been found yet.

Inverse Compton Scattering using Laser Wakefield Accelerators

In laser wakefield acceleration (LWFA), the intense laser driver is intrinsically synchronised to the relativistic electron beam that trails behind it and the electron source size is small, allowing complete overlap with a tightly focused laser pulse. This makes LWFA well suited to study inverse Compton scattering at high intensities.

Colliding-pulse or ICS experiments using LWFA have been successfully performed by different groups over the past years, gradually improving the control over the process, increasing the laser intensities and the energies of the electrons involved, and subsequently of the generated radiation [120–125, 296, 297] (see Figure 6.1). The energy and the tunability of the radiation produced in these experiments are good indicators for their continuing progress. More specifically of interest for measuring radiation reaction is the quantum non-linearity parameter, $\eta = 2\gamma E_L/E_{crit}$ [131, 298], that indicates the strength of the electric field of the laser, E_L, in the rest frame of the electron relative to the critical electric field of QED, $E_{crit} = m_e^2 c^3/\hbar e$, also called the *Schwinger field* [25, 26].

Inverse Compton Scattering using a plasma mirror

A single intense laser pulse can be used to accelerate electrons to relativistic energies via LWFA and to scatter the electrons after backreflecting the laser from a close-to-normal plasma mirror [72], e.g. tape [121] (see Table 6.1 for an overview of recent experimental results achieved in this geometry). In this geometry, the laser beam and the electrons are timed intrinsically. In [121] electrons of an energy $\sim 100\,\mathrm{MeV}$ were collided at a laser intensity of $a_0 \approx 1.2$ (weakly non-linear). The radiation measured was a broadband X-ray spectrum and reached up to 100‘s keV photon energies. In [299] a low energy spread electron beam of up to 90 MeV was scattered at a laser intensity $a_0 \approx 0.9 - 1.2$, producing an X-ray spectrum peaked at 180 keV. In [300] a laser of intensity a_0 was scattered from electrons of 400 MeV energy emitting gamma rays of up to 2 MeV energy. By now the highest recorded gamma-ray energies from ICS in LWFA using this scheme were reported

All-optical experiments with plasma mirror					
Name	**Journal**	**Year**	**ϵ [MeV]**	**a_0**	**ϵ_γ [MeV]**
Ta Phuoc et al.	Nat. Photonics **11**	2012	100	1.2	0.1
Tsai et al.	Phys. Plasmas **22**	2015	90	1.2	0.18
Doepp et al.	PPCF **58**	2016	150	1.0	0.05
Yu et al.	Sci. Rep. **6**	2016	400	1.0	2
Shaw et al.	arXiv:1705.08637	2017	2000	0.5	85

Table 6.1: Overview of all-optical inverse Compton experiments using a plasma mirror, colliding electrons of energy ϵ and a laser pulse of peak intensity a_0 reaching maximum gamma energies of ϵ_γ.

in [297], reaching photon energies of up to 85 MeV in a collision with electrons of energies up to 2 GeV.

Whilst this technique avoids issues with timing and overlap, the intensity of the laser pulse is limited as it is partly depleted when interacting with the electron bunch after driving a wake [301] and is typically not tightly focused due to diffraction. At the same time, the acceleration can not be pushed to its depletion limit as the laser pulse has to remain intense enough for a suitable interaction. Further problems might arise as controlling or measuring the wavefront of the depleted laser pulse is challenging. The electrons will also produce radiation from bremsstrahlung when passing through the plasma mirror [300], which overlays the ICS signal, although in [299] the measured signal was claimed to be insignificant. These details are important for a precise measurement of radiation reaction, but might be of secondary concern if a well-defined spectrum is not crucial for the application. At facilities housing the next generation of petawatt lasers, the reflective scheme will also be able to yield very promising results to probe radiation reaction due to the high intensities involved.

Inverse Compton Scattering with two lasers

If two separate lasers are available or maybe one very powerful laser pulse can be split into two parts, one can be used to accelerate electrons via LWFA and one to scatter off them. An overview of recently published experimental results in this geometry are shown in Table 6.2. Electrons produced from LWFA are typically very short in duration $\sim 10 `s$ fs [77] and only few microns small [78] when leaving the accelerating cavity. This allows focusing the second laser very tightly to reach high intensities and to interact with a large fraction of the electron bunch at comparable intensities without a large background from linear ICS. Using two laser pulses opens the gateway to combine higher intensities and

All-optical experiments with two lasers					
Name	**Journal**	**Year**	**ϵ [MeV]**	**a_0**	**ϵ_γ [MeV]**
Chen et al.	Phys. Rev. Lett. **110**	2013	250	0.4	4
Powers et al.	Nature Photonics **8**	2014	300	0.3	0.1
Liu et al.	Optics Letters **39**	2014	450	0.1	9
Sarri et al.	Phys. Rev. Lett. **113**	2014	400	2	18
Khrennikov et al.	Phys. Rev. Lett. **114**	2015	50	0.9	0.04
Yan et al.	Nature Photonics **8**	2017	200	12	20

Table 6.2: Overview of all-optical inverse Compton experiments using two lasers, colliding electrons of energy ϵ and a laser pulse of peak intensity a_0, reaching maximum gamma energies of ϵ_γ.

electron energies at the interaction point, and gives more control over the interaction itself. However, it is challenging to overlap the micron-sized electron bunch with the ultra-short tightly-focused laser pulse, compressed in time and space, and to maintain this alignment over an extended period of time [302]. A very powerful laser can also be used to interact at slightly larger spot sizes, which improves the probability of interactions as it mitigates relative pointing fluctuations. If the laser spot is larger than the electron beam, the theoretical modelling of the interaction can be simplified as all electrons approximately experience the same field and focusing effects are negligible [303].

Tunability at narrow electron energy spread was demonstrated at 300 MeV and tens of MeV electron energies and laser intensities $a_0 < 1$ in [123] and [125]. In [122] relativistic electrons were scattered at an angle of 10 degrees and up to 4 MeV gamma rays were produced. In [296] an electron beam of $\epsilon = 450$ MeV was scattered with a second harmonic laser at $\epsilon_{ph} = 3$ eV reaching up to 9 MeV gamma energies. In [124] electrons at an energy of 400 MeV were successfully collided at an laser intensity of $a_0 \approx 2$, resulting in broadband radiation extending up to 18 MeV. In [120] electrons of energy ~ 200 MeV were collided with an intense laser at $a_0 \sim 12$ reaching photon energies just above 20 MeV, resulting in the generation of over 500 orders of higher harmonics.

Future LWFA Studies on Inverse Compton Scattering and Radiation Reaction

Future laser facilities will be able to perform ICS studies at even higher electron energies and laser intensities. Several PW laser systems have already or are soon to commence their operation, with some existing laser systems being upgraded to the PW-level as well (for instance ELI-NP [35], ELI-Beamlines [36], EPAC [44], HERCULES [46] and ZEUS [45], Apollon [37], SULF [38], SEL [40], BELLA [41, 304], XCELS [42], CALA [43] and many

more [10]). At this point, QED studies are already considered for the 100 PW regime [39, 40]. Maximum electron energies from LWFA, on the other hand, have reached the multi-GeV regime [213, 215] with up to 8 GeV recently [76].

The combination of both, highly relativistic electron beams and highly intense lasers, opens up a wide variety of research topics in the strongly non-linear quantum regime probing radiation reaction[130], photon-photon scattering [62] and pair production from the Breit-Wheeler mechanism [141, 149] or by reaching supercritical field strengths [104]. The high laser intensities will also enable studies of vacuum birefringence [152].

Considering the cost and variety of facilities, it is important to investigate the limitations of current all-optical ICS setups, the feasibility of future measurements and explore potential ways to improve them [302].

Inverse Compton Scattering at conventional accelerator facilities

Inverse Compton Scattering has been employed at conventional accelerator facilities for some time as well, but at much lower laser intensities to measure the beam polarisation (polarimetry, e.g. [87, 93]), in particular in the context of (de)polarisation of beams due to the Sokolov-Ternov effect [305, 306], as beam diagnostic [295], to study nuclear processes [97] or as tool to diagnose high-density or high-temperature plasmas in the context of fusion research [307, 308].

As the field of applications for large-scale accelerators widens and the access to 10 TW laser systems and even commercially available PW-class lasers becomes easier [10], conventional accelerators combine their high-quality relativistic particle beams with intense laser pulses. At XFELs, for instance, this is interesting for the study of warm-dense-matter states and high-energy-density physics [85, 309, 310], involving pump-probe measurements, where X-rays from an insertion device probe matter structures and changes induced in them in the interaction with an intense laser pulse. In the wake of increasing interest in measuring QED phenomena in laser interactions, ICS has also moved into the focus of conventional accelerator facilities. New dedicated projects like LUXE at the European X-FEL [31, 32] and the SFQED project at FACET-II [33] aim to continue the success of the seminal E144 experiment at SLAC conducted in the 90s [99, 100]. Whilst the high-quality beams at these facilities are superior to LWFA studies in terms of charge, energy and energy stability, these projects are facing other challenges such as the temporal synchronisation of the laser pulse and the electron beam or the typically longer and larger electron bunch sizes resulting in a significant overlay from linear scattering events in an ICS setup. Another measurement of radiation reaction was performed at CERN [145], however using positrons and planar channeling in crystals [143, 144] as tool to probe radiation reaction [142] instead of ICS. An overview over the high field QED projects currently being undertaken can be found in [33].

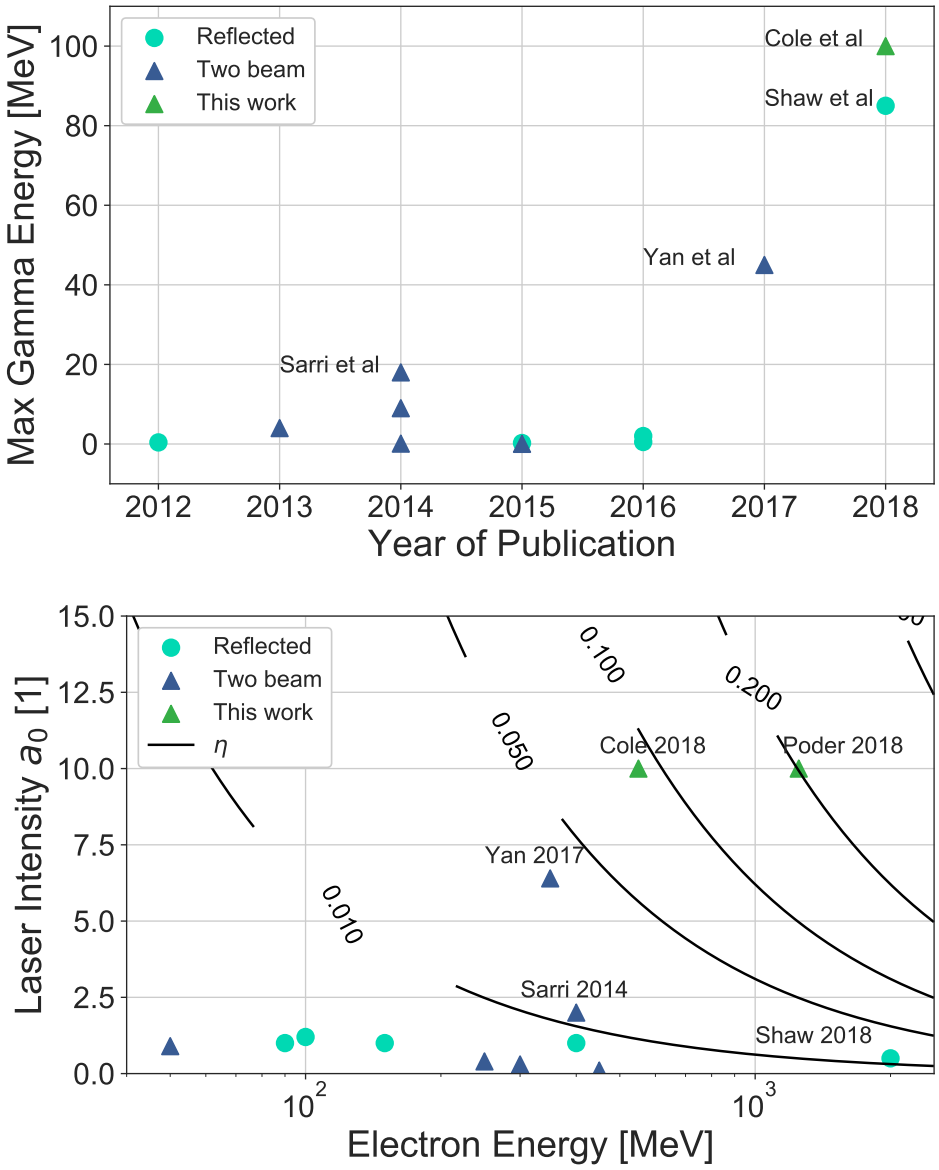


Figure 6.1: Comparison of all-optical ICS experiments using LWFA. The circles (cyan) indicate one-beam experiments that use a plasma mirror to reflect the LWFA driver beam and scatter off the electron bunch it accelerated before. The triangles (blue and green) indicate experiments that used two laser beams, one to accelerate electrons from LWFA and one separate laser to scatter off them. Top: Maximum gamma energies measured and their year of publication. Bottom: Electron energies and laser intensities in recent ICS experiments using LWFA. The contour lines indicate the corresponding values of the quantum nonlinearity parameter η.

6.2 Chapter Outline

The work presented in this Chapter relates to an experiment aimed at measuring radiation reaction through inverse Compton scattering (ICS). It was performed at the GEMINI laser facility in late 2015. Our experimental team succeeded in colliding electrons of energy $\epsilon \approx 550\,\mathrm{MeV}$ at a laser intensity of $a_0 \approx 10$, reaching critical gamma-ray energies, ϵ_{crit}, in excess of 30 MeV. This was the highest gamma-ray energy from an all optical ICS source published at that point and consists the first published measurement of radiation reaction in an LWFA setup [162].

This Chapter includes significant contributions to this publication, in particular devising a method to identify successful collisions and characterise the electron spectra. As a result, the reader will find several parallels and in some instances a similar line of arguments between [162] and this Chapter.

In order to make a measurement of radiation reaction, we need to observe that when a laser-electron beam collision occurs the electron energy is lower. However, in a laser wakefield accelerator (LWFA) experiment there are two key challenges: first, the electron spectrum varies from shot to shot, and second, not all attempted collisions will be successful. To overcome these difficulties, the statistical fluctuations of the electron beam need to be characterised when there is not a collision, and the sub-set of successful collisions needs to be identified.

After an outline of the experimental setup in Section 6.3, such a method to identify successful collisions is presented in Section 6.4. For this purpose, the yield on the gamma detectors is correlated with the energy in the electron beam on a shot-to-shot basis. Without the second scattering beam, the measured radiation is produced from bremsstrahlung as dispersed electrons interact with the walls of the vacuum chamber. It is assumed that the second laser adds ICS as an additional source of radiation and that particularly intense interactions produce a significant excess signal on the gamma detector.

The Chapter continues in Section 6.5 with an analysis of the electron spectra measured in this dataset. The electron spectra consistently exhibit a distinct spectral feature in shape of a sharp edge-like fall-off in charge at $\sim 550\,\mathrm{MeV}$ (see Figure 6.7). The intrinsic fluctuations of the electron source are characterised in a statistical analysis after removing correlations.

Then key results from the analysis of the gamma spectra, performed by Jason Cole (Imperial College London) and Keegan Behm (University of Michigan), are introduced. The spectra are inferred by fitting the simulated response of the detector, a stack of scintillating caesium-iodide (CsI) crystals, to the signal measured in the experiment. Details of this procedure can be found in [162, 263] or Section 4.6.2 of the Experimental Methods. Combining all of the previous results, the measurements are compared to

different models of radiation reaction to explore whether they are in agreement.

Finally, the electron spectra from this experiment are compared to a second measurement of radiation reaction at the same laser system using a gas cell target, and colliding electrons of up to 2 GeV energy at $a_0 \approx 10$ [163]. The analysis of the stability of the electron energies of both measurements are used to estimate the minimum number of successful collisions one would require in an experiment to reach a 'discovery' 5σ level of confidence that a model excluding energy loss from radiation reaction is not describing the data accurately. In [179, 180] this discussion is expanded to a wider set of parameters and the discrimination of different models of radiation reaction, but this is beyond the scope of this thesis.

6.3 Experimental Setup

The experiment described in the following was conducted at the dual 300 TW Ti:Sa GEMINI laser system at the Central Laser Facility, Rutherford Appleton Laboratory, UK, in late 2015. Both arms provide two linearly polarised laser beams of central wavelength 800 nm at a pulse duration of 45 ± 5 fs FWHM and collimated beam diameter of ~ 150 mm before being focused. A sketch of the setup is shown in Figure 6.2.

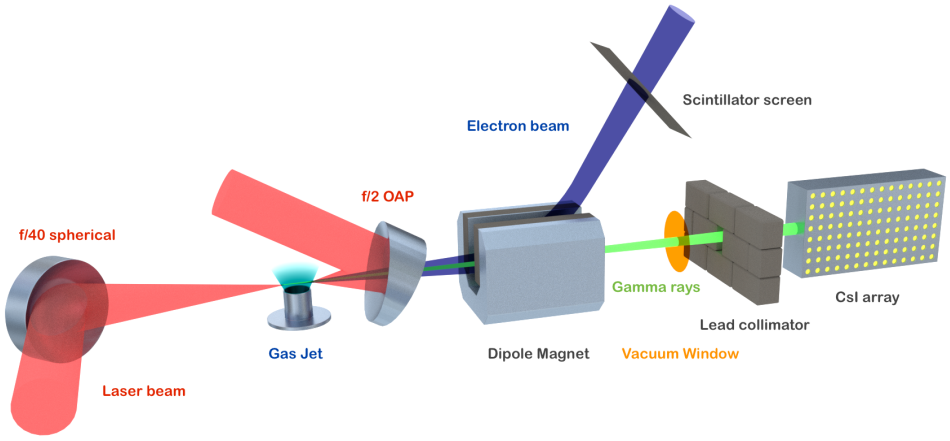


Figure 6.2: Conceptual sketch of the experimental setup, rendered with Blender. Based on a sketch made by J. Cole (Imperial College) for [162], adapted for this work and for [263]. From left to right: a high intensity laser beam (red) focused with an $f/40$ spherical mirror generates GeV*-scale electrons (blue) in a gas jet (LWFA). A second laser beam (red) is focused down tightly at the edge of the gas jet by an $f/2$ off-axis parabola (OAP) to scatter the electron beam shortly after it leaves the jet. The electrons are dispersed by a dipole magnet and detected on a scintillating lanex screen (grey). Finally, gamma rays (green) emitted in the interaction propagate through a Kapton vacuum window (orange) and a lead aperture onto a stack of scintillating CsI crystals acting as gamma detector.*

The first part of the experiment is set up to produce a relativistic electron bunch from laser wakefield acceleration (LWFA): a laser beam, linearly polarised in the horizontal plane, is focused down by an $f/40$ spherical mirror with 6 m focal length onto the leading edge of a 15 mm conical supersonic helium gas jet target. The top edge of the gas jet is positioned 6 mm below the laser axis in order to avoid damage to the nozzle from the second, more divergent laser beam. Electrons are accelerated via LWFA and propagate further downstream, where they are dispersed by a permanent dipole magnet of integrated field strength $\int B(x)\mathrm{d}x = 0.4\,\mathrm{Tm}$ onto a scintillating standard Lanex screen, which is imaged by a cooled 16-bit CCD camera (Andor Neo) to measure their spectrum. The typical FWHM focal spot of the driving laser pulse measures $37 \times 49\,\mu\mathrm{m}$ with an energy on target of $(8.6 \pm 0.6)\,\mathrm{J}$, which corresponds to a normalised vector potential $a_0 = 1.9 \pm 0.1$. The electron density of the target was interferometrically measured to be $(3.7 \pm 0.4) \times 10^{18}\,\mathrm{cm}^{-3}$.

The second laser beam, linearly polarised in the vertical plane, is focused down tightly onto the opposite edge of the gas jet, at 180 degrees from the driver laser, using an $f/2$ off-axis parabola (OAP). This laser is used to scatter from the electron bunch accelerated through LWFA to generate a bright flash of gamma rays from inverse Compton scattering (ICS). The OAP is fitted with a central hole, 21 mm in diameter, to enable propagation of the electrons, gamma rays and the remaining laser light of the $f/40$ wakefield driver beam. In addition, a plastic ring of 28 mm radius around the hole protects the optics and the laser chain upstream from potential driver laser light scattered in an interaction with the plasma. The combined loss of reflective surface leads to a decrease in intensity of the flat-top beam of around 16%. The energy on target was typically $(10 \pm 0.6)\,\mathrm{J}$ focused into a spot of $2.4 \times 2.8\,\mu\mathrm{m}$ FWHM, corresponding to a peak normalised vector potential of $a_0 = 24.7 \pm 0.7$. The peak value of the quantum non-linearity parameter, η, in a head-on collision is $\eta = 2\gamma a_0 \hbar\omega_0 / m_e c^2$. Based on the laser parameters, the maximum values of η achievable in this configuration are $\eta = 0.15$ for electrons at 0.5 GeV and $\eta = 0.3$ at 1 GeV electron energy, respectively.

The two laser beams are overlapped in space and time using spatial interferometry as detailed in Section 4.3 of the Experimental Methods.

The narrow cone of gamma rays from ICS propagates through the hole of the $f/2$ OAP, the aperture of the dipole magnet, then through a $50\,\mu\mathrm{m}$ aluminium laser beam block and finally leaves the vacuum chamber through a $250\,\mu\mathrm{m}$ thick Kapton vacuum window. In air, the gamma rays are incident onto a stack of caesium-iodide (CsI) crystals that measures the spectrum of the high energy radiation and is imaged by a cooled 14-bit EMCCD camera (Andor iXon). More details on the composition of the detector can be found in

Section 4.6.2 (labelled 'RAL stack with steel front plate'). The entire stack is housed and shielded in a lead enclosure with a circular aperture of 15 mm diameter, corresponding to an acceptance angle of 6.8 mrad at 2.2 m from the interaction point.

6.4 Identifying Successful Collisions

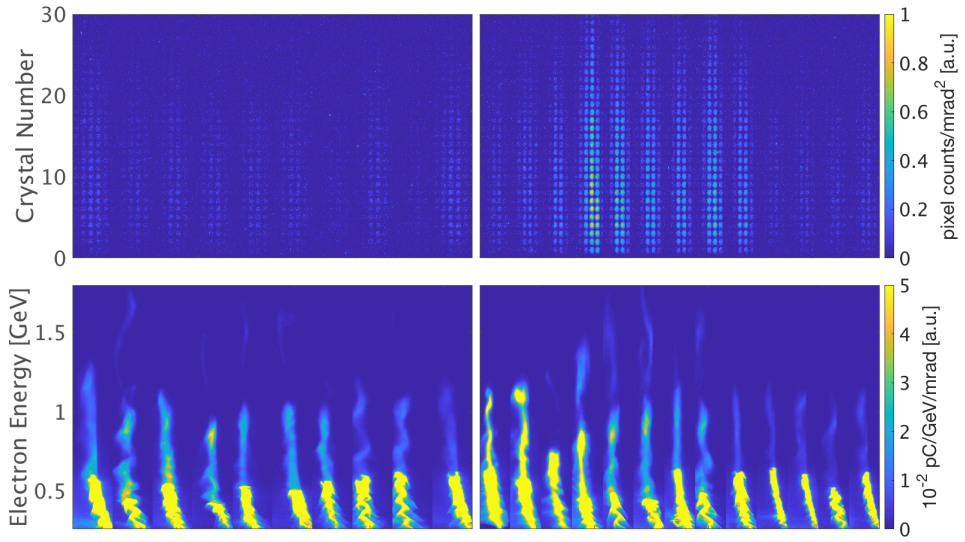


Figure 6.3: Montage of images from the gamma ray spectrometer (upper row) and electron spectrometer (bottom row) at shots with the colliding laser beam off (left) and on (right), using the same colour scale. Some shots with the colliding beam show bright signals on the scintillator array that indicate a successful collision.

To identify successful collisions, we compare the radiation yield from the electron beams with and without scattering laser, as measured with the gamma detector (see Figure 6.3). The electrons will emit broadband bremsstrahlung with photon energies extending up to the maximum electron energy when interacting with matter in their trajectory [52]. Especially high-Z materials such as the vacuum chamber walls are efficient converters. This radiation is in a spectral range comparable to the expected ICS signal and is also measured by the gamma-ray detectors. The electrons are dispersed upwards and collide with the roof of the aluminium vacuum chamber producing the main source of bremsstrahlung. It is located off-axis and a large fraction is shielded efficiently by blocking the direct line of sight with sufficient amounts of lead. This reduces the total background signal on the detector and improves the signal-to-noise ratio, but also allows a spectral retrieval of the bremsstrahlung component as it now only enters the stack from one defined side.

The total energy emitted through bremsstrahlung by a relativistic electron is proportional to its energy squared (e.g. [52] and Section 2.2.4). The total energy deposited in the caesium-iodide crystals of the gamma spectrometer is assumed to convert linearly into

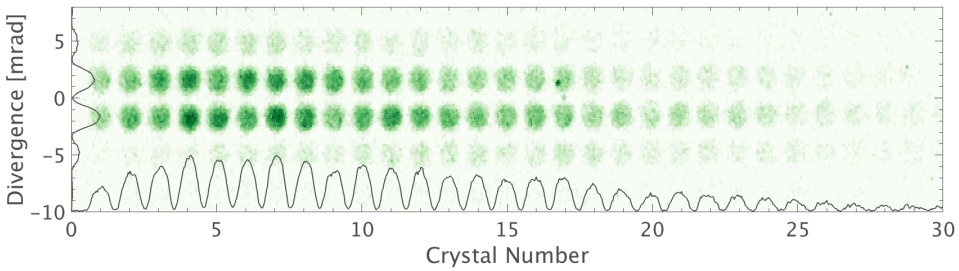


Figure 6.4: Example of a measured gamma-detector signal. The gamma rays propagate from the left into the stack and deposit their energy. Higher energy radiation penetrates the stack deeper. The y-axis indicates divergence.

scintillation light [258] at an efficiency of $\approx 5 \times 10^4$ photons/MeV. The total yield of the detected bremsstrahlung signal on the camera chip, S_{BG}, should then follow this relation:

$$\boxed{S_{BG} = c_{BG} \int_{\gamma_{min}}^{\gamma_{max}} [\mathrm{d}N_e/\mathrm{d}\gamma]\ \gamma^2 \mathrm{d}\gamma \approx c_{BG} Q \left\langle \gamma^2 \right\rangle ,} \tag{6.4.1}$$

where c_{BG} is a constant in units of [pixel counts $\mathrm{pC}^{-1}\,\mathrm{MeV}^{-2}$] that encapsulates the complicated details of the interaction and the experimental setup that remain the same over the course of the shots, such as the conversion efficiencies of electron energy to bremsstrahlung photons, photons depositing their energy in the detector crystals, number of photons emitted from the scintillator per deposited energy, viewing angle of the camera, collection efficiency of the imaging system, and quantum efficiency of the camera. $\mathrm{d}N_e/\mathrm{d}\gamma$ is the charge distribution of the measured electron spectrum, $Q = \int (\mathrm{d}N_e/\mathrm{d}\gamma)\mathrm{d}\gamma$ the total charge and γ is the relativistic Lorentz factor of the electrons. Other sources of background (dark field, stray light on the camera etc.) are removed efficiently and do not need to be included in this equation. By measuring the total counts (yield) on the gamma detector and the electron spectrum, one can then determine c_{BG} experimentally.

Figure 6.5 shows the relation of the experimentally measured $Q \left\langle \gamma^2 \right\rangle$ to the total number of pixel counts (yield) on the gamma-ray detector for 10 shots without the scattering beam (blue). Figures 6.7 and 6.4 show examples of an electron spectrum and the gamma detector. The data points follow a linear trend with a slope corresponding to c_{BG} at a linear correlation coefficient of 0.71.

Successful collisions of the electron bunch and the scattering beam produce a beam of gamma rays from inverse Compton scattering (ICS). At the detector, the signal is then a combination of bremsstrahlung as without the scattering beam, following the same relation with slope c_{BG}, and the ICS signature. The emitted energy of the ICS radiation and hence the resulting detector signal, S_{ICS}, is also proportional to γ^2, similarly as for

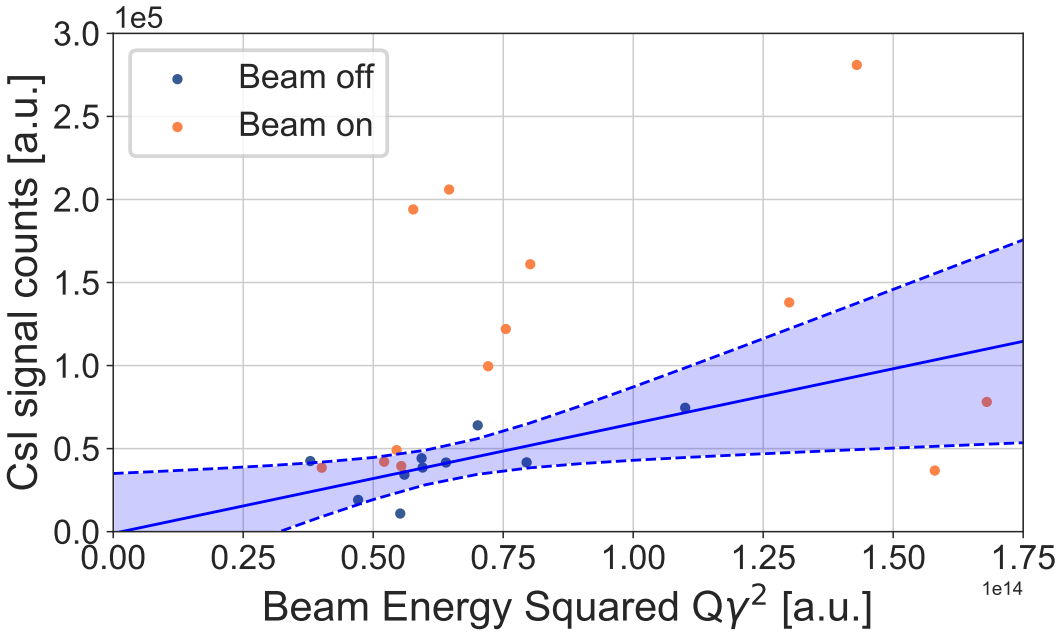


Figure 6.5: Yield on the gamma detector in pixel counts (y-axis) as a function of the squared electron beam energy (x-axis). The reference shots without the scattering beam are indicated in blue with a regression line, where the gradient corresponds to c_{BG}. The shaded region indicates the 95% confidence interval. In orange shots with both laser beams on.

the bremsstrahlung process, but also scales with the normalised vector potential a_0 in interaction with an electron with energy γ, valid for $\gamma a_0^2 < 5.5 \times 10^5$ [80, 133]:

$$\boxed{S_{ICS} = c_{ICS} \int a_0^2 \left[\mathrm{d}N_e/\mathrm{d}\gamma\right] \gamma^2 \mathrm{d}\gamma,} \tag{6.4.2}$$

where now c_{ICS} similarly encapsulates all the complex physics of coupling constants, the imaging system, cross sections and conversion efficiencies. In this case, the value of a_0 at the interaction is not constant from shot to shot as a varying overlap of the laser pulse and the electron beam will result in changing interaction conditions. a_0 can also vary throughout the interaction, if the duration of the interaction is comparable to the time it takes for the laser pulse to pass through its focus, either due to a short Rayleigh length or long electron bunches [303]. The better the overlap and the higher the intensity at the interaction, the stronger the ICS signal and the easier will it be to distinguish from the background bremsstrahlung. In addition, whilst we expect all of the electrons to produce bremsstrahlung, only a variable fraction of electrons will interact with the laser pulse. If the laser pulse is larger than the electron beam, the variation in intensity the electrons experience will be reduced.

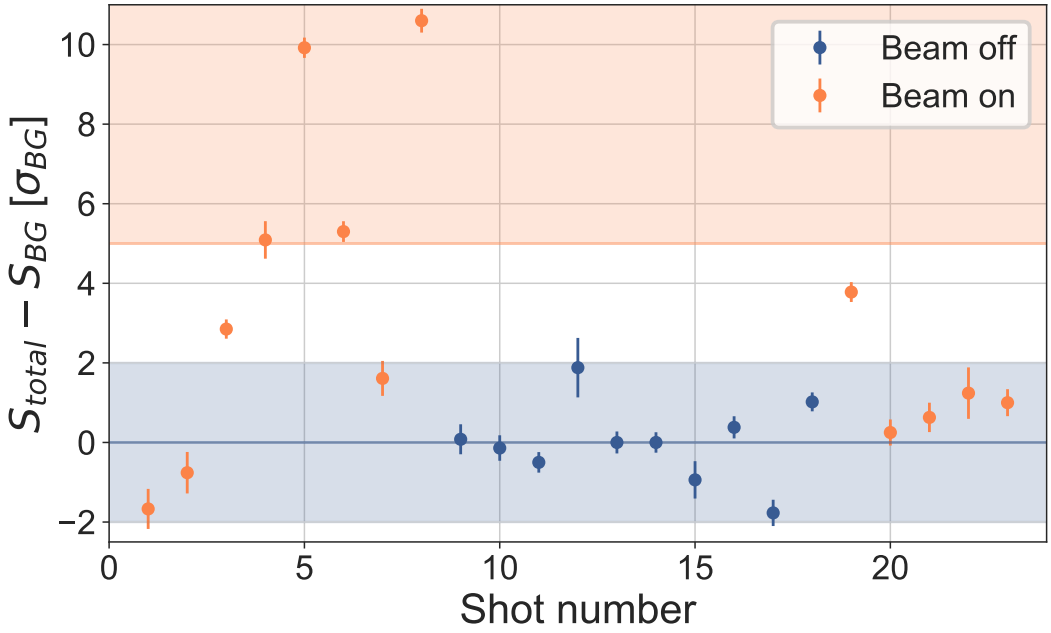


Figure 6.6: Deviation from the expected background gamma signal in units of the standard deviation of the background, σ_{BG}, as a function of the shot number (order data was taken) without the scattering beam on (blue) and with both laser beams (orange). The shaded blue area indicates a 2 sigma interval for the background centred around zero (blue line). The orange line at $5\sigma_{BG}$ and the shaded area above it indicates the parameter space satisfying our criterion for successful collisions, here including 4 shots. The absence of any successful collisions after shot 18 indicates a drift in alignment.

The total signal measured on the detector, S_{total}, combines to

$$S_{total} = S_{BG} + S_{ICS} = c_{BG} \int [\mathrm{d}N_e/\mathrm{d}\gamma]\ \gamma^2 \mathrm{d}\gamma + c_{ICS} \int a_0^2\, [\mathrm{d}N_e/\mathrm{d}\gamma]\ \gamma^2 \mathrm{d}\gamma. \tag{6.4.3}$$

In Figure 6.5, the shots with the scattering beam (orange) are more spread than the shots without the colliding beam (blue). Some of the data points with the colliding beam follow the linear relationship determined for the reference data relatively well. This indicates poor overlap of the electron bunch with the scattering beam. A few shots exhibit a much higher detector signal than predicted by the fit for an electron spectrum of comparable charge and energy, signalling good overlap.

To quantify how much higher the detected signal is than predicted by the background fit, it is more useful to look at the difference of measured to expected signal, i.e. by subtracting the expected bremsstrahlung background from the total signal to extract the ICS contribution:

$$S_{ICS} = S_{total} - c_{BG} Q \left\langle \gamma^2 \right\rangle, \tag{6.4.4}$$

or in relative terms:

$$S_{ICS,rel}(Q\left\langle\gamma^2\right\rangle) = \frac{S_{ICS}}{c_{BG}Q\left\langle\gamma^2\right\rangle} = \frac{S_{total} - c_{BG}Q\left\langle\gamma^2\right\rangle}{c_{BG}Q\left\langle\gamma^2\right\rangle}. \tag{6.4.5}$$

For shots without the scattering beam, the ICS signal, S_{ICS}, determined by this method and $S_{ICS,rel}$ fluctuate around a mean of zero. Assuming a normal distribution we can calculate the standard deviation σ_{BG} of the fluctuating background and estimate how likely a bright gamma signal would be produced by the characterised background signal:

$$S_{ICS,norm} = \frac{S_{ICS,rel}}{\sigma_{BG}} \tag{6.4.6}$$

Figure 6.6 presents the shots in the order their data was taken in the experiment. The normalised signal above expected background, $S_{ICS,norm}$, is indicated on the y-axis, which now encapsulates the information of both the gamma signal and the electron spectrum. As we can see, most of the shots follow the expected trend within 2 standard deviations (shaded blue area), with some exceeding this. 4 shots show a signal more than 5 standard deviations higher than expected from background measurements (shots in shaded orange area). Based on a normal distribution, the probability for one shot to be as bright as 5 standard deviations above the mean background is 1 in 3,500,000. This is very unlikely and hence a suitable confirmation that these are successful collisions.

$$S_{ICS,norm}[\sigma_{BG}] \begin{cases} \text{if } \geq 5 & \longrightarrow \text{Successful Collision} \\ \text{if } 5 < x < 1 & \longrightarrow \text{Partial Overlap} \\ \text{if } \leq 1 & \longrightarrow \text{No Collision} \end{cases} \tag{6.4.7}$$

This method not only allows the identification of successful collisions, but on the other hand also enables us to identify collisions where ICS was negligible on dual-beam shots if the normalised excess signal is for instance within one standard deviation of zero.

6.5 Characterisation of the Electron Spectrum

In the previous section, the comparison of the measured gamma-ray signal with the expected bremsstrahlung noise produced by the electron beam enabled the identification of successful collisions. The next step is to quantify whether there was a measurable lower energy (potential energy loss) visible in the electron spectrum on these collisions and to estimate the statistical significance of this.

To estimate the energy loss accurately, we have to take the intrinsic variations of the electron source and correlations to other fluctuating variables such as the laser energy into account. For this purpose, we will characterise the typical electron spectrum and its

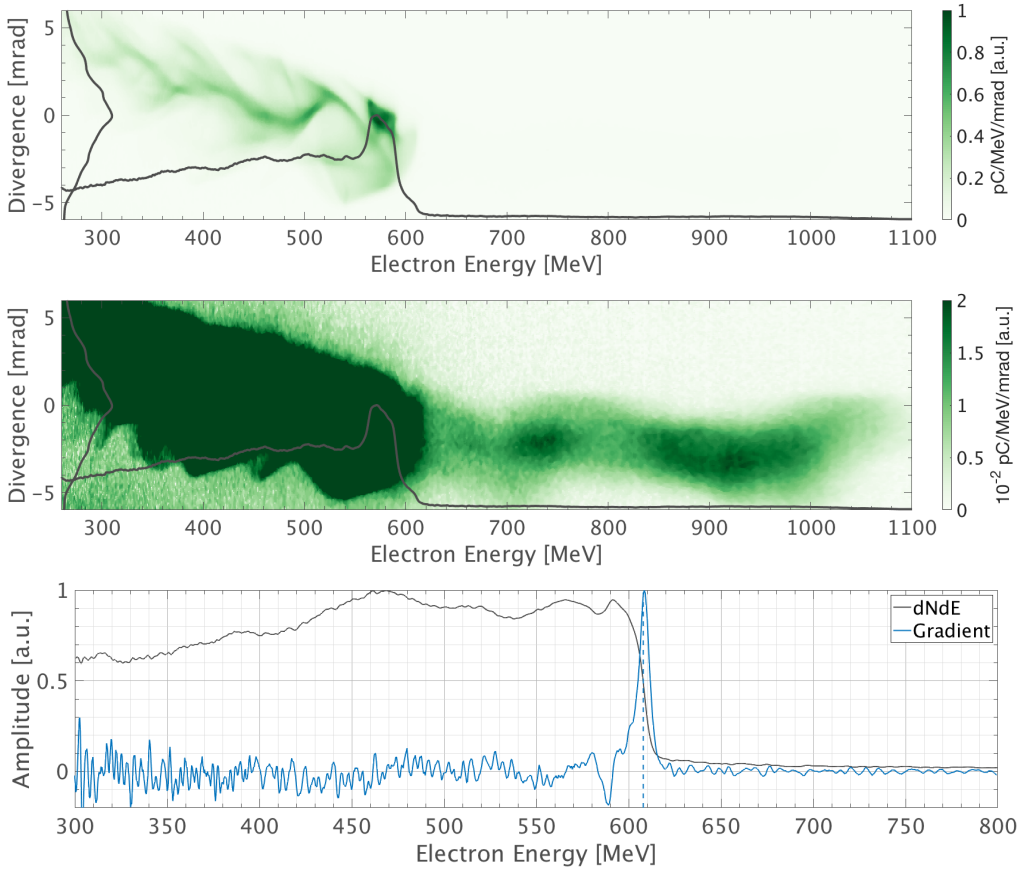


Figure 6.7: Top/centre: Example of a typical electron spectrum measured in the experiment. The x-axis indicates the energy, the y-axis the divergence of the electrons. The spectrum is integrated in the dispersion and divergence axis and shown on the respective axes. The colour scale indicates the charge per divergence and energy (pC per mrad and MeV) scaled to the maximum value in the image (top) or saturated by a factor 50 to show the low-charge high-energy tail of the e-beam (centre). Bottom: Lineout of an electron spectrum (grey) normalised to its peak charge as a function of electron energy. The first derivative of the spectrum (blue) exhibits a sharp peak at the edge-like spectral feature around 600 MeV *(dashed blue line). This peak is used to identify the spectral feature on a shot-to-shot basis.*

statistical fluctuations for shots without the scattering beam or where ICS is negligible based on the previous argument.

Characterising a typical spectrum

The characteristic electron spectrum consists of two components (see Figure 6.7): one is a low charge but high energy tail reaching $800 - 1000$ MeV (centre), the other part contains a high charge at lower energy that falls off rapidly at an edge-like spectral feature at around 550 MeV (top). The position of this spectral feature is identified by finding a maximum in the derivative of the integrated spectrum (bottom). The electron spectrum is cut off at 250 MeV due to limitations in the spectrometer setup. The high energy component resembles spectra from self-injection [311] measured at GEMINI before (see for instance

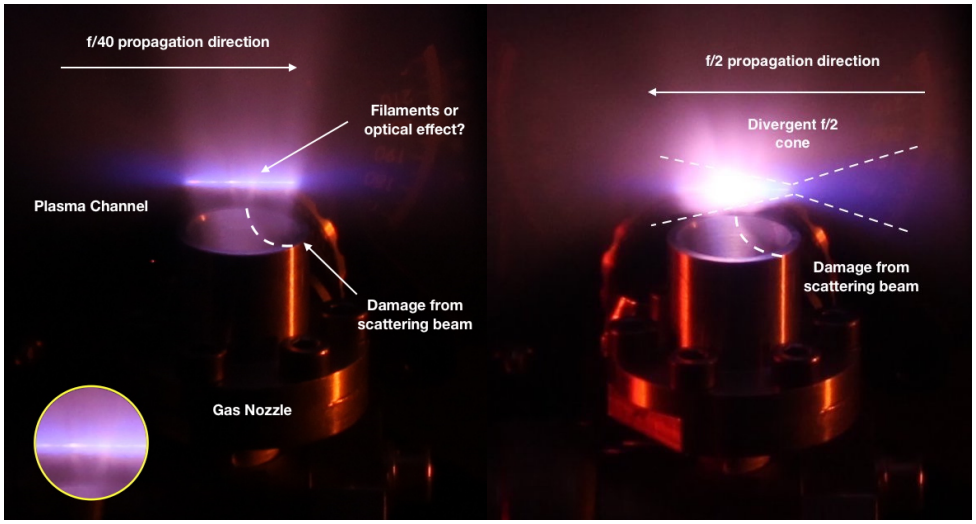


Figure 6.8: Photograph of the plasma channel and plasma self emission taken with a Canon DSLR camera. A supersonic helium gas jet is traversed by the wakefield driver beam from left to right forming a plasma channel (left image). A second divergent beam arriving from the right side is used to scatter off electrons accelerated in the wakefield, producing a bright and divergent cone of emission on top of the channel (right image). The gas nozzle was scorched by the divergent beam and rotated by 180 degrees. Subsequently, the nozzle was lowered to avoid further damage. Apparent structuring in the plasma channel (left, zoomed in) could indicate density perturbations or could be an optical effect.

[69]). The high charge component with the distinct spectral feature is consistent with shock injection [230] measured at GEMINI, e.g. see Chapter 5, potentially caused by either the nozzle design or potential damage to it. The optical image seen in Figure 6.8 indicates some damage to the nozzle. Shock injection has been observed by other groups introducing a blade [228, 230, 275, 276] or a wire [312] into the supersonic gas flow to generate a shock front. Note that the electron beams observed at GEMINI are qualitatively different from these results and the high quality properties commonly associated with the term 'shock injection' in literature.

Extending the dataset for the statistical analysis of the electron source

The dataset that includes the potential high-intensity interactions and its immediate null shots is relatively limited with 23 shots in total, 10 of which are reference data without the scattering beam. A small sample size like this (10) is not sufficient to draw reliable conclusions about the general character of the fluctuations of the accelerator, i.e. more reference data is required. In order to gain access to a larger pool of reference shots, we now consider a second dataset that was taken immediately after the small dataset discussed so far. Here the accelerator was operated at comparable conditions, i.e. the general properties of the electron beam are the same, but the scattering beam was strongly defocused, such that interactions only occurred at low intensities ($a_0 < 1$) without measurable effect of

radiation reaction. The scattering beam was active on all shots and translated relative to the electron beam, such that now radiation from linear ICS was produced at varying overlap. In order to obtain 'clean' reference shots without any significant interaction between the scattering beam and the electron bunch, we only consider shots with a gamma-ray yield within 1 standard deviation of the expected background. This additional set of references consists of 89 shots, and will help to investigate correlations with other experimental parameters and to characterise the 'intrinsic' fluctuations of the accelerator statistically.

Temporal drift in the electron energy

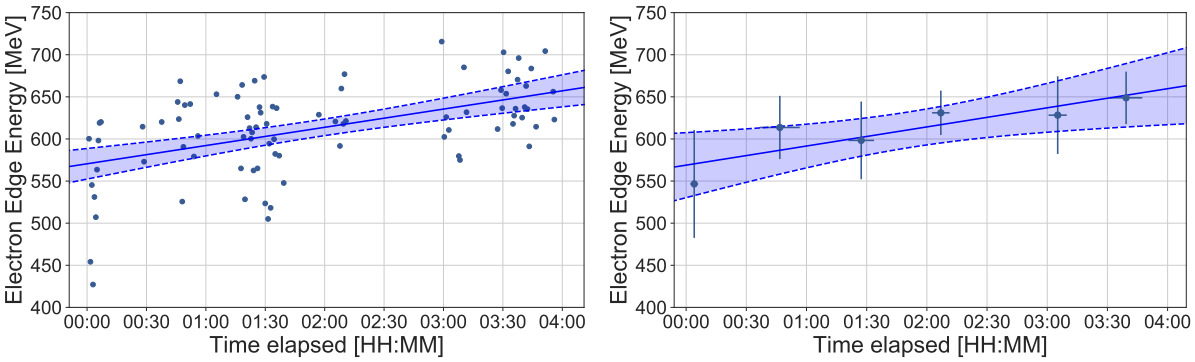


Figure 6.9: Left: Distribution of the energy of the spectral feature for null shots or negligible ICS signal plotted as a function of the relative time the data was taken. The energies are scattered around a line that slowly increases with time. A regression with corresponding 95% *confidence interval (shaded area) is drawn. Right: By assuming a random distribution around a slowly drifting mean the dataset was split into individual time slices. The data points show the average energy of the spectral feature within the individual time slices as a function of the elapsed time. The error bars indicate the standard deviation in time and energy assuming a normal distribution.*

When tracing the time the data was taken and the electron energy of the spectral feature, a slow drift in the mean energy becomes apparent (see Figure 6.9). The correlation coefficient for the driver laser energy over time is -0.11, and the 95% confidence interval for the slope of the linear regression includes negative and positive values. This indicates that the mean laser energy does not drift significantly over this time period, and only fluctuates around a constant or very slowly decreasing mean (see Figure 6.10). The same applies to the injected charge at a correlation coefficient of -0.13.

Self-injection depends strongly on the evolution of the laser in the medium and hence on the performance of the laser. If the mean electron energy increases over time without changes to the laser properties and energy, changes in the medium can be suspected to have caused this drift. The appearance of the high charge component of the spectrum is consistent with other electron beams injected through shock features at Gemini (see

Chapter 5). The shock could be generated due to a damage in the gas nozzle (see Figure 6.8) or intrinsically due to its design. The drifting mean is consistent with a shock shifting position closer to the leading edge of the gas target, increasing the acceleration length and energy over time. This behaviour typical for shock injection has been observed at lower intensities at other laser systems, typically though producing narrow energy spread beams [228, 230, 276]. The self-emission of the plasma appears to show some structuring which could indicate density modulations (see Figure 6.8). Unfortunately, there is no optical probe data, e.g. from a shadowgraphy or interferometry, to provide conclusive evidence in form of density measurements for this theory. Progressing damage to the nozzle material could provide the seed for a shifting shock position.

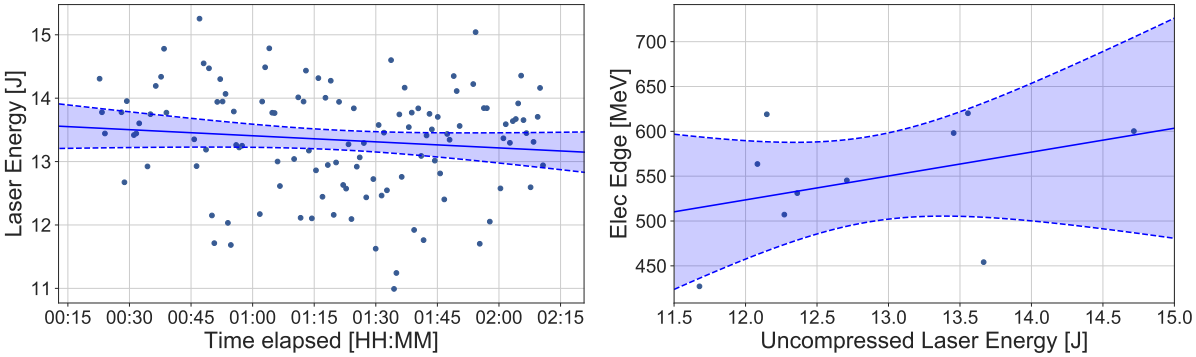


Figure 6.10: Left: On-shot driver laser energy as a function of elapsed time. The dataset is truncated earlier than in Figure 6.9, since this diagnostic failed about 2 hours into the measurement. Right: Correlation of laser energy with spectral feature for the core dataset.

Despite the lack of conclusive evidence to explain the origin of the drift, we can measure and account for it when characterising the intrinsic fluctuations of the electron spectrum. We split the varying components into two parts: one is random noise fluctuating from shot to shot, the second is the mean around which the fast fluctuations take place, which is slowly increasing with time. The increase of the mean correlates well with time at a correlation coefficient of 0.86 at a rate of 21.6 MeV/hour.

After removing the slow drift from the data, we can check if the remaining fluctuations correlate with the on-shot laser energy and the injected charge. There appears to be a correlation but only at a coefficient of 0.35 (0.22 with drift) across the entire dataset and even lower for the potential high-intensity dataset. The same holds for the injected charge at a correlation coefficient of 0.39 (0.38 with drift). The gradient of the regression is small compared to the shot-to-shot fluctuation in the laser energy and the 95% confidence interval indicates no significant correlation (see Figure 6.10, right). We will hence ignore this factor in our analysis.

Intrinsic statistical fluctuations of the accelerator

Any deviation in energy $\Delta\epsilon$ from this slow drifting mean now represents a characteristic intrinsic fluctuation of the accelerator. Figure 6.11 shows a histogram of relative differences in energies, $\Delta\epsilon/\epsilon$, along with an estimate of the underlying density distribution using a Kernel Density Estimate (KDE) and a Gaussian fit. The Gaussian fit agrees with the 99% confidence interval of the KDE, but there seems to be a slight skew in the distribution.

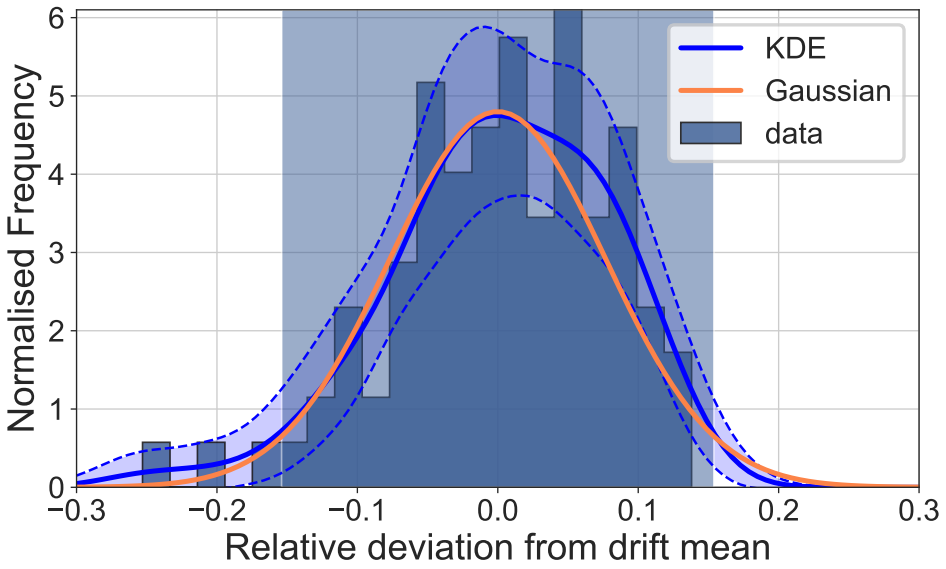


Figure 6.11: Histogram of relative deviation of the spectral edge energy from the expected slowly varying mean ($\Delta\epsilon/\epsilon$). The total distribution is overlaid with a KDE, its 95% confidence intervals and a Gaussian distribution (orange). The shaded area indicates a 2 sigma (95%) confidence interval assuming a normal distribution.

Continuing with the assumption of a normal distribution we can assign probabilities to observing certain energies. The standard deviation of this distribution is $\sigma_{Cole} = 7.7\%$. In other words we expect 68 percent of all shots to take a value of $\Delta E/E$ between $\pm 7.7\,\%$ ($1\,\sigma_{Cole}$), and 95 percent between $\pm 15.4\,\%$ ($2\,\sigma_{Cole}$).

Electron spectra in the collision dataset

Having now characterised the fluctuations of the energy of the spectral feature in the electron beam, we can estimate how likely it is that we measure low energies by chance or at what confidence this could be due to energy loss from radiation reaction. The collision dataset was taken over the course of ~ 20 minutes, such that the slow drift identified in the previous section becomes negligible and is not included in the following analysis.

In the previous section, we identified 4 successful collisions. The corresponding electron spectra on those four shots exhibit a lower energy for the edge-like spectral feature than

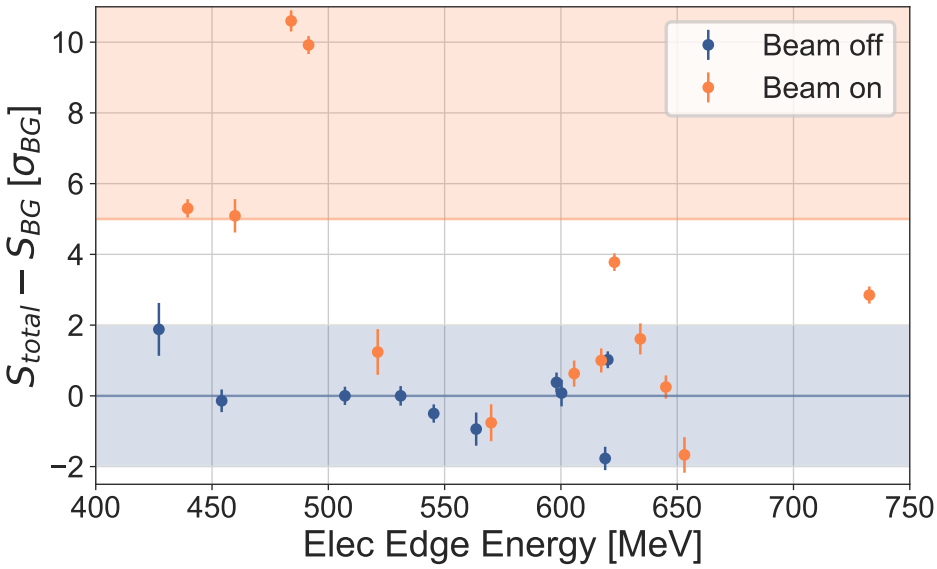


Figure 6.12: Gamma ray signal above the expected radiation background (y-axis) in units of standard deviation from the reference mean as a function of the electron energy of the spectral edge feature (x-axis). Reference shots without the scattering beam ('beam off') are shown in blue, dual-beam shots ('beam on') are indicated in orange. The 2 sigma interval of the reference shots is shaded in blue, whereas the parameter space for successful collisions is shaded orange.

on most of the other shots. Figure 6.12 shows a plot of the electron energy of the spectral feature and its relation to the excess signal on the gamma detector.

For a normal distribution of mean 550 MeV and a standard deviation $\sigma_{Cole} = 7.7\%$, the cumulative probability to observe a spectral feature below 500 MeV on one shot is 12%. To observe this on all four successful collisions is then $(12\%)^4 = 0.02\%$. We conclude that the lower energies measured on these shots are due to energy loss in the successful collision and statistically significant.

To estimate whether the energy loss relates to a realistic intensity at the interaction, we use the analytic expression for energy loss from the classical Landau-Lifschitz radiation reaction force for a plane wave with a Gaussian temporal envelope, valid for $\gamma a_0 \ll 1.6\times10^5$ [133]:

$$\frac{\Delta\gamma}{\gamma_0} = \frac{\sqrt{\pi/2}\tau_0 t_L \omega_0^2 \gamma_0 a_0^2}{1+\sqrt{\pi/2}\tau_0 t_L \omega_0^2 \gamma_0 a_0^2}, \tag{6.5.1}$$

where $\tau_0 = e^2/6\pi\epsilon_0 m_e c^3 = 6\times10^{-24}$ s, the pulse duration $t_L = 45$ fs, the wavelength be $\lambda = 800$ nm. We then solve for the normalised vector potential

$$a_0 = \sqrt{\left[\frac{\Delta\gamma/\gamma_0}{1-\Delta\gamma/\gamma_0}\right]\frac{1}{\sqrt{\pi/2}\tau_0 t_L \omega_0^2 \gamma_0}}. \tag{6.5.2}$$

For an 80 ± 10 MeV energy loss from the mean of 550 ± 20 MeV down to 470 ± 10 MeV, for instance, we obtain $a_0 = 8.9 \pm 1$. In a quantum model, on the other hand, the required peak intensity to effect the same energy loss is 10 ± 2 as electrons lose energy at $\approx 75\%$ the rate as in a classical model [132]. This is lower than the estimated peak intensity of $a_0 \sim 25$ reachable at the focus of the laser, based on the measured laser energy and the focal spot characterised in the experiment. This mismatch will be investigated in the following section.

6.6 Estimating the laser intensity at the interaction

The intensity of the laser pulse estimated through the energy loss is significantly lower than the peak a_0 achievable in this geometry. Since the calibration of the on-shot laser energy measurement is relatively reliable, this indicates a spatio-temporal offset and that the interaction is not occurring at the focal plane of the laser.

The two laser pulses were synchronised in vacuum using spatial interferometry to an estimated accuracy of 30 fs. This timing is only valid if both laser pulses travel through vacuum. In a shooting scenario, however, the driving laser pulse propagates through plasma to accelerate electrons via LWFA. The propagation in a medium reduces the group velocity of the laser pulse and delays its arrival relative to the vacuum timing. In addition, we are trying to overlap the scattering beam with the electrons accelerated by the driver pulse, not the driver itself. The LWFA electron bunch trails behind the driving laser pulse and arrives even later at the interaction point. Since the scattering beam arrives before both at its focal plane and the designated interaction point, the real collision will occur beyond this point and at a slightly defocused spot size. To estimate the intensity of the laser pulse at the interaction, we have to determine the real collision point and the size of the scattering beam at this plane. For this purpose we can use Equation (4.3.8) derived in Section 4.3.3 to determine the distance δz from the intended collision point [162]:

$$\boxed{\delta z = \frac{3d}{4}\frac{n_e}{n_c} + N\frac{\lambda_0}{2}\sqrt{\frac{n_c}{n_e}},} \tag{6.6.1}$$

where d is the distance of the injection point from the front of the gas jet, n_c the critical density, n_e the density of the plasma, λ_0 the wavelength of the laser, and N the number of plasma wavelengths the electron bunch is trailing behind the laser pulse ($N = 1/2$ at the dephasing limit).

For a normal distribution of ± 30 fs of the relative temporal jitter and by sampling from a uniform distribution for the injection point d between 0 and 10 mm, the intensity expected at the interaction averaged over an area of 10 μm^2, the estimated size of the

electron beam and its spatial shot-to-shot fluctuations, reaches $a_0 = 12 \pm 1$ [162].

Estimating Collision Probability based on Jitter

With knowledge of the approximate focal spot size at the interaction and realistic spatio-temporal fluctuations, we can estimate the number of successful collisions we would expect under these conditions. These calculations have been performed by Jason Cole (Imperial College) and Chris Baird (York) by running Monte-Carlo simulations based on the spatio-temporal shot-to-shot jitter measured in the experiment and estimating the amount of radiation produced for different overlaps using particle-in-cell (PIC) simulations. It was estimated that 1 in 3 ($\sim 33\%$) collisions would under these circumstances be on average successful, which closely matches the observed 4 in 13 ($\sim 31\%$) successful collisions in this experiment.

6.7 Gamma spectra with and without interaction

For this work the spectral retrieval has been conducted by Jason Cole (Imperial College) and Keegan Behm (Michigan University), and their results will be presented in this context. More details on the procedure can be found in [162, 263] and also in Section 4.6.2 of the Experimental Methods as this technique is used in different variations to infer the spectra of high energy radiation in the other two experiments presented throughout this thesis (see Chapters 5 and 7).

The gamma spectra were inferred by analysing the signal on the gamma detector, a stack of scintillating caesium-iodide crystals (see Experimental Methods), and comparing the shape of the energy deposition throughout the detector with the detector response simulated in GEANT4 [262]. An example of the experimentally measured raw detector signal is shown in Figure 6.4.

In Section 6.4 we already established that the total counts on this diagnostic, related to the energy deposition and yield of the radiation on-shot, are composed of bremsstrahlung from electrons interacting with matter, such as the chamber walls, and the ICS signal. By characterising the relation between the electron beam and the bremsstrahlung signal, the excess yield is a useful indicator of successful collisions. If we consider not only the yield but also the spectrum of the gamma radiation itself, we expect to see different behaviour depending on whether there is a significant interaction between the electron beam or not: On shots without the scattering beam, the gamma detector characterises only the bremsstrahlung background. On shots with the scattering beam and sufficiently bright signal, the overlaying ICS signal will be dominant. On some shots with both beams, the

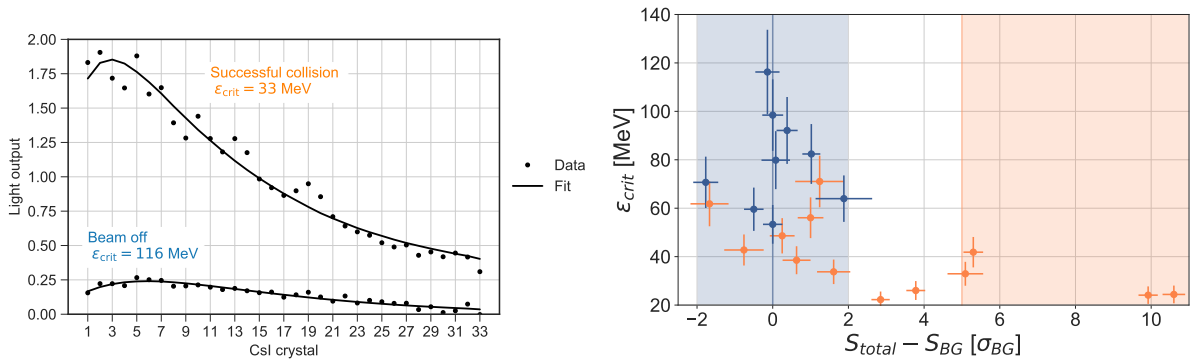


Figure 6.13: Left: Fitted detector response with critical energies for exemplary shots with scattering beam on and off, from [162]. Right: Fitted critical energies ϵ_{crit} (y-axis) as function of the yield on the gamma detectors above expected background (x-axis) with the $\pm 2\sigma$ interval for the background (blue shaded) and $> 5\sigma$ indicating successful collisions (shaded orange).

contribution of bremsstrahlung and ICS might be of similar level, so that the inferred characteristic energies take an intermediate level.

In simulations of the inverse Compton scattering process[1], it was found that the spectral shape of the expected radiation is well parametrised by

$$\frac{\mathrm{d}N_\gamma}{\mathrm{d}\epsilon_\gamma} \propto \epsilon_\gamma^{-2/3} e^{-\epsilon_\gamma/\epsilon_{crit}}, \tag{6.7.1}$$

where we used an exponential spectrum with a critical energy ϵ_{crit} as approximation to the high energy component of the synchrotron-like non-linear ICS spectrum. In this parametrisation about half of the energy is radiated below and above ϵ_{crit}, with a mean photon energy of $\epsilon_{crit}/3$.

Figure 6.13 (left) shows two examples of fits using this spectral shape: a single beam shot where we characterise only bremsstrahlung (blue) and a successful collision (orange). The successful collision is, as defined by our identification criterion, brighter than the bremsstrahlung shot. In addition, the critical energy of the fitted spectrum is lower for the collision than for bremsstrahlung only.

In Figure 6.13 (right), we now see the critical energies for all shots in this run, but this time with the yield on the detectors on the x-axis. We see that all shots with one beam only have high critical energies fitted to their detector response. The energies on shots with both beams that have low signal are also quite high. All shots that have a higher yield, however, decrease in critical energy and all identified shots are < 50 MeV.

[1] performed by Tom Blackburn (Chalmers) and Jason Cole (Imperial College)

Figure 6.14 considers how the critical energy of the fitted spectra changes with the energy of the measured electrons: the critical energy of the gamma spectrum seems to be anti-proportional to the energy of the electron beam. A positive correlation is expected if the electron energy was converted into radiation after the spectrometer screen as in the interaction with the vacuum chamber resulting in bremsstrahlung. Similarly, ICS without significant energy loss would be expected to result in a positive correlation, too. This is another indicator that the energy loss and the measured high energy radiation are related. The probability of observing such a negative correlation and electron energies below 500 MeV on four shots by chance is 1 in 3000, which further supports the hypothesis that we have measured energy loss from radiation reaction and increases the statistical significance of this finding. Since the spectrum of non-linear ICS changes with intensity, we can also use the retrieved spectra to further constrain the intensity at the interaction.

6.8 Agreement with models of radiation reaction

To summarise, we considered a dataset of 23 shots, 10 reference shots without the scattering beam and 13 dual beam shots. We devised a method to identify successful collisions of the electron beam and the scattering laser pulse (Section 6.4). We identified 4 successful collisions in 13 shots, which is consistent with the measured spatio-temporal jitter of the accelerator and the laser. On the 4 identified collisions, the energy of the spectral feature in the electron spectrum was lower than on most of the other shots. A statistical analysis of the intrinsic fluctuations of the accelerator showed that this is statistically significant with a probability of 1 in 350 to occur by chance (Section 6.5). Using the LL equation we estimated that the intensity at the interaction point must have been around $a_0 \sim 9 \pm 1$ (or 10 ± 2 in a quantum model) which slightly undervalues the experiment conditions of $a_0 \approx 12 \pm 1$ suspected due to a mismatch in the timing (Section 6.6). We inferred the gamma spectrum of the radiation and see that it qualitatively changes in significant collisions, which further supports that we have measured a non-linear interaction. The critical energies and the electron energies anti-correlate which indicates energy loss from radiation reaction and a non-linear interaction at a 1 in 3000 chance (Section 6.7).

We made a statistically significant measurement of energy loss from radiation reaction and also measured the corresponding radiation that was produced in the interaction. We will now discuss if this is consistent with different models of radiation reaction. This analysis was conducted by Jason Cole (Imperial College) and Tom Blackburn (Chalmers University of Technology).

Figure 6.14 shows the 4 successful collisions with the fitted critical energies for the gamma spectra on the y-axis and the measured electron energy of the spectral feature on

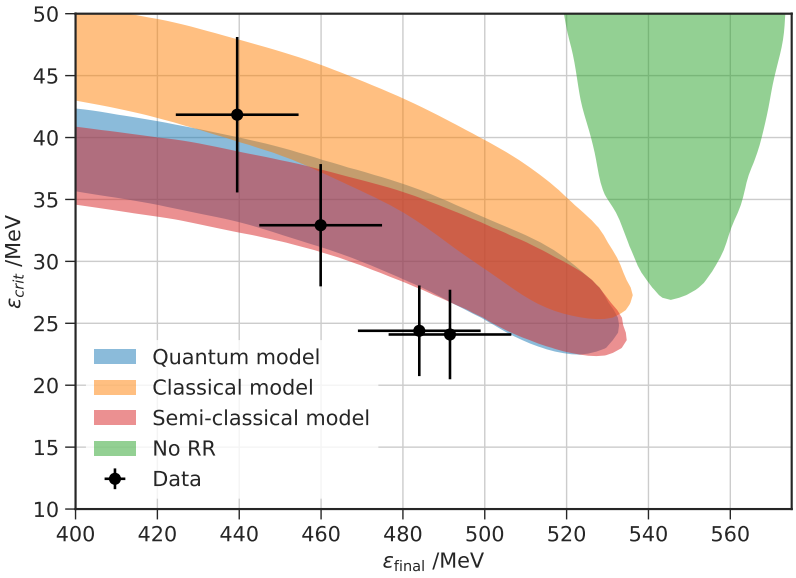


Figure 6.14: Critical energies, ϵ_{crit}, and energies of spectral feature, ϵ_{final}, in the electron spectrum for the 4 identified successful collisions along with different model predictions (1σ contours) including experimental uncertainties for a mean initial electron energy of $\epsilon_i = 550\,\mathrm{MeV}$ and a range of $a_0 = 4$ to 20. Adapted from Figure 9 in [162].

the x-axis. We will now use different models for this interaction to determine where in this parameter space events would be most likely. For this purpose, we sample experimental parameters from distributions incorporating the experimental fluctuations and uncertainties we characterised (energy stability, overlap, fitting errors), and calculate the energy loss of the electron beam with mean energy $\epsilon = 550 \pm 40\,\mathrm{MeV}$ and the generated radiation spectra in the respective model for intensities ranging from $a_0 = 4$ to 20. The respective 1σ contours are then plotted onto Figure 6.14 as comparison to the experimentally measured data.

First, we consider a classical description. The orange contour represents the results for an interaction described by the Lorentz force and the classical LL radiation reaction force, only considering the dominant term as higher order terms are suppressed by at least $1/2\gamma^2 \ll 1$. The red contour is generated using a semi-classical model. Here the equation of motion of the particles is governed by a classical description and is deterministic, but the emission power is reduced to match the quantum description, using the Gaunt factor which in the limit of low-intensity and low-energy interactions approaches 1 [132, 181]. Due to the reduced emission spectrum, the predicted critical energies are lower than for the classical model (orange) for the same final electron energy, which means that the purely classical description systematically underestimates a_0 relative to the semi-classical model.

The blue contour indicates the parameter space most likely to be occupied by interac-

tions correctly described by a quantum model, which includes the stochastic nature of emissions in the interaction, derived in the locally constant field approximation [131]. In this model, the electrons follow a classical trajectory between discrete emission events. The contour closely aligns with the semi-classical model as the average emission power is by definition matched. However, at lower final energies, i.e. more intense interactions, the contour starts to separate towards higher critical energies. The finite radiation lifetime allows electrons to propagate unperturbed between different radiation events and to release the equivalent energy within one single emission event. In the astrophysical context, this phenomenon is referred to as *'energy straggling'* [136]. This only occurs when the stochastic nature of the process is considered and leads then to a spectral hardening of the emitted radiation. Finally, we consider a model without energy loss. The electrons follow an equation of motion governed by the Lorentz force and the emitted radiation is calculated as in the quantum case, but the electrons do not lose energy in the process. This is indicated as a green contour, centred on the initial mean energy. For both the semi-classical and the full quantum model the local constant field approximation (LCFA) was used in the derivation [131], either to calculate only the emission power or also the stochastic emission rates, respectively.

The measurements related to the 4 successful collisions are consistent with models that include energy losses from radiation reaction (all contours except green). The no-RR (green) contour does not overlap with any of the measurements, and the results could only be part of a no-RR description if the intensity is lowered to about $a_0 = 5$ and the contours are extended to 2σ. The negative correlation of the data points along with the confidence in the experimental uncertainties make this very unlikely.

On a 1σ level, it appears that the data points are in better agreement with models including quantum corrections (semi-classical and quantum model, red and blue) than with the purely classical LL description (orange). To improve the confidence, we would require more data points, interactions at higher intensities and electron energies or use a different set of observables that is more sensitive to differences in the models [132]. A technique to determine a_0 at the interaction on-shot [120, 260] would also help to constrain the experimental conditions further, in particular if the value of the inferred intensity were model-independent [172] separating experimental from model uncertainties.

6.9 Electron beam stability and model distinction for future measurements

The experimental results show agreement with models including radiation reaction, discarding the hypothesis of a no-RR model at $> 2\sigma$ confidence. In addition, the data seems

to be more consistent with the models including quantum corrections at the 1σ level. However, due to the low number of shots and the intrinsic fluctuations of the setup, a more definite discrimination of radiation reaction models is not possible at this point. More data, stability, higher electron energies, laser intensities and additional observables could enable this as part of a future precision measurement of radiation reaction.

The following section will investigate the stability of gas targets used in two measurements of radiation reaction at GEMINI under similar experiment conditions. One is the already presented data from a gas jet (*Cole et al.* [162]), the second is from a gas cell target (*Poder et al.* [163]). For this purpose, the electron spectra of the second experiment undergo a statistical analysis similarly as described before.

The results from the statistical analysis are then being used to estimate how many shots are required to achieve 5σ confidence, the established standard for a 'discovery', that an explanation of the measurements requires energy loss from radiation reaction. For this purpose, normal electron distributions with and without energy loss, relying here on an analytic expression for the energy loss in the Landau-Lifschitz model (LL), are compared over a range of electron energies with different standard deviations. This analysis could help to make more informed decisions about gas targetry and interaction regimes and complements with simple methods other recent analyses on this topic [179, 180].

Experimental setup in Poder et al.

The experimental setup in [163] is very similar to the experiment described at the beginning as it is based at the same facility, and relies on similar optics and beam line designs. A sketch of the setup is show in Figure 6.15.

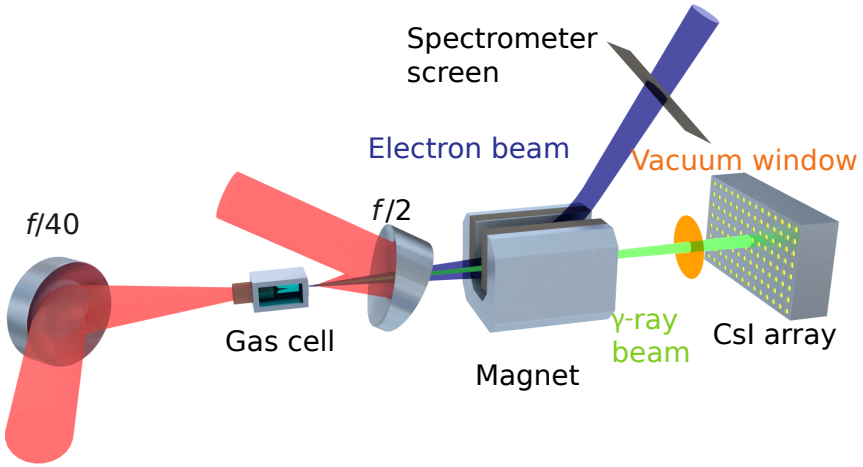


Figure 6.15: Conceptual sketch of the experimental setup as used on the radiation reaction campaign [163]. Adapted from Figure 1 in [162].

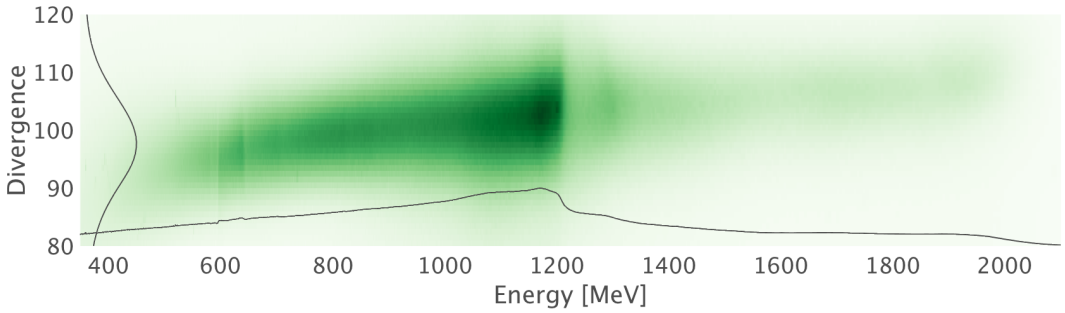


Figure 6.16: Example of a typical electron spectrum taken on this experiment. The distinct lines in the spectrum are the edges of a second layer of Lanex that was placed on the main screen to increase the yield.

The first laser is focused by an $f/40$ spherical mirror to a spot of FWHM dimensions $(59 \pm 2)\,\mu\text{m} \times (67 \pm 2)\,\mu\text{m}$ into the 20 mm long gas cell filled with helium at an electron density of $2 \times 10^{18}\,\text{cm}^{-3}$. The energy delivered on target at a FWHM pulse duration of $40 \pm 3\,\text{fs}$ is on average about 9 J reaching a peak normalised vector potential of $a_0 = 1.7$.

The focal plane of the colliding laser was positioned approximately 1 cm downstream from the exit of the gas cell. The focusing optic was the identical $f/2$ OAP with a central hole as in the previously described setup. The energy on-target was measured to be $(8.8 \pm 0.7)\,\text{J}$, already taking into account the loss in intensity due to the hole, at a FWHM pulse duration of $42 \pm 3\,\text{fs}$. The intensity at the interaction point was $a_0 \approx 10$ at a spot size of 7 µm FWHM. Both lasers were synchronised to about 40 fs accuracy using spectral interferometry [239].

The electrons accelerated via LWFA are dispersed by a dipole magnet of integrated field strength $\int B(x)\text{d}x \approx 0.15\,\text{Tm}$ onto a scintillating Lanex screen. The gamma rays from ICS are measured by the same scintillator stack as described previously, but this time it is rotated such that the long side of the crystals is oriented in the longitudinal direction. The stack acts as a profile screen instead of a spectrometer and the brightness of the measured scintillation light is proportional to the total energy deposited in the crystal stack.

Characterisation of Electron Spectra

Figure 6.16 shows an exemplary electron spectrum produced from the gas cell target. The average shape is an exponential spectrum reaching energies in excess of 1.5 GeV. At the lower end, the spectrum is cut off at around 400 MeV due to limitations in the magnetic electron spectrometer setup. The spectra from the gas cell originate from self-injection and lack a consistent sharp feature comparable to the spectral edge described in the previous

section related to shock injection. The distinct lines visible in Figure 6.16 are a result of stacking several Lanex layers to enhance the light yield. The change of intensity and the spatial features are removed in course of the analysis. The dataset consists of 19 shots.

The value characterising each spectrum is the cut-off energy, which is in [163] defined as the energy at which the spectral intensity reaches 10 percent of its peak value. The cut-off energy of the spectrum scales linearly with the energy in the driver beam (see Figure 6.17). The linear correlation is very strong at a correlation coefficient of 0.9. The linear fit follows the equation $\epsilon_{cutoff} = 0.07\,\mathrm{GeV/J} \times E_{laser} + 0.57\,\mathrm{GeV}$.

After scaling the spectra according to the linear relation found in Figure 6.17, we can analyse again the 'intrinsic' fluctuations of the source. The distribution of cut-off energies in terms of $\Delta E/E$ follow a normal distribution after removing the correlation with the on-shot measured laser energy. The standard deviation of the cut-off energy distribution is $\sigma_{Poder} = 3.5\%$, so 95 percent of the expected energies will fall within $\pm 7\,\%$ of the mean energy.

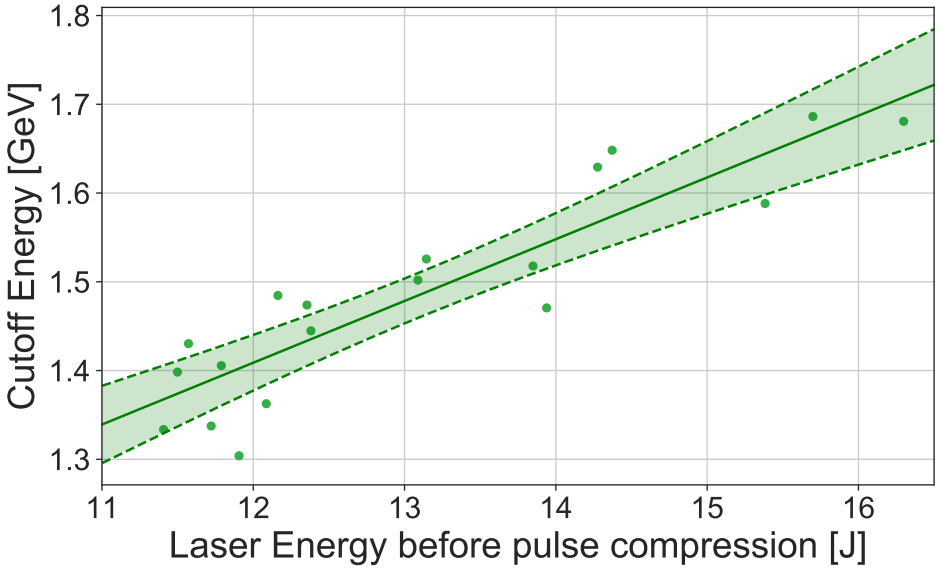


Figure 6.17: Laser energy of the wakefield driver beam before pulse compression plotted against the cutoff energy of the electron spectrum. The data points clearly follow a linear trend drawn in the straight green line with a gradient of 0.07 GeV/J. *The shaded area indicates the 95 percent confidence interval of the fitting function. The correlation coefficient for a linear fit is* 0.9.

Comparison of intrinsic fluctuations in both datasets

By factoring out known correlations of the spectra, scaling them accordingly [slow drift for gas jet data (*Cole et al.*) and laser energy for gas cell data (*Poder et al.*)], and by normalising the spectra to their total charge, it is possible to compare the spectra.

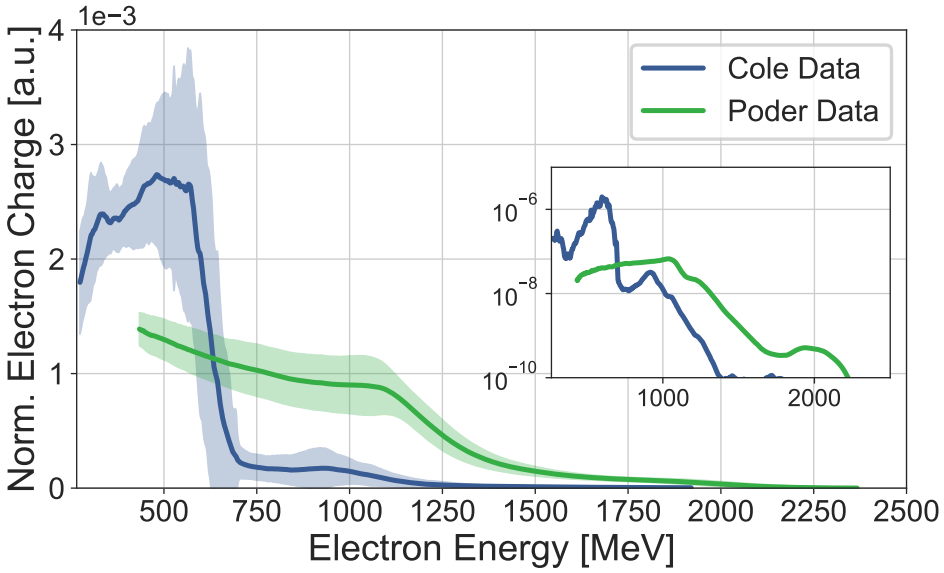


Figure 6.18: Averaged and scaled electron spectra for data from Cole (blue) and Poder (green). The spectra are normalised to a total charge of 1. The error bars indicate the energy dependent variance of the spectra. Inset: Energy-dependent variance of the average spectra, following the same colour scheme. The total variance for Cole et al. was 1.5×10^{-7} *and* 1.98×10^{-8} *in the case of Poder et al.*

Expected intrinsic or non-attributed fluctuations can be characterised and taken into consideration.

Figure 6.18 shows the scaled and averaged spectra from the two experiments. The spectra were processed as outlined before and then averaged over all available data shots. The lineouts are normalised by their total charge such that the integral of each spectrum is set to 1. The typical energy reached in the gas cell from *Poder et al.* is significantly higher, by at least a factor two for the majority of the charge distribution. The higher electron energy also enables a potentially higher η parameter in an interaction as $\eta \propto \gamma$. The shaded region around the scaled spectra indicates the standard deviation of the averaged spectrum at that particular energy. The energy-dependent variances are also shown in the inset of Figure 6.18 on a logarithmic y-axis. The variations for the data taken with the gas jet (blue) are in particular strong around the important position of the spectral edge and the variance reaches a 10-times higher peak and total value.

The spread of cut-off energies for the gas cell data is narrower than the spread of energies of the edge feature produced with the gas jet target. The shaded areas in Figure 6.19 indicate the $\pm 2\sigma$ or 95 percent confidence intervals based on a normal distribution. The *Poder* data has a typical fluctuation of the cut-off energy of around 7 percent. The spectral feature from the gas jet varies with 15 percent by the double amount. The gas cell data from *Poder et al.* is superior in terms of energy stability (cut-off for gas cell, spectral feature for gas jet) and stability of the spectral shape (variance).

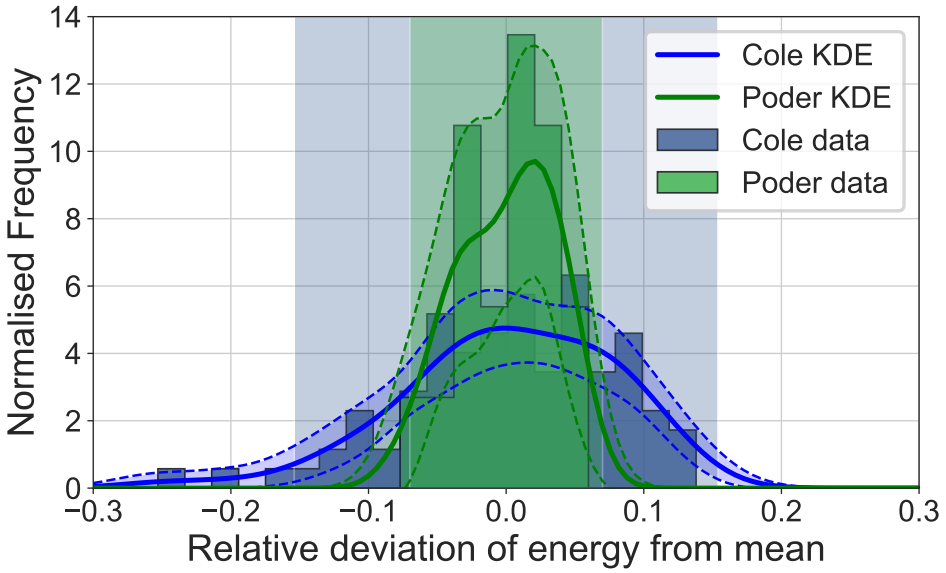


Figure 6.19: Distribution of the relative energy deviations from the mean ($\Delta\epsilon/\epsilon$ for Cole et al. (blue) and Poder et al. (green) after scaling. The overlaid lines are kernel density estimates (KDEs). The shaded areas indicate the ±2 sigma intervals assuming a normal distribution.

Relevance for measurements of radiation reaction

Based on the statistical analysis of the electron spectra from both experiments, we want to investigate now how these fluctuations affect the confidence in the identification of radiation reaction effects in the electron spectra.

For this purpose, we sample electron energies from two normal distributions with the same mean energy $\epsilon = 550\,\mathrm{MeV}$ and the measured standard deviations $\sigma_{Cole} = 7.7\%$ and $\sigma_{Poder} = 3.5\%$. The sampled energies are shown in Figure 6.20 in blue for a normal distribution with σ_{Cole} and in green with σ_{Poder} as previously.

We then calculate the energy loss for the sampled electron energies based on the Landau-Lifschitz model, using again the analytic expression for a plane wave with a Gaussian temporal envelope given in [133, 177]

$$\frac{\Delta\gamma}{\gamma_0} = \frac{\sqrt{\pi/2}\tau_0 t_L \omega_0^2 \gamma_0 a_0^2}{1 + \sqrt{\pi/2}\tau_0 t_L \omega_0^2 \gamma_0 a_0^2}, \tag{6.9.1}$$

where $\tau_0 = 2e^2/3m_e c^3 = 6.4\times10^{-24}\,\mathrm{s}$, the pulse duration, $t_L = 45\,\mathrm{fs}$, and the wavelength is $\lambda = 800\,\mathrm{nm}$.

The histograms in Figure 6.20 show the electron energies sampled from unperturbed normal distributions without radiation reaction, labelled 'RR off', along with the corresponding post-interaction distribution of energies (orange), calculated using Equation (6.9.1) for $a_0 = 8$, which is the lower end of the estimated interaction intensity in [162].

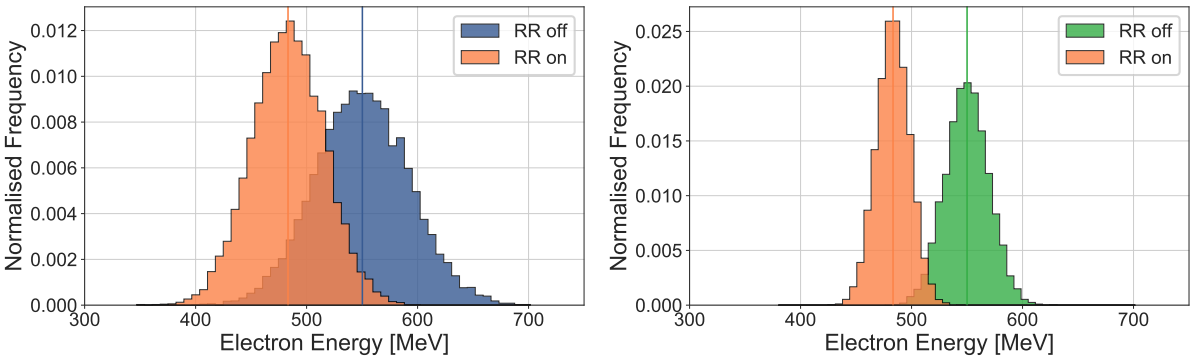


Figure 6.20: Electron energies sampled from normal distributions with standard deviation $\sigma_{Cole} = 7.7\%$ *(left, blue) and* $\sigma_{Poder} = 3.5\%$ *(right, green), and the corresponding post-interaction energy distribution (orange) calculated with Equation* (6.9.1) *at* $a_0 = 8$.

For both 'RR on' distributions, the mean energy has shifted down by more than 50 MeV and the width of the normal distribution is reduced. Equation (6.9.1) predicts a higher absolute energy loss for higher initial electron energies which over the entire spectrum leads to a 'cooling' and reduction of the spread of energies [132]. Due to the larger initial spread of sampled energies, the overlap of the initial and final distribution is larger for the blue distribution. This intuitively tells us that it will be more challenging for the distribution with σ_{Cole} than for the one with $\sigma_{Poder} < \sigma_{Cole}$ to confidently identify whether a measured electron spectrum was produced from a model without radiation reaction, 'RR off', or for instance from a 'RR on' model (here LL).

To quantify this, we perform a statistical Z-test. The parameter Z indicates the confidence at which two normal distributions can be distinguished from each other and is equivalent to a σ confidence level. There are similar tests that can be applied to other types of distributions or without assuming a specific shape at all. Z is calculated by comparing the mean and the standard deviation on the mean of two normal distributions:

$$Z = \frac{\overline{\mu}_1 - \overline{\mu}_2}{\sqrt{\sigma_{\mu_1}^2 + \sigma_{\mu_2}^2}}, \tag{6.9.2}$$

where $\sigma_X = \sigma/\sqrt{n}$ is standard deviation on the mean. $\overline{\mu}_1$ and σ_1 are $\epsilon = 550\,\text{MeV}$, and σ_{Cole} or σ_{Poder}, respectively. The mean $\overline{\mu}_2$ and standard deviation σ_2 are calculated from the post-interaction distribution.

If we assume a fixed relation of number of successful collisions and reference shots, we can estimate the number of shots we require to distinguish a 'no RR' from a 'LL-RR' distribution at a confidence of Z sigma. In the case of an equal number of successful

collisions and reference shots, the minimum number of shots required is given by

$$\boxed{N_{min} = Z^2 \frac{\sigma_1^2 + \sigma_2^2}{(\overline{\mu}_1 - \overline{\mu}_2)^2}.} \tag{6.9.3}$$

In an experiment, we also have to consider that only 1 in X shots with both beams will result in a successful collisions. In this case, it was estimated to be a 1 in 3 chance, so the total number of shots would then be $4 \times N_{min}$ or in general terms $(1 + X)N_{min}$ shots. We assume that we can identify successful collisions using the method described at the beginning of this Chapter, and that we know the intensity at the interaction which for now remains constant throughout the dataset.

The number of shots that we have to take to be able to make statistically significant observations is a crucial factor in complex experiments like this all-optical setup that requires a spatio-temporal overlap to the micrometre (10^{-6}m) and femtosecond (10^{-15}s) accuracy.

At $a_0 = 8$ and $\epsilon = 550\,\mathrm{MeV}$, the number of collisions shots required to reach $Z = 5$ is then $n = 15.7$ for σ_{Cole} and $n = 3.4$ for σ_{Poder}, for $Z = 3$ we obtain $n = 5.6$ and $n = 1.2$, respectively. A single shot level $n = 1$ still requires a proper characterisation of the reference ('no RR') distribution.

At a 0.05 Hz repetition rate like at the Gemini laser system (1 shot/20 s), we would then take at least 21 minutes to reach 5σ for σ_{Cole}, given no failed shots and stable conditions. If we would require 100 shots for a confident discrimination, a scan at the same laser system would take more than 2 hours, during which conditions might change. This includes drift in spatial alignment and temporal synchronisation, laser performance, failing of diagnostics and exhaustion of the target [302]. In addition, more data is produced and has to be stored.

Using this method, we can easily determine N_{min} for a range of standard deviations and electron energies. Figure 6.21 shows the minimum shot numbers for $Z = \{5, 3\}$ and $a_0 = \{8, 20\}$ for standard deviations between 1-10%, and 100 to 2500 MeV electron energy, spanning a realistic parameter space of electron properties at Gemini. The blue and green markers now indicate the conditions of *Poder* and *Cole et al.* If we include the higher electron energy measured by *Poder et al.*, the number of successful collisions required to distinguish the cases no-RR and RR (LL) falls to 1, i.e. one successful collision suffices as long as the unperturbed electron spectrum is characterised well enough. This is consistent with the findings in [163].

As one would intuitively expect, at a fixed a_0, lower energies and higher shot-to-shot energy fluctuations result in a higher value of N_{min} to reach the same confidence level Z.

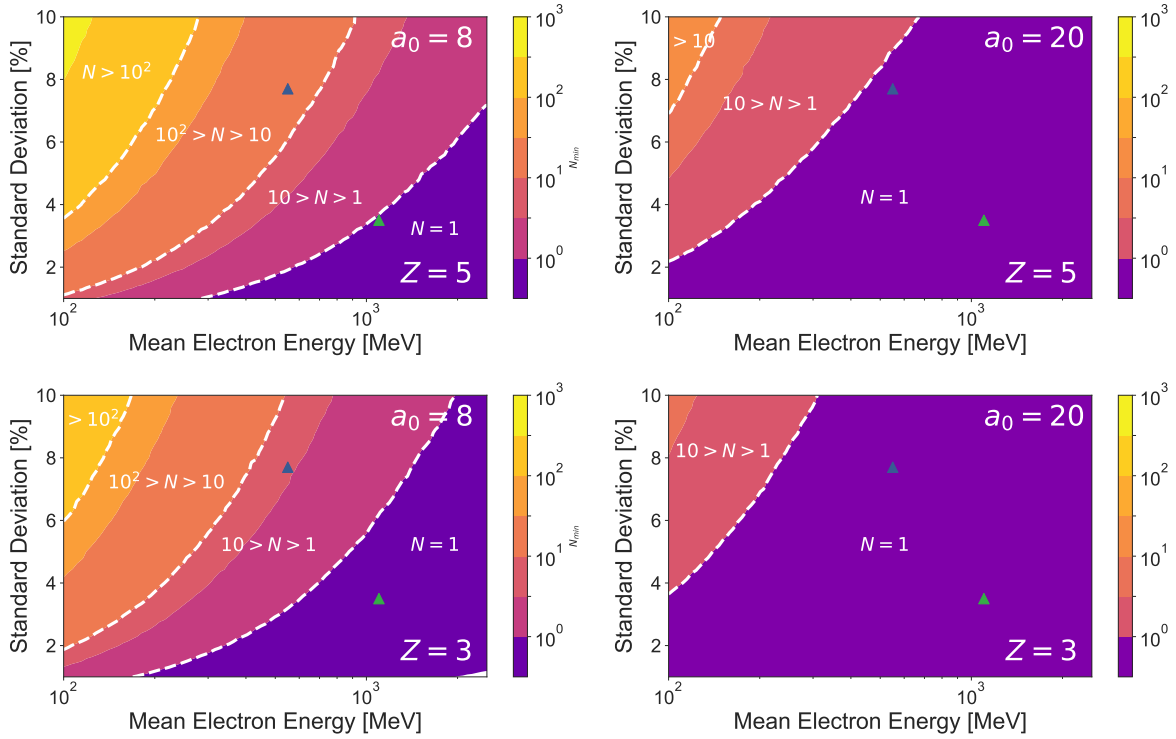


Figure 6.21: Minimum number of successful collisions required, N_{min}, to reach a 5σ confidence level for a range of standard deviations and mean electron energies at $a_0 = 8$. The colour scale is logarithmic. The dashed white lines indicate the contours for the different regions for each order of magnitude. The blue and green triangle mark the conditions Cole et al. [162] and Poder et al. [163] were taken at, respectively.

From $a_0 = 8$ to $a_0 = 20$ (see Figure 6.21, left to right panels), the region $N_{min} = 1$ (purple) quickly expands and it is possible to distinguish the models in both cases within one single shot, even for energy fluctuations of 10 percent. This means that at lower intensities and energies the fluctuations in the electron energy have a stronger impact on the ability to identify energy losses from radiation reaction, whereas higher intensities and electron energies mitigate the imperfect performance of the accelerator. In this context, the accelerator using a gas jet (*Cole et al.*) had a worse performance than the gas cell (*Poder et al.*), which means more shots are required to build up statistical confidence. However, whilst the gas cell produced more stable and higher energetic electron beams, gas jets allow in principle an interaction closer to the exit of the accelerator without damaging components and producing debris, if the nozzle is far enough below the laser axis.

Close to the exit the electron beam is still very small $\sim$ µm and a tightly focused laser spot can interact at a comparable intensity with a large fraction of the beam. These interactions are then likely to occur in a parameter space where $N_{min} = 1$ again. If the laser focus is larger than the electron beam, the interaction can be reduced to a 1D problem which simplifies the modelling process. Gas jets have in the past produced very stable electron beams with narrow energy spread [226] and have also reached energies beyond

1 GeV [215, 216, 313], which indicates that the performance of this target was maybe not representative of what is achievable to-date. In addition, using a gas jet would allow us to use controlled, rather than accidental, shock injection as mechanism which has the potential of producing high-charge beams with narrow energy spread [228], and would also constrain the injection point and as a result the relative timing.

In summary, it appears that the benefits of using a gas jet target outweigh in principle the stability of the electron beams produced with this gas cell and are hence recommended to be used in future studies.

Finally, it should emphasised that the scope of this analysis is limited and based on a series of assumptions: It is assumed that successful collisions can be identified, for instance using the method described at the start of this Chapter, and that the laser intensity remains fixed in all interactions. Fluctuations or uncertainties are only considered for the electron beam in terms of energy, and for both laser and electron beam for the spatio-temporal jitter, but are not extended to other laser or electron parameters.

We also only considered the binary scenario where either the entire electron beam or nothing interacts. This might be approximately true in the case where the waist of the laser pulse is at the interaction wider than the electron beam, but is not the case if the opposite is true. In this scenario, the exact on-shot laser profile and wavefront becomes more important, and the radiation reaction signature is hidden under the remaining, unperturbed electron beam. This could represent an avenue to achieve an on-shot reference on upcoming more powerful laser systems [314].

This analysis also neglects effects that could become important for longer interactions and tight focusing, such as change in intensity due to focusing effects and a chirp in the electron beam energy [303].

Furthermore, we used the Landau-Lifschitz description to calculate the post-interaction distribution. It would be of interest, in particular for future precision studies, to discriminate different radiation reaction models, for instance the full quantum model including stochasticity and the semi-classical model introduced in the previous section. Limitations of the local constant field approximation (LCFA) [131], which is basis for the models including quantum corrections, are also an active field of research and require experimental validation [315].

For these cases, it will become beneficial to consider other or additional observables that are more sensitive than the mean energy loss to the respective differences in the models (e.g. [132]). This is beyond the scope of this analysis but has been looked at for the models discussed previously in more detail in [179, 180].

6.10 Conclusion

We measured radiation reaction in an all-optical setup by colliding a tightly focused laser beam of $a_0 \approx 10$ with a relativistic electron beam from LWFA of energy $\sim 550\,\mathrm{MeV}$ [162], producing gamma radiation of critical energies $\epsilon_{crit} > 30\,\mathrm{MeV}$.

Successful high-intensity collisions were signalled by bright bursts of gamma radiation recorded on the gamma detectors. The expected radiation background from bremsstrahlung was found by correlating the electron spectra and the signal on the gamma-detector on shots without the scattering laser. Over the course of 13 shots, this method identified 4 successful collisions with an excess signal of more than 5 standard deviations above background, i.e. at a probability of 1 in 3,500,000 to occur by chance on one shot, assuming a normal background distribution.

On the 4 identified collisions, the energy of the spectral feature was lower than the average of the shots without the scattering laser. Considering a larger dataset, the statistical fluctuations of the spectral feature without the scattering laser were characterised and correlations to other experiment parameters explored. Based on this statistical analysis, the combined probability of measuring 4 spectral features at such low energies is about 0.3%, rendering this a statistically significant measurement of energy loss.

This information was combined with a spectral analysis of the gamma signal to confirm the conditions at the interaction from another perspective. The characteristic energy of the gamma spectrum is higher on shots without the scattering laser as the detector response is dominated by bremsstrahlung, whilst exhibiting a lower yield. The characteristic energies of the 4 identified collisions are anti-correlated with the electron energy, all below 500 MeV, which is not consistent with radiation produced after measuring the energy of the electron beam. The likelihood for this to occur by chance is 1 in 3000. This supports the hypothesis that we have measured radiation reaction and that this result is statistically significant.

The measurements were in agreement with models including radiation reaction and indicate a better agreement at the 1σ level with models including quantum corrections. The intrinsic fluctuations of the experiment and the low number of successful collisions do not allow more confident association to one specific model.

The statistical analysis of the stability of the electron beam has shown to be useful to estimate the significance of lower electron energies, but also provides a powerful tool to quantify the scale of data required to distinguish different models of radiation reaction.

A comparative analysis of the stability of electrons from a gas jet and a gas cell target,

both used for radiation reaction measurements, was used to estimate the scale of data required to reach 'discovery' 5σ confidence discarding a no-RR scenario. In this case, the stability of the electron beam energy and of the spectral shape was superior for the data using a gas cell target [163], with half of the standard deviation on a normal distribution for the energies.

The improved stability was weighed against the advantages of using a gas jet target, which are the ability to perform very close interactions without producing debris or damaging the target, as well as easy diagnostic access. The possibility to use shock injection for improved control over the injection point and potentially a lower energy spread is favouring gas jet targets.

This method can be expanded to other source parameters, including the spectral shape of the electron beam and gamma spectra, to identify observables that discriminate models more efficiently. This is beyond the scope of this thesis, but can be found in [179, 180].

Chapter 7

Characterisation of a LWFA Bremsstrahlung Source for a Measurement of the Linear Breit-Wheeler Process

7.1 Motivation and Introduction

In the Breit-Wheeler mechanism, two (linear) or more (non-linear) photons combine to produce an electron-positron pair — in other words matter is created from light. The linear Breit-Wheeler process is the simplest mechanism by which photons can create matter and is one of the most fundamental interactions of quantum electrodynamics (QED) that can be represented by minimally-sized Feynman diagrams (see Figure 7.1). However, despite its simplicity, it is the last of these fundamental interaction that has not been definitively observed in isolation in vacuum yet, i.e. without the presence of other particles or external fields. Its measurement is particularly relevant for the field of high-energy astrophysics [109, 110, 316]. The inverse process is the more commonly observed Dirac annihilation [183], where an electron and a positron decay into two photons.

The non-linear Breit-Wheeler process, on the other hand, has been measured and confirmed as part of the E144 experiment at SLAC in the '90s, where an ultrarelativistic electron beam of 46.6 GeV energy was collided with an intense laser pulse of $a_0 \sim 0.3$, resulting in highly energetic gamma photons from inverse Compton scattering [99, 100]. These gamma photons in turn interacted with up to $n \approx 7$ laser photons to produce electron-positron pairs [101]. The researchers detected about 100 positrons that match the momentum profile for products from the non-linear Breit-Wheeler and the Trident process [317] over the course of 22,000 laser shots.

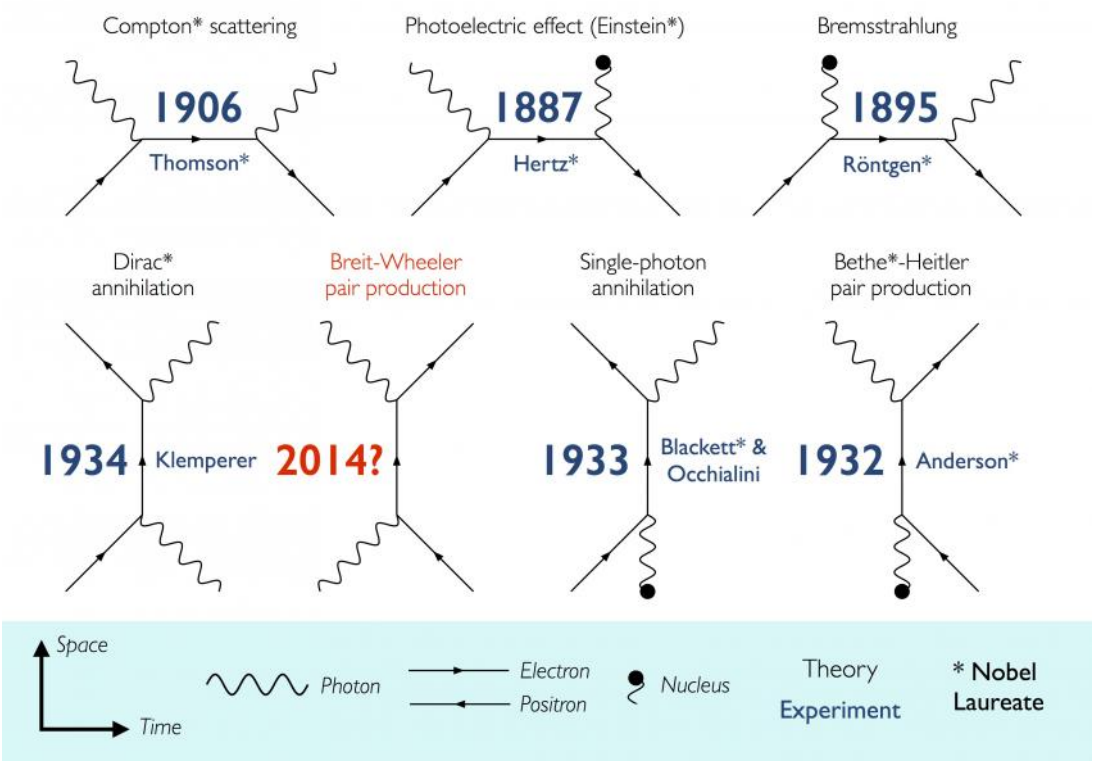


Figure 7.1: Overview of fundamental QED processes shown in their Feynman representation along with the year the process was validated experimentally. Each of the processes has been observed in experiment, with exception of the Breit-Wheeler pair production. Figure courtesy O. Pike [320].

The measurement of other photon-photon interactions, elastic and inelastic scattering processes, is additionally very challenging as these are higher order processes with cross sections that are suppressed by at least $\sim \alpha^2 \approx (1/137)^2$ [164], where α is the fine-structure constant. As a result, similarly few events have been measured for other photon-photon interactions without background fields, for instance at CERN [318]: the ATLAS collaboration reported 13 candidate events for light-light scattering in heavy-ion collisions [62, 63], whereas the OPAL Collaboration measured inelastic photon-photon interactions at LEP [319]. Photon collisions have also been proposed to probe even rarer processes such as the production of axionlike particles [65, 66], sleptons and dark matter candidates [64].

Pair annihilation is easily measured in radioactive decays [187] as its cross section is very high at low energies ($\sigma_{e^+e^-} \propto 1/\epsilon$ [164]) and an abundance of electrons in ordinary matter provides an abundance of attracted partners for positrons to annihilate with. Pair creation from radiation, on the other hand, requires high energy photons and/or a very high photon density, for instance a tightly focused laser, to overcome the production

threshold in the centre-of-mass frame:

$$\boxed{s = \frac{\epsilon_1 \epsilon_2}{2 m_e^2 c^4}(1 - \cos\theta) > 1,} \tag{7.1.1}$$

where $\sqrt{s}$ is the centre-of-mass energy, ϵ_1, ϵ_2 the energy of the first and second photon, respectively, and θ is the angle between the two photons. Any excess energy can provide the created pair with sufficient momentum to avoid an immediate decay through Dirac annihilation. The quantities of the Breit-Wheeler and annihilation total cross-sections are related by $\sigma_{\gamma\gamma} = 2\beta^2 \sigma_{e^+e^-}$, where $\beta = \sqrt{1 - 1/s}$ (see Figure 2.14). However, delivering two bright energetic photon sources at suitable energies at the same location is very challenging and hence mainly mediated pair production processes in presence of a background field have been measured instead [99, 185, 321–325].

Directed high energy radiation in the keV range can be produced from highly relativistic electrons, for instance, at XFELs and synchrotron sources using bending magnets and insertion devices [68], and equivalently in plasma accelerators through betatron radiation [282, 326]. Another approach is to heat solid targets with a laser, for instance hohlraums [327–330] or burn-through foils [246].

Directed energetic gamma radiation can be generated by passing highly relativistic electrons through solid material to produce bremsstrahlung [274, 331–337] or relying on inverse Compton scattering [120–125, 150, 296, 297].

In 2014, *Pike et al.* [149, 338] proposed to measure the linear Breit-Wheeler process by combining a low-divergence ($\theta \sim \ln(\gamma)/\gamma$ [339]) bremsstrahlung source, consisting of a GeV-class electron beam generated by a high-intensity laser [212] and a gold foil [274, 331–337], with a blackbody radiation field formed in a hohlraum heated by a high-energy laser [327–330] (see Figure 7.2). For 10^9 electrons at 2 GeV energy, a 5 mm thick gold foil and a 1 cm long hohlraum at 400 eV temperature, the researchers predicted up to 10^5 pairs to be generated from the linear Breit-Wheeler process [149]. The asymmetry of the energies produced by the two photon sources results in an emission of pairs in the direction of the more energetic gamma ray beam. This is referred to as pair beaming [193], which in principal allows the extraction and measurement of all produced pairs, better separation of signal and noise, and using smaller detectors. The setup also opens up the possibility to investigate elastic photon-photon scattering of the gamma-rays in the X-ray field [62].

The experiment presented here was based on this proposed layout [149, 338]: two lasers were employed to provide simultaneously an X-ray and a gamma-ray source to overcome the mass threshold and to produce electron-positron pairs from the linear Breit-Wheeler

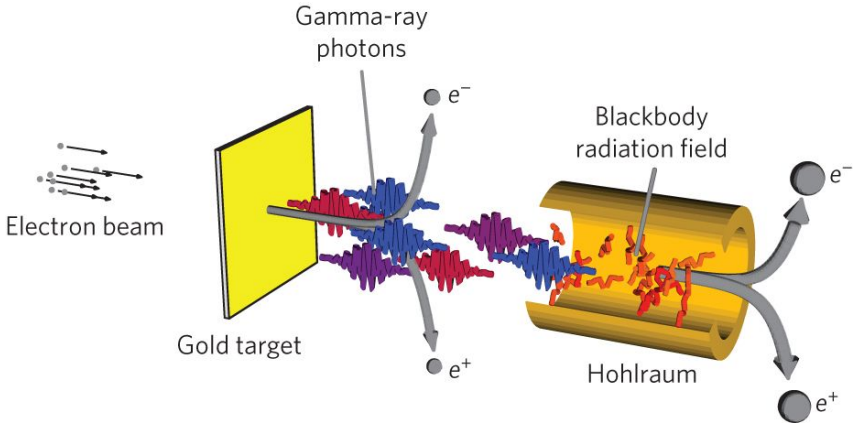


Figure 7.2: Experimental setup for a photon-photon collider to produce and measure pair production from the linear Breit-Wheeler process as proposed by Pike et al. in 2014 [149]. From left to right: an electron beam (grey circles with black momentum arrows) from a laser wakefield accelerator is incident on a gold target (yellow) and produces gamma-ray photons (red, blue and purple wave packets) from bremsstrahlung. The remaining electrons and electron-positron pairs produced in the interaction with the solid are removed from the system using a dipole magnet. The gamma-ray photons enter the blackbody radiation field (red) generated by heating a hohlraum (gold). In the interaction of the gamma-rays and the radiation field, electron positron pairs (grey) are produced and emitted in the propagation direction of the gamma-rays. The pairs are dispersed by a magnetic field and directed onto suitable detectors (not shown). This is Figure 1 in [149] reprinted by permission from Nature Photonics, copyright (2019).

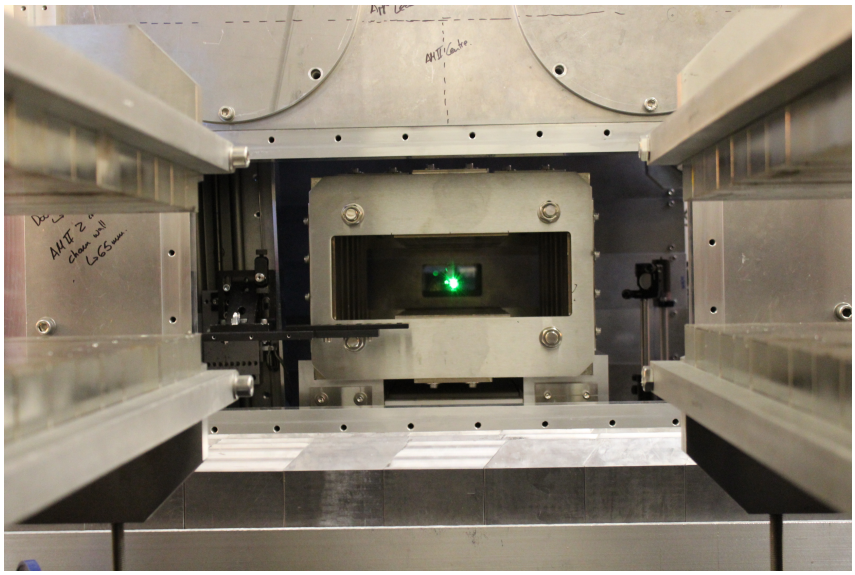


Figure 7.3: In pursuit of creating matter from light. Photo taken during the experiment campaign aimed at measuring the linear Breit-Wheeler process at the Gemini *facility in 2018. View upstream on the gamma-ray axis, indicated by a green alignment laser, through the magnetic chicane that is designed to transport generated electron-positron pairs from the Breit-Wheeler process to designated single particle detectors.*

process. A detailed description can be found in Section 7.3 (see also Figure 7.4). The gamma rays were produced, as proposed, by bremsstrahlung from LWFA electrons [274, 331–337], but in this instance typically at electron energies $\epsilon_{e^-} < 1\,\mathrm{GeV}$. The metal bismuth (Bi, $Z = 83$) was used as converter, which allows reducing the material thickness with respect to the proposed gold foil ($Z = 79$) at comparable conversion efficiency, but at lower maximum cut-off energy due to the lower electron energies. Instead of using a high-energy laser and a hohlraum, a replenishable germanium target was used as burn-through foil in conjunction with another high-intensity laser [246], producing an X-ray spectrum with emission lines peaked around 1.5 keV [340]. This balances out the lower gamma-ray energy and the narrow bandwidth of the spectrum constrains the interaction conditions. Using a replenishable foil target and a high-intensity instead of a high-energy laser also allows making use of high repetition rate systems. By removing the X-ray target from the beam axis, we also reduced the production of secondary Bethe-Heitler pairs [185] from gamma rays interaction with solids that might be mistaken for pairs created in the linear Breit-Wheeler process.

7.2 Chapter Outline

This Chapter relates to an experimental campaign aimed at measuring the linear Breit-Wheeler process [184] conducted at the Gemini laser system in spring 2018. Two high-intensity lasers were used to provide highly energetic gamma radiation and an X-ray source that combined exceed the production threshold of a centre-of-mass energy of $\sqrt{s} > 1$. The experiment can be divided in three major components: the gamma-ray source, the X-ray source and the single-particle detectors. This work focuses on the commission, characterisation and considerations related to the gamma-ray source. This is the main contribution of the author to the overall analysis of the experimental data. In some parts, this Chapter will refer to analysis from diagnostics related to the other two areas where the author has not directly contributed to the analysis itself. The X-ray data has been analysed by Cary Colgan (Imperial College) and Brendan Kettle (Imperial College), with John Morton (AWE) providing simulations for the X-ray spectra. Data related to the single particle detectors has been analysed by Brendan Kettle (Imperial College) and Guillermo Marrero Samarin (QUB) with significant contribution from Dominik Hollatz (Jena) for the tracking of particles through the magnetic chicane.

In this experiment, the gamma-ray source was generated by bremsstrahlung from LWFA electrons traversing a solid target [274, 331–337]. The properties of the electrons determine the properties of the generated radiation, but LWFA electrons underlie intrinsic fluctuations and their performance varies from experiment to experiment [22]. Hence, the

electron beams are first characterised in general and then more specifically its variation in performance on three relevant shot days. The primary properties of interest are charge, electron energy, divergence and the stability of the shot-to-shot beam pointing. The properties of radiation that the electron beam produces are investigated for two different density regimes of the accelerator and two converter materials at two different thicknesses. The performance of the source in its different configurations is analysed and optimised in terms of yield enclosed within a certain divergence angle and the number of background events registered on the single-particle detectors. Using the optimised parameters for the bremsstrahlung source, the performance and its variations are characterised for the three shot days. Then, the measured spectra of the X-ray source, analysed by Cary Colgan (Imperial College), and its performance for the shot days are presented. Combining the characterisation of the gamma-ray source and the X-ray source the impact of the varying performance of both on the total Breit-Wheeler cross section for the three shot days is analysed and discussed. To provide the context and significance of this Chapter, a brief overview of the overall analysis is given. Finally, the results are summarised and potential improvements for a future measurement are discussed.

7.3 Experimental Setup

The experiment was performed at the dual 300 TW Ti:Sa GEMINI laser at the Central Laser Facility, UK, in early 2018. The aim of this setup was to create and to measure electron-positron pairs from the linear Breit-Wheeler process [184]. For this purpose, high-energy bremsstrahlung gamma-rays produced by LWFA electrons [274, 331–337] were collided with X-rays from a heated burn-through foil [246]. One beam of the GEMINI laser system provided the X-rays, the other one the gamma source. A sketch of the experimental setup is shown in Figure 7.4.

Burn-through foil X-ray source

In this experiment, the heating laser beam was temporally detuned to a pulse duration of 40 ps FWHM in order to heat the solid target efficiently [246]. The beam was focused onto the target by an $f/2$ off-axis parabola (OAP), delivering 10.72 ± 0.28 J energy on target. After optimising the angle of the OAP, a phase plate was inserted in the collimated beam which results in a smoothing of the spot and an increase of its size to an ellipse with a characteristic speckled profile [238], measuring $(77 \pm 6)\,\mu\text{m} \times (217 \pm 6)\,\mu\text{m}$ and containing about 80% of the energy in the laser pulse. The base of the burn-through foil target was a 25 µm thick Kapton tape. 800 µm wide squares were etched into the tape, reducing the thickness of the tape to 5 µm at these spots. The thinned out parts of the

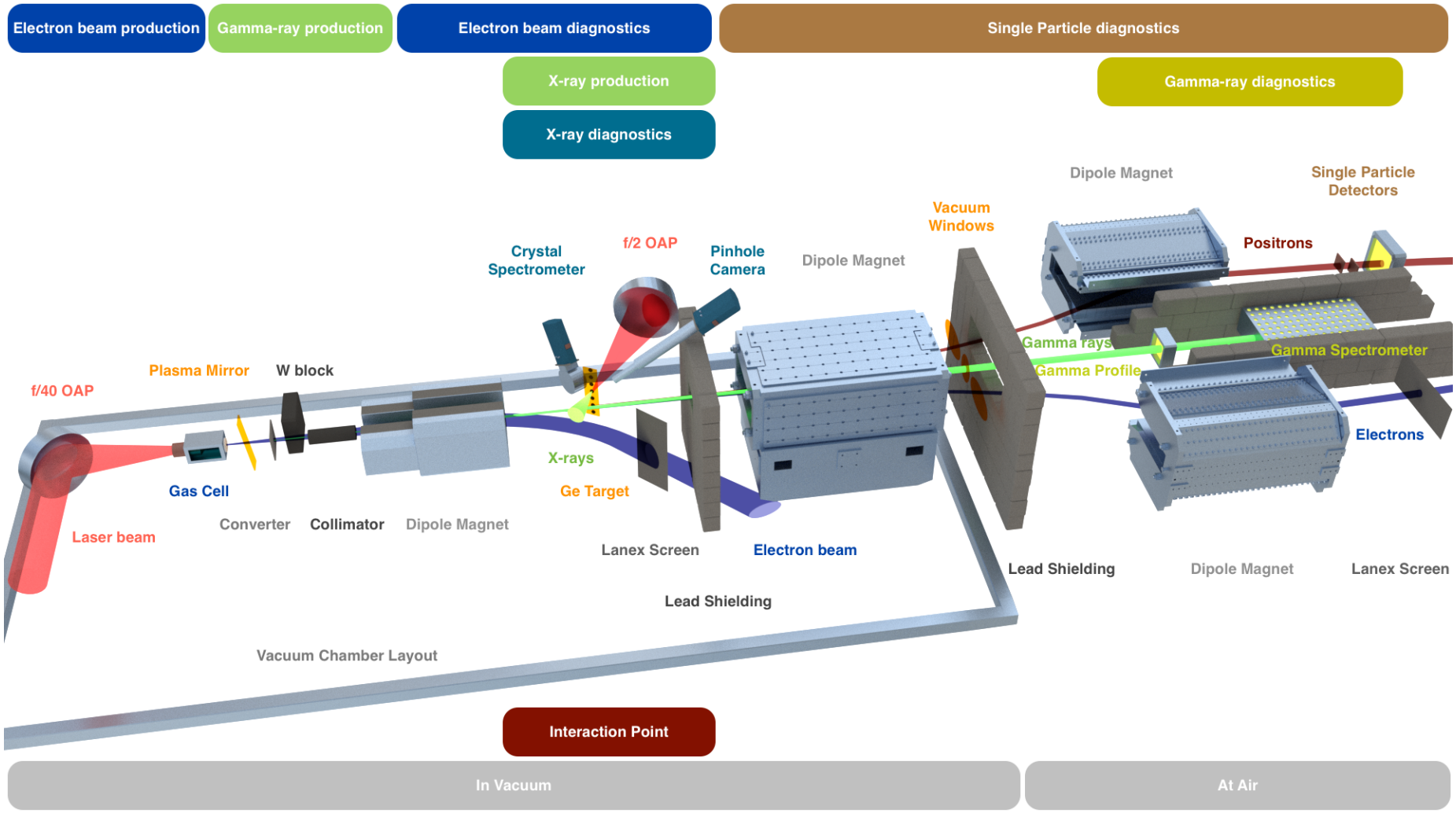


Figure 7.4: Sketch of the experimental setup indicating its main components. From left to right: The first laser pulse (left, red) is focused by an $f/40$ OAP into a gas cell target (blue), producing an electron beam (blue) via LWFA leaving the cell on the right side. The remainders of the laser pulse are removed after the cell by a Kapton tape acting as plasma mirror (orange). The electron beam passes through the tape, and then traverses a metal converter target producing gamma radiation from bremsstrahlung (green) in forward-direction. A tungsten (W) collimator removes the divergent components of the radiation and a thick block of tungsten shields the direct line of sight to the X-ray target further downstream. When the converter (and the collimator) are not in the path of the electron beam, it is characterised by a magnetic spectrometer using a permanent dipole magnet. A second laser (red) is focused onto a Kapton tape with germanium (Ge) dots (orange) to act as source of X-rays (green) that are characterised by a crystal spectrometer and a pinhole camera (turquoise). Positrons (dark red) produced in the interaction of the X-rays and gamma-rays propagate downstream and are directed through a magnetic chicane and onto single particle detectors (brown). The gamma-rays are measured by a profiler and a spectrometer (gold).

tape are coated with a 750 µm wide and 100 nm thick layer of germanium (Ge)[1]. The motion of the tape drive is motorised[2] and a fresh Ge target can be provided on each shot. When the germanium is heated by the laser, it expands and produces a plasma plume facing the focusing optic. The hot plasma emits X-rays with distinct emission lines around 1.5 keV in the ML emission band on top of a black-body like emission[3]. Radiation that travels in the opposite direction, away from the focusing optic, traverses the Kapton tape and is spectrally filtered in the process. This is the component of the emitted radiation that was used for the photon-photon interaction.

The X-ray source was diagnosed by a pinhole camera setup with two 25 µm tantalum pinholes, measuring the flux and the source size at a magnification $M = 2.03 \pm 0.02$. One pinhole was filtered with 5 µm of aluminium, the other one with 6 µm of PTFE. The preliminary estimate for the X-ray source size in the experiment is 240 µm × 255 µm. A crystal spectrometer using a thallium-hydrogen-phthalate (TlAP) crystal measured the spectrum of the X-rays in a spectral range spanning ~ 700 eV from just under 1.3 keV to 1.9 keV including emission lines around 1.5 keV (see Section 7.7). Both cameras are back-illuminated deep-depletion in-vacuum X-ray CCD cameras (Andor DX420-BR-DD). Both measurements were conducted from the side of the target that was heated by the laser and are hence not spectrally filtered by the Kapton tape. Based on the X-ray yield the preliminary estimate for the conversion efficiency from laser light into X-rays in this spectral range was about 4.9 ± 0.3 percent. The X-ray source comprises the first component of the two-photon interaction.

Laser wakefield accelerator and gamma-ray source

The second laser beam was focused down by a 6 m focal length $f/40$ OAP onto the edge of a 17.5 mm long gas cell target[4] to drive a wakefield and accelerate electrons to relativistic energies. The cell was filled with helium and 2 percent nitrogen as dopant at an electron density of $(2.6 \pm 0.4) \times 10^{18}\,\mathrm{cm}^{-3}$. The typical spot size was (44 ± 2) µm × (53 ± 2) µm at 5.51 ± 0.64 J energy on target at a pulse duration of 45 ± 5 fs, corresponding to a normalised vector potential $a_0 = 1.13 \pm 0.18$. The energy on target was limited by the damage threshold of mirrors in the focusing beam. The remaining laser light exiting the cell was disposed of by another replenishable Kapton tape acting as plasma mirror [72].

The two laser beams were synchronised temporally using a fast photodetector and an oscilloscope to an estimated accuracy of ±3 ps (see Section 4.3).

[1] Target and fabrication techniques were developed by the Target Fabrication Division at the Central Laser Facility, in particular Sam Astbury and Chris Spindloe.

[2] The tape drive was designed and built by Brendan Kettle (Imperial College).

[3] The emission spectrum was simulated by John Morton (AWE) using [340, 341].

[4] Gas cell of variable density and length from 1 to 20 mm, designed and built by Nelson Lopes (Imperial College/IST).

The electrons were dispersed downwards by a permanent dipole magnet of integrated field strength $\int B\mathrm{d}x = 0.4\,\mathrm{Tm}$ onto a scintillating Lanex screen measuring their energy and charge. The yoke of the magnet was blocking the path of dispersed electrons with energy below 300 MeV, which results in a corresponding low-energy cut-off in the spectral measurement on the Lanex screen. The screen is imaged by a cooled 16-bit CCD camera (Andor Neo) equipped with an objective and a bandpass filter transmitting (546 ± 10) nm. A (153 ± 3) mm thick lead wall held together on both sides by (9.5 ± 1) mm thick aluminium plates separates the part of the vacuum chamber containing the laser wakefield accelerator, the X-ray source and the magnet spectrometer from the remaining experimental setup. This prevents radiation and secondary particles generated outside the interaction point to propagate further downstream. An aperture of size $(100 \pm 1)\,\mathrm{mm} \times (50 \pm 1)\,\mathrm{mm}$ (horizontal $\times$ vertical) is fitted to the wall, centred on the laser beam axis, to allow, on the other hand, on-axis particles and radiation to pass through.

High-Z foils of various thicknesses are mounted on a motorised linear stage (190 ± 1) mm downstream from the exit of the accelerator and can be driven into the path of the electrons to act as bremsstrahlung converters. This interaction produces copious amounts of directed bremsstrahlung in propagation direction and stops or scatters most of the electrons in the process [274, 331–337]. The gamma-ray beam propagates through the aperture of the dipole magnet used to disperse the electron beam, then through the aperture of the lead wall, and a large aperture dipole magnet. It then passes through a 125 µm thick Kapton window with circular aperture of 80 mm diameter at the end of the chamber into air.

At air, a stack of 20×20 caesium-iodide (CsI) crystals of dimensions 2 mm $\times$ 2 mm $\times$ 20 mm, each individually wrapped in aluminium foil ($\sim 15 - 20$ µm) and held together in a 1 cm thick aluminium casing, measures the transverse profile and yield of the gamma-ray beam. The total transverse area is 40 mm $\times$ 40 mm which corresponds to an acceptance angle of 11.8 mrad, based on a distance of 3.39 m measured from the converter targets to the profile screen. Another larger stack of 33×47 CsI crystals doped with thallium, each of dimensions 5 mm $\times$ 5 mm $\times$ 50 mm and spaced by 1 mm aluminium dividers, measures the decay of the signal in propagation direction to deduce the spectrum [263]. Both CsI arrays are imaged by sensitive cooled 14-bit EMCCD cameras (Andor iXon) equipped with suitable objectives and bandpass filters. The arrays are described in more detail in Section 4.6 of the Experimental Methods.

Divergent gamma-rays are likely to collide with the apertures of either magnet and lead wall as well as other components along the beam axis, for instance the burn-through foil target, producing leptons close to the axis with comparable properties as the Breit-Wheeler pairs [185]. This also motivates the use of a large aperture magnet as the yoke material

is retracted as far as possible from the main axis to avoid any interaction of particles or radiation with the solid. To remove these divergent components of the gamma-ray beam, a tungsten (W) collimator of length 100 mm, inner diameter 2 mm and outer diameter 20 mm is inserted at 180 ± 1 mm distance downstream of the converter target. The field of view from the position of the converter targets through the collimator is $2\,\text{mm}/0.28\,\text{m} = 7.14\,\text{mrad}$. In addition, a 50 mm thick block of tungsten was placed (85 ± 1) mm downstream from the converter targets to obstruct its direct line of sight onto the Ge target drive to prevent the production of Bethe-Heitler pairs [185] in the interaction of the gamma-rays and the tape. By placing the collimator and the block in front of the magnet, any secondary particles produced from an interaction with them are also removed. The tungsten shield effectively bisects the gamma-ray beam. As a result, when introducing the collimator and the shield, only a collimated half-circle of gamma-rays will be incident on the interaction point, providing the second component for the two-photon interaction.

Magnetic Chicane and Single-Particle Detectors

Potential electron-positron pairs from the photon-photon interaction are emitted in the propagation direction of the gamma-ray beam [193]. The pairs enter the field of the permanent large aperture (10 cm gap) dipole magnet with integrated field $\int B(x)\mathrm{d}x = 0.35\,\text{Tm}$ that disperses the electrons and positrons horizontally in opposite directions. Electrons and positrons with an energy < 220 MeV collide with the yoke of the magnet, producing a low-energy cut-off in the particles leaving the magnet. Electrons and particles, dispersed in opposite directions, are then leaving the vacuum chamber into air through two separate, elongated Kapton windows of dimensions 150 mm $\times$ 35 mm (horizontal $\times$ vertical) that flank the circular Kapton window for the gamma radiation on either side. (60 ± 1) mm downstream of the vacuum window a second 150 mm thick lead wall is installed to shield radiation and secondary particles produced in the chamber. The wall is fitted with a (598 ± 2) mm $\times$ (150 ± 1) mm wide aperture centred on the radiation axis, allowing the dispersed particles and the gamma-ray beam to propagate through. The dispersed positrons are then caught by an oppositely polarised permanent magnet[5] of field strength $B \sim 0.5\,\text{T}$ that bends the positrons onto the narrow aperture of a lead-shielded enclosure and onto a set of detectors that are housed within. The acceptance bandwidth of the chicane is $220 - 380$ MeV. The positrons pass through two TimePix3 [342] silicon detectors[6] that are used as tracking layers [343] and onto a CsI array attached to an intensified CCD camera (4 Picos ICCD camera by Stanford Computer Optics) that acts as a single-particle detector[7]. On the other side, the electrons also encounter a dipole

[5]The design of the magnets and the chicane as well as the supervision of the magnet assembly and positioning was performed by D. Hollatz (Jena).

[6]Provided by the Medipix Collaboration, CERN

[7]Developed by the Helmholtz Institute Jena.

magnet with opposite polarisation. It is identical to the magnet on the positron side, positioned symmetrically with respect to the gamma-ray axis, and bends the electrons onto a scintillating Lanex screen. By driving out the first electron spectrometer magnet in the system and translating in a Lanex screen behind the large aperture magnet, the set of two oppositely polarised magnets can be used to measure the LWFA electron beam on these two Lanex screens. The electron beam can then be used to confirm that the setup of the magnetic chicane is working according to its design parameters.

7.4 Characterisation of Electron Spectra

In this experiment electrons are accelerated in a gas cell target to relativistic energies by laser wakefield acceleration to be then passed through a metal foil to produce directed and highly energetic bremsstrahlung [274, 331–337]. The properties of the generated radiation are determined strongly by the properties of the electron beam [52, 339] and hence need to be characterised. Introducing the bremsstrahlung converter foils into the beam path of the electron beam leads to a conversion of electron energy into radiation and also scattering [272, 273], such that we can not characterise the electron spectra and the gamma radiation simultaneously. As a consequence, the electron spectra presented as follows were measured with a clear beam path.

High and low density accelerator settings

During the commission of the bremsstrahlung source, the accelerator was initially operated in two configurations: one uses a higher electron density of $(3.8 \pm 0.5) \times 10^{18}\,\mathrm{cm}^{-3}$, the other one a lower density of $(2.6 \pm 0.4) \times 10^{18}\,\mathrm{cm}^{-3}$. The 'low density' accelerator produced electron beams reaching energies up to 800 MeV at ~ 30 pC charge and < 3 mrad divergence (Figure 7.5, bottom). The electron spectra in the 'high density' setting, on the other hand, reached ~ 500 MeV at an divergence of > 3 mrad and up to ~ 50 pC of beam charge (Figure 7.5, top), but at lower reproducibility on a shot-to-shot basis. On the final shot days aimed at photon-photon collisions, the accelerator was operated at the 'low density' configuration.

Performance of the accelerator on shot days

The performance of the wakefield accelerator can vary from day to day [22] and is hence characterised separately for three shot days that we will simply refer to as days A, B and C. On day A, one dataset was taken to characterise the performance of the accelerator, on days B and C two and three datasets were taken, respectively. The lineouts for the average electron spectra for those days are shown in Figure 7.6. An overview of the key properties

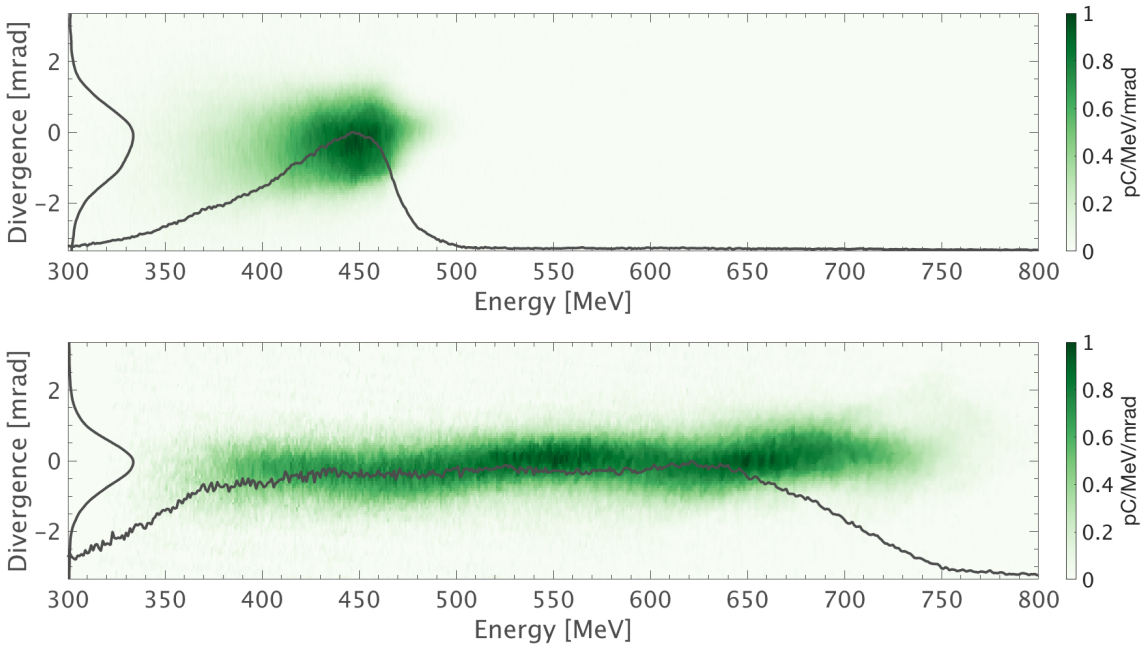


Figure 7.5: Example of electron spectra measured on the experiment operating the accelerator at 'high' (top) and 'low' electron densities (bottom). The electron densities were (3.8 ± 0.5) *and* $(2.6 \pm 0.4) \times 10^{18}\,\mathrm{cm}^{-3}$*, respectively. The x-axis indicates the electron energy in MeV, the y-axis the divergence of the beam in mrad. The colour scale encodes the charge per MeV and per mrad of the beam scaled to the maximum in the image, with darker regions containing more charge.*

of the electron beam (charge, maximum energy, divergence and beam pointing) on the three shot days are shown in Table 7.1 and Figure 7.7.

In general, the measured electron beams have a relatively flat spectrum with large energy spread and no quasi-monoenergetic feature. This is consistent with previous measurements of electron beams injected by ionisation injection at GEMINI or comparable laser systems [203, 204, 256]. The spectrum reaches up to 550 MeV for days B and C, and just over 700 MeV for day A. The average beam charge is the highest on day A with $(26.26 \pm 3.8)\,\mathrm{pC}$, whereas it only amounts to about half of this on the other two days. Across the days, the FWHM divergence of the electron beams was $< 3\,\mathrm{mrad}$ with a beam pointing of $< 1\,\mathrm{mrad}$, with day A exhibiting the lowest divergence and pointing followed by day B and then C. Between the three shot days, the performance of the accelerator was the best on day A, reaching the highest electron energies at the highest beam charge at the lowest divergence and pointing.

The maximum energy and the charge in the electron beams is lower than typically achieved at GEMINI, where electron beams of charge $> 100\,\mathrm{pC}$ and energies of $\sim 1\,\mathrm{GeV}$ are routinely measured [83, 251, 344] with peak energies exceeding 2 GeV in some instances [69, 163]. Here the on-target energy in the wakefield driver laser was limited to $5.51 \pm 0.64\,\mathrm{J}$ due to the damage threshold of the mirrors in the focusing beam, which is about half of

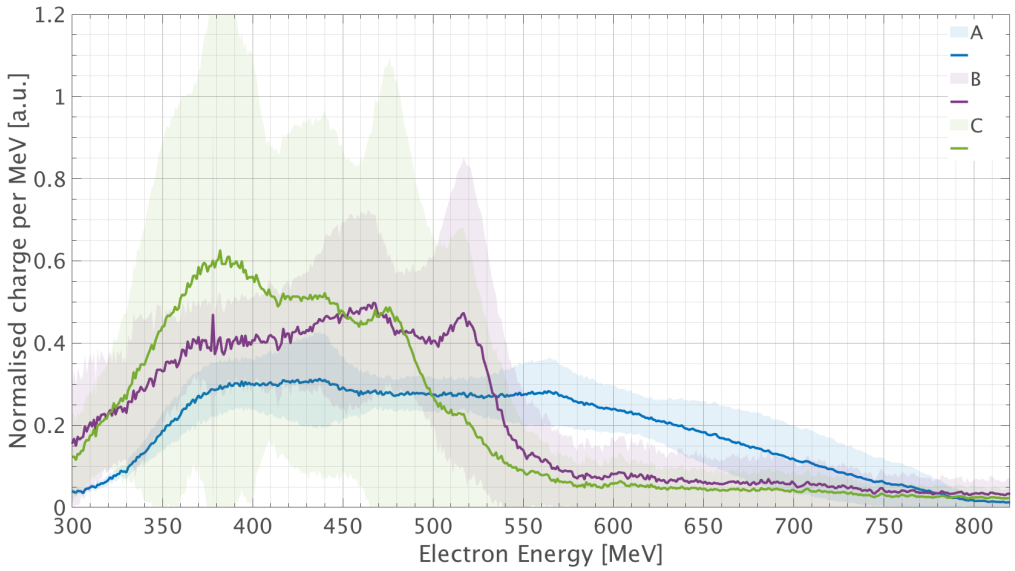


Figure 7.6: Average electron spectra for the relevant shot days (A in blue, B in purple and C in green). The spectra are normalised such that the total charge is equal for each spectrum. The shaded areas indicate 1 standard deviation from the average spectrum.

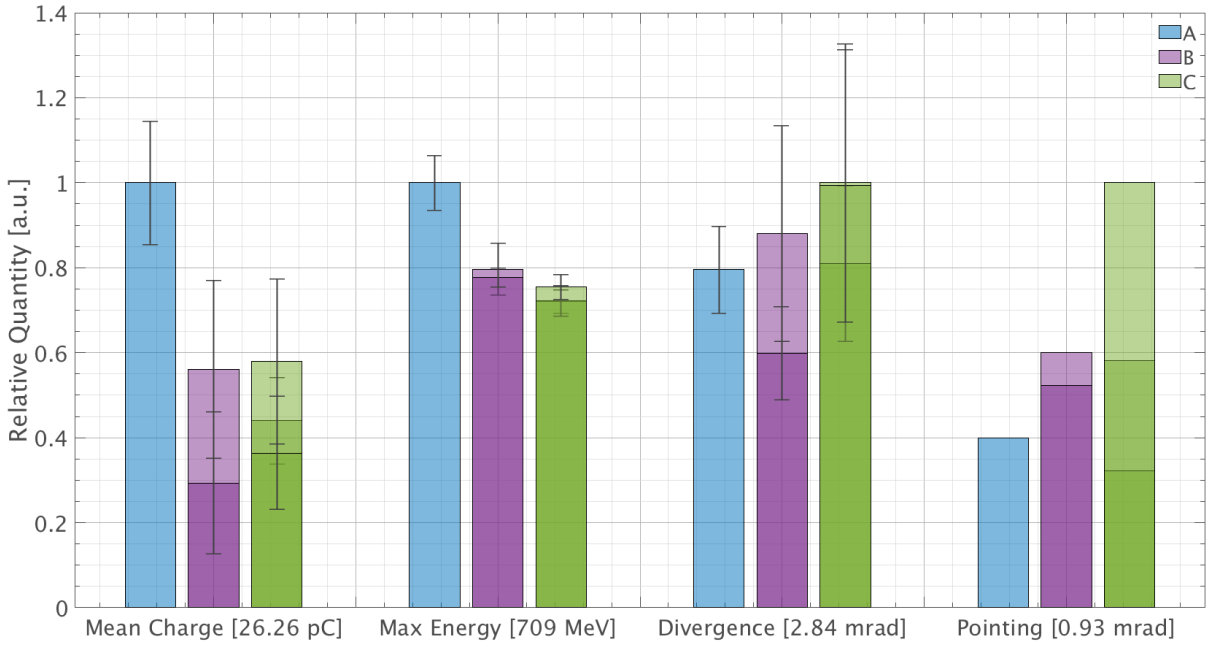


Figure 7.7: Bar charts summarising the average electron beam properties measured on the relevant shot days A, B and C. The height of the bars are for each group normalised to the maximum of the respective group. Multiple overlapping bars indicate several data sets for that particular day (2 data sets for B, 3 for C). From left to right: average electron beam charge, maximum energy, divergence and beam pointing. The error bars indicate 1 standard deviation from the average value assuming a normal distribution.

Overview of Electron Beam Properties						
Day	**Run**	**Charge [pC]**	**E_{max} [MeV]**	**θ [mrad]**	**σ_X [mrad]**	**N_{shots}**
A	1	26.26 ± 3.8	709 ± 46	2.26 ± 0.29	0.62	10
B	1	14.73 ± 5.5	565 ± 43	2.5 ± 0.72	0.93	18
B	2	7.7 ± 4.4	551 ± 16	1.7 ± 0.31	0.81	12
C	1	11.55 ± 2.7	511 ± 19	2.84 ± 0.93	0.90	22
C	2	15.24 ± 5.1	512 ± 26	2.3 ± 0.52	0.50	6
C	3	9.56 ± 3.5	535 ± 21	2.82 ± 0.91	1.55	21

Table 7.1: Overview of electron beam properties for the relevant shot days A,B, *and* C, *and the data set for those days (runs). The maximum energy E_{max} is defined as the energy when the spectral intensity falls to 10 percent of its peak value. θ is the* FWHM *divergence angle and σ_X is the beam pointing fluctuation in the horizontal, non-dispersion axis. N_{shots} is the number of shots within a data set (run).*

the energy used in other experiments at Gemini [69, 163], which might have resulted in a lower maximum energy and lower charge in the electron beam overall [222].

7.5 Characterisation of Bremsstrahlung Targets

The properties of the bremsstrahlung depend on the interplay of the electron beam, which we just characterised, and the choice of the converter material. We will investigate in the following the properties of bremsstrahlung produced with two different materials (tungsten and bismuth) at two target thicknesses and in two different accelerator settings. Based on the yield of gamma-rays, the divergence and the noise measured on the positron detectors, we will then identify the most suitable configuration to use for the photon-photon collisions.

Gamma yield for different materials and electron regimes

An overview of the of the targets is shown in Table 7.2. The materials used in this experiment are tungsten (W) and bismuth (Bi). Both are high-Z materials ($Z = 74$ and 83), which means energy can be efficiently converted to radiation within thinner targets resulting in less scattering and divergence [52, 339]. Tungsten is very dense at $\rho = 19.3\,\mathrm{g/cm^3}$, whereas bismuth is about half as dense [345]. Both materials are also readily available and easy to handle. The converter materials were mounted on 0.5 mm plastic (PTFE) and placed on a motorised linear stage that allows switching between the materials or removing the converter targets from the beam path completely. The specific target thicknesses used were 2 mm and 4 mm for tungsten (W), which correspond to just

Overview of Bremsstrahlung Converter Targets					
Material	**Z**	**ρ [g/cm^3]**	**X_0 [mm]**	**d [mm]**	**d [X_0]**
Tungsten (W)	74	19.3	3.504	4	1.14
				2	0.57
Bismuth (Bi)	83	9.747	6.454	1	0.15
				0.5	0.08

Table 7.2: Overview of bremsstrahlung converter targets used in the experiment. Tungsten (W) and bismuth (Bi) targets of density ρ were used at two different thicknesses, d, each, also expressed in units of the radiation length, X_0.

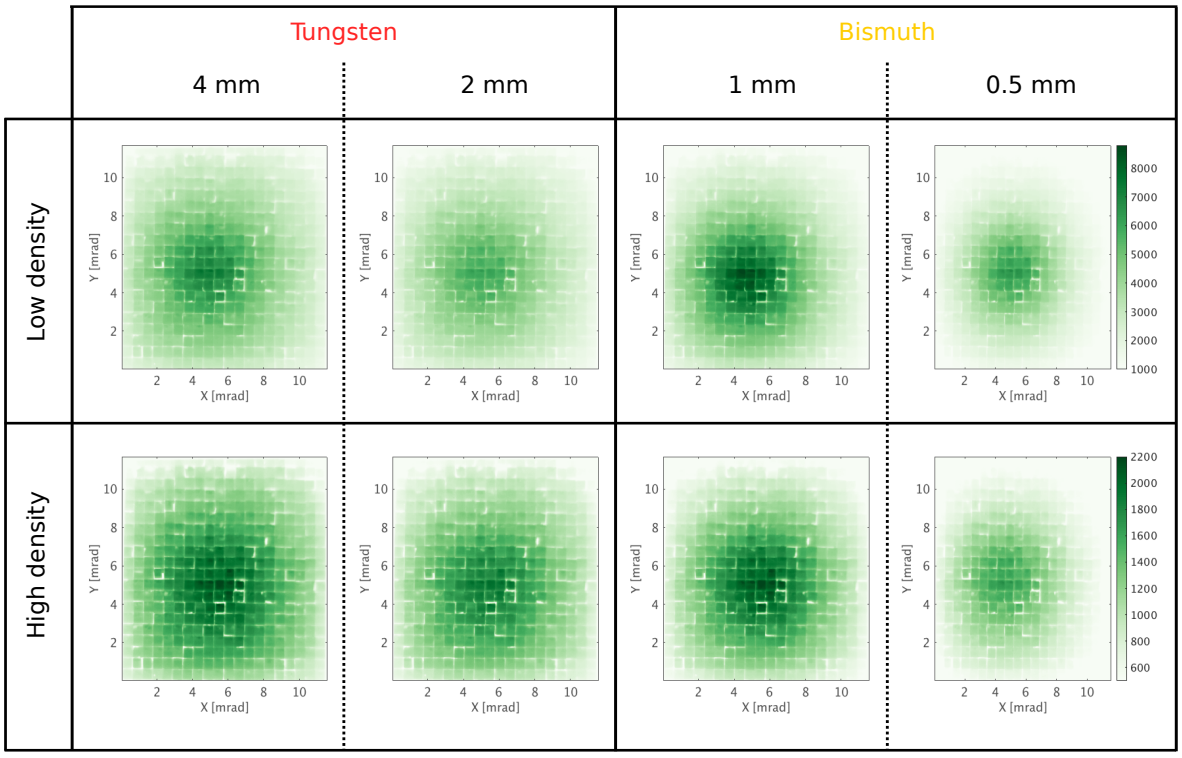


Figure 7.8: Montage of over 10 shots averaged gamma profile images for different materials and accelerator configurations. The rows (vertical) indicate the accelerator configuration the image is representative of, whereas each column refers to a different target material or thickness. The thickness of targets decreases from left to right. The colour scale shows the number of pixel counts on the camera which is proportional to the number of emitted scintillation photons per mrad^2. The images on the top row and the images on the bottom row are at the same colour scale, respectively.

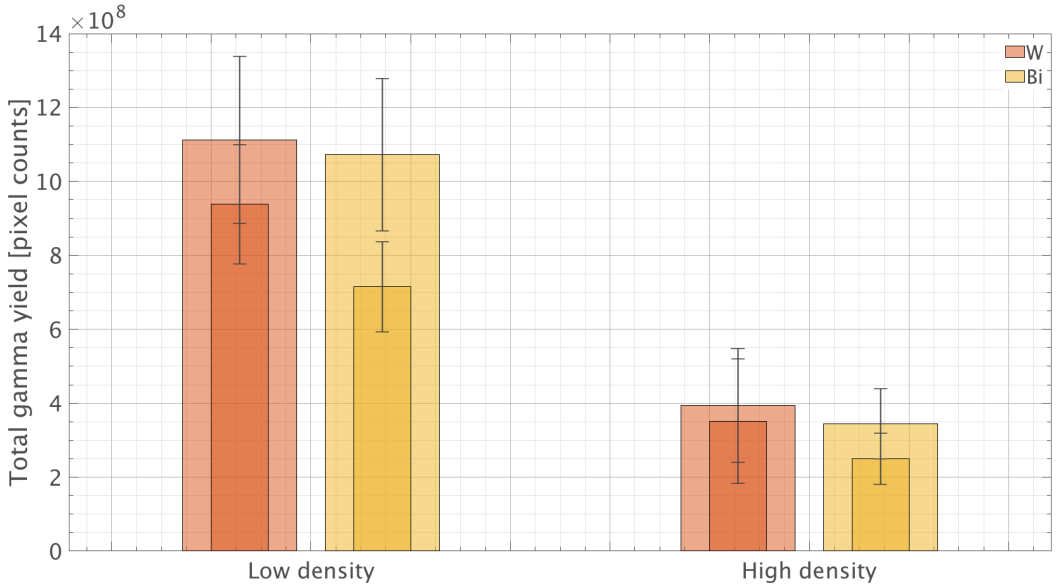


Figure 7.9: Total measured gamma yield of the gamma-ray beam at two accelerator configurations (low and high electron densities) for tungsten (W, red) and bismuth (Bi, yellow). The values for the thin and the thick targets are shown by the thin and thick bars, respectively. The error bars indicate the standard deviation from the mean assuming a normal distribution of the data.

over 0.5 and 1 radiation lengths, X_0 [52, 345]. The bismuth (Bi) targets were 0.5 and 1 mm thick, which corresponds to 0.08 and $0.15X_0$. From the thicknesses and radiation lengths, we expect that the tungsten targets will convert more of the electron energy into bremsstrahlung but that the bismuth targets produce a more collimated beam of radiation [339]. We will investigate this in the following. We also consider the two accelerator configurations discussed in the previous section. 10 shots were taken for each target and accelerator setting. Figure 7.8 shows a montage of the averaged gamma profile response in each configuration.

Figure 7.9 presents the average yield of gamma-rays measured on the gamma profile screen for each of the configurations in form of a bar chart, where each bar represents the average of a 10-shot dataset and the error bars indicate the standard deviation. The materials are colour-coded, with results related to tungsten coloured in red and bismuth in yellow. The thick red bars indicate that the thicker tungsten target ($d = 4\,\text{mm}$) was used, the thin bar relates to the thinner target ($d = 2\,\text{mm}$). Similarly, the thick yellow bar corresponds to the bismuth target of thickness $d = 1\,\text{mm}$ and the thin one for $d = 0.5\,\text{mm}$. The bars are presented in two groups, one labelled with 'low density', the other one with 'high density', which relates to the configuration of the accelerator.

In general, the bremsstrahlung source achieves consistently a higher yield at the 'low

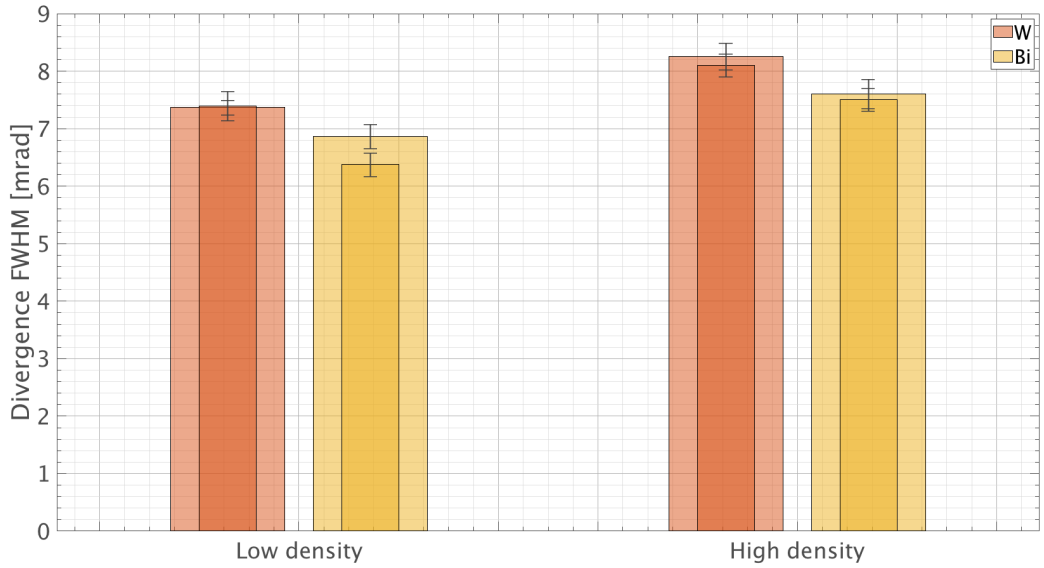


Figure 7.10: FWHM *divergence of the gamma-ray beam at two accelerator configurations (low and high electron densities) for tungsten (W, red) and bismuth (Bi, yellow). The values for the thin and the thick targets are shown by the thin and thick bars, respectively. The error bars correspond to* ± 1 *standard deviation from the mean under the assumption of a normal distribution.*

density' configuration. Thicker targets produce in all configurations a higher yield than their thin counterparts of the same material, as expected from their respective thickness in radiation lengths. This trend is more pronounced for bismuth. Despite the different thicknesses, the yield is very similar at each configuration, with mainly the thin bismuth target producing a significantly lower yield.

The FWHM divergence of the measured radiation profiles is shown in a similar format in Figure 7.10. The divergences are in general larger at high densities than at low densities, which might be due to the larger initial divergence of the electron beam, θ_e, and the decrease in energy. We expect the divergence of the radiation to roughly scale as [339]

$$\theta \sim \sqrt{{\theta_e}^2 + \left(\frac{\ln \gamma}{\gamma}\right)^2}, \tag{7.5.1}$$

where the divergences of the radiation cone and the electron beam become additive if one clearly dominates. The divergence is $> 6\,\mathrm{mrad}$ in all configurations. At a fixed accelerator configurations, thicker targets result on average only in a slightly increase in divergence, with exception of tungsten at low densities which shows no significant difference. The slight increase might be due to small-angle scattering of the electron beam in the material [272, 273], but has overall only a small effect. The radiation with the lowest divergence

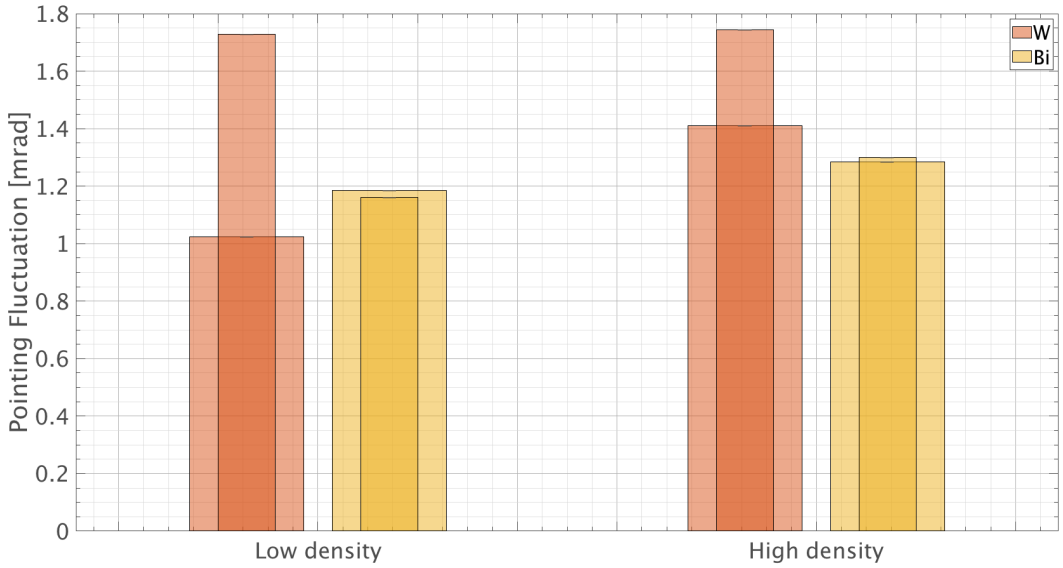


Figure 7.11: Pointing of the gamma-ray beam at two accelerator configurations (low and high electron densities) for tungsten (W, red) and bismuth (Bi, yellow). The values for the thin and the thick targets are shown by the thin and thick bars, respectively.

was measured using the thinnest target, bismuth of $d = 0.5\,\text{mm}$, also at the low density configuration of the accelerator. The thin bismuth target, however, produced the lowest yield, which indicates that yield and divergence have to be weighted against each other. The low density configuration seems to be favourable for the accelerator.

Finally, the pointing variations of the gamma-ray beam are shown in Figure 7.11. The pointing should not be material-dependent but inherited from the electron beam [339]. In all cases, the pointing of the beam centroid is $> 1\,\text{mrad}$, reaching a maximum for the thin tungsten targets at just over $1.7\,\text{mrad}$ at both accelerator configurations. However, there does not seem to be a general trend as for the divergence and the yield, which indicates that these fluctuations are due to variations in the electron beam performance and not due to the change in converter material.

The survey of the gamma-ray beam properties so far has shown that thicker targets produce a higher yield of gamma radiation with a slight increase in the divergence of the beam profile in some cases, and that a low density configuration is favourable in either case. The tungsten collimator is $100\,\text{mm}$ long and its aperture permits an optical field of view of $7.14 \pm 0.1\,\text{mrad}$ full angle, with an acceptance angle at its entrance of $11.11 \pm 0.1\,\text{mrad}$. The choice of material is then based on the effective yield that is transported through the collimator and is incident on the interaction point. An example of a gamma-profile measurement with and without collimator is shown in Figure 7.12. The circular aperture

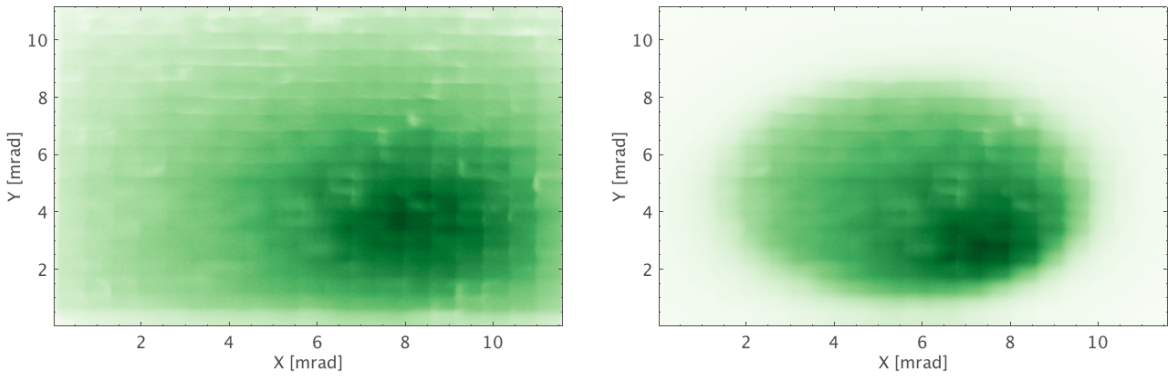


Figure 7.12: Examples of gamma profile measurements of the bremsstrahlung source with the tungsten collimator in (right) and out (left) in units of mrad. The x-axis indicates the divergence in the horizontal direction, the y-axis in the vertical axis. The colour scale indicates the number of pixel counts on the camera which is proportional to the number of emitted scintillation photons per mrad^2.

seen on the profile monitor has a FWHM of 6.2 mrad which corresponds to 10.5 mrad width to decay to $1/e^2$ of its peak value, assuming a Gaussian distribution[8]. This is larger than the predicted field of view of 7.14 ± 0.1 mrad and matches more the acceptance angle of the collimator at its entrance. The soft edges indicate this is due to hard and slowly expanding radiation penetrating parts of the collimator.

Considering the collimator and the measured divergences of the gamma rays, we can now estimate the fraction of the gamma-ray beam that will be transmitted through the collimator. We will use the measured FWHM divergences and model the intensity profile after a two-dimensional Gaussian. We will also assume that the peak of the distribution is centred on the collimator and ignore any beam pointing as it does not depend on the material. We then integrate in both dimensions up to a transverse cut-off at 11.11 mrad, assuming that any radiation beyond this angle is terminated efficiently by the collimator. Figure 7.13 shows the transmitted gamma yield estimated this way. Similarly as before, the low-density accelerator achieves a higher yield as the high density configuration, which has a lower initial yield and higher divergence. In general, thicker targets still produce a higher yield of gamma rays that is transmitted through the collimator than their thinner counterparts of the same material. The highest yield after the collimator is achieved using bismuth of thickness $d = 1$ mm, followed by tungsten of $d = 4$ mm. Based on this bismuth of $d = 1$ mm in a low density configuration of the accelerator seems to be the most suitable choice for the bremsstrahlung source as the highest yield is transported to the interaction point.

[8]The FWHM divergence of the unperturbed Gaussian gamma-ray profile and the field of view of the collimator are of comparable size. As a result, the profile is truncated at the tails of the distribution, narrowing its width but preserving its overall Gaussian shape.

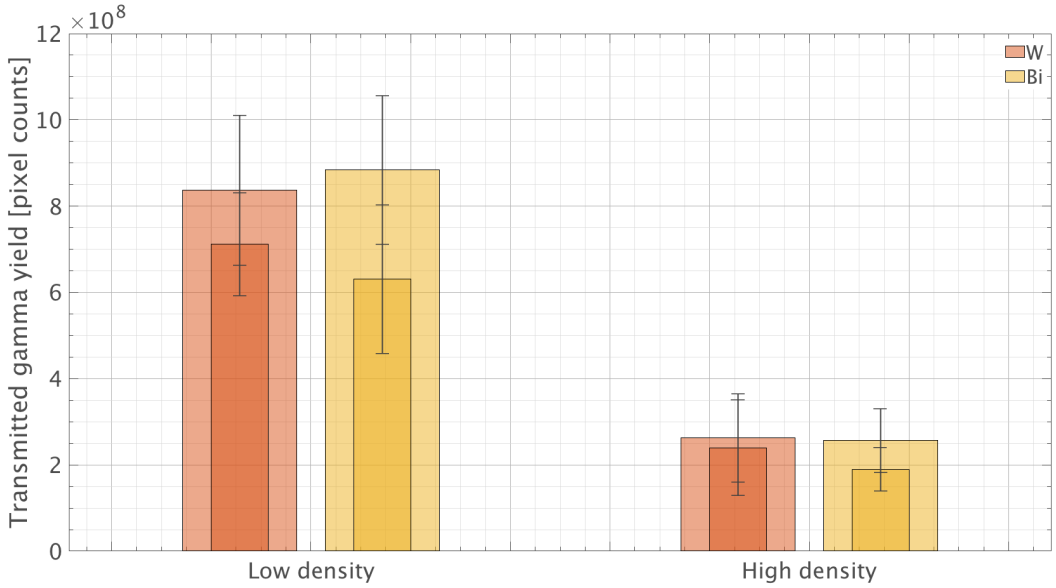


Figure 7.13: Estimated transmitted yield through the collimator assuming a cut-off at 11.11 mrad at two accelerator configurations (low and high electron densities) for tungsten (W, red) and bismuth (Bi, yellow). The values for the thin and the thick targets are shown by the thin and thick bars, respectively. The error bars indicate the standard deviation from the mean value assuming a normal distribution.

Background candidate events

The positrons produced by the Breit-Wheeler process are detected by the TimePix3 detectors[9] [342] (see Figure 7.14). These are sensitive to gamma rays and charged particles over a wide range of energies. The shape of the tracks in the detector allows some events to be excluded [343]. For example, low energy charged particles produce wiggly tracks, high energy particles or gammas produce straight tracks, the length of which provides information about the angle of incidence. As positrons transported through the magnetic chicane from the collision point enter the detectors within a specific range of angles, this can be used to exclude some high energy events. Events which are not excluded are 'candidate events'.

Gamma rays can interact with material in the chamber (e.g. the magnets, lead walls, Kapton tape) and produce positrons via the Bethe-Heitler process that have similar characteristics (energy, angle into the chicane) so that they are indistinguishable from Breit-Wheeler positrons on the detector. Gamma rays striking the vacuum windows can also scatter into the detector at an angle corresponding to a candidate event. We might expect that the number of these noise events will depend on the gamma yield. The following section examines this for the scenarios discussed previously.

[9]The detectors were provided by the MediPix Collaboration (CERN), simulated by Robbie Watt (Imperial College) and the data was analysed by Brendan Kettle (Imperial College).

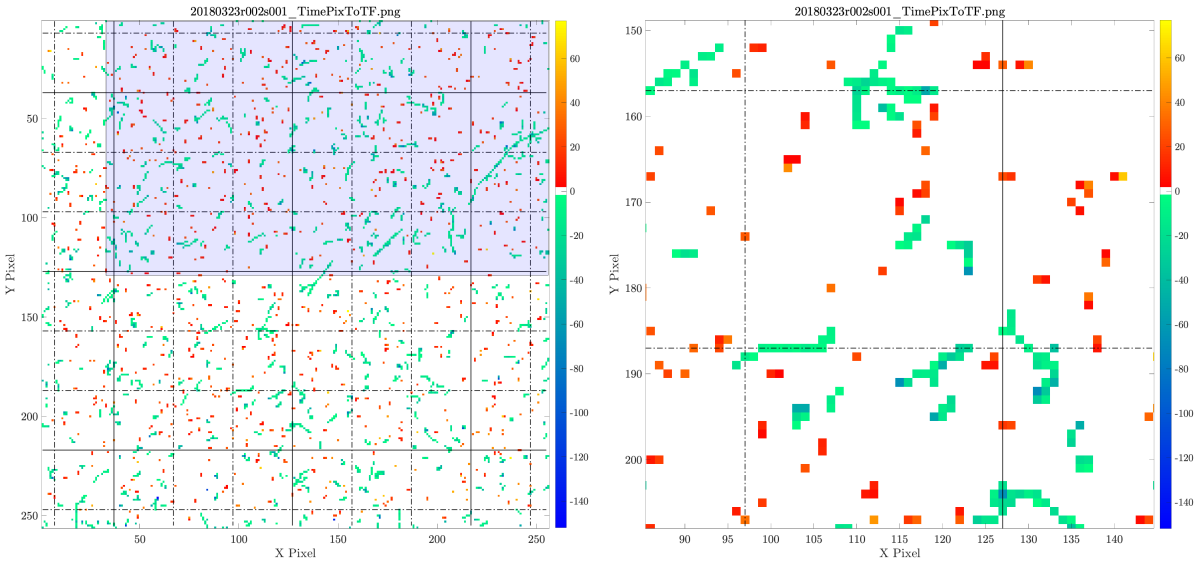


Figure 7.14: On-shot data from a 255 × 255 pixels wide TimePix3 chip (left, zoomed in on the right). The colour scale indicates potential candidate events (red, above zero, localised) and excluded events (green/blue, below zero, extended tracks). The shaded blue area shows the overlap of this chip with a second TimePix3 chip, which can be used to exclude even more events by tracking hits between the two layers. Figure courtesy of Brendan Kettle.

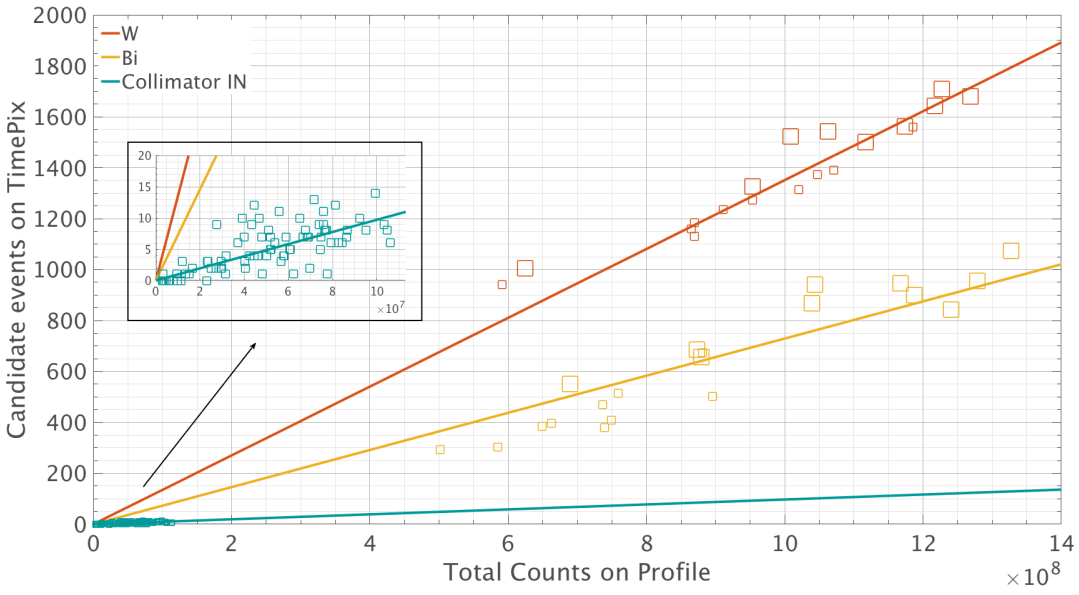


Figure 7.15: Candidate events on the TimePix detectors as function of the yield measured on the gamma profiles for tungsten (W, red), bismuth (Bi, yellow) and with the collimator in the beam path (cyan). The large squares indicate results from thick, the smaller ones from thin converter targets. The gradients indicate a material-dependent noise-to-yield ratio. The inset enlarges the region of low profile counts and few candidate events.

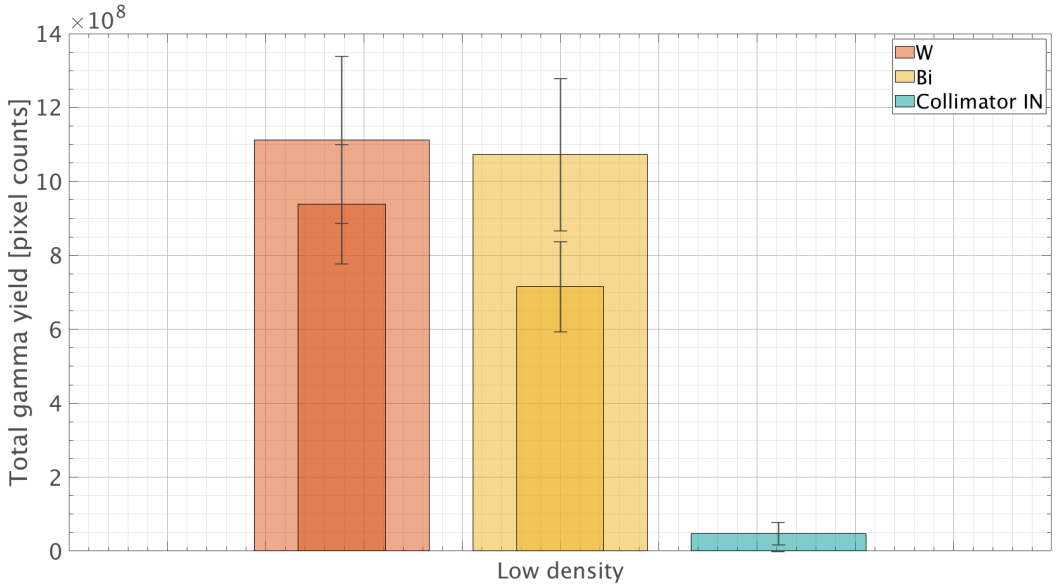


Figure 7.16: Total measured gamma yield at low density accelerator configuration for tungsten (W, red) and bismuth (Bi, yellow). In turquoise the gamma yield measured using the thick bismuth target and the collimator in the beam path. The values for the thin and the thick targets are shown by the thin and thick bars, respectively. The error bars are the standard deviation from the mean assuming a normal distribution of the data.

The number of background candidate events measured on the TimePix3 detector is shown in Figure 7.15 as a function of the gamma yield on the same shot. Here we only considered the results taken at the 'low density' configuration of the accelerator, where red markers again indicate results from tungsten targets and yellow from bismuth targets, respectively. Larger markers refer to results from thick and smaller markers to results from thinner targets. For each material, the gamma yield seems to correlate well linearly with the number of measured candidate events. The linear correlation coefficient for tungsten is 0.97 and for bismuth 0.95. The gradient of the linear fit indicates the number of background candidate events produced per yield measured on the gamma profile detector, i.e. is an indicator of noise over yield (which is used to generate a signal). The inverse of the gradient is then an indicator of yield over noise or signal to noise. The gradient for tungsten is steeper than for bismuth which indicates that more noise is being produced per unit gamma yield reaching the gamma detector. A material of higher density scatters the electron beam more strongly, which results in more gamma rays being emitted at angles that allow for interaction with the magnet and shielding apertures. Interestingly, the thickness of the targets itself does not seem to have an as large impact on the noise production as the material itself.

Figure 7.15 also includes the dataset with the tungsten collimator in the beam path

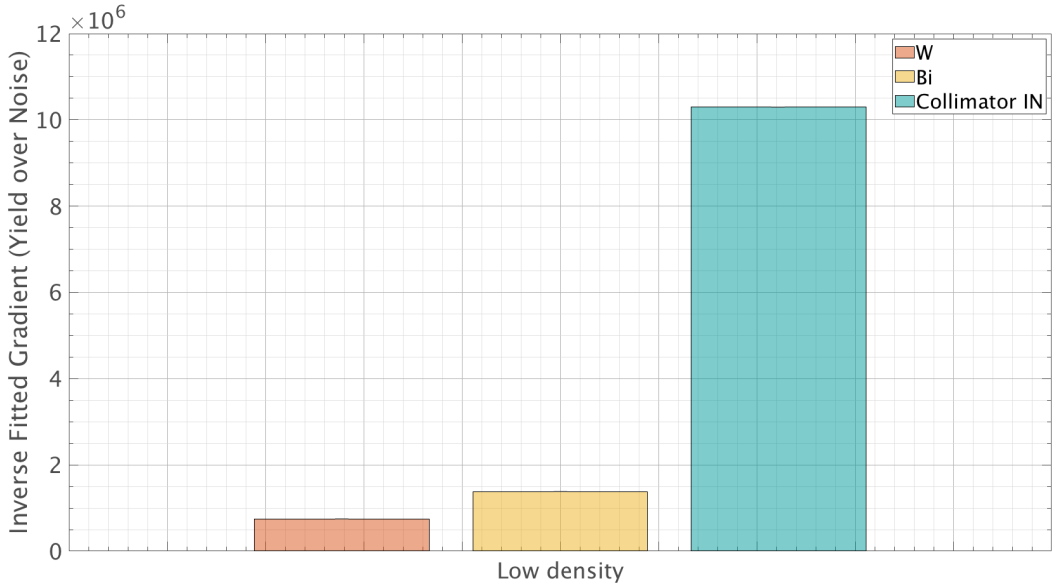


Figure 7.17: Inverse of fitted gradient (yield over noise) from Figure 7.15 at low density accelerator configuration for tungsten (W, red) and bismuth (Bi, yellow). In turquoise the gradient fitted for the data using the thick bismuth target and the collimator in the beam path.

(cyan, enlarged in inset). For this dataset we used the optimum conditions determined so far (low density, bismuth at $d = 1\,\mathrm{mm}$). The gamma yield and the number of candidate events is much lower than the results without collimator (see also Figure 7.16), but we also see that the gradient of the linear fit relating to the data with the collimator is much lower than for the data without. The inverse gradient, an indicator for the signal-to-noise ratio, is then much higher with the collimator in the beam path (see Figure 7.17). This clearly shows that the collimator is performing as intended, by spatially filtering the components of the radiation that are most likely to generate Bethe-Heitler pairs.

Summary

In this section, we compared the performance of a LWFA driven bremsstrahlung source for tungsten and bismuth at two thicknesses and two accelerator configurations. We found that the highest yields were achieved at the low-density configuration of the accelerator and thicker converter targets produce higher radiation yields. Tungsten of thickness $d = 4\,\mathrm{mm}$ and bismuth of $d = 1\,\mathrm{mm}$ reached the highest yields. The divergences of the radiation profiles were found to be slightly larger for thicker targets and the high-density configuration of the accelerator, but $> 6\,\mathrm{mrad}$ in all settings. Factoring in the field of view of the tungsten collimator, the effective yield reaching the interaction point was the highest for bismuth of thickness $d = 1\,\mathrm{mm}$. We also considered the correlation of gamma yield and the production of noise in form of background candidate events measured by the TimePix3

detectors that are used to measure the positrons created in the Breit-Wheeler process. A material-dependent linear relation was found linking measured gamma yield and the number of detected candidate events. The number of events generated per gamma yield was lower for bismuth than for tungsten, which again favours bismuth as choice. In this context, we also confirmed that the tungsten collimator performs well and improves the signal to noise by a factor of 7 for bismuth. As a result, bismuth of thickness $d = 1\,\text{mm}$ at a low density configuration appears to be the best choice as it produces the highest yield reaching the interaction point through the collimator and generates the lowest amount of noise in form of background candidate events.

7.6 Characterisation of Gamma Spectra

We will now characterise the gamma spectra and their variations for the relevant shot days at the optimum conditions identified before. Due to the intrinsic variations of the wakefield accelerator characterised in Section 7.4, we also expect the emitted gamma spectrum to vary on those days. To estimate the range of spectra that can be produced on these days, we selected three different examples of electron spectra measured in the experiment, shown in Figure 7.18 (top left). One spectrum (blue) has a very flat energy distribution from 350 to just under 700 MeV, with a fall-off reaching up to 800 MeV electron energy. The next spectrum (green) is sharply peaked at 350 MeV with a slow roll-off up to 800 MeV. The third spectrum is strongly peaked at 450 MeV electron energy with a shoulder falling off to lower energies and a sharp cut-off at 500 MeV, and a maximum energy reaching just under 600 MeV. We then simulated the bremsstrahlung spectrum produced by these electron spectra in an interaction with a 1 mm bismuth foil using GEANT4 [262]. The resulting bremsstrahlung spectra are also shown in Figure 7.18 (top right), where the gamma-ray spectra are coloured as their corresponding electron spectra. Despite the different spectral shapes of the electron spectra, the simulated gamma spectra are close in shape and follow the same exponential fall-off for up to 400 MeV. The maximum energies of the radiation spectra match the maximum energies of the related electron spectra, which introduces the main difference between the spectra. The bremsstrahlung process mitigates the intrinsic fluctuations in spectral shape and energy of the wakefield electron beam efficiently and reduces the fluctuations to its high-energy tail, which contributes only a low number of photons to the overall spectrum.

Figure 7.18 (bottom left) shows the response of the gamma spectrometer to the respective gamma spectra: the responses for both peaked spectra (orange and green) are visually not distinguishable, whereas the response for the gamma spectrum reaching the highest energies (blue) is shifted slightly towards to higher crystal numbers. The response of the detector is dominated by the spectrum below 400 MeV and is not able to

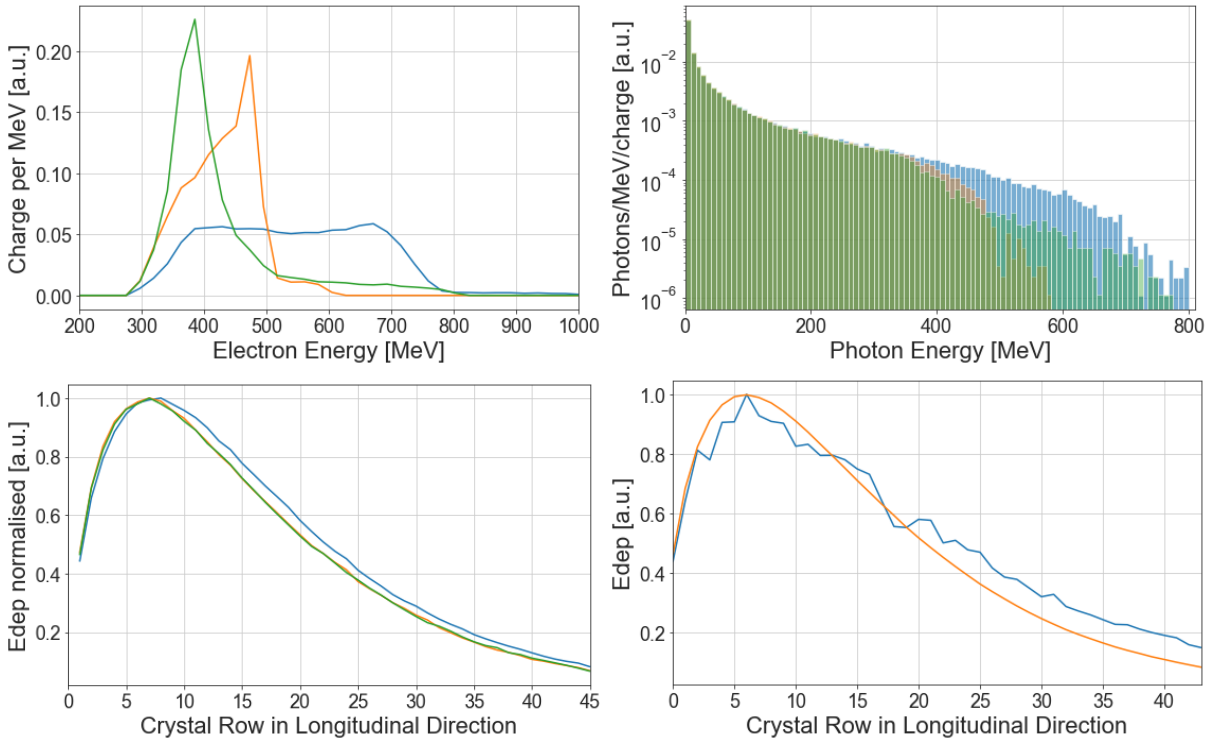


Figure 7.18: Top left: Examples of electron spectra measured in the experiment (normalised by charge) and used as simulation input. Top right: Resulting gamma spectra per unit charge based on GEANT4 simulations of the spectra on the left. Bottom left: Simulated detector responses for the simulated spectra. Bottom right: Example of an experimentally measured raw response (blue) and corresponding simulation (orange).

clearly resolve a spectral change as induced by the variation in shown spectra. Figure 7.18 (bottom right) shows an example of an experimentally measured response curve. Due to experimental uncertainties of background noise and imperfections in the detector setup, we are also not able to measure the small difference in the responses shown in Figure 7.18 (bottom left), which would have given indication of significant changes in the spectrum. As we are unable to measure the electron beam on-shot when the converter targets are inserted into the beam path, we are not able to resolve any shot-to-shot fluctuations in the high-energy tail of the gamma spectrum on-shot. Instead, we are limited to confirm experimentally only that the mean energy of the bremsstrahlung source remains stable on a shot-to-shot basis and on all three days, without measurable deviations from the simulated detector response. The spectrometer also provides the on-shot yield of the radiation, which is linearly correlated with the yield measured on the gamma profile screen at a correlation coefficient of > 0.99, so that either diagnostic provides an equivalent measurement of this observable.

In order to quantify the variation in performance for the shot days nonetheless, we will rely on the characterisation of the electron beams presented in Section 7.4. The reference electron spectra for each shot day are used to simulate the corresponding gamma spectra

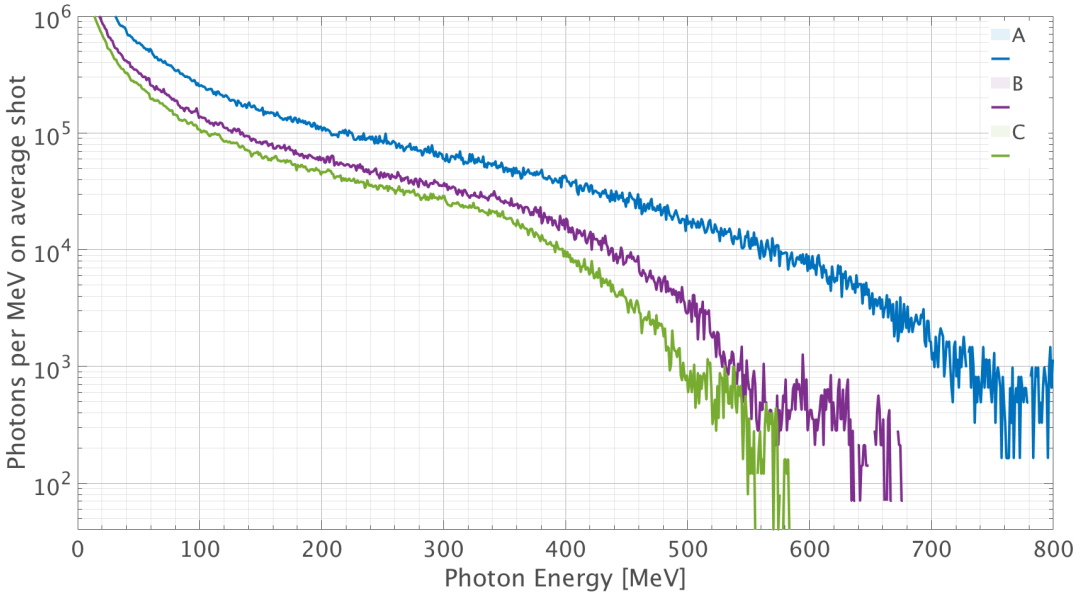


Figure 7.19: Average gamma spectra for the relevant shot days (A, B and C), obtained by simulating gamma spectra for electron beams measured in the experiment. The average number of photons per shot per MeV is shown as a function of the photon energy. The spectra were scaled relative to each other such that their integrated yield matches the measured relative yield of radiation measured experimentally on the shot days.

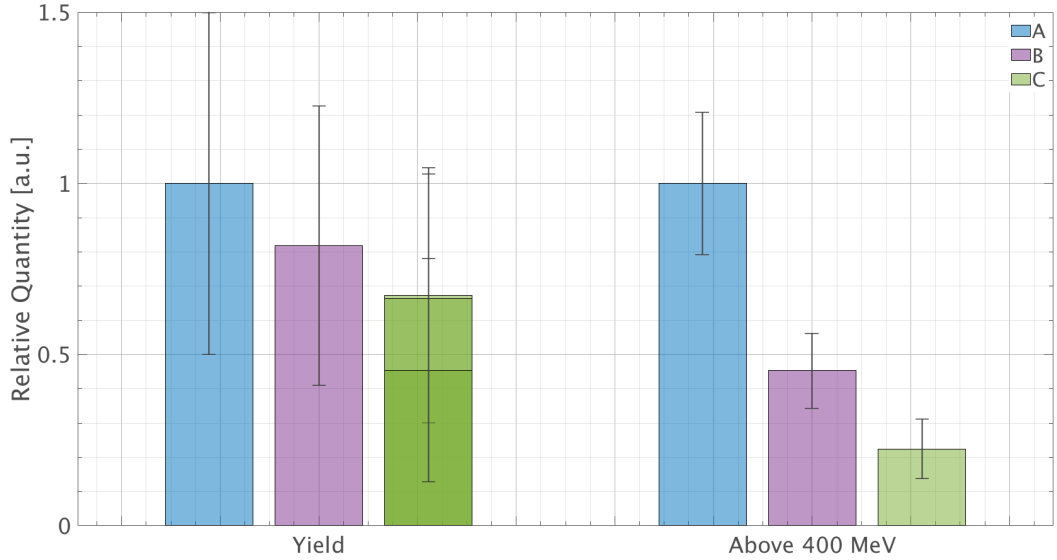


Figure 7.20: Left: Average gamma-ray yield measured with the gamma profile on shot days A (blue), B (purple) and C (green), normalised to the maximum value in the group. The error bars indicate the standard deviation from the average assuming a normal distribution. Right: Fraction of photons above 400 MeV contributing to the overall spectrum based on the average gamma spectra simulated in GEANT4 (Figure 7.19). The error bars indicate the change induced by the standard deviation on the spectral shape of the electron beams.

in GEANT4 and, using in turn these simulated spectra, an average gamma spectrum is determined for each day (see Figure 7.19). As the average electron spectra are representative of the performance of the accelerator on that day, the simulated gamma spectra will also, within limits, reflect the performance of the bremsstrahlung source. It should, however, be noted that this does not capture changes in performance throughout the process of data taking and that this link becomes less reliable the more the characterisation of the electron source and a particular data shot are separated in time. However, the experimental response of the gamma spectrometer did not change shape measurably over the course of the relevant shot days. This suggests that the mean energy, dominated by the large number of photons at low energies, remained stable. On the other hand, this is by itself not sufficient to determine whether the same holds for the full spectral shape, in particular in the high energy tail and at low photon numbers. The simulated gamma spectra in Figure 7.19 for days B (purple) and C (green) are similar in spectral shape with a cut-off at a photon energy of just under 700 MeV and 600 MeV, respectively. On day A (blue), the electron spectra reached on average higher maximum energies, which results in producing the highest energy photons of up to 800 MeV. The average radiation yield measured experimentally (see Figure 7.20, left) and the proportion of photons above 400 MeV (right) was also the highest on day A (blue), followed by B (purple) and C (green). In short, the bremsstrahlung source performed the best in terms of yield on day A, followed B and C, and also emitted higher energy radiation on day A, based on the performance of the electron source characterised in Section 7.4.

7.7 Characterisation of X-ray spectra

The analysis of the X-ray data has been conducted by Cary Colgan (Imperial College) and Brendan Kettle (Imperial College). John Morton (AWE) provided simulations of the emitted X-ray spectra using [340, 341]. The simulation assumed a laser pulse of wavelength 800 nm, 15 J energy and 50 ps pulse duration incident at a beam diameter of 450 µm on 50 nm of germanium with 5 µm of plastic as backing layer. Note that in the experiment the germanium target was thicker, and the pulse energy, pulse duration and beam diameter were lower, resulting in a comparable intensity on target as in the simulation, but necessitating further simulations at the exact experimental parameters.

Figure 7.21 (top) shows the simulated X-ray spectrum with filtering (red) and without filtering (blue) by the Kapton tape. The spectrum exhibits two distinct emission peaks, one between 1.2 and 1.5 keV, another lower one between 1.6 and 1.9 keV. The spectrum underlying these two emission peaks appears to fall off exponentially from lower to higher X-ray energies, such that the emission peaks are $2-3$ orders of magnitude higher than

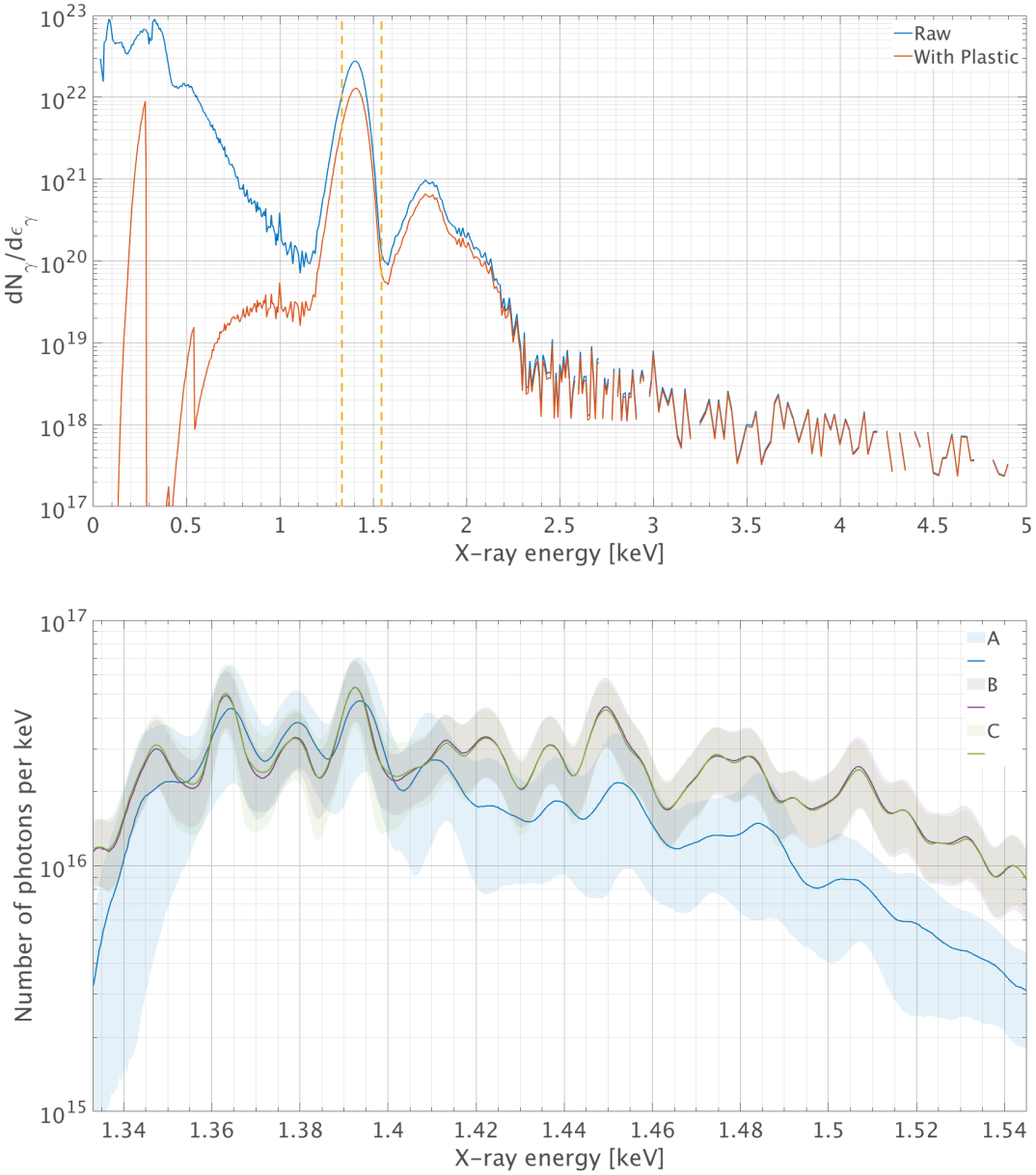


Figure 7.21: X-ray spectra produced with the burn-through foil. Top: Simulated X-ray spectra for a 5 keV energy window as emitted by 100 nm germanium target heated by a high-intensity laser pulse. The y-axis indicates the number of photons per keV, the x-axis the energy of the X-ray photons (blue) and after being filtered by 5 µm of Kapton as used in the experiment (red). The dashed yellow lines indicate the spectral interval measured with the crystal spectrometer in the experiment. Bottom: X-ray spectra measured experimentally averaged for each of the three shot days A, B *and* C *using a crystal spectrometer setup. The shaded regions indicate the standard deviation from the mean assuming a normal distribution.*

the surrounding spectrum. When including the spectral filtering of the radiation by the layer of Kapton, most of the photons below 1 keV X-ray energy are cut out efficiently with exception of the spectral K-edge which leaves a narrow bandwidth at photon numbers comparable to the high emission peak. The experimentally measured spectral range is marked in the simulation data presented in Figure 7.21 (top) with two yellow dashed lines.

Similarly as before, we will characterise the properties of the source on the three shot days A, B and C. Figure 7.21 (bottom) shows the average spectra measured by the crystal spectrometer on the three days, flat-field and background corrected, and on a logarithmic y-scale. The standard deviation of the shot-to-shot fluctuations from the mean is indicated in the shaded regions. The range of X-ray energies shown on the x-axis is representative of the spectral range measured effectively with the crystal spectrometer setup throughout the three shot days. The measured spectrum falls off sharply on either side of the spectral window presented here as the end of the crystal is reached. The height of the spectra is indicative of the relative X-ray yield on the different days. The distinct peaks are emission lines of the material and slight spectral shifts are due to smaller calibration and alignment errors. Note that these emission lines are not shown in the simulated spectrum as the code is based on an average atom model that does not resolve the electronic structure well enough. The spectral shape on day B and C is very consistent, whereas on day A the spectral lines above 1.4 keV are less pronounced and the spectrum falls off. This is probably due to varying plasma conditions as a hotter or colder plasma will shift the emission lines and rates. The fall off is more consistent with the simulated spectrum than the spectral shape observed on days B and C, which indicates that the plasma conditions are closer related as well. The spectrum on day A is also cut off at around 1.33 keV, which is due to misalignment of the crystal and not a physical phenomenon. In general, the shape of the X-ray spectra is consistent from shot-to-shot, whereas the shaded regions indicate that the total yield of photons can change significantly.

The yield of the X-ray source is measured by a pinhole camera setup with two pinholes, one filtered with aluminium, the other one with PTFE. Figure 7.22 shows the X-ray yield for an example dataset. On the top, the yield measured through both pinholes is compared. The measured quantities are linearly correlated at a correlation coefficient of 0.99, which indicates that the relative distribution of photons in the spectrum, i.e. the spectral shape, remains consistent throughout the shots or that changes only occur in a spectral region that causes the same response for both pinholes (above 1 keV [346]). On the bottom, the yield measured by the crystal spectrometer in the limited spectral window is shown together with the yield measured by the pinhole camera setup on the same shots. Both

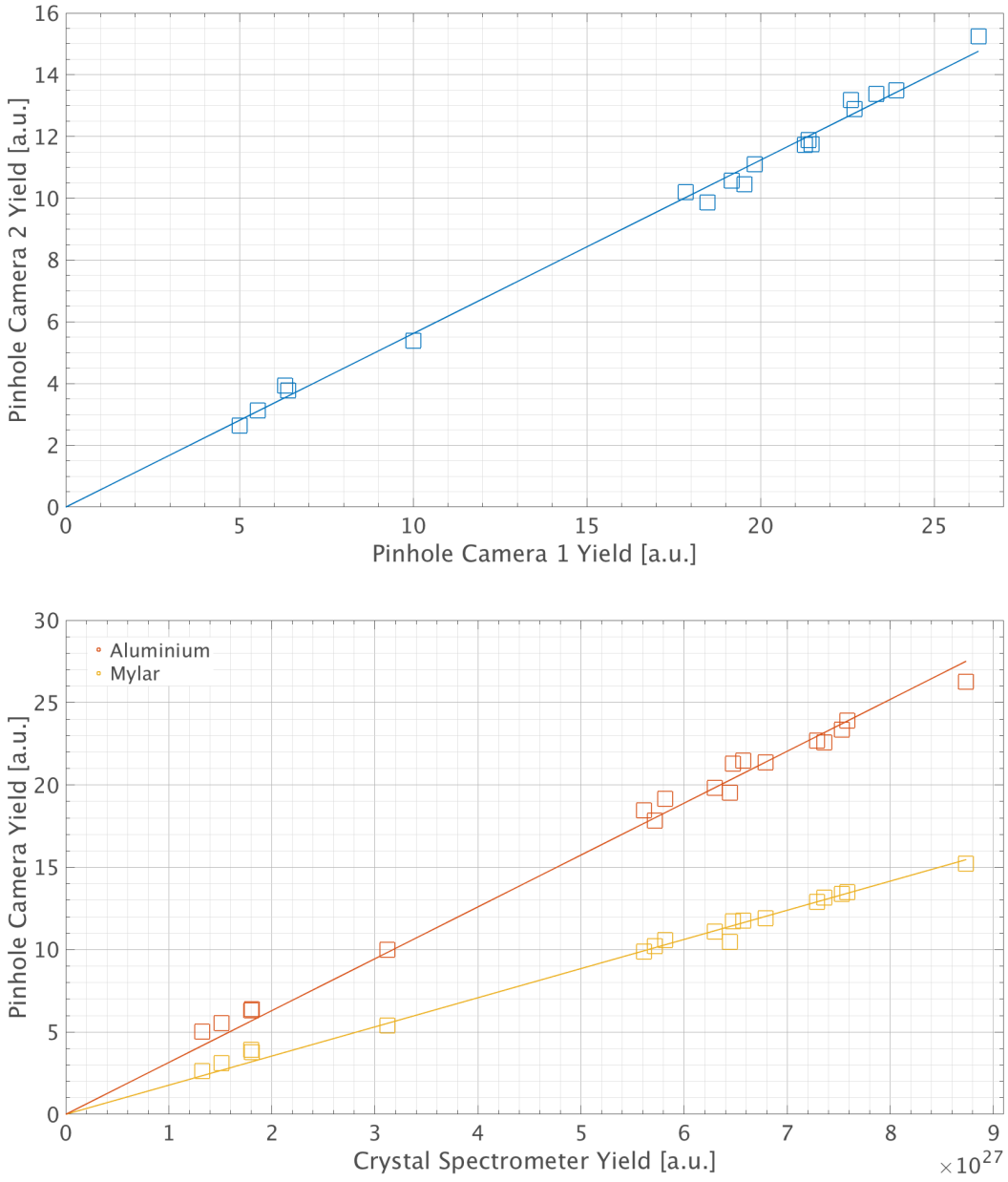


Figure 7.22: X-ray yield measured with the pinhole camera and the crystal spectrometer. Top: Comparison of the yield measured through both pinholes. The yield on pinhole 2 (filtered with mylar) as a function of the yield on pinhole 1 (filtered with aluminium). Bottom: The yield detected with the pinhole camera, separately for the two pinholes, one filtered with aluminium (red) and the other one with mylar (yellow), as a function of the yield measured with the crystal spectrometer.

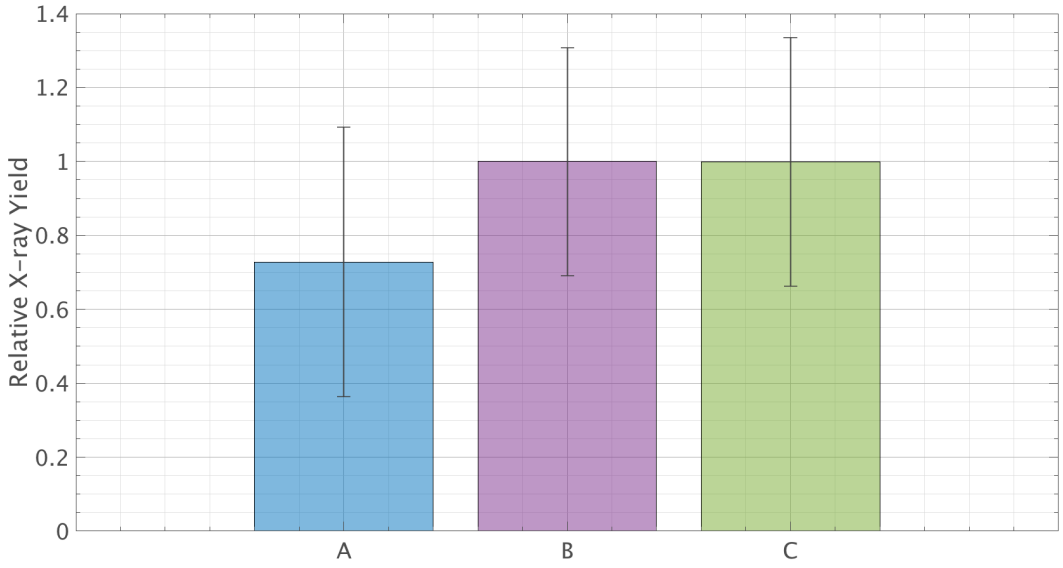


*Figure 7.23: Average X-ray yield as measured by the crystal spectrometer on the different shot days (*A,B *and* C*) normalised by the maximum X-ray yield in the group. The error bars indicate the standard deviation of the total yield for the respective shot day assuming a normal distribution.*

pinhole measurements correlate linearly with the result from the crystal spectrometer at a correlation coefficient of 0.90. This indicates that the spectral range measured by the crystal spectrometer contributes consistently a similar fraction to the overall yield as measured through either pinhole camera, which in turn confirms the consistency of the spectral shape on a shot-to-shot basis. As a result, the yield measured by the crystal spectrometer is also a good indicator for the relative changes in the yield of the entire X-ray emission. Overall, we can observe that shot-to-shot yield varies significantly, but there are strong indications that the spectral shape remains consistent.

Returning to the variations in performance of the X-ray source, the average X-ray yield on the three shot days is shown relative units in a bar chart in Figure 7.23, where the error bars indicate the standard deviation from the mean. The average yield is very consistent on days B and C, but was about 30% lower on day A. However, on all three days the standard deviation is large at $> 30\%$ of the mean value, reaching $> 50\%$ on day A. Determining the absolute X-ray yield and its temporal distribution are still subject of the ongoing analysis.

7.8 Spatio-temporal overlap of photon sources

In order to produce electron-positron pairs from the Breit-Wheeler process, we have to overlap the high-energy photons emitted from the two sources in time and space. The

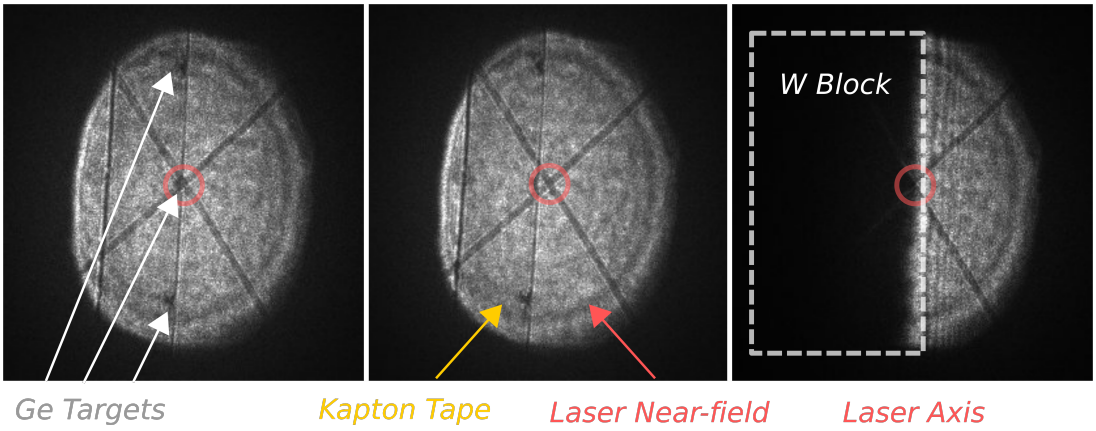


Figure 7.24: Alignment of the germanium (Ge) X-ray target relative to the wakefield beam axis (red circle). The cross-hair indicates the centre of the wakefield driver beam. First, the Ge target is placed on the beam axis (left). Then it is translated 1 mm away from the axis (centre) and the side of the driver beam containing the X-ray target is blocked by a tungsten (W) block.

two laser pulses driving the photon sources were spatially overlapped to within the width of a thin metal alignment wire $\sim 100\,\mu m$. They were then synchronised to each other to within an accuracy of $\pm 3\,ps$ using a fast photodiode and a suitable oscilloscope (see Section 4.3.1). The wakefield driver beam is $45 \pm 5\,fs$ long and the pulse duration of the X-ray heater beam is 40 ps FWHM.

The typical temporal shot-to-shot fluctuations between the two laser arms at GEMINI were measured to be of order of $10's\,fs$ with slow long-term drifts of up to $\sim 100\,fs$ in more extreme cases (see [243] and Section 4.3.3). Considering the long pulse duration of the X-ray heater beam, these fluctuations are negligible. The LWFA electron bunch that produces the gamma ray beam is delayed relative to the laser driver (see Section 4.3.3). For a gas target of length 17.5 mm and density $\sim 2 \times 10^{18}\,cm^{-3}$, this is at most $\sim 180\,fs$, which by itself is also negligible. The heated X-ray target, on the other hand, is expected to produce X-rays almost instantaneously. Combining all components discussed so far, the centres of the laser pulses are at most temporally offset by $< 3.5\,ps$, such that the temporal overlap is guaranteed throughout. Shot-to-shot fluctuations are in general expected to be negligible.

After having considered the temporal overlap, we will now discuss the spatial overlap. The gamma ray beam that is transmitted through the collimator is confined to a cone of 10.5 mrad divergence (see Section 7.5), which expands to a beam size of $(9.01 \pm 0.05)\,mm$ at the interaction point located $865 \pm 4.5\,mm$ downstream from the converter target. A tungsten block is used to bisect the gamma ray beam to shield the X-ray target tape from direct gamma hits such that the beam size is halved to $(4.54 \pm 0.03)\,mm$ (see Figures 7.24 and 7.25). The shot-to-shot pointing fluctuations of the gamma ray beam were measured

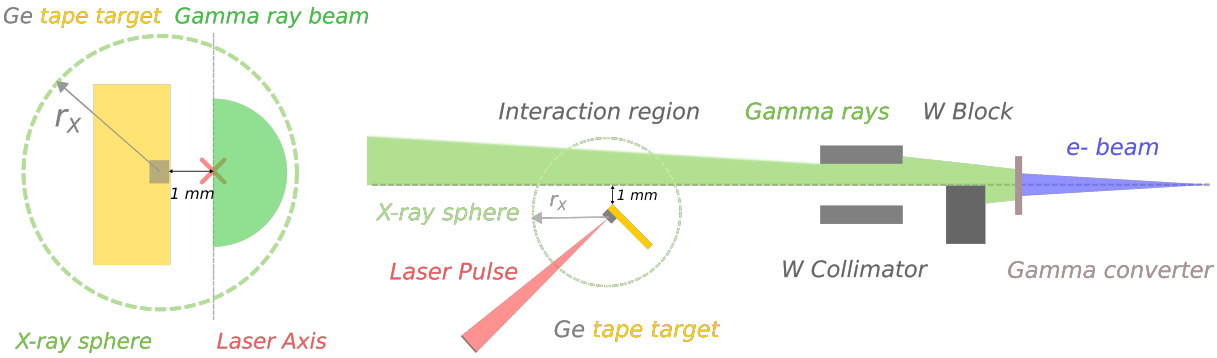


Figure 7.25: Sketch of the spatial overlap between the two high-energy photon sources. Right: Sketch of the top-down view of the interaction region. The electron beam (blue, on the right) passes through a gamma converter (brown) producing gamma radiation (green) from bremsstrahlung. Half of the beam is blocked by a thick tungsten (W) block and the remaining radiation is spatially filtered in a long W collimator. The remaining collimated half circle of radiation is then incident on the interaction region. The X-ray source is driven by a laser pulse that heats a germanium dot (grey) on a Kapton tape (yellow). The X-rays are emitted in 4π such that a sphere of X-rays is formed around the heated target (dashed circle), with an expanding radius r_X. The intersection of the sphere and the half-circle is the interaction region. Left: Sketch of the front view showing the position of the germanium target relative of the laser axis (red cross) and the overlap region of the X-ray sphere (dashed circle) and the transmitted gamma ray beam (green half-circle).

to be 1.2 mrad, which corresponds to a spatial shift of 1.04 mm at the interaction point. However, we expect any pointing variations to be mitigated by the tungsten block and the collimator such that spatial shifts simply result in different parts of the beam being transmitted.

The X-rays, on the other hand, are emitted from 1 ± 0.1 mm off-axis in a 4π sphere that expands over time. At the arrival of the gamma ray beam, the radius is > 5.95 mm, such that the region beyond the laser axis is at least 4.95 ± 0.1 mm wide. The half-sphere of X-rays crossing the laser axis and the half circle of gamma rays are of comparable size, and it is expected that both overlap fully with each other even in the previously identified largest timing offset of 3.5 ps (see Figure 7.25). As a result, we can safely assume that both photon sources will consistently overlap in space and time. If we assume that the temporal intensity profile of the X-ray heater is related to the temporal X-ray yield, a temporal offset of the relative beam timing results in a systematic shift in the number of X-rays that share an interaction volume with the gamma ray flash, where a late arrival of the X-ray heater increases this number.

7.9 Variations in the number of produced pairs

In the previous sections, we characterised the experimental fluctuations of the two photon sources for the three shot days A, B and C. We showed that due to fluctuations in the

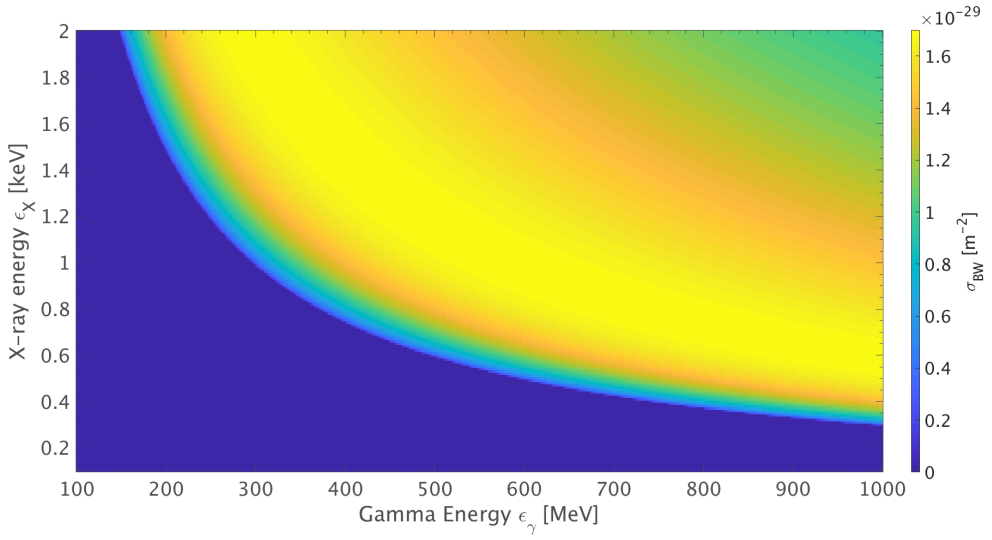


Figure 7.26: Total Breit-Wheeler cross section in m^{-2} (colour scale) for an X-ray photon of energy ϵ_X (y-axis) interacting with a gamma-ray of energy ϵ_γ (x-axis) at an interaction angle of $\theta = 140°$.

electron beam the performance of the bremsstrahlung source also varies from day to day. However, due to the characteristic emission spectrum of the bremsstrahlung process the fluctuations are mainly in the high energy tail of the spectrum and at low photon numbers. These high-energy gamma-rays might still be able to contribute significantly to the total number of produced pairs, if their higher energy enables them to interact with a large number of low-energy photons that were not accessible on the shot days B and C. On the other hand, we showed that the performance of the X-ray source was similar for days B and C, but had an about 30% lower average yield of photons on day C. The X-ray yield varied strongly from shot-to-shot at a standard deviation $\sigma > 30\%$ of the mean, but the spectral shape remained very consistent on a shot-to-shot basis. To estimate the impact of the fluctuations in both photon sources on the number of produced pairs, we have to combine both spectral measurements and calculate the Breit-Wheeler cross section, σ_{BW}, for these interactions. The Breit-Wheeler cross section depends on the invariant mass of the collision, s, which incorporates the energy of the two photons involved in the interaction, ϵ_1 and ϵ_2 and the angle, θ, between them:

$$s = \frac{\epsilon_1 \epsilon_2 (1 - \cos\theta)}{2 m_e^2 c^4}. \tag{7.9.1}$$

The central angle between the two photon sources in the experiment was set to be $140° \pm 10°$. Due to the strong collimation of the gamma-ray beam to $< 10\,\text{mrad}$ and pointing fluctuations of $< 2\,\text{mrad}$, the maximum spread of angles is $\theta < 0.7°$ and hence negligible. In this setting, the main angular spread is then dominated by the angular distribution of the $\sim 4\pi$ X-ray emission. Due to the wide emission angle of the X-ray

source, the geometry is less sensitive to angular and spatial variations on a shot-to-shot basis or between shot days, for instance when the tape target is being replaced. Considering this factor and since the analysis of the directionality of the X-ray source is still ongoing, we will for now also ignore any angular variation within the spectrum and calculate the cross-sections at a fixed crossing angle, $\theta = 140°$, and investigate how the cross-section, σ_{BW}, varies for a deviation in $\theta \pm 20°$.

Figure 7.26 shows σ_{BW} for $\theta = 140°$ and a range of X-ray and gamma-ray energies accessible in this experiment. Since $s \sim \epsilon_1\epsilon_2$ or in this scenario $s \sim \epsilon_X\epsilon_\gamma$, the energy of the most likely interaction partner for one photon to produce a Breit-Wheeler pair with changes with its energy. For instance, the higher the gamma-ray energy, ϵ_γ, the lower the X-ray energy, ϵ_X, of the partner photon that would be most likely to produce a pair in an interaction. The bulk of the gamma radiation produced in the experiment was in a spectral range up to 400 MeV, which is well matched with the emission peak measured in the X-ray spectrum. The fluctuations of the gamma spectrum in the high-energy tail around 600-800 MeV, on the other hand, are most likely to interact with X-rays of energy $< 1\,\mathrm{keV}$. However, this part of the X-ray spectrum is efficiently filtered out by the Kapton base of the burn-through foil, such that the impact of the high-energy fluctuations in the gamma-ray spectrum onto the total cross-section is suppressed. The bandwidth of X-rays that is transmitted through the plastic at $\epsilon_X \sim 0.2\,\mathrm{keV}$ requires a gamma photon of energy $\sim 1.5\,\mathrm{GeV}$ to meet the threshold for pair production and does not contribute. Since the normalised vector potential, a_0, associated with the X-ray field [347] is well below unity, multi-photon processes are also negligible.

We now estimate the average number of produced pairs evaluated for a specific day, $N_{BW,day}$, and at a fixed angle, θ, by combining the spectra of the X-ray source, $\mathrm{d}N_X/\mathrm{d}\epsilon_X$, the gamma-ray spectra, $\mathrm{d}N_\gamma/\mathrm{d}\epsilon_\gamma$, and convolving it with the cross section, σ_{BW}:

$$\boxed{N_{BW}|_{day,\theta} \sim \int \frac{N_{ph,X}}{\mathrm{d}\epsilon_X}\frac{N_{ph,\gamma}}{\mathrm{d}\epsilon_\gamma}\sigma_{BW}(\epsilon_X,\epsilon_\gamma,\theta)\mathrm{d}\epsilon_\gamma\mathrm{d}\epsilon_X.} \tag{7.9.2}$$

We calculate this for the average X-ray and gamma-ray spectra as experimentally measured on the three shot days, but also consider the simulated X-ray spectra presented in Figure 7.21 to understand how much the filtering of the X-ray spectrum by the Kapton base affects the result. In addition, we consider not only the central angle $\theta = 140°$ but also deviations of $\pm 20°$ to estimate how a global angle would change the number of pairs produced in total but also how much deviation a spread of angles would cause. In the experiment a change in the central angle could, for instance, occur when the spool of tape for the burn-through foil was replaced, or intermittently if the tape was not brought to full tension during the alignment procedure. Due to the 4π emission of the X-ray source, however, this effect is mitigated and a large spread of angles is expected on every shot.

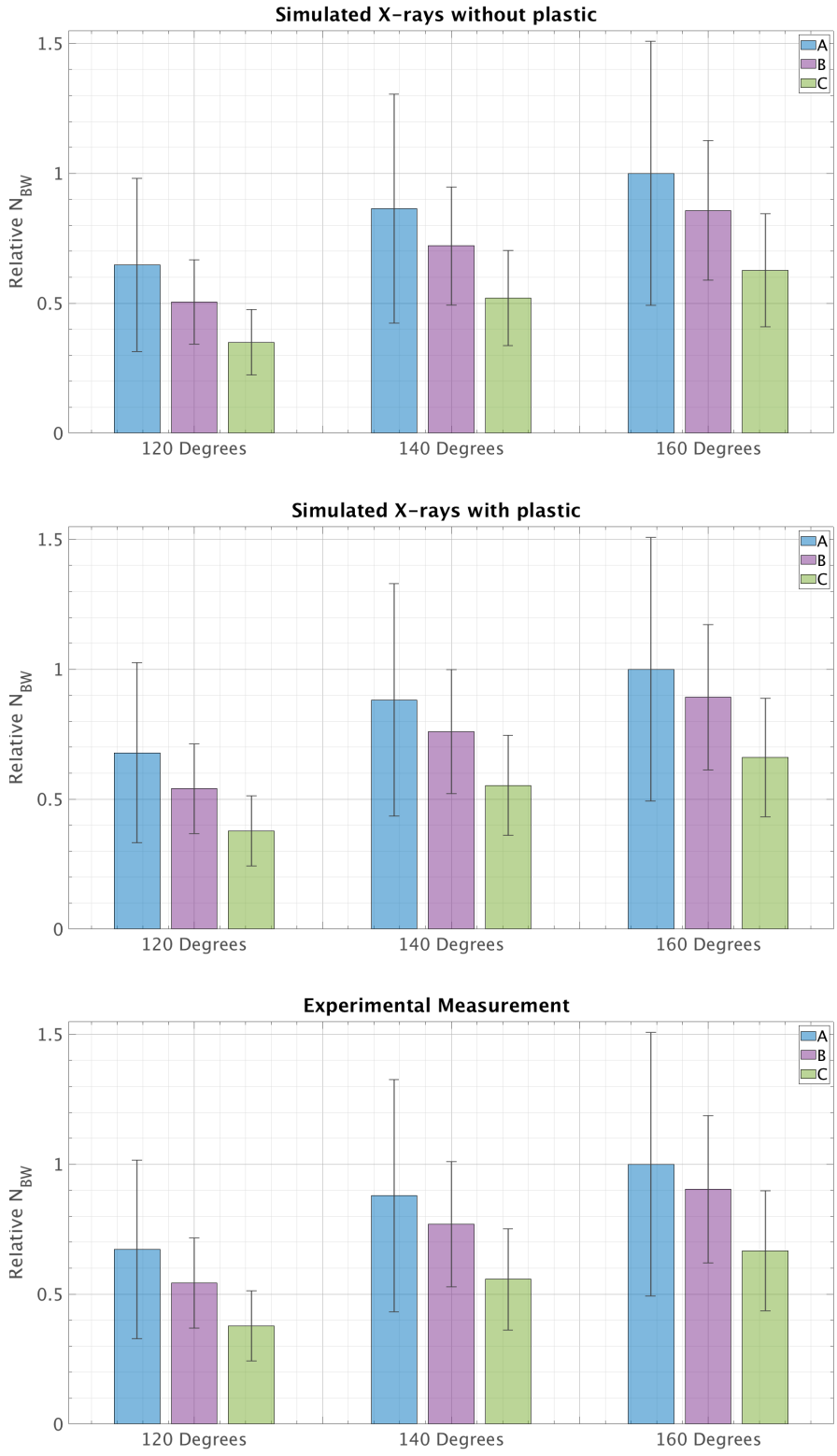


Figure 7.27: Estimated relative number of pairs produced calculated with Equation (7.9.2) *for the three shot days* A, B *and* C *at the interaction angles* $\theta = 140° \pm 20°$ *using the experimentally measured gamma-ray spectrum and a simulated X-ray spectrum (top), a simulated X-ray spectrum including plastic filtering (centre) and using the experimentally measured X-ray spectrum. The error bars indicate the standard deviation from the mean value combining the fluctuations in the X-ray and gamma-ray source, assuming a normal distribution in either case.*

In all cases, we assume that as a prerequisite the gamma-ray beam and the X-rays are overlapped in space and time (see Section 7.8). Figure 7.27 presents the different values of N_{BW} that were calculated for the different scenarios in a bar chart. Since the absolute yield of the photon sources is still subject of an ongoing analysis, here the *relative* variations in N_{BW} between the days and scenarios are considered. The results using the simulated X-ray spectrum, scaled by the experimentally measured X-ray yield, are shown without spectral filtering in the top chart and with filtering in the chart in the centre of the Figure. The chart on the bottom shows the results using the experimentally measured X-ray spectrum. The relative number of pairs is calculated for three groups using $\theta = 140° \pm 20°$ as interaction angle for each chart. The height of the bars is normalised to the maximum value of N_{BW} within a chart. The error bars indicate the standard deviation from the average value on a shot-to-shot basis, which is dominated by the variation in the X-ray yield.

In all cases, the number of produced pairs is the highest for day A, followed by B and then C. The order holds for both the average value and the maximum potential number of pairs produced on a single shots. This shows that the higher gamma-ray yield and peak energy are outweighing the lower X-ray yield. Also consistent across all three scenarios is that decreasing the interaction angle, θ, reduces N_{BW} by $> 10\%$ per 20° step. When including the spectral filtering of the simulated X-rays (centre), the average values of days B and C rise by about 5%, bringing A and B to within $\sim 10\%$ of each other. The calculations using the experimentally measured X-ray spectrum yield similar results to the simulated X-ray spectra *with* the plastic filtering, which indicates that the emission line in the X-ray spectrum around 1.5 keV provides the most important and dominant contribution to the total production of pairs. The interaction of low-energy X-rays with the high-energy tail of the gamma spectrum, on the other hand, constitutes only a small contribution that can be removed efficiently through the plastic filter. This is important since we showed that we are not able to resolve the differences in the gamma-ray spectrum on a shot-to-shot basis, resulting in an uncertainty on the expected N_{BW} on each shot. Also note that the X-ray yield varies strongly from shot-to-shot, but since the spectral shape is stable, and the yield and spectrum are measured on-shot, the resulting on-shot uncertainty introduced by the X-ray source remains small.

As a result, despite significant variations in the performance of the X-ray and gamma-ray sources, our ability to determine the number of expected pairs on a single shot is not significantly impaired by the limitations in the spectral measurements, within the assumptions made. A more detailed analysis including the angular distribution of the X-ray source could, however, alter this conclusion.

7.10 Status of the Breit-Wheeler Analysis

This section aims to place the results presented so far in the context of the overall effort of analysing the experimental data of this campaign[10]. After having discussed the commission and performance of both high-energy photon sources, here we will now describe the installation of the last component, the detector system composed of a magnetic chicane and single-particle detectors. We will then indicate briefly how eventually all components worked together towards the main goal of this campaign, but will fall short of presenting details or results of the ongoing complex analysis as this is outside the scope of this work.

Magnetic Chicane

Since only a small number of pairs is expected to be created in this setup, a magnetic chicane is used to extract only particles with matching properties from the interaction point and guides them onto well-shielded detectors that are capable of detecting single particles. The design, supervision of the positioning and the analysis related to the magnetic chicane were conducted by Dominik Hollatz (Jena). Guillermo Marrero Samarin (QUB) provided FLUKA [348] simulations to model the generation of background noise and designed the radiation shielding for this setup.

The magnetic chicane consisted of three magnets, one dipole magnet separating the electrons and positrons near the interaction point, and one dipole magnet each on opposite arms to bend the electrons and positrons, respectively, back onto detectors. The magnets for the chicane were set up symmetrically on both sides using identical magnets. The performance of the chicane of tested by removing the dipole magnet that was used as electron spectrometer from the beam path and allowing the electron beam from LWFA to propagate through the electron arm of the chicane. A Lanex screen was inserted after each of the two dipole magnets of the electron chicane. The first screen acted as electron spectrometer, the second screen measured the properties of the electron beam at the end of the chicane equivalent to the measurement plane of the single-particle detectors on the positron arm. The experimental results were consistent with tracking simulations and this result was assumed to hold similarly for the positron arm of the chicane within experimental measurement errors.

Single-particle detectors

Two types of single-particle detectors were placed at the end of the positron arm of the magnetic chicane. First, two subsequent silicon-based Timepix3 detectors in order to discriminate particles from noise by tracking lepton hits through both layers. The detectors

[10]Brendan Kettle (Imperial College) was the experimental lead on this campaign and coordinates the efforts around the ongoing analysis.

were provided by the MediPix Collaboration (CERN), simulated by Robbie Watt (Imperial College), and the data was analysed by Brendan Kettle (Imperial College). Second, a caesium-iodide stack coupled to a gated intensified CCD camera capable of identifying single lepton hits. This data was analysed by Guillermo Marrero Samarin (QUB) [349]. Only the positrons were measured as the Breit-Wheeler cross section peaks at $s = 2$ resulting together with the asymmetry of the photon energies in an unequal momentum distribution which makes a coincidence measurement more difficult and not feasible in this setup (see Figure 2.16 in Section 2.4.2). The single-particle detectors were calibrated by producing Bethe-Heitler pairs with similar properties as the Breit-Wheeler pairs by scattering the gamma-ray beam from solid targets placed on purpose near the interaction point or the gamma-ray axis. A small cube of tungsten was used to produce a localised source of pairs, whereas a wide scattering screen was re-purposed as wide-angle converter target to produce hundreds of pairs with a momentum distribution that is accepted by the magnetic chicane. With an abundance of signal enough data was produced to identify the characteristic shape and energy deposition of the positrons on both detector types. After removing the calibration sources again, the varying background of positrons from the Bethe-Heitler process was characterised on single-beam shots driving either the gamma-ray beam or the X-ray source.

Photon-photon collider

Finally, the two photon sources and the single-particle detectors were used simultaneously in dual-beam shots aimed for photon-photon collisions to produce pairs from the Breit-Wheeler process. This was achieved on three shot days at the end of the experimental campaign which in total lasted 8 weeks. The number of weeks required to prepare the experimental setup and to develop the right techniques to reach the stage to take dual-beam shots is indicative of the challenging nature of this experiment. Over the course of the three shot days, for which the variations in the performance of the X-ray and gamma-ray source were characterised in the previous sections, 217 dual-beam shots were taken for photon-photon collisions and 334 single-beam shots as background references. The reference and data shots were then used to perform a statistical analysis of the number of registered candidate events to identify whether there was a statistically significant excess of events measured on dual-beam shots, indicating pair production from the Breit-Wheeler process. A large fraction of this analysis was performed 'blindly' to remove potential bias from the process, and was predominantly conducted by Brendan Kettle (Imperial College), Stuart Mangles (Imperial College), Guillermo Marrero Samarin (QUB) and Peter Hatfield (Oxford). The analysis is still ongoing but is now slowly reaching its completion. We expect the verdict on the outcome of this campaign in the near future.

7.11 Improvements for a future measurement

In this section, we will explore, based on the analysis presented in this Chapter, how a potential future measurement of the linear Breit-Wheeler process could be improved. For this discussion, we will remain within the framework of the present experimental layout as we were able to field the three main components (gamma-ray source, X-ray source and single-particle detectors) successfully, and we demonstrated that the components worked individually and in tandem as designed. In the following, we will discuss how to improve their performance, focusing on the topics of this Chapter, mainly the commission of the bremsstrahlung source but also in smaller parts its interplay with the X-ray source.

The bremsstrahlung source in general produced a directed high-energy gamma-ray beam. The bremsstrahlung process efficiently mitigated the intrinsic spectral variability of the electron beam. Areas of improvement concern the overall yield, spectral shaping, noise production and the resolution of the spectral measurement. The X-ray source was spectrally very stable, but its yield of X-rays varied strongly from shot to shot. The areas of improvement are hence increasing the stability of the source, further spectral shaping and improving its characterisation. Finally, the single-particle detectors and the chicane performed as designed, but we will not discuss any alterations to these components here and focus on the light sources instead.

7.11.1 Gamma-ray source

Laser wakefield accelerator

On the best shot day (A), the electron beam reached a maximum electron energy of $709 \pm 46\,\mathrm{MeV}$ at an average beam charge of $26.26 \pm 3.8\,\mathrm{pC}$, using $5.51 \pm 0.64\,\mathrm{J}$ energy on-target. The laser energy was limited by the damage threshold of the optics in the focusing beam, which might have also limited the performance of the accelerator. Electron energies at GEMINI, on the other hand, are routinely in excess of 1 GeV at hundreds of pC charge [83, 251, 344], and have in individual cases reached more than 2 GeV with beam charges of $> 300\,\mathrm{pC}$ [69, 163]. This indicates that the accelerator was not performing at its optimum and significant improvements of the performance should be possible within the scope of this setup and this laser system. At a fixed electron spectrum, a tenfold increase in beam charge would equally increase the yield of gamma-rays and, as a result, also the number of potentially produced pairs, but also the number of candidate events from noise (see Section 7.5). A detailed investigation of how many 'real' and noise candidate events are produced in absolute terms per additional yield is still subject of an ongoing analysis. A rise in the electron energy would lead to a potentially higher yield in radiation overall, distributed over the entire bandwidth of the bremsstrahlung spectrum with the largest number of photons per unit energy at lower photon energies. The stability and the

charge of the electron beam could be improved by using density gradients in the plasma to inject electrons into the accelerator. Shock injection has been demonstrated to produce high-quality and high-charge electron beams at high shot-to-shot stability [228, 230]. The results presented in Chapter 5 also indicate that the density gradients can be used to produce a wide range of spectral shapes.

Converter Material

In Section 7.5 we found that, out of the materials investigated, bismuth of thickness $d = 1\,\text{mm}$ was producing the highest yield of radiation at suitable collimation. The bismuth target generated a comparable yield to the thick tungsten target although, based on the corresponding radiation lengths, it is not expected that a comparable amount of energy is being converted. This indicates that a higher atomic number, Z, is for this application more favourable than a high material density, ρ. Since bismuth is already at the upper end of readily available high-Z materials, followed in the periodic table predominantly by radioactive (synthetic) or reactive elements, we could still explore whether 1 mm is already the optimum thickness or whether a thicker bismuth target would increase the radiation yield whilst maintaining a suitable amount of collimation.

A rise in the electron energy will increase the cut-off energy of the bremsstrahlung spectrum and boost the number of high-energy photons and the fraction they hold of the entire spectrum. At a fixed X-ray energy, this then also increases the maximum energy of generated Breit-Wheeler pairs and due to the distribution of momentum amongst the electron and positron in turn a broadening of the bandwidth. In order to measure a larger bandwidth, one would have to adjust the acceptance window of the magnetic chicane which, however, could also result in more noise reaching the detectors as the access is widened. In an unaltered chicane setup, on the other hand, the additional pairs would not be measured and could potentially act as additional source of noise. In addition, higher-energy radiation penetrates matter deeper, generating cascades of particles and radiation, which make it harder to shield. This indicates that higher electron energies are only within limits desirable in this context.

Alternatively, the higher energy photons can be converted to lower energies by increasing the thickness of the converter targets significantly to stimulate the production of Bethe-Heitler pairs and re-conversion to gamma radiation through bremsstrahlung. Each conversion shifts the spectrum of the gamma radiation towards lower energies [52]. This, however, requires multiple radiation lengths of material resulting in scattering and an increase in divergence of the beam, which reduces the fraction of radiation transmitted through the collimator arrangement. In addition, the increased scattering and cascading of the radiation might increase the noise production, which would require additional shielding

or a different design of the collimator. A detailed study would be needed to evaluate the gains and drawbacks quantitatively for this scenario but also more generally to understand the production of candidate events better to identify stay-clear areas and prevent their production in the first place.

The analysis presented in Section 7.6 has shown that an accurate spectral measurement is challenging in this regime as the detector response is dominated by the largest component of the spectrum and changes in the spectral shape are not well resolved. In [264] it was demonstrated that a spectrometer setup based on a scintillator array [263], as used in this experiment, can in conjunction with a gamma converter spectrometer [286] be used to unfold the full spectrum. This would be of interest for a future measurement to decrease the on-shot uncertainty on the gamma spectrum, but also requires a detailed consideration of detection limits, potential noise production and space constraints when introducing additional measurement screens and magnets on-axis.

7.11.2 X-ray source

In the experiment, the spectral shape of the X-ray emission was shown to be very stable from shot-to-shot and across several shot days (see Section 7.7). The X-ray source and its spectral filtering by the plastic base are designed to limit the bandwidth of the X-rays, which reduces the spectral bandwidth of the generated pairs. This is reinforced further when considering the shape of the Breit-Wheeler cross section and the exponential decay in the gamma spectrum towards high photon energies. This allows the use of a magnetic chicane with small acceptance bandwidth and more practicable diagnostic shielding. However, the X-ray yield varied strongly from shot-to-shot. Whilst the variation in the yield and the impact on the pair production can be diagnosed on-shot when assuming spectral stability, it reduces the number of suitable shots with sufficient probability to generate Breit-Wheeler pairs above the background. Analysis by Cary Colgan (Imperial College) shows that the strong variations in the X-ray yield are not correlated with the on-shot laser energy of the driver. This suggests that either the shot-to-shot alignment of the burn-through foil was not reproducible or that the properties of the target itself varied, for instance the thickness of the germanium coating. Note also that an increase in the X-ray yield does not increase the noise on the single particle detectors as it does for the gamma source and is hence highly desirable.

The spectrum reaching the interaction point passes through a 5 µm layer of Kapton, which absorbs low energy X-rays (see Section 7.7). The plastic, however, also allows transmission of a narrow bandwidth of photons around 200 eV (K-edge) [346] at comparable photon numbers per unit energy interval as the main emission line. These photons were

not energetic enough to produce pairs in this experiment, but could contribute if the gamma ray energy exceeded $\sim 1.5\,\mathrm{GeV}$. The transmission could be reduced by increasing the thickness of the plastic base or, for instance, flash coating the tape with aluminium, which, however, would also reduce the transmission of the remaining spectrum. A future measurement of the Breit-Wheeler process could also benefit from an on-shot spectral measurement of the transmitted spectrum to confirm its spectral content at the interaction point. In general, a wider *in-situ* survey of the properties of the X-ray source might be required to evaluate the design of the targetry more thoroughly, in particular regarding the directionality of the source to estimate the range of angles interactions might occur at and whether a more directed source could be beneficial.

7.12 Conclusion

In this Chapter, we presented the setup of an experimental campaign to measure the production of electron-positron pairs from the linear Breit-Wheeler process by colliding a gamma-ray beam from bremsstrahlung [274], using an electron beam from LWFA and a bismuth target, with X-rays from a burn-through foil driven by a high-intensity laser [246].

The focus of the Chapter was on the commission and optimisation of the bremsstrahlung source in terms of yield within a narrow cone of divergence and the number of background candidate events measured on a set of single-particle detectors by varying the material, target thickness and the accelerator setting. The performance of the gamma-ray source was then characterised for its optimum condition across several shot days.

Electron beams from LWFA underlie intrinsic fluctuations and the performance of the accelerator can vary from day to day. The impact of these fluctuations on the properties of the generated radiation was mitigated by deciding on bremsstrahlung as mechanism. It was demonstrated that the radiation generated in the electron-solid interaction is relatively insensitive to the spectral shape of the electron beam, reducing the variations of the electron beam to fluctuations in the high energy tail of the spectrum at low photon numbers. The gamma-ray spectrometer used in this experiment was not able to resolve these fluctuations as its response is dominated by the spectral range of the bremsstrahlung spectrum containing most of the photons, which remained consistent in shape throughout the days despite the fluctuations in the electron beam.

However, the influence of the gamma-ray fluctuations was mitigated by the characteristic shape of the Breit-Wheeler cross-section itself and by limiting the spectrum of X-rays that reaches the interaction point. A plastic filter removed low-energy X-rays, the likeliest interaction partners of high-energy gamma-rays, and mitigated the uncertainty introduced by the fluctuations.

Finally, we placed the work of this Chapter in the context of the ongoing larger analysis of the experimental results which tries to determine whether we successfully measured pairs from the Breit-Wheeler process and provided a brief status update. This was followed by a discussion of potential improvements for a future measurement of the linear Breit-Wheeler process within the framework of the laser-wakefield accelerator setup discussed here.

Chapter 8

Conclusion and Outlook

8.1 Summary of Results

The experimental results presented in this work demonstrate the capability of laser wakefield acceleration (LWFA) to produce highly energetic radiation from few to hundreds of MeV photon energies, and their application in the context of fundamental studies of quantum electrodynamics (QED):

- **Chapter 5** described how relativistic electron beams with energies up to 1.3 GeV were collided with a laser pulse at $a_0 \sim 0.2 - 1$, producing radiation from **linear inverse Compton scattering** of variable spectral shape in the range of 10s of MeV photon energies. The radiation yield and spectrum were used to diagnose the properties of the electron and the laser beam at the interaction. Linear inverse Compton scattering promises to become a useful **beam diagnostics and alignment tool** for future studies of radiation reaction.

- **Chapter 6** outlined how relativistic electron beams of energy $\epsilon \approx 550$ MeV were collided with a highly intense laser pulse of intensity $a_0 \approx 10$, producing broadband synchrotron-like radiation with a critical energy $\epsilon_{crit} > 35$ MeV from **non-linear inverse Compton scattering**. The high energy of the emitted photons lead to a measurable energy loss in the electron spectra due to **radiation reaction**.

- **Chapter 7** reported how electron beams were propagated through a solid target to produce an energetic gamma-ray beam from **bremsstrahlung** reaching photon energies of several hundreds of MeV. The yield and collimation of the source were optimised for its application in a photon-photon collider experiment with the aim to produce electron-positron pairs from the **linear Breit-Wheeler process**. The second photon source was a ∼keV X-ray source from a burn-through foil heated by a second high-intensity laser.

8.2 Discussion and Outlook

The experimental results presented in this work demonstrate that an all-optical colliding-pulse geometry using a laser wakefield accelerator (LWFA) is suited to investigate fundamental (strong-field) QED (SFQED) phenomena (see Chapters 6 and 7), and can contribute significantly to this emerging research field [149, 162, 163]. Whilst this bears exciting research opportunities, especially at the next generation of multi-PW laser systems [35–46], the results have also shown the need for a better control over the laser system and the accelerator [302], and motivate the development of suitable diagnostics to facilitate precision measurements with statistical significance [179, 180].

Since the first reported measurement of quasi-monoenergetic electron beams in 2004 [19–21], maximum electron energies have increased by a factor of 100 [76] – a rapid increase that aligns with the rate of energy gain observed historically in conventional accelerator technology [58], e.g. see Figure 1.1 [49] in Section 1.1. The progress in the field of LWFA has over the past decades been strongly driven by the enhanced control over high-intensity lasers and the exponentially rising peak intensities [22]. Along with an increase of the maximum electron energies, there have been significant improvements to the overall beam quality [75] and an enhanced control over the final properties of the accelerated bunch [350], which can be attributed to a better understanding of the evolution of the bubble [223], injection mechanisms [228], and the ability to tailor both. LWFA electron beams and the energetic radiation they generate are suited for a wide range of applications [81], including the study of fundamental QED phenomena discussed here [149, 162, 163].

However, LWFA is still an actively evolving accelerator technology that has not yet reached a level of maturity comparable to those of accelerators based on radio-frequency (RF) cavities: current challenges are, for instance, the stability or shot-to-shot reproducibility of the accelerator (see also Sections 5.4, 6.9 and 7.4), and the production of low emittance and low energy spread beams, for instance to be used in free-electron lasers [351]. Another key challenge is to operate the accelerator at a high repetition rate and efficiency [10], and to fully diagnose the accelerator and the electron beam it produces [232]. This indicates that a particle collider solely based on plasma technology still lies further in the future as the prerequisite for precision measurements is the full characterisation of the probe. The designs for the proposed next generations of lepton colliders, e.g. CLIC [54] or ILC [55], are hence still based on superconducting RF cavities, but the increasing scale and cost of RF-based accelerators eventually require the use of high-field technology as found in plasmas. For now, the wakefield community provides crucial impulses and expertise to enhance existing conventional accelerator facilities with beam-driven wakefield technology [352], e.g. as final amplification stage (PWFA afterburner) [56], and explores the potential of hybrid collider schemes [353].

The following sections will briefly recapitulate research opportunities in SFQED that can be explored in all-optical colliding-pulse setups using LWFA, and will, based on the results presented in this work (Chapters 5, 6 and 7), discuss specific experimental considerations for the accelerator, scattering geometries and diagnostics that will facilitate measurements in the future.

8.2.1 Research Opportunities

All-optical colliding-pulse setups where an LWFA electron beam collides with a counter-propagating intense laser pulse are uniquely suited for studies of inverse Compton scattering, radiation reaction and other high-field phenomena (see Chapter 6 and [162, 163]): in LWFA setups an intense laser system and a relativistic electron accelerator are co-located, and both are intrinsically synchronised to each other. Moreover, the small size of the electron beam at the end of the accelerator [78] and its short bunch duration [77] allow a full overlap with the tightly focused (and hence very intense) laser pulse such that the interaction occurs with almost all of the electrons at a comparable intensity [303]. Since relativistic electron beams and intense laser pulses can produce a wide range of energetic radiation, this setup can also be converted into a real photon-photon collider (see Chapter 7 and [149]). As a result, LWFA and the next generation multi-PW laser systems [10, 35–46] are in this context in direct competition with state-of-the-art particle accelerators [31–34, 64–66, 142–146].

Colliding-pulse geometries with relativistic particles and highly intense laser pulses will enable a detailed investigation of Compton scattering in different regimes, from the classical [120] to the perturbative quantum description [99] and in the non-perturbative strong-field regime [99, 121–126]. Approaching a quantum nonlinearity parameter, η, of unity, we can measure quantum radiation reaction [130–135, 145] and perform statistically significant precision measurements [179, 180] of the transition from a regime where classical descriptions hold to a regime where quantum effects dominate. This includes the manifestations of the stochastic quantum nature of radiation reaction [182], such as energy straggling [136] and radiation quenching [137], visible in the emission spectrum and the post-interaction electron spectrum [132]. The emission might also result in a spin-polarisation of the electron beam [138–140] through the Sokolov-Ternov effect [305].

In this regime, intense interactions also give rise to (multi-step) cascades and showers [141, 147], which are particularly relevant in the astrophysical context. At $\eta \sim 1$ we reach the regime of nonperturbative strong-field QED [103–105], where quantum effects dominate. Here QED cascades can produce dense pair plasmas [116], which are of interest for high-energy density studies [118].

Suitable radiation diagnostics will enable measuring the formation length of the photon

emission via breakdown of the local-constant field approximation (LCFA) [131, 160, 315] and it will allow to scrutinise the range of applicability of state-of-the-art numerical methods [354–357].

This geometry also enables the investigation of pair production processes such as two (linear) [149, 150] and multi-photon (nonlinear) Breit-Wheeler pair production [100], and at $\eta \sim 1$ vacuum pair production (vacuum breakdown) [101, 298, 317]. In these extreme fields, it also facilitates probing the quantum fluctuations and the vacuum acts as nonlinear medium manifested in phenomena like vacuum birefringence [152, 153], vacuum dichroism [154], and vacuum recollision processes [155, 156]. Photon-photon interactions are also a potential route for probing physics beyond the Standard Model, e.g. sleptons [64] and axions [65, 66].

At more extreme conditions, the Hawking-Unruh effect [358, 359] and the conjectured strong-coupling regime of QED, the Ritus-Narozhny conjecture [157–159], become accessible.

8.2.2 Experimental Considerations

A prerequisite for useful measurements of new phenomena in the SFQED regime is the detailed knowledge of the conditions at the interaction, e.g. electron spectra and laser properties, the capability to diagnose the reaction products accurately, and to maintain conditions consistently such that the results gain statistical significance. The results presented in this work (Chapters 5, 6, 7) can help to identify specific aspects of the experimental setup or technique that can be addressed in order to design an experiment that fulfils these criteria.

Laser Wakefield Accelerator

In a colliding-pulse setup, the performance and choice of the targetry of the laser wakefield accelerator is crucial (see Sections 4.4 and 6.9). The ideal accelerator has to provide over long periods of time consistently a stable but also tunable electron beam, where low-energy spread, high charge and high maximum electron energies are examples of favourable properties [179, 180].

Gas cells have in some instances demonstrated to produce electron beams of higher quality than gas jets at the same laser system [75], but gas jets offer wide access for diagnostics (see Figure 8.1) and are easier to align, also avoiding potential damage from the wakefield driver beam. Moreover, it enables the use of shock injection which has demonstrated to produce high-quality electron beams of high charge and low energy spread with great tunability and stability [228, 230, 275, 276]. Electron beams with

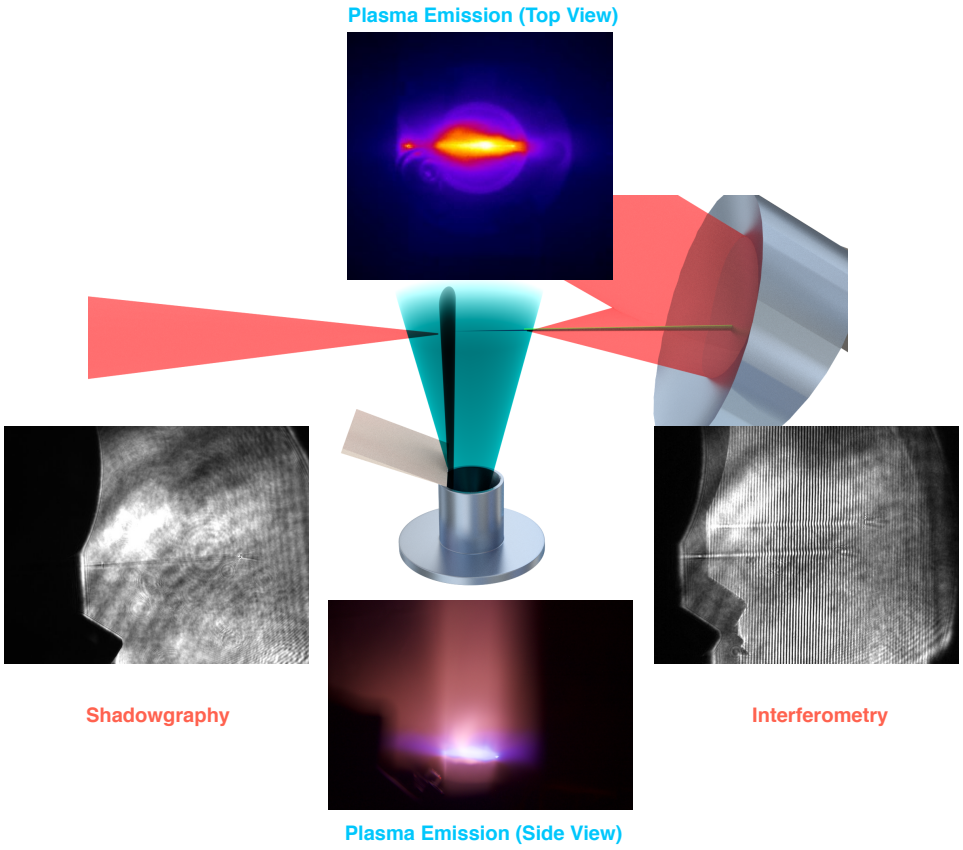


Figure 8.1: Sketch of a gas jet and example images from diagnostics that characterise the plasma: An optical transverse probe was used to obtain a shadowgram and an interferometry image. The self-emission of the plasma was imaged from the side and the top.

these properties are in particular suited for precision studies of radiation reaction (see for instance Section 6.9 and [132, 179, 180]).

Gas jets facilitate a debris-free interaction close to the accelerator where the electron beam is small such that the entire bunch can interact with the intense laser pulse. Gas cells, on the other hand, risk damage if an interaction occurs close to it, which could result in a degradation of its performance. Moreover, the production of debris and scattered light could in turn damage optics in the vicinity. To use a gas cell sustainably, interactions would need to take place further away from the target where the electron beam is larger. In this scenario, a plasma lens could be used to focus the electron beam onto a second interaction point. As a consequence, for now gas jets appear to be the most suitable targets for colliding-pulse experiments.

Electron diagnostics

As the properties of electron beam from a LWFA vary from shot-to-shot, it is necessary to measure its properties on-shot or characterise its fluctuations statistically (see Sections 6.5 and 6.9). In a typical LWFA setup, the energy of the electron beam is measured

in a magnetic spectrometer (see Section 4.5), where multiple screens [257] and spatial references [360] can be used to account for beam pointing and divergence to improve the energy resolution. In a colliding-pulse setup, this allows an on-shot measurement of the *post*-interaction electron spectrum and a statistical characterisation of the *pre*-interaction spectrum when the scattering beam is not used. Given a sufficiently populated reference dataset, the statistical approach can yield significant results but requires more shots depending on the stability of the source and the strength of the interaction (see Sections 6.5 and 6.9 or [162, 179, 180]). Ideally, we would also measure the on-shot pre-interaction spectrum, which is, for instance, discussed in [314].

Observables that are in particular important in the context of colliding-pulse setups are the pointing variations of the electron beam, to estimate overlap, and its divergence or ellipticity, in the context of on-shot intensity measurements. These are commonly measured with beam profile screens, e.g. Lanex, in the undispersed electron beam. This approach is, however, not suitable for on-shot measurements in colliding-pulse setups as any material in the beam path produces energetic radiation from bremsstrahlung which affects the spectral retrieval of the Compton signal (see Section 4.6.2). Such a screen would also be prone to damage from the intense laser pulse. Moreover, the response of a Lanex beam profile screen is dominated by low-energy electrons [284] which are commonly abundant in wakefield accelerators.

Section 5.11 outlines how inverse Compton scattering can be used as beam profile monitor to measure beam properties such as the ellipticity of the electron beam, its pointing and to resolve spatial features from the emitted gamma radiation. Due to the dependence of the energy of the emitted radiation on the electron energy, this technique is also less sensitive to low-energy ($\sim$ MeV) electrons (see Section 5.8). At low laser intensities, this enables a non-invasive on-shot diagnostic of the electron beam profile. At high intensities the scattering process becomes nonlinear and the emission profiles becomes elongated in the polarisation axis (see Section 2.2.3). At high intensities and electron energies radiation reaction becomes significant (see Section 2.3). Consequently, this is a suitable for a statistical characterisation of the pre-interaction beam profile. Its more specific use on-shot at high interactions is discussed in the following section.

A more challenging measurement is the chirp of the electron beam and its bunch duration. These factors, together with the beam size, can influence the shape of the post-interaction spectrum similarly as changes in intensity and focusing effects, and, if not considered, could lead to wrongly inferred conditions at the interaction and deviations from radiation reaction models. These properties can be measured using electro-optical sampling, transverse deflecting structures or transition radiation [232]. Once radiation

reaction is well characterised, it might, on the other hand, be possible to use inverse Compton scattering and radiation reaction in reverse as diagnostics for both properties by considering energy loss and stochastic effects [132]. For now shorter electron bunches, for instance narrow-energy spread beams injected from shock injection, and short laser pulse durations could be used to avoid a significant impact [303].

Finally, at high intensities electron beams can be spin-polarised [138–140], similarly as in beam storage rings through the Sokolov-Ternov effect [305]. In conventional accelerators the spin-polarisation of beams is measured using Compton scattering [93]. Since an intense laser-electron interaction already produces a large gamma-ray signal, this would require diverting the electron beam, then performing the scattering and divert the electron beam again to separate two gamma signals and the electron beam from the radiation. The scattering laser could be a low-intensity laser pulse (see Section 5.7). Suitable diagnostics to measure gamma radiation are outlined in Section 8.2.2. On the other hand, an appropriate choice of polarisation for the scattering beam results in a 'splitting' of the electron beam which could be measured on a magnetic spectrometer and the scattered radiation [140].

Scattering geometry and choice of focusing optics

Simplistically, it is preferable to achieve the highest possible value of the quantum non-linearity parameter, η, in an interaction as a higher value gives access to a wider range of phenomena and also produces a stronger response of the system. A stronger response in turn facilitates statistically significant measurements requiring fewer data points. η increases with the electron energy, γ, and the laser intensity, I_L:

$$\boxed{\eta = \frac{(1-\cos\theta)\gamma E_L}{E_S} \propto (1-\cos\theta)\gamma\sqrt{I_L}.} \tag{8.2.1}$$

Neglecting the properties of the electron beam as they were discussed already, it is becomes evident that it is preferable to focus the laser pulse tightly to increase the peak intensity. On the other hand, at the exit of the wakefield accelerator the electron beam is of $\sim$ µm size: the optimum spot size is then at least of similar magnitude or even slightly larger such that the electron beam acts as a real probe and is not affected by wavefront and intensity variations that would then need to be considered in the modelling process as well. At the same time, very short focal lengths place the optic into the vicinity of the interaction and risk damage to it. Longer focal length optics maintain a high intensity over a wider distance and larger z_R facilitate overlap between the laser pulse and the electron bunch, but also result in larger absolute pointing fluctuations. In all experiments discussed in this work, an $f/2$ off-axis parabola was used with a Rayleigh length of $z_R \sim 8\,\mu\text{m}$.

At a fixed electron energy and laser intensity, η is maximised in a head-on collision, i.e.

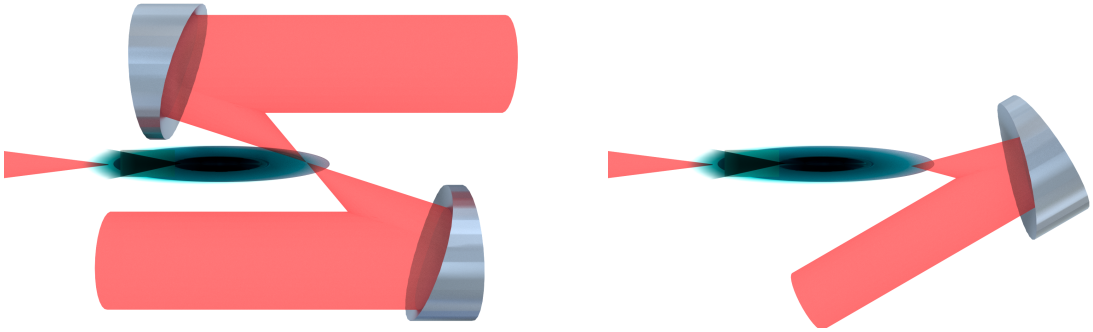


Figure 8.2: Scattering geometries using either a head-on geometry (right) or an off-axis parabola at an off-angle (left). Here we also use a second parabola to re-collimate the light. The wakefield driver beam enters from the left and is incident onto the gas jet (blue).

$\theta = \pi$, such that it is desirable to place the focusing optic as close as possible to the laser axis. One can then either place the OAP directly onto the axis [see Figure 8.2 (right) and Chapters 5 and 6], which then requires a hole in the optics, or place it close but off-axis at an angle [see Figure 8.2 (left) and Chapter 7].

The hole in the optic has to be large enough to avoid any interaction with particles and radiation as it would affect measurements downstream. In particular, it has to be large enough to avoid being hit by the wakefield driver beam, also considering that the laser might drift or defocus in the plasma, as this could damage the optics and, more importantly, the laser chain upstream. However, the larger the hole, the more energy is lost in the process. Larger beam optics that might be used at multi-PW facilities could reduce the relative impact of the hole (assuming a flat-top beam profile) and make the relative angle more relevant, but the high intensities increase the risk of damage to the laser.

On the other hand, the position on-axis maximises η through θ, and also allows easier alignment of the two laser pulses and facilitates longer overlap over a wider spatial range. In the experiments presented in Chapters 5 and 6, the loss of energy through the hole and potential loss of η due to an angle were of a similar value ($\sim 5\%$), such that the on-axis position was chosen for the ease of alignment. Consistent overlap was demonstrated in Chapter 5 and also enabled the alignment procedure based on spatial correlation (laser raster scan) outlined in Section 5.5, which would only be applicable in a limited fashion in an off-angle geometry.

The extended temporal overlap of the laser pulse and the electron beam might also be beneficial to induce cascades [141]. Moreover, in this head-on geometry the polarisation vector of the laser pulse is always orthogonal to the electron axis, whereas in an off-axis geometry this would only be true in one axis and the projected polarisation vector would be smaller in the other axis.

When placing the parabola off-axis, on the other hand, the full energy of the beam is

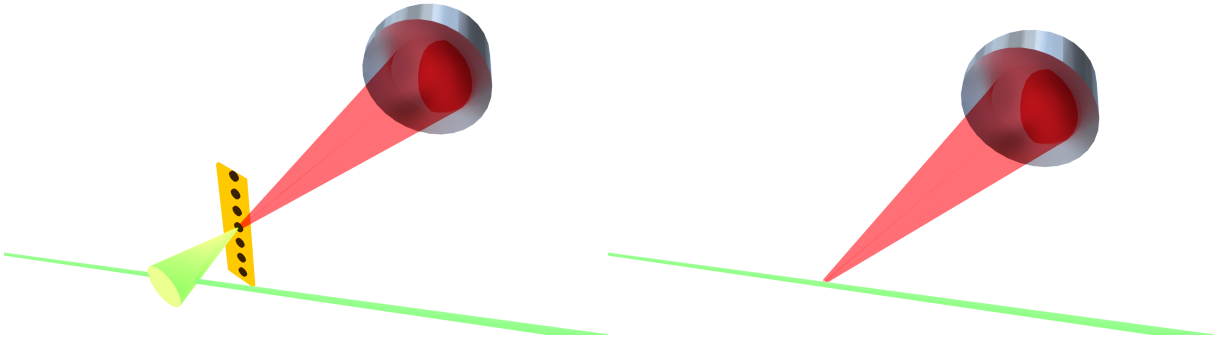


Figure 8.3: Scattering geometries for photon-photon collisions using an off-axis parabola at an oblique angle either heating an X-ray target with an intense laser (red) for a measurement of the linear Breit-Wheeler process (left) or colliding the laser pulse directly with the gamma-ray beam (green) to produce pairs from the nonlinear Breit-Wheeler process (right).

used, and potential diffraction effects caused by the hole are avoided, but at cost of the reduced scattering angle. This geometry reduces the risk of damage to the laser system, and also enables the use of a second OAP to recollimate the beam and transport it to appropriate laser diagnostics [32, 33] [see Figure 8.2 (left)]. This would also reduce the production of potential debris around the interaction region as the laser pulse is terminated far away from it.

As a result of the angle, the relative alignment is slightly more involved, and the overlap of the electron bunch and the scattering pulse is reduced. Whilst this is not the ideal configuration to study cascades, especially if the experimental conditions are at the threshold to study these phenomena, it is being proposed that an oblique angle of incidence might even be *required* to achieve critical or even supercritical η and to avoid losses through radiation and particle production before reaching the peak η [104]. This geometry is also well suited for photon-photon collisions at a second interaction point as shown in Chapter 7. Here any material close to the axis is a potential source of noise that should be avoided. In a photon-photon collider, the off-axis geometry would also allows switching between a direct collision using the scattering laser, e.g. to study the nonlinear Breit-Wheeler process, and a laser-heated X-ray target as discussed in Chapter 7 for a measurement of the linear Breit-Wheeler process (see Figure 8.3).

In summary, both geometries (see Figure 8.2) are associated with a trade-off of specific advantages and disadvantages (see Table 8.1), and it might be beneficial to switch between configurations for different research questions, in particular for reaching high effective η (supercritical) and photon-photon interactions in the on-axis, and cascades in the off-axis geometry. At high intensities of multi-PW laser facilities, the risk of damage to optics and the laser chain upstream might be too significant to implement a head-on geometry.

Category	On-axis (with hole)	Off-axis
η (+)	Optimum angle θ	Full laser energy
η (–)	Energy loss (hole)	Reduced angle θ
Overlap	Maximised	Reduced
Phenomena	Radiation Reaction	Supercritical η
	Showers and Cascades	Photon-photon coll.
Main Risks	Laser/Optic Damage	No Overlap

Table 8.1: Comparison of scattering geometries under different aspects.

High-intensity laser diagnostics and laser controls

In order to probe new physics, the uncertainties on the laser beam properties have to be decoupled from the model or theoretical uncertainties. A major challenge for high-intensity lasers is the characterisation of the actual full power (not attenuated) high-intensity laser focus on-shot. Typically, the laser pulse is characterised in a low-power configuration (attenuated) and it is assumed that the properties of the low-power and full-power laser focus are comparable such that both can be related by simply scaling the total energy contained in the laser pulse accordingly. However, at ultrahigh intensities this assumption might not be true anymore. There are multi-shot methods that propose a full wave front measurement of transmitted beams [361], but the key challenge remains the measurement of the intensity *at the focus*. There have been multiple proposals how to do this using gas jets, relying on ionisation rates [362, 363] and ponderomotive effects onto the relativistic electrons [364].

Especially in the context of inverse Compton scattering, there have been proposals that are also suitable on-shot, e.g. by considering the yield of the radiation in the linear case (limit $a_0 \sim 0$) in Chapter 5, the contribution of higher harmonic radiation in the approach of $a_0 \to 1$ (at moderate intensities) [287] or the ellipticity of the emitted gamma signal in the highly nonlinear regime [120, 172, 260]. This can be measured using the setup described in Chapter 5, but needs to decoupled from the electron beam properties. In the future when radiation reaction is well characterised, these counterpropagating experiments might themselves become a tool to characterise the intense laser pulse by passing them through specially tailored electron beams. The rate of electron positron pairs produced in the process is particularly sensitive (exponential) to the laser intensity and is suited for a precise measurement of the laser intensity.

In addition to the capability to characterise the laser pulse and the intense focus, we

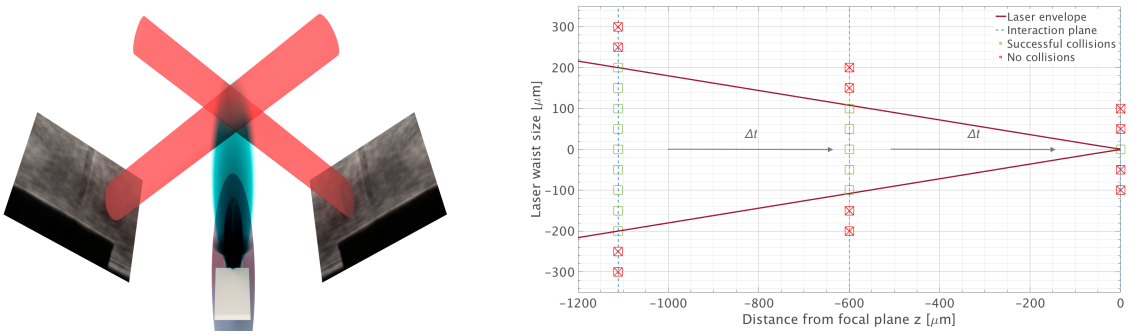


Figure 8.4: Monitoring spatio-temporal overlap. Left: Two optical transverse probes (red) are crossing perpendicular to each other through a gas jet (blue) and are used as shadowgraphy (planes). Right: Sketch of a laser raster scan (see Figure 5.8 in Section 5.5 for more details).

also require a good control over the properties of the laser pulse for certain measurements. For instance, changing the polarisation either from linear to circular or rotating the polarisation axis, e.g. using waveplates, is of interest for on-shot intensity measurements (observing the elongated axis) and to measure polarisation-dependent cross sections. The control over the spatio-temporal shape and energy distribution might be required to achieve supercritical values of η [104] and to stimulate emissions early in an interaction to study cascades. Finally, the capability to operate at high repetition rates and stability increases the discovery reach, similarly as the luminosity in conventional accelerators.

Spatio-temporal synchronisation

One of the key challenges in colliding-pulse experiments is the spatio-temporal overlap of the electron bunch and the laser pulse, or the light sources in case of photon-photon interactions, respectively. Two laser pulses can be synchronised in an attenuated low-power mode, e.g. using a combination of photodiodes and interferometry techniques (see Section 4.3). For on-shot full power shots, there are three main issues to consider (see Section 6.6): first, the alignment and the time of arrival of the laser pulses is varying from shot-to-shot (jitter). Second, the spatial and temporal alignment might be drifting over time such that the electron bunch and the laser pulse do not remain overlapped indefinitely (see Section 4.3.3). Third, there is an offset between the wakefield driver beam and the electron bunch it accelerates (see Section 4.3.3), which might also vary from shot-to-shot due to fluctuating injection points.

A spectral interferometry setup measures the relative delay between two laser pulses [239, 243] and could monitor said *temporal* jitter and drifts, for instance by combining components of the beams that are transmitted through optics or the post-interaction laser pulses.

In the experiment described in Chapter 5, the optical transverse probe (shadowgraphy) and the recombination light of the plasma channel were useful diagnostics to monitor, on the other hand, the *spatial* overlap and drifts in the alignment, but at a limited spatial and temporal resolution. Two transverse optical probes with high magnification crossing through the plasma perpendicular with respect to each other could resolve jitter and drifts in the spatial position of the plasma channel [see Figure 8.4 (left)]. A *fast* shadowgraphy [365–367] could, on the other hand, enable a more accurate localisation of the bubble (instead of an expanded channel), but would require significant efforts to maintain and would add complexity to an already complex multi-beam setup. The pointing variations of the scattering beam, on the other hand, could be characterised by a far-field diagnostic.

The offset between the electron bunch and the wakefield driver beam depends on the density of the plasma, its length, and the point at which the electrons are injected into the bubble. Due to the complex interplay of nonlinear effects in the plasma, the injection point might vary from shot to shot (bubble evolution). It is desirable to reduce the variability of the injection point, e.g. through shock injection, and to measure the offset and relative jitter, e.g. from a shot-to-shot shift of the shock position, between the electron bunch and the laser pulse to find a systematic route to consistent overlap between the scattering laser pulse and the electron beam.

Chapter 5 demonstrated that inverse Compton scattering itself can be used as tool for this purpose: Section 5.5 described a spatial-correlation technique that can be used to align the electron beam and the scattering laser pulse over multiple shots and that could systematically facilitate high-intensity interactions [see Figure 8.4 (right)].

Section 5.9, on the other hand, outlined that the radiation yield measured in a low-intensity interaction can be used to infer the intensity at the interaction on a single shot and, as a consequence, effectively characterises the *temporal jitter* between the scattering laser and the electron bunch. By comparing this with a measurement of the jitter between the two laser pulses, e.g. using spectral interferometry, one could also infer the jitter between the wakefield driver and the electron bunch it accelerates.

A statistical measurement of the temporal jitter and offset is useful, but especially at high intensities where there are significant model uncertainties an independent on-shot measurement is required. Diagnostics that measure the relative timing between an electron bunch and a laser pulse are, for instance, electro-optical sampling (EOS) [368, 369] and magneto-optic sampling [232], which have been demonstrated at the femtosecond level accuracy.

Considering the rising number of laser pulses and diagnostics in such a setup and the potential danger of spatio-temporal drifts and misalignment (see Section 4.3.3), it might be useful to automate some parts of the alignment process according to selected quantities

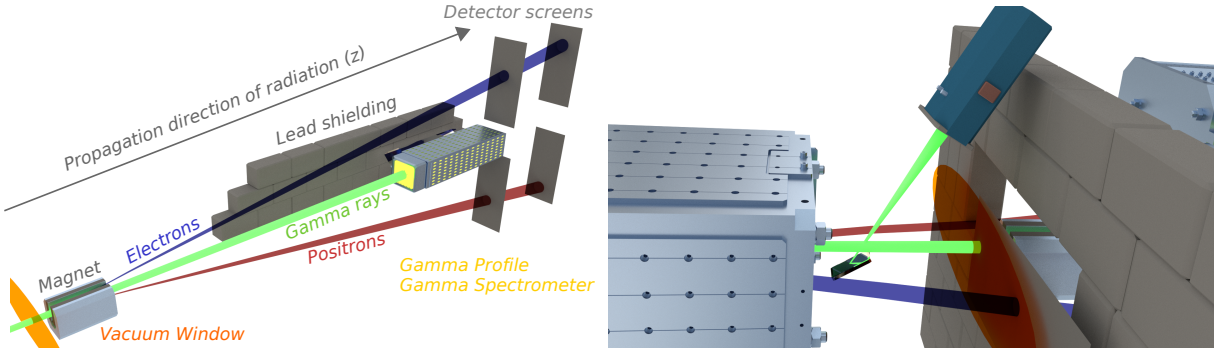


Figure 8.5: Measuring high-energy radiation: Left: Gamma spectrometer design combining a scintillator array as used in this work with a gamma converter spectrometer. The gamma rays (green) pass through a vacuum window or converter target (orange) and produce electron-positron pairs. A magnet (grey) disperses them and the particles are measured on detector screens. The gamma-ray beam propagates into the scintillator stack (yellow) where its profile and spectrum are measured. Right: A crystal (black) is used to disperse divergent low-energy X-rays onto the CCD of a X-ray camera (blue).

[280] and to evaluate data immediately 'on the fly'. Multi-shot diagnostics, statistical characterisations and automation benefit from high repetition rates. The two techniques introduced in Sections 5.5 and 5.9 are well suited to be automated with machine learning, for instance Bayesian inference which can reduce the number of shots required to optimise parameters in a multi-dimensional scan. Quantitative measurements of alignment drifts could then also be corrected in real-time and increase the number of successful collisions and ultimately the discovery reach.

Radiation diagnostics

The spectral retrieval of highly energetic gamma radiation is in this context a crucial capability to infer the conditions at the interaction, e.g. of the electron beam and the laser pulse (see Chapters 5 and 6), and to estimate expected cross sections for photon-photon interactions (see Chapter 7). In the study of strong-field effects, we anticipate a wide bandwidth of energetic radiation ranging from keV to several GeV photon energies.

X-ray energies in the tens of keV range are routinely measured in LWFA experiments, for instance, using direct or indirect detection X-ray cameras with filter packs [218]. The setup described in Chapter 7, on the other hand, included a crystal spectrometer setup, which could be employed to measure the formation length of a photon in the breakdown of the local-constant field approximation (LCFA) in the halo of the main emission cone [131, 160, 315] [see Figure 8.5 (right)].

An accurate spectral retrieval over a large bandwidth and particularly at high photon energies is, however, challenging. This work demonstrated that the retrieval of a gamma spectrum from a spectrometer on scintillating crystals relies on a good knowledge of the spectral shape as the response of the detector is insensitive to small changes to it (see

Sections 4.6.2, 5.10 and 7.6). An alternative spectrometer setup uses the spectrum of Compton scattered electrons, and at higher energies electron-positron pairs, from gamma rays passing through a converter foil to infer the spectrum [286]. However, as the pair production cross sections plateaus at few tens of MeV photon energies this diagnostic also loses sensitivity with increasing photon energies.

A potential solution sees both diagnostics, a scintillator array and a pair spectrometer, combined to infer the spectrum more accurately from the two independent measurements [32, 264] [see Figure 8.5 (left)]. In this configuration, a thin converter target, for instance a wire, and multiple detector screens measuring the spectrum of the pairs could give access to a double differential gamma spectrum or even a triple differential spectrum with suitable deconvolution methods. However, such a spectrometer still has to be fielded experimentally at hundreds of MeV to GeV-scale photon energies and requires a detailed analysis of signal-to-noise ratios and shielding concepts.

A crucial development area towards the measurement of absolute cross sections is the absolute calibration of radiation detectors. In this work and commonly done in the LWFA community, radioactive sources (here Na-22 and Cs-137, emitting particles or radiation at an energy of around $0.5 - 1$ MeV) were used to calibrate the energy deposition in the scintillator arrays. Whilst good agreement of the calibration with expected radiation yields was demonstrated in Section 5.8, the fundamentally different response of the detector at higher photon energies motivates the use of a light source that provides photons of comparable energy. Linear inverse Compton scattering and bremsstrahlung are well understood phenomena and reach similar energies (see Sections 4.6.2 and 5.8), and are hence suitable candidates for this purpose.

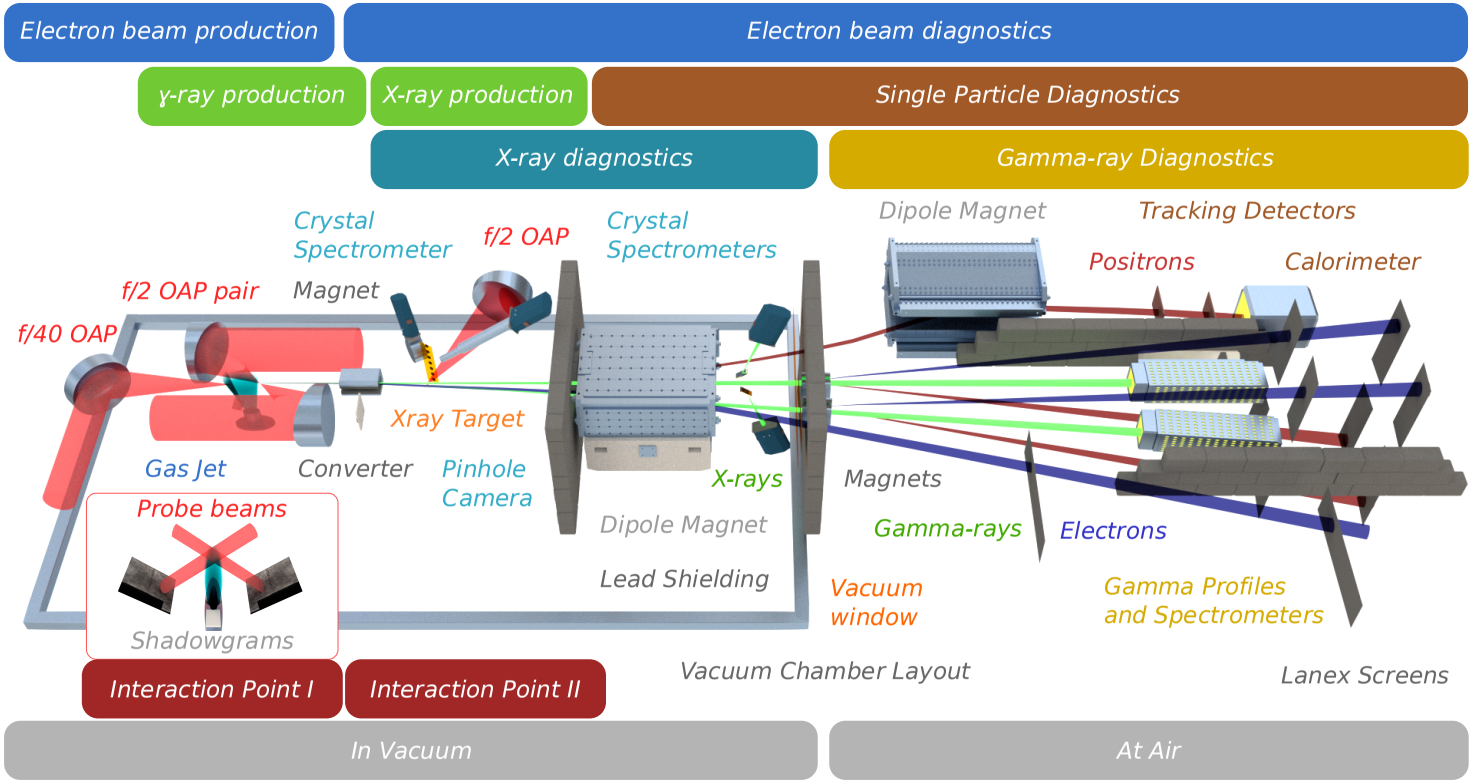


Figure 8.6: Sketch of an experimental setup to measure strong-field QED phenomena incorporating some of the ideas and concepts discussed in this work and this section. From left to right: An $f/40$ off-axis parabola (OAP) focuses an intense laser pulse (red) onto the edge of a gas jet (blue) to accelerate electrons (blue) via LWFA. The flow of the gas jet is perturbed by a blade to induce shock injection. The plasma is diagnosed by two orthogonal probe beams (inset). A pair of $f/2$ OAPs is used for radiation reaction studies: the first OAP focuses the second laser pulse onto the LWFA electron beam to produce energetic gamma-rays (green) from inverse Compton scattering (ICS), the second OAP recollimates it and transports it away to diagnostics. In a photon-photon (PhPh) setup the OAP pair can be replaced by a bremsstrahlung converter (grey). A dipole magnet (grey) disperses the electron beam to separate it from the gamma-ray cone. Another $f/2$ OAP is either used to collide with the gamma-ray beam directly (PhPh, nonlinear Breit-Wheeler) or heats an X-ray target (orange, PhPh, linear Breit-Wheeler), which is then characterised by a crystal spectrometer and a pinhole camera (turquoise). In an ICS setup, this laser pulse scatters off the electron beam at low intensity to act as beam profile and polarisation measurement. Electrons and positrons are dispersed by another dipole magnet: electrons pass through the vacuum window (orange) and multiple Lanex screens. The positrons are redirected by another dipole magnet (magnetic chicane) and through multiple tracking screens (brown) onto a calorimeter (gold). The gamma-rays from both interaction points pass through the vacuum window where they produce electron-positron pairs. Magnets disperse these onto Lanex screens, while the gamma-ray cones are incident onto sets of gamma profile and crystal spectrometers. A set of crystal spectrometers are, on the other hand, measuring the divergent low-energy X-rays predicted by the breakdown of the locally constant field approximation. Components such as collimators and laser diagnostics were omitted due to space constraints.

8.3 Concluding remarks

Strong-field QED is a novel research field that bears ample research opportunities into fundamental phenomena and novel diagnostics. Laser wakefield accelerators are a powerful tool to explore high-field phenomena in colliding-pulse geometries where electric field strengths are greatly enhanced in the rest frame of relativistic electrons and can realise real photon-photon colliders.

The stringent requirements of these studies on laser systems, accelerators and diagnostics are expected to drive innovation, but will also make experimental setups more complex such that purpose-built facilities and designated target areas will be needed to facilitate precision measurements. High repetition rates and automated alignment procedures, e.g. guided by machine learning, might become a necessity to cope sustainably with the large number of diagnostics in real time and to achieve a similar standard for 'discoveries' as particle accelerators.

The overlapping interests of the conventional accelerator, and the high-intensity laser and laser-plasma community might also signal the opportunity for a closer alignment of the fields beyond PWFA research, which could stimulate a fruitful exchange between the disciplines and establish plasma-based technology further into the mainstream of accelerator science.

Appendix A

Symbols and constants

A.1 Symbols

Symbol	Name	Symbol	Name
a_0	Normalised vector potential	ω_p	Plasma frequency
B	Magnetic field	P	Power
β	Relativistic velocity	q	Particle charge
E	Electric field strength	Q	Total charge
$\mathcal{E}, \epsilon$	Energy, e.g. ϵ_γ gamma energy	r	Radius
η	Quantum nonlinearity param.	r_β	Betatron radius
g	Gaunt factor	ρ	(Material) density
γ	Relativistic Lorentz factor	R_c	Classical radiation reaction param.
I	Intensity	s	Centre-of-mass energy
K	Wiggler parameter	σ	Standard deviation
λ	Wavelength	σ_X	Cross section for process X
N	Number of particles/photons	θ	Divergence or angle
n_c	Critical density	v	Velocity
n_e	Electron density	w	Waist size
∇	Nabla operator	X_0	Radiation length
ω	Frequency	z_R	Rayleigh length
Ω	Solid angle	Z	Atomic Number

Table A.1: Overview of symbols used in this work.

A.2 Abbreviations

Abbreviation	Meaning
BW	Breit-Wheeler (process)
CCD	Charge-coupled device
CLF	Central Laser Facility
CM	Centre of mass
CPA	Chirped-pulse amplification
FROG	Frequency resolved optical gating
FWHM	Full width at half maximum
IC	Imperial College
ICS	Inverse Compton scattering
KDE	Kernel density estimate
LWFA	Laser wakefield acceleration
LAD	Lorentz-Abraham-Dirac (equation)
LCFA	Locally constant field approximation
LL	Landau-Lifschitz (equation)
OAP	Off-axis parabola
PWFA	Plasma wakefield accleration
QED	Quantum electrodynamics
QUB	Queen's University Belfast
RAL	Rutherford Appleton Laboratory
RR	Radiation reaction
SI	Internation System of Units
(X)FEL	(X-ray) free-electron laser

Table A.2: List of abbreviations used in this work.

A.3 Notations

Notation	Meaning
Bold	Vector
$()^t$	Transposed Vector/Matrix
$\langle ... \rangle$	Average
$\hbar$	Reduced quantity, $h/2\pi$
$\dot{x}$	Time derivative of x

Table A.3: List of notations used in this work.

A.4 Fundamental constants

Symbol	Name	Value (SI)	Unit (SI)
α	Fine-structure constant	7.3×10^{-3}	1
c	Vacuum speed of light	3×10^{8}	m/s
e	Electron charge	1.6×10^{-19}	C
E_S	Schwinger field	1.32×10^{18}	V/m
ϵ_0	Vacuum permittivity	8.9×10^{-12}	F/m
h	Planck constant	6.6×10^{-34}	J · s
λ_C	Compton wavelength	2.4×10^{-12}	m
m_e	Electron mass	9.1×10^{-31}	kg
μ_0	Vacuum permeability	1.3×10^{-6}	N · A
r_e	Classical electron radius	2.8×10^{-15}	m
σ_T	Thomson cross section	6.7×10^{-29}	m^2

Table A.4: Summary of relevant fundamental constants.

Most of the thesis uses SI units. In a few exceptions, natural units ($\hbar = c = \epsilon_0 = 1$) are used, which is then explicitly indicated.

Appendix B

Single particle motion

B.1 Electron in a cylindrically symmetric electric field

Here we discuss the motion of an electron in a cylindrically symmetric electric field, which resembles the case of an electron in a plasma channel. This derivation is based on [218].

Assume a relativistic electron moving in the longitudinal direction and an electric field that is cylindrically symmetric around the propagation axis. We ignore any vector potential contributions and only use a scalar potential. The Lagrangian of this scenario is described by

$$L(\mathbf{r}, \mathbf{v}, t) = -m_e c^2 \gamma^{-1} - q\Phi, \tag{B.1.1}$$

where Φ is the scalar potential describing the electrostatic field of the channel. The scalar potential is the solution matching the radial Poisson equation in cylindrical symmetry

$$\frac{1}{r}\frac{\partial}{\partial r}\left(r\frac{\partial \phi}{\partial r}\right) = \frac{-e(n_0 - n_e)}{\epsilon_0}, \tag{B.1.2}$$

with the solution

$$\phi = -\frac{(n_0 - n_e)er^2}{4\epsilon_0}, \tag{B.1.3}$$

where n_0 is the ion charge density and n_e the electron density in the channel. In the limit of a completely evacuated channel, $n_e \to 0$, $\phi = -n_0 e r^2/(4\epsilon_0)$. As before $\mathbf{E} = -\nabla\phi$ and in this case $E_r = -\partial_r \phi$. The equation of motion for the radial component is then

$$\frac{d}{dt}\mathbf{p} = -\frac{e^2 n_0}{2\epsilon_0} r, \tag{B.1.4}$$

with $\mathbf{p} = \gamma m_e \dot{\mathbf{r}}$. Assume there is no axial acceleration field, the radial component of the velocity is small compared to c and the longitudinal component is close to c: $\dot{\gamma}$ is then

close to zero. The equation then takes the shape of a harmonic oscillator

$$\ddot{r} = -\frac{e^2 n_0}{2\epsilon_0 m_e \gamma} r = -\omega_\beta^2 r, \tag{B.1.5}$$

with the betatron frequency, ω_β, which is related to the plasma frequency, ω_p, by $\omega_\beta = \omega_p/\sqrt{2\gamma}$. The plasma frequency is derived explicitly in Section 3.1.3. As this is the standard harmonic oscillator equation, it follows a solution of shape

$$r(t) = A\cos(\omega_\beta t + \varphi), \tag{B.1.6}$$

and with initial conditions $r(t=0) = r_\beta$ and $\dot{r}(t=0) = 0$, we obtain

$$r(t) = r_\beta \cos(\omega_\beta t), \tag{B.1.7}$$

where r_β is the amplitude of the oscillation, also referred to as the betatron radius.

If we continue with the assumption $\dot{\gamma} = 0$, this requires $\beta^2 = \beta_r^2 + \beta_z^2 = constant$. This gives $\beta_z = \sqrt{\beta^2 - \beta_r^2} \approx \beta(1 - \beta^2/2)$, where we used a Taylor expansion and $\beta \approx 1$. If we use the solution for $r(t)$ derived above, $\beta_r = \dot{r}/c$ and $\sin^2 x = (1 - \cos 2\theta)/2$, we obtain:

$$\beta_z \approx \beta\left(1 - \frac{r_\beta^2 \omega_\beta^2}{4c^2}\right) + \beta\frac{r_\beta^2 \omega_\beta^2}{4c^2}\cos(2\omega_\beta t). \tag{B.1.8}$$

Integrating this with the initial condition $z(t=0) = z_0$

$$\frac{z}{c} \approx \frac{z_0}{c} + \beta\left(1 - \frac{r_\beta^2 \omega_\beta^2}{4c^2}\right)t + \beta\frac{r_\beta^2 \omega_\beta}{8c^2}\sin(2\omega_\beta t), \tag{B.1.9}$$

where we identify the drift velocity $\beta c\left(1 - \frac{r_\beta^2 \omega_\beta^2}{4c^2}\right)$ and in the moving frame the familiar figure-of-eight motion.

B.2 Electron in a cylindrically symmetric electric field with axial field

Now we add a constant axial field in the longitudinal (direction of electron propagation) to the previous case. This comes closer to the reality of a laser wakefield accelerator where electrons experience radial focusing and axial accelerating fields at the same time. Significant parts of this derivation are based on [218, 370].

The electric field component shall now be E_z, with z being the longitudinal axis. This gives us the extra term $\frac{\partial \phi}{\partial z} = -E_z$. The Euler-Lagrangian now has two non-trivial equations of motions. First, as before

$$\frac{d}{dt}(\gamma m_e \dot{r}) = \frac{\partial}{\partial r} L = -\frac{e^2 n_0}{2\epsilon_0} r, \tag{B.2.1}$$

and, second, the z-component

$$\frac{d}{dt}(\gamma m_e \dot{z}) = \frac{\partial}{\partial z} L = eE_z = const. \tag{B.2.2}$$

The change in momentum is now not negligible any more, $\dot{\gamma} \neq 0$, and we have to expand the brackets on the left-hand side of Equations (B.2.1) and (B.2.2). The radial component is then

$$\dot{\gamma} m_e \dot{r} + \gamma m_e \ddot{r} = -\frac{e^2 n_0}{2\epsilon_0} r. \tag{B.2.3}$$

The axial component is equal to a constant, so we can simply integrate

$$\gamma m_e \dot{z} = -eE_z t + const. \tag{B.2.4}$$

If we assume that the electron is highly relativistic $\dot{z} \to c$, so $\dot{\gamma} = eE_z/m_e c$ and

$$\gamma \beta_z \approx \gamma = -\frac{eE_z t}{m_e c} + \gamma_0 \beta_0, \tag{B.2.5}$$

where $\gamma_0 \beta_0$ are the initial conditions. Inserting the result from Equation (B.2.5) into Equation (B.2.1), we obtain the differential equation

$$eE_z \dot{r} + (eE_z t + \gamma_0 \beta_0 m_e c)\ddot{r} = -\frac{e^2 n_0 c}{2\epsilon_0} r, \tag{B.2.6}$$

which we can write as

$$(At + B)\ddot{r} + A\dot{r} + Cr = 0, \tag{B.2.7}$$

by using the abbreviations $A = eE_z$, $B = \gamma_0 \beta_0 m_e c$ and $C = e^2 n_0 c/2\epsilon_0$. The analytic

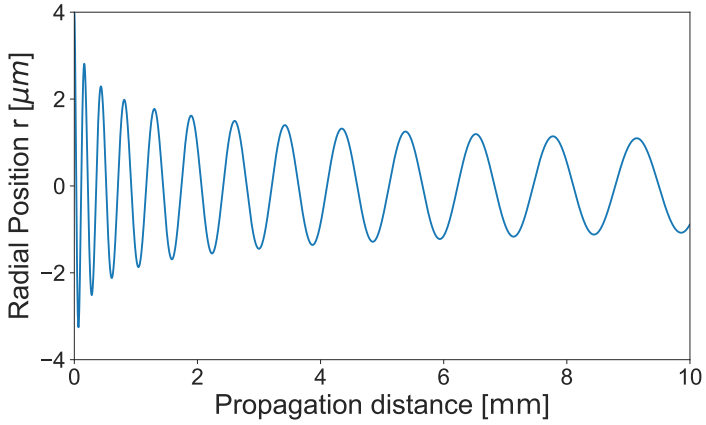


Figure B.1: Particle trajectory of an electron in a cylindrically symmetric electric field with a constant axial accelerating field as described in Equation (B.2.8) *for a plasma of density* $n_e = 2 \times 10^{18} cm^{-3}$ *as a function of propagation distance.*

solution for this differential equation is [218]:

$$r(t) = \frac{\pi\sqrt{CB}}{A} r_{\beta 0} \Bigg[J_1\left(2\sqrt{CB}/A\right) Y_0\left(2\sqrt{C(B+At)}/A\right) - Y_1\left(2\sqrt{CB}/A\right) J_0\left(2\sqrt{C(B+At)}/A\right) \Bigg], \tag{B.2.8a}$$

with the initial conditions $r(t=0) = r_{\beta 0}$ and $\dot{r}(t=0) = 0$. J_1, J_0 are Bessel functions of first kind of order 1 and 0, respectively. Y_1, Y_0 are Bessel function of the second kind of order 1 and 0. This motion is shown in Figure B.1. We see that the oscillations quickly lose amplitude and fall to a settled value, whereas the wavelength of the oscillations increases as the electron gains momentum and inertia.

Appendix C

Synchrotron radiation

C.1 Synchrotron Radiation

The angularly integrated spectral intensity for synchrotron radiation is given by [52, 218]:

$$\frac{dI}{d\omega} = \frac{\sqrt{3}}{4}\frac{e^2}{\pi c \epsilon_0}\gamma\frac{\omega}{\omega_c}\int_{\omega/\omega_c}^{\infty} K_{5/3}(x)dx, \tag{C.1.1}$$

where e is the electron charge, ϵ_0 the dielectric constant and c is the speed of light. γ is the relativistic Lorentz factor of an electron. $K_{5/3}$ is a modified Bessel function of the second kind. ω_c is the characteristic or *critical frequency* given by

$$\omega_c = \frac{3}{2}\gamma^3\frac{c}{r_L}, \tag{C.1.2}$$

where r_L is the bending radius, e.g. the Larmor radius. The doubly differential spectral intensity reads

$$\frac{d^2I}{d\epsilon d\Omega} = \frac{3e^2}{16\pi^3\hbar c\epsilon_0}\gamma^2\frac{\epsilon^2}{\epsilon_c^2}\left(1+\gamma^2\theta^2\right)^2\left[K_{2/3}^2(\psi) + \frac{\gamma^2\theta^2}{1+\gamma^2\theta^2}K_{1/3}^2(\psi)\right], \tag{C.1.3}$$

with

$$\psi = \frac{\epsilon}{2\epsilon_c}(1+\gamma^2\theta^2)^{3/2} \tag{C.1.4}$$

C.2 Undulator and Wiggler Radiation

A set of alternating magnets can be used to harvest and direct the radiation of an accelerated relativistic electron more efficiently. The electron oscillates and emits radiation preferentially at the turning points as the acceleration is the strongest there. The radiation is emitted in a forwards-pointing cone with a diameter proportional to K/γ and $1/\gamma$ [52] in and out of plane of the oscillation, respectively.

The rapid change of direction in the field and hence forced trajectory of the electron in the transverse results in a change of effective Lorentz factor in the forward direction.

$$\langle\gamma\rangle \approx \frac{\gamma}{\sqrt{1+0.5K^2}} \tag{C.2.1}$$

Commonly, two regimes are identified based on the *wiggler parameter*, K:

$$K = \frac{eB_0}{m_e c k_u} = \frac{eB_0\lambda_u}{2\pi m_e c}, \tag{C.2.2}$$

where B_0 is the amplitude of the magnetic field, λ_u the wavelength of the alternating magnetic field, and k_u is the corresponding wave vector. e is charge of the electron, m_e its mass and c is the speed of light. $K \ll 1$ refers to the *undulator regime*, whereas large $K \gg 1$ indicate the *wiggler regime*. In the wiggler regime, the divergence of the cone is large and the radiation has a broad bandwidth. In the undulator regime the radiation is strongly collimated and interference can occur resulting in single harmonics being emitted. The constructive interference occurs with the nth harmonic of wavelength:

$$\lambda = \frac{\lambda_u}{2n\gamma^2}\left(1+\frac{K^2}{2}+\gamma^2\theta^2\right), \tag{C.2.3}$$

where γ is the relativistic Lorentz factor of the electron and θ is the observation angle relative to the beam axis. The equations introduced for synchrotron radiation work similarly for wiggler radiation. The reference to the bending radius is usually replaced by an expression including the magnet periodicity or the K parameter. The critical frequency of a wiggler is then, for instance:

$$\omega_c \sim \frac{3}{2}\gamma^2 K k_u c \tag{C.2.4}$$

C.3 Betatron Radiation

Just as the evacuated 'bubble' in a wakefield accelerates particles in a similar way as conventional RF cavities would, the generation of X-rays draws another parallel in conventional devices.

Due to initial transverse momentum on injection, and the focusing and defocusing fields of the cavity, electrons start to oscillate around the central axis. The electrons oscillate at the betatron frequency, ω_β [79, 218]

$$\omega_\beta = \omega_p/\sqrt{2\gamma}, \tag{C.3.1}$$

which depends on the plasma frequency ω_p and the energy of the electrons, here given by the relativistic Lorentz factor γ.

Similarly to electrons in an insertion device (undulator or wiggler), these oscillations lead to the emission of radiation in a narrow forward pointing cone due to the relativistic forward momentum of the particles. Unsurprisingly, the equations describing both processes are very similar.

The collimation depends on K, the wiggler parameter (for insertion devices) or betatron strength parameter

$$K = \gamma k_\beta r_\beta, \tag{C.3.2}$$

where $k_\beta = \omega_\beta/c$ is the wavenumber and r_β is the betatron radius, the amplitude of the oscillations. If $K \gg 1$, it is called the undulator parameter.

The generated radiation follows the on-axis synchrotron radiation with a critical energy

$$\boxed{\epsilon_c = \frac{3}{4}\hbar\gamma^2\omega_p^2 r_\beta/c,} \tag{C.3.3}$$

where this characteristic energy indicates when approximately half the energy is radiated above and below this value.

The oscillation of the particles and hence the emission of radiation can be enhanced in wakefield experiments by tailoring the wavefront [371, 372], density profile [373, 374] or by using different injection mechanisms [283]. In LWFA betatron radiation typically reaches the soft X-ray regime of a few to tens of keV [282].

Appendix D

Radiation Length

The radiation length, X_0, is a material-specific quantity that indicates how much energy a high-energy particle converts into radiation and secondary particles when passing through a material. A particle passing through a material of thickness x and radiation length X_0 loses energy at a rate [52]:

$$\frac{\mathrm{d}\epsilon}{\mathrm{d}x} = -\frac{\epsilon}{X_0}, \tag{D.0.1}$$

with $\epsilon(x) = \epsilon_0 e^{-x/X_0}$ and X_0 is given by [285, 375]:

$$\boxed{X_0 = \left[4\alpha r_e^2 \frac{N_A}{A}\left\{Z^2\left(L_{rad} - f(Z)\right) + ZL'_{rad}\right\}\right]^{-1},} \tag{D.0.2}$$

with the atomic weight, A, and $4\alpha r_e^2 \frac{N_A}{A} = (716.408\,\mathrm{g\,cm^{-2}})^{-1}$ for $A = 1$ g/mol. For up to uranium, $f(Z)$ can be approximated by

$$f(Z) = a^2\left[(1+a^2)^{-1} + 0.20206 - 0.0369a^2 + 0.0083a^4 - 0.002a^6\right], \tag{D.0.3}$$

with $a = \alpha Z$. The radiation length in a mixture or compound of n components can be approximated by the sum of radiation lengths of the individual components weighted by their weight

$$\frac{1}{X_0} = \sum_{j=1}^{n} \frac{w_j}{X_j}. \tag{D.0.4}$$

Appendix E

Bremsstrahlung

E.1 Bremsstrahlung in the Born approximation

The (in energy) differential cross section for electron-nucleus bremsstrahlung in a fixed field in the Born approximation, neglecting the recoil of the nucleus, is given by [109, 338]

$$\begin{aligned}\frac{\mathrm{d}\sigma_{eZ}}{\mathrm{d}\omega} = \frac{\alpha Z^2 r_e^2}{\omega}\frac{u'}{u}\Bigg\{&\frac{4}{3} - 2\gamma\gamma' c^2\frac{u^2+u'^2}{u^2u'^2} + c^3\left(\frac{\epsilon\gamma'}{u^3} + \frac{\epsilon'\gamma}{u'^3} - \frac{\epsilon\epsilon'^3}{uu'c}\right) \\ &+ L\Bigg[\frac{8}{3}\frac{\gamma\gamma' c^2}{uu'} + \frac{(\hbar\omega)^2c^2}{m_e^2u^3u'^3}(\gamma^2\gamma'^2 + u^2u'^2/c^4) \\ &+ \frac{\hbar\omega}{2m_euu'}\left(\frac{\gamma\gamma'+u^2/c^2}{u^3/c^3} - \frac{\gamma\gamma'+u'^2/c^2}{u'^3/c^3} - \frac{2\hbar\omega\gamma\gamma' c^2}{m_eu^2u'^2}\right)\Bigg]\Bigg\},\end{aligned} \tag{E.1.1}$$

where

$$\begin{aligned}L &= \ln\left(\frac{\gamma\gamma' + uu'/c^2 - 1}{\hbar\omega/m_ec^2}\right), \\ \epsilon &= 2\ln(\gamma + u/c), \\ \epsilon' &= 2\ln(\gamma' + u'/c).\end{aligned}$$

u is the momentum of the electron, γ its energy and m_e its mass. $\hbar\omega$ is the energy of the photon and c is the speed of light. Primed quantities denote post-interaction values and $\gamma m_ec^2 = \hbar\omega + \gamma' m_ec^2$, assuming all energy is transferred into radiation. r_e is the electron radius, α the fine-structure constant and Z the atomic number.

E.2 Bremsstrahlung including screening

The (in energy) differential cross section for electron-nucleus bremsstrahlung is in the ultra-relativistic limit, including electron contributions and screening, given by [285, 375]

$$\frac{\mathrm{d}\sigma_{eZ}}{\mathrm{d}\omega} = \frac{\alpha r_e^2}{\omega}\Bigg\{\left(\frac{4}{3}-\frac{4}{3}y+y^2\right)\times\left[Z^2\left(\phi_1-\frac{4}{3}\ln Z-4f\right)+Z\left(\psi_1-\frac{8}{3}\ln Z\right)\right] + \frac{2}{3}(1-y)\left[Z^2(\phi_1-\phi_2)+Z(\psi_1-\psi_2)\right]\Bigg\}, \tag{E.2.1}$$

with $y = \hbar\omega/\gamma m_e c^2$, the ratio of the emitted photon energy to the initial electron energy. r_e is the electron radius, α the fine-structure constant and Z is the atomic number. The ϕ and ψ terms are given by

$$\begin{aligned}
\phi_1 &= 2\left[1+\ln\left(a^2Z^{2/3}m_e^2\right)\right]-2\ln(1+b^2)-4b\tan^{-1}(b^{-1}),\\
\phi_2 &= 2\left[\frac{2}{3}+\ln\left(a^2Z^{2/3}m_e^2\right)\right]-\ln(1+b^2)+8b^2\left[1-b\tan^{-1}(b^{-1})-\frac{3}{4}\ln(1+b^{-2})\right],\\
\psi_1 &= 2\left[1+\ln\left(a'^2Z^{4/3}m_e^2\right)\right]-2\ln(1+b'^2)-4b'\tan^{-1}(b^{-1}),\\
\psi_2 &= 2\left[\frac{2}{3}+\ln\left(a'^2Z^{4/3}m_e^2\right)\right]-2\ln(1+b'^2)+8b'^2\left[1-b\tan^{-1}(b'^{-1})-\frac{3}{4}\ln(1+b'^{-2})\right],
\end{aligned}$$

with $a = 184.15(2.718)^{-1/2}Z^{-1/3}/m_e$, $a' = 1194(2.718)^{-1/2}Z^{-2/3}/m_e$, $b = a\delta$, $b' = a'\delta$, $\delta = m_e^2\hbar\omega/(2\gamma m_e c^2(\hbar\omega-\gamma m_e c^2))$. The Coulomb correction term for the atomic electrons, f, is given by

$$f(z) \approx 1.202z - 1.0369z^2 + 1.008z^3/(1+z). \tag{E.2.2}$$

E.3 Bremsstrahlung in terms of radiation length

The differential cross section for the bremsstrahlung process is in the ultrarelativistic limit approximated by a simplified expression in terms of the radiation length, X_0 (see Section D) [285, 375]

$$\frac{\mathrm{d}\sigma}{\mathrm{d}(\hbar\omega)} = \frac{A}{X_0 N_A \hbar\omega}\left(\frac{4}{3}-\frac{4}{3}y+y^2\right), \tag{E.3.1}$$

where $\hbar\omega$ is the energy of the emitted photon, Z is the atomic number and A the atomic weight and N_A the Avogadro number. $y = \hbar\omega/\epsilon$, i.e. the fraction of the emitted photon energy relative to the initial electron energy.

Appendix F

Nonlinear Compton Scattering

The emission/scatter rates for the n-th harmonic depend on the laser polarisation: the scattering rate (spin-averaged and unpolarised states in/out) for n scattered photons for circular polarisation is given (in natural units) by [131, 173]

$$\frac{\mathrm{d}W_n}{\mathrm{d}x} = \frac{\alpha m^2}{4\epsilon}\left[-4J_n^2 + a_0^2\left(1 - x + \frac{1}{1-x}\right)\left(J_{n-1}^2 + J_{n+1}^2 - 2J_n^2\right)\right], \tag{F.0.1}$$

and for linear polarisation by

$$\frac{\mathrm{d}W_n}{\mathrm{d}x} = \frac{2\alpha m^2}{\pi\epsilon}\int_0^{\pi/2}\left[-A_0^2 + a_0^2\left(1 - x + \frac{1}{1-x}\right)\left(A_1^2 - A_0 A_2\right)\right]\mathrm{d}\varphi. \tag{F.0.2}$$

The energy of the incoming photons is ω and the scattered photon carries an energy $\omega' = x\epsilon$, i.e x is the fraction of energy the photon carries away. a_0 is the normalised vector potential of the laser pulse. J_n is shorthand for $J_n(z)$, and $A_i = A_i(n, a, b)$, with

$$z = \frac{2a_0}{\sqrt{1+a_0^2}}\frac{\sqrt{x[nu - (1+nu)x]}}{u(1-x)}, \tag{F.0.3}$$

$$u = \frac{2k\cdot q}{q^2} = \frac{4\epsilon\omega}{m^2(1+a_0^2)}. \tag{F.0.4}$$

The function A_i and its arguments are defined as

$$A_i(n, a, b) = \frac{1}{\pi}\int_0^{\pi}\cos^i\phi\cos[(a + 2b\cos\phi)\sin\phi - n\phi]\mathrm{d}\phi, \tag{F.0.5}$$

$$a = \frac{\sqrt{8}Qna_0}{1 + a_0^2 + Q^2}\cos\varphi, \tag{F.0.6}$$

$$b = -\frac{(n/2)a_0^2}{1 + a_0^2 + Q^2}, \tag{F.0.7}$$

$$Q^2 = (1 + a_0^2)\left[nu\left(\frac{1}{x} - 1\right) - 1\right]. \tag{F.0.8}$$

Appendix G

Quantum synchrotron function

The quantum synchrotron function, F, is given as a function of the two invariants, η and χ, by [173]

$$F(\eta,\chi)=\frac{4\chi}{3\eta^2}\left[\left(1-\frac{2\chi}{\eta}+\frac{1}{1-2\chi/\eta}\right)K_{2/3}(\delta)-\int_\delta^\infty K_{1/3}(t)\mathrm{d}t\right], \tag{G.0.1}$$

where $\chi=\gamma b, \eta=\hbar\omega b/2m_ec^2$ are quantum parameters with $b=|\mathbf{E}_\perp+\mathbf{v}\times\mathbf{B}|/E_S$, and E_S is the Schwinger field. $K_{2,3}, K_{1/3}$ are Bessel functions of the second kind, and δ is given by

$$\delta=\frac{4\chi}{3\eta^2}\left(1-\frac{2\chi}{\eta}\right)^{-1}. \tag{G.0.2}$$

The classical part of the quantum synchrotron function is here

$$F_{cl}(\eta,\chi)=\delta_{cl}\left[2K_{2/3}(\delta_{cl})-\int_{\delta_{cl}}^\infty K_{1/3}(t)\mathrm{d}t\right], \tag{G.0.3}$$

where $\delta_{cl}=4\chi/3\eta^2$. The emission power in terms of χ for an electron of energy ϵ reads

$$\frac{\mathrm{d}P}{\mathrm{d}\chi}=\frac{2\epsilon\chi}{\eta}\frac{\mathrm{d}W_\gamma}{\mathrm{d}\chi}=\frac{\sqrt{3\alpha}}{\pi}\frac{mc^2}{\tau_c}F(\eta,\chi). \tag{G.0.4}$$

The total emission power of the classical synchrotron emission and the quantum description are related by the *Gaunt factor*, $g(\eta)$:

$$P=\frac{2\alpha}{3}\frac{mc^2}{\tau_c}\eta^2 g(\eta), \tag{G.0.5}$$

were $\tau_C=\hbar/mc^2=1.29\times10^{-21}\,\mathrm{s}$ is the Compton time and $g(\eta)$ is defined as

$$g(\eta)=\frac{3\sqrt{3}}{2\pi\eta^2}\int_0^\infty F(\eta,\chi)\mathrm{d}\chi. \tag{G.0.6}$$

In two limits of η, the Gaunt factor can be approximated by

$$g(\eta) \approx \begin{cases} 1 - (55\sqrt{3}/16)\eta + 48\eta^2 & \text{for } \eta \ll 1, \\ 0.5564\eta^{-4/3} & \text{for } \eta \gg 1, \end{cases} \tag{G.0.7}$$

or by an analytic approximation that holds over the entire parameter space to within few percent [181]

$$g(\eta) = [1 + 4.8(1+\eta)\ln(1+1.7\eta) + 2.44\eta^2]^{-2/3}. \tag{G.0.8}$$

Examining these expressions, we see that the rate at which the power emission increases falls at high intensities to $P \propto \eta^{2/3}$ and as $\eta \propto a_0$, $P \propto a_0^{2/3}$.

Appendix H

Radiation Reaction

H.1 Landau-Lifschitz Equation

The Landau-Lifschitz radiation reaction force, $\mathbf{F}_{LL}$, can be written in terms of 3-vectors as follows [127]:

$$\begin{aligned}\mathbf{F_{LL}} = \frac{2e^3}{3m_e c^3\sqrt{1-\frac{v^2}{c^2}}}&\left\{\left(\frac{\partial}{\partial t}+(\mathbf{v}\cdot\nabla)\right)\mathbf{E}+\frac{1}{c}\left[\mathbf{v}\times\left(\frac{\partial}{\partial t}+(\mathbf{v}\cdot\nabla)\right)\mathbf{B}\right]\right\}+\\ &+\frac{2e^4}{3m_e^2c^4}\left\{\mathbf{E}\times\mathbf{B}+\frac{1}{c}(\mathbf{B}\times(\mathbf{B}\times\mathbf{v}))+\frac{1}{c}\mathbf{E}(\mathbf{v}\cdot\mathbf{E})\right\}-\\ &-\frac{2e^4}{3m_e^2c^5\left(1-\frac{v^2}{c^2}\right)}\mathbf{v}\left\{\left(\mathbf{E}+\frac{1}{c}\mathbf{v}\times\mathbf{B}\right)^2-\frac{1}{c^2}(\mathbf{v}\cdot\mathbf{E})^2\right\},\end{aligned}$$

where c is the speed of light, e is the electron charge, m_e its mass, $\mathbf{v}$ its velocity and $v=|\mathbf{v}|$. $\mathbf{E}$ and $\mathbf{B}$ are the electric and magnetic field, respectively.

H.2 Stochastic Operator

The stochastic operator, S, in Section 2.3.4 is given by [132]

$$S(\eta) = \frac{55\alpha c}{24\sqrt{3}\bar{\lambda}_c} m_e^2 c^4 \eta^4 g_2(\eta), \tag{H.2.1}$$

where α is the fine-structure constant, c the speed of light, m_e the electron mass and $\bar{\lambda}_c$ is the reduced Compton wavelength. $b = |\mathbf{E}_\perp + \mathbf{v} \times \mathbf{B}|/E_S$, i.e. the relative magnitude of the Lorentz force, and E_S is the Schwinger field. η is the quantum nonlinearity parameter. $g_2(\eta)$ is similarly defined as the Gaunt factor, g, (see Appendix G) in terms of the quantum synchrotron function, F, and the classical synchrotron function, F_{cl}:

$$g_2(\eta) = \frac{\int_0^{\eta/2} \chi F(\eta, \chi) \mathrm{d}\chi}{\int_0 \chi F_{cl}\left(\frac{4\chi}{3\eta^2}\right)} = \frac{144}{55\pi\eta^4} \int_0^{\eta/2} \chi F(\eta, \chi) \mathrm{d}\chi. \tag{H.2.2}$$

An accurate fit for g_2 is parametrised as follows:

$$g_2(\eta) \approx [1 + (1 + 4.528\eta) \ln(1 + 12.29\eta) + 4.632\eta^2]^{-7/6} \tag{H.2.3}$$

The limits are $g_2 \approx 1$ for $\eta \ll 1$, and $g_2 \approx 0.167\eta^{-7/3}$ for $\eta \gg 1$.

For an electron beam with a Gaussian energy distribution colliding with a plane wave in the limits $\eta \ll 1$ and $\sigma \ll \langle\gamma\rangle$, i.e. the width is much smaller than the mean of the Gaussian, the evolution of the variance can be written as:

$$\left(\frac{\mathrm{d}\sigma^2}{\mathrm{d}t}\right)_{st} \approx \frac{\alpha b^2}{\bar{\lambda}_c} \left(\frac{55b}{24\sqrt{3}} \langle\gamma\rangle^4 - \frac{8}{3}\sigma^2 \langle\gamma\rangle\right). \tag{H.2.4}$$

Appendix I

Pair Production

I.1 Nonlinear Breit-Wheeler cross section

The probability of pair production by one photon of momentum l in interaction with n laser photons of momentum k per unit volume in unit time (circular polarisation) [109]:

$$P_{\gamma\gamma} = \frac{e^2 m_e^2}{16 l_0} \sum_{n>n_0}^{\infty} \int_1^{\nu} \frac{\mathrm{d}\nu}{\nu^{3/2}(1+\nu)^{1/2}} [2J_n^2(z) + \eta^2(2\nu-1)(J_{n+1}^2 + J_{n-1}^2 - 2J_n^2)], \quad \text{(I.1.1)}$$

with $\nu = (kl)^2/4(kq)(kq')$, $\nu_n = n/n_0$, $n_0 = 2m_*^2/(kl)$ and Bessel functions $J_n(z)$, where

$$z = 4m_e^2 \frac{\eta(1+\eta^2)^{1/2}}{(kl)} \left[\frac{\nu}{\nu_n}\left(1 - \frac{\nu}{\nu_n}\right)\right]^{1/2}. \quad \text{(I.1.2)}$$

Alternatively, in the high-field limit the rates can be related to the (quantum) synchrotron function (App. G), such that the differential probability rate is given by [173]

$$\boxed{\frac{\mathrm{d}W_{\pm}}{\mathrm{d}\eta_+} = \frac{\alpha}{\tau_C}\frac{mc^2}{\hbar\omega}\chi\frac{\mathrm{d}T(\chi)}{\mathrm{d}\eta_+},} \quad \text{(I.1.3)}$$

where $\tau_C = \hbar/mc^2 = 1.288 \times 10^{-6}\,\mathrm{fs}$ is the Compton time, χ is the quantum parameter and

$$\frac{\mathrm{d}T(\chi)}{\mathrm{d}\eta_+} = \frac{1}{2\sqrt{3}\pi\chi^2}\left[\left(\frac{2\chi}{\eta_+} - 1 + \frac{1}{2\chi/\eta_+ - 1}\right)K_{2/3}(\delta) - \int_{\delta}^{\infty} K_{1/3}(t)\mathrm{d}t\right], \quad \text{(I.1.4)}$$

with

$$\delta = \frac{4\chi}{3\eta_+^2}\left(\frac{2\chi}{\eta_+} - 1\right)^{-1}. \quad \text{(I.1.5)}$$

The total rate of the Breit-Wheeler pair production is obtained by integrating Equation

(I.1.3):

$$\boxed{W_{\pm} = \frac{\alpha}{\tau_C}\frac{mc^2}{\hbar\omega}\chi T(\chi),} \tag{I.1.6}$$

where $T(\chi)$ can analytically be approximated by [194]

$$T(\chi) \approx \frac{0.16}{\chi} K_{2/3}^2\left(\frac{2}{3\chi}\right), \tag{I.1.7}$$

or in two limits of χ by

$$T(\chi) = \begin{cases} \frac{3\sqrt{3}}{8\sqrt{2}}\exp\left(-\frac{4}{3\chi}\right) & \chi \ll 1, \\ 0.6\chi^{-1/3} & \chi \gg 1. \end{cases} \tag{I.1.8}$$

I.2 Bethe-Heitler Pair Production

The differential cross section of the Bethe-Heitler pair production process is given by crossing symmetry from bremsstrahlung (compare with Appendix E.1) [109]:

$$\begin{aligned}\frac{\mathrm{d}\sigma_{\gamma Z}}{\mathrm{d}\gamma_+} = \frac{\alpha Z^2 r_e^2 u_+ u_-}{\omega^3}\Bigg\{ &-\frac{4}{3} - 2\gamma_+\gamma_- c^2\frac{u_+^2+u_-^2}{u_+^2u_-^2} + c^3\left(\frac{\epsilon_-\gamma_+}{u_-^3} + \frac{\epsilon_+\gamma_-}{u_+^3} - \frac{\epsilon_-\epsilon_+^3}{u_-u_+c}\right) \\ &+ L\Bigg[\frac{8}{3}\frac{\gamma_+\gamma_-c^2}{u_+u_-} + \frac{(\hbar\omega)^2c^2}{m_e^2u_+^3u_-^3}(\gamma_+^2\gamma_-^2 + u_+^2u_-^2/c^4) \\ &- \frac{\hbar\omega}{2m_eu_+u_-}\left(\frac{\gamma_+\gamma_- - u_+^2/c^2}{u_+^3/c^3} + \frac{\gamma_+\gamma_- - u_-^2/c^2}{u_-^3/c^3} + \frac{2\hbar\omega\gamma_+\gamma_-c^2}{m_eu_+^2u_-^2}\right)\Bigg]\Bigg\},\end{aligned} \tag{I.2.1}$$

where

$$\begin{aligned}L &= \ln\left(\frac{\gamma_+\gamma_- + u_+u_-/c^2 - 1}{\hbar\omega/m_ec^2}\right), \\ \epsilon_\pm &= 2\ln(\gamma_\pm + u_\pm/c),\end{aligned}$$

where r_e denotes the electron radius, $u_\pm$ the momentum of the positron and electron, respectively, and α is the fine-structure constant. $\gamma_\pm$ is the energy of the electron and positron, and c is the speed of light.

Similarly as for bremsstrahlung (see Appendix E.3), the differential cross section can in the ultrarelativistic regime be approximated by a simplified equation in terms of the radiation length, X_0 (see Appendix D) [285, 375]:

$$\frac{\mathrm{d}\sigma_{\gamma Z}}{\mathrm{d}x} = \frac{A}{X_0N_A}\left[1 - \frac{4}{3}x(1-x)\right], \tag{I.2.2}$$

with $x = \epsilon/k$, where k is the incident photon energy and ϵ the energy of the produced electron or positron. A is the atomic weight and N_A the Avogadro constant. In the high-energy limit, the total cross section becomes

$$\sigma_{\gamma Z} = \frac{7}{9}\frac{A}{X_0N_A}, \tag{I.2.3}$$

which is accurate to within a few percent at 1 GeV and high-Z materials.

Appendix J

Linear correlation coefficient

The Pearson correlation coefficient, ρ, is a measure of the linear dependence of two variables. For two two random variables, A and B, and N data points is defined as [376]:

$$\boxed{\rho(A,B) = \frac{1}{N-1}\sum_{i=1}^{N}\left(\frac{A_i - \mu_A}{\sigma_A}\right)^*\left(\frac{B_i - \mu_B}{\sigma_B}\right),} \tag{J.0.1}$$

or alternatively in terms of the covariance

$$\rho(A,B) = \frac{\mathrm{cov}(A,B)}{\sigma_A \sigma_B}, \tag{J.0.2}$$

where μ denotes the mean and σ the standard deviation of the distribution. The correlation coefficient can take values in the interval $[-1,1]$, where negative values indicate a negative linear correlation and positive value a positive linear correlation. Values close to 1 or -1 imply a strong linear dependence, whereas small values close to zero suggest that there is no strong linear dependence between A and B.

Bibliography

[1] P. W. Higgs. *Broken symmetries and the masses of gauge bosons*. Physical Review Letters **13**, 508 (1964).

[2] F. Englert and R. Brout. *Broken symmetry and the mass of gauge vector mesons*. Physical Review Letters **13**, 321 (1964).

[3] G. S. Guralnik et al. *Global conservation laws and massless particles*. Physical Review Letters **13**, 585 (1964).

[4] G. Aad et al. *Observation of a new particle in the search for the Standard Model Higgs boson with the ATLAS detector at the LHC*. Physics Letters B **716**, 1 (2012).

[5] S. Chatrchyan et al. *Observation of a new boson at a mass of 125 GeV with the CMS experiment at the LHC*. Physics Letters B **716**, 30 (2012).

[6] T. Shears. *The Standard Model*. Philosophical Transactions of the Royal Society A: Mathematical, Physical and Engineering Sciences **370**, 805 (2012).

[7] D. A. Deacon et al. *First operation of a free-electron laser*. Physical Review Letters **38**, 892 (1977).

[8] P. Emma et al. *First lasing and operation of an ångstrom-wavelength free-electron laser*. nature photonics **4**, 641 (2010).

[9] D. Strickland and G. Mourou. *Compression of amplified chirped optical pulses*. Optics communications **55**, 447 (1985).

[10] C. N. Danson et al. *Petawatt and exawatt class lasers worldwide*. High Power Laser Science and Engineering **7**, (2019).

[11] G. Mourou. *Nobel Lecture: Extreme light physics and application*. Rev. Mod. Phys. **91**, 030501 (2019).

[12] M. Protopapas et al. *Atomic physics with super-high intensity lasers*. Rep. Prog. Phys. **60**, 389 (1997).

[13] K. Schafer et al. *Above threshold ionization beyond the high harmonic cutoff*. Phys. Rev. Lett. **70**, 1599 (1993).

[14] P. B. Corkum. *Plasma perspective on strong field multiphoton ionization*. Phys. Rev. Lett. **71**, 1994 (1993).

[15] R. Freeman et al. *Above-threshold ionization with subpicosecond laser pulses*. Phys. Rev. Lett. **59**, 1092 (1987).

[16] F. Calegari et al. *Ultrafast electron dynamics in phenylalanine initiated by attosecond pulses*. Science **346**, 336 (2014).

[17] W. Mori. *The physics of the nonlinear optics of plasmas at relativistic intensities for short-pulse lasers*. IEEE Journal of Quantum Electronics **33**, 1942 (1997).

[18] B. Albertazzi et al. *Laboratory formation of a scaled protostellar jet by coaligned poloidal magnetic field*. Science **346**, 325 (2014).

[19] S. P. D. Mangles et al. *Monoenergetic beams of relativistic electrons from intense laser-plasma interactions.* Nature **431**, 535 (2004).

[20] J. Faure et al. *A laser-plasma accelerator producing monoenergetic electron beams.* Nature **431**, 541 (2004).

[21] C. G. R. Geddes et al. *High-quality electron beams from a laser wakefield accelerator using plasma-channel guiding.* Nature **431**, 538 (2004).

[22] E. Esarey et al. *Physics of laser-driven plasma-based electron accelerators*. Reviews of Modern Physics **81**, 1229 (2009).

[23] V. I. Denisov et al. *Vacuum nonlinear electrodynamic polarization effects in hard emission of pulsars and magnetars*. J. Cosmol. Astropart. Phys. **09**, 004 (2017).

[24] R. P. Mignani et al. *Evidence for vacuum birefringence from the first optical-polarimetry measurement of the isolated neutron star RX J1856.5–3754*. Mon. Not. R. Astron. Soc. **465**, 492 (2017).

[25] F. Sauter. *Über das Verhalten eines Elektrons im homogenen elektrischen Feld nach der relativistischen Theorie Diracs*. Zeitschrift für Physik **69**, 742 (1931).

[26] W. Heisenberg and H. Euler. *Folgerungen aus der diracschen theorie des positrons*. Zeitschrift für Physik **98**, 714 (1936).

[27] J. Schwinger. *On gauge invariance and vacuum polarization*. Physical Review **82**, 664 (1951).

[28] E. Brézin and C. Itzykson. *Pair production in vacuum by an alternating field*. Physical Review D **2**, 1191 (1970).

[29] V. Popov. *Production of e+ e-Pairs in an Alternating External Field*. Soviet Journal of Experimental and Theoretical Physics Letters **13**, 195 (1971).

[30] W. Scandale. *Proton–Proton and Proton–Antiproton Colliders*. Reviews of Accelerator Science and Technology **7**, 9 (2014).

[31] F. Burkart et al. *LUXE-a QED Experiment at the European XFEL. 10th Int. Partile Accelerator Conf.(IPAC'19), Melbourne, Australia, 19-24 May 2019.* JACOW Publishing, Geneva, Switzerland. 2019, 1694.

[32] H. Abramowicz et al. *Letter of Intent for the LUXE Experiment*. arXiv preprint arXiv:1909.00860, (2019).

[33] M. Altarelli et al. *Summary of strong-field QED Workshop*. arXiv preprint ArXiv:1905.00059, (2019).

[34] M. Hogan. *Preliminary Conceptual Design Report for the FACET-II Project at SLAC National Accelerator Laboratory*, (2016).

[35] S. Gales et al. *The extreme light infrastructure – nuclear physics (ELI-NP) facility: New horizons in physics with 10 PW ultra-intense lasers and 20 MeV brilliant gamma beams*. Reports on Progress in Physics **81**, 094301 (2018).

[36] S. Weber et al. *P3: An installation for high-energy density plasma physics and ultra-high intensity laser–matter interaction at ELI-Beamlines*. Matter and Radiation at Extremes **2**, 149 (2018).

[37] J. Zou et al. *Design and current progress of the Apollon 10 PW project*. High Power Laser Science and Engineering **3**, (2015).

[38] R. Li et al. *Progress of the SULF 10 PW laser project. 1st AAPPS-DPP meeting.* 2017.

[39] B. Shen et al. *Exploring vacuum birefringence based on a 100 PW laser and an x-ray free electron laser beam*. Plasma Physics and Controlled Fusion **60**, 044002 (2018).

[40] *The light fantastic* (2018).

[41] C. Toth et al. *Transition of the bella PW laser system towards a collaborative research facility in laser plasma science*. *AIP Conference Proceedings*. **1812**. AIP Publishing. 2017, 110005.

[42] A. Bashinov et al. *New horizons for extreme light physics with mega-science project XCELS*. The European Physical Journal Special Topics **223**, 1105 (2014).

[43] A. Kessel et al. *Relativistic few-cycle pulses with high contrast from picosecond-pumped OPCPA*. Optica **5**, 434 (2018).

[44] *Introducing the Extreme Photonics Applications Centre (EPAC)* (2019).

[45] A. Maksimchuk et al. *Zettawatt-Equivalent Ultrashort Pulse Laser System (ZEUS) at the University of Michigan*. Bulletin of the American Physical Society, (2019).

[46] V. Yanovsky et al. *Ultra-high intensity- 300-TW laser at 0.1 Hz repetition rate.* Opt. Express **16**, 2109 (2008).

[47] A. Di Piazza et al. *Extremely high-intensity laser interactions with fundamental quantum systems*. Reviews of Modern Physics **84**, 1177 (2012).

[48] *The scale of the LHC* (2019).

[49] W. Panofsky. *Evolution of particle accelerators*. SLAC Beam Line **27**, 36 (1997).

[50] L. De Broglie. *Research on the theory of quanta*. *Annales de Physique*. **10**. 1925, 22.

[51] R.-L. Geng et al.
World record accelerating gradient achieved in a superconducting niobium RF cavity. *Proceedings of the 2005 Particle Accelerator Conference*. IEEE. 2005, 653.

[52] J. D. Jackson. *Classical Electrodynamics, 3rd ed.*
American Journal of Physics **67**, 841 (1999).

[53] M. Benedikt and F. Zimmermann. *Future circular colliders*.
Proc. Int. Sch. Phys. Fermi **194**, 73 (2016).

[54] *CLIC Conceptual Design Report No. CERN-2012-007*. Tech. rep. 2012.

[55] *ILC Technical Design Report Nos. CERN-ATS-2013-037*. Tech. rep. 2013.

[56] S. Lee et al. *Energy doubler for a linear collider*.
Phys. Rev. ST Accel. Beams **5**, 011001 (2002).

[57] J. M. Dawson. *Nonlinear electron oscillations in a cold plasma*.
Physical Review **113**, 383 (1959).

[58] A. Chao et al. *2001 Snowmass Accelerator R & D Report*. Tech. rep.
Fermi National Accelerator Lab.(FNAL), Batavia, IL (United States), 2001.

[59] G. Apollinari et al.
High-luminosity large hadron collider (HL-LHC): Preliminary design report.
Tech. rep.
Fermi National Accelerator Lab.(FNAL), Batavia, IL (United States), 2015.

[60] *Collider Reach (tool) Website* (2013).

[61] ATLAS-collaboration et al. *Physics at a High-Luminosity LHC with ATLAS*.
Tech. rep. ATL-COM-PHYS-2012-1118, 2012.

[62] D. d'Enterria and G. G. da Silveira. *Observing light-by-light scattering at the Large Hadron Collider*. Physical review letters **111**, 080405 (2013).

[63] M. Aaboud et al. *Evidence for light-by-light scattering in heavy-ion collisions with the ATLAS detector at the LHC*. Nature Physics **13**, 852 (2017).

[64] L. Beresford and J. Liu. *Search strategy for sleptons and dark matter using the LHC as a photon collider*. Physical Review Letters, (2019).

[65] S. Knapen et al. *Searching for axionlike particles with ultraperipheral heavy-ion collisions*. Physical review letters **118**, 171801 (2017).

[66] C. Baldenegro et al. *Searching for axion-like particles with proton tagging at the LHC*. Journal of High Energy Physics **2018**, 131 (2018).

[67] S. Boutet and G. J. Williams. *The coherent X-ray imaging (CXI) instrument at the Linac Coherent Light Source (LCLS)*.
New Journal of Physics **12**, 035024 (2010).

[68] P. Emma et al. *First lasing and operation of an ångstrom-wavelength free-electron laser*. nature photonics **4**, 641 (2010).

[69] K. Poder.
Characterisation of self-guided laser wakefield accelerators to multi-GeV energies.
PhD thesis. Imperial College London, 2016.

[70] P. Gibbon. *Short pulse laser interactions with matter*.
World Scientific Publishing Company Singapore, 2004.

[71] P. Sprangle et al. *Relativistic self-focusing of short-pulse radiation beams in plasmas*. IEEE transactions on plasma science **15**, 145 (1987).

[72] H. C. Kapteyn et al. *Prepulse energy suppression for high-energy ultrashort pulses using self-induced plasma shuttering*. Opt. Lett. **16**, 490 (1991).

[73] A. Pukhov and J. Meyer-ter-Vehn. *Laser wake field acceleration: the highly non-linear broken-wave regime*. Applied Physics B **74**, 355 (2002).

[74] I. Kostyukov et al. *Phenomenological theory of laser-plasma interaction in 'bubble' regime*. Physics of Plasmas **11**, 5256 (2004).

[75] J. Osterhoff et al. *Generation of Stable, Low-Divergence Electron Beams by Laser-Wakefield Acceleration in a Steady-State-Flow Gas Cell*.
Phys. Rev. Lett. **101**, 085002 (2008).

[76] A. J. Gonsalves et al. *Petawatt Laser Guiding and Electron Beam Acceleration to 8 GeV in a Laser-Heated Capillary Discharge Waveguide*.
Phys. Rev. Lett. **122**, 084801 (2019).

[77] O. Lundh et al. *Few femtosecond, few kiloampere electron bunch produced by a laser–plasma accelerator*. Nature Physics **7**, 219 (2011).

[78] R. Weingartner et al. *Ultralow emittance electron beams from a laser-wakefield accelerator*. Phys. Rev. ST Accel. Beams **15**, 111302 (2012).

[79] D. H. Whittum. *Electromagnetic instability of the ion-focused regime*.
Physics of Fluids B: Plasma Physics **4**, 730 (1992).

[80] S. Corde et al. *Femtosecond x rays from laser-plasma accelerators*.
Rev. Mod. Phys. **85**, 1 (2013).

[81] F. Albert and A. G. Thomas. *Applications of laser wakefield accelerator-based light sources*. Plasma Physics and Controlled Fusion **58**, 103001 (2016).

[82] J. Cole et al. *Tomography of human trabecular bone with a laser-wakefield driven x-ray source*. Plasma Physics and Controlled Fusion **58**, 014008 (2015).

[83] B. Kettle et al. *Single-Shot Multi-keV X-Ray Absorption Spectroscopy Using an Ultrashort Laser-Wakefield Accelerator Source*.
Physical Review Letters **123**, 254801 (2019).

[84] *The Astra Gemini Facility* (2019).

[85] S. Vinko et al. *Creation and diagnosis of a solid-density plasma with an X-ray free-electron laser*. Nature **482**, 59 (2012).

[86] R. Schoenlein et al. *New science opportunities enabled by LCLS-II x-ray lasers*.
SLAC Report-R-1053, (2015).

[87] D. Barber et al. *The HERA polarimeter and the first observation of electron spin polarization at HERA*.
Nuclear Instruments and Methods in Physics Research Section A: Accelerators, Spectrometers, Detectors and Associated Equipment **329**, 79 (1993).

[88] R. Alley et al. *A laser-based beam profile monitor for the SLC/SLD interaction region*.
Nuclear Instruments and Methods in Physics Research Section A: Accelerators, Spectrometers, Detectors and Associated Equipment **379**, 363 (1996).

[89] W. Leemans et al. *X-ray based subpicosecond electron bunch characterization using 90 Thomson scattering*. Physical review letters **77**, 4182 (1996).

[90] H. Sakai et al. *Measurement of an electron beam size with a laser wire beam profile monitor*.
Physical Review Special Topics-Accelerators and Beams **4**, 022801 (2001).

[91] H. Sakai et al. *Measurement of a small vertical emittance with a laser wire beam profile monitor*.
Physical Review Special Topics-Accelerators and Beams **5**, 122801 (2002).

[92] H. Sakai et al. *Performance studies of a laser wire beam profile monitor*.
Japanese journal of applied physics **41**, 6398 (2002).

[93] M. Baylac et al. *First electron beam polarization measurements with a Compton polarimeter at Jefferson Laboratory*. Physics Letters B **539**, 8 (2002).

[94] Y. Honda et al. *Upgraded laser wire beam profile monitor*.
Nuclear Instruments and Methods in Physics Research Section A: Accelerators, Spectrometers, Detectors and Associated Equipment **538**, 100 (2005).

[95] H. Utsunomiya et al. *Energy calibration of the NewSUBARU storage ring for laser Compton-scattering gamma rays and applications*.
IEEE Transactions on Nuclear Science **61**, 1252 (2014).

[96] T. Okugi et al. *Evaluation of extremely small horizontal emittance*.
Phys. Rev. ST Accel. Beams **2**, 022801 (1999).

[97] T. Nakano et al. *Multi-GeV laser-electron photon project at SPring-8*.
Nuclear Physics A **684**, 71 (2001).

[98] E. Esarey et al. *Nonlinear Thomson scattering of intense laser pulses from beams and plasmas*. Phys. Rev. E **48**, 3003 (1993).

[99] C. Bula et al. *Observation of nonlinear effects in Compton scattering*.
Physical Review Letters **76**, 3116 (1996).

[100] D. Burke et al. *Positron production in multiphoton light-by-light scattering*.
Physical Review Letters **79**, 1626 (1997).

[101] H. Hu et al. *Complete QED theory of multiphoton trident pair production in strong laser fields*. Physical review letters **105**, 080401 (2010).

[102] T. Blackburn. *Radiation reaction in electron–beam interactions with high-intensity lasers*. Reviews of Modern Plasma Physics **4**, 1 (2020).

[103] V. Yakimenko et al. *Prospect of Studying Nonperturbative QED with Beam-Beam Collisions*. Physical review letters **122**, 190404 (2019).

[104] T. G. Blackburn et al. *Reaching supercritical field strengths with intense lasers*.
New Journal of Physics **21**, 053040 (2019).

[105] C. Baumann et al. *Probing non-perturbative QED with electron-laser collisions*.
Scientific reports **9**, 9407 (2019).

[106] A. K. Harding. *The physics of gamma-ray bursts*. Phys. Rep. **206**, 327 (1991).

[107] D. A. Uzdensky and S. Rightley. *Plasma physics of extreme astrophysical environments*. Rep. Prog. Phys. **77**, 036902 (2014).

[108] R. D. Blandford and R. L. Znajek. *Electromagnetic extraction of energy from Kerr black holes*. Mon. Not. R. Astron. Soc. **179**, 433 (1977).

[109] R. Ruffini et al. *Electron–positron pairs in physics and astrophysics: from heavy nuclei to black holes*. Physics Reports **487**, 1 (2010).

[110] A. I. Nikishov. *Absorption of high-energy photons in the universe*.
Sov. Phys. JETP **14**, 393 (1962).

[111] A. Kandus et al. *Primordial magnetogenesis*. Phys. Rep. **505**, 1 (2011).

[112] D. Grasso and H. R. Rubinstein. *Magnetic fields in the early universe*. Phys. Rep. **348**, 163 (2001).

[113] K. Yokoya and P. Chen. *Beam-beam phenomena in linear colliders*. *Frontiers of Particle Beams: Intensity Limitations*. Springer, 1992, 415.

[114] J. Esberg et al. *Strong field processes in beam-beam interactions at the Compact Linear Collider*. Phys. Rev. ST Accel. Beams **17**, 051003 (2014).

[115] T. Grismayer et al. *Seeded QED cascades in counterpropagating laser pulses*. Physical Review E **95**, 023210 (2017).

[116] C. P. Ridgers et al. *Dense Electron-Positron Plasmas and Ultraintense γ rays from Laser-Irradiated Solids*. Phys. Rev. Lett. **108**, 165006 (2012).

[117] E. Nerush et al. *Laser field absorption in self-generated electron-positron pair plasma*. Physical review letters **106**, 035001 (2011).

[118] *Plasma: at the frontier of scientific discovery – Report of the Panel on Frontiers of Plasma Science* (2015).

[119] E. National Academies of Sciences, Medicine, et al. *Opportunities in Intense Ultrafast Lasers: Reaching for the Brightest Light*. National Academies Press, 2018.

[120] W. Yan et al. *High-order multiphoton Thomson scattering*. Nature Photonics **11**, 514 (2017).

[121] K. Ta Phuoc et al. *All-optical Compton gamma-ray source*. Nature Photonics **6**, 308 (2012).

[122] S. Chen et al. *MeV-energy X rays from inverse compton scattering with laser-wakefield accelerated electrons*. Physical Review Letters **110**, 1 (2013).

[123] N. D. Powers et al. *Quasi-monoenergetic and tunable X-rays from a laser-driven Compton light source*. Nature Photonics **8**, 28 (2014).

[124] G. Sarri et al. *Ultrahigh brilliance multi-MeV γ-ray beams from nonlinear relativistic Thomson scattering*. Physical review letters **113**, 224801 (2014).

[125] K. Khrennikov et al. *Tunable All-Optical Quasimonochromatic Thomson X-Ray Source in the Nonlinear Regime*. Physical Review Letters **114**, 1 (2015).

[126] F. Mackenroth and A. Di Piazza. *Nonlinear Double Compton Scattering in the Ultrarelativistic Quantum Regime*. Phys. Rev. Lett. **110**, 070402 (2013).

[127] S. V. Bulanov et al. *Lorentz-Abraham-Dirac versus Landau-Lifshitz radiation friction force in the ultrarelativistic electron interaction with electromagnetic wave (exact solutions)*. Phys. Rev. E **84**, 056605 (2011).

[128] L. D. Landau and E. M. Lifshitz. *The Classical Theory of Fields*. Butterworth-Heinemann, 1975.

[129] W. Baylis and J. Huschilt. *Energy balance with the Landau–Lifshitz equation*. Physics Letters A **301**, 7 (2002).

[130] T. G. Blackburn et al. *Quantum Radiation Reaction in Laser–Electron-Beam Collisions*. Phys. Rev. Lett. **112**, 015001 (2014).

[131] V. Ritus. *Quantum effects of the interaction of elementary particles with an intense electromagnetic field*. Journal of Russian Laser Research **6**, 497 (1985).

[132] C. Ridgers et al. *Signatures of quantum effects on radiation reaction in laser–electron-beam collisions*. Journal of Plasma Physics **83**, (2017).

[133] A. G. R. Thomas et al. *Strong Radiation-Damping Effects in a Gamma-Ray Source Generated by the Interaction of a High-Intensity Laser with a Wakefield-Accelerated Electron Beam*. Phys. Rev. X **2**, 041004 (2012).

[134] M. Vranic et al. *All-Optical Radiation Reaction at* $[10^{21}]Wcm^2$. Phys. Rev. Lett. **113**, 134801 (2014).

[135] V. Dinu et al. *Quantum Radiation Reaction: From Interference to Incoherence*. Phys. Rev. Lett. **116**, 044801 (2016).

[136] C. S. Shen and D. White. *Energy Straggling and Radiation Reaction for Magnetic Bremsstrahlung*. Phys. Rev. Lett. **28**, 455 (1972).

[137] C. N. Harvey et al. *Quantum Quenching of Radiation Losses in Short Laser Pulses*. Phys. Rev. Lett. **118**, 105004 (2017).

[138] D. Del Sorbo et al. *Spin polarization of electrons by ultraintense lasers*. Phys. Rev. A **96**, 043407 (2017).

[139] D. Seipt et al. *Theory of Radiative Electron Polarization in Strong Laser Fields*. Physical Review A **98**, 23417 (2018).

[140] Y. Li et al. *Ultrarelativistic electron-beam polarization in single-shot interaction with an ultraintense laser pulse*. Phys. Rev. Lett. **122**, 154801 (2019).

[141] T. G. Blackburn et al. *Scaling laws for positron production in laser–electron-beam collisions*. Phys. Rev. A **96**, 022128 (2017).

[142] A. Di Piazza et al. *Investigation of classical radiation reaction with aligned crystals*. Physics Letters B **765**, 1 (2017).

[143] X. Artru and M. Chevallier. *Channeling radiation: Theory, semi-classical simulations*. Radiation Effects and Defects in Solids **130**, 415 (1994).

[144] V. Katkov, V. M. Strakhovenko, et al.
Electromagnetic processes at high energies in oriented single crystals.
World Scientific, 1998.

[145] T. N. Wistisen et al. *Experimental evidence of quantum radiation reaction in aligned crystals*. Nature communications **9**, 795 (2018).

[146] T. N. Wistisen et al. *Quantum radiation reaction in aligned crystals beyond the local constant field approximation*. Phys. Rev. Research **1**, 033014 (2019).

[147] S. S. Bulanov et al. *Electromagnetic cascade in high-energy electron, positron, and photon interactions with intense laser pulses*. Phys. Rev. A **87**, 062110 (2013).

[148] I. V. Sokolov et al. *Pair Creation in QED-Strong Pulsed Laser Fields Interacting with Electron Beams*. Phys. Rev. Lett. **105**, 195005 (2010).

[149] O. Pike et al. *A photon–photon collider in a vacuum hohlraum*.
Nature Photonics **8**, 434 (2014).

[150] I. Drebot et al. *Matter from light-light scattering via Breit-Wheeler events produced by two interacting Compton sources*.
Physical Review Accelerators and Beams **20**, 043402 (2017).

[151] A. Di Piazza. *Nonlinear Breit-Wheeler Pair Production in a Tightly Focused Laser Beam*. Phys. Rev. Lett. **117**, 213201 (2016).

[152] B. King and N. Elkina. *Vacuum birefringence in high-energy laser-electron collisions*. Phys. Rev. A **94**, 062102 (2016).

[153] Y. Nakamiya and K. Homma. *Probing vacuum birefringence under a high-intensity laser field with gamma-ray polarimetry at the GeV scale*.
Phys. Rev. D **96**, 053002 (2017).

[154] S. Bragin et al. *High-Energy Vacuum Birefringence and Dichroism in an Ultrastrong Laser Field*. Phys. Rev. Lett. **119**, 250403 (2017).

[155] S. Meuren et al. *High-Energy Recollision Processes of Laser-Generated Electron-Positron Pairs*. Phys. Rev. Lett. **114**, 143201 (2015).

[156] M. Y. Kuchiev. *Production of High-Energy Particles in Laser and Coulomb Fields and the e+ e- Antenna*. Phys. Rev. Lett. **99**, 130404 (2007).

[157] V. Ritus. *Radiative corrections in quantum electrodynamics with intense field and their analytical properties*. Annals of Physics **69**, 555 (1972).

[158] N. Narozhny. *Expansion parameter of perturbation theory in intense-field quantum electrodynamics*. Physical Review D **21**, 1176 (1980).

[159] A. Fedotov. *Conjecture of perturbative QED breakdown at* $\alpha\chi^{2/3} \geq 1$.
Journal of Physics: Conference Series. **826**. IOP Publishing. 2017, 012027.

[160] A. Ilderton. *Note on the conjectured breakdown of QED perturbation theory in strong fields*. Phys. Rev. D **99**, 085002 (2019).

[161] A. G. R. Thomas. *Studies of laser propagation and mono-energetic electron beam injection in laser-wakefield accelerators*.
PhD thesis. Imperial College London (University of London), 2007.

[162] J. Cole et al. *Experimental evidence of radiation reaction in the collision of a high-intensity laser pulse with a laser-wakefield accelerated electron beam*.
Physical Review X **8**, 011020 (2018).

[163] K. Poder et al. *Experimental signatures of the quantum nature of radiation reaction in the field of an ultraintense laser*. Physical Review X **8**, 031004 (2018).

[164] M. E. Peskin and D. V. Schroeder. *An introduction to quantum field theory*.
CRC Press, 2018.

[165] W. Furry. *On bound states and scattering in positron theory*.
Physical Review **81**, 115 (1951).

[166] D. Wolkow. *Über eine klasse von lösungen der diracschen gleichung*.
Zeitschrift für Physik **94**, 250 (1935).

[167] D. Seipt. *Strong-Field QED Processes in Short Laser Pulses*.
PhD thesis. Technische Universitaet Dresden, 2012.

[168] A. H. Compton. *A quantum theory of the scattering of X-rays by light elements*.
Physical review **21**, 483 (1923).

[169] O. Klein and Y. Nishina. *Über die Streuung von Strahlung durch freie Elektronen nach der neuen relativistischen Quantendynamik von Dirac*.
Zeitschrift für Physik **52**, 853 (1929).

[170] J. J. Thomson. *Conduction of electricity through gases*.
Cambridge University Press, 1906.

[171] J. Krämer et al. *Making spectral shape measurements in inverse Compton scattering a tool for advanced diagnostic applications*.
Scientific reports **8**, 1398 (2018).

[172] T. G. Blackburn et al. *Model-independent inference of laser intensity*.
Phys. Rev. Accel. Beams **(accepted)**, (2020).

[173] T. G. Blackburn. *QED effects in laser-plasma interactions*.
PhD thesis. Oxford University, UK, 2015.

[174] A. Di Piazza et al. *Quantum Radiation Reaction Effects in Multiphoton Compton Scattering*. Phys. Rev. Lett. **105**, 220403 (2010).

[175] S. S. Bulanov et al. *Multiple Colliding Electromagnetic Pulses: A Way to Lower the Threshold of e^+e^- Pair Production from Vacuum*.
Phys. Rev. Lett. **104**, 220404 (2010).

[176] D. A. Burton and A. Noble. *Aspects of electromagnetic radiation reaction in strong fields*. Contemporary Physics **55**, 110 (2014).

[177] S. V. Bulanov et al. *Lorentz-Abraham-Dirac versus Landau-Lifshitz radiation friction force in the ultrarelativistic electron interaction with electromagnetic wave (exact solutions)*. Phys. Rev. E **84**, 056605 (2011).

[178] H. Spohn. *The critical manifold of the Lorentz-Dirac equation*.
EPL (Europhysics Letters) **50**, 287 (2000).

[179] C. Arran et al. *Optimal parameters for radiation reaction experiments*.
Plasma Physics and Controlled Fusion **61**, 074009 (2019).

[180] C. Arran et al. *Potential to measure quantum effects in recent all-optical radiation reaction experiments*. Proc. SPIE **11039**, (2019).

[181] V. Baier et al. *Quasiclassical theory of radiation and pair creation in crystals at high energy*. Radiation Effects and Defects in Solids **122**, 527 (1991).

[182] F. Niel et al. *From quantum to classical modeling of radiation reaction: A focus on stochasticity effects*. Phys. Rev. E **97**, 043209 (2018).

[183] P. A. Dirac. *On the annihilation of electrons and protons*.
Mathematical Proceedings of the Cambridge Philosophical Society. **26**.
Cambridge University Press. 1930, 361.

[184] G. Breit and J. A. Wheeler. *Collision of two light quanta*.
Physical Review **46**, 1087 (1934).

[185] H. Bethe and W. Heitler. *On the stopping of fast particles and on the creation of positive electrons*. Proceedings of the Royal Society of London. Series A, Containing Papers of a Mathematical and Physical Character **146**, 83 (1934).

[186] P. A. M. Dirac. *Quantised singularities in the electromagnetic field*.
Proceedings of the Royal Society of London. Series A, Containing Papers of a Mathematical and Physical Character **133**, 60 (1931).

[187] O. Klemperer. *On the annihilation radiation of the positron*.
Mathematical Proceedings of the Cambridge Philosophical Society. **30**.
Cambridge University Press. 1934, 347.

[188] C. D. Anderson. *Energies of cosmic-ray particles*. Physical Review **41**, 405 (1932).

[189] C. D. Anderson. *The positive electron*. Physical Review **43**, 491 (1933).

[190] D. L. Bailey et al. *Positron emission tomography*. Springer, 2005.

[191] R. J. Gould and G. P. Schréder. *Pair production in photon-photon collisions*. Physical Review **155**, 1404 (1967).

[192] X. Ribeyre et al. *Electron–positron pairs beaming in the Breit–Wheeler process*. Plasma Physics and Controlled Fusion **59**, 014024 (2016).

[193] X. Ribeyre et al. *Effect of differential cross section in Breit–Wheeler pair production*. Plasma Physics and Controlled Fusion **60**, 104001 (2018).

[194] T. Erber. *High-energy electromagnetic conversion processes in intense magnetic fields*. Reviews of Modern Physics **38**, 626 (1966).

[195] H. Bethe and L. Maximon. *Theory of bremsstrahlung and pair production. I. Differential cross section*. Physical Review **93**, 768 (1954).

[196] H. Davies et al. *Theory of bremsstrahlung and pair production. II. Integral cross section for pair production*. Physical Review **93**, 788 (1954).

[197] W. Kruer. *The physics of laser plasma interactions*. CRC Press, 2018.

[198] I. H. Hutchinson. *Principles of plasma diagnostics*. Plasma Physics and Controlled Fusion **44**, 2603 (2002).

[199] L. V. Keldysh. *Ionization in the field of a strong electromagnetic wave*. Soviet Physics JETP **20**, 1307 (1965).

[200] Z. Z. Latypov et al. *Ionizing Collisions of Electrons with Ions and Atoms*. Sov. Phys. JETP **19**, (1964).

[201] A. M. Perelomov et al. *Ionization of atoms in an alternating electrical field*. Sov. Phys. JETP **23**, 924 (1966).

[202] H. R. Reiss. *Semiclassical electrodynamics of bound systems in intense fields*. Physical Review A **1**, (1970).

[203] C. McGuffey et al. *Ionization Induced Trapping in a Laser Wakefield Accelerator*. Phys. Rev. Lett. **104**, 025004 (2010).

[204] A. Pak et al. *Injection and Trapping of Tunnel-Ionized Electrons into Laser-Produced Wakes*. Phys. Rev. Lett. **104**, 025003 (2010).

[205] J. M. Cole. *Diagnosis and application of laser wakefield accelerators*. PhD thesis. Imperial College London, 2015.

[206] R. Wagner et al. *Electron acceleration by a laser wakefield in a relativistically self-guided channel*. Physical Review Letters **78**, 3125 (1997).

[207] A. Thomas et al. *Effect of laser-focusing conditions on propagation and monoenergetic electron production in laser-wakefield accelerators*. Physical review letters **98**, 095004 (2007).

[208] E. Esarey et al. *Optically guided laser wake-field acceleration*.
Physics of Fluids B: Plasma Physics **5**, 2690 (1993).

[209] J. Mendonça and L. O. e Silva. *Regular and stochastic acceleration of photons*.
Physical Review E **49**, 3520 (1994).

[210] J. T. Mendonça. *Theory of photon acceleration*. CRC Press, 2000.

[211] C. Murphy et al. *Evidence of photon acceleration by laser wake fields*.
Physics of Plasmas **13**, 033108 (2006).

[212] C. B. Schroeder et al. *GeV electron beams from a centimetre-scale accelerator*.
Nature Physics **2**, 696 (2006).

[213] W. P. Leemans et al. *Multi-GeV Electron Beams from Capillary-Discharge-Guided Subpetawatt Laser Pulses in the Self-Trapping Regime*.
Phys. Rev. Lett. **113**, 245002 (2014).

[214] S. Steinke et al. *Multistage coupling of independent laser-plasma accelerators*.
Nature, (2016).

[215] H. T. Kim et al. *Enhancement of Electron Energy to the Multi-GeV Regime by a Dual-Stage Laser-Wakefield Accelerator Pumped by Petawatt Laser Pulses*.
Phys. Rev. Lett. **111**, 165002 (2013).

[216] S. P. D. Mangles. *An Overview of Recent Progress in Laser Wakefield Acceleration Experiments*. CERN Proceedings **001**, 23 (2016).

[217] A. Akhiezcr and R. Polovin. *On the theory of wave motions of relativistic plasma*.
JETP **3**, 696 (1956).

[218] J. C. Wood.
Betatron radiation from laser wakefield accelerators and its applications.
PhD thesis. Imperial College London, 2016.

[219] A. G. R. Thomas. *Scalings for radiation from plasma bubbles*.
Physics of Plasmas **17**, 056708 (2010).

[220] S. P. Mangles et al. *Self-injection threshold in self-guided laser wakefield accelerators*.
Physical Review Special Topics-Accelerators and Beams **15**, 011302 (2012).

[221] C. Decker et al. *The evolution of ultra-intense, short-pulse lasers in underdense plasmas*. Physics of Plasmas **3**, 2047 (1996).

[222] W. Lu et al. *Generating multi-GeV electron bunches using single stage laser wakefield acceleration in a 3D nonlinear regime*.
Physical Review Special Topics - Accelerators and Beams **10**, 061301 (2007).

[223] E. Guillaume et al. *Electron Rephasing in a Laser-Wakefield Accelerator*. Phys. Rev. Lett. **115**, 155002 (2015).

[224] A. Debus et al. *Circumventing the Dephasing and Depletion Limits of Laser-Wakefield Acceleration*. Phys. Rev. X **9**, 031044 (2019).

[225] W. Lu. *Nonlinear plasma wakefield theory and optimum scaling for laser wakefield acceleration in the blowout regime*. PhD thesis. University of California, 2006.

[226] J. Faure et al. *Controlled injection and acceleration of electrons in plasma wakefields by colliding laser pulses*. Nature **444**, 737 (2006).

[227] C. G. R. Geddes et al. *Plasma-Density-Gradient Injection of Low Absolute-Momentum-Spread Electron Bunches*. Physical Review Letters **100**, 215004 (2008).

[228] A. Buck et al. *Shock-Front Injector for High-Quality Laser-Plasma Acceleration*. Phys. Rev. Lett. **110**, 185006 (2013).

[229] A. Deng et al. *Generation and acceleration of electron bunches from a plasma photocathode*. Nature Physics, 1 (2019).

[230] K. Schmid et al. *Density-transition based electron injector for laser driven wakefield accelerators*. Phys. Rev. ST Accel. Beams **13**, 091301 (2010).

[231] S. Bulanov et al. *Particle injection into the wave acceleration phase due to nonlinear wake wave breaking*. Physical Review E **58**, R5257 (1998).

[232] M. C. Downer et al. *Diagnostics for plasma-based electron accelerators*. Rev. Mod. Phys. **90**, 035002 (2018).

[233] C. Hooker et al. *The Astra Gemini project–A dual-beam petawatt Ti: Sapphire laser system*. *Journal de Physique IV (Proceedings)*. **133**. EDP sciences. 2006, 673.

[234] C. J. Hooker et al. *Commissioning the Astra Gemini petawatt Ti: sapphire laser system*. *Conference on Lasers and Electro-Optics*. Optical Society of America. 2008.

[235] R. Trebino. *Frequency-resolved optical gating: the measurement of ultrashort laser pulses*. Springer Science & Business Media, 2012.

[236] M. Streeter. *Ultrafast dynamics of relativistic laser plasma interactions*. PhD thesis. Imperial College London, 2013.

[237] C. Gregory et al. *Optimisation of the f/2 Gemini focal spot using full beam adaptive optics*. Tech. rep. 2015.

[238] Y. Kato et al. *Random Phasing of High-Power Lasers for Uniform Target Acceleration and Plasma-Instability Suppression*. Phys. Rev. Lett. **53**, 1057 (1984).

[239] D. J. Corvan et al. *Optical measurement of the temporal delay between two ultra-short and focussed laser pluses*. Opt. Express **24**, 3127 (2016).

[240] *"Index of Refraction of Air,"in the Engineering Metrology Toolbox of the National Institute of Standards and Technology (NIST)* (2011).

[241] D. Carroll and C. D. Murphy. *Measurement of the difference in the Gemini gate valve windows thickness by its effect on timing between the North and South beams*, (2013).

[242] I. Malitson. *Interspecimen comparison of the refractive index of fused silica*. Josa **55**, 1205 (1965).

[243] R. Shalloo et al. *Measurement of femtosecond-scale drift and jitter of the delay between the North and South Beams of Gemini*, (2016).

[244] S. C. Wilks et al. *Energetic proton generation in ultra-intense laser-solid interactions*. Physics of Plasmas **8**, 542 (2001).

[245] a. Maksimchuk et al. *Forward ion acceleration in thin films driven by a high-intensity laser*. Physical review letters **84**, 4108 (2000).

[246] J. Edwards et al. *Measurement and analysis of radiation transport in laser-irradiated targets*. EPL (Europhysics Letters) **11**, 631 (1990).

[247] S. Semushin and V. Malka. *High density gas jet nozzle design for laser target production*. Review of Scientific Instruments **72**, 2961 (2001).

[248] D. J. Spence and S. M. Hooker. *Investigation of a hydrogen plasma waveguide*. Physical Review E - Statistical, Nonlinear, and Soft Matter Physics **63**, 1 (2001).

[249] S. W. Jolly et al. *Stereolithography based method of creating custom gas density profile targets for high intensity laser-plasma experiments*. Review of Scientific Instruments **83**, 073503 (2012).

[250] M. Vargas et al. *Improvements to laser wakefield accelerated electron beam stability, divergence, and energy spread using three-dimensional printed two-stage gas cell targets*. Applied Physics Letters **104**, (2014).

[251] S. Kneip et al. *Near-GeV acceleration of electrons by a nonlinear plasma wave driven by a self-guided laser pulse*. Physical review letters **103**, 035002 (2009).

[252] F. G. Desforges et al. *Reproducibility of electron beams from laser wakefield acceleration in capillary tubes*. Nuclear Instruments and Methods in Physics Research Section A: Accelerators, Spectrometers, Detectors and Associated Equipment **740**, 54 (2014).

[253] M. C. Kaluza. *Ultrafast Plasma Imaging*.
Laser-Driven Sources of High Energy Particles and Radiation. Springer, 2019, 165.

[254] R. Bracewell. *The Fourier Transform and its Applications*. McGraw-Hill, 1978.

[255] S. P. D. Mangles.
Measurements of relativistic electrons from intense laser-plasma interactions.
PhD thesis. Imperial College London (University of London), 2005.

[256] C. E. Clayton et al. *Self-Guided Laser Wakefield Acceleration beyond 1 GeV Using Ionization-Induced Injection*. Phys. Rev. Lett. **105**, 105003 (2010).

[257] A. A. Soloviev et al. *Two-screen single-shot electron spectrometer for laser wakefield accelerated electron beams*. Review of Scientific Instruments **82**, (2011).

[258] E. Frlež et al. *Cosmic muon tomography of pure cesium iodide calorimeter crystals*.
Nuclear Instruments and Methods in Physics Research Section A: Accelerators, Spectrometers, Detectors and Associated Equipment **440**, 57 (2000).

[259] J. B. Birks. *The theory and practice of scintillation counting: International series of monographs in electronics and instrumentation*. Vol. 27. Elsevier, 2013.

[260] O. Har-Shemesh and A. D. Piazza. *Peak intensity measurement of relativistic lasers via nonlinear Thomson scattering*. Opt. Lett. **37**, 1352 (2012).

[261] *Cesium Iodide Scintillation Material (CsI(Tl) and CsI(Na) Datasheet)* (2017).

[262] S. Agostinelli et al. *GEANT4: a simulation toolkit*.
Nuclear instruments and methods in physics research section A: Accelerators, Spectrometers, Detectors and Associated Equipment **506**, 250 (2003).

[263] K. T. Behm et al. *A spectrometer for ultrashort gamma-ray pulses with photon energies greater than 10 MeV*. Review of Scientific Instruments **89**, 113303 (2018).

[264] L. Lisi et al. *Spectral Analysis of 50–100 MeV Thomson Backscatter Gamma-rays from GeV Laser-Plasma Accelerator*.
2018 IEEE Advanced Accelerator Concepts Workshop (AAC). IEEE. 2018, 1.

[265] K. Chouffani et al. *Determination of electron beam parameters by means of laser-Compton scattering*. Phys. Rev. ST Accel. Beams **9**, 050701 (2006).

[266] G. Weber et al. *Compton polarimetry using double-sided segmented x-ray detectors*.
Journal of Physics: Conference Series **583**, (2015).

[267] S. Banerjee et al. *Compact source of narrowband and tunable X-rays for radiography*. Nuclear Instruments and Methods in Physics Research Section B: Beam Interactions with Materials and Atoms **350**, 106 (2015).

[268] J. C. Wood et al. *Ultrafast imaging of laser driven shock waves using betatron x-rays from a laser wakefield accelerator*. Scientific reports **8**, 11010 (2018).

[269] A. Jochmann et al. *High resolution energy-angle correlation measurement of hard x rays from laser-Thomson backscattering*.
Physical review letters **111**, 114803 (2013).

[270] G. Golovin et al. *Intrinsic beam emittance of laser-accelerated electrons measured by x-ray spectroscopic imaging*. Scientific reports **6**, 24622 (2016).

[271] *Kevlar Aramid Fiber: Technical Guide* (2019).

[272] C. Møller. *Zur theorie des durchgangs schneller elektronen durch materie*.
Annalen der Physik **406**, 531 (1932).

[273] H. A. Bethe. *Moliere's theory of multiple scattering*.
Physical review **89**, 1256 (1953).

[274] Y. Glinec et al. *High-Resolution γ-Ray Radiography Produced by a Laser-Plasma Driven Electron Source*. Phys. Rev. Lett. **94**, 025003 (2005).

[275] K. K. Swanson et al. *Control of tunable, monoenergetic laser-plasma-accelerated electron beams using a shock-induced density downramp injector*.
Phys. Rev. Accel. Beams **20**, 051301 (2017).

[276] H.-E. Tsai et al. *Control of quasi-monoenergetic electron beams from laser-plasma accelerators with adjustable shock density profile*.
Physics of Plasmas **25**, 043107 (2018).

[277] J. Kirschner et al. *Adaptive and Safe Bayesian Optimization in High Dimensions via One-Dimensional Subspaces*. arXiv preprint arXiv:1902.03229, (2019).

[278] A. Edelen et al. *Opportunities in Machine Learning for Particle Accelerators*.
arXiv preprint arXiv:1811.03172, (2018).

[279] C. Emma et al. *Machine learning-based longitudinal phase space prediction of particle accelerators*. Phys. Rev. Accel. Beams **21**, 112802 (2018).

[280] M. Streeter et al. *Temporal feedback control of high-intensity laser pulses to optimize ultrafast heating of atomic clusters*.
Applied Physics Letters **112**, 244101 (2018).

[281] M. Galletti et al. *An ultra short pulse reconstruction software applied to the GEMINI high power laser system*.
Nuclear Instruments and Methods in Physics Research Section A: Accelerators, Spectrometers, Detectors and Associated Equipment **829**, 442 (2016).

[282] S. Kneip et al. *Bright spatially coherent synchrotron X-rays from a table-top source*.
Nature Physics **6**, 980 (2010).

[283] L. M. Chen et al. *Bright betatron X-ray radiation from a laser-driven-clustering gas target*. Scientific Reports **3**, (2013).

[284] Y. Glinec et al. *Absolute calibration for a broad range single shot electron spectrometer*. Review of scientific instruments **77**, 103301 (2006).

[285] M. Tanabashi et al. *Review of particle physics*.
Physical Review D **98**, 030001 (2018).

[286] D. J. Corvan et al. *Design of a compact spectrometer for high-flux MeV gamma-ray beams*. Review of Scientific Instruments **85**, 065119 (2014).

[287] M. Babzien et al. *Observation of the Second Harmonic in Thomson Scattering from Relativistic Electrons*. Phys. Rev. Lett. **96**, 054802 (2006).

[288] Y. Y. Lau et al. *Nonlinear Thomson scattering: A tutorial*.
Physics of Plasmas **10**, 2155 (2003).

[289] E. Sarachik and G. Schappert. *Classical theory of the scattering of intense laser radiation by free electrons*. Physical Review D **1**, 2738 (1970).

[290] J. Koga et al. *Nonlinear Thomson scattering in the strong radiation damping regime*. Physics of plasmas **12**, 093106 (2005).

[291] F. E. Carroll. *Tunable monochromatic X rays: a new paradigm in medicine*.
American Journal of Roentgenology **179**, 583 (2002).

[292] V. T. DeVita et al.
DeVita, Hellman, and Rosenberg's cancer: principles & practice of oncology. Vol. 2.
Lippincott Williams & Wilkins, 2008.

[293] P. Oliva et al. *Quantitative evaluation of single-shot inline phase contrast imaging using an inverse compton x-ray source*. Applied Physics Letters **97**, 134104 (2010).

[294] G. Baldwin and G. Klaiber. *X-ray yield curves for γ- n reactions*.
Physical Review **73**, 1156 (1948).

[295] A. Bosco et al. *A two-dimensional laser-wire scanner for electron accelerators*.
Nuclear Instruments and Methods in Physics Research Section A: Accelerators, Spectrometers, Detectors and Associated Equipment **592**, 162 (2008).

[296] C. Liu et al. *Generation of 9 MeV γ-rays by all-laser-driven Compton scattering with second-harmonic laser light*. Optics letters **39**, 4132 (2014).

[297] J. Shaw et al. *Bright 5-85 MeV Compton gamma-ray pulses from GeV laser-plasma accelerator and plasma mirror*.
arXiv preprint arXiv:1705.08637, (2017).

[298] A. R. Bell and J. G. Kirk. *Possibility of Prolific Pair Production with High-Power Lasers*. Phys. Rev. Lett. **101**, 200403 (2008).

[299] H.-E. Tsai et al. *Compact tunable Compton x-ray source from laser-plasma accelerator and plasma mirror*. Physics of Plasmas **22**, 023106 (2015).

[300] C. Yu et al. *Ultrahigh brilliance quasi-monochromatic MeV γ-rays based on self-synchronized all-optical Compton scattering*. Scientific reports **6**, 29518 (2016).

[301] B. A. Shadwick et al. *Nonlinear laser energy depletion in laser-plasma accelerators*. Physics of Plasmas **16**, 056704 (2009).

[302] G. M. Samarin et al. *Radiation reaction studies in an all-optical set-up: experimental limitations*. Journal of Modern Optics **65**, 1362 (2017).

[303] C. Harvey et al. *Focusing effects in laser-electron Thomson scattering*. Phys. Rev. Accel. Beams **19**, 094701 (2016).

[304] W. Leemans et al. *BELLA laser and operations*. Proc. of PAC2013, THYAA11097 (2013).

[305] A. A. Sokolov and I. M. Ternov. *On Polarization and Spin Effects in the Theory of Synchrotron Radiation*. Soviet Physics Doklady **8**, 1203 (1964).

[306] V. Baier and V. Katkov. *Radiational polarization of electrons in inhomogeneous magnetic field*. Physics Letters A **24**, 327 (1967).

[307] S. H. Glenzer and R. Redmer. *X-ray Thomson scattering in high energy density plasmas*. Reviews of Modern Physics **81**, 1625 (2009).

[308] S. Prunty. *A primer on the theory of Thomson scattering for high-temperature fusion plasmas*. Physica Scripta **89**, 128001 (2014).

[309] A. Schropp et al. *Imaging shock waves in diamond with both high temporal and spatial resolution at an XFEL*. Scientific reports **5**, 11089 (2015).

[310] M. Harmand et al. *X-ray absorption spectroscopy of iron at multimegabar pressures in laser shock experiments*. Physical Review B **92**, 024108 (2015).

[311] S. V. Bulanov et al. *Transverse-Wake Wave Breaking*. Phys. Rev. Lett. **78**, 4205 (1997).

[312] M. Burza et al. *Laser wakefield acceleration using wire produced double density ramps*. Physical Review Special Topics - Accelerators and Beams **16**, 11301 (2013).

[313] M. Mirzaie et al. *Demonstration of self-truncated ionization injection for GeV electron beams*. Scientific reports **5**, 14659 (2015).

[314] C. D. Baird et al. *Realising single-shot measurements of quantum radiation reaction in high-intensity lasers*. New Journal of Physics **21**, 053030 (2019).

[315] A. Di Piazza et al. *Implementing nonlinear Compton scattering beyond the local-constant-field approximation*. Phys. Rev. A **98**, 012134 (2018).

[316] S. Bonometto and M. Rees. *On possible observable effects of electron pair production in QSOs*. Monthly Notices of the Royal Astronomical Society **152**, 21 (1971).

[317] A. Ilderton. *Trident Pair Production in Strong Laser Pulses*. Phys. Rev. Lett. **106**, 020404 (2011).

[318] K. Piotrzkowski. *Tagging two-photon production at the CERN Large Hadron Collider*. Physical Review D **63**, 071502 (2001).

[319] G. Abbiendi, O. collaboration, et al. *Total hadronic cross-section of photon-photon interactions at LEP*. The European Physical Journal C-Particles and Fields **14**, 199 (2000).

[320] *Fundamental Feynman diagrams and their experimental validation* (2014).

[321] W. Heitler. *The quantum theory of radiation*, (1954).

[322] C. Gahn et al. *Generating positrons with femtosecond-laser pulses*. Applied Physics Letters **77**, 2662 (2000).

[323] H. Chen et al. *Relativistic Positron Creation Using Ultraintense Short Pulse Lasers*. Phys. Rev. Lett. **102**, 105001 (2009).

[324] G. Sarri et al. *Table-top laser-based source of femtosecond, collimated, ultrarelativistic positron beams*. Physical review letters **110**, 255002 (2013).

[325] G. Sarri et al. *Generation of neutral and high-density electron–positron pair plasmas in the laboratory*. Nature communications **6**, 6747 (2015).

[326] A. Rousse et al. *Production of a keV X-ray beam from synchrotron radiation in relativistic laser-plasma interaction*. Physical review letters **93**, 135005 (2004).

[327] J. D. Lindl et al. *The physics basis for ignition using indirect-drive targets on the National Ignition Facility*. Physics of plasmas **11**, 339 (2004).

[328] C. Decker et al. *Hohlraum radiation drive measurements on the Omega laser*. Physical review letters **79**, 1491 (1997).

[329] R. Town et al. *Analysis of the National Ignition Facility ignition hohlraum energetics experiments*. Physics of Plasmas **18**, 056302 (2011).

[330] S. Glenzer et al. *Demonstration of ignition radiation temperatures in indirect-drive inertial confinement fusion hohlraums*. Physical review letters **106**, 085004 (2011).

[331] R. Edwards et al. *Characterization of a gamma-ray source based on a laser-plasma accelerator with applications to radiography*. Applied Physics Letters **80**, 2129 (2002).

[332] A. Giulietti et al. *Intense γ-ray source in the giant-dipole-resonance range driven by 10-TW laser pulses*. Physical review letters **101**, 105002 (2008).

[333] A. Ben-Ismail et al. *Optimization of gamma-ray beams produced by a laser-plasma accelerator*.
Nuclear Instruments and Methods in Physics Research Section A: Accelerators, Spectrometers, Detectors and Associated Equipment **629**, 382 (2011).

[334] Y. Oishi et al. *Evaluation of Yields of γ-Rays Produced by Electrons from Gas Jets Irradiated by Low-Energy Laser Pulses: Towards "Virtual Radioisotopes"*.
Japanese Journal of Applied Physics **50**, 042702 (2011).

[335] S. Cipiccia et al. *A tuneable ultra-compact high-power, ultra-short pulsed, bright gamma-ray source based on bremsstrahlung radiation from laser-plasma accelerated electrons*. Journal of Applied Physics **111**, 063302 (2012).

[336] A. Döpp et al. *A bremsstrahlung gamma-ray source based on stable ionization injection of electrons into a laser wakefield accelerator*.
Nuclear Instruments and Methods in Physics Research Section A: Accelerators, Spectrometers, Detectors and Associated Equipment **830**, 515 (2016).

[337] N. Lemos et al. *Bremsstrahlung hard x-ray source driven by an electron beam from a self-modulated laser wakefield accelerator*.
Plasma Physics and Controlled Fusion **60**, 054008 (2018).

[338] O. J. Pike. *Particle Interactions in High-Temperature Plasmas*. Springer, 2017.

[339] M. Stearns. *Mean square angles of bremsstrahlung and pair production*.
Physical Review **76**, 836 (1949).

[340] P. Roberts et al. *The stability of multiple-shell ICF targets*.
Journal of Physics D: Applied Physics **13**, 1957 (1980).

[341] W. Lokke and W. Grasberger.
XSNQ-U: A non-LTE emission and absorption coefficient subroutine. Tech. rep.
California Univ., Livermore (USA). Lawrence Livermore Lab., 1977.

[342] T. Poikela et al. *Timepix3: a 65K channel hybrid pixel readout chip with simultaneous ToA/ToT and sparse readout*.
Journal of instrumentation **9**, C05013 (2014).

[343] B. Bergmann et al. *3D track reconstruction capability of a silicon hybrid active pixel detector*. The European Physical Journal C **77**, 421 (2017).

[344] A. E. Hussein et al. *Laser-wakefield accelerators for high-resolution X-ray imaging of complex microstructures*. Scientific reports **9**, 3249 (2019).

[345] *Atomic and Nuclear Properties of Materials* (2019).

[346] B. L. Henke et al. *X-ray interactions: photoabsorption, scattering, transmission, and reflection at E= 50-30,000 eV, Z= 1-92*.
Atomic data and nuclear data tables **54**, 181 (1993).

[347] F. Hartemann et al. *Compton scattering in ignited thermonuclear plasmas*.
Physical review letters **100**, 125001 (2008).

[348] G. Battistoni et al. *The FLUKA code: Description and benchmarking*.
AIP Conference proceedings. **896**. AIP. 2007, 31.

[349] G. J. Marrero Samarin. *Experimental studies of radiation reaction and photon-photon collisions in ultrahigh intensity regimes*.
PhD thesis. Queen's University Belfast, 2019.

[350] S. Banerjee et al. *Stable, tunable, quasimonoenergetic electron beams produced in a laser wakefield near the threshold for self-injection*.
Phys. Rev. ST Accel. Beams **16** (issue), 031302 (2013).

[351] K. Nakajima et al. *A table-top X-ray FEL based on the laser wakefield accelerator-undulator system*.
Nuclear Instruments and Methods in Physics Research Section A: Accelerators, Spectrometers, Detectors and Associated Equipment **375**, 593 (1996).

[352] A. Caldwell et al. *Proton-driven plasma-wakefield acceleration*.
Nature Physics **5**, 363 (2009).

[353] E. Adli et al. *A beam driven plasma-wakefield linear collider: from Higgs factory to multi-TeV*. arXiv preprint arXiv:1308.1145, (2013).

[354] A. Di Piazza et al. *Improved local-constant-field approximation for strong-field QED codes*. Phys. Rev. A **99**, 022125 (2019).

[355] N. V. Elkina et al. *QED cascades induced by circularly polarized laser fields*.
Phys. Rev. ST Accel. Beams **14**, 054401 (2011).

[356] C. P. Ridgers et al. *Modelling gamma-ray photon emission and pair production in high-intensity laser–matter interactions*. J. Comput. Phys. **260**, (2014).

[357] A. Gonoskov et al. *Extended particle-in-cell schemes for physics in ultrastrong laser fields: Review and developments*. Phys. Rev. E **92**, 023305 (2015).

[358] R. Schützhold et al. *Signatures of the Unruh Effect from Electrons Accelerated by Ultrastrong Laser Fields*. Phys. Rev. Lett. **97**, 121302 (2006).

[359] P. Chen and T. Tajima. *Testing Unruh Radiation with Ultraintense Lasers*.
Phys. Rev. Lett. **83**, 256 (1999).

[360] X. Wang et al. *Quasi-monoenergetic laser-plasma acceleration of electrons to 2 GeV*. Nature communications **4**, 1988 (2013).

[361] G. Pariente et al. *Space–time characterization of ultra-intense femtosecond laser beams*. Nature Photonics **10**, 547 (2016).

[362] M. F. Ciappina et al. *Progress toward atomic diagnostics of ultrahigh laser intensities*. Phys. Rev. A **99** (issue), 043405 (2019).

[363] M. Ciappina and S. Popruzhenko. *Diagnostics of ultra-intense laser pulses using tunneling ionization*. Laser Physics Letters **17**, 025301 (2020).

[364] F. Mackenroth et al. *Ultra-intense laser pulse characterization using ponderomotive electron scattering*. New Journal of Physics **21**, 123028 (2019).

[365] A. Buck et al. *Real-time observation of laser-driven electron acceleration*. Nature Physics **7**, (2011).

[366] A. Sävert et al. *Direct Observation of the Injection Dynamics of a Laser Wakefield Accelerator Using Few-Femtosecond Shadowgraphy*. Phys. Rev. Lett. **115**, 055002 (2015).

[367] E. Siminos et al. *Modeling ultrafast shadowgraphy in laser-plasma interaction experiments*. Plasma Physics and Controlled Fusion **58**, 065004 (2016).

[368] A. L. Cavalieri et al. *Clocking Femtosecond X Rays*. Phys. Rev. Lett. **94**, 114801 (2005).

[369] X. Yan et al. *Subpicosecond electro-optic measurement of relativistic electron pulses*. Physical Review Letters **85**, 3404 (2000).

[370] Y. Glinec et al. *Direct observation of betatron oscillations in a laser-plasma electron accelerator*. EPL (Europhysics Letters) **81**, 64001 (2008).

[371] S. Mangles et al. *Controlling the spectrum of x-rays generated in a laser-plasma accelerator by tailoring the laser wavefront*. Applied Physics Letters **95**, 181106 (2009).

[372] J. Ferri et al. *Effect of experimental laser imperfections on laser wakefield acceleration and betatron source*. Scientific reports **6**, 27846 (2016).

[373] K. Ta Phuoc et al. *Betatron radiation from density tailored plasmas*. Physics of Plasmas **15**, 063102 (2008).

[374] M. Kozlova et al. *Hard X Rays from Laser-Wakefield Accelerators in Density Tailored Plasmas*. Physical Review X **10**, 011061 (2020).

[375] Y.-S. Tsai. *Pair production and bremsstrahlung of charged leptons*. Reviews of Modern Physics **46**, 815 (1974).

[376] M. G. Kendall et al. *The advanced theory of statistics. Vols. 1.* The advanced theory of statistics. Vols. 1. (1948).